Metadata of the book that will be visualized online

BookTitle	Induction Accelerators	
Book Sub-Title		
Book CopyRight - Year	Springer-Verlag Berlin Heidelberg 2011 (This will be the copyright line in the final PDF)	
Series Name	Particle Acceleration and Detection	
Book Editor	Family Name	**Takayama**
	Particle	
	Given Name	**Ken**
	Suffix	
	Email	takayama1@milk.kek.jp
	Organization	High Energy Accelerator Research
	Division	Organization (KEK), Neutron Science Laboratory
	Address	Oho 1-1, Tsukuba, Ibaraki-ken, 305-0801, Japan
Book Editor	Family Name	**Briggs**
	Particle	
	Given Name	**Richard J.**
	Suffix	
	Email	
	Organization	
	Division	
	Address	Bolla Avenue 279, Alamo, 94507, USA

Induction Accelerators

UNCORRECTED PROOF

Particle Acceleration and Detection

springer.com

The series *Particle Acceleration and Detection* is devoted to monograph texts dealing with all aspects of particle acceleration and detection research and advanced teaching. The scope also includes topics such as beam physics and instrumentation as well as applications. Presentations should strongly emphasize the underlying physical and engineering sciences. Of particular interest are

- contributions which relate fundamental research to new applications beyond the immediate realm of the original field of research
- contributions which connect fundamental research in the aforementioned fields to fundamental research in related physical or engineering sciences
- concise accounts of newly emerging important topics that are embedded in a broader framework in order to provide quick but readable access of very new material to a larger audience

The books forming this collection will be of importance for graduate students and active researchers alike.

Series Editors:

Alexander Chao
SLAC
2575 Sand Hill Road
Menlo Park, CA 94025
USA

Christian W. Fabjan
CERN
PPE Division
1211 Genève 23
Switzerland

Frank Zimmermann
CERN
SL-Division
AP Group
1211 Genève 23
Switzerland

For further volumes:
http://www.springer.com/series/5267

UNCORRECTED PROOF

Ken Takayama · Richard J. Briggs
Editors

Induction Accelerators

UNCORRECTED PROOF

Springer

Editors
Ken Takayama
High Energy Accelerator Research Organization (KEK)
Neutron Science Laboratory
Oho 1-1
305-0801 Tsukuba, Ibaraki-ken
Japan
takayama1@milk.kek.jp

Richard J. Briggs
Bolla Avenue 279
94507 Alamo California
USA
richardbriggs@sbcglobal.net

Portions of this document were prepared as an account of work sponsored by an agency of the United States government. While this document is believed to contain correct information, neither the United States government nor Lawrence Livermore National Security, LLC, nor any of their employees, nor the Regents of the University of California, nor any of their employees, makes any warranty, expressed or implied, or assumes any legal liability or responsibility for the accuracy, completeness, or usefulness of any information, apparatus, product, or process disclosed, or represents that its use would not infringe privately owned rights. Reference herein to any specific commercial product, process, or service by trade name, trademark, manufacturer, or otherwise does not necessarily constitute or imply its endorsement, recommendation, or favoring by the United States government or Lawrence Livermore National Security, LLC, or the Regents of the University of California. The views and opinions of authors expressed herein do not necessarily state or reflect those of the United States government or Lawrence Livermore National Security, LLC, or The Regents of the University of California and shall not be used for advertising or product endorsement purposes.

ISSN 1611-1052
ISBN 978-3-642-13916-1 e-ISBN 978-3-642-13917-8
DOI 10.1007/978-3-642-13917-8
Springer Heidelberg Dordrecht London New York

Library of Congress Control Number: 2010933077

© Springer-Verlag Berlin Heidelberg 2011
This work is subject to copyright. All rights are reserved, whether the whole or part of the material is concerned, specifically the rights of translation, reprinting, reuse of illustrations, recitation, broadcasting, reproduction on microfilm or in any other way, and storage in data banks. Duplication of this publication or parts thereof is permitted only under the provisions of the German Copyright Law of September 9, 1965, in its current version, and permission for use must always be obtained from Springer. Violations are liable to prosecution under the German Copyright Law.
The use of general descriptive names, registered names, trademarks, etc. in this publication does not imply, even in the absence of a specific statement, that such names are exempt from the relevant protective laws and regulations and therefore free for general use.

Cover design: Integra Software Services Pvt. Ltd., Pondicherry

Printed on acid-free paper

Springer is part of Springer Science+Business Media (www.springer.com)

UNCORRECTED PROOF

This book is dedicated to the memory of two pioneers of induction accelerators: Nicholas Christofilos, the inventor and leader of its early development; and Daniel Birx, a prolific innovator of high repetition rate induction linacs.

Nick Christofilos *circa* 1964 standing in front of the Astron fusion experiment at the Lawrence Livermore National Laboratory

Daniel Birx in 1998 working at the Lawrence Berkeley National Laboratory on beam breakup instability impedance measurements of DARHT-II cells

UNCORRECTED PROOF

Preface

This book grew out of a three-day international workshop, *Recent Progress in Induction Accelerators*, which was held at KEK October 29–31, 2002. The original concept was to produce a book which dealt with the principles and applications of modern induction accelerators in a comprehensive manner – including developments which had occurred in the past decade. Unique distinguishing features of induction accelerators, such as the low impedance and the pulse operation are fully described. Emphasis is placed on aspects of induction accelerators that are distinct from RF accelerators including issues associated with the transport of bright, high-intensity beams. All aspects of modern induction accelerators are covered including both linear and circular geometry machines for electrons, protons, and heavy-ions.

The authors of this book were invited from a select list of active experts in the field including the workshop attendees. It is written both as a reference for graduate students and researchers. Introductory material is presented that should aid newcomers wanting a thorough and systematic introduction to the principle of induction acceleration as well as pulsed power technology supporting induction accelerators, beam dynamics, and unique induction accelerator applications. Needs of more experienced physicists and engineers involved in the design or operation of accelerator facilities are also covered. Beam dynamics material presented can be applied to both RF accelerators as well as induction accelerators.

Material presented is organized such that the first six chapters provide an introduction to the essential features of induction accelerators at a level appropriate for students and researchers new to the field. Key technologies necessary to realize a modern induction accelerator are covered in these chapters. Subsequent chapters deal with more specialized and advanced topics. Chapters 7 and 8 cover electron linacs and their applications, whereas Chaps. 9 and 10 cover ion accelerators and their applications. Chapters 11 and 12 are devoted to circular hadron induction machines. Beam physics applicable to both RF and induction accelerators is systematically developed in Chaps. 7, 9, and 11. SI units are used throughout the book except where noted otherwise.

Acknowledgments are well deserved for the many contributions that have made this book possible. The authors somehow found time in their very busy schedules to organize and prepare their contributions. Steven Lund deserves special recognition for his tireless work refining the LaTeXformat and editing all Chapters~~besides his~~

UNCORRECTED PROOF

~~own~~. Yoji Michishita assisted in assembling the LaTeXinput, editing, and figure processing for the book at KEK. Prabir Roy carried out preliminary LaTeXconversions of several chapters. Numerous other colleagues graciously contributed to the examples and figures presented and provided valuable guidance and insights. The chapters benefited from reviews and comments provided by the following colleagues: Roger Bangerter, Tom Fessenden, Alex Friedman, Antatoly Krasnykh, Grant Logan, Art Molvik, Peter Seidl, and Will Waldron. Finally, our editor Dr. Christian Caron and his team from Springer Verlag including Gabriele Hakuba were patient and provided valuable help and encouragement.

Tsukuba, Japan Ken Takayama
July 2010

UNCORRECTED PROOF

Contents

1 Introduction 1
Ken Takayama and Richard J. Briggs
References 5

2 Historical Perspectives 7
Richard J. Briggs and Glen Westenskow
2.1 Introduction 7
2.2 Invention of the Linear Induction Accelerator by Christofilos 8
2.3 Early History of Short-Pulse Induction Accelerators at LLNL and LBNL 9
2.4 Long-Pulse Induction Accelerators 13
2.5 High Repetition-Rate Induction Technology Developments 13
2.6 Recirculating Induction Linacs 14
2.7 Former USSR Induction Accelerators and "Coreless" LIA's 15
2.8 Summary Tables of Induction Accelerators World-Wide 16
References 19

3 Principles of Induction Accelerators 23
Richard J. Briggs
3.1 Introduction 23
3.2 Basic Features of an Induction Accelerator System 23
3.3 Comparison Between RF Accelerators and Induction Accelerators 26
3.4 Physical Processes Inside a Typical Induction Module 28
3.5 Magnetic Core Considerations 32
3.6 Ferromagnetic Laminated Cores 34
3.7 Ferrites 35
References 36

UNCORRECTED PROOF

4 Modulators 39
Edward G. Cook and Eiki Hotta
4.1 General Discussion on Induction Accelerator Modulators 39
4.1.1 Line-Type Modulators 40
4.1.2 Solid-State Modulators 50
4.2 Switching Devices 60
4.2.1 Closing Switches 60
4.2.2 Closing Switches with an Opening Capability 69
References 72

5 Magnetic Materials 75
Louis L. Reginato
5.1 Introduction 75
5.2 Ferrites 75
5.3 Ferromagnetic Materials 78
5.4 Energy Loss 81
5.5 Other Materials 83
5.6 Summary 85
References 85

6 Induction Cell Design Tradeoffs and Examples 87
Louis L. Reginato and Richard J. Briggs
6.1 Introduction 87
6.2 Cell Configurations 87
6.3 Long-Pulse Cell Design 91
6.4 Short-Pulse Cell Design 92
6.5 Comparison Between Amorphous and Ferrite Cells 93
6.6 Core Segmentation and Flux Equalizing 95
6.7 Core Reset Techniques 97
6.8 High Voltage Design Issues 97
6.9 Voltage and Electrical Stress Distribution in Laminated Cores 99
6.10 Coupling Impedance 107
6.10.1 General Form of the Transverse Impedance 107
6.10.2 Minimizing the Transverse Impedance in Induction Cell Designs 109
6.10.3 Measurement of the Transverse Impedance 110
6.11 High Average Power 112
6.12 Summary of Cell Design 113
References 114

7 Electron Induction Linacs 117
George J. Caporaso and Yu-Jiuan Chen
7.1 Introduction 117
7.2 Electron Sources 119

UNCORRECTED PROOF

7.2.1 Cathodes 119
7.2.2 Electron Guns 120
7.3 Beam Dynamics in Induction Machines 123
7.3.1 Basic Force Equation 123
7.3.2 Coordinate Description of a Beam 124
7.3.3 Focusing in a Solenoidal Field 125
7.4 Envelope Equations 131
7.4.1 Lee-Cooper Envelope Equation 131
7.4.2 KV Envelope Equations 135
7.5 Corkscrew Motion 136
7.5.1 Corkscrew Amplitude 136
7.5.2 Tuning Curve Algorithm 139
7.6 Instabilities 141
7.6.1 Image Displacement Instability 141
7.6.2 Beam Breakup Instability (BBU) 144
7.7 Induction Linac Design Considerations 152
7.7.1 Optimal Focusing Strategy 152
7.8 Nonlinear Focusing to Suppress BBU 155
7.8.1 Motivation for Nonlinear Focusing Systems 155
7.8.2 Laser Generated Ion Channel 155
7.8.3 Phase Mix Damping of BBU 157
References 162

8 Applications of Electron Linear Induction Accelerators 165
Glen Westenskow and Yu-Jiuan Chen
8.1 Linear Induction Accelerators Built for Flash X-Ray Radiography 167
8.1.1 Induction Accelerators Built for Radiography 167
8.1.2 Beam Requirements 169
8.1.3 Target Issues 171
8.2 Free Electron Lasers Driven by LIAs 171
8.2.1 ELF Experiments on the ETA Accelerator 172
8.2.2 Short Wavelength Radiation Production Using the ATA Accelerator 173
8.2.3 Use of Induction Accelerators to Produce Millimeter Wavelength Power for Tokamak Heating 175
8.3 Two-Beam Accelerators 176
8.4 High Average Power Applications 179
8.5 Conclusion 180
References 181

9 Ion Induction Accelerators 185
Steven M. Lund, John J. Barnard, and Kazuhiko Horioka
9.1 Ion Sources and Injectors 185

UNCORRECTED PROOF

9.1.1 Physics of High Current-Density Ion Sources 186
9.1.2 Ion Sources 194
9.1.3 Example Injectors 197
9.2 Longitudinal Beam Dynamics 200
9.2.1 Fluid Equation Approach 200
9.2.2 "g-Factor" Descriptions of E_z 201
9.2.3 Rarefaction Waves 202
9.2.4 "Ear Fields" 204
9.2.5 Longitudinal Waves 205
9.2.6 Longitudinal Instability 206
9.2.7 Effects of Capacitance on Longitudinal Instability 208
9.3 Transverse Dynamics Issues 210
References 211

10 Applications of Ion Induction Accelerators 215
John J. Barnard and Richard J. Briggs
10.1 Driver for Heavy Ion Fusion (HIF) 215
10.1.1 Requirements Set by Target Physics 216
10.1.2 Final Focus Limits 217
10.1.3 Accelerator Architectures for Inertial Fusion Energy 219
10.1.4 Induction Acceleration and Energy Loss Mechanisms 222
10.1.5 Scaling of the Focusing Systems 224
10.1.6 Accelerator Scaling with Charge-to-Mass Ratio 227
10.1.7 Multi-Beam Linac with Quadrupole Focusing 228
10.1.8 Modular Drivers 230
10.1.9 Recirculator 232
10.1.10 Beam Manipulations 233
10.2 Other Applications of Ion Induction Accelerators 235
10.2.1 High Energy Density Physics and Warm Dense Matter Physics 235
10.2.2 Neutron Spallation Source 243
References 244

11 Induction Synchrotron 249
Ken Takayama
11.1 Principle of Induction Synchrotron 249
11.1.1 Review of Phase Dynamics in an RF Synchrotron 251
11.1.2 Phase Dynamics in the Induction Synchrotron 254
11.2 Beam Handling 257
11.2.1 Beam Injection 258
11.2.2 Beam Stacking and Super-Bunch Formation 261
11.2.3 Transition Crossing 261

UNCORRECTED PROOF

11.3 Induction Devices for an Induction Synchrotron 263
11.3.1 Equivalent Circuit Model 264
11.3.2 Induction Cell 266
11.3.3 Switching Power Supply (Power Modulator) 269
11.4 Proof of Principle Experiment 273
11.4.1 Beam–Cell Interaction: Beam Loading 273
11.4.2 Scenario of Proof of Principle Experiment 275
11.4.3 Induction Acceleration of an RF Bunch 276
11.4.4 Confinement by Induction Barrier Voltages 279
11.4.5 Induction Acceleration of a Trapped Barrier Bunch – Full Demonstration of the Induction Synchrotron 279
11.5 Perspective 283
References 284

12 Applications of Induction Synchrotrons 287
Ken Takayama
12.1 Typical Accelerator Complex Capable of Employing the Induction Synchrotron Scheme 287
12.2 Hybrid Synchrotrons 287
12.2.1 Quasi-adiabatic Focusing-Free Transition Crossing 288
12.3 Super-Bunch Hadron Colliders 291
12.3.1 Introduction 291
12.3.2 Contrast of Coasting Beam, RF Bunch Collider, and Super-Bunch Colliders 291
12.3.3 Generation of the Super-Bunch 293
12.3.4 Luminosity 295
12.3.5 Beam–Beam Effects and Crossing Geometry 300
12.3.6 Typical Super-Bunch Collider's Parameters 304
12.3.7 Beam Physics Issues for the Super-Bunch Hadron Collider 305
12.4 All-Ion Accelerator – An Injector-Free Induction Synchrotron 316
12.4.1 Introduction 316
12.4.2 Concept 319
12.4.3 Digital Acceleration and Switching Frequency 320
12.4.4 Longitudinal Confinement 322
12.4.5 Stacking and Beam Handling Through the Acceleration 322
12.4.6 Transverse Focusing 323
12.4.7 Space Charge Limited Ion-Beam Intensity 325
12.4.8 Vacuum 325
12.4.9 Ion Source and Injector 326
12.4.10 Summary 327
References 327

Index 331

UNCORRECTED PROOF

Contributors

John J. Barnard Lawrence Livermore National Laboratory, Livermore, CA 94550, USA, jjbarnard@llnl.gov

Richard J. Briggs Alamo, CA 94507, USA, richardbriggs@sbcglobal.net

George J. Caporaso Lawrence Livermore National Laboratory, Livermore, CA 94550, USA, caporaso1@llnl.gov

Yu-Jiuan Chen Lawrence Livermore National Laboratory, Livermore, CA 94550, USA, yjchen@llnl.gov

Edward G. Cook Lawrence Livermore National Laboratory, Livermore, CA 94550, USA, cook5@llnl.gov

Kazuhiko Horioka Department of Energy Sciences, Tokyo Institute of Technology, Yokohama 226-8502, Japan, khorioka@es.titech.ac.jp

Eiki Hotta Department of Energy Sciences, Tokyo Institute of Technology, Yokohama 226-8502, Japan, ehotta@es.titech.ac.jp

Steven M. Lund Lawrence Livermore National Laboratory, Livermore, CA 94550, USA, smlund@llnl.gov

Louis L. Reginato Lawrence Berkeley National Laboratory, Berkeley, CA 94720-8201, USA, LLReginato@lbl.gov

Ken Takayama High Energy Accelerator Research Organization (KEK), Tsukuba 305-0801, Japan, ken.takayama@kek.jp; takayama1@milk.kek.jp

Glen Westenskow Lawrence Livermore National Laboratory (Retired), USA, GWestenskow2@gmail.com

UNCORRECTED PROOF

Chapter 1
Introduction

Ken Takayama and Richard J. Briggs

The motivation for the initial development of linear induction accelerators starting in the early 1960s came mainly from applications requiring intense electron pulses with beam currents and a charge per pulse above the range accessible to RF accelerators, and with particle energies beyond the capabilities of single stage pulsed-power diodes. The linear induction accelerators developed to meet these needs utilize a series of induction cells containing magnetic cores (torroidal geometry) driven directly by pulse modulators (pulsed power sources). This multistage "one-to-one transformer" configuration with non-resonant, low impedance induction cells accelerates kilo-Ampere-scale electron beam current pulses in induction linacs.

The flexibility in the accelerating voltage waveform with induction accelerator cells has also been a key feature of interest. This waveform flexibility aspect, together with the capability for high efficiency when accelerating high beam currents, lead to linear heavy ion induction accelerators being the central focus of the US inertial fusion energy program for the past several decades. More recently, the waveform flexibility has been utilized in the application of induction technology as the acceleration system in ion synchrotrons, even with relatively low ion beam currents. A unique aspect of the synchrotron application is the requirement for MHz repetition rates of the modulator systems, much higher than with any of the linear induction accelerators.

International workshops were held in 2002 and 2006 to review recent induction accelerator developments and applications. On-going projects based on linear induction accelerators for electrons and heavy ions, and circular induction accelerators for ions, were presented together with the related novel technology. These workshops were the origin of this book. To support a wider understanding and utilization of induction accelerator technology, it was felt that a comprehensive coverage of the basic principles and underlying science and technology elements of modern induction systems was needed.

K. Takayama (✉)
High Energy Accelerator Research Organization (KEK), Tsukuba 305-0801, Japan
e-mail: ken.takayama@kek.jp

K. Takayama, R.J. Briggs (eds.), *Induction Accelerators*, Particle Acceleration and Detection, DOI 10.1007/978-3-642-13917-8_1,
© Springer-Verlag Berlin Heidelberg 2011

UNCORRECTED PROOF

The terminology we use in this book is as follows. The overall accelerator system will generally contain a number of individual accelerator modules that each add a given increment of energy to the charged particles that pass through it. Each module is comprised of a pulse modulator (a pulsed power source) that powers one or more induction cells containing a magnetic core. Focusing systems that provide radial confinement of the charged particles are another important element of the overall accelerator system. These focusing systems are sometimes integrated into the individual induction cells to provide more continuous focusing and/or save axial space. The charged particle beam source and the injector that contains it are also essential elements of the accelerator system.

The field of charged particle accelerators is very broad, so that it is important to provide a perspective on how the induction accelerator subjects covered in this book fit into some kind of overall context. Simple charts that attempt to summarize all the categories of particle accelerators will always have some deficiencies, but the one derived from Humphries text [1] shown in Fig. 1.1 is a useful one for our purposes.

As is well known, the vast majority of high-energy particle accelerators employ radio frequency (RF) or microwave fields as the acceleration medium. These fields are created in various resonant structures ("cavities") fed by RF or microwave power sources. This class of accelerators is the "resonant" category of electromagnetic accelerators shown in Fig. 1.1. Circular versions of this "resonant" category include cyclotrons (circa 1931) and RF synchrotrons (circa 1945). Linear versions include electron RF linacs (circa 1928) and ion RF linacs, composed of one or more specific types of acceleration structures depending on the ion speed [drift tube linac, coupled cavity linac, RF quadrupole (RFQ), etc.]. (Readers interested in a detailed comparison between RF accelerators and induction accelerators, including the advantages and disadvantages of each, should see Sect. 3.3.)

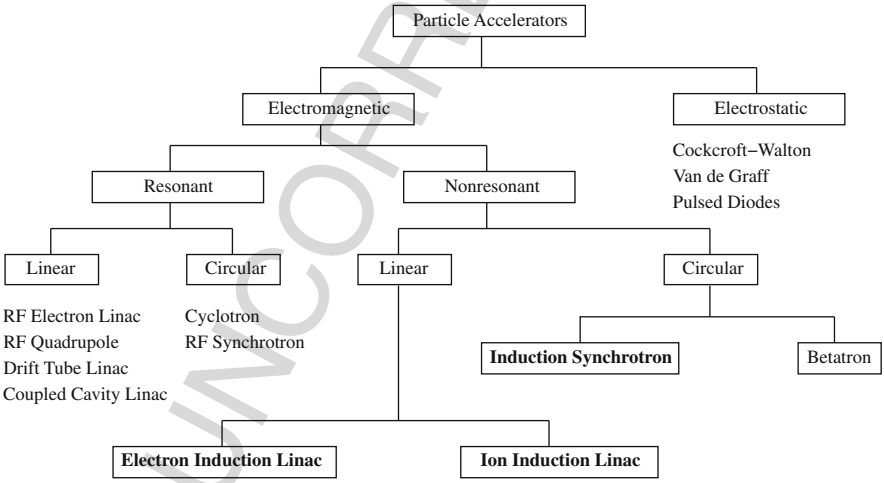

Fig. 1.1 Simple classification of particle accelerators

UNCORRECTED PROOF

The induction systems discussed in this book use non-resonant structures (induction cells) energized by pulsed (non-sinusoidal) electromagnetic sources (pulse modulators). These systems constitute most of the accelerators in the "non-resonant" category of electromagnetic accelerators in Fig. 1.1. One exception is the Betatron (circa 1940). The acceleration electric field in this circular device is created by pulsing a magnetic core (that the closed particle orbits encircle) on a timescale many orders of magnitude longer than in our typical induction cell. It is an important class of particle accelerator, with some relatively recent attempts to extend its capabilities, but the technology components and longitudinal beam dynamics have little overlap with the core subjects in the present book. Humphries text [1] has an excellent discussion of the basic physics and technology of the betatron, including a comparison with the induction accelerators discussed in this book.

In addition to the "electromagnetic" accelerator category, a class of accelerators termed electrostatic are also shown in Fig. 1.1. Included here are the common Van de Graaff DC accelerators, and we also include short-pulse single-stage pulsed diodes. The logic for including pulsed diodes in the "electrostatic" category is that the timescale for the particles to move through the diode acceleration region is short compared to the voltage pulse duration. Once again, these devices are an important technology but pulsed power diode physics has little overlap of with most of the core subjects in the present book, especially in the beam dynamics areas. One exception is the "inductive voltage adder" (IVA) technology used as recent diode pulsed power sources; the IVA was actually an outgrowth of early electron induction accelerator injectors [2]. Accelerators that are not classified fully under the "linear" or "circular" characterizations include various forms of "recirculating linacs." Such recirculating linacs have been developed for RF accelerators, and also for electron and ion induction accelerators (see Sects. 2.6 and 10.1.8). Generally, these systems are best considered as a subset of the "linac" category with special beam dynamics and modulator issues.

In the initial development of very high current "nonresonant" electron linear accelerators, several different approaches were used to couple the pulse modulator output to the electron beam. In this book, we focus exclusively on approaches that use magnetic material in a toroidal configuration inside the coupling cell. With very short pulses, "~~line-type~~" or "coreless" induction accelerators that use (for example) radial transmission lines without any magnetic material as the coupling cell can be used [1, 3]. The basic principles of line-type nonresonant linacs are similar to the magnetic core induction systems, but we do not cover them in detail here since the magnetic core systems are the ones in common use in modern induction accelerators.

The main objectives of this book are as follows:

- Explain the basic principles of induction acceleration at a level consistent with a graduate course reference text.
- Discuss the essential component technologies in modern induction accelerator systems, including recent advances in switching, magnetic materials, etc., that are enabling new applications.

UNCORRECTED PROOF

– Describe the three main examples of induction accelerators; electron linac, ion linac, and induction synchrotron with corresponding coverage of the most important beam physics and beam dynamics phenomenology involved in their design and operation.
– Introduce some of the major applications and the top level beam requirements that have motivated designs of induction accelerators to meet these requirements.
– Describe the designs of several induction accelerators that have been built and operated, to provide the reader with perspectives on the tradeoffs involved in typical induction module designs

This book is organized as follows (see Fig. 1.2). Chapter 2 presents a brief historical overview and extensive summary tables of induction accelerators constructed worldwide. Chapters 3, 4, 5, and 6 contain the basic material common to all the different types of induction accelerators. Chapter 3 describes the basic features of induction accelerator systems, including comparisons with RF accelerators. A detailed discussion of the physical processes involved in the induction cell itself is the main focus of most of this chapter. Modulators are covered in Chap. 4 while Chap. 5 reviews the properties of the magnetic materials that constitute the main key component in the induction cell. Details involved in the design of typical induction modules are covered in Chap. 6, including discussions of the tradeoffs involved in the design of several previous induction accelerators. The following six chapters cover specific details and applications of the three main types of induction accelerator systems developed to date: electron linacs, ion linacs, and induction synchrotrons.

Readers interested in the historical background of the development of induction accelerators as well as the basic principles involved in their operation should start with Chap. 2 and proceed to Chap. 3. More experienced researchers mainly interested in the technological background needed to design induction acceleration systems should follow Chaps. 4, 5, and, 6 after a brief reading of Chap. 3.

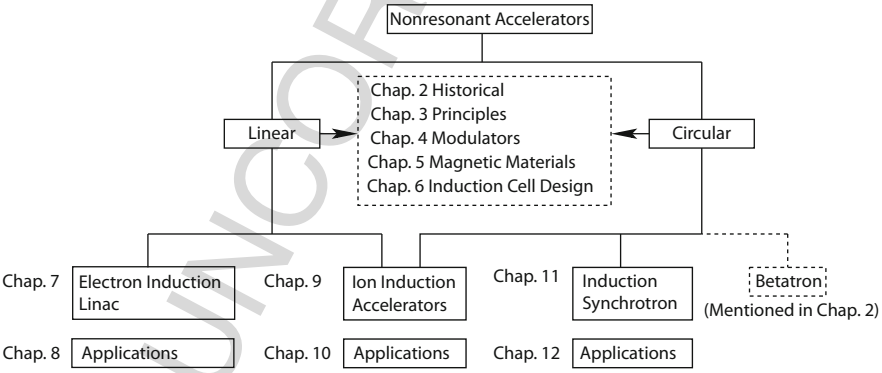

Fig. 1.2 Organization of the book

UNCORRECTED PROOF

Readers with specific interests in the beam dynamics issues of electron induction linacs and/or ion induction linacs may want to go directly to Chaps. 7 and 9, respectively. However, the physics of transverse ion dynamics in induction linacs is not covered. ~~because most basic transverse dynamics topics such as beam focusing optics and envelope matching are essentially common to both electron (see Chap. 7) and ion machines.~~

Recently a circular induction accelerator called an induction synchrotron has been rapidly developed and established as one of the standard types of induction accelerators. Chapter 11 covers the basic principles and the unique technologies of the induction synchrotron, especially those related to the very high repetition rate operation of the induction module. In Chap. 12 several attractive applications of the induction synchrotron, such as super-bunch hadron colliders and all-ion accelerators, are described.

Beam physics in the various types of induction accelerators described in this book have a number of unique features compared to their resonant (RF) accelerator counterparts. In electron induction linacs the transverse beam dynamics are generally dominated by issues associated with the very high beam intensities, for example, the beam breakup instability. The variation of particle energy over the beam pulse in induction linacs can also lead to time-dependent beam displacements (corkscrew); these various transverse beam dynamics features are discussed in Chap. 7. In ion induction linacs and the induction synchrotron, on the other hand, longitudinal beam physics is notably different from that of resonant accelerators where the gradient of the RF voltage in time provides the longitudinal focusing forces. The special features associated with longitudinal control of beam pulses in ion induction accelerators are described in Chaps. 9 and 11.

References

1. S. Humphries. *Principles of Charged Particle Acceleration*, Wiley, New York, NY 1986.
2. I. Smith. Induction Voltage Adders and the Induction Accelerator Family. *Phys. Rev. Spec. Topics Accel. Beams*, 7:064801, 2004.
3. J. Leiss. Induction Linear Accelerators and Their Applications. *IEEE Trans. Nucl. Sci.*, NS-26:3870, 1979. (Proceedings of the 1979 Particle Accelerator Conference, San Francisco, CA, 12–14 Mar., IEEE).

UNCORRECTED PROOF

Chapter 2
Historical Perspectives

Richard J. Briggs and Glen Westenskow

AQ1

UNCORRECTED PROOF

2.1 Introduction

The main objective of this chapter is to provide an overall perspective on the historical evolution of induction accelerator technology, and the applications that motivated its initial development. Understanding the context of these early developments might help the reader appreciate why particular technical approaches were followed in the past, and why new applications might push induction accelerator developments in different directions in the future. However, the main emphasis in all cases is to provide historical perspectives on the technical features of the accelerator technology, and not a detailed history of the projects that motivated their development.

Because the authors have personal knowledge of many of the early pioneering linear induction accelerator developments in the USA, these will be covered in the greatest detail. We will attempt to balance this emphasis by also providing references and brief summaries of the parameters of various induction accelerators built in other countries throughout the world.

The Betatron also uses pulsed voltages on a magnetic core to generate an inductive acceleration field, and its development preceded linear induction accelerator developments by a couple of decades. As we noted in Chap. 1, the technology and beam dynamics of the Betatron are fundamentally different from the induction accelerators discussed in this book. Pulsed voltages many orders of magnitude smaller with pulse lengths many orders of magnitude longer than linear induction accelerators are used to accelerate the electrons that circulate around the transformer core of the Betatron, and the pulsed magnetic fields of the core are an integral part of the magnetic focusing system of the electrons. We therefore consider a detailed discussion of the history of the Betatron development, like the history of RF accelerators, to be outside the scope of this book.

R.J. Briggs (✉)
Alamo, CA 94507, USA
e-mail: richardbriggs@sbcglobal.net

K. Takayama, R.J. Briggs (eds.), *Induction Accelerators*, Particle Acceleration and Detection, DOI 10.1007/978-3-642-13917-8_2,
© Springer-Verlag Berlin Heidelberg 2011

2.2 Invention of the Linear Induction Accelerator by Christofilos

The Astron controlled-fusion concept invented by N. C. Christofilos required very high pulsed currents of relativistic electrons [1, 2]. The objective was to create an intense enough electron ring for its self magnetic field on axis to be stronger than the applied solenoidal magnetic field. The resulting closed magnetic field lines would be an ideal magnetic bottle to confine a thermonuclear plasma. Radiofrequency accelerators could not provide the 100's of Amp currents required in this application. To explore this fusion concept, Christofilos conceived of, and developed, the linear induction accelerator technology to serve as the injector for the Astron.

The original Astron Injector shown in Fig. 2.1 began operation in 1963 [3]; it produced a 300 ns, 350 A electron beam at around 3.7 MeV. The upgrade to 6 MeV and 800 A shown in Fig. 2.2 was completed in 1968 [4]. Both of the Astron Injectors used commercial coaxial cables charged to 25 kV as the energy storage medium, switched by thyratrons, to deliver a 400 ns pulse to magnetic "transformer" cores constructed out of Ni–Fe tape. (See Sects. 6.2 and 6.3 for more details on the Astron Injector modules themselves). With individual core voltages of ∼12.5 keV (half the charge voltage on the energy storage cable), a large number of switch modules were required and the average acceleration gradient was relatively low (0.2–0.3 MeV/m). But these machines did have the remarkable capability to produce a burst of up to 100 electron pulses (limited by the energy stored in a rotating generator) at repetition rates of order 1 kHz. This burst output capability was required to study the build up of the electron ring by "stacking" successive electron beam pulses in the plasma confinement vessel on a fast enough time scale.

The Astron Injectors produced very repeatable and high quality electron beam pulses, and the energy variation within the pulse on the Astron Upgrade accelerator

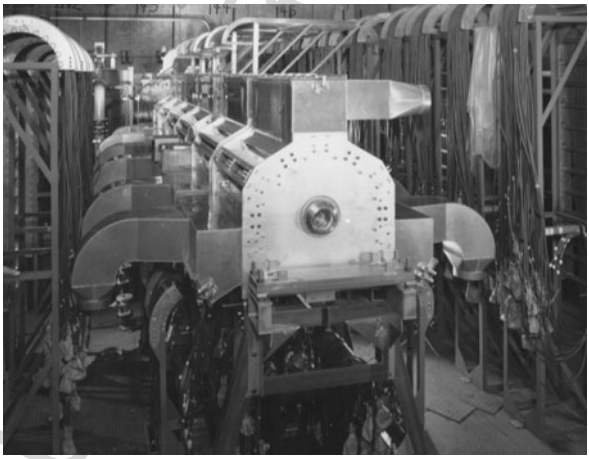

Fig. 2.1 Original Astron Injector (1963)

UNCORRECTED PROOF

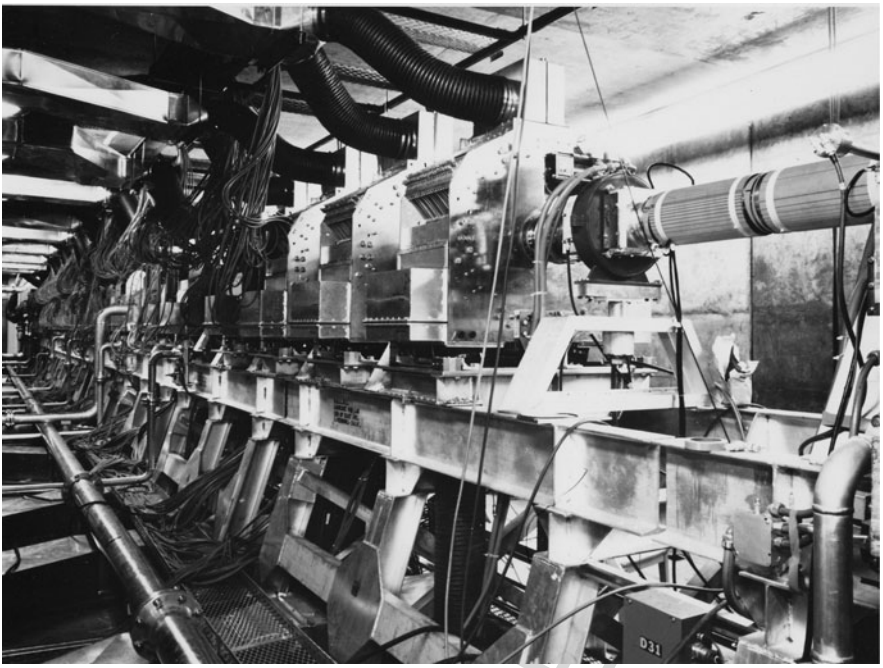

Fig. 2.2 Astron Injector upgrade (1968)

could be reduced to less than 0.1–0.2% with careful tuning of the pulse compensation networks in the drive system. This precision was felt to be important for controlling the trapping of the electron pulses injected into the confinement vessel.

It should be noted that the beam current in the Astron Upgrade, originally designed to produce a 1 kA beam, was limited to about 800 A by the beam breakup instability (BBU), and for a good quality beam the current needed to be less than 500–600 A [4]. The BBU instability in induction accelerators was poorly understood at that time but its observation in the Astron Injector did serve as a warning in the design of subsequent machines to study and to minimize cell resonances.

2.3 Early History of Short-Pulse Induction Accelerators at LLNL and LBNL

Lawrence Livermore National Laboratory (LLNL) and Lawrence Berkeley National Laboratory (LBNL; formerly denoted LBL) continued to pioneer the linear induction accelerator technology following its origination by N.C. Christofilos in the early 1960s. A summary of some of the key parameters of these accelerators and the Astron Injectors is given in Table 2.1. Switch modules listed drive the accelerator cells.

UNCORRECTED

Table 2.1 Early history of induction accelerators in the USA

Accelerator	Kinetic energy [MeV]	Current [A]	Pulse length [ns]	Repetition rate [Hz]		Core type	HV modules	Number switch modules	Modulator voltage [kV] cell (core)	Length [m]
				Max. Avg.	Burst (pulses)					
Astron injector, LLNL (1963)	3.7	350	300	60	1,440 (100)	Ni–Fe tape	Thyratron	300	250 (12.5)	∼10
Astron upgrade, LLNL (1968)	6.0	800	300	60	800 (100)			550		30
NBS prototype, NBS (1971)	0.8	1 k	2,000	< 1	–	Steel tape	Spark gap	2	200 (40)	1.3
ERA injector, LBNL (1970)	4	1 k	30	5	–	Ferrite	Spark gap	17	250	14
ETA, LLNL (1979)	4.5	10 k	40	2	900 (5)	Ferrite	Spark gap	10	250	10
FXR, LLNL (1982)	18	3 k	70	0.3	–	Ferrite	Spark gap	54	250	40
ATA, LLNL (1983)	50	10 k	60	5	1,000 (10)	Ferrite	Spark gap	200	250	53

UNCORRECTED PROOF

At LBNL a program to investigate the electron ring collective ion accelerator (ERA) concept, following successful initial experiments in the USSR by Sarentsev and his group, led to the development of a new type of shorter pulse induction accelerator in the late 1960s [5]. In the electron ring collective ion accelerator concept, invented by V.I. Veksler, a small radius electron ring was loaded with a few ions by ionization of a background gas. The electron ring and its ion load were then accelerated along the axis of the ring; the ions trapped within the ring could be accelerated at a much higher gradient than in conventional accelerators. To create the electron ring, an injected electron beam pulse of 10's of ns at beam currents of a few 100 Amps was required. Following successful initial experiments using the Astron Injector, the 4 MeV ERA Injector at LBNL shown in Fig. 2.3 was built to study the formation of these electron rings. It introduced the use of ferrite tiles for the magnetic core material, and it used much higher voltage pulsers driving each core than the Astron Injector (the electrical energy storage was based on oil-filled Blumleins operating at 250 kV, as described in Chap. 4). The current through the accelerator was generally around 1–1.5 kA, but collimation systems were used to separate out a high quality beam of a few 100 Amps.

Fig. 2.3 Electron Ring Accelerator Injector, the first induction linac to use ferrite cores (1970)

UNCORRECTED PROOF

A program aimed at the study of electron beam propagation in air for directed energy weapon applications lead to the development and construction of similar shorter pulse machines at LLNL in the late 1970s and early 1980s. The predicted requirements for stable propagation of a self-focused beam in air was a peak current of order 10 kA or more, and a one kHz "burst mode" capability was needed to explore the creation of rarefied channels in the air to extend the propagation range. A 4.5 MeV Experimental Test Accelerator (ETA) was constructed to develop the technologies required for this high current, high burst repetition-rate operation [6]. Individual cores in both the ETA and the 50 MeV Advanced Test Accelerator (ATA) shown in Fig. 2.4 were driven by 250 kV Blumleins switched by spark gaps. These pulse power units were capable of 1 kHz burst operation [7], and the Blumleins used water with its high dielectric constant as the energy storage medium to produce the required output current of 20 kA. The gradient in the 50 MeV ATA was on the order of 1 MeV/m, considerably higher than the earlier longer pulse machines. These accelerators were used to study self-focused beam propagation in air, and also to investigate high gain Free Electron Laser (FEL) amplifiers in the mm and infrared wavelength bands (discussed in Chap. 8).

The requirement for an intense pulsed X-ray source for radiography in non-nuclear hydrodynamic experiments supporting nuclear weapons research (see Chap. 8) lead to the construction of the 18 MeV FXR machine at LLNL [8]. FXR was built in the same timeframe as ATA, with a design based on the ERA injector and ETA. It has been a workhorse in "flash radiography" of hydro experiments for the last several decades. The 20 MeV first axis of DARHT-I built at Los Alamos National Laboratory (LANL) in the early 1990s [9] made several improvements on the FXR design, and it has been providing an even more robust radiography capability.

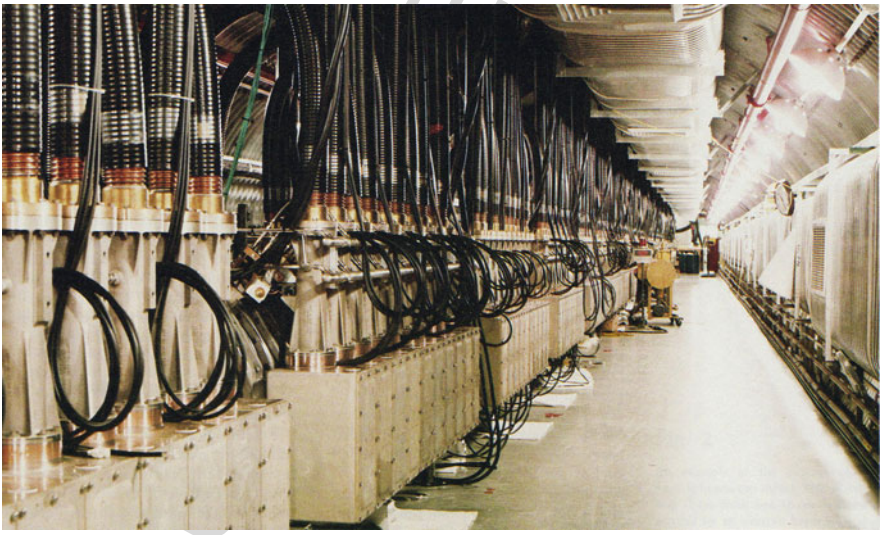

Fig. 2.4 Advanced Test Accelerator, the highest energy induction linac (1983)

UNCORRECTED PROOF

2.4 Long-Pulse Induction Accelerators

At the same time that the LBNL/LLNL programs were developing the short-pulse ferrite core induction technology, a program was initiated at the National Bureau of Standards (NBS, now NIST) to extend the induction linac technology to much longer pulse lengths (∼2 μs) to get higher total charge per pulse [10]. It was recognized that much longer pulse length induction accelerators extended to higher energies would require a more cost effective way to construct induction cores with a larger energy gain per module. Cost considerations lead to the choice of thin mild-steel foil wound with Mylar sheet insulation into tape-wound cores, and radial segmentation to enhance the acceleration gradient (see Chap. 6). The prototype modules constructed at NBS accelerated a 1 kA beam by 400 keV, held constant within a few percent over the full 2 μs pulse (see Table 2.1).

The legacy of this long-pulse induction linac development continued in the Heavy Ion Fusion Program at LBNL. In the mid 1970s, it was recognized by Maschke and others that an intense multi-GeV beam of heavy ions could be an attractive driver for inertial fusion energy (see Chap. 10). Because very high intensity beams are required in this application, the USA Heavy Ion Fusion (HIF) program has focused on driver concepts based on linear induction accelerator technology for the past three decades. The heavy ion beam must be eventually compressed to pulse lengths of order 10 ns at the target, but space charge limitations in the beam transport in the earlier sections of the linac lead to multi-μs induction cores for much of the accelerator. In the late 1980s, a 1 MeV heavy ion induction accelerator test bed (MBE-4) was built to accelerate four parallel 10 mA Cesium ion beams through the same induction cores [11]. The Astron cores were reused in the MBE-4, and the beam pulse lengths varied from 2.0–0.5 μs.

The recent construction of a long-pulse electron induction linac for multiple pulse radiography at LANL, the ∼18 MeV second axis of DARHT (DARHT-II), represents a significant advance in the long-pulse induction technology [12]. The DARHT-II cell design and its application to radiography are both discussed in the later chapters of this book (Chaps. 6 and 8).

2.5 High Repetition-Rate Induction Technology Developments

Motivated by applications requiring high average power, like microwave power sources for heating of magnetically confined plasmas, and short-wavelength FELs for directed energy weapon applications, the technology of magnetic modulators for induction accelerators was pioneered at LLNL by the late Dan Birx in the early 1980s. A watershed in this development was the construction of the MAG-I-D modulator in the early 1980s [13]. Using thyratrons as the primary switch, this pulsed power system produced 125 kV, 8 GW peak, 70 ns pulses at a 5 kHz repetition-rate (quasi-CW) for an average power of ∼3 MW. The efficiency of this multistage magnetic pulse compression system exceeded 90%; this made it a viable candidate

UNCORRECTED PROOF

for induction linac pulsed power systems in applications where high conversion efficiencies were needed.

Three MAG-I-D units were used to power the 60-cell ETA-II accelerator constructed at LLNL in the late 1980s [14]. This accelerator was built as a testbed for the development of high average power, high brightness electron beams. ETA-II produces a 6 MeV, 2 kA, 40 ns flat-top, very high brightness electron beam. It was used as the electron beam source to drive a mm wavelength FEL for heating a Tokamak plasma (discussed in Chap. 8). It has been used in recent years as a test bed for advanced radiography development.

A smaller induction accelerator, SNOMAD-II, used solid state primary switches to drive the magnetic pulse compressors [15]. The more recent advances in solid state switching technology and their application to induction accelerator modulators are described in Chaps. 4 and 11.

2.6 Recirculating Induction Linacs

Since linear induction accelerators (LIAs) generally have relatively low gradients, around one MeV per meter with short-pulse LIA's like ATA and even lower with long-pulse LIA's, the idea of recirculating the beam through the cores several times with independent beam transport lines has often been considered. The main objective is to obtain significant savings in cost, size, and weight of a high energy induction accelerator. Note that this "recirculating linac" architecture is very different from the induction synchrotron discussed in Chaps. 11 and 12, or a Betatron. The approach discussed here is more closely related to the Microtron, a "recirculating RF linear accelerator."

With a long-pulse electron beam (multi-μs, hundreds of meters in length) of "modest" current (a few kA), passing the beam several times through a few modules during the time of one voltage pulse on the induction cores can significantly reduce the number of modules required for a given final beam energy. The large bore of long-pulse induction cores and the low impedance of the pulsed power drivers are key here, since the bore must accommodate the simultaneous presence of several beam transport sections at once, and the total beam current load on the induction module (over most of the pulse length) is increased by the number of recirculations. This approach was considered at NBS, and experimental studies of electron beam recirculation through long-pulse induction cores with a two-pass facility delivering 20 keV per pass were carried out [16].

With shorter electron beam pulses a more reasonable recirculation scheme is to apply voltage pulses lasting slightly longer than the duration of a single beam pulse on a set of induction modules. The cores would then be reset during the recirculation time, and the pulse reapplied when the beam pulse comes around again. This approach, with a novel beam transport system utilizing static magnetic guide fields on the separate beam transport lines, was developed at PSI [17]. The spiral shape of

UNCORRECTED PROOF

the transport lines motivated its name, the Spiral Line Induction Accelerator (SLIA). Transport and acceleration of a 10 kA, 30 ns beam pulse around one turn of a SLIA with minimal emittance growth was demonstrated, and a 2 kA beam was accelerated around two turns to 9 MeV.

The Heavy Ion Fusion (HIF) program has also considered beam recirculation to reduce the cost of a heavy ion beam driver (see Chap. 10). In a conceptual inertial fusion power plant design, the induction acceleration stages would be relatively long and circular, and the beam pulse would occupy less than half the circumference. The cores would have fast resets, and the (burst) repetition rate of the pulsed power systems would be very high (∼10–100s of kHz). An experimental test bed to study the beam transport in a heavy ion recirculator was constructed at LLNL, but only 1/4 turn of a 80 mA beam with 5 induction cells were completed before the project was terminated [18]. Recirculation of an intense space-charge dominated beam has continued to be studied using a low energy electron beam at the University of Maryland (UMER) [19].

2.7 Former USSR Induction Accelerators and "Coreless" LIA's

A number of "magnetic core-type" induction accelerators were constructed and operated in the former USSR during the same general time frame as the developments in the USA discussed in the previous sections. The first machine, the 1.5 MeV LIA-3000 at JINR, was completed around 1966 [20]. It was similar in many respects to the original Astron Injector, with Permalloy cores and a thermionic BaO cathode, and it operated at similar beam currents. As mentioned in Sect. 2.3, the collective ion acceleration results with an electron ring accelerator using this machine as the injector were a major stimulus for the initiation of the ERA program at LBNL.

A list of the other core type induction accelerators in the former USSR that the authors are aware of, and their key parameters, are given in Table 2.3. Detailed information on these accelerators was in general not publicly available until recently, and gaps still remain.

The so-called "coreless" or "line-type" induction accelerator was pioneered in the former USSR starting in the late 1960s [21, 22]. The accelerator modules in a "core-less" induction accelerator do not contain magnetic material; instead, short-duration acceleration voltage pulses are generated (for example) by firing closing switches on one side of a radial Blumlein configuration charged to several MeV. These modules are generally very low impedance, operate at a very high voltage per stage, and can accelerate extremely high electron beam currents. For example the highest energy accelerator (the LIA-30) accelerated 50–100 kA, 25 ns beam pulses to 40 MeV [23]. The applications that motivated these developments were not known at the time they were first reported, but were thought to be nuclear weapons effects simulation and radiography.

UNCORRECTED PROOF

The initial reports of these developments at VNIEF (former USSR, presently Sarov, Russia) stimulated the development of high current radial line accelerators in the USA. The RADLAC-I accelerated a 25 kA, 15 ns pulse length electron beam to 9 MeV using 4 radial line stages operating at around 1.75 MeV each [24, 25]. Issues with beam transport at these high currents lead to the development of a follow-on machine (RADLAC-II) reconfigured into an Inductive Voltage Adder (IVA) – basically, a single stage high voltage diode with a ∼12 MeV stalk voltage generated by inductive addition of the stages [26].

As mentioned in Chap. 1, these "coreless" induction accelerators represent significant technological achievements but we do not cover their designs in detail in this book. We should note, however, that there is recent interest in the development of very short pulse length "coreless" induction linacs with extremely high gradients [27].

2.8 Summary Tables of Induction Accelerators World-Wide

To give an overall perspective on the development of induction accelerator technology over the past decades throughout the world, summary tables with references are provided in this section. The accelerators included in these tables are all the machines we are aware of that have been constructed and operated. The parameters listed are the energy, current, pulse length, and repetition rate of the output beam. In cases where the information was available, the repetition rate is qualified with the burst rate value and the number of shots (in parenthesis) that the burst rate could be maintained. The authors made a "best effort" to determine these beam parameters from published descriptions, but caution should be exercised by the reader. For example, pulse lengths are often not measured consistently and it is generally not clear whether quoted parameters are "typical" operating conditions or the occasional "best shot." Table entries where parameters could not be determined are indicated with dashes. The beam particles are electrons unless otherwise indicated.

In Table 2.2 the "core type" induction accelerators in the USA are listed. For completeness, this table includes the machines already discussed in some detail in the earlier sections. A major objective of the HBTS, SNOMAD-II, and ETA-II accelerators, for example, was the development of high average power capability of induction linacs. The recirculator was intended as an induction based ring with modulators capable of rapid pulse bursts as the beam pulse circulated in the ring.

The "core type" induction accelerators in the former USSR are listed in Table 2.3. Most of these accelerators operated at relatively modest beam voltages, with the exception of the LIA-30/250. This machine reportedly had the unique combination of a high beam voltage (30 MeV) and a relatively long pulse length.

Several "coreless" (also referred to as "radial line" type) induction accelerators are listed in Table 2.4. As discussed in Sect. 2.7, the development of this type of

UNCORRECTED PROOF

Table 2.2 USA "core-type" induction accelerators

	Institute	Energy [MeV]	Current [A]	Pulse [ns]	Rep.-rate [Hz]	Operational years	References
Astron	LLNL	3.7	350	250	60 Burst 1.4 k (100)	1963–1967	[3]
Astron upgrade	LLNL	6	800	300	60 Burst 0.8 k (100)	1968–1975	[4]
ERA	LBNL	4	3 k	30	∼1	∼1970	[5]
NBS prototype	NBS	0.8[a]	1 k	2,000	< 1	∼1975	[10]
ETA	LLNL	4.5	10 k	30	2 Burst 900 (5)	1977–1987	[6]
FXR	LLNL	17	3 k	60	0.3	1980–Present	[8]
ATA	LLNL	45	10 k	75	5 Burst 1 k (10)	1983–1995	[7]
HBTS	LLNL	3	2 k	50	∼100 Burst 5 k	1984–1990	[28]
MBE-4	LBNL	1	0.04[b] Cs^+	500	< 1	1984–2000	[11]
ETA-II	LLNL	6.5	3 k	50	∼1 Burst 2 k (50)	1989–Present	[14]
SNOMAD-II	MIT	0.5	500	50	∼1 Burst 5 k	∼1991	[15]
SLIA	PSI	5.5	10 k	∼30	? Burst 10 M	∼ 1996	[17]
CLIA	PI	0.75	10 k	100	100 (5 k) 1 k (5)	∼1993	[29]
RTA	LBNL	1	1.2 k	250	4	1998–2001	[30]
Recirculator	LLNL	0.08[c]	0.002[b] K^+	4,000	0.1 Burst 100 k (100)	∼1999	[18]
DARHT-I	LANL	19.8	2 k	60	< 1	1999–Present	[9]
DARHT-II	LANL	17	2.1 k	1,600	< 1	2003–Present	[12]

Abbreviations: LLNL – Lawrence Livermore National Laboratory (formerly LRL-Livermore), LBNL – Lawrence Berkeley National Laboratory (formerly LRL-Berkeley), NBS – National Bureau of Standards (presently NIST), MIT – Massachusetts Institute of Technology, PSI – Pulse Science Inc., San Leandro, CA, PI – Physics International Company, San Leandro, CA.

[a]Induction cells boosted injector voltage by 400 kV.

[b]Current of ion machines are distinguished by listing the ion and charge state ~~below~~ the current.

[c]Only one quarter turn installed. Energy boost by 5 induction cells was 500 V.

accelerator was pioneered in the former USSR, culminating in the construction of a 40 MeV, 100 kA accelerator (LIA-30). The USA RADLAC machines are also included in this table.

A number of linear induction accelerators were constructed in Japan for FEL and Two Beam Accelerator (TBA) research projects (see Table 2.5). The application of induction accelerator technology to high energy synchrotrons is included in the table. This technology has been pioneered at KEK in Japan and is discussed in detail in Chaps. 11 and 12.

UNCORRECTED PROOF

Table 2.3 Former USSR "core-type" induction accelerators

	Institute	Energy [MeV]	Current [kA]	Pulse [ns]	Repetition-rate [Hz]	~Start year	References
LIA-3000	JINR	1.5	0.25	250	5	1967	[20]
SILUND	JINR	1.7	0.7	15	1	1973	[20]
SILUND-2	JINR	0.8	1.0	20	50	1978	[20]
SILUND-10	JINR	0.25	8	20	1	1980	[20]
SILUND-20	JINR	2	1	20	50	1982	[20]
LEUK-20	JINR	1.5	–	60	20	1985	[20]
LIA-30/250	JINR	30	0.25	500	50	–	[31]
					Dual pulse		
LIA-5/5000	ITEP	4	2	200	1 K design	1977	[32]
LIA-0.8/5000	MRTI	0.8	5	80	100	–	[31]
LIA-0.4/10000	NPI	0.4	10	100	10	–	[31]
					Burst 50 (2 k)		
LIA-0.5/5000	NPI	0.5	5	100	100	–	[31]
					Burst 1 k (10)		
LIA-4/2	NPI	4	2	80	100	–	[31]
SILUND-21	JINR	10(5)	1	60	–	1995	[33]

Abbreviations: JINP – Joint Institute for Nuclear Research, Dubna, NPI – Nuclear Physics Institute at Tomsk Pollytechnic University, Tomsk, MRTI – Moscow Radio Technical Institute, Moscow, ITEP – Institute for Theoretical and Experimental Physics, Moscow.

Table 2.4 Former USSR and USA coreless ("radial line") induction accelerators

	Institute	Energy [MeV]	Current [kA]	Pulse [ns]	Rep.-Rate [Hz]	~Start year	References
LIA-2	VNIEF	2	25	35	$\ll 1$	1967	[34]
LIU-10	VNIEF	14	40	20	$\ll 1$	1977	[34]
Copy of LIU-10	NIIP	14	40	20	$\ll 1$	–	[34]
LIU-30	VNIEF	40	50–100	~25	$\ll 1$	1988	[34, 23]
I-3000	VNIEF	3.5	20	16	$\ll 1$	–	[34]
STAUS	VNIEF	2.7	15	40	$\ll 1$	–	[34]
STRAUS-2	VNIEF	3.3	50	40	$\ll 1$	–	[34]
LIU-10M	VNIEF	20	50	20	$\ll 1$	1994	[34]
RADLAC-I	SNL	9	25	15	$\ll 1$	1981	[24]
RADLAC-II	SNL	9	40	20	$\ll 1$	1984	[25]

Abbreviations: VNIEF – All-Russian Scientific and Research Institute of Experimental Physics (formerly Arzamas, presently Sarov), NIIP – Lytkarino (built for use by radiation researchers), SNL – Sandia National Laboratory, Albuquerque, NM.

The linear induction accelerators built in France are listed in Table 2.6. The 20 MeV AIRIX accelerator was built for flash radiography. Its design is similar to DARHT-I, and it achieved record-setting performance in the combination of beam current (dose) and emittance (spot size). China is the most recent country to construct a major linear induction accelerator for flash radiography, the DRAGON-I accelerator in Table 2.7.

UNCORRECTED PROOF

Table 2.5 Japanese "core-type" induction accelerators

	Institution	Energy [MeV]	Current [A]	Pulse [ns]	Rep.-rate [Hz]	∼Start year	References
FEL–KEK	KEK	1.6	3 k	80	0.1	1987	[35]
KEK+JLA	Naka, JAERI	4	1 k	80	1	1997	–
LAX-1	Naka, JAERI	1	3 k	100	1	1991	[36]
JLA	Naka, JAERI	2.5	3 k	100	1	1988	[37]
ETIGO-III	Nagaoka Univ.	8	5 k	30	< 1	1997	[38]
12 GeV PS Ring	KEK	0.01/Turn	~~4.8 = 6.4 ×10^−5~~ [a]	500–100	1 M	2006	[39]
RAIDEN	ILE	4	1.2 k	100	< 1	1990	[40]

Abbreviations: KEK – National Laboratory for High Energy Physics, Tskuba, JAERI – Japan Atomic Energy Research Institute, ILE – Institute for Laser Engineering, Osaka University, Osaka.
[a]Proton current.

Table 2.6 French "core-type" induction accelerators

	Institution	Energy [MeV]	Current [kA]	Pulse [ns]	Rep.-rate [ns]	Operational	References
LELIA	CESTA	3	1	80	∼1 (∼1k burst)	1991–2002	[41]
PIVAR	CESTA	8	3.5	80	< 1	2000–2002	[42]
AIRIX	B3–M/PEM	20	4	80	< 1	1999–Present	[43]

Abbreviations: CESTA – Centre d'Etudes Scien. et Tecniques d'Aquitaine, Le Barp, B3–M/PEM – Institute at Pontfaverger–Moronvilliers.

Table 2.7 Chinese "core-type" induction accelerators

	Institution	Energy [MeV]	Current [kA]	Pulse [ns]	Rep.-rate [Hz]	Operational	References
LIAXF (LIAXFU)	Institute of Fluid Physics	12	2.6	90	< 1	∼1990–Present	[44, 45]
DRAGON-I	Institute of Fluid Physics	20	3	90	< 1	∼2007–Present	[46]

References

1. N. Christofilos. Astron thermonuclear reactor. In *Second UN International Conference on Peaceful Uses of Atomic Energy*, Vol. 32, page 279, Geneva, Switzerland, 1958.
2. N. Christofilos. Energy Balance in the Astron Device. *Nucl. Fusion Suppl. I*, page 159, 1962.
3. N. Christofilos, R. Hester, W. Lamb, D. Reagan, W. Sherwood, and R. Wright. High current linear induction accelerator for electrons. *Rev. Sci. Inst.*, 35:886, 1964.

UNCORRECTED PROOF

4. J. Beal, N. Christofilos, and R. Hester. The Astron linear accelerator. *IEEE Trans. Nucl. Sci.*, 16:294, 1969.
5. R. Avery, G. Behrsing, W. Chupp, A. Faltens, E. Hartwig, H. Hernandez, C. MacDonald, J. Maneghetti, R. Nemetz, W. Popenuck, W. Salsig, and D. Vanecek. The ERA 4 MeV Injector. In *Proceedings of the 1971 Particle Accelerator Conference*, page 497, San Francisco, CA, 5–9 May 1971.
6. T. Fessenden, W. Atchison, D. Birx, J. Clark, E. Cook, R. Hester, L. Reginato, D. Rogers Jr. R. Spoerlein, K. Sturve, and T. Yokota. The Experimental Test Accelerator (ETA). *IEEE Trans. Nucl. Sci.*, 28:3401, 1981. (Proceedings of the 1981 Particle Accelerator Conference, Washington, DC, 11–13 Mar., 1981).
7. L. Reginato. The Advanced Test Accelerator (ATA), a 50-MeV 10-kA Induction Linac. *IEEE Trans. Nucl. Sci.*, 30:2970, 1983. (Proceedings of the 1983 Particle Accelerator Conference, Santa Fe, NM, 21–23 March, 1983).
8. B. Kulke and R. Kihara. Recent Performance Improvements on FXR. *IEEE Trans. Nucl. Sci.*, 30:3030, 1983. (Proceedings of the 1983 Particle Accelerator Conference, Santa Fe, NM, 21–23 Mar., 1983).
9. M. Burns, B. Carlsten, T. Kwan, D. Moir, D. Prono, S. Watson, E. Burgess, H. Rutkowski, G. Caporaso, Y.-J. Chen, Y. (Judy) Chen, S. Sampayan, and G. Westenskow. DARHT Accelerators Update and Plans for Initial Operation. In *Proceedings of the 1999 Particle Accelerator Conference*, page 617, New York City, NY, 27 Mar.–2 Apr. 1999.
10. J. Leiss, N. Norris, and M. Wilson. The design and performance of a long-pulse high-current linear induction accelerator at the National Bureau of Standards. *Part. Accel.*, 10:223, 1980.
11. R. T. Avery, C. S. Chavis, T. J. Fessenden, D. E. Gough, T. F. Henderson, D. Keffe, J. R. Meneghetti, C. D. Pik, D. L. Vanecek, and A. I. Warwick. MBE-4, A Heavy Ion Multiple-Beam Experiment. *IEEE Trans. Nucl. Sci.*, 32:3187, 1985. (Proceedings of the 1985 Particle Accelerator Conference, Dallas TX, 1–5 May, 1985).
12. C. Ekdahl, E. Abeyta, L. Candill, K. Chan, D. Dalmas, S. Eversole, R. Gallegos, J. Harrison, M. Holzscheiter, J. Johnson, E. Jacquez, B. McCuistian, N. Montaya, K. Nielsen, D. Oro, L. Rodrequez, P. Rodrigues, M. Sanchez, M. Schauer, D. Simmons, H.V. Smith, J. Studebaker, G. Sullivan, C. Swinney, R. Temple, Y. Chen, T. Houck, E. Henestroza, S. Eylon, W. Fawley, S. Yu, B. Bender, W. Broste, C. Carson, G. Durtschi, D. Frayer, D. Johnson, K. Jones, A. Meidinger, K. Moy, R. Sturgess, C. Tom, T. Hughes, and C. Mostrom. First Beam at DARHT–II. In *Proceedings of the 2003 Particle Accelerator Conference*, page 558, Portland, OR, 12–16 May 1971.
13. D. Birx, E. Cook, S. Hawkins, S. Poor, L. Reginato, J. Schmidt, and M. Smithand. Magnetic Switching. In *Proceedings of the 4th IEEE International Pulsed Power Conference*, page 231, Albuquerque, NM, 6–8 June 1983.
14. D. Prono, D. Barrett, E. Bowles, G. Caporaso, Y.-J. Chen, J. Clark, F. Coffield, M. Newton, W. Nexsen, D. Ravenscroft, W. Turner, and J. Watson. High Average Power Induction Linacs. In *Proceedings of the 1989 Particle Accelerator Conference*, page 1441, Chicago, IL, 20–23 Mar. 1989.
15. D. Goodman, D. Brix, and B. Danly. Induction Linac Driven Relativistic Klystron and Cyclotron Autoresonant Maser Experiments. In *Proceedings of SPIE Vol. 1407, Intense Microwave and Particle Beams II*, page 217, Los Angles, CA, 21–24 Jan. 1991.
16. M. Wilson. Recirculation acceleration of high current relativistic electron beams – a feasibility study. *IEEE Trans. Nucl. Sci.*, 28:3375, 1981. (Proceedings of the 1981 Particle Accelerator Conference, Washington DC, 11–13 March, 1981).
17. J. Smith, V. Bailey, H. Lackner, and S. Putnam. Performance of the Spiral Line Induction Accelerator. In *Proceedings of the 1997 Particle Accelerator Conference*, page 1251, Vancouver, Canada, 12–16 May 1997.
18. L. Ahle, T. Sangster, D. Autrey, J. Barnard, G. Craig, A. Friedman, D. Grote, E. Halaxa, B. Logan, S. Lund, G. Mant, A. Molvik, W. Sharp, S. Eylon, A. Debeling, and W. Fritz. Current Status of the Recirculator Project at LLNL. In *Proceedings of the 1999 Particle Accelerator Conference*, page 3248, New York City, NY, 27 Mar.–2 Apr. 1997.

UNCORRECTED PROOF

19. R. Kishek, G. Bai, B. L. Beaudoin, S. Bernal, D. Feldman, R. Fiorito, T. Godlove, I. Haber, T. Langford, P. O'Shea, C. Papadopoulous, B. Quinn, M. Reiser, D. Stratakis, D. Sutter, J. Thangaraj, K. Tian, M. Walter, and C. Wu. The University of Maryland Electron Ring (UMER) Enters a Neegime of High-Tune-Shift Rings. In *Proceedings of the 2007 Particle Accelerator Conference*, page 820, Albuquerque, NM, 25–29 June 2007.
20. G. Dolbilov. High Current Induction Linacs at JINR and Perspective of their Application for Acceleration of Ions. In Y. K. Batygin, editor, *AIP Conference Proceedings 480, Space Charge Dominated Beam Physics for Heavy Ion Fusion*, pages 85–98, Saitama, Japan, Dec. 2008.
21. A. Pavlovskii, A. Gerasimov, D. Zenkov, V. Bosamykin, A. Klementev, and V. Tananakin. Ironless induction linear accelerator. *Sov. Atom. Energy*, 28:432–434, 1970.
22. A. Pavlovskii, V. Bossamykin, V. Savchenko, A. Klementev, K. Morunov, V. Nikolskii, A. Gerasimov, V. Tananakin, and V. Basmanov D. Zenkov. The LIU-10 High-Power Electron Accelerator. *Dokl. Akad. Nauk. USSR*, 250:1118, 1980.
23. V. Bossamykin, A. Koshelev, A. Gerasimov, V. Gordeev, A. Grishin, V. Averchenkov, S. Lazarev, G. Maslov, and Yu. Odintsov. Intensive Neutron Source Based on Powerful Electron Linear Accelerator LIA-30 and Pulsed Nuclear Reactor FR-1. In K. Jungwirth and J. Ullschmied, editors, *Proceedings of the 11th International Conference on High Power Particle Beams*, page 619, Prauge, Czech Republic, 10–14 June 1996.
24. R. Miller, J. Poukey, B. Epstein, S. Shope, T. Genoni, M. Franz, B. Godfrey, R. Adler, and A. Mondelli. Beam Transport issues in high current linear accelerators. *IEEE Trans. Nucl. Sci.*, 28:3343, 1981. (Proceedings of the 1981 Particle Accelerator Conference, Washington, DC, 11–13 Mar., 1981).
25. R. Miller. RADLAC Technology Review. *IEEE Trans. Nucl. Sci.*, 32:3149, 1985. (Proceedings of the 1985 Particle Accelerator Conference, Vancouver, Canada, 13–16 May, 1985).
26. M. Mazarakis, J. Poukey, S. Shope, C. Frost, B. Turman, J. Ramierez, and K. Prestwich. SMILE, a Self-Magnetically Insulated Transmission Line Adder for the 8-Stage RADLAC II Accelerator. In R. White and K. Prestwich, editors, *Proceedings of the 8th IEEE International Pulsed Power Conference*, pages 86–89, San Diego, CA, 15–19 June 1991.
27. G. Caporaso, S. Sampayan, Y.-J. Chen, D. Blackfield, J. Harris, S. Hawkins, C. Holmes, M. Krogh, S. Nelson, W. Nunnally, A. Paul, B. Poole, M. Rhodes, D. Sanders, K. Selenes, J.Sullivan, L. Wang, and J. Watson. High Graident Induction Accelerator. In *Proceedings of the 2007 Particle Accelerator Conference*, page TUYC02, Albuquerque, NM, 25–29 June 2007.
28. G. Caporaso and D. Birx. Brightness Measurements on the Livermore High Brightness Test Stand. *IEEE Trans. Nucl. Sci.*, 32:2608, 1985. (Proceedings of the 1985 Particle Acceleator Conference, Vancouver, Canada, 13–16 May, 1985).
29. S. Ashby, D. Drury, P. Sincerny, L. Thompson, and L. Schlitt. CLIA – A Compact Linear Induction Accelerator System. In D. Mosher and G. Cooperstein, editors, *Proceedings of the 9th International Conference on High Power Particle Beams, BEAMS' 92*, pages 1855–1860, Washington, DC, 25–29 May 1991.
30. G. Westenskow, D. Anderson, S. Eylon, E. Henestroza, T. Houck, J. Kim, S. Lidia, L. Reginato, D. Vanecek, and S. Yu. Relativistic Klystron Two-Beam Accelerator Studies at the RTA Test Facility. In C. Hill and M. Vretenar, editors, *Proceedings of the 17th International Linear Accelerator Conference*, pages 393–395, Geneva, Switzerland, 26–30 Aug. 1996.
31. Private communication with A. Krasnykh.
32. S. Martynov, V. Pershin, V. Plotnikov, and N. Popova. Experimental Investigation of the beam of the LIA-5/5000 Electron Gun. In W. Bauer and W. Schmidt, editors, *Proceedings of the 7th International Conference on High Power Particle Beams, BEAMS' 88*, pages 950–955, Karlsruhe, Germany, 4–8 July 1991.
33. A. Fateev, G. Dolbilov, I. Ivanov, V. Kosukhin, N. Lebedev, V. Petrov, V. Razuvakin, V. Shvetsov, and M. Yurkov. Status of the First Stage of Linear Induction Accelerator SILUND-21. In *Proceedings of the 1995 Particle Accelerator Conference*, pages 1272–1273, Dallas, TX, 1–5 May 1995.

UNCORRECTED PROOF

34. M. Voinov, A. L. Gerasimov, A. V. Grishin, N. Zavyalov, A. Koshelev, M. Kuvshinov, V. Punin, V. Savchenko, and I. Smimov. Complexes on the Basis of High-Current Linear Induction Accelerators and Pulse Nuclear Reactors. *Nucl. Phys. Res.*, 34:82–84, 1999.
35. K. Takayama. 1.5 MeV Ion-Channel Guided X-Band Free-Electron Laser Amplifier. In R.C. Fernow, editor, *AIP Conference Proceedings 337, Pulsed RF Sources for Linear Colliders*, pages 244–260, Montauk, NY, Oct. 1994.
36. K. Sakamoto, T. Tobayashi, S. Kawasaki, Y. Kishirmoto, S. Musyoki, A. Watanabe, M. Takahashi, H. Ishizuka, M. Sato, and M. Shiho. Millimeter Wave Amplification in a Free Electron Laser with a Focusing Wiggler. *J. Appl. Phys.*, 75:36–42, 1994.
37. M. Shiho, S. Kawasaki, K. Sakamoto, H. Maeda, H. Ishizuka, Y. Watanabe, A. Tokuchi, Y. Yamashita, and S. Nakajima. Design and Construction of an Induction Linac for mm Wave Free Electron Laser for Fusion Research. *Nucl. Inst. Meth. A*, 341:412–416, 1991.
38. K. Yatsui, W. Masuda, C. Gregoriu, K. Masugata, W. Jiang, G. Imada, K. Imanari, T. Sonegawa, and E. Chisiro. Pulse-Power and Its Application at LBT. In *Proceedings of the 11th International Conference on High Power Particle Beams*, Vol. 1, page 27, Prauge, Czech Republic, 10–14 June 1996.
39. T. Dixit, Y. Shimosaki, and K. Takayama. Adiabatic Damping of the Bunch Length in the Induction Synchrotron. *Nucl. Inst. Meth. A*, 582:294–302, 2007.
40. T. Akiba, K. Imasaki, K.Tanaka, S. Miyamoto, K. Mima, Y. Kitagawa, S. Nakai, S. Kuruma, C. Yamanka, M. Fukuda, N. Ohigashi, and Y. Tsunawaki. Induction Linac FEL Experiment at ILE. In *Proceedings of the 7th International Conference on High Power Particle Beams*, pages 1306–1310, Kongresszentrum, Karlsruhe, Federal Republic of Germany, 4–7 July 1988.
41. P. Eyharts, Ph. Anthouard, J. Bardy, C. Bonnafond, Ph. Delsart, A. Devin, P. Eyl, P. Grua, J. Labrouche, J. Launspach, P. Le Taillandier, J. de Mascureau, E. Merle, A. Roques, M. Thevenot, and D. Villate. First Operation of the LELIA Induction Accelerator at CESTA. In *Proceedings of the 1993 Particle Accelerator Conference*, pages 670–672, Washington, DC, 17–20 May 1993.
42. P. Anthouard, J. Bardy, C. Bonnafond, P. Delsart, A. Devin, P. Eyharts, P. Eyl, D. Guilhem, J. LaBrouche, J. Launspach, J. de Mascureau, E. Merle, J. Picon, A. Roques, M. Thevenort, D. Villate, and L. Voisin. AIRIX at CESTA. In *Proceedings of the 11th International Conference on High Power Particle Beams*, pages 628–631, Prague, Czech Republic, 10–14 June 1996.
43. E. Merle, R. Boivinet, M. Mouillet, O. Pierret, Ph. Anthouard, J. Bardy, C. Bonnafond, A. Devin, P. Eyl, and C. Vermare. Installation of the AIRIX Induction Accelerator. In *Proceedings of the 19th International Linear Accelerator Conference*, pages 391–393, Chicago, IL, 23–28 Aug. 1998.
44. J. Deng, B. Ding, J. Shi, Y. He, J. Li, Q. Li, G. Cao, L. Wen, and G. Dai. Upgrading of Linear Induction Accelerator X-Ray Facility (LIAXF). In *Proceedings of the 19th International Linear Accelerator Conference*, pages 389–390, Chicago, IL, 23–28 Aug. 1998.
45. D. Dainam, D. Jianjun, H. Shenzong, S. Jinsui, Z. Wenjun, L. Qing, and H. Yi. Free Electron Laser Amplifier Experiment Based on 3.5 MeV Linear Inuction Accelerator. In *Proceedings of the 1995 Particle Accelerator Conference*, pages 246–247, Dallas, TX, 1–5 May 1995.
46. J. Deng, B. Ding, L. Zhang, H. Wang, G. Dai, N. Chen, Z. Dai, K. Zhang, J. Shi, W. Zhang, J. Li, X. Liu, Y. Xie, M. Wang, L. Wen, H. Li, J. Wang, Z. Xie, and M.H. Wang. Design of the DRAGON-I Linear Induction Accelerator. In *Proceedings of the 21st International Linear Accelerator Conference*, pages 40–42, Gyeongju, Korea, 19–23 Aug. 2002.

UNCORRECTED PROOF

Chapter-2

Query No.	Query
AQ1	Please provide organization name for "Richard J. Briggs".

UNCORRECTED PROOF

Chapter 3
Principles of Induction Accelerators

Richard J. Briggs

AQ1

UNCORRECTED PROOF

3.1 Introduction

The basic concepts involved in induction accelerators are introduced in this chapter. The objective is to provide a foundation for the more detailed coverage of key technology elements and specific applications in the following chapters. A wide variety of induction accelerators are discussed in the following chapters, from the high current linear electron accelerator configurations that have been the main focus of the original developments, to circular configurations like the ion synchrotrons that are the subject of more recent research. The main focus in the present chapter is on the induction module containing the magnetic core that plays the role of a transformer in coupling the pulsed power from the modulator to the charged particle beam. This is the essential common element in all these induction accelerators, and an understanding of the basic processes involved in its operation is the main objective of this chapter. (See [1] for a useful and complementary presentation of the basic principles in induction linacs.)

3.2 Basic Features of an Induction Accelerator System

As described in the historical summary in the previous chapter, linear induction accelerators were originally developed to fill a need for higher charged particle energies than a single stage diode could provide, at pulse currents beyond the capability of RF accelerators. The multistage induction accelerator configurations developed to accelerate particles to these higher energies are similar in overall appearance to the more common RF linac. In an induction accelerator module, however, as we describe in more detail in this chapter, the pulsed power source is directly coupled to the beam through a low impedance structure, the *induction cell*. This induction cell plays the same role as the resonant cavities used in RF accelerators. It is more

R.J. Briggs (✉)
Alamo, CA 94507, USA
e-mail: richardbriggs@sbcglobal.net

K. Takayama, R.J. Briggs (eds.), *Induction Accelerators*, Particle Acceleration and Detection, DOI 10.1007/978-3-642-13917-8_3,
© Springer-Verlag Berlin Heidelberg 2011

appropriate for accelerating high beam currents and/or providing general (non-sinusoidal) acceleration waveforms since the accelerating voltage comes directly from the pulse modulator.

Induction accelerators can be thought of in simple terms as a series of 1:1 transformers where pulsed voltage sources form the transformer primary circuit and the charged particle beam pulse acts as the secondary (as illustrated by the cartoon in Fig. 3.1). The rise time (τ_r), fall time (τ_f), and duration (τ_p) of a typical source voltage pulse (see Fig. 3.2) and the beam current pulse are generally in the range of tens of nanoseconds to several microseconds. In these cases the transit time of electromagnetic waves over the dimensions of a typical accelerator cell (fractions of a meter) are short compared to these characteristic pulse times. The electromagnetic fields in the accelerator cell can then generally be modeled in a quasi-static approximation. As a consequence, lumped circuit models of the accelerator module are often very useful approximations, as we show in the following sections.

A key point about this multistage accelerator module configuration as compared to single stage pulsed diodes is the fact that the peak voltages on drive cables, vacuum insulators, and other elements in the system are limited to the output of the pulse source driving one module. The charged particles, in effect, do the integration of the axial electric field in the vacuum beam pipe to achieve a final energy equal to the sum of all the individual module voltages. The *total* voltage corresponding

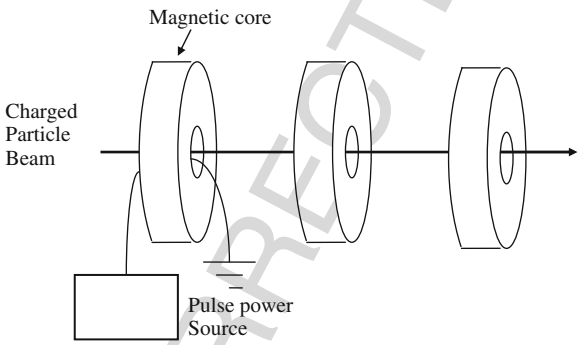

Fig. 3.1 Induction accelerator as a series of 1:1 transformers

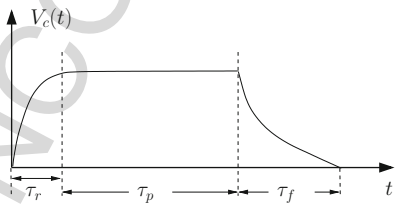

Fig. 3.2 Typical source voltage waveform applied to primary of induction core for constant acceleration over the pulse duration (τ_p). More complex waveforms can also be used as discussed in the following chapters

UNCORRECTED PROOF

to the sum of the individual module voltages doesn't appear on physical structures anywhere in the system, even if the voltage pulse length is much longer than the transit time of electromagnetic waves, or particles, through the entire system.

The basic functional elements that make up an induction accelerator system are the following.

1. The *induction cell* that couples the electromagnetic energy to the charged particle beam. This cell contains the magnetic core material that acts as the transformer. It must also provide the vacuum barrier (an insulator structure) between the evacuated beam line transporting the charged particles and the rest of the system. The basic physical processes involved in its operation are discussed in Sect. 3.3. A detailed discussion of the magnetic material properties of the core is covered in Chap. 5.
2. The *pulse power system* that delivers the pulsed voltage (accelerating electric field) to the accelerating gap in the cell. These systems are discussed in Chap. 4. Depending on the specific application, the pulsed power system can range from very low rep rates (single shot) to very high rep rates.
3. An *injector* including a charged particle source that creates the charged particle beam pulse (in a linac system). Injectors for high current electron beam applications are discussed in Chap. 7, while Chap. 9 covers ion sources for induction linacs.
4. A *focusing system* to transport the charged particle beam through the accelerator cells, similar to those used in RF linacs and synchrotrons. In linear accelerators, the magnetic elements of this transport system (solenoids, quads) are often integrated into the cell to economize on axial space and achieve the highest possible acceleration gradient. Focusing systems for high current electron beam induction linacs are discussed in Chap. 7, while ~~Chap. 9 covers~~ focusing systems for ion induction linacs.

The design of an induction module, consisting of an induction cell and the pulsed power system that drives it, often involves a number of tradeoffs. These tradeoffs and other design considerations are discussed in Chap. 6, using a number of examples from accelerators that have actually been constructed and operated.

In addition to these hardware elements, the *beam transport and beam-cell interaction* are key physics issues in the design of an induction accelerator. Indeed, as discussed in Chap. 6, in high current applications minimization of the transverse and/or longitudinal interaction impedance of the accelerator module (the "wake fields") often dominates various parameter choices (like the gap width and the beam pipe diameter).

In typical electron linear induction accelerators, the particles are highly relativistic right out of the injector. The defocusing from the radial electric field created by the beam space charge is canceled to a high degree by the azimuthal magnetic field created by the beam current (within $1/\gamma^2$, where γ is the electron energy in rest mass units). As a consequence, the design of the transverse focusing system for a high current relativistic electron induction linac is generally dominated by control of coherent *transverse* instabilities (beam breakup and image displacement

UNCORRECTED PROOF

instabilities described in Chap. 7), rather than the basic considerations of particle optics and available aperture.

In contrast, in the high current, high brightness ion induction accelerators discussed in ~~Chap. 9~~, the design of the focusing systems are generally dominated by consideration of the basic particle optics in the presence of strong radial space charge forces. Instability concerns are more often dominated by the *longitudinal* dynamics and the longitudinal interaction impedance that controls it, when the particles are only mildly relativistic.

In the induction synchrotrons discussed in Chaps. 11 and 12, the beam currents are much lower than in induction linacs but the repetition rates of the power systems are much higher. The transverse beam focusing systems are basically unchanged in the conversion from RF power systems to induction systems. Many novel aspects of the longitudinal dynamics are encountered, however, as discussed in these chapters.

3.3 Comparison Between RF Accelerators and Induction Accelerators

For readers familiar with RF accelerators [2], a discussion of the comparisons between RF accelerators and induction accelerators might be helpful at this point. Readers without any background in RF accelerators should probably skip this section until they have read the subsequent two sections in this chapter.

A typical linear induction accelerator has identical modules adding an increment of energy to the charged particle beam, as described in Sect. 3.2. This basic configuration is very similar in appearance to the more common radio frequency accelerator. The features that distinguish the two technologies can be describes in several different ways, from several different points of view.

From the perspective of the charged particle beam being accelerated: In an RF accelerator, a short "micro-bunch" passes through successive acceleration modules (or makes repetitive trips through the same module in a synchrotron) carefully timed to match a given phase of the sinusoidally varying acceleration "voltage" (axial electric field) waveform. A series of these "micro bunches" is typically used to form much longer duration "macro-bunches" (or DC particle currents). Any axial focusing of the micro-bunch that is required can be automatically provided by locating the bunch on a sloping part of the sinusoidal waveform rather than the peak of the voltage.

In an induction accelerator the beam pulse length is typically several orders of magnitude longer than the charged particle transit time through an individual module. The accelerating electric field in the region of the accelerating gap and inside the beam pipe is essentially quasi-static in character. The basic acceleration voltage waveform is also most often a flat-topped pulse. In electron induction linacs, no axial focusing is required. In ion induction linacs or induction synchrotrons, "ear pulses" or "barrier pulses" at the ends of the bunch might be provided by

UNCORRECTED PROOF

tailoring the induction module pulsed power drive pulse, or by using separate modules designed for that function.

From the perspective of the power coupling to the beam: An essential role of the high Q resonant cavities in RF accelerators is to provide a large transformer step-up ratio. That is, the high Q cavity provides an impedance match between the relatively low impedance of the RF (or microwave) transmission lines feeding energy into the cavity (10's – 100's of ohms) loaded by a relatively high (typically mega-ohm class) "beam impedance" (beam voltage gain per module divided by the beam current). The electromagnetic energy is stored in the cavity for times the order of Q/ω.

The induction cell, as already noted, is a non-resonant (low Q) structure containing a magnetic core that basically serves as a 1:1 isolating auto-transformer. This allows the modulators to drive the beam current directly and be summed to any energy using a series of modules. The electromagnetic energy from the pulsed power sources flow directly into the beam without being stored in the cell. With multi-kilo-Amp charged particle beam pulses, and cell voltages of several hundred kilovolts, the beam impedance in high current linac systems often provides a reasonable match when coupled directly to the pulsed power sources and their transmission line feeds. The induction accelerator in these situations can operate at relatively high efficiencies as discussed in more detail in Chap. 6.

From the perspective of the accelerator cell voltage gradient and wake impedances: High Q RF cavities can provide relatively high acceleration gradients per watt of source drive power. At the same time, the high Q cavity does make the suppression of transverse and longitudinal instabilities more of an issue in high beam current applications.

Induction accelerators generally have a lower acceleration gradient than RF accelerators. The "packaging" issues, vacuum insulator voltage stress limits, and volt-second limitations in the magnetic core material are all important constraints particularly for pulse durations of order a microsecond or longer. The non-resonant character of the cell itself, however, does facilitate reductions in the wake field impedances to very low values by insertion of damping elements at strategic locations.

Considering these basic differences we see that the induction approach is, in general, more suitable for the acceleration of high beam currents with relatively long ("micro-bunch") pulse lengths compared to RF accelerators. Indeed, as the discussion in the previous chapter illustrated, the primary motivation for the early development of multistage linear induction accelerators for electrons was the achievement of high instantaneous beam currents, from hundreds to thousands of Amps, in pulse lengths ranging from tens of nanoseconds to several microseconds. For some applications, like radiography of fast processes, this combination of current and pulse length comes from the requirement for a high charge per pulse to make a sufficient radiation dose, in a pulse length less than the dynamic timescale of the process (e.g., like 50–100 ns). Multistage accelerators, as opposed to single stage diode configurations, are necessary, or perhaps favored, when the required particle energy is high, and/or the beam quality requirement is demanding.

UNCORRECTED PROOF

The flexibility in the acceleration waveform is another attribute of induction acceleration that motivates its use in various ion accelerators, as indicated above and discussed in more detail in the following chapters, even when the beam current is low enough for RF acceleration to be used.

3.4 Physical Processes Inside a Typical Induction Module

To illustrate the basic physical processes in an induction module, a cutaway view of an induction cell like those used in the electron linear accelerators built in the 1970s and 1980s at LLNL and LBNL is shown in Fig. 3.3.

A voltage pulse generated by the pulsed power system (for example, by switching stored energy out of a charged transmission line or PFN) is transmitted to the induction module through a balanced set of coaxial lines as shown. Symmetrical drives through two (or more) lines are generally used to avoid deflection forces on the beam from multi-kilo-Amp drive currents.

In the presence of a charged particle beam moving down the axis and being accelerated, a return current I_B flows in the beam pipe wall and up the gap as shown in Fig. 3.3. The beam current will therefore appear as a load on the drive transmission lines connecting the pulsed power source to the cell.

A fundamental design objective in all induction accelerator systems is to have the cylindrical magnetic core present a relatively high impedance to the drive

This figure will be printed in b/w

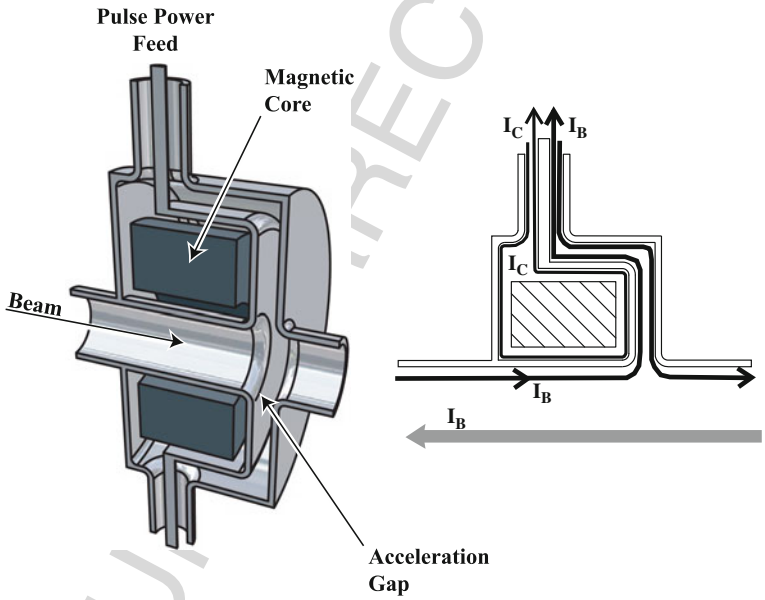

Fig. 3.3 Cutaway view of induction cell and the current flow during the pulse flat top in an induction module (the direction of the beam current is illustrated for electrons)

UNCORRECTED PROOF

transmission lines and the pulsed power source to minimize the "magnetizing current" I_c flowing into the core region (shown in Fig. 3.3). In high current induction accelerators, a key metric for how well the design meets this objective is a comparison of the magnetizing current with the beam current. As discussed in Chap. 6, when multi-kilo-Amp beams are accelerated, the magnetizing current can be made a small fraction of the total drive current resulting in high energy transfer efficiency. In all cases, however, minimization of the magnetizing current is desirable to minimize core losses and to simplify the compensation of voltage "droop" from this nonlinear, rate dependent load.

It is implicit in this picture that the beam and voltage pulse durations (and rise and fall times) are long compared to the electromagnetic propagation time through the radial gap structure so that the fields can be treated in a quasi-static approximation. Note in particular that the electric field in the vicinity of the accelerating gap is quasi-static in character, as illustrated in the sketch in Fig. 3.4. There is no electromagnetic coupling between the modules as long as the beam pipe length between successive gaps is longer than the evanescent decay length of the quasi-static electric field (one or two beam pipe radii). Note also that all the charged particles passing through the gap region gain V_c electron volts independent of their trajectory or distance from the axis, in the same way as having a DC voltage across the gap. In the rise time and fall time of the voltage pulse, the charging (and discharging) of the gap voltage leads to a displacement current flowing through the feed line to the cell, in addition to the currents I_c and I_B indicated in Fig. 3.3.

The circuit schematic presented in Fig. 3.5 that follows from these physical considerations can be used for zero-order modeling of the accelerator module operation. Note that the beam current load on the drive transmission line is accurately represented as a current source in this equivalent circuit, since this load current is not dependent on the voltage of that stage as it would be in a diode. A gap capacitance C_g has also been added to this simple circuit model to account for the displacement current flow during the rise time and fall time transients discussed above.

The magnetic core is represented in the schematic by an equivalent load impedance Z_c. This core load is nonlinear and rate dependent (dispersive), as we discuss in the following subsection, so that the relationship between the cell voltage and the time dependent "magnetizing current" I_c is quite complicated in general.

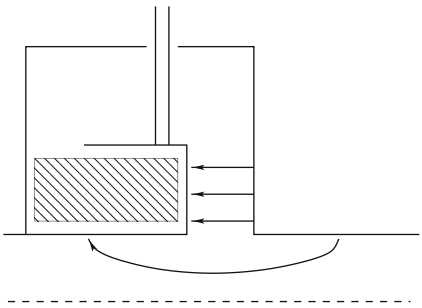

Fig. 3.4 Sketch of the electric field in the gap region and inside the beam pipe

UNCORRECTED PROOF

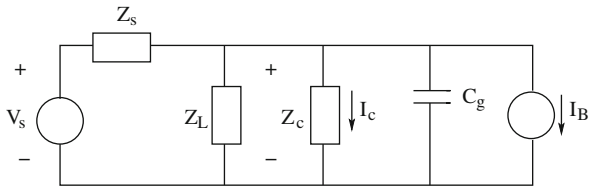

Fig. 3.5 Simplified circuit schematic of induction unit. The pulsed power source (including any transmission line cables that connect it to the cell) is represented by an equivalent voltage source V_s and series impedance Z_s. External compensation circuits at the cell junction are represented by the impedance Z_L. The core impedance (nonlinear in general) is Z_c, the gap capacitance is C_g, and the time dependent beam current load is the current source I_B

When the nonlinearities are not dominating the response (early times in the pulse and/or operation at lower amplitudes), the core impedance of ferromagnetic laminated cores can often be adequately represented by a parallel L-R circuit. The core inductance can be estimated from small amplitude permeability measurements, and the parallel resistance value chosen to reproduce the core losses for the magnetization rates of interest.

The pulsed power source is represented in the schematic by a voltage generator V_s with internal impedance Z_s as shown. An external compensation circuit with an impedance Z_L is also included in the schematic. In most induction accelerators this network is placed in an external oil filled (to provide-high voltage insulation) box and connected across the drive line just outside the induction module. This external load can be used to help flatten the acceleration voltage pulse, compensating for the rise time transients and time-dependent core currents, and also to absorb energy when the beam is absent (i.e., suppress ringing in the drive transmission lines and possible voltage doubling).

To illustrate the usefulness of this equivalent circuit in the design and operation of an induction accelerator, let us consider a simple case where the magnetic core impedance is very high ($I_c \simeq 0$), and the source and compensation load impedances are purely resistive. With the simple "step function" source voltage of amplitude V_0 and pulse duration τ_0 as illustrated in Fig. 3.6a, the cell voltage rise time is limited by the cell capacitance. Without any beam loading the cell voltage prior to the end of the pulse is given by

$$V_c(t) = V_{co}[1 - \exp(-t/\tau_R)], \tag{3.1}$$

where

$$\begin{aligned} V_{co} &= \left(\frac{Z_L}{Z_L + Z_S}\right) V_0, \\ \tau_R &= R_{\text{net}} C_g, \\ R_{\text{net}} &= \frac{Z_L Z_s}{Z_L + Z_s}. \end{aligned} \tag{3.2}$$

UNCORRECTED PROOF

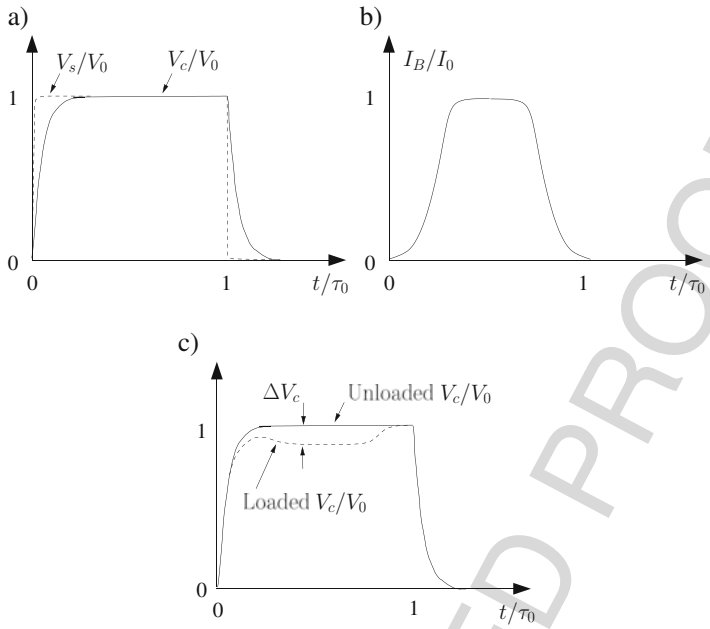

Fig. 3.6 Illustration of (**a**) time dependent cell voltages in a simple case, (**b**) beam current pulse example, and (**c**) cell voltage waveform with beam current loading (assumed to be 20%) compared with the unloaded cell voltage waveform

This cell voltage waveform is also sketched in Fig. 3.6a for the case when the rise time (and fall time) τ_R is equal to about 5% of the total pulse length.

If a beam pulse of duration less than the source voltage pulse and peak amplitude I_0 passes through the cell, as sketched in Fig. 3.6b, the cell voltage would have the form indicated in Fig. 3.6c. This cell voltage waveform is easily derived by superposition of the response to each of the two sources, V_s and I_B. The "loading" by the beam drops the cell voltage by an amount

$$\Delta V = R_{\text{net}} I_0 \tag{3.3}$$

in the flat top region of the waveform. (In Fig. 3.6c it is assumed that this loading is 20%). The power into the beam in the flat top region is therefore

$$V_c I_B = \left(\frac{Z_L}{Z_L + Z_s} \right) (V_0 - Z_s I_0) I_0. \tag{3.4}$$

With a given source impedance and source voltage, as a function of beam current the maximum energy transfer is obtained when $I_B = V_s/2Z_s$.

It is apparent from the cell voltage sketches in Fig. 3.6 that it is difficult to avoid significant beam energy variations on the head and tail of the beam pulse in a heavily loaded (efficient) induction accelerator driven by simple pulse forming line (PFL) or

UNCORRECTED PROOF

pulse forming network (PFN) sources. Compensating for a time-varying beam load current is possible in principle but difficult in practice with these drive systems. This objective might be easier to achieve with modern ("programmable") solid state drive systems.

The equivalent circuit also illustrates that the module voltage rise time is controlled by the product of the gap capacitance and the parallel combination of the source impedance and the compensation circuit impedance. Minimization of this gap capacitance is often an important consideration in the design of short pulse induction accelerators to achieve a fast enough voltage rise time. However, as discussed in Chap. 6, the gap spacing has upper limits because of transverse instability (BBU) considerations.

3.5 Magnetic Core Considerations

The basic function of the magnetic core in an induction cell is to serve as a 1:1 isolating auto-transformer so that each individual modulator can be grounded in the voltage summing process. In addition, as we emphasized in Sect. 3.4, the core should present a relatively high impedance to the drive system so that the power from the modulator flows primarily into the beam and not into the core region.

Let $\Phi(t)$ represent the total azimuthal magnetic flux in the magnetic core located inside the induction module, illustrated in Fig. 3.3. From Faraday's law, this total magnetic flux must change in time to maintain the accelerating voltage, so that

$$\Delta\Phi(t) = \int_0^t V_c(t')\,\mathrm{d}t' \tag{3.5}$$

where we take $t = 0$ as the time when the cell voltage begins. The magnetic flux is the integral of the azimuthal induction field over the core cross section,

$$\Phi = \int B_\theta(r, z, t)\,\mathrm{d}A. \tag{3.6}$$

To predict the magnetizing current I_c flowing into the core region (illustrated in Fig. 3.3) and the time-dependent "impedance" of the core, we need to know the B–H relationship of the magnetic core material. As we discuss in an elementary way in this chapter (as an prelude to the more complete discussions in Chap. 5), the electromagnetic properties of typical magnetic materials used in induction cores are very complicated to describe and to model. Their response is nonlinear, exhibiting hysteresis, and rate dependent (dispersive), as illustrated in the sample B–H relation in Fig. 3.7. It is perhaps surprising that a "zero-order" design of the induction module can be done with only limited modeling of the detailed space-time dependence of the electromagnetic fields in the magnetic material. The objective in the design, once again, is to make all these "complications" as irrelevant as possible,

UNCORRECTED PROOF

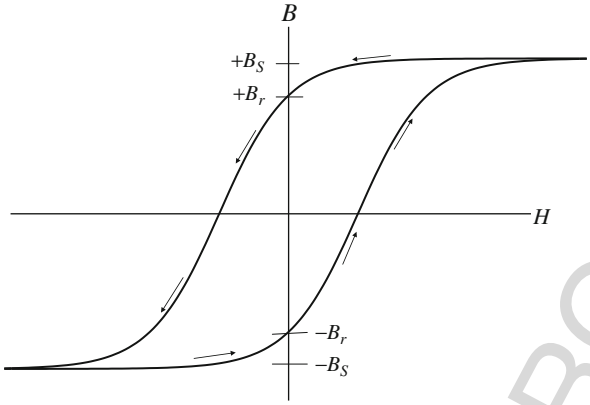

Fig. 3.7 Illustration of nonlinear B–H relation for a typical magnetic core material going from saturation at $-B_s$ to saturation at $+B_s$. The shape of this "trajectory" in B–H space depends on the rate of change of the magnetic flux

by ensuring that the magnetizing current remains as small a perturbation as possible for the full duration of the acceleration voltage pulse. At a minimum, the magnetic core impedance should be as large as possible compared to the pulsed power driver impedance for reasonable waveform control.

The main constraint on the choice of magnetic material and the required volume of material follows from Eq. (3.5). When the voltage pulse is first applied, we assume the core has been reset to $-B_r$. (Circuitry for ensuring this reset occurs is discussed in Chap. 6). During the voltage pulse, the magnetic induction field at any given position will start moving from $-B_r$ towards $+B_s$ (saturation). The details of how various regions of the core move towards saturation can be complicated, since the H field varies throughout the core; we discuss some of these aspects in the following discussions of ferrite and tape wound cores. It is clear, independent of these details, that the product of the pulse voltage and pulse length is limited by the "volt-seconds" product of the core, i.e.,

$$\int V_c \, \mathrm{d}t \sim \text{Average}[V_c]\tau_p \leq \Delta B A_c \text{ volt-s}, \tag{3.7}$$

where A_c is the cross sectional area of the core and ΔB is the total flux swing available ($B_r + B_s$ with the assumed reset to $-B_r$). When this volt-s limitation is reached, and all the regions of the core are saturated (i.e., the magnetic flux is on the upper flat part of the B–H curve), the impedance of the core collapses and I_c rapidly rises.

We must also ensure, that the impedance of the core *prior* to saturation is large compared to the pulsed power driver impedance. This constraint is generally satisfied when the volt-second constraint is satisfied, as long as we chose magnetic core material with a relatively high effective permeability prior to saturation.

UNCORRECTED PROOF

Equation (3.7), together with other considerations like the magnetization rate and the rep rate (average power and heating), constitute the zero order basis for the choice of magnetic material and the specification of the volume of core material. Examples of how these choices were made in the design of several induction accelerators that were built and operated are discussed in Chaps. 5 and 6.

The details of the space-time dependence of the nonlinear magnetics with a given cell aspect ratio ultimately determine the time dependence and magnitude of the magnetizing current, of course. Compensation for this magnetizing current with networks in the drive circuitry and/or the compensation box are often required to achieve adequate flat top on the module voltage pulse, as can be predicted from the equivalent circuit in Fig. 3.5. In practice the design and "tuning" of these networks are generally done empirically.

One area where the details of the nonlinear magnetics can be important is in the distribution of electrical stresses in the core region. This phenomenology is very different with ferrite magnetic material or tape wound cores, as we discuss below.

3.6 Ferromagnetic Laminated Cores

For long pulse induction accelerators, the large flux swings available with ferromagnetic materials like nickel-iron, silicon steel, and amorphous magnetic material makes their use compelling. Ferromagnetic materials are those in which magnetization is produced by cooperative action between domains of collectively oriented molecules yielding a higher flux density and permeability [3, 4]. However, the conductivity of these materials is many orders of magnitude higher than the ferrites. Basically they are conductors so that it is necessary to manufacture the cores by wrapping thin ribbons (10–40 μm thick) of the material with electrical insulation between the layers to avoid excessive eddy current losses. This is the same technique used to manufacture 50–60 Hz power transformers with this material where the thickness of the laminations can be much greater since the frequency is much lower.

With a laminated core inside an induction cell, the azimuthal H field in the core region is quasi-static and proportional to the magnetizing current. It penetrates "instantly" throughout the insulating layers in the core region since these insulating layers suppress any (bulk) radial currents that would shield it from the core region interior. As we discuss in more detail in Chap. 6, however, the micro-picture of the magnetic field penetration does involve partial shielding of the magnetic flux from the ribbon interiors because of local eddy currents circulating around each ribbon. If the rate of rise of the magnetizing current is slow enough, so that the ribbon thickness is small compared to an equivalent skin depth, this shielding effect and the associated eddy current losses are a small perturbation. In this case, the core impedance one can use in the equivalent circuit in Fig. 3.5 (prior to saturation) is simply the low frequency inductance of the core. This inductance should use the effective rate dependent permeability, for an improved estimate, and a resistor in

UNCORRECTED PROOF

parallel to model the losses. The magnetizing current with a flat topped drive voltage pulse, then, will increase linearly in time.

A major difference in the construction of laminated cores for induction cells as opposed to 60 Hz transformers is the requirement for much better layer to layer insulation, as well as thinner ribbons to reduce eddy current losses. With magnetization rates of many Tesla per microsecond, the layer to layer voltages can be tens of volts in the induction cell application as opposed to a millivolt or less in the 60 Hz case, where no additional insulation is required except for the surface discontinuity insulation. The distribution of the pulsed voltages throughout the induction cell is in fact a much more complicated problem than it would first appear; this issue is discussed in detail in Sect. 6.9.

3.7 Ferrites

For pulse lengths much less than a microsecond, the volt-second requirements are more modest and the use of ferrimagnetic materials like ferrite can become attractive. Ferrimagnetic materials are those in which spontaneous magnetic polarization occurs in non equivalent sub-lattices; the polarization in one sub-lattice is aligned anti-parallel to the other yielding a lower flux density and permeability [3, 4]. However, the resistivity of Ni–Zn ferrite is very high ($\sim 10^4 \Omega$-m typically) so that the equivalent skin depth is many meters at the frequencies of interest. The losses of the ferrite material in induction cell applications are dominated by the magnetic losses associated with the spin resonance, as discussed in Chap. 5. Spin resonance absorption at microwave frequencies is similar in principle to nuclear and electronic spin resonance [5]. The magnetic moment of the material precesses about the direction of the static magnetic field and energy is absorbed strongly from a transverse radio frequency field when its frequency is equal to the precessional frequency. At this frequency, the permeability shows an increase and above this frequency the real part of the permeability decreases while the imaginary or lossy part increases.

At frequencies well below the spin resonance, the (small amplitude) permeability can be quite high (several hundred to thousands). This relatively high permeability, together with a dielectric constant of order 10 in typical ferrites, means that the basic electromagnetic propagation speed in ferrite is of order 1% of the speed of light in vacuum. In contrast to all the other regions in an induction cell, therefore, where the electromagnetic fields are quasi-static in character, the ferrite core region will generally involve wave propagation dynamics for an adequate description [1]. The wave amplitudes are generally too large for a linear model of the ferrite to be an adequate description, however.

Induction cell designs using ferrite cores are therefore basically ferrite loaded transmission lines. In later generation designs it was recognized that the wave propagation dynamics in the ferrite could be used to advantage to make the core impedance resistive and also to remain relatively constant throughout the entire duration of the drive voltage pulse. This constant core impedance feature is desirable

UNCORRECTED PROOF

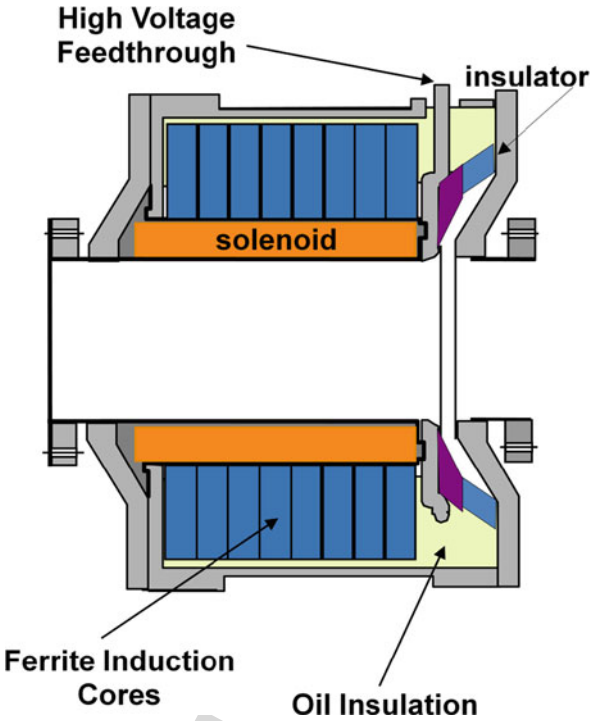

Fig. 3.8 ETA-II induction cell

This figure will be printed in b/w

because it greatly simplifies the compensation requirements to achieve a constant acceleration voltage.

The ETA-II induction cell pictured in Fig. 3.8 illustrates how this feature can be optimized in the cell design as discussed more fully in Sect. 6.2. The 20 cm long coaxial ferrite induction core in ETA-II was driven from one end at the acceleration gap. The two-way propagation time of small amplitude voltages in this line is of order 120–140 ns, slightly longer than the actual pulse length. At the normal operating voltages in ETA-II, the ferrite is driven into saturation and the propagation of the "saturation wave" through the ferrite core cannot be treated adequately as a small amplitude wave. Nonetheless, the measured core impedance in ETA-II up to saturation of the entire core did remain roughly constant at around 200 Ω [6]. This constant core impedance in ETA-II was in marked contrast to the ATA configuration where the drive was applied at the outer radius of the ferrite toroid.

References

1. S. Humphries. *Principles of Charged Particle Acceleration*, Wiley, New York, NY, 1986.
2. T. Wangler. *RF Linear Accelerators*, Wiley, New York, NY, 1998.
3. D. Gray, editor. *American Institute of Physics Handbook*, McGraw-Hill, New York, NY, 1972. see Sect. 5–4.

UNCORRECT

4. A. Deckker, editor. *Electrical Engineering Materials*, Prentice Hall, New Jersey, 1959. page 96.
5. C. Kittel. *Introduction to Solid State Physics*, Wiley, New York, NY, 8th edition, 2005. see page 363.
6. W. Turner, G. Caporaso, G. Craig, J. De Ford, L. Reginato, S. Sampayan, R. Kuenning, and I. Smith. Impedance Characteristics of Induction Accelerator Cells. In *Proceedings of the 7th International Conference on High-Power Particle Beams*, page 845, Karlsruhe, Germany, 4–8 July 1988.

UNCORRECTED PROOF

Chapter-3

Query No.	Query
AQ1	Please provide Organization name for "Richard J. Briggs."

UNCORRECTED PROOF

Chapter 4
Modulators

Edward G. Cook and Eiki Hotta

4.1 General Discussion on Induction Accelerator Modulators

High power modulator circuit topologies useful for driving induction accelerators are always limited by the capabilities of the available switching devices. These switch limitations are usually in the form of maximum operating voltage and current, maximum repetition rate and minimum pulse width. Most high power switching devices can be characterized as closing devices that are capable of very fast turn-on times but are limited in their ability to support voltage immediately after conduction.

Conventional modulators capable of generating rectangular voltage pulses to drive induction cells and using closing switches are limited to line-type topologies, comprised of either transmission lines or pulse forming networks (PFNs) that simulate transmission lines. Line-type modulators have the advantages of limited stored energy, moderate cost, and relative ease of design and fabrication, however, line-type modulators have severe limitations regarding pulse-width agility, maximum repetition rate, and the ability of driving nonlinear or time varying loads. Historically, modulator topologies using the grid-controlled switching capabilities of vacuum tubes (hard-tube pulsers) overcame many of the limitations of line-type modulators. However, the intrinsic high internal impedance of vacuum tubes results in low energy transfer efficiencies and precludes their use in high power, high current modulators. Recent developments in high peak-power semiconductor devices that are capable of both fast turn-on and fast turn-off have rekindled interest in these hard-tube-type modulator topologies for induction accelerator applications. These solid-state switched modulators vastly broaden the capabilities of linear induction accelerators with regard to average power, variable pulse width, and peak repetition rate and will allow their use in applications not previously envisioned.

E.G. Cook (✉)
Lawrence Livermore National Laboratory, Livermore, CA 94550, USA
e-mail: cook5@llnl.gov

K. Takayama, R.J. Briggs (eds.), *Induction Accelerators*, Particle Acceleration and Detection, DOI 10.1007/978-3-642-13917-8_4,
© Springer-Verlag Berlin Heidelberg 2011

UNCORRECTED PROOF

4.1.1 Line-Type Modulators

Line-type pulsers of both the transmission line configuration and pulse forming networks (PFNs) are the most commonly used high voltage pulse generating circuits for accelerator applications. Basic transmission line theory as it pertains to pulse generation followed by a more detailed discussion of PFN design is presented. For a more detailed discussion on transmissions lines and line type pulser see Smith or Pai [1, 2]. Variants of basic transmission line circuits such as Blumlein lines are discussed.

Line-type pulsers are those in which all the stored electrical energy is delivered to the load during the pulse. The energy storage is usually in the form of transmission lines (usually coaxial in geometry) or lumped element (discrete capacitors and inductors) transmission lines that also perform the function of pulse shaping. In lumped element lines, commonly referred to as pulse forming networks (PFNs), the electrical energy may be stored in either the electrostatic field (capacitors) or magnetic field (inductors). Circuits using capacitor energy storage (voltage fed) require a closing switch (see Fig. 4.1) and circuits using inductive energy storage (current fed) require an opening switch (see Fig. 4.2) and are not used very much due to the lack of fast high-voltage switches capable of opening at high currents. Line-type pulsers are based on the properties of transmission lines as pulse generating devices. When transmission lines are used in pulse applications, the output pulse parameters are directly related to the electrical length (one-way propagation time), τ, and line characteristic impedance, Z_o. In normal usage, the transmission line as shown in Fig. 4.3 is charged by a voltage source and subsequently discharged into the load impedance through a series switch. A simplified equivalent circuit for this topology would be shown as a pulse generator having an output pulse of duration 2τ and internal impedance Z_o. Transmission line pulsers generally generate fairly nice rectangular pulses but suffer from a number of disadvantages including being bulky, having a limited range of characteristic impedance, low energy density, and the difficulties in making connections at high operating voltages.

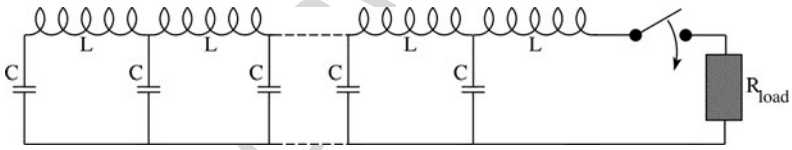

Fig. 4.1 Voltage fed PFN

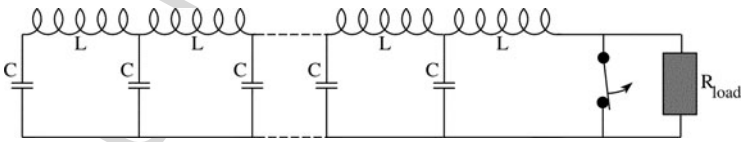

Fig. 4.2 Current fed PFN

UNCORRECTED PROOF

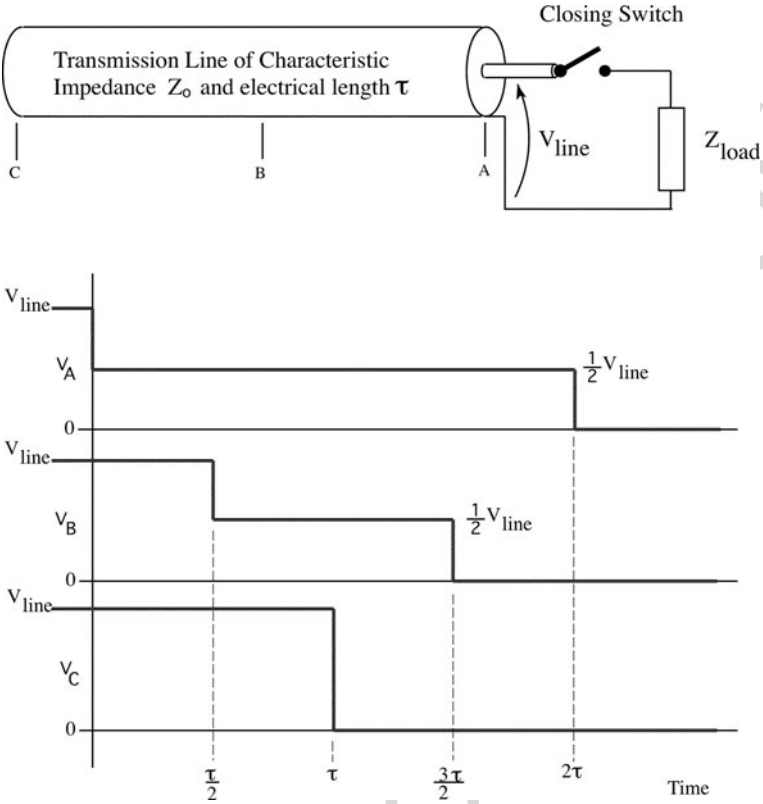

Fig. 4.3 Transmission line pulser

4.1.1.1 Simplified Theory of Operation

The transmission line is initially charged to voltage V_{line}. At switch closure time ($t = 0$), the line voltage, as measured at the output of the transmission line, point A in Fig. 4.3, drops to the value determined by the ratio of the voltage divider determined by the load impedance, Z_L, and line characteristic impedance, Z_o. When the two impedances are equal, that load voltage is $V_{\text{line}}/2$ and a voltage wave of amplitude $-V_{\text{line}}/2$ begins propagating towards the open circuit end of the transmission line (point C) reducing the line voltage to $V_{\text{line}}/2$ as it propagates. At time τ, the voltage wave arrives at the end of the line and gets reflected off the open circuit resulting in a voltage wave of amplitude $-V_{\text{line}}/2$ propagating back towards the load. This voltage wave reduces the transmission line voltage to zero as it propagates and, when it reaches the load at time 2τ, the line is fully discharged. The voltage appearing across the load beginning at time $t = 0$, has an amplitude of $V_{\text{line}}/2$ and has a pulse duration 2τ.

When a voltage pulse propagating along a transmission line encounters an impedance, Z_L, not equal to Z_o, the amplitude and polarity of reflected voltage

UNCORRECTED PROOF

waves from that impedance mismatch is calculated as the product of the voltage pulse amplitude and the reflection coefficient, Γ, where $\Gamma = (Z_L - Z_o)/(Z_L + Z_o)$. The effect of mismatching the load impedance of a line type pulser is to introduce a series of voltage steps into the transient discharge across the load. As seen at the load, these steps are all the same polarity when $Z_L > Z_o$ and alternate in polarity when $Z_L < Z_o$. A mismatch between the load and the line results in the line not fully discharging in the first pass and the energy remaining in the line must dissipate into the load later in time. In most induction linacs using pulse forming lines, a long transmission line cable is used to connect the pulse forming line to the induction cell (see Sect. 6.2). In this case, the load impedance to use in Fig. 4.3 for calculating the modulator output pulse is the characteristic impedance of the connecting transmission line cable, and not the cell impedance discussed in Chap. 3.

The Astron accelerator (see Sect. 2.1) used transmission line pulsers in the form of thyratron switched coaxial cables as the pulse source for it induction cells. Coaxial line pulsers, usually with a liquid dielectric and using a magnetic compression circuit as the output switch, were used in HBTS, ETA-II, SNOMAD-II, and CLIA.

4.1.1.2 PFN Theory and Design

When transmission lines are used to generate long pulses (microsecond time scale), the transmission lines become very long. PFNs are an attempt to replace the distributed inductance and capacitance of a transmission line with lumped elements arranged as shown in Fig. 4.1 [3, 4, 2]. In this circuit topology, the number of discrete elements needed to accurately represent a transmission line becomes very large and, in practice, the efforts to accurately simulate a transmission line in this manner have waveshape limitations of a fundamental nature:

- Voltage overshoot on leading edge
- Excessive oscillation on pulse top

Guillemin determined that these perturbations to the waveshape are due to the attempt to generate discontinuous (very fast rise-time) pulses by means of lumped parameter networks. He ascertained that instead of infinitely fast rise and fall-times, the desired pulse shape should have a reasonable and finite rise and fall time. This approach is represented as a repetition of bipolar pulses having a flattop with finite rise and fall times, as shown in Fig. 4.4, on which a Fourier analysis can be performed. The Fourier expansion of the current required to generate a waveform of this shape into a constant resistive load consists of only sine terms with the Fourier coefficients b_n.

$$I(t) = I_{pk} \sum_{n=1,3,5,\ldots}^{\infty} b_n \sin\left(\frac{n\pi t}{\tau}\right) \tag{4.1}$$

UNCORRECTED PROOF

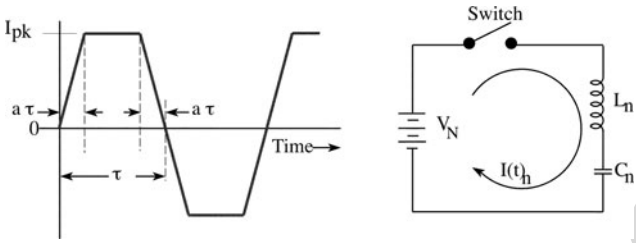

Fig. 4.4 Bipolar pulse train with finite rise and fall times and electrical circuit that generates sinusoidal currents

where

$$b_n = \frac{2}{\tau}\int_0^{\tau} \frac{I(t)}{I_{pk}} \sin\left(\frac{n\pi t}{\tau}\right) \mathrm{d}t \tag{4.2}$$

Equation (4.2) when solved for the waveshape in Fig. 4.4 yields:

$$b_n = \frac{4}{n\pi}\frac{\sin(n\pi a)}{n\pi a} \tag{4.3}$$

where $n = 1, 3, 5, \cdots$, and a is defined as the pulse rise-time as a percentage of the pulse width (τ) as shown in Fig. 4.4. Each sinusoid in this series may be produced by the electrical circuit having the topology shown in Fig. 4.4. The loop current for this series resonant circuit is:

$$I(t) = \frac{V_N}{\sqrt{L_n/C_n}} \sin\left(\frac{t}{\sqrt{L_n C_n}}\right) \tag{4.4}$$

$$I(t) = \frac{V_N}{Z_N} \sin \omega_o t \tag{4.5}$$

where Z_N represents the characteristic impedance and ω_o is the natural resonant frequency of the LC circuit. Comparing the amplitude and frequency terms for the Fourier coefficients to the loop equations and solving for the value of the inductance and capacitance gives:

$$L_n = \frac{Z_N \tau}{n\pi b_n} \quad \text{where} \quad Z_N = \frac{V_N}{I_{pk}} \tag{4.6}$$

$$C_n = \frac{\tau b_n}{n\pi Z_N} \tag{4.7}$$

A physical implementation of this series expansion is a parallel array of series resonant circuits as shown in Fig. 4.5. In practice, for this circuit topology, stray capacitance across the inductors and mutual inductance between the parallel circuits degrades the pulse waveshape. In addition, each capacitor in this topology has a different value and makes this approach expensive to implement.

UNCORRECTED PROOF

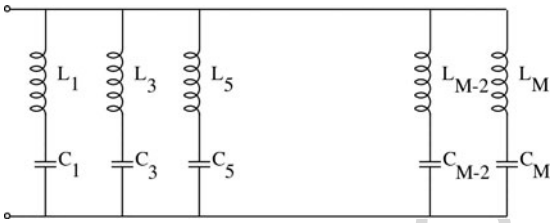

Fig. 4.5 Circuit topology implementing the Fourier series expansion

This form of analysis and network synthesis may be performed on waveshapes other that the trapezoidal waveshape shown in Fig. 4.4. If the waveshape is chosen to have a flattop and parabolic rise and fall times, the Fourier series is seen to converge to a clean waveshape more rapidly than the trapezoidal series. This is summarized in Table 4.1 where the Fourier coefficients and inductance and capacitance values are shown for rectangular, trapezoidal and parabolic rise/fall time pulses.

Other circuit topologies capable of generating equivalent waveshapes can be easier to build. The mathematical approach to finding these other circuits is to use the impedance function for this circuit and, from this impedance function, derive networks having other topologies. The Laplace transform equations for the admittance and equivalent impedance functions for the circuit in Fig. 4.5 are:

$$Y(s) = \frac{C_1 s}{L_1 C_1 s^2 + 1} + \frac{C_3 s}{L_3 C_3 s^2 + 1} + \ldots \tag{4.8}$$

$$Z(s) = \frac{1}{Y(s)} \tag{4.9}$$

Expanding $Z(s)$ about its poles yields equivalent networks have other circuit topologies. In practice, six topologies have been identified. These networks are normally identified as Type A – Type F. Network topologies Type A, B, C, and F require

Table 4.1 Values of b_n, L_n, and C_n for the circuit in Fig. 4.5

Waveform	b_n	L_n	C_n
Rectangular	$\frac{4}{n\pi}$	$\frac{Z_N \tau}{4}$	$\frac{4\tau}{n^2\pi^2 Z_N}$
Trapezoidal	$\frac{4}{n\pi}\frac{\sin(n\pi a)}{n\pi a}$	$\frac{Z_N \tau}{4\frac{\sin(n\pi a)}{n\pi a}}$	$\frac{4\tau}{n^2\pi^2 Z_N}\frac{\sin(n\pi a)}{n\pi a}$
Flat top with parabolic rise and fall times	$\frac{4}{n\pi}\left[\frac{\sin\left(\frac{1}{2}n\pi a\right)}{\frac{1}{2}n\pi a}\right]^2$	$\frac{Z_N \tau}{4\left[\frac{\sin\left(\frac{1}{2}n\pi a\right)}{\frac{1}{2}n\pi a}\right]^2}$	$\frac{4\tau}{n^2\pi^2 Z_N}\left[\frac{\sin\left(\frac{1}{2}n\pi a\right)}{\frac{1}{2}n\pi a}\right]^2$

UNCORRECTED PROOF

capacitors having different values (not cost effective) for each section. While the Type D network requires equal or near equal value capacitors in each section, it also has negative value inductors in series with the capacitors. The negative inductance in the Type D network represents the mutual inductance between adjacent inductors and may be realized in physical form by properly spacing coils on a single tubular form (solenoid). This derivative of the Type D network is designated as the Type E network. The quality of the output pulse of each of these networks is dependent on the number of sections used. For a waveform having a desired rise time that is ~8% of the total pulse width, five sections (each consisting of one inductor and one capacitor) adequately produces the desired waveshape. A sixth section provides only slight improvement. This corresponds to the relative amplitude of the Fourier-series components for the corresponding steady-state alternating current wave. The relative amplitude of the fifth to the first Fourier coefficient is ~4% while the sixth to the first is ~2%. If faster risetimes are required, this increases the number of sections required to satisfy that risetime and still provide a quality pulse.

The Type E PFN is one of the more commonly used network topologies due to the simplicity of the design/fabrication and the cost effectiveness of using equal value capacitors and inductors of solenoidal form. The important design equations are simple once the PFN characteristic impedance, Z_o, and output pulse width, 2τ, are selected.

$$Z_o = \sqrt{\frac{L_N}{C_N}} \tag{4.10}$$

$$\tau = \sqrt{L_N C_N} \tag{4.11}$$

Where L_N is equal to the total PFN inductance and C_N is equal to the total PFN capacitance. The total PFN inductance (including mutual inductances) and capac-

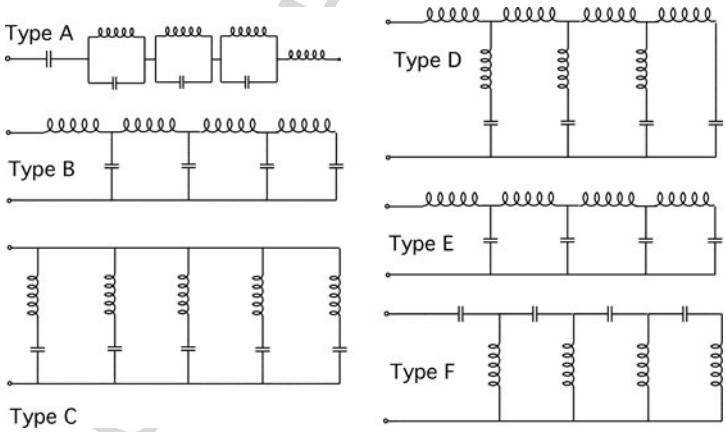

AQ1

Fig. 4.6 Network equivalents to Fig. 4.5

UNCORRECTED PROOF

itance are divided equally between the number of sections comprising the PFN. Empirical data have shown that the best overall waveshape can be achieved when the end inductors have 20–30% more self inductance than the other sections. The mutual inductance should be approximately 15% of the self inductance for each section and can be achieved fairly easily when the inductor is wound as a solenoid.

Within a limited range, the impedance of individual PFN sections may be adjusted to match an impedance change in the load. As an example; each section of a 5 section PFN drives approximately 20% of the load pulse duration. If the load impedance is 10% lower for the first 20% of the pulse, designing the first section of the PFN (section closest to the load) to be 10% lower than the rest of the PFN will make a better match and generate a flatter pulse at the load. This approach only works if the load impedance is repeatable on a pulse-to-pulse basis. See Sect. 6.3 for a discussion of the application of this tapering technique to flatten the voltage pulse on the DARHT-II cell.

A number of PFN variations can be used to overcome limitations and restrictions caused by switch capabilities, capacitor operating voltage, etc. As depicted in Fig. 4.7, PFNs may be stacked to achieve higher output voltage with the tradeoff of requiring floating (non grounded) switches and PFNs. To generate a clean output pulse, the output switches must also be triggered simultaneously and have low jitter. For the DARHT-II accelerator, series connected PFNs with spark gap switches were chosen to drive their long pulse induction cells. As mentioned in the previous paragraph, these PFNs were also designed to have a tapered impedance.

The PFN variation of the Blumlein line is also often used. In this configuration two identical lines, configured as shown in Fig. 4.8, are discharged into a load impedance that has twice the characteristic impedance of each of the lines. A major attractiveness of this configuration is that the load voltage is equal to the line charge voltage with the tradeoff being that the single, ground-referenced switch must be capable of handling twice the current of a normal PFN switch. This topology may be

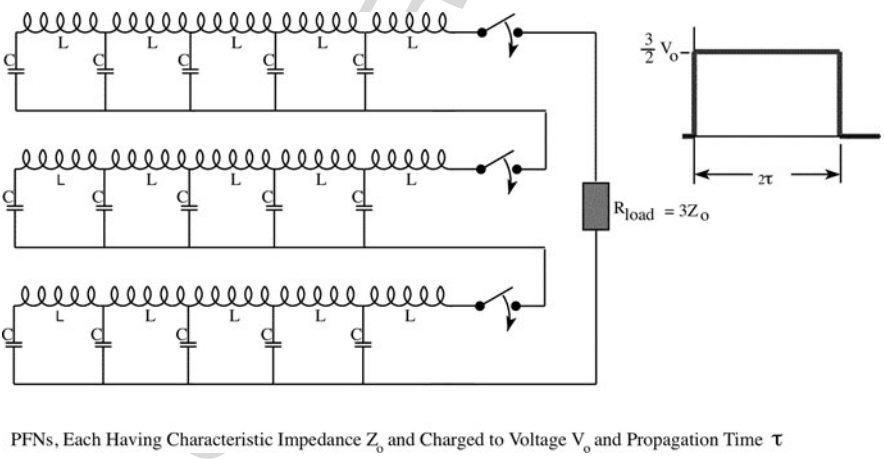

Fig. 4.7 Series connected PFNs

UNCORRECTED PROOF

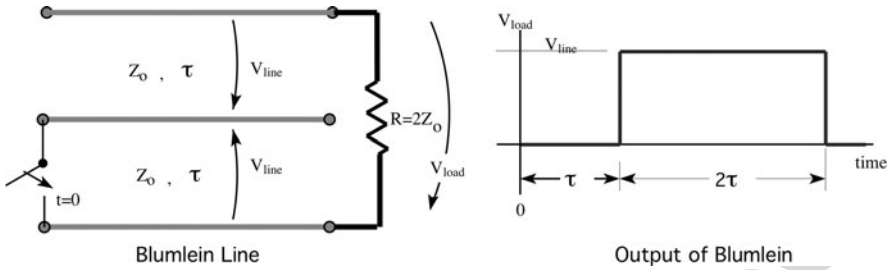

Fig. 4.8 Blumlein line

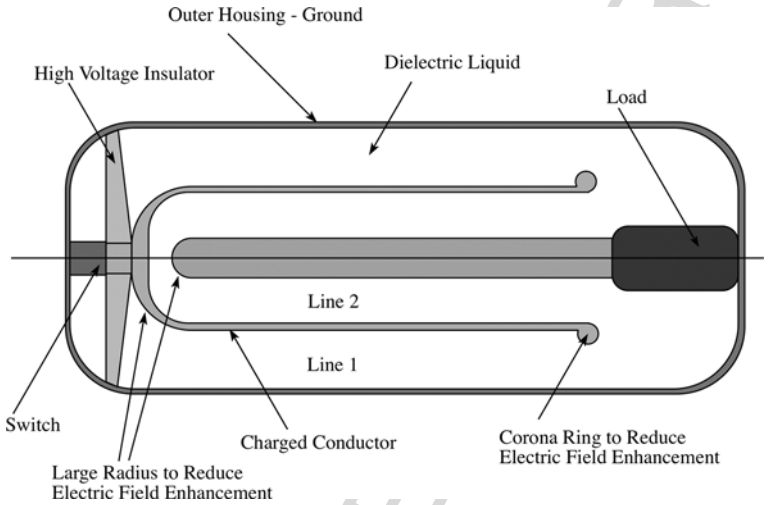

This figure will be printed in b/w

Fig. 4.9 Coaxial Blumlein configuration

implemented with either transmission lines or PFNs but the liquid-dielectric, coaxial version (see Fig. 4.9) has been successfully used in several induction accelerators (e.g., see Sect. 6.4) including ETA, FXR, ATA, ERA, and DARHT-I. The Blumlein line configuration may also be stacked similarly to the series connected PFNs if higher voltages are required. As with the stacked lines, the floating high voltage switches must be triggered simultaneously.

4.1.1.3 Summary

In summary, line-type pulsers are commonly used in accelerator pulsed power applications. These devices in general have several positive and negative attributes. In addition, both the transmission line based and PFN pulse circuits have distinct and separate characteristics.

UNCORRECTED PROOF

- General advantages of line-type pulsers:
  - Limited stored energy
  - Fairly simple circuits to design and fabricate
  - Inexpensive
  - Requires a closing high-voltage switch
  - Efficient
- General disadvantages of line-type pulsers:
  - Fixed output pulsewidth
  - Fixed characteristic impedance
  - High-voltage switch must operate at twice load voltage (except Blumlein line)
  - Must be recharged between pulses
- Transmission Line Pulser
  - Advantages
    - Produces rectangular pulses with good rise and fall times
    - Capable of producing short duration pulses
  - Disadvantages
    - Tends to be large and bulky for very high voltage or long pulse width
    - Limited range of characteristic impedance (may require impedance matching pulse transformer to couple to the load)
    - Very low inductance connections can be difficult at high voltages
- Lumped Element PFNs
  - Advantages
    - Compact
    - Can be scaled to both very high voltages and currents and long pulse duration
    - Considerable flexibility in characteristic impedance
  - Disadvantages
    - Slow rise and fall time unless many sections used
    - Pulse waveshape prone to having overshoot and ringing on flattop

4.1.1.4 Marx Generators

Marx generators are versatile devices capable of generating fast rise time, high voltage pulses and are often used in conjunction with PFN systems [5]. Originally developed by Erwin Marx in the 1920s, these device are used as fast charging systems and as simple low impedance sources for many applications. In their basic configuration, as shown in Fig. 4.10, a number of impedance isolated capacitors (C1–C4) are charged by a single voltage source and, when the interconnecting

UNCORRECTED PROOF

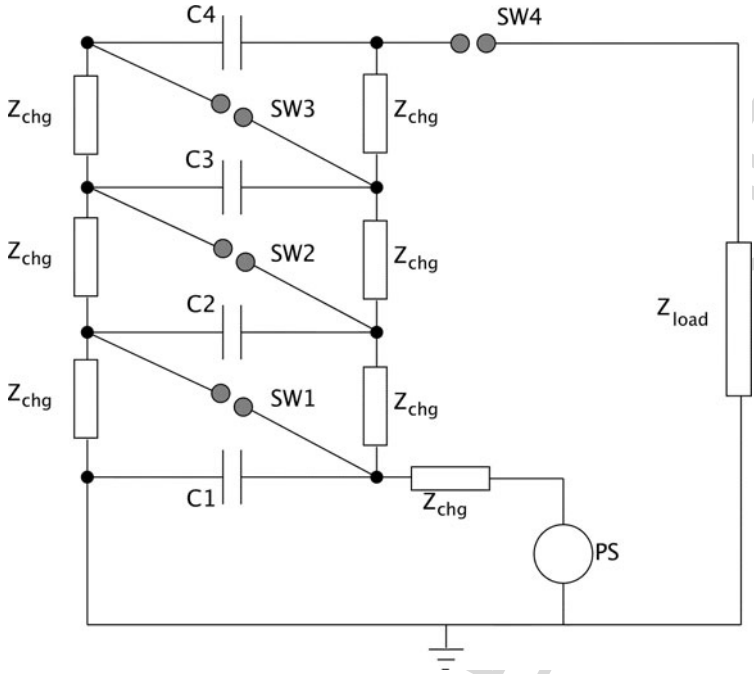

Fig. 4.10 Simplified Marx generator circuit

switches (SW1–SW4) close, the capacitors discharge in series thereby providing voltage gain. Commonly, spark gaps are used as the closing switch and resistors as the isolating elements. In Fig. 4.10, when SW1 is triggered, the additional voltage stress across SW2 causes it to self break and subsequently leads to the closing of all the switches. These cascading switch closures, usually described as the "erection of the Marx," can generate very fast rise time voltage pulses across the load impedance. While the fast rise time of a Marx generator is one of its strongest attributes, the fall time can be much slower as the load impedance determines the wave shape and duration of the voltage fall time.

There are some subtleties involved in designing the system so that the gaps will properly trigger to erect the Marx. The stray capacitance to ground in series with the switch capacitance forms a voltage divider that determines the peak voltage appearing across the switch. If the capacitance ratio is not correct, the switch may not see sufficient voltage to initiate self breakdown. This effect may be completely avoided by triggering each switch although this increases the overall complexity of the system.

As with any pulsed power system, many variations exist. Inductors are often used as isolating elements in order to reduce the energy losses. In either case, the capacitors charge on different time scales due to the different series impedances and this limits both the charge rate and the repetition rate of a traditional Marx. This limitation can be reduced by replacing the isolation impedances with high voltage

UNCORRECTED PROOF

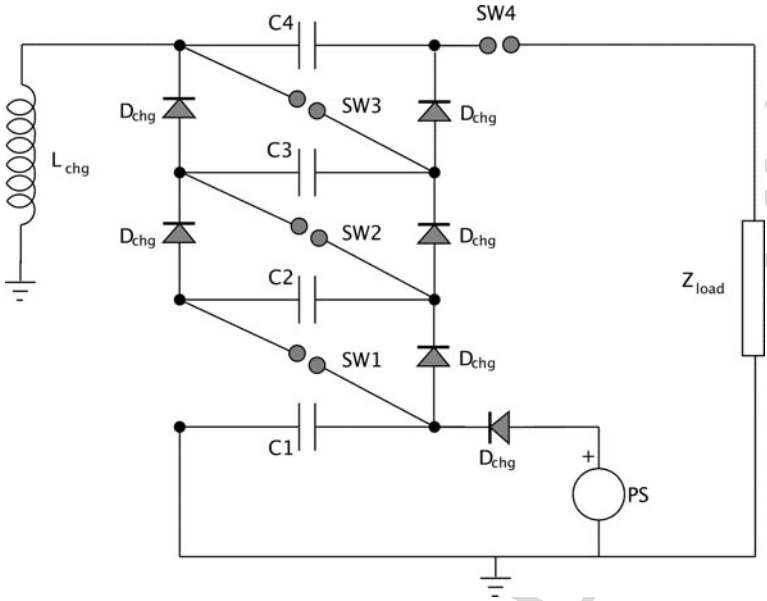

Fig. 4.11 Simplified Marx generator circuit

diodes and adding a charging inductor between ground and the output as seen in Fig. 4.11. While spark gaps are often the switch of choice, the use of other devices such as thyratrons and thyristors are not precluded. With the emergence of solid-state switches having moderately high operating voltages, another significant variation of Marx generators exists. Replacing conventional switches with solid-state opening switches in a diode charged Marx provides many intriguing opportunities to modify the wave shape. Since the switches can interrupt the load current, a more rectangular pulse can be generated. In addition, the diodes provide a current path in the event that a switch is not conducting thereby providing an additional means of changing the wave shape: the voltage contribution from a single capacitor can be added or removed at will by controlling the "on" time of the switch during the pulse. Solid-state switched Marx generators do not currently have the rise time or peak voltage/current capabilities of a spark gap switched Marx but they do provide a broad expansion into applications having waveform requirements usually satisfied only by PFN type systems.

4.1.2 Solid-State Modulators

High-power modulators, not of the line-type configuration, that use solid-state devices are approaching the peak and average power capabilities of line-type pulsers but without many of their limitations. Traditionally referred to as hard-tube modulators, these are pulsers in which only a portion of the stored electrical energy is

UNCORRECTED PROOF

delivered to the load during the pulse. This class of modulator requires a switch that can open while conducting at full load current. The "hard-tube" nomenclature is a reference to the nature of the switch originally used in this circuit topology: hard-vacuum tubes with a control grid(s). Vacuum tubes are high voltage devices capable of very fast switching speeds, however their large internal resistance limits their use in high power, high current modulators particularly when efficiency is an issue. Developments in high power solid-state devices have increased their switching speeds and have led to their incorporation in designs previously utilizing vacuum tubes. Solid-state devices are generally capable of efficiently conducting much higher peak currents (10's–1,000's Amps) than vacuum tube devices but their peak operating voltages are usually substantially less (1–6 kV). Consequently, solid-state switch circuit topologies are utilized that take advantage of the strengths of the devices and minimize their weaknesses.

A basic circuit topology as shown on the left side of Fig. 4.12 is very simple. Essentially, the modulator is a series circuit that consists of a large capacitor bank, a high-voltage switch and a load impedance. If the internal switch impedance is small, the full capacitor voltage appears across the load when the switch closes and disappears when the switch opens. The capacitor bank must be capable of sourcing the load current for the required pulse duration while also satisfying voltage sag requirements at the load. The high voltage switch must be capable of interrupting the full load current while having the switching speed needed to meet the load rise and fall time requirements. Discussed circuit topologies include series switch and inductive adder configurations. The detailed design of an inductive adder is included as an example.

4.1.2.1 Series Switch Configuration

When using solid-state switch components, multiple series connected devices (right side of Fig. 4.12) are usually required to meet the voltage requirements. Such series switch configurations have issues regarding the simultaneity of turn-on and turn-off times as well as voltage grading between devices – particularly during turn-off. The series switch configuration requires power and trigger circuits isolated from ground and additional controls are needed to provide protection to the switch for

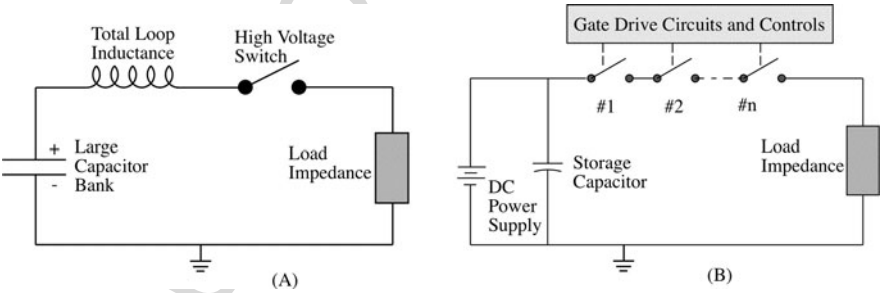

Fig. 4.12 Simplified modulator topology using a fast opening switch

UNCORRECTED PROOF

load and output faults and a load crowbar may be needed to protect the load from switch faults. In a series connected switch, failure of an individual switching device increases the voltage stress on the other series elements and, if enough devices fail, can result in catastrophic failure of the entire switch. Circuit parasitics such as stray loop inductance and stray capacitance to ground affect the rise and fall times of the load voltage and increase the voltage stress across the switch during turn-off due to $L\mathrm{d}I/\mathrm{d}t$. These issues/requirements are solvable and modulators based on this configuration are commercially available. Note that the circuit position of the switch and capacitor are interchangeable in this topology although the grounded switch adds two requirements: isolation from the power supply during the pulse and a load or load shunt impedance tolerant of the charge/recharge current through the capacitor. In either circuit configuration, load voltage of either polarity may be obtained by changing the power supply polarity and reversing the switch terminals. A major advantage of the series switch configuration is the wide range of pulsewidth control. Limited only by the average and peak current ratings for the specific devices used, modulators of this topology have a capability for high repetition rate, high average power, and high peak power. A potential limitation of this configuration is the commutation times and the minimum pulse width: often the controls and switch protection circuitry limit the switch turn-on and turn-off times in order to maintain voltage grading between the series devices.

4.1.2.2 Transformer Coupled

There are other circuit topologies that address some of the issues of the series switch configuration while often creating additional issues. The use of a step-up pulse transformer (see Fig. 4.13) reduces the voltage requirements for the switch and simplifies the trigger/controls by allowing ground referenced circuits. The major issues of this configuration are the potential for very large switch current ($I_{pk} = NI_{\mathrm{load}}$) and a very large $\mathrm{d}I/\mathrm{d}t$ when fast switching times are required. For very fast commutation times or very short pulses, the transformer design is challenging due to the difficulty in meeting the requirement for very tight coupling (low leakage inductance) between

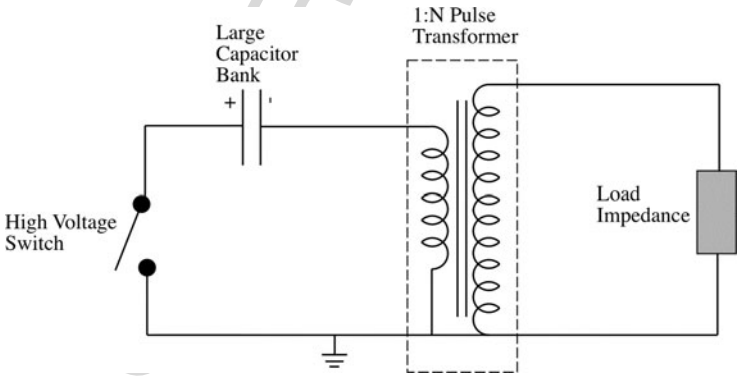

Fig. 4.13 Transformer coupled modulator

UNCORRECTED PROOF

the primary and secondary windings while also satisfying the hold-off requirements for operation at high voltage.

The large peak current and dI/dt issues can partially be resolved by using multiple parallel devices as current sharing between parallel devices is not difficult to achieve. Protection of solid-state devices from very fast voltage transients can be a significant issue as failure of a single device essentially shorts out the switch (and disables the modulator). Consequently, reducing the stray and leakage inductances and the subsequent stored inductive energy in this topology is critical in order to reduce voltage stress during turn-off. It should be noted that the total number of solid-state devices required for a transformer coupled modulator is essentially equivalent to the number of devices used in a modulator using a series connected switch provided that the peak current is the same for all devices and each device operates at the same DC voltage. Operational limitations of the transformer coupled circuit topology are a finite maximum pulse width as determined by the volt-second product of the transformer and a pulse repetition rate limitation due to the transformer needing to be reset between pulses to avoid saturation. For a single turn primary, the volt-second product of a specific magnetic core is equal to the available magnetic flux density, ΔB, times the effective cross sectional area of the core (see Chap. 5).

4.1.2.3 Inductive Adder

A circuit topology that overcomes the major issues of the step-up pulse transformer circuit (very high peak current, dI/dt, and single point failure) is the inductive adder [6–10] as seen in Fig. 4.14. Essentially, the inductive adder consists of modules each having the same circuit topology shown in Fig. 4.14 but with the transformer having a low turns ratio – usually 1:1. The secondary winding of each of these transformers is connected in series and subsequently the step up ratio of $1{:}N$ is achieved by using N modules. In this topology the switch current for each module is the same as the load current and usually each module operates at the same voltage although that is not a requirement. Failure of a single switching device does not result in modulator failure but is seen as the loss of the contribution to the output voltage of that specific module. The voltage stress does not change for the other modules and, since the load current decreases, the current in each module also decreases. As with the transformer coupled topology, the operational limitations of the inductive adder are a finite maximum pulse width as determined by the volt-second product of the transformer and a pulse repetition rate limitation due to the transformer needing to be reset between pulses. This pulse repetition rate limitation is true except in short duration pulse, burst mode operation whereby the volt-second product (average voltage times the pulse width) of the individual pulses is less than the volt-second product of the magnetic core. In burst mode, the maximum number of short duration pulses is limited such that their cumulative volt-second product cannot exceed the magnetic core volt-second product. Modulators based on inductive adder circuit topology have demonstrated great versatility with regard to pulse width and pulse repetition rate while maintaining pulse rise and fall times of less than 10 ns.

UNCORRECTED PROOF

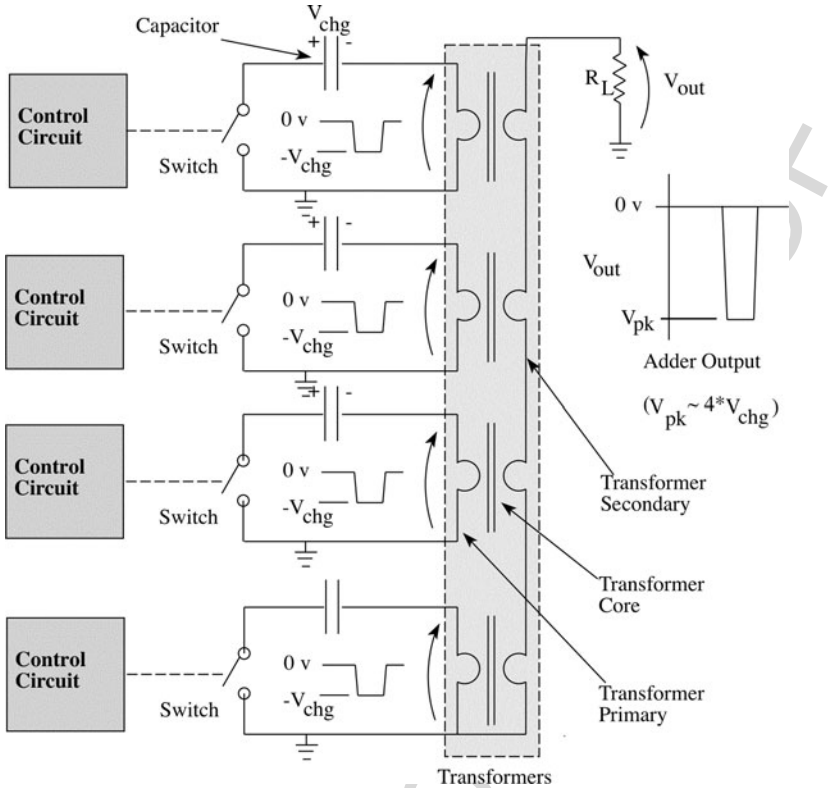

Fig. 4.14 Four module inductive adder

They have demonstrated MHz burst frequencies and, with appropriate cooling, are capable of kHz average repetition rates [11]. At slower rise and fall times, slower solid-state devices that have higher operating voltages and/or higher peak currents can be used thus allowing modulators to be designed for instantaneous peak powers approaching 10^9 watts and average power levels of 500 kW.

When very fast rise and fall times are required, the adder transformer should be designed to look like an induction cell as described in Chaps. 3 and 6, i.e., a single turn primary that totally encloses the magnetic core (often having a toroidal geometry). The leakage inductance of this geometry is negligible and rise times measured in single digit nanoseconds are achievable. The transformer assemblies can be stacked and aligned on the axial center line. The secondary winding for this topology is usually a metal rod extending through the center of the transformer structure and may be grounded at either end of the stack so that an output voltage of either polarity can be attained. It is possible to have a multi-turn secondary winding although this substantially complicates the design and assembly. It should be noted that an inductive adder is very similar, in concept, to the injector for a linear

UNCORRECTED PROOF

induction accelerator whereby multiple inductive cell voltages are added to create a high gradient voltage at the cathode-anode gap.

To further take advantage of the adder topology, solid-state devices should not be series connected so that voltage grading is not required and gate/trigger/control circuits can be ground referenced. In general, faster switching speeds can be achieved when voltage grading is not required. Devices connected in parallel allow for higher load currents and a distributed component layout can be used to reduce the total circuit loop inductance. The parallel operation of solid-state devices does require that turn-on and turn-off jitter be very small; an easily achieved requirement for solid-state devices. Additionally turn-on and turn-off delay times need to be very consistent for all the devices used in the modulator which, in general, precludes the mixing of device types. When the fastest possible switching speeds are required, dedicated closely-coupled gate/trigger drive circuits for each solid-state device are essential. It is also advantageous to use a parallel array of smaller capacitors for the main storage capacitor to further reduce the loop inductance. If the components are mounted on printed circuit boards and connected with wide conductor pads, the loop inductance may be further reduced.

Adder modulator design example: The design of an inductive adder modulator is primarily focused on the design of a single module where a module is defined to be a single pulse transformer and the drive electronics/energy storage for that transformer. The design process is somewhat iterative in that the transformer and drive board should be designed as an integrated unit to achieve the best performance. This may mean that the physical dimensions of one component may need to change to accommodate the physical requirements of another. However, once a module is designed and tested, it may be duplicated as required to build up the entire the modulator assembly. As long as the switches used in a module can handle the peak current, the modules may be stacked up to achieve the required voltage. Consider a modulator with the following requirements:

- Output voltage = 10 kV
- Pulse width (flattop) = 100 ns
- Pulse rise and fall times < 20 ns
- 5 Pulse burst @ 1 MHz repetition rate
- Intra-pulse load voltage < 200 V
- 1 burst/second
- Time jitter < 1 ns
- Load impedance = 50 Ω
- Voltage droop during burst $< 1\%$

In the following sections, we will describe a design process leading to a solid-state adder modulator capable of achieving these parameters.

Solid-state switch: Switch options are driven by the pulse width and rise/fall time requirements. For this specific example, MOSFETs (Metal Oxide Semiconductor Field Effect Transistors) are the only devices currently capable of meeting the switching time requirements. Note that IGBTs (Insulated Gate Bipolar Transistors)

UNCORRECTED PROOF

may be the preferred switching technology for slower switching speeds. MOSFETs have a peak operational voltage of 1,000–1,200 V and there are a number of vendors that manufacture devices with a peak pulse current rating of 40–150 A per device. The required load current is 200 A to which must be added the magnetizing current of the transformer to determine the total switch current. Let's assume that a 1,000 V device is chosen and that these devices are to operate at 700 V DC. The decision on the number of parallel devices used is deferred until other components are selected. Selecting the operating voltage to be 700 V and assuming a nominal voltage drop across the MOSFETs of ~20 V, sets the number of modules required to generate 10 kV pulses at 14.7 which is rounded up to 15.

The MOSFETs shown in the simplified circuit schematic in Fig. 4.15 have their source lead connected to ground. This is chosen so that all the gate drive circuits are also ground referenced, thereby eliminating the need for floating and isolated power supplies. In the physical layout, the pulsed power ground and the drive circuit ground have a common point at the MOSFET source connection but otherwise do not share common current paths; thereby reducing switching transients being coupled into the low-level gate drive circuits.

Excessive voltage transients can be generated across the solid-state device during fast turn-off due to energy stored in the stray loop inductance, energy stored in the transformer primary, and/or voltage coupled into the primary circuit from the secondary (usually due to fault condition or trigger timing differences in stages of the adder). Transient protection for the MOSFETs is provided by the series combination of a snubber capacitor and diode tightly coupled to the MOSFET (see Fig. 4.15). The capacitor is initially charged to the same voltage as the DC capacitor bank and the diode prevents the snubber capacitor from discharging into the MOSFET during the turn-on or conduction intervals. As the MOSFET turns off, transient voltages that exceed the voltage on the snubber capacitor turn the diode on so that the capacitor can absorb the excess energy. A resistor in parallel with the diode allows the excess capacitor energy to discharge into the DC capacitor bank between bursts. Good performance of the over-voltage circuit requires a low inductance capacitor and a diode with a low forward recovery voltage. Additional

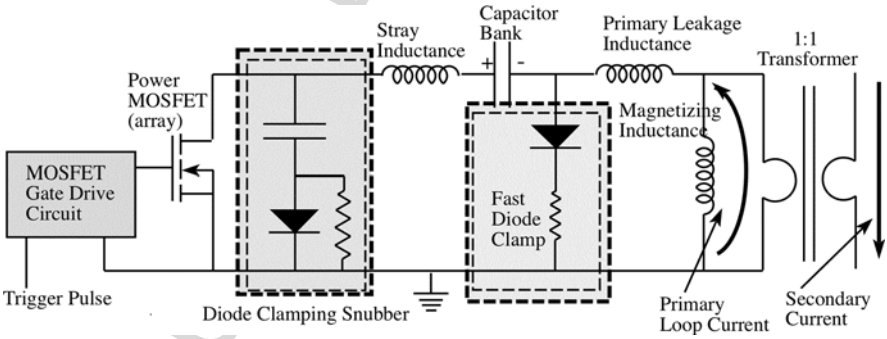

Fig. 4.15 Simplified schematic of adder drive circuit

UNCORRECTED PROOF

protection to the MOSFETs may be provided by a fast diode clipper placed across the primary of the transformer. This diode provides a shunt path for the transformer magnetization current and for current induced into the primary circuit from the secondary winding and is most important if the gate pulse to a specific module is intentionally delayed with respect to the other modules (the latter consideration is not a concern for this design example but may be relevant for other applications).

Transformer design: Two decisions need to be made prior to continuing the design of the pulse transformer; selection of the physical geometry and selection of the magnetic material. The dI/dt for this modulator is on the order of 10 kA/μs which necessitates a very low leakage inductance in the transformer as well as a very small loop inductance in the remainder of the transformer primary circuit. These requirements are easily met by the use of a single-turn primary winding that totally encloses the magnetic core. Structurally, this transformer will look very much like the induction cells described in Chap. 3 when a magnetic core of toroidal geometry is selected. Several magnetic materials can be used including Ferrites, amorphous metals, and nanocrystalline amorphous metals (see Chap. 5). A design using amorphous material will require substantially less material due to their high flux swing and their high permeability reduces the magnetization current. At these voltages, insulating the core from the housing is not difficult so let us choose the magnetic core material to be a spiral-wound toroid wound of amorphous or nanocrystalline metal tape that has a total available flux swing ($-B_{\text{sat}}$ to $+B_{\text{sat}}$) of 2 T. A square-loop annealed core will have the lowest magnetization current and is recommended.

The core cross-sectional area must be sized to accommodate the volt-seconds of the entire burst as there is not sufficient time to reset the cores between pulses in the burst (as set by the intra-pulse voltage requirement). With an average operating voltage of 700 V, the total voltage hold-off (Δt) time of 600 ns (5 pulses each having a pulse duration of 120 ns (full width half maximum)), the area of the magnetic core (A_m) is determined from: $V_{\text{avg}} = N A_m \frac{\Delta B}{\Delta t}$ and $A_m = 700\ \text{V} * 600\ \text{ns}/(2\text{T}) = 2.1\ \text{cm}^2$. To protect the solid-state switches, the transformer should never saturate (a saturated single-turn transformer represents a very low impedance and will result in very large discharge currents through the solid-state switches), so that a volt-second safety factor of at least two is advised. This increases the core area to $\sim 4.2\ \text{cm}^2$. Spiral wound tape cores have a packing factor associated with the gaps between turns and coatings that may be applied. Typical packing factors ranges between 0.7 and 0.85. Choosing the more conservative number the total required core area is now $4.2\ \text{cm}^2/0.7 = 6.0\ \text{cm}^2$. A square cross-section yields a core approximately 2.5 cm on a side. This is a very conservative core design that should provide a substantial safety margin for most operating conditions. The core cost is a small percentage of the total modulator cost and this additional level of safety can usually be justified. The aspect ratio of the toroidal core (outside diameter to inside diameter) is dependent on the operating voltage (used to set the minimum inside diameter) and the physical layout of the drive electronics (these need to be closely connected to the primary winding in order to minimize the loop inductance).

UNCORRECTED PROOF

Capacitor bank: The DC capacitor bank provides the peak current during the pulse but must also be large enough to limit the voltage sag during the burst to $<1\%$. The peak current is the sum of the load current plus the magnetizing current of the transformer. Additionally, the inductance of the capacitor should be small in order that the rise and fall times are not compromised. The inductance of a standard capacitor package designed to have a low-inductance has a range of 10–50 nH and this is roughly independent of the capacitance value. The voltage developed across a stray inductance of 10 nH is 100 V for a $\mathrm{d}I/\mathrm{d}t$ of 10 kA/μs. To further reduce the inductance, a parallel array of capacitors is used. The total capacitance required easily determined from the relation: $i_{\mathrm{avg}} = C\Delta V/\Delta t$ where i_{avg} is the average current ~~during the pulse times the number of pulses in the burst~~, ΔV is the voltage droop during the burst, and Δt is ~~the total pulse duration~~. For this design, let's use a value of magnetizing current of 30 A. With a 230 A total load current, a 600 ns total pulse duration, and 1% voltage droop requirement for a ΔV of 7 V, the total capacitance is calculated to be 19.7 μF. Standard plastic film capacitors at this operating voltage are available in values up to ~1 μF thus requiring the array to consist of a minimum of 20 capacitors.

General component layout: Since the transformer core and transformer have a toroidal geometry, it is reasonable to arrange the components in a circular pattern around the transformer. This gives a compact layout and also achieves a very important design criteria: in a symmetrical circular pattern, it is easy to generate a conduction path (loop consisting of the capacitor(s), MOSFET, and transformer primary) for each MOSFET that has geometrically identical inductances. Since this is a very fast, low impedance circuit it is very important that each MOSFET see the same series inductance to ensure current sharing during both turn-on and turn-off.

Following these general guidelines, a reasonable layout is for the DC bank capacitors to be arranged in a symmetric circular pattern around the outside diameter of the transformer, the MOSFETs to be arranged radially just outside the capacitors, and since the MOSFET gate drivers should be closely coupled to their switches, they will be located radially just beyond the MOSFETs. This layout also satisfies the need to decouple the low level signal of the gate drive circuit from the high currents in the transformer primary circuit. Note that since the number of MOSFETs and DC capacitors are the same (20 of each required per module), it is very reasonable to couple the two components closely together in the layout and achieve very good symmetry and therefore virtually identical loop inductances. If the number of capacitors were slightly less than the number of required MOSFETs, it would be reasonable and prudent to increase the number of capacitors used in order to achieve this symmetry.

As a radial layout tends to increase the spacing between components as the diameter increases, additional space is available for the transient suppression circuit while still maintaining the required close coupling to the MOSFETs. A final layout consideration is that the gate drive circuits need to be triggered simultaneously so that the electrical lengths (propagation times) of the paths from the trigger source to the gate drive circuits are identical. This timing requirement also applies to all the boards in the adder assembly. Careful consideration of the distribution of the low level trigger to modules is important. Fortunately, since the noise levels are low,

UNCORRECTED PROOF

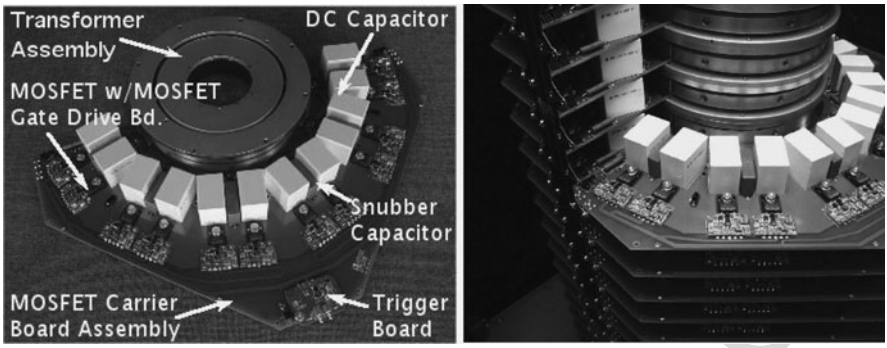

Fig. 4.16 Examples of an adder module consisting of a drive board and transformer and an adder assembly

this distribution can usually be achieved by using cables having identical lengths between the trigger source and the modules. A representation of how the final component layout could appear and an assembly of modules are shown in Fig. 4.16.

Reset/bias circuit: Not shown in the simplified adder circuit layout (see Fig. 4.15) is a reset circuit for the magnetic cores. The cores require reset prior to operation so that they do not saturate during a voltage pulse. If this circuit operates in a pulse burst format or if the interval between pulses is long, a DC reset circuit can be used and is implemented by connecting a DC power supply through a large isolation inductor to the ungrounded end of the secondary winding of the adder stack. In the long interval between bursts or for low duty cycle pulses, the reset current will reset and bias the magnetic cores. When the magnetic cores must be reset quickly between pulses, active (pulsed) reset applied to either the primary or secondary side of the transformer is often used. Active reset circuits are more complicated than DC reset and usually require a controlled switch, charged capacitor, timing/trigger pulse and associated control circuitry as well as some circuit element to isolate the reset circuit from the high-voltage pulse.

- Inductive Adder
  - Advantages
    - Fast rise and fall times
    - Very high dI/dt
    - Very high Burst Frequencies
    - Burst frequency agility
    - Pulse width agility
    - Easy to control and trigger
    - Modular
  - Disadvantages
    - Not compact
    - Many components required
    - Pulse width limitation

UNCORRECTED PROOF

4.2 Switching Devices

As mentioned at the beginning of this chapter, the performance and capabilities of the various modulators are determined by the capabilities and limitations of the switches used. This section will discuss switches commonly used as well as some less commonly used devices and present a glimpse into components that will be incorporated into future designs of induction accelerators particularly as applications for high repetition rate accelerators advance. This section is not intended to provide detailed insight into the physics of device operation but to provide an overview. Detailed information of device operation and performance capabilities may be found at vendor websites and published literature.

4.2.1 Closing Switches

Most high voltage, high power switches are closing devices. These may only be used in modulator topologies such as PFNs, Blumlein lines, and Marx generators which historically have dominated linac pulsed power designs. Commonly used closing switches are spark gaps, thyratrons, and thyristors. Magnetic switches are not pure closing switches as they do not have a DC blocking capability but they have been used in high average power and high repetition rate applications.

4.2.1.1 Spark Gaps

Spark gaps are the most commonly used closing switch for very high voltage, high current circuits [10]. In their basic form they consist of two electrodes between which an electrical discharge is initiated to close the switch. The region between these electrodes may be high vacuum, gases (usually at high pressure), liquids, and even solid materials with the choice being determined by the hold-off voltage and the switch package size/inductance. Each of these gap mediums has its own breakdown characteristics which determines the overall performance and capabilities as well as the limitations of that specific spark gap. Spark gaps are commercially available and specific information regarding performance and lifetimes for specific designs may be found in vendors literature.

The method by which breakdown is initiated in the spark gap is critical in order to achieve low time jitter, one of the essential requirements for an induction accelerator. The actual time required for a spark gap to begin conduction is a strong function of how close to self breakdown (untriggered) the device is operated but statistically spark gaps will occasionally break down at voltages substantially lower than the peak self breakdown voltage. Synchronization of inductive cell acceleration voltages must usually be controllable and repeatable on ns time scales and this jitter requirement precludes the use of untriggered spark gaps and essentially mandates the use of either vacuum or gas filled spark gaps. Once a spark gap is triggered, it will remain in an ON state throughout the discharge and remain conductive until all the plasma and ionization products generated by the pulse discharge

UNCORRECTED PROOF

have completely dissipated. This time interval is strongly dependent on the external circuit and how it couples energy into the spark gap after the main conduction pulse and can easily extend into milli-second time scales. This is the cause of a fundamental repetition rate limitation for spark gaps. Heroic measures such as the use of high velocity blower ~~system~~ are required to push operation of a spark gap to the kHz repetition rates achieved in the ETA/ATA , accelerator modules (see Sect. 2.3). Electrode erosion is also a serious issue that results in spark gaps having relatively short life times – on the order of single shots to a few million shots depending on the total charge transfer in the switch, the pulse duration, and electrode materials.

The overall performance of a spark gap is determined by so many factors that it is not practical to list all the possible variations of electrode material, electrode geometry, electrode separation, gas mixtures, operating pressures, and trigger methods. It is sufficient to note that much research and testing has been done and is still being performed to improve the performance and capabilities of spark gaps.

- Spark Gaps
  - Advantages
    - Low cost
    - Operates at voltages of kilovolts to megavolts
    - Can switch mega-Amp currents and very high $\mathrm{d}I/\mathrm{d}t$
    - Fast switching times
    - Can be very compact
  - Disadvantages
    - Limited lifetimes
    - Low repetition rates
    - Low turn-on jitter requires fast trigger (high-voltage, laser, etc)

4.2.1.2 Thyratrons

Thyratrons are extensively used in high power modulators, particularly those with high repetition rate requirements. These devices are grid controlled, gas filled tubes having a basic configuration consisting of three electrode structures: anode, cathode, and a grid although an extra grid may be added to reduce turn-on delay times and jitter. The cathode is the electron emitting surface and is most readily available in a heated oxide coated version although cold cathode tubes are also available. Heated cathode devices are used when low time jitter is required. Internal gas reservoirs may also be added to extend the operational lifetime and to control performance. Adjustments to the reservoir heater supply permit the internal gas pressure to be controlled. Lower internal gas pressure gives thyratrons a higher voltage hold-off capability and a decreased recovery time but with the trade-off of lower $\mathrm{d}I/\mathrm{d}t$. Higher reservoir voltages increase gas pressure thereby enabling higher $\mathrm{d}I/\mathrm{d}t$ and longer pulse conduction but with reduced hold-off voltage and increased tube recovery time. Several different gases including mercury vapor, xenon, hydrogen, and

UNCORRECTED PROOF

deuterium have been used in thyratrons. As the lighter gases recover more quickly and allow higher repetition rate operation, hydrogen and deuterium filled tubes are most often used in pulsed power applications. Thyratrons are commercially available from multiple vendors with a wide range of operating voltage and peak current ratings in either glass or ceramic housings.

Single-gap triode and tetrode thyratrons have an operational anode-cathode range of a few kV to approximately 40 kV. The operational voltage can be extended to greater than 150 kV by using multiple gaps. Thyratrons are capable of switching peak currents in the range of 10's of Amps to 10's of kilo-Amps although the average current ratings are usually less than 5 A. The total charge for a given pulse is limited by the size of the cathode electrode and exceeding that charge limit can damage the tube. With fast trigger voltages, thyratrons in pulse modulator applications routinely achieve time jitter of less than 1 ns and dI/dt approaching 10 kA/μs. When operated within their ratings, thyratrons exhibit long lifetimes as measured by total number of pulses (10^{10}–10^{11} pulses), however, their total on-time life is usually limited by cathode depletion (oxide cathodes) to 1–2 years. Operational lifetime may be extended by operating the cathode filaments at DC, accurately controlling internal gas pressure, and by using magnetic assists (non-linear magnetic switch) in the anode circuit. Operational lifetime is shortened by large dI/dt and long duration currents that can cause hard internal arcs due to quenching which can subsequently result in anode damage.

Operationally, when the grid is negatively biased (−20 to −100 V) with respect to the cathode, the thyratron is able to support full rated voltage. A positive trigger voltage pulse (usually less than 1 kV) applied to the grid turns the thyratron on and initiates current conduction. After the thyratron has been triggered, a glow discharge is initiated and the grid loses control. The thyratron can only be turned off and grid control regained when the anode voltage is reduced below the ionization potential of the fill gas. The low anode voltage must be maintained for a time period sufficient for the internal plasma to dissipate and the high impedance state regained before anode voltage can be reapplied. Thyratron recovery time is largely dependent on the external circuit but maximum recovery time is on the order of 10–100 μs for single gap tubes and much longer for multi-gap tubes. Negative grid bias can substantially reduce recovery times. A small inverse voltage (less than 5% of the peak operating voltage) after current conduction is also useful in decreasing the recovery time but thyratrons do need to be protected from large inverse voltages for at least 25 μs after conduction in order to prevent hard internal arcs and tube damage.

- Thyratrons
  - Advantages
    - High repetition rate capability
    - Low jitter
    - Moderate operational voltage
    - Fast switching times
    - Compact

UNCORRECTED PROOF

- Moderate lifetime
- Easy to trigger

– Disadvantages

- Moderate cost
- Requires auxiliary power supplies
- Low average current capability
- Prone to timing drift
- Can generate X-rays at higher operating voltages

4.2.1.3 Thyristors

Thyristors or Silicon Controlled Rectifiers (SCRs) are gate triggered solid state devices that operate in a manner very similar to thyratrons. As the power switching capabilities and switching speeds of thyristors increase, they are increasingly being incorporated into new high power modulator circuit designs and replacing thyratrons in existing systems. Thyristors are three terminal devices (anode, gate, and cathode) and have the highest power switching capability of all solid state devices.

The dominating attribute of thyristors is their very high peak and average current switching capability. Devices are available that have current ratings of greater than 5,000 A RMS and peak surge current ratings of approximately 100 kA. The highest power, highest voltage thyristors are normally fairly slow devices that have found extensive applications as phase control devices in the power industry. However, devices optimized for pulsed power applications are now available that have very respectable operating voltages (in the range of 8 kV), RMS current ratings greater than 5 kA, and perhaps most importantly high dI/dt (ratings $\geq$ 5,000 A/μs). Thyristors are manufactured by many vendors with a wide range of operating voltages and peak current ratings. The standard package for most of the high voltage devices consists of a low inductance cylindrical ceramic housing with electrodes on both ends (hockey puck configuration) that requires substantial compression force to make up the electrical connections.

Most thyristors are capable of handling equal peak forward and reverse voltages although some devices trade off a small reverse blocking capability for lower forward conduction losses. With a positive voltage across the anode-cathode electrodes, thyristors are turned on when a small positive gate voltage and the corresponding current injection is applied to the gate-cathode junction. Once the anode current exceeds the latching current, gate drive is no longer required and the device will remain in conduction until the anode-cathode current returns to a value less than the holding current. The holding current is the minimum value that the device requires to remain in the conduction state in the absence of gate drive current. As with the thyratron, a finite recovery time (on the order of 15–100 μs) is required after current conduction before positive anode voltage can be reapplied. This recovery time is the time required for recombination of carriers within the device and may be reduced by material processing techniques that introduce recombination sites such as irradiation

UNCORRECTED PROOF

and the implanting of various impurities. The recovery time can also be reduced by application of an inverse anode-cathode voltage by the external circuit.

The trigger input is a p–n junction and the gate drive requirements for a thyristor are modest in terms of voltage and current. Internally, the thyristor gate-cathode structure is a self regenerative circuit and reliable, low jitter triggering is easily achievable with a gate drive voltage of less than 2 V and a drive current on the order of 10's–100's of milli-Amps. However, this turn-on mechanism is rather slow and some devices may take 50–100 μs to become fully conductive thereby limiting the peak dI/dt. Most fast or inverter grade devices increase the dI/dt capability by incorporating a highly interdigitated gate electrode and may then require Amp scale gate drive currents. Recently thyristors have become available that are light triggered devices whereby a laser diode is coupled to the thyristor via fiber optics thereby providing both a very fast turn-on capability (high dI/dt) and excellent voltage isolation between the device and the gate drive circuit.

Thyristors are not as robust as spark gaps or thyratrons in that they can suffer catastrophic failure if their maximum voltage ratings or their peak dI/dt rating is exceeded. They are also susceptible to self triggering if the anode-cathode dV/dt rating is exceeded. However, with appropriate design and device protection, thyristors can exhibit very long lifetimes. Devices may also be connected in series or parallel to meet system voltage and current requirements. Being solid-state devices, thyristors are instant on devices that do not require the heater supplies or warm up times associated with thyratrons.

In addition to the fast inverter grade thyristors and devices optimized for pulsed power applications, several other variations have been developed. Gate turn-off (GTO) thyristors use an extremely highly interdigitated gate structure that provides a capability of turning off the thyristor provided sufficient reverse gate drive is provided. When first developed, these devices provided a unique capability but the continuing development of IGBTs has reduced their attractiveness. The Static Induction Thyristor (SIT) was developed to be a substantially faster device while still being capable of switching higher voltages [12] and high currents at very high dI/dt. While normally used as a closing switch, in some circuit configurations, the SIT has been operated as an opening switch.

- Thyristors
  - Advantages
    - High repetition rate capability
    - High average current capability
    - Low jitter
    - Long lifetime
    - Compact
    - Easy to trigger
    - Low cost and simple gate drive circuit
    - Moderate cost

UNCORRECTED PROOF

– Disadvantages

- High voltage ratings may require series connected devices
- Catastrophic failure can result from exceeding voltage and dI/dt ratings

4.2.1.4 Magnetic Switches

A unique modulator topology that has found applications in high repetition rate power systems is based on the energy compression capabilities of magnetic switches [13–15]. Magnetic switches are devices that rely on the non-linear properties of magnetic materials to perform an energy transfer from input to output. They do not have a DC hold-off capability and therefore, with few exceptions, require the use of another "real" switch such as a thyratron or thyristor [16]. Magnetic switches are of special interest because of their high peak power switching capability and inherent robustness. Because the magnetic switches handle the very stringent final switching requirements required by some loads, they facilitate the use of other switching devices either by extending their lifetimes or by allowing those devices to operate within a safe operating regime. Since magnetic switches are not generally available commercially and must be designed by the user, a more detailed discussion follows. Historical information on high repetition rate induction technology applications employing magnetic switches can be found in Sect. 2.5.

In its most simple form, a magnetic switch is a coil or winding which has a core material composed on a non-linear ferromagnetic or ferrimagnetic material. The critical property of the magnetic material is that it exhibits a distinct change of state from high to low permeability when certain voltage and time parameters (volt-second product) are met. The change of permeability results in the coil inductance "switching" from a high (unsaturated) to low (saturated) inductance value. The permeability change can have a range of several hundred to several thousand and is dependent on the type of magnetic material selected. The term magnetic compression describes the process whereby energy is transferred sequentially through multiple magnetic switches with each energy transfer occurring in a shorter time period thereby resulting in higher peak power levels. Voltage gain can be obtained in magnetic compression circuits by using pulse transformers between or after stages of compression. Most magnetic switch geometries use either a toroidal, solenoidal, or racetrack coil geometry; i.e. geometries for which inductances are well defined and may be more easily calculated.

The general circuit topology for a magnetic compression circuit is shown in Fig. 4.17. This figure depicts intermediate stages whereby the inductances of the magnetic switches are represented as L_{n-1} and L_n in their unsaturated state and L_{n-1}^{sat} and L_n^{sat} in their saturated state. The energy storage capacitors, C_{n-1}, C_n, and C_{n+1}, are usually equal or nearly equal in value for high efficiency energy transfer.

A stage of magnetic compression has three components: an input capacitance, a saturating inductance, and a load which is usually another capacitor. To describe the operation of the circuit shown in Fig. 4.17, begin by assuming that there is a voltage of amplitude V_{pk} on C_{n-1} and that L_{n-1} is about to saturate to its low inductance

UNCORRECTED PROOF

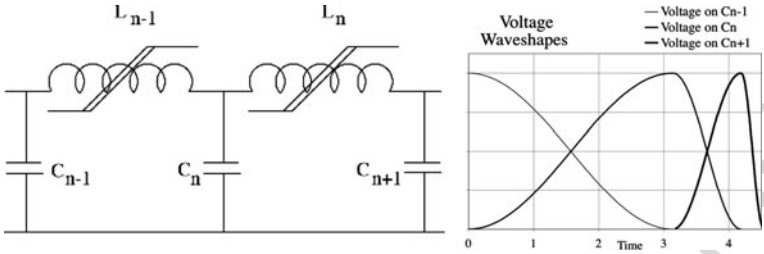

Fig. 4.17 Intermediate stages and voltage waveforms of a magnetic compression circuit

value. Upon saturation of L_{n-1}, the time required for C_{n-1} to discharge through L_{n-1}^{sat} and charge C_n is:

$$\tau_{C_n}^{\text{chg}} = \pi\sqrt{L_{n-1}^{\text{sat}}\frac{C_n}{2}} \tag{4.12}$$

The waveform of the current through the inductor is sinusoidal and the charge voltage waveform on C_n has the form of $1 - \cos\omega t$. When designed properly, L_n will remain in its unsaturated state until the voltage peaks on C_n at which point L_n will saturate and energy will be transferred to C_{n+1} at a rate faster than C_n was charged.

The gain of the magnetic switch stage L_n can be defined as the ratio of the charge time to discharge time for the capacitor C_n for the circuit shown in Fig. 4.17. For efficient operation, the time to saturation (hold-off time) of a magnetic switch is set approximately equal to the charge time on the capacitor. This hold-off time is defined by algebraic manipulation of Faraday's Law to be:

$$\Delta t = \tau_{C_n}^{\text{chg}} = \frac{N_n A_n \Delta B}{V_{\text{avg}}} \tag{4.13}$$

where N_n is the number of turns in the switch winding, A_n is the cross-sectional area of the magnetic core, ΔB is the total magnetic flux swing available in the core, and V_{avg} is the average voltage during the interval Δt. The previous two equations can be solved for L_{n-1}^{sat} to yield:

$$L_{n-1}^{\text{sat}} = \frac{\left(\frac{2N_n A_n \Delta B}{\pi}\right)^2}{\frac{1}{2}C_n {V_{pk}}^2} = \frac{\left(\frac{2N_n A_n \Delta B}{\pi}\right)^2}{E_{C_n}} \tag{4.14}$$

where E_{C_n} is the peak energy stored on C_N and noting that V_{avg} is equal to $V_{pk}/2$ for the charging waveshape of the form of $1 - \cos\omega t$.

To minimize the required core area and subsequently the total core volume, the magnetic flux density of the core is normally operated in the range from either $-B_{\text{sat}}$ or $-B_r$ to $+B_{\text{sat}}$. The capacitor discharge time is proportional to the $\sqrt{L_n^{\text{sat}}}$ which is purely a function of the winding dimensions of the switch inductor without

UNCORRECTED PROOF

its magnetic core (i.e. its air core inductance). Maximum gain is achieved by minimizing the air core inductance which, in turn, requires that the winding be placed as close as possible to the magnetic core. Typical stage gains are in the range of 3–10 and, subsequently, multiple stages are required to achieve high overall energy compression. For example: a compression circuit consisting of three stages, each stage having a gain of 3, yields an overall gain of approximately 27 and can convert a 1 μs charge time at the input into a 37 ns charge time at the output.

In operation it is also desirable to minimize the prepulse on the switch output, so the unsaturated inductance must be much larger than the saturated inductance of the previous switch ($L_n >> L_{n-1}^{\text{sat}}$). The performance of a magnetic switch is strongly dependent on both the properties of the magnetic material and the form factor of the winding that encloses the core. If the winding is not closely coupled to the core material, the saturated inductance will be larger and the switch will have a smaller gain.

Design of a magnetic switching circuit can be divided into two parts. After selection of the core material and the required switch gain, the electrical design consists of calculation of the core cross-sectional area and calculation of the number of turns (N) for the selected core/winding geometry. The second part of the design is the mechanical design. This can be very challenging as it entails meeting the usually contradictory requirements of close spacing of the winding to the magnetic core while also satisfying the turn-to-turn and turn-to-core spacing requirements for a winding operating at high voltages. Maintaining low inductance connections to the capacitors is also essential as stray connection inductance reduces the overall performance of a magnetic compression circuit. Additionally, the mechanical design must also support the weight of the switch assembly as well as handle the forces generated by the peak currents. The final design is an iterative process whereby the core geometry and winding geometry are adjusted until the number of turns is a reasonable integral number.

The most commonly used switch designs are based on the use of toroidal magnetic cores. The inductance of a toroidal winding of rectangular cross section is:

$$L = \frac{1}{2\pi}\mu_r\mu_o w N^2 \ln\frac{\text{OD}}{\text{ID}} \tag{4.15}$$

where μ_r and μ_o are the relative and free space permeability, w is the length of the winding and OD and ID are the winding outside and inside diameters. Substituting the saturated values for switch L_n into this equation gives:

$$L_n^{\text{sat}} = \frac{1}{2\pi}\mu_r^{\text{sat}}\mu_o w N^2 \ln\frac{\text{OD}}{\text{ID}} \tag{4.16}$$

Dividing this into Eq. (4.12) and noting that $L_{n-1}^{\text{sat}}/L_n^{\text{sat}} = (\tau_{C_n}^{\text{chg}}/\tau_{C_{n+1}}^{\text{chg}})^2 = \text{Gain}^2$ yields the following expression that relates per stage gain to material properties, winding geometry and per stage energy transfer thereby providing a means to compare switch designs.

UNCORRECTED PROOF

$$\frac{L_{n-1}^{\text{sat}}}{L_n^{\text{sat}}} = \text{Gain}^2 = \frac{8\Delta B_s^2 A_n^2}{\pi \mu_r^{\text{sat}} \mu_o w_n \ln \frac{\text{OD}}{\text{ID}} E_{C_n}} \tag{4.17}$$

Another useful approximation can be derived by taking the expansion for the natural log term, $w_n \ln(\text{OD}/\text{ID}) \sim w_n \Delta r / r_{\text{avg}} = A_n / r_{\text{avg}}$ and substituting into the previous equation to get:

$$\text{Vol}_n \sim \frac{\text{Gain}^2 E_{C_n} \pi^2 \mu_r^{\text{sat}} \mu_o}{4\Delta B_s^2} \tag{4.18}$$

Where Vol_n represents the minimum volume of magnetic material (and therefore minimum loss) required for a switch, L_n, given a required gain, per pulse switched energy, and ΔB_s. This equation assumes that the entire toroidal winding volume is filled with magnetic material and while this is never achievable, it is a viable figure of merit. Further examination of this relationship shows that the minimum core volume increases rapidly as the stage gain increases and means that an efficient design (considering only magnetic core losses) is achieved with several stages of compression rather than with a single, high gain compression stage. Another observation is that the volume scales inversely with the square of the available flux swing. This limits the practical gain of a ferrite ($\Delta B \sim 0.6$ T) switch to a design value of $\sim$3 while the substantially higher flux swing of an amorphous metal ($\Delta B \sim 3.2$ T) allows switch gains approaching 10.

An important design consideration is related to how the magnetic switch or switches are prepared for operation. After saturation, the magnetic core material must be "reset" to a repeatable magnetic state prior to the next switching event. If low time jitter is important, the core needs to be reset such that the available flux swing does not vary on a pulse to pulse basis. A DC reset consisting of a low voltage DC power supply and an isolation inductor and connected through the center of the magnetic core is a simple means of satisfying this requirement. After saturation at $+B_{\text{sat}}$, the current flowing in the inductor acts as a current source and will provide whatever voltage is necessary to drive the magnetic core back along its B–H curve towards $-B_{\text{sat}}$. Once reset, the H-field generated by the current will bias and hold the core to the stable and repeatable initial operating point needed for low jitter pulse generation. Another method of resetting a magnetic core uses a pulsed source such as a charged capacitor and a switch. Pulsed reset circuits have the advantage of shorter reset times (necessary in high repetition rate systems) but have the issues of increased circuit complexity and higher costs.

A single magnetic switch can also be connected directly in series with a closing switch. In this application, the magnetic switch (commonly referred to as magnetic assist) is used to provide a time delay prior to the closing switch conducting the full peak current. This time delay with its accompanying leakage current can provide the time necessary for the closing switch to prepare for a large $\mathrm{d}I/\mathrm{d}t$ and/or a large peak current. Magnetic assists have been found to be particularly useful in fast thyristor circuits and in extending the operational life of thyratrons.

UNCORRECTED PROOF

- Magnetic Switches
  - Advantages
    - Extremely robust
    - Very high voltage and very high current capabilities
    - Long life
    - High repetition rate capability
    - Capable of generating short duration pulses
  - Disadvantages
    - Complicated to design
    - Not compact
    - High weight
    - Requires a closing switch
    - Requires a reset circuit
    - Low jitter is achievable but requires external control circuitry or precision voltage supplies

4.2.2 Closing Switches with an Opening Capability

There are only a few switches that have an inherent capability of not only being gated ON but also gated OFF with very short switching transition times. Devices with these characteristics are used in modulator applications requiring high repetition rates or high burst frequencies. Most of the switches that have a turn-off capability are solid-state devices that are limited in their peak voltage and peak power ratings to values considerably lower than gas switches or thyristors. These solid state devices often require special circuit topologies such as inductive adders or Marx configurations to reach system requirements. Vacuum tube devices, while having unique high speed, high voltage switching capabilities, are not often considered for pulsed power systems due to their high intrinsic internal impedance and subsequent poor energy efficiency and will not be discussed.

4.2.2.1 Metal Oxide Field Effect Transistors – MOSFETs

MOSFETs are the fastest of the solid state devices and have demonstrated switching times, both ON and OFF, of less than 10 ns. MOSFETs are voltage controlled, three terminal devices (drain, gate, and source) and are commercially available from a large number of vendors with peak voltage ratings of 1,000–1,200 V and peak current ratings in the range of 30–150 A. While their peak power capability is modest, these devices may easily be operated in parallel. Series operation is also possible but does require more effort to achieve equal voltage grading for each series device and deliver adequate gate (trigger) pulses. Being solid state devices they inherently have sub-nanosecond jitter. Vendors usually provide MOSFETs in standard power

UNCORRECTED PROOF

semi-conductor packages (TO-220, TO-247, TO-264, etc) but devices are increasingly becoming available in the lower inductance packages that are needed to fully capitalize on MOSFET's switching capabilities.

A major advantage of MOSFETs over other switching devices is their ease of gating ON and OFF and their very small gate trigger power requirements. The gate-source junction is essentially a capacitance (whose value scales with the average current rating of the MOSFET) and must be charged and discharged to effect the switching transitions. Once the device is gated ON, no additional power is required to keep the device ON. While the energy required to turn on a MOSFET can be measured in μJ, the peak gate current for the very fastest switching times requires 10's of Amps and may require a dedicated gate drive circuit for each device. Fortunately, there are a number of commercial gate drive circuits that can satisfy all but the most stringent switching requirements. The commercial sector is also continually improving the performance of both MOSFETs and MOSFET drivers with regard to their peak power capability and switching speeds.

Most power MOSFETs are N-channel enhancement mode devices. They block positive polarity drain to source voltages and are gated ON with positive polarity gate to source voltages. Their internal structure includes an intrinsic anti-parallel diode. Consequently, these devices do not have a reverse blocking capability. MOSFET current conduction is initiated when the gate voltage exceeds a device dependent threshold voltage and terminates when the gate voltage drops below the threshold. MOSFETs are normally rated as having a finite ON resistance that tends to limit the peak pulse current during fault conditions but are prone to catastrophic failure due to inductive voltages generated during high dI/dt turn-off.

- MOSFETs
  - Advantages
    - Very fast switching transitions
    - High repetition rate capability
    - Capable of generating short duration pulses
    - Long life potential
    - Easy to control
    - Low jitter
  - Disadvantages
    - Low voltage, low current devices
    - Parallel devices needed for high current
    - Special circuit topologies needed to obtain high voltage
    - Voltage induced failure usually catastrophic

4.2.2.2 Insulated Gate Bipolar Transistors – IGBTs

IGBTs are a three terminal device (Collector, gate, and emitter) and are essentially a bipolar transistor with a MOSFET input. They have the advantages of a MOSFET

UNCORRECTED PROOF

with regard to ease of triggering and trigger circuit design and the increased peak power, current density, and voltage rating of bipolar transistors. While not having the ultimate switching speeds of MOSFETs, IGBTs are capable of switching transitions of less than 20 ns for smaller devices and approximately 200–500 ns for larger devices. IGBTs are now used in many high average power applications and are replacing thyristors in many new designs. As the manufacturers increase their switching speeds, IGBTs are replacing MOSFETs in moderate frequency switching power supply designs. With large modules having peak operational voltages of 6.5 kV in conjunction with average currents of 600 A, IGBTs dominate the traction and motor control industry. Many vendors offer IGBTs and these devices are available in the same power semiconductor packages as MOSFETs as well as larger module and hockey puck configurations.

Currently few of the large power IGBTs are optimized for pulsed power applications particularly with regard to low inductance packages and distribution of gate triggers. That has not prevented them from being used in pulse applications requiring short duration (μs) pulses at peak power levels approaching 10^9 W. As with MOSFETs, these devices can easily be operated in parallel to increase peak current capability and very high voltage operation requires the use of special circuit topologies or series connection. The turn-off characteristics of most IGBTs are not as clean as MOSFETs and they tend to have a tail current that can take μs to extinguish. As with most solid-state devices, IGBTs are subject to catastrophic failure when subjected to voltages exceeding their maximum peak rating. While the devices have a reasonable surge rating, sense circuitry coupled to the gate drive is usually needed to protect the devices from short circuit conditions.

- IGBTs
  - Advantages
    - Fast switching transitions
    - High repetition rate capability
    - Long life potential
    - Easy to control
    - Low jitter
    - Moderate peak voltage ratings
    - Moderate to high peak current ratings
  - Disadvantages
    - Limited capability for generating short duration pulses
    - Voltage induced failure usually catastrophic
    - Special circuit topologies needed to obtain very high peak voltage

4.2.2.3 Capacity of Semiconductor Switches

Several types of semiconductor switching device have been invented as described above. Figure 4.18 is a performance map of high power semiconductor switches,

UNCORRECTED PROOF

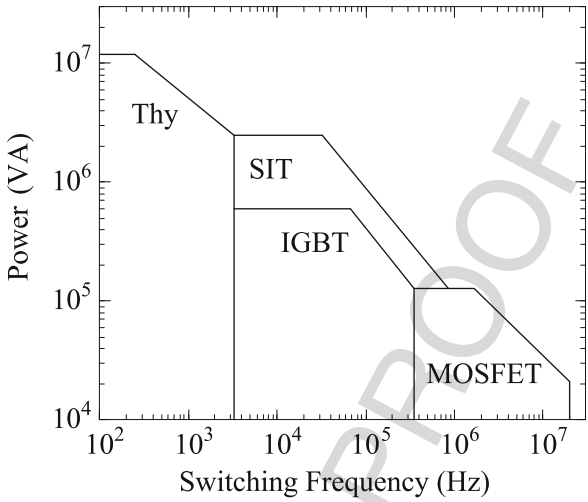

Fig. 4.18 Performance map of typical switching devices

in which the maximum capacities of thyristors (Thy), static induction thyristors (SIT), insulated gate bipolar transistors (IGBT) and metal oxide semiconductor field effect transistors (MOSFET) are schematically shown. The power in the figure is the product of rating voltage and current, and the frequency is a reciprocal number of switching time divided by 10.

4.2.2.4 Silicon Carbide Devices

Silicon Carbide is often recognized as the most likely candidate solid state material for the next generation of high power devices. Silicon Carbide has a much higher electrical breakdown strength and thermal conductivity when compared with silicon which would allow higher voltage, high temperature devices to be manufactured. They are also anticipated to have excellent switching transition times. Currently, the only devices commercially available are diodes but, as the quality of base material improves and manufacturing techniques advance, these devices are expected to be available in the form of high voltage MOSFETs [17] and IGBTs within a few years.

References

1. S. Pai and Q. Zhang. *Introduction to High Power Pulse Technology*, World Scientific, Singapore, 1995.
2. P. Smith. *Transient Electronics Pulsed Circuit Technology*, Wiley, West Sussex, England, 2002, see Chapters 2–4.
3. G. Glasoe and J. Lebacqz, editors. *Pulse Generators*, Dover Publications, Inc., New York, NY, reprinted 1965, see Chapter 6, same as Ref. [4].
4. L. Ridenour, editor. *Radiation Laboratory Series 5. Pulse Generators*, McGraw-Hill, New York, NY, 1948, see Chapter 6, same as Ref. [3].

UNCORRECTED PROOF

5. T. Gallagher and A. Pearmain. *High Voltage Measurement, Testing and Design*, Wiley, New York, NY, 1983, see page 105.
6. H. Kirbie, S. Hawkins, B. Hickman, B. Lee, M. Newton, C. Ollis, C. Brooksby, D. Gilbert, D. Longinotti, and E. Eubank. Development of Solid-State Induction Modulators for High PRF Accelerators. In *Proceedings of the 10th IEEE International Pulsed Power Conference*, pages 441–447, Albuquerque, New Mexico, 10–13 July 1995.
7. E. Cook, B. Lee, S. Hawkins, F. Allen, E. Anaya, E. Gower, B. Hickman, and J. Sullivan. Solid-State Kicker Pulser for DARHT-2. In *Proceedings of the 13th IEEE International Pulsed Power Conference*, pages 632–635, Las Vegas, Nevada, 20–23 June 2001.
8. E. Cook, B. Lee, F. Allen, E. Anaya, E. Gower, S. Hawkins, B. Hickman, J. Sullivan, J. Watson, C. Brooksby, J. Yuhas, R. Cassel, M. Nguyen, C. Pappas, and J. deLamare. Solid-State Modulator R&D at LLNL. In *Proceedings of the International Workshop on Recent Progress in Induction Accelerators*, Tsukuba, Japan, 29–31 Oct. 2002. High Energy Accelerator Research Organization.
9. E. Cook, G. Akana, E. Gower, S. Hawkins, B. Hickman, C. Brooksby, R. Cassel, J. deLamare, M. Nguyen, and C. Pappas. Solid-State Modulator for RF and Fast Kickers. In *Proceedings of the 2005 Particle Accelerator Conference*, pages 637–641, Knoxville, Tennessee, 16–20 May 2005.
10. I. Smith. Induction Voltage Adders and the Induction Accelerator Family. *Phys. Rev. Spec. Topics Accel. Beams*, 7:064801, 2004.
11. K. Takayama, K. Torikai, Y. Shimosaki, T. Kono, T. Iwashita, Y. Arakida, E. Nakamura, M. Wake, and H. Sato. Present Status of the Incuction Synchrotron Experiment in the KEK PS. In *Proceedings of the International Workshop on Recent Progress in Induction Accelerators*, page 1, Tsukuba, Japan, 7–10 Mar. 2006. High Energy Accelerator Research Organization.
12. R. Hironaka, M. Watanabe, E. Hotta, A. Okino, M. Maeyama, K.-C. Ko, and N. Shimizu. Performance of Pulsed Power Generator Using High-Voltage Static Induction Thyristor. *IEEE Trans. Plasma Sci.*, 28:1524, 2000.
13. W. Melville. The Use of Saturable Reactors as Discharge Devices for Pulse Generators. In *Proceedings of the Institute of Electrical Engineers*, Vol 98, pages 185–207, London, England, 10 Jan. 1951.
14. D. Birx. Basic Principles Governing the Design of Magnetic Switches. Technical Report UCID 18831, Lawrence Livermore National Laboratory, 1980.
15. E. Chu. Design Considerations of Magnetic Switching Modulator. In *Proceedings of the 4th IEEE International Pulsed Power Conference*, pages 242–245, Albuquerque, New Mexico, 6–8 June 1983.
16. G. Coate and L. Swain Jr. *High-Power Semiconductor Magnetic Pulse Generators*, The MIT Press, Cambridge, MA, 1966. Research Monograph No. 39.
17. H. Honma, T. Yokoo, and W. Jiang. Evaluation of Switching Characteristics of SiC-JFET. In *Proceedings of the International workshop on Recent Progress in Induction Accelerators*, page 84, Tsukuba, Japan, 7–10 Mar. 2006. High Energy Accelerator Research Organization.

UNCORRECTED PROOF

Chapter-4

Query No.	Query
AQ1	Figure 4.6 has not been cited in the text. Please check.

UNCORRECTED PROOF

Chapter 5
Magnetic Materials

Louis L. Reginato

5.1 Introduction

The magnetic material is a key element of the induction accelerator cell. The choice of material will generally involve a number of trade offs. Desirable properties of magnetic materials include high flux density (B_s), low coercive force (H_c), high permeability (μ), and low loss at high rates of magnetization ($\mathrm{d}B/\mathrm{d}t$), but any given application will emphasize some of these properties at the expense of the others. The acceleration gradient, pulse duration, and integration of focusing systems in the cell design place constraints on the cell aspect ratio such as the outside/inside radii. Further constraints are imposed by the limits of the modulator on parameters such as repetition rate, peak power, and rise time. Finally the budgetary constraints, particularly when several hundred tonnes of magnetic materials are required, must be included in the tradeoffs.

A large variety of ferrimagnetic (see Sects. 3.6 and 3.7) and ferromagnetic materials are available to cover induction ~~cells~~ designs with pulse durations from nanoseconds to microseconds. The application of ferrimagnetic materials such as ferrites and ferromagnetic materials such as silicon steel, nickel iron and amorphous magnetic materials in short- and long-pulse accelerator designs will be discussed in this chapter.

5.2 Ferrites

Ferrites are an essential class of magnetic materials used extensively in linear and nonlinear microwave applications. The application of ferrites for the induction cells in the electron ring accelerator (ERA) in the early 1970s to produce 30 ns pulses at high currents was quite novel [1]. At that time, the large diameter toroids could not be pressed as a unit so they were made by gluing bricks together to achieve the

L.L. Reginato (✉)
Lawrence Berkeley National Laboratory, Berkeley, CA 94720–8201, USA
e-mail: LLReginato@lbl.gov

K. Takayama, R.J. Briggs (eds.), *Induction Accelerators*, Particle Acceleration and Detection, DOI 10.1007/978-3-642-13917-8_5,
© Springer-Verlag Berlin Heidelberg 2011

UNCORRECTED PROOF

desired diameter. Subsequent continued development provided better materials and toroids of over one meter in diameter.

The ferrite properties of particular interest to short-pulse accelerators are their high resistivity (ρ) and moderately high permeability (μ_r) at high frequencies (short pulse). A ferrite toroid is made by pressing together a mixture of powders composed of oxides containing ferric ions. The magnetic properties arise from the interaction between metallic ions and oxygen ions in the crystal structure of the oxide. By mixing divalent metal ions such as Mn, Co, Ni, Cu, Mg, and Zn in the compound, properties can be tailored for a variety of short-pulse induction accelerator cell designs.

The solid state physics issues of ferrites are covered extensively in many textbooks [2–5]. The two most common ferrites are nickel–zinc (Ni–Zn) and the manganese–zinc (Mn–Zn). The resistivity of the Ni–Zn ferrites is in the range of 10^4–10^7 Ω-cm and for Mn–Zn it is in the range of 10–10^4 Ω-cm. The flux density swing for the Ni–Zn is 0.7 T and for Mn–Zn it can exceed 1.2 T. The relative permeability for both ferrites is in the range of 10–10^4 and the permittivity is typically about 10 but can be as high as 10^5 in some low conductivity Mn–Zn ferrites.

The properties of the Mn–Zn ferrites appear to be a good choice for medium pulse duration in transitioning from short-pulse to long-pulse since they offer twice the flux density of the Ni–Zn. However, because some of the higher flux density Mn–Zn ferrites have several orders of magnitude lower resistivity, they have much greater losses than the Ni–Zn ferrites at high frequencies. Besides the eddy current losses, another effect has been observed in Mn–Zn ferrites called dimensional resonance [6]. Associated with the low resistivity of the Mn–Zn ferrites there is an effective permittivity (ϵ_r) which can be as high as 10^5. Analytical studies have been made for typical Mn–Zn ferrites and the resonances have been calculated. The high value of permeability and permittivity give rise to standing waves within the ferrite. Under these conditions the measured permeability drops to near zero. This occurs when the smallest dimension of the cross section perpendicular to the electric field equals half a wavelength. Mn–Zn ferrites have not been used in induction cells for the above mentioned reasons and also because great advances have been made in thin ribbon metallic magnetic materials which can be used at any pulse duration depending on the actual accelerator requirements.

The maximum flux swing for ferrites is set by the crystal structure and there is little that can be done to change it. The resistivity of 10^6 Ω-cm or larger leads to negligible eddy current losses even with very short pulses. The property which can be most affected by variations of the divalent metal ions Ni–Zn is the permeability or ferromagnetic resonance frequency. By reducing the nickel content and replacing it with zinc, the relative permeability can be increased from 10 to 10^4. The higher the permeability the lower will be the spin resonance or the point where the ferrite losses begin to dominate. Figure 5.1(A–E) shows that if the compositional ratio of Ni/Zn is increased, the spin resonance goes from 1–100 MHz and the real part of the permeability [7] goes from 1,000 down to ten. In an induction accelerator it is desirable to have a high permeability to reduce the nonlinear portion of the magnetizing current. The composition of the ferrite can actually be tailored to a

UNCORRECTED PROOF

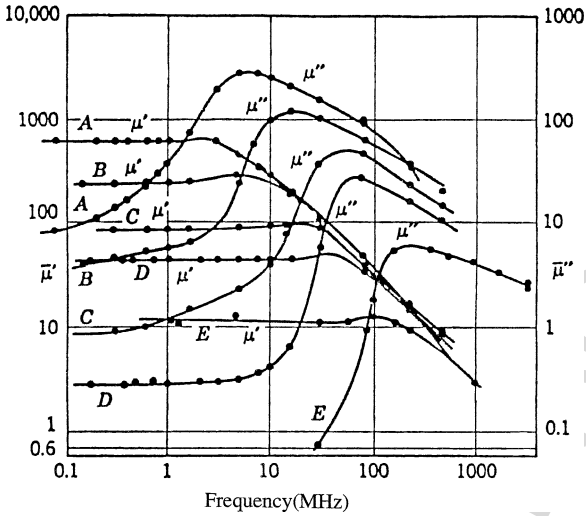

Fig. 5.1 Frequency dependence of real and imaginary parts of permeability for Ni–Zn ferrite as Zn is substituted by Ni from A–E

defined pulse duration so that the optimum pulse can be achieved with very low losses as was done with the Advanced Test Accelerator (ATA).

Figure 5.2 shows the hysteresis loop of PE11B, a Ni–Zn ferrite which was used in the ATA accelerator. This ferrite was developed by TDK for this specific application and required ~500 A-turns per meter of magnetizing current to achieve the full flux swing. The energy density losses, $U = (1/2)BH$ J/m^3, can be obtained by integrating the forward hysteresis loop from $-B_r$ to $+B_r$, where B_r is the remnant flux at zero coercive force ($H_c = 0$). A low level pulse of much longer duration and of opposite polarity to the main pulse is applied to reset the core from $+B_r$ to $-B_r$. For PE11B ferrite the energy density loss with a 100 ns saturation pulse is about 120 J/m^3.

The selection of ferrites instead of ferromagnetic materials for pulse durations less than 100 ns is not a firm criterion. It depends on many factors determined by the accelerator requirements such as current, efficiency, gradient, power dissipation and cost. A design example in the next chapter will show that if efficiency is important, ferrites may well be the right choice. If Ni–Zn ferrites are the optimum choice, a guideline which has been used in several previous accelerators is that the fundamental frequency of the pulse is at or near the spin resonance (see Sect. 3.7). This insures that the permeability is still high and the losses are low for the duration of the pulse.

Although core losses for Ni–Zn ferrites are relatively low, in high repetition rate accelerators cooling will be required to keep the temperature rise below certain limits. The flux swing decreases with temperature and improper cooling can lead to runaway conditions if the magnetic material temperature approaches the Curie point where the flux density approaches zero. More will be said on this issue in Sect. 6.11 discussing cell losses and cooling.

UNCORRECTED PROOF

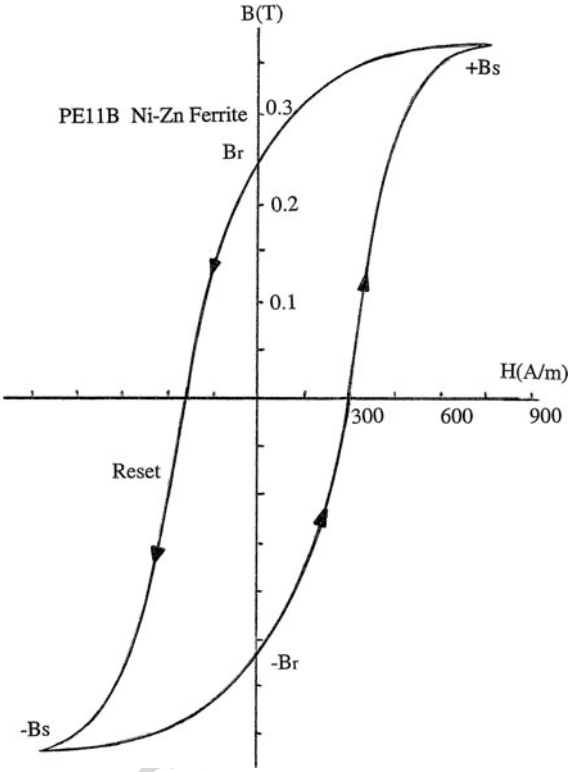

Fig. 5.2 Hysteresis loop for PE11B Ni–Zn ferrite with a saturation time of 100 ns

5.3 Ferromagnetic Materials

For long-pulse applications, the cross-section(volume) of the cell using ferrite becomes impractically large and leads to very low accelerating gradients. A magnetic material with much greater flux swing is required to make the design practical. All the ferromagnetic materials have flux swings two to five times greater than the nickel–zinc ferrites but all have resistivities many orders of magnitude lower. As it is well known, a changing magnetic flux in a conductive medium will induce eddy currents in that medium which will result in energy loss. The magnitude of that loss depends on the rate of change, the resistivity, the permeability and most importantly the shape or size of the conductive medium. As ~~was~~ in the case of the first induction accelerator, the Astron, the only way to reduce the losses and make the ferromagnetic nickel-iron (Ni–Fe) practical for the induction cell is to subdivide the core material into very small electrically insulated regions or laminations [8]. In the early 1960s the manufacturing of these cores with 25 μm insulated ribbon required considerable development and was very costly. During the last three decades, researchers have developed a new class of magnetic materials called metallic glasses and nanocrystalline metals that are manufactured by various companies

UNCORREC

under different trade names. These materials have high flux swing, low magnetization fields and a higher resistivity than the well known ferromagnetic materials and they can easily be manufactured as a very thin ribbon 15–40 μm thick [9–13].

The development of these materials was initially driven by the energy saving potential of the 60 Hz power distribution system. Since the primary windings of the distribution transformers are always connected to the power grid, the magnetic material continuously cycles around the hysteresis loop at power line frequency draining a small but not insignificant fraction of the power and turning it into heat. It was estimated in the early 1980s that over 10^{10} kW-h could be saved in the United States in one year if all of the transformers in usage could have been replaced by amorphous magnetic material. This incentive drove a number of companies in the US, Japan and Europe to develop manufacturing techniques that could produce very large quantities of the thin ribbon at very low cost from inexpensive alloys. Initial research on the amorphous metals can be attributed to several universities and corporations, but the composition of many alloys and the development of Metglas production techniques that revolutionized the manufacturing process were led by Allied Corporation. There are several techniques for producing an amorphous phase metal, but the most common is melt spinning where the alloy is ejected onto a cold, rapidly rotating wheel by a nozzle up to a few tens of centimeters wide. The ribbon thickness of 15–40 μm is controlled by adjusting the proximity of the nozzle to the wheel. The rapid cooling of the melt at greater than 10^5°C/s avoids crystallization and the amorphous alloy is created at very high speeds (tonnes/hour). The term metallic glass appears to be contradictory but the structure of these amorphous materials does resemble that of glass and their electrical conductivity is much like that of ferromagnetic metals.

The amorphous alloys have found applications in nonlinear pulse compression modulators, induction accelerators and many other areas requiring thin ribbon [14, 15]. Magnetic materials for pulse applications are subjected to very high rates of magnetization where dB/dt can exceed 10 T/μs. In comparison, the magnetization rates at 60 Hz are four to five orders of magnitude lower. This is a relevant difference because the voltage generated for each layer of ribbon is in the hundreds of microvolts at 60 Hz and can be in the tens of volts for pulsed applications. The significance of this difference is that for applications at 60 Hz the surface resistance between layers is sufficiently high to block eddy current flow without additional insulation. For pulse applications with tens of volts between layers, the resistance is not sufficient to block current flow and additional insulation is required to isolate the individual layers. Without insulation between layers excessive eddy currents would render the magnetic material useless.

During the development of the amorphous alloys for the 60 Hz industry, it was found that the as-cast magnetic properties were not very desirable for transformers regardless of cost. In order to achieve the required high flux swing, low coercive force and high permeability, the material had to be field annealed. That is, the material was cast and wound into a core, a circumferential field was applied and the temperature was raised to 300–400°C. Figure 5.3 shows the hysteresis loops for the as-cast and for the field-annealed metallic glasses. It was concluded that for these

UNCORRECTED PROOF

alloys to be competitive with existing materials transverse field annealing would be required.

Recalling that for pulsed applications many volts can appear between layers, studies to provide additional inter-laminar insulation of annealed cores were initiated. One option for achieving the optimized properties in pulse applications was to field-anneal prior to winding the core with additional insulation between ribbon layers. Unfortunately, annealing of most alloys embrittles the material to such an extent that it becomes very difficult to wind into a core and the labor intensive winding process eliminates all cost advantages. Some annealed alloys such as 2605CO have been successfully wound into large cores but in these particular applications cost and energy loss were not deciding factors. Coatings that withstand annealing temperatures have been successfully developed by several companies and are becoming more cost competitive with the as-cast material [16–18]. At the time of the design studies of heavy ion fusion and for DARHT-II, tests made on magnetic materials with commercial coatings for inter-laminar insulation offered inconsistent results. Some of the magnetic properties had deteriorated and inter-laminar shorts developed that made the application of this coating technique a very risky proposition. In the last several years, inter-laminar insulation that holds off several volts has proven to be reliable and economically viable but not yet cost competitive with the as-cast material. Since the cost difference between the as-cast and the annealed materials was not acceptable for the heavy ion and the DARHT-II accelerators, it was essential to determine if the as-cast material offered a viable solution simply by winding the ribbon with 2.5 μm Mylar as inter-laminar insulation.

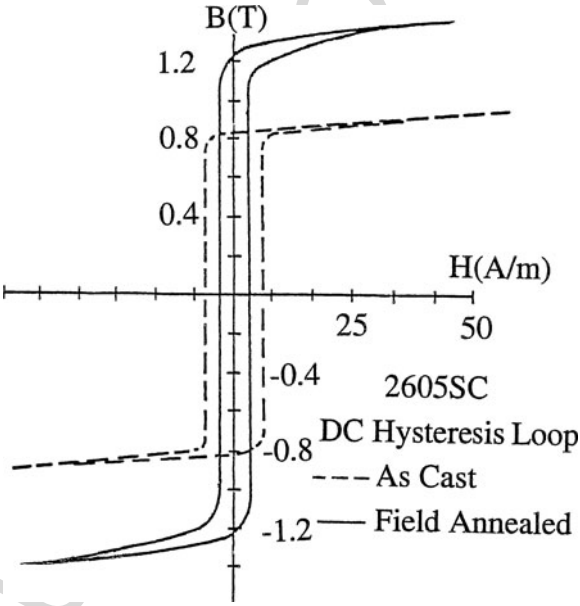

Fig. 5.3 Hysteresis loops for as-cast and field-annealed 2605SC

5.4 Energy Loss

The dominant loss mechanism in ferromagnetic ribbon at high magnetization rates is basically due to the eddy current losses (see Sect. 6.9 for a discussion of the electromagnetic fields and the eddy currents in a ferromagnetic ribbon core). A full description of the dynamics of all magnetization losses is more complicated, but for rates above about one T/μs a model sometimes referred to in the literature as the "saturation wave theory" has proven useful in showing how the losses scale with magnetization rate, ribbon thickness, etc. This theory models the major components of the excitation losses in terms of the eddy currents within the magnetic ribbon and the time required for the field to fully penetrate. In this model the coercive field, H_a, required to fully magnetize the material from $-B_r$ to $+B_s$ is given by

$$H_a = H_c + \frac{d^2}{8\rho}\frac{\Delta B}{2B_s}\frac{\mathrm{d}B}{\mathrm{d}t}, \tag{5.1}$$

where H_c is the DC coercive field, $\Delta B = B_r + B_s$, and d and ρ are the ribbon thickness and resistivity respectively. The half cycle energy density $\mathcal{E}$ lost in magnetizing the core to B_s is:

$$\mathcal{E} = H_c \Delta B + \frac{d^2}{8\rho}\frac{\Delta B^2}{2B_s}\frac{\mathrm{d}B}{\mathrm{d}t}, \tag{5.2}$$

where the first term ($H_c \Delta B$) is the DC anisotropy energy and the second term represents dynamic (eddy current) losses which dominate at high magnetization rates [19, 20]. To accurately quantify the magnetic material losses at high $\mathrm{d}B/\mathrm{d}t$ rates, the hysteresis curve is always measured at those rates and the energy loss per unit volume (J/m^3) is obtained by integrating the area under the B–H loop [19, 21]. It is evident from Eq. (5.1) that the coercive field, H_a, is proportional to the magnetization rate and the ribbon thickness squared but inversely proportional to the resistivity.

To evaluate the benefits of annealing when operating at high magnetization rates, hysteresis loop measurements of large as-cast amorphous cores of 2605SC were made with $\mathrm{d}B/\mathrm{d}t = 1$ T/μs. These measurements show that unlike the 60 Hz results taken at very low magnetization rates the saturation flux, B_s, is nearly the same as that of the annealed cores. Figure 5.4 shows the hysteresis loop for the as-cast 2605SC at 2 μs saturation time. The losses per unit volume are about the same as the annealed material but the hysteresis loop is more S-shaped, so more compensation is required to maintain constant voltage during the pulse. The remanent flux is also lower which leads to lower flux swing from $-B_r$ to $+B_s$. This reduction in flux swing, however, can be avoided by maintaining a reset current flow just prior and during the forward pulse ("active reset"). This reverse current flow is typically a pulse of much longer duration and orders of magnitude lower power than the main pulse, but still sufficient to bias the core near $-B_s$ instead of $-B_r$. This gains back most of the $(B_s - B_r)$ that would be lost without the use of this "active reset".

UNCORRECTED PROOF

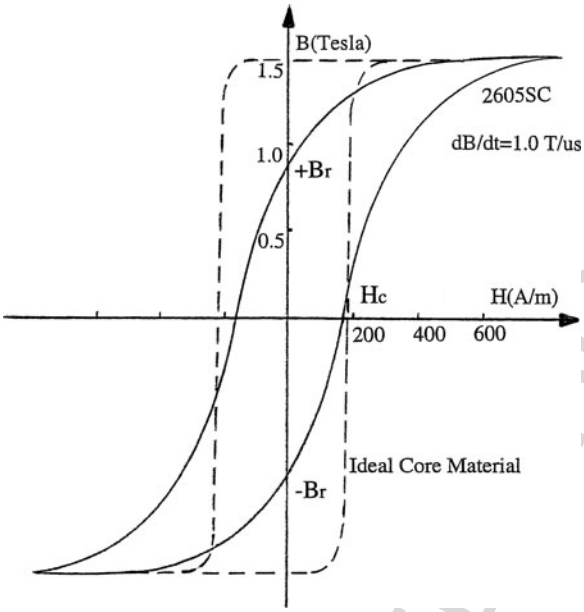

Fig. 5.4 Hysteresis Loop for 2605SC amorphous material

A clear advantage of the annealed amorphous or nanocrystalline materials is that the hysteresis loop approaches the squareness of the ideal material shown in Fig. 5.4. Although the overall losses may be comparable to the as-cast material, the compensation network to achieve constant voltage during the pulse is much easier, or not required, since the magnetizing current is constant (time independent).

In the material selection process the different trade offs need to be evaluated. As previously mentioned, for 60 Hz operation, field annealing of the as-cast amorphous ribbon is essential in order to obtain full saturation flux with low magnetization or coercive field. Although it was believed initially that annealing would also be required for applications with high magnetization rates, the as-cast material offered more than satisfactory performance. This made the DARHT-II accelerator economically feasible since coatings that could withstand annealing were unreliable or prohibitively expensive at that time.

Empirically obtained loss data for annealed and as-cast materials are shown on Fig. 5.5. The losses and measured flux swing at high magnetization rates are quite comparable. Several alloys and Ni–Zn ferrite are shown on this chart. The alloy 2605CO, which could be wound after annealing, shows more than twice the losses of the as-cast 2605SC and also costs considerably more due to the cobalt content. Note that the PE11B ferrite losses are approximately an order of magnitude lower than 2605SC and do not become significant until dB/dt is above 10 T/μs. There are several alloys such as 2705M and 2714 that have losses lower than 2605SC but their flux swing is considerably less and their cost is greater. These alloys should

UNCORRECTED PROOF

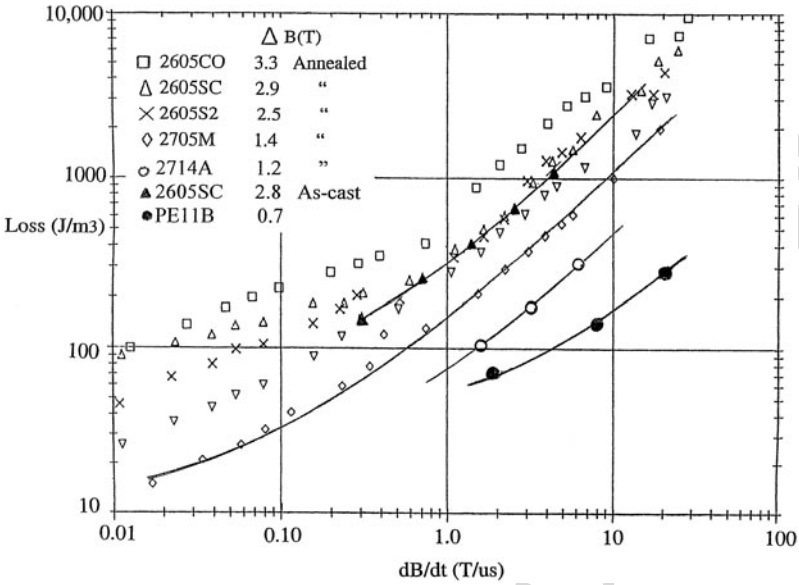

Fig. 5.5 Magnetic material losses versus magnetization rate

definitely be considered in cell designs where high efficiency is required and low cost is not the deciding factor [20, 22].

The discussion of energy loss in this section has concentrated on the case where the full flux swing of the magnetic material is utilized, since that minimizes the material cost for a given pulse length and core voltage. At very high repetition rates, however, the optimum design choice may lead to situations where only a fraction of the available flux swing is used . This case is discussed in Chap. 11, where it is shown that the magnetization energy loss with a minor hysteresis loop has a different scaling than presented in Eq. (5.2).

5.5 Other Materials

The discussion on ferromagnetic materials for long-pulse accelerators has concentrated mainly on amorphous metals since in the past they were readily available and offered a viable solution to achieving the technical requirements at a reasonable cost. The fact that the amorphous metals have similar flux swing to the nickel–iron or silicon steel, have a higher resistivity and can be mass produced in thinner and wider ribbon by very low cost manufacturing techniques make them the compelling choice for long-pulse accelerators and many other applications where large quantities are needed.

Over the last decade, the cost of some amorphous metals dropped nearly one order of magnitude making the DARHT-II long-pulse accelerator economically

UNCORRECTED

viable. Studies of induction linac accelerators to drive a heavy ion fusion power plant (see Sect. 10.1) estimate that over 10^7 kg of magnetic material would be required and to make the linac economically feasible the cost would have to decrease by nearly another order of magnitude. There are many other applications for induction cells such as induction synchrotrons, recirculating linacs, relativistic two beam accelerators for microwave generation, linacs for food processing and muon phase rotation where the material's cost is not a major driving factor. In these cases, the cell designer has considerable latitude in the material choices, and this allows the final selection to be based primarily on the cell performance and not cost.

There are several manufacturers that produce a variety of materials by various techniques that are competitive in both magnetic properties and cost with the amorphous alloys Metglas. Hitachi Metals Ltd. (Japan) has developed a number of alloys that have comparable properties to the amorphous metals. These alloys, including Finemet, are produced as a nanocrystalline material by adding small fractions of copper and Niobium. Some of these alloys have lower losses than the amorphous metals and are currently being manufactured as complete cores with sufficient inter-laminar insulation on the ribbon to be applicable at high magnetization rates. Although still not cost competitive with the as-cast alloys, these cores have found extensive usage in induction synchrotrons, step-up transformers and nonlinear pulse compression modulators. There are other magnetic materials that are produced as a thin ribbon by various methods in several countries. Vitroperm is an alloy similar to Finemet manufactured by Vacuumschmelze (Germany) and Moscow Radio Technical Institute (MRTI-Russia) also produces many comparable amorphous materials [23–27].

Extensive material studies were undertaken by Molvik and Faltens for the heavy ion fusion application since the induction cells would be a major cost factor for inertial fusion accelerators. Many small cores from several different manufacturers were tested and all the magnetic properties such as flux density, coercive field, losses at different magnetization rates and other issues such as coatings and annealing were investigated. Table 5.1 below shows a small data sample from that report for coated/annealed materials [28–30].

The sample data shows that the amorphous materials 2605SA1 and 2605SC have losses approximately twice those of the nanocrystalline materials which have slightly lower flux density. This report describes in detail the progress which has been made in the last decade. The coating/annealing process seems to have been

Table 5.1 Sample data from [28–30]

Material @ $dB/dt = 1$ T/μs		ΔB [T]	$\mathcal{E}$ [J/m^3]
Metglas	2605A1	2.2	350
	2605SC	2.4	400
Finemet	FT-1H	2.1	150
	FT-2H	2.4	200
Vitroperm	NAM-2	2.2	150
	NAM-3	2.1	120
MRTI	2605A1	2.1	300
	2605SC	2.2	400

UNCORRECTED PROOF

satisfactorily resolved and future cores with improved magnetic properties will be readily available from several different manufacturers. Clearly, advancements have been made and will continue to be made but an important point which should not be lost about the as-cast amorphous alloys is that their magnetic properties at high magnetization rates are comparable to the annealed materials and at the time of the DARHT-II design the cores were available at one fifth the cost. It has yet to be established if in the future the new and improved annealed materials with sufficient inter laminar insulation for high magnetization rates will be cost competitive with the as-cast [30].

5.6 Summary

There are several manufacturers of ferrite in the US, Europe and Asia that offer many types of ferrites that are competitive in quality and prices to those mentioned in the text. The induction cell designer should investigate and compare the magnetic properties of all available materials to assess their impact on the complete system. It may well be that if a more expensive material with lower losses and a square hysteresis loop is used, it could lead to a simpler pulse generator and compensation network and ultimately result in better performance and overall lower cost. After reviewing the performance data of available materials, it is advisable to test many samples under the same conditions as the specific application for which they are intended. Once the parameters are well characterized, the cell designer can choose the magnetic material to meet all technical and economic goals be it ferrite, amorphous or nanocrystalline. The cell designer should evaluate and eliminate any weak points, and maximize the safety factors that influence the future performance of the cells particularly if they are produced in large quantities. Events such as deterioration of magnetic properties due to mechanical stress, deterioration of inter-laminar insulation due to pulsing or movement and deterioration of voltage holding caused by improper impregnation of the insulating medium must also be carefully considered. The final prototype cell should then be tested at elevated levels well above the normal operating level to insure that the final design will give reliable performance for the desired life expectancy of the accelerator.

References

1. A. Faltens and E. Hartwig. Preliminary Hardware Concepts for an Electron Ring Accelerator. *IEEE Trans. Nucl. Sci.*, NS-18:484–487, 1971. (Proceedings of the 1971 Particle Accelerator Conference, Chicago, IL, 1–3 Mar., IEEE-NPSS).
2. C. Kittel. *Introduction to Solid State Physics*, Wiley, New York, NY, 8th edition, 2005.
3. E. Snelling. *Soft Ferrites: Properties and Applications*, Butterworth, London, 2nd edition, 2000.
4. J. Smit and H. Wijn. *Ferrites*, Wiley, New York, NY, 1959.
5. R. Bozorth. *Ferromagnetism*, D. Van Nostrand Co. Inc., New Jersey, 1951.
6. F. Brockman. Dimensional Effects Resulting from High Dielectric Constant Found in a Ferromagnetic Ferrite. *Phys. Rev.*, 77:85, 1950.

UNCORRECTED PROOF

7. E. Gorter. Magnetization in Ferrites: Saturation Magnetization of Ferrites with Spinel Structure. *Nature*, 165:798, 1950.
8. S. Winter, R. Kuenning, and G. Berg. Pulse Properties of Large 50–50 Ni–Fe Tape Cores. *IEEE Trans. Magn.*, 6:41–45, 1970.
9. R. O'Handley, S. Murray, and S. Allen. Low-Field Magnetic Properties of Fe80B20 Glass. *J. Appl. Phys.*, 47:4460, 1976.
10. F. Luborsky. Perspective on Applications of Amorphous Alloys in Magnetic Devices. In R. A. Levy and R. Hasegawa, editors, *Amorphus Magnetism II*, page 345, Plenum Press, New York, NY, 1977.
11. A. Glaser and R. Tagirov. Amorphous Magnetic Materials. *Acad. Sci. USSR Phys. Ser.*, 42–48:1600, 1978.
12. P. Chaudhari, B. Giessen, and D. Turnbull. Magnetic Glasses. *Sci. Am.*, 242:98, 1980.
13. L. Davis, N. de Cristofaro, and C. Smith. Technology of Metallic Glasses. In *Proceedings of the Conference on Metallic Glasses: Science and Technology*, page 125, Budapest, Hungary, 30 June–4 July 1980. Springer, The Netherlands.
14. C. Smith. Metallic Glasses for Magnetic Switches. In *Proceedings of the 15th Power Modulator Symposium*, page 22, Baltimore, MD, 14–16 June 1982.
15. C. Smith. Magnetic Shielding to Multi-Gigawatt Magnetic Switches: Ten Years of Amorphous Magnetic Applications. *IEEE Trans. Magn.*, MAG-18:1376, 1982.
16. C. Smith, B. Turman, and H. Harjes. Insulations for Metallic Glasses in Pulsed Power Systems. *IEEE Trans. Electron Devices*, 38:750, 1991.
17. A. Molvik, W. Meier, R. Moir, and A. Faltens. Implications of New Induction Core Materials and Coatings for High Power Induction Accelerators. In *Proceedings of the 1999 Particle Accelerator Conference*, pages 1503–1505, New York, NY, 29 Mar.–2 Apr. 1999.
18. C. Smith, A. Faltens, and S. Rosenblum. Insulation for Metallic Glasses in Pulse Power Systems. *J. Appl. Phys.*, 57:3508, 1985.
19. R. Jones, A. Collins, and N. Cleaver. A Comparison of the Step $\mathrm{d}B/\mathrm{d}t$ Pulse Magnetization Losses in Some Amorphous Ribbon and Conventional Toroids. *IEEE Trans. Magn.*, MAG-17:2707, 1981.
20. C. Smith and D. Nathasingh. Magnetic Properties of Metallic Glasses Under Fast Pulse Excitation. In *Proceedings of the 16th Power Modulator Symposium*, page 240, Arlington, VA, 18–20 June 1984. IEEE, New York, NY.
21. R. Jones. Step $\mathrm{d}B/\mathrm{d}t$ Magnetization Losses in Toroidal Amorphous Ribbon and Polycrystalline Cores. *IEEE Trans. Magn.*, MAG-18:1559, 1982.
22. C. Smith and L. Barberi. Dynamic Magnetization of Metallic Glasses. In *Proceedings of the 5th IEEE Pulse Power Conference*, page 664, Arlington, VA, 10–12 June 1985. IEEE/NPSS.
23. Y. Yoshizawa, S. Oguma, and K. Yamauchi. New Fe-Based Soft Alloys Composed of Ultrafine Grain Structure. *J. Appl. Phys.*, 64:6044, 1988.
24. S. Nakajima, S. Arakawa, Y. Yamashita, and M. Shiho. Fe-Based Nanocrystalline FINEMET Cores for Induction Accelerators. *Nucl. Inst. Meth. A*, 331:5556, 1993.
25. G. Mamaev, I. Bolotin, A. Ctcherbakov, and S. Mamaev. Fe-Based Nanocrystalline FINEMET Core for Induction Accelerators. In *Proceedings of the 1997 Particle Accelerator Conference*, page 1313, Vancouver, Canada, 12–16 May 1997.
26. S. Nakajima, S. Arakawa, Y. Yamashita, and M. ~~Shino~~, Fe-Based Nanocrystalline FINEMET Core for Induction Accelerators. *Nucl. Inst. Meth. A*, 331:318, 1993.
27. S. Vonsovskii and E. Turov. Metallic Glasses and Amorphous Magnetism. *Acad. Sci. USSR Phys. Ser.*, 42:1570, 1978.
28. A. Molvik and A. Faltens. Induction Core Alloys for Heavy-Ion Inertial Fusion-Energy Accelerators. *Phys. Rev. Spec. Topics Accl. Beams*, 5:080401, 2002.
29. R. Hasegawa. Properties and Applications of Nanocrystalline Alloys from Amorphous Precursors. *NATO Sci. Ser.*, 184:189–198, 2006.
30. R. Wood and R. Lathlaen. Amorphous Material Coatings. In *Proceedings of the 12th Pulsed Power Conference*, page 1313, Monterey, CA, 27–30 June 1999.

UNCORRECTED PROOF

Chapter 6
Induction Cell Design Tradeoffs and Examples

Louis L. Reginato and Richard J. Briggs

6.1 Introduction

A brief history of induction accelerator development was covered in Chap. 2. The induction accelerators constructed since the early 1960s can be categorized as short-pulse if the pulse duration is less than 100 ns and long-pulse if it is longer. The distinction between short-pulse and long-pulse is arbitrary; it mainly reflects the type of magnetic material that was typically used in the cell. Examples of short-pulse induction accelerators are the electron ring accelerator (ERA, $\Delta t = 30$ ns) [1], the advanced test accelerator (ATA, $\Delta t = 70$ ns) [2] and the experimental test accelerator (ETA-II, $\Delta t = 70$ ns) [3]. Examples of long-pulse accelerators are the Astron ($\Delta t = 400$ ns) [4, 5] and the second axis of the dual axis radiographic hydro test accelerator (DARHT-II, $\Delta t = 2{,}000$ ns) [6]. In this chapter the cell design of several of these accelerators will be described in detail. We will discuss how the physics, economics, and space requirements often lead to a non-optimum design from the accelerator systems vantage point. Although modulators are covered in Chap. 4, some specific designs will be discussed on how the constant voltage (flat-top) was achieved in concert with the cell design and compensation network.

6.2 Cell Configurations

Induction cell designs for the short and long-pulse accelerators are as varied as the applications for which they were intended. The long-pulse cell cross-section of the Astron and the DARHT-II accelerators are contrasted in Fig. 6.1. The short-pulse cell cross-section of the ATA and the ETA-II accelerators are shown in Fig. 6.2.

A comparative analysis of each design reveals important features distinctive to each cell. The constraints imposed by the physics requirements often limited the optimization process to achieve the best performance and efficiency at a minimum cost.

L.L. Reginato (✉)
Lawrence Berkeley National Laboratory, Berkeley, CA 94720-8201, USA
e-mail: LLReginato@lbl.gov

K. Takayama, R.J. Briggs (eds.), *Induction Accelerators*, Particle Acceleration and Detection, DOI 10.1007/978-3-642-13917-8_6,
© Springer-Verlag Berlin Heidelberg 2011

UNCORRECTED PROOF

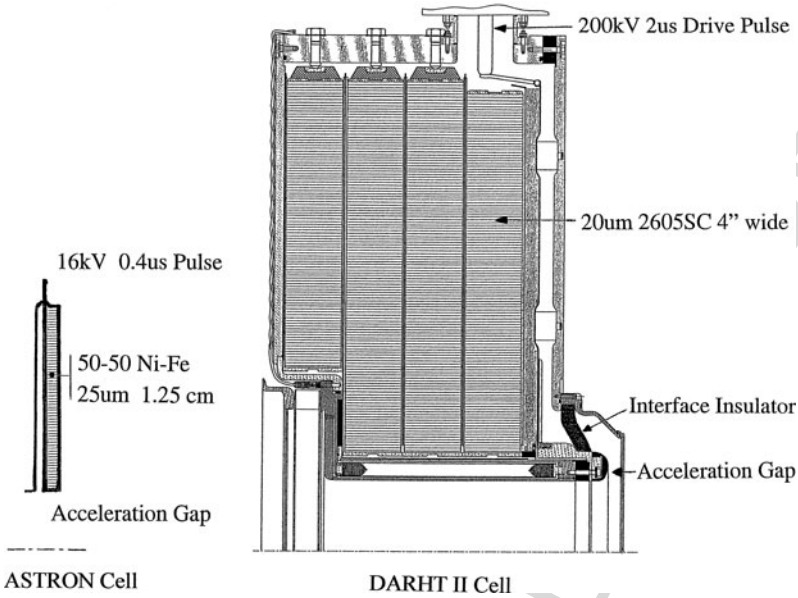

Fig. 6.1 Cell cross-section of the Astron and DARHT-II accelerators

It has been customary to show the induction cell as a one-to-one coupled transformer, but it may actually be represented more accurately as an auto-transformer. The simplified equivalent circuit discussed in Chap. 3 is repeated here in Fig. 6.3 for continuity. V_s and Z_S are the voltage and impedance of the pulse generator, Z_L is the compensation load, L_c is the inductance of the cell, I_c represents the core magnetizing current which includes losses, C_g is the acceleration gap capacitance, I_B is the beam load and V_c is the acceleration voltage. It is evident that the beam current is supplied directly from the pulse generator and that the sole function of the magnetic core in the cell is to provide a high impedance to ground for the full duration of the pulse. As discussed in Sect. 3.5, the core volt-seconds product $V_c \Delta t = A_c \Delta B$ must be sufficient so that the magnetic material does not go into saturation during the pulse. Here, A_c is the core cross-sectional area, Δt is the pulse duration and ΔB is the flux swing averaged over the core cross section.

Turner presents comparative measurements of the ETA-II and the ATA core impedances [7]. The ETA-II cell design by Birx shown in Fig. 6.2 shows considerably less impedance variation than the ATA. The ETA-II cell configuration closely resembles a ferrite loaded transmission line while the ATA is driven from the outside diameter and behaves more as a lumped element with more impedance variation. Another design improvement on the ETA-II cell is that the ferrite cores, just behind the interface ceramic insulator, were closely coupled to the BBU RF modes and provided the necessary damping without additional ferrites. Despite the lower impedance variation of the ETA-II cell, a compensation network was still required to maintain a constant voltage because the magnetizing current (sometimes

UNCORRECTED

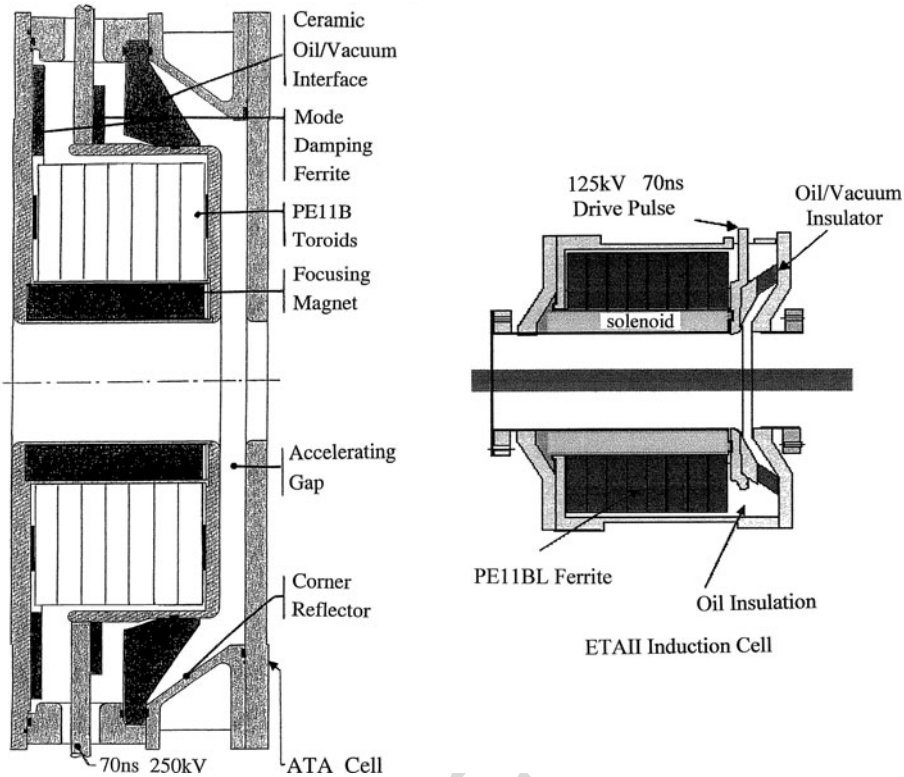

Fig. 6.2 Cell cross-section of the ATA and the ETA-II accelerators

called leakage current) was a much larger fraction of the total current than was the case in the ATA drive system.

From the simplified equivalent circuit in Fig. 6.3, it can be seen that with a constant V_s, the time-varying current required for core magnetization flowing through Z_s will cause a time-varying acceleration voltage, V_c. This is not acceptable since most experimental programs require a constant voltage during the pulse flat-top.

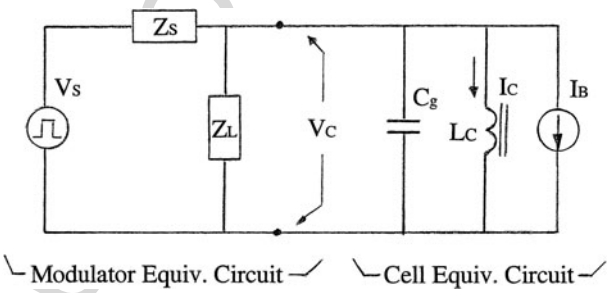

Fig. 6.3 Simplified equivalent circuit of induction unit

There are several techniques or combinations thereof that can be used to insure that the acceleration voltage, V_c, remains constant. They are:

(a) Make the core magnetizing current, I_c, much smaller than the total current from the source.
(b) Introduce an impedance, Z_L, in shunt with the cell impedance which complements it in such a way as to make the combination approximate a constant load on the source.
(c) Design the source impedance, Z_s, so that it varies in time and supplies the current required by the core.
(d) Make the source impedance much smaller than the core impedance.

In describing the simplified equivalent circuit, Z_s has represented the source impedance of the pulse generator or modulator. In most cases, induction cells are driven by long cables from a modulator located a distance away. Typically, the cable length is chosen so that the two way travel time is equal to or greater than the pulse duration τ_p. That is, the cable length $\ell > (\tau_p/2)v$ where v is the wave speed in the cable. This is done to avoid cell-to-cell interaction when they are driven from the same modulator. It also eliminates reflections from beam head induced transients from reflecting back during the pulse and locates the modulator in a radiation free environment for easy maintenance. In this case, Z_s, actually represents the cable impedance and not the source impedance of the modulator. In most accelerators, the cable impedance is matched to that of the modulators so it is also correct to say that Z_s represents the source impedance.

It is apparent from the simplified equivalent circuit that the voltage on the cell will droop with an exponential decay time determined by the L_c/Z_{eq}, where L_c is the inductance of the cell and Z_{eq} is the parallel combination of Z_s and Z_L. The inductance is dependent on the aspect ratio of the cell but mostly on the properties of the magnetic material. With square loop materials, the droop can be fairly simple to compensate but with materials with a complex B–H relationship it can be a difficult task. As discussed in Sect. 6.4, the pulse flat-top on the ATA was achieved by choosing method (a) listed above. That is, the ferrite magnetizing current was made sufficiently small that the droop was less than 1%, thus requiring no compensation. In the Astron accelerator, method (b) was used by installing the pulse-shaper circuit to maintain the flat top over the 400 ns pulse. Note that in this case the beam was a small fraction of the total current and because of the highly nonlinear L_c, the compensation network was quite complex and used most of the energy. In the DARHT-II accelerator with cable length a small fraction of the total pulse duration, method (c) was used. In this case, the pulse forming network characteristic impedance was tapered to make the equivalent modulator source impedance, Z_s, time-varying to compensate for the magnetic material nonlinearities. With the development of solid state modulators (see Chap. 4), method (d) offers a viable solution to maintaining the flat-top during the pulse. The energy in an on/off solid state modulator comes from a large capacitor where the source pulse impedance is essentially zero except for some small stray series inductance. In this case, the modulator can supply any

UNCORRECTED PROOF

amount of current and still maintain a flat-top as long as it is in close proximity of the cell. If long cables are used to power the cell, then the issue becomes more complex and compensation may be required.

6.3 Long-Pulse Cell Design

For optimum efficiency and best performance it is always advantageous to minimize the magnetizing current. It is important to choose a magnetic material with high permeability and a cell aspect ratio (outer to inner radius) which leads to high inductance. The high gradient required by the Astron accelerator led to a cell design with very short axial length and large ratio of outer to inner radius as shown in Fig. 6.1. This design resulted in a small and very nonlinear cell inductance since the inductance is proportional to the length of the cell and to the log ratio of outer to inner radius. The large nonlinear load current was further aggravated by saturation at the inner core radius. The Astron drive system is shown in Fig. 6.4. The modulator was implemented by using six parallel cables to form a pulse forming line (PFL) switched by a thyratron. The six cables had a linear source impedance of 8.33 Ω and the nonlinear magnetizing current was compensated by the three harmonics "pulse-shaper" to produce a constant acceleration voltage. The PFL delivered a total of 2 kA into a matched load with 400 A going to the beam and 1,600 A to the magnetizing current and pulse-shaper. It is interesting to compare this design to one with lower gradient had it been allowed by the physics design. For example, maintaining the same core cross-sectional area, if the cell had been made 5 cm long axially, it would have resulted in 48% greater inductance and a core volume reduction of 60% leading to a simpler pulse shaper and considerably lower modulator energy and cost. This observation does not suggest that the physics design or requirements should be compromised but simply points to the importance of carefully studying the tradeoffs between the physics design and the engineering implementation since they can have a significant impact on the system performance and cost.

The DARHT-II induction cell shown in Fig. 6.1 also required a large aspect ratio in order to satisfy the pulse duration and energy gain while fitting within a pre-existing building. The initial beam current required was 2 kA with allowance for future expansion to 4 kA. Once the beam transport physics determined the inside

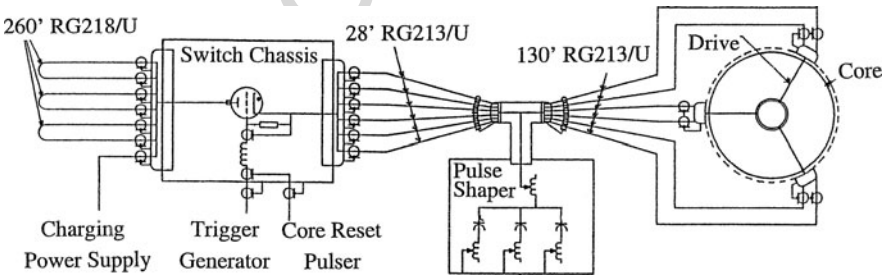

Fig. 6.4 Astron accelerator drive system

UNCORRECTED PROOF

radius to achieve transverse stability, as discussed in Sect. 6.10, the cell geometry was pretty well established. All that remained to be done was to choose the highest ΔB material that fit within the economic boundary dictated by the project. A number of materials from several manufacturers were considered and tested. Budgetary constraints quickly eliminated all of them except the as-cast 2605SC Metglas produced by Allied Signal Corporation. In order to stay within the allotted budget, the 20 μm material had to be cast in widths of 10 cm or wider. The hysteresis loop for a full size core for the DARHT-II accelerator is shown in Fig. 5.4 and it shows that the nonlinear portion of the magnetizing field will have a peak value of ~500 A/m which translates to 1.6 kA of peak current for the DARHT-II cell. It was decided that in order to meet all the programmatic requirements, a total current drive of 10 kA would be chosen. Since the nonlinear portion of the current was about 16% of the total, the constant voltage requirement was met by designing a pulse forming network (PFN) with temporally decreasing impedance which matched the nonlinear (time-varying) impedance of the core. The PFN chosen was a modified type-E network with an average impedance of 20 Ω and a 2 μs output pulse of 200 kV into a matched load. The capacitors were chosen to have the same value and in order to achieve the decreasing impedance, the inductors were reduced in value from the front to the back of the pulse (PFN). Figure 6.5 shows the acceleration voltage waveform for the DARHT-II cell at 20% below operating level. The amplified waveform shows that a ±1% variation could be achieved by careful tuning of the PFN stage inductance.

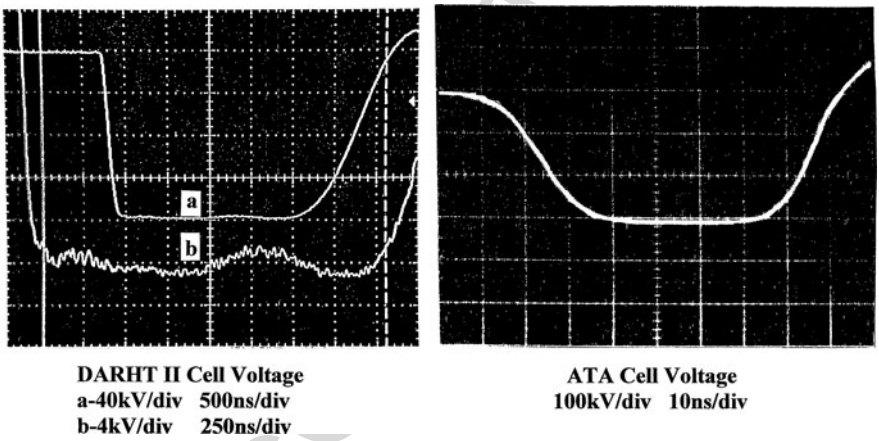

Fig. 6.5 DARHT-II and ATA cell voltages

6.4 Short-Pulse Cell Design

The cross-section of the ATA and ETA-II induction cells are shown in Fig. 6.2. The ETA-II cell was an improved design that could operate at high repetition rates with one half the gradient and one tenth the current of the ATA. Since the ATA cell was

UNCORRECTED PROOF

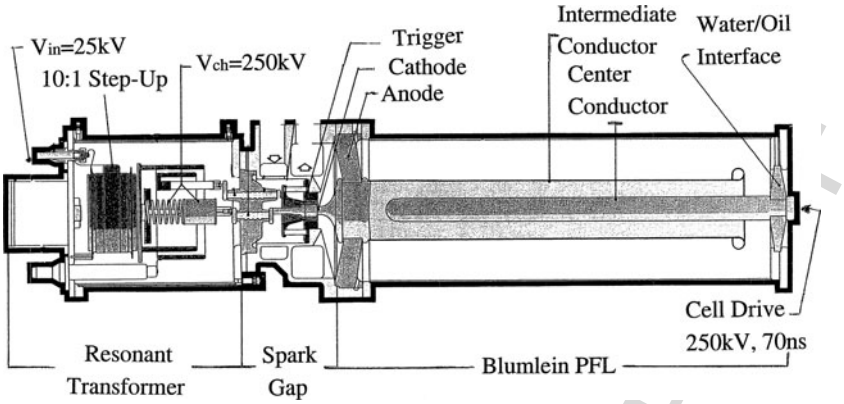

Fig. 6.6 ATA 250 kV, 70 ns pulse generator

the more challenging design, it will be discussed in more detail. Each of the 200 ATA cells ~~was~~ designed to deliver a 70 ns, 250 kV pulse at 20 kA for a total of 50 MeV. The modulator is shown in Fig. 6.6. It consists of a 12.5 Ω Blumlein PFL charged by a double resonant transformer and switched by a gas-blown spark gap. The pulse is delivered to the cell symmetrically by two 25 Ω oil filled cables. The cell was considered to be very nearly an optimum design in that it delivered the desired gradient and energy uniformity with high efficiency without a compensation network. The core material was TDK's PE11B Ni–Zn ferrite which required only ~500 A of magnetizing current to achieve full flux swing from $-B_r$ to $+B_s$. The equivalent series impedance of 12.5 Ω resulted in a voltage droop of about ±1% during the 70 ns pulse. The beam transport system allowed for this variation and no compensation network was needed to improve it. Except for the heavy ion fusion program, efficiency is usually not a high priority in induction accelerators. However, it is interesting to note that had the ATA accelerator been able to transport a 20 kA beam, the cell efficiency in energy delivery would have been 97%. The voltage waveform is shown in Fig. 6.5 and because the cell is being driven 25% above the operating level, core saturation shortens the pulse and the voltage flat-top.

6.5 Comparison Between Amorphous and Ferrite Cells

The previous examples have shown how the induction cell design for previous long- and short-pulse accelerators were implemented using unique engineering designs in order to satisfy the physics requirements. A number of tradeoffs were required which in some cases led to non optimum designs from the standpoint of pulse waveform compensation and efficiency. It was shown that if a high gradient is required, large diameter and short axial length cores lead to a highly nonlinear (time-varying) current drive which makes the compensation for constant voltage during the pulse considerably more difficult.

UNCORRECTED PROOF

As previously mentioned, the cross-over point between short-pulse and long-pulse was arbitrarily selected at 100 ns. It was pointed out that ferrites are more applicable to the short pulse while the ferromagnetic materials are preferred for the long pulse. However, the ferromagnetic materials, in particular the amorphous and nanocrystalline ones, have also been used in short-pulse applications such as nonlinear pulse compression modulators as well as induction cells. Their use has not been confined exclusively to long pulses so their application depends on many factors.

The following example will show that 100 ns is a reasonable cross over point between the usage of ferrites and amorphous materials in induction cells. Design parameters for two cells are presented for the following parameters:

Accel. Voltage	100 kV
Pulse Duration	100 ns
Axial Length	0.1 m
Inside Radius	0.1 m

One design employs the PE11B Ni–Zn ferrite used in the ATA and the other is based on the 2605SC as-cast amorphous material used in DARHT-II. The voltage gradient will be the same as will be the inside radius and the pulse duration. Two comparisons are made. In Case I the maximum flux swing for each material will be used and in Case II the cross-sectional area (including packing-factor) of the amorphous material is made the same as that of the ferrite. The results are shown in Table 6.1. The packing factor which is the ratio of the cross-sectional area occupied by the magnetic material to the total cross sectional area is assumed to be 0.75 for 2605SC and 1.0 for PE11B. The losses are obtained from Fig. 5.5 by applying the respective magnetization rates (dB/dt) for the two cases. In Case I where the maximum flux swing applicable to each material is utilized, the losses for PE11B are 2.3 J and for 2605SC the losses are 23.7 J. In Case II, where the same cross sectional area is used resulting in a lower magnetization rate for the 2605SC material, the losses actually increase. This result is somewhat surprising and can be explained by the fact that at the lower magnetization rates, the total losses for the amorphous material 2505SC increase because the decrease in losses per unit volume are offset

Table 6.1 Comparison of losses between PE11B Ni–Zn Ferrite and the 2605SC as-cast amorphous material used in the DARHT-II induction cells

	Ferrite	Metglas 2605SC	
Quantity	PE11B	Case I	Case II
Flux swing [T]	0.6	2.4	0.8
Coercive force [kA/m]	0.2	2.9	2.5
Outer radius [m]	0.267	0.156	0.267
Magnetization rate [T/μs]	6	24	8
Energy loss [J]	2.3	23.7	28.8
Volume [m^3]	0.0193	0.0045	0.0145

UNCORRECTED PROOF

by the proportionally greater increase in total volume. The large increase in total volume also explains the fact that that average coercive force is nearly the same in the two cases. In either case, the amorphous material is not competitive with the Ni–Zn ferrite in terms of losses. For low current accelerators using 2605SC, the magnetizing current would be excessively large and the modulator peak power would have to be ten times greater than that for the ferrite.

There are other factors that should also be taken into consideration. For example, the choice of material also depends on the total beam current that must be accelerated, the nonlinearity of the respective B–H loops, modulator cost and the cost and quantity of magnetic material that is needed. If the beam load is much larger than the magnetization losses, the core losses will not be the major deciding factor in choosing the material. Other important factors to be considered before making a final choice include repetition rate, high voltage integrity of the cell and the influence of the core material on the damping of the beam break-up instabilities. Ferrites with very high resistivity are basically an insulator and high voltage integrity is much easier to achieve than with amorphous materials. The other very important factor to consider is the attenuation of the high frequency modes that cause beam instability. Accelerator cells that use amorphous materials must have ferrites near the acceleration gap to attenuate the BBU modes. In cells that use PE11B or PE11BL, such as the ETA-II in Fig. 6.2, if the ferrite is exposed to the acceleration gap the additional BBU absorbers are not required.

The accelerator designer needs to take into consideration all the issues that were mentioned in making the final decision on whether to use ferrites, amorphous or nanocrystalline materials at any pulse duration. However, the use of ferrite at pulse durations of 100 ns or less appears to offer several distinct advantages. If the core dimensions are such that the ferrites cannot be manufactured as a toroid or very high gradients are required, then the only choice may well be to use an amorphous or nanocrystalline material.

6.6 Core Segmentation and Flux Equalizing

The conventional low gradient three-cell configuration giving a voltage gain 3 V is shown in Fig. 6.7a. To achieve a three times higher gradient and still maintain a linear drive and avoid core saturation, two techniques have been used as shown in Fig. 6.7b, c. One such technique called core-segmentation has been used in the injector at the National Bureau of Standards in the 1970s, the relativistic two-beam accelerator (RTA) in the late 1990s, and the prototype cells of the Heavy Ion Fusion Accelerator [8–11]. It can be seen from Fig. 6.7c that in cases where large ratios of outside to inside diameters are unavoidable, the core can be split radially in several sections resulting in lower core saturation on the inside diameter thus reducing the non-linearity of the magnetizing current. The high voltage feed must encircle each core individually and is V in value. If as shown in Fig 6.7c there are three segments, the total voltage gain is 3 V and the total current consisting of beam plus magnetizing current will be slightly greater than that of the drive for the three

UNCORRECTED PROOF

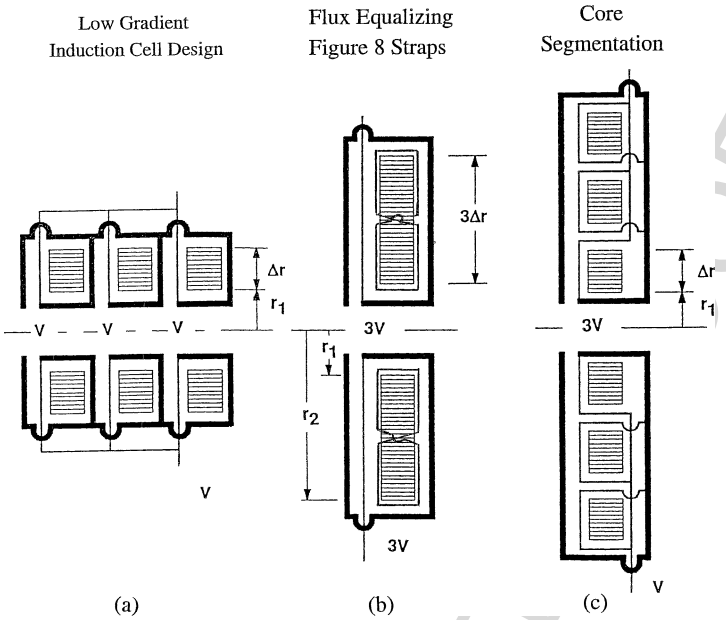

Fig. 6.7 Conventional low-gradient, three-series cells (**a**), higher-gradient, single-cell with figure eight strapping (**b**), and higher-gradient cell with core segmentation (**c**)

low gradient cells. In order to maintain the required high voltage safety factors in the drive conductors, radial and axial space must be added to the cell design. The loss of radial and axial packing factor, the increased complexity of the high voltage feeds and a lower impedance reduce the effectiveness of core-segmentation. It does not necessarily lead to a better or more desirable overall system configuration. To satisfy the high gradient requirements, the cell designer must consider the advantages of core segmentation against the disadvantages of increased complexity in the network compensation to achieve linearity of drive and constant voltage. Since core-segmentation has mainly been used in injectors, the beam break-up cell impedance issues have not been addressed for this configuration.

Another technique which has been suggested to equalize the flux density from the inside to the outside radius of the core is to couple the flux from the inside half to the outside half by a figure eight conductor as shown in Fig. 6.7b. Since the magnetization rate is greater on the inside portion, the figure eight conductor couples the flux to the outside half forcing them to be equal. The voltage drive in this configuration is 3 V and the current will be about one third that of the three-core drive leading to a nine times higher impedance. Similarly to the core segmentation case, to insure high voltage integrity of the figure eight conductors, the packing factor is also decreased axially and radially reducing the effectiveness of this technique. In actual prototype tests, flux equalizing between the inside and outside halves of the core were only partially effective. This lack of agreement with the expected results can partly be

UNCORRECTED PROOF

attributed to the leakage coupling between the inside to the outside loops and may be made more effective by additional figure eight radial straps.

The need to apply core segmentation or flux equalizing in high gradient cells where the ratio of outside to inside diameter is large in order to reduce impedance nonlinearities must be decided on an individual basis. One needs to insure that the benefits outweigh the increased complexity of the compensation network [12–14].

6.7 Core Reset Techniques

In all short- and long-pulse accelerators in order to make full usage of the flux swing, the magnetic core in the cell must be reset from the remanent flux $+B_r$ back to $-B_r$ or $-B_s$ after the forward or main acceleration pulse. The reset is usually accomplished by applying a pulse of opposite polarity to the core through an isolation inductor such as in the Astron and DARHT-II accelerators. The core reset can also be accomplished by directing the PFL charging current through the core in the opposite direction of the forward pulse as was done in the ATA accelerator avoiding the need for a separate pulse generator. As discussed in Sect. 5.4, the reset pulses are typically of much longer duration and much lower energy than the main pulse, but sufficient to provide enough current to bias the core near $-B_s$.

In high gradient cases where it is critical to achieve the absolutely maximum flux swing, it is possible to gain additional ΔB from $-B_r$ to near $-B_s$ by maintaining the reset current flowing through the core during the main pulse as was done in the ATA and DARHT-II. This technique is particularly beneficial in magnetic materials with low remanence such as the as-cast 2605SC or some Ni–Zn ferrites.

In the ATA, the Blumlein charging current flows in the reverse direction through the cell resetting the core to $-B_r$. If the spark gap is triggered just prior to the peak resonant voltage, the current maintains the core near $-B_s$ rather than $-B_r$. In the DARHT-II cell, the reset is accomplished by a separate pulser and the reset current is likewise kept flowing prior to the forward pulse beginning the cycle near $-B_s$ gaining additional ΔB. A considerable amount of magnetic material can be saved using "active reset" at the expense of a slightly more complex compensation network to maintain constant voltage. The active reset may also be used as a tuning knob to make small adjustments on the operating range of the hysteresis curve.

6.8 High Voltage Design Issues

The magnetic material (core), the high voltage cable feeds and the compensation network are typically immersed in oil. The beam undergoing acceleration and focusing in the accelerator is in high vacuum. The interface separating these two regions is a critical component of the cell (see Figs. 6.1 and 6.2). This insulator must reliably hold off the acceleration voltage without arcing and it must resist shocks and not deteriorate if arcing does occur. This insulator is typically hidden from the beam

UNCORRECTED PROOF

line of sight since it is believed that stray particles landing on the insulator lead to surface breakdowns. As discussed in Sect. 6.10, another very important function of this insulator is to allow the transmission of the beam break-up modes into the ferrite dampers located just behind it on the oil side so the high frequency properties are also very important. The choice and the angle of this insulator must follow established high voltage practices covered extensively in the literature.

To satisfy the vacuum requirements in the ETA-II and the ATA, the interface insulators were made of ceramic and the DARHT-II used Mycalex. Figure 6.1 and 6.2 show the interface insulators for the long- and short-pulse induction cells which satisfy both the equipotential angle requirement for optimum voltage holding and BBU mode transmission to the ferrite dampers. As discussed in Sect. 6.10, the acceleration gap spacing directly impacts the growth of the beam instabilities. That is, the narrower the acceleration gap, the lower will be the growth. This is in direct conflict with the voltage holding requirements which demand a wide gap for reliable operation. At the desired beam current, a balance must be achieved which satisfies both the beam transport stability and the high voltage requirements with acceptable risk factors.

In the last decade, a new type of insulator has been developed which has achieved voltage gradients several times greater than the conventional angled insulator. It is less sensitive to bipolar voltage pulses, is not susceptible to the presence of high current beams and also satisfies the BBU transmission requirements [15]. This insulator is based on a well known fact that the more grading that is applied to a vacuum surface, the greater will be the voltage that it can hold without arcing. The high gradient insulator concept takes the grading to extremes by alternating layers of conductors and insulators with a period of about one millimeter. The properties of this insulator have been well established and the only drawback appears in the manufacturing of different shapes and sizes. In recent times, however, techniques for manufacturing this insulator in large quantities at reasonable cost have made great strides and it will undoubtedly be used in future induction cells [16].

Another very important issue in the cell design is the voltage distribution between the cores and the cell. In short pulse accelerators where Ni–Zn ferrite with high resistivity is used, the voltage distribution is relatively uniform and it is not an issue. In long-pulse cells with many individual cores of amorphous material such as the DARHT-II cell shown in Fig. 6.1, the voltage distribution must be carefully analyzed since statically these cores act like a short and dynamically they act as voltage generators dependent on the radial distribution of the flux density in the core. It is evident that the voltage induced by each core will be proportional to the cross sectional area and in this case will be approximately one fourth of the total voltage. Also intuitively one can estimate that if the core-to-core and the core-to-end plate spacing is identical and the capacitance from the outside diameter of the cores to the inside diameter of the vessel is negligibly small, equal voltages should appear core-to-core and core-to-end plates. As discussed in Sect. 6.9, however, because of radial core saturation effects, unequal core-to-core and core-to-end plates capacitance and non negligible core-to-inside vessel capacitance, the voltage will not be equally distributed. Accurate analysis of the voltage distribution is essential to determine

UNCORRECTED PROOF

the proper high voltage insulation from core-to core and core-to-end plates to insure that safe operating voltage gradients are maintained.

To insure that there are no high voltage breakdowns, the cell is typically filled with insulating oil. Critical to reliable voltage holding is the removal of all air from the cell prior to filling with out-gassed oil. Furthermore, in cores that are wound with as-cast amorphous alloys with inter-laminar insulation, the ribbon must be carefully wound so that individual layers do not protrude or shift after winding to create razor edges with excessively high gradients which might lead to voltage breakdown.

6.9 Voltage and Electrical Stress Distribution in Laminated Cores

In this section we analyze the electrical stress distribution in laminated cores like the DARHT-II cell shown in Fig. 6.1. In the long-pulse regime where laminated cores are used, a quasi-static approximation for the electromagnetic fields generally suffices because the timescale for the fields to change is much longer than the EM wave propagation time. Applying this approximation has subtle features because the electric field is a mixture of an "inductive emf field" (having a nonzero curl, with $\dot{B}$ the source) and a "quasi-electrostatic field" (the source being electric charges on the various metal surfaces).

"*Micro-scale" core fields*: We first discuss the EM field structure on the "micro-scale" of the individual layers of magnetic ribbon (for example, Metglas) and the insulation between them (for example, Mylar). Inside the Metglas the radial electric field (normal to the interface) is negligible. It is shorted out by the high Metglas conductivity ($1/\sigma \approx 1.25 \times 10^{-6}$ Ωm) on the timescale ϵ/σ for surface charges to build up on the interface.

The magnetizing current flowing around the entire core creates an $H_\theta \sim 1/r$ field that is constant throughout an individual Mylar sheet. To illustrate the main features of the "micro-scale" EM fields, we first analyze the simplest case where the effective "skin depth" is much larger than the Metglas thickness d_M, and take both H_θ and $B_\theta = B_M$ as constant throughout the Metglas tape as well. (This approximation is valid in DARHT-II, for example [17]). Inside the Metglas (see Fig. 6.8) Maxwell's equations require

$$\left(\frac{\partial E_z}{\partial r}\right)_M = \frac{\partial B_M}{\partial t}. \tag{6.1}$$

The net current in the z direction in any Metglas tape section must be zero, otherwise free charge at the ends of the tape would rapidly build up. The axial electric field inside a given Metglas layer must therefore be an odd function of $r - r_n$, where r_n is the center of the nth Metglas layer;

$$E_z = (r - r_n)\frac{\partial B_M}{\partial t}. \tag{6.2}$$

UNCORRECTED PROOF

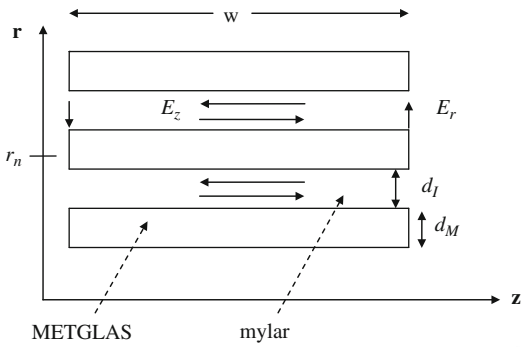

Fig. 6.8 Expanded view of Metglas and Mylar ribbon tape

Since this solution is essentially the same in adjacent tapes (H_θ varies slowly on this scale), the E_z field must vary in the periodic fashion indicated in Fig. 6.8 from tape to tape. Therefore the slope of $E_z(r)$ in the Mylar region must be $-d_M/d_I$ times the slope of $E_z(r)$ in the Metglas region given by Eq. (6.1).

In the case treated here where the skin depth is larger than the ribbon thickness, the eddy current flowing in the axial direction in the ribbon (σEz) varies linearly in r across the ribbon. Integrating the power dissipation in the ribbon (σE_z^2) across its thickness using Eq. (6.2), we see that the average power per unit volume dissipated in the core from the resistive losses is proportional to

$$P_d \sim \sigma \left(\frac{\mathrm{d}B}{\mathrm{d}t}\right)^2 d_M^2. \tag{6.3}$$

The energy loss associated with the eddy currents is the dominant loss mechanism in a laminated core at high magnetization rates, as discussed in Sect. 5.4. From Eq. (6.3) we see that the energy loss magnetizing the core through one cycle is proportional to the square of the ribbon thickness, the Metglas conductivity, and the rate of magnetization [see Eq. (5.2)].

In the Mylar where B is very small in comparison to B in the Metglas, $\nabla \times E$ is approximately zero, so

$$\left(\frac{\partial E_r}{\partial z}\right)_I = \left(\frac{\partial E_z}{\partial r}\right)_I = -\frac{d_M}{d_I}\frac{\partial B_M}{\partial t}, \tag{6.4}$$

where $(E_r)_I$ is the radial electric field in the Mylar (normal to the interface).

Outside of the core region, the "smooth" radial electric field in gaps between cores, or between the core and an end plate, should be set equal to the mean value of the radial field (averaged over the layers of Metglas and Mylar tape) at the core boundary:

UNCORRECTED PROOF

$$\langle E_r \rangle = \frac{(E_r)_I d_I}{d_M + d_I}. \tag{6.5}$$

Using Eq. (6.4), we have

$$\frac{\partial \langle E_r \rangle}{\partial z} = -\frac{d_M}{d_M + d_I}\frac{\partial B_M}{\partial t} = -p_f \frac{\partial B_M}{\partial t}, \tag{6.6}$$

with the last equality defining the "packing factor" p_f. Since the magnetic field in any individual Metglas tape winding is constant in z, $\langle E_r \rangle$ varies linearly in z across the tape width w.

In cases where the effective "skin depth" is not much larger than the Metglas thickness, the magnetic field B_M will have significant radial variation within each individual Metglas ribbon (as a "saturation wave" propagating inward, for example). In these more general cases, it is easy to show that Eq. (6.6) is still valid as long as we use a radial average over the ribbon of the magnetic field B_M on the right hand side.

In moving over to a "macro" description of the EM fields, note that the maximum value of E_z is of order $d_M/w \sim 10^{-3} - 10^{-4}$ compared to the peak value of $\langle E_r \rangle$. We can therefore safely ignore the z-directed electric field in a "macro-picture," even though it is a critical factor in the "micro-picture" of the fields in the Metglas that create the eddy currents and associated losses.

Also note that in a macro description, the equivalent radial dielectric constant for calculating the radial displacement current using the mean radial electric field [see Eq. (6.5)] is

$$\epsilon_r = \frac{\epsilon_I}{1 - p_f}, \tag{6.7}$$

where ϵ_I is the Mylar dielectric constant.

We have implicitly modeled the tape sections as individually-nested cylinders instead of the actual continuous helical winding of (typically) thousands of layers. This approximation is valid as long as the radial displacement current is much larger than the real current in the helical windings, which it should be considering the resistance and inductance impeding the real current flow.

Modeling a core as an equivalent homogeneous media: The previous discussion of the "micro-fields" motivates the following description of the "spatially averaged" EM fields (macro-fields) in a core region. These are the fields that will be matched onto the EM fields in gap regions, for example.

The magnetic fields in the core region are basically magnetostatic in character because the large inductance constrains the rate of rise of the magnetizing current I_M, so $H_\theta = I_M(t)/(2\pi r)$. In our formulation we assume that the macroscopic (mean) azimuthal magnetic field $B_\theta(r, t) = p_f B_M$ in any one core is a function of r and t only. Otherwise, one is free to use arbitrary models of the nonlinear magnetization including eddy currents, saturation, etc., as inputs. Since in an equivalent

UNCORRECTED PROOF

homogeneous core model, $E_z = E_\theta = 0$, Maxwell's equations reduce to [see Eq. (6.6)]

$$\frac{\partial E_r}{\partial z} = -\frac{\partial B_\theta(r,t)}{\partial t}, \tag{6.8}$$

with the simple solution

$$E_r(r,z,t) = -z\frac{\partial B_\theta}{\partial t} + E_r^c(r,t), \tag{6.9}$$

where E_r^c is independent of z, but otherwise an arbitrary function of r and t at this point. We take $z = 0$ as the center of the core.

For the purpose of matching onto the gap fields, we define "voltages" along the left and right side of the core as

$$\begin{aligned} \psi_L(r,t) &\equiv -\int_a^r \mathrm{d}r'\ E_r(r', z = -w/2), \\ \psi_R(r,t) &\equiv -\int_a^r \mathrm{d}r'\ E_r(r', z = +w/2), \end{aligned} \tag{6.10}$$

where a is the inner radius of the core. We introduce the following definitions of the "inductive" and "electrostatic" voltage components, respectively

$$\begin{aligned} V &\equiv -w\int_a^r \mathrm{d}r'\ \frac{\partial B_\theta(r',t)}{\partial t}, \\ \Phi &\equiv -\int_a^r \mathrm{d}r'\ E_r^c(r',t). \end{aligned} \tag{6.11}$$

Then

$$\begin{aligned} \Psi_L &= \Phi + V/2, \\ \Psi_R &= \Phi - V/2. \end{aligned} \tag{6.12}$$

The inductive voltage $V(r,t)$ is assumed to be known from the magnetostatic modeling of the core. The sources for Φ, as we will see, are the free charges which redistribute themselves on each Metglas layer to short out the internal E_z and E_θ. A differential equation for Φ can be obtained by applying the constraint of no radial conductivity. Consider the "pillbox" shown in Fig. 6.9 encompassing a radial slice Δr that extends over the full width of the core. (Note that this radial slice contains many individual layers of ribbon, since we are treating the core as an equivalent homogeneous media in making a connection with the smooth fields outside the core.) The net displacement current out of the pillbox must vanish, since no charge can flow out of it radially, so

UNCORRECTED PROOF

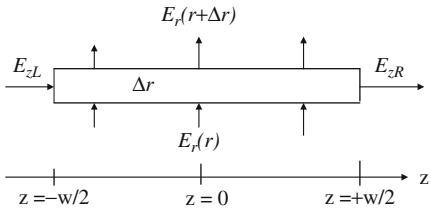

Fig. 6.9 Pillbox used to apply constraint of no net charge flow out of each Δr layer of the core

$$2\pi r \Delta r \epsilon_g (E_{zR} - E_{zL}) + 2\pi \epsilon_r \int_{-w/2}^{+w/2} \mathrm{d}z \, [(r + \Delta r) E_r(r + \Delta r) - r E_r(r)] = 0. \tag{6.13}$$

Here E_{zR} and E_{zL} are the axial electric field components just outside the core at the right and left sides of the core, respectively, ϵ_r is the effective radial dielectric constant given in Eq. (6.7), and ϵ_g is the dielectric constant of the insulating media in the gap region between the core and end plates, or between adjacent cores.

Using the solution for E_r from Eq. (6.9) and the voltage definitions, and taking the limit $\Delta r \to 0$, we have

$$E_{zR} - E_{zL} = \frac{\epsilon_r w}{\epsilon_g} \frac{1}{r} \frac{\partial}{\partial r} \left(r \frac{\partial \Phi}{\partial r} \right). \tag{6.14}$$

In a multicore situation, coupled differential equations for the $\Phi_n(r, t)$ of each core would result from relating E_{zR}, E_{zL} to the voltages on adjacent cores (or between the core and the conducting end plates).

Single core example: Application of the model to the case of a single core will illustrate the key features that play a role in the distribution of the stresses in the core region. The situation we consider is a one core version of the general geometry of the DARHT-II cell (see Fig. 6.1), as indicated in the sketch in Fig. 6.10.

The core is separated from end plates on the left and right sides by Δ_1 and Δ_2, respectively. These separations are assumed to be small compared to the core radii, so we can take the axial electric field in the gaps between the conducting end plates and the core to be approximately constant. Since the electric field in the gap region is purely electrostatic (has zero curl), we can relate these axial electric fields to the voltages we defined along the core boundary as

$$\begin{aligned} E_{zL} &= -\Psi_L(r)/\Delta_1, \\ E_{zR} &= \Psi_R(r)/\Delta_2. \end{aligned} \tag{6.15}$$

Using these relations in Eq. (6.14) together with the voltage definitions in Eq. (6.12) we have the following differential equation for the "electrostatic voltage" Φ,

UNCORRECTED PROOF

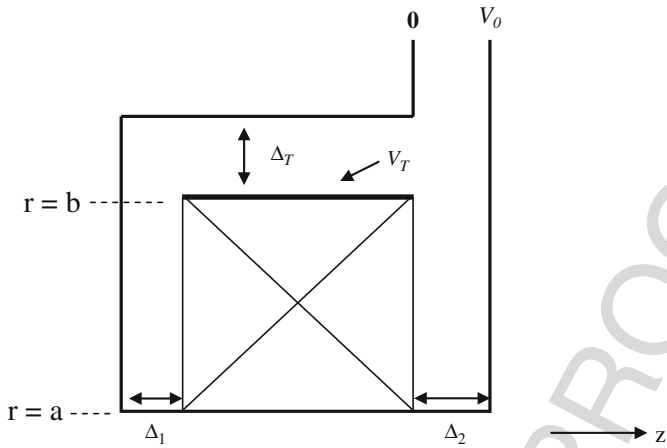

Fig. 6.10 Single core example. Note that the terminal voltage $V_0 = \Psi_L(b) - \Psi_R(b) = V(b)$ is the total inductive voltage across the core

$$\frac{1}{r}\frac{\partial}{\partial r} r \frac{\partial \Phi}{\partial r} - \kappa^2 \Phi = \kappa^2 \left(\frac{\Delta_2 - \Delta_1}{\Delta_2 + \Delta_1} \right) \frac{V(r,t)}{2} \tag{6.16}$$

Here,

$$\kappa^2 \equiv \frac{\epsilon_g}{\epsilon_r w} \left(\frac{1}{\Delta_1} + \frac{1}{\Delta_2} \right).$$

The solution of the homogeneous equation is a linear combination of modified Bessel functions, $I_0(\kappa r)$ and $K_0(\kappa r)$. The scale length of the exponential decay and growth described by these functions ($K_0(\kappa r) \sim \exp(-\kappa r)/\sqrt{\kappa r}$) can be quite short. For example, using parameters similar to those of the DARHT-II cell, $\Delta_1 = \Delta_2 = 1/4$ in., $w = 4$ in., $\epsilon_r = 12$, and $\epsilon_g = 2.3$, we have $1/\kappa \equiv \ell_c = 1.7$ in. compared to an outer radius of the core of order 30 in. With equal gap spacings the inductive voltage source term on the right hand side of Eq. (6.16) vanishes, and Φ contains only the homogeneous solution. Boundary conditions on $\Phi(r = b)$ will come from the condition of no net charge on the outer metallic band (or outermost winding) of the core. Since the inductive component of $E_r(r, z, t)$ as we have defined it in Eq. (6.9) has no average value over the core width w, no net charge requires

$$-\epsilon_r \left(\frac{\partial \Phi}{\partial r} \right)_{r=b} = \frac{\epsilon_T V_T}{\Delta_T}. \tag{6.17}$$

Here the voltage on the outer metallic band V_T is equal to $\Psi_L(r = b)$, ϵ_T is the dielectric constant of the media between the outer band and the conducting enclosure (see Fig. 6.10), and Δ_T is the separation between them (assumed to be much less than the core width w).

Assuming $\ell_c \ll b$ the approximate solution for the electrostatic voltage is

$$\Phi = \Phi(b) e^{-(b-r)/\ell_c}. \tag{6.18}$$

UNCORRECTED PROOF

Using this approximation, the following expression for the voltage on the top band can be derived

$$V_T = \frac{V_0/2}{1 + \frac{\ell_c \epsilon_T}{\Delta_T \epsilon_r}}. \tag{6.19}$$

Here $V_0 = V(r = b)$ is the total voltage across the core. If the outer enclosure was a long distance from the core ($\Delta_T \to \infty$), the outer band would be at 1/2 the total voltage, and the axial electric fields on the left and right side would be equal, as might be expected with equal gap widths.

Using the above "DARHT-II like" parameter set with $\Delta_T = 1$ inch and $\epsilon_T = \epsilon_g = 2.3$, we find $V_T = 0.76(V_0/2)$ and a ratio of electric fields at the outer radius of $E_{zR}/E_{zL} = 1.6$. The capacitive coupling from the outer band of the core to the adjacent metallic enclosure at ground potential depresses its potential and makes for a 60% inequality in the gap stresses. As we come in from the outer radius, however, the gap stresses become equal since $\Phi(r)$ decays exponentially. This "equipartition" of the electrical stress in the gaps well inboard of the outer band is actually a very general property. It also applies to unequal gaps and multicore geometries when the scale length for decay of the electrostatic voltage is small compared to the scale length over which $V(r)$ varies. With unequal gaps in the single core case, for example, the approximate particular solution to the inhomogeneous Eq. (6.16) under these assumptions is

$$\Phi_P(r, t) = \frac{\Delta_1 - \Delta_2}{\Delta_1 + \Delta_2} \frac{V(r, t)}{2}. \tag{6.20}$$

At radial distances of several ℓ_c inward from the outer band, where the homogeneous contribution to Φ has decayed away, from Eq. (6.20) we find the same axial electric field in the left and right sides:

$$E_{zL} \approx E_{zR} \approx -\frac{V(r, t)}{\Delta_1 + \Delta_2}. \tag{6.21}$$

Physical interpretations: A physical interpretation of the exponentially decaying character of the homogeneous solution for $\Phi(r)$ in Eq. (6.18) can be obtained from an analysis of the distributed circuit model shown in Fig. 6.11. If we consider a layer of the core between r and $r + \delta r$, the net radial displacement current I_{disp} passing through the core at this radius r is given by

$$I_{\text{disp}} = \frac{2\pi r w \epsilon_r}{\delta r} \frac{\partial}{\partial t} [\Phi(r + \delta r) - \Phi(r)]. \tag{6.22}$$

This identifies the "core capacitance" of that layer $C_r = \epsilon_r 2\pi r w/\delta r$ as illustrated in Fig. 6.11.

The radial displacement current through the core decreases as we move inward since it is "shunted out" each side through the gap capacitances at each layer given by $C_{g1,2} = \epsilon_g 2\pi r \delta r/\Delta_{1,2}$. If we write down the differential equation for the

UNCORRECTED PROOF

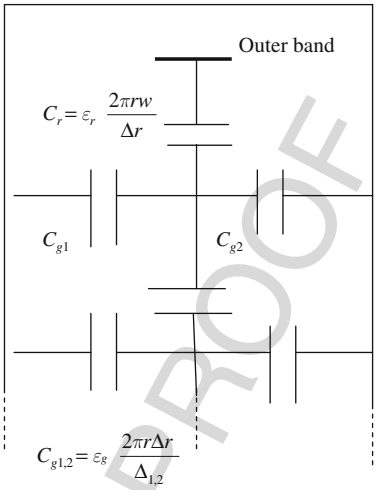

Fig. 6.11 Distributed circuit model of core-gap capacitive "ladder line"

electrostatic voltage $\Phi(r)$ that follows from this distributed "capacitive ladder line" model, we obtain the homogeneous version of Eq. (6.16).

Since the total electrostatic voltage drop from the outer band to ground is $\Phi(b)$, it makes sense to define an "effective core-gap capacitance" as

$$q = C_{\text{eff}}\Phi(b), \tag{6.23}$$

with q the total charge on the *inside* of the outer band. Using the approximate solution for $\Phi(r)$ in Eq. (6.18) to get the radial electric field, we have

$$C_{\text{eff}} = \epsilon_r \frac{2\pi b w}{\ell_c}. \tag{6.24}$$

Note that C_{eff} can be measured directly by applying an AC voltage between the outer band and the grounded end plates (with the outer cylinder removed). The capacitance of the outer band to the cylindrical enclosure is $C_T = \epsilon_T 2\pi b w/\Delta_T$. In the equal gap case where the band voltage is $V_T = V(b)/2 + \Phi(b)$, the condition of no net charge on the outer band leads directly to

$$V_T = \frac{V(b)/2}{1 + C_T/C_{\text{eff}}}, \tag{6.25}$$

in agreement with Eq. (6.19). This illustrates the physical point that the deviation from a simple equal division of inductive voltage across the two gaps is due to the capacitance of the outer band to the outer wall at ground potential. It also shows that it is the ratio of this capacitance to an "effective core-gap" capacitance that enters into the voltage distribution.

Generalizations: The generalization of this analytical model to multi-core situations is straightforward but tedious [17]. In that case a set of decay lengths equal to

UNCORRECTED PROOF

the number of cores is obtained, but the general features of enhanced stress between the cores (and between laminations near the outer band) from capacitive coupling to the surrounding enclosure apply there also. The enhanced stress can be quite substantial as was found in the DARHT-II cell refurbishment project.

6.10 Coupling Impedance

Linear induction accelerators for electrons have almost always been designed for beam currents of a kiloAmp or more. At these currents, reduction of the transverse impedance that controls the growth rate of the "beam breakup instability" (BBU) has been a dominant concern. In linear induction accelerators for ions, or induction synchrotrons, the longitudinal impedance is generally of greater concern than the transverse impedance since the beam is not as "stiff" longitudinally. A typical induction cell can support a number of RF modes in the frequency band below the cutoff frequency for propagation in the beam pipe. These modes are confined to the vicinity of that cell, and the modes with the highest Q's are the main contributors to the interaction impedance. The reduction of the Q's of these modes has therefore been a major factor in the design of induction cells.

Since the vast majority of the induction cells that have been designed and constructed have been for electron linear accelerators, the reduction of the transverse impedance has been studied to a much greater extent than the longitudinal impedance. We will therefore use it as our example to illustrate the general approaches used to minimize the coupling impedances in induction cells.

6.10.1 General Form of the Transverse Impedance

We consider induction cavities of the general form shown in Figs. 6.1 and 6.2. The accelerating gap has a width w of the shortest point across the rounded electrodes, and the beam tube radius is b. The objective in this section is to derive a general form for the transverse impedance in terms of the RF magnetic fields in the gap region. In Sect. 6.10.3 we discuss how measurements of these fields can be used to deduce the transverse impedance.

To formulate an expression for the transverse impedance, consider a relativistic electron beam of current I oscillating transversely with a small amplitude Δ_x in the x direction at a frequency ω as $\exp(i\omega t)$. Inside a conducting beam tube (away from the gap region), the beam displacement induces a dipole component of the surface current on the tube wall equal to

$$K_Z = -\frac{I\Delta_x}{\pi b^2}\cos\theta = K_{z0}\cos\theta. \tag{6.26}$$

UNCORRECTED PROOF

The beam also induces a dipole surface charge K_z/c on the tube wall. The collective forces from the dipole surface charge (attractive) and the dipole surface current (repulsive) cancel inside a smooth conducting tube for a highly relativistic beam, as is well known. When the beam passes through an accelerating gap region, the dipole surface current flows out into the accelerator cell, destroying this force balance. We consider here the frequency spectrum below the cutoff for propagation in the beam tube ($\omega < \omega_{co} = 1.84c/b$) where the dipole RF modes of the cell excited by the beam oscillation lead to localized deflection forces on the beam.

To describe the cell RF excitation and the fields that produce a net transverse force, the following superposition construct is useful. Place ideal surface current and surface charge sources at the radius b across the gap equal to those that would be induced in a smooth conducting tube given above. The net force from these sources and the surface current and charge on the beam tube outside the gap region will sum to zero, obviously, since the fields are the same as in a smooth tube without the gap. Then, we must add surface current and surface charge sources across the gap of the opposite sign to return to the actual situation. The fields created by these localized "negative" surface current and surface charge sources across the gap (the "cell fields") give the net force on the beam.

To determine the net transverse impulse imparted to the electrons passing through the gap region of one cell, we need to integrate the transverse electromagnetic force $E+v\times B$ along the electron trajectory in z (assumed to be at a constant displacement from the axis through the gap region). For highly relativistic electrons, the case we consider here, it can be proven that this integral is independent of radial position anywhere inside the beam tube. Using this theorem, we can relate the change in transverse momentum to the radial magnetic field and azimuthal electric field *at* the gap (i.e., at the beam tube radius). With a gap width much less than the beam tube radius and the wavelength, it is physically obvious that the integral of the azimuthal electric field will be very small since it is shorted out on both sides of the gap. With this assumption, the change in transverse momentum is given by

$$\delta p_x = -e\int \mathrm{d}z\; B_r(r=b,\theta=\pi/2). \tag{6.27}$$

The radial magnetic field at the gap is linearly proportional to the strength of the oscillating beam's dipole moment, or equivalently the surface current source K_{zo} (and it varies as $\sin\theta$). The electromagnetic response of the cell itself can therefore be incorporated into a dimensionless (complex, frequency dependent) parameter defined by

$$\eta(\omega) = -\frac{1}{w}\int \mathrm{d}z\; \frac{B_r(b)}{\mu_0 K_{z0}} = -\left\langle \frac{B_r(b)}{\mu_0 K_{z0}} \right\rangle. \tag{6.28}$$

Here, $B_r(b)$ is shorthand notation for the radial field at $r = b$ and $\theta = \pi/2$ in Eq. (6.27), and we use $\langle\ \rangle$ to imply an average in z over the gap. We introduce the definition of transverse interaction impedance Z_t through

UNCORRECTED PROOF

$$\delta p_x = -i\frac{e}{c}Z_t I \Delta_x. \tag{6.29}$$

Inserting this definition in Eq. (6.27), and using Eqs. (6.26) and (6.28), we obtain

$$Z_t = -i\sqrt{\frac{\mu_0}{\epsilon_0}}\frac{w}{\pi b^2}\eta \tag{6.30}$$

with η defined by Eq. (6.28).

We expect there will be one or more dipole eigenmodes of the induction cell. Calculations (or measurements) of $\eta(\omega)$ and $Z_t(\omega)$ will exhibit the usual resonance structure with a peak in the real part of $Z_t(\omega)$ at any given eigenmode frequency and a bandwidth proportional to $1/Q$.

A similar form for the peak value of the resistive part of the transverse impedance was introduced originally in computational studies of the transverse impedance in induction cells [18], as

$$Z_{tr} = \sqrt{\frac{\mu_0}{\epsilon_0}}\frac{w}{\pi b^2}\eta_f. \tag{6.31}$$

At that time η_f was considered to be a convenient figure of merit, a dimensionless "form factor" that could be reduced to of order unity in a well damped induction cell. The derivation here identifies η_f as the peak value of Im $\eta(\omega)$ as defined by Eq. (6.28), and it also provides a physical interpretation of this form factor in terms of the cell fields and equivalent source currents.

6.10.2 Minimizing the Transverse Impedance in Induction Cell Designs

Equation (6.30) shows that the fundamental geometrical scaling factor in the transverse impedance is w/b^2. The peak electric field stress on the negative electrode generally constrains how small the gap width can be for a given acceleration voltage. As far as the beam pipe radius is concerned, the voltage gradient, and the cost, are adversely affected by significant increases in the inner bore as discussed in the previous subsections. So the main emphasis in the cell design has generally been placed on minimizing the Q's to make $\eta_f = \max$ Im $\eta(\omega)$ as small as possible, with w/b^2 determined mainly by voltage holding and economic constraints.

In contrast to RF linacs, an induction cell does not need to support a high Q acceleration mode. In ferrite induction cells, the ferrite core itself provides significant absorption of the RF modes. In addition, the placement of smaller amounts of ferrite damping material in strategic locations in the cell to further lower the Q's of the transverse modes has now become standard practice in the design of high current electron induction accelerators. In the ATA accelerator, for example, the Q of the

UNCORRECTED PROOF

dominant mode at 820 MHz was reduced from ~~70–10~~ by adding the "mode damping ferrite" tiles on the flat-faced drive blades and back plate indicated in Fig. 6.2.

Judicious choices of ferrite tile thickness can also be used to minimize wave reflection over the most important frequency band, a well known feature of ferrite material used as UHF absorbers when they are placed against a highly conducting plate (thinner is sometimes better!). In general, the utilization and optimization of these ferrite dampers is the most powerful technique that one can use to minimize the transverse interaction impedance in induction linacs.

The other geometrical feature that can be exploited to minimize the impedance is the shape of the conductors in the vacuum region adjacent to the insulator. The importance of this geometrical feature was shown many years ago in ATA cell impedance studies [19]. In the ATA cell the insulator was located between the outer cylindrical walls just beyond the outer radius of the radial line, as shown in Fig. 6.2. The corner reflector shown in Fig. 6.2 faced the insulator at the Brewster angle (in that case) to reduce wave reflections from the vacuum-insulator interface. With this corner reflector and the ferrite dampers on the drive blades and the back wall, the Q of the dominant mode was reduced even further, to about 4.

Computational models of increasing complexity have also been developed more recently as a tool to optimize the design of induction cells for minimum transverse impedance. These computational tools were not available when the ATA, FXR, and ETA-II machines were designed and constructed, but they have proven to be a useful tool in the design of the short pulse DARHT-I cell as well as the DARHT-II cell shown in Fig. 6.1. Form factors for some of these accelerators have been calculated with these tools [18].

6.10.3 Measurement of the Transverse Impedance

The first measurements of transverse impedance were made using the same kind of techniques used to characterize RF cavities, namely excitation and detection of the modes in the cell with small RF loops placed at two different locations inside the cell. The Q of a given mode was measured by sweeping the frequency through its resonance, and the $Z_\perp/Q$ was inferred from shifts of the resonant frequency induced by inserting a conducting rod (for example) along the axis of the beamtube [19]. Unfortunately, this technique cannot be used to measure the impedance of a damped cell where the Q's are reduced to small values, because the frequency shifts are then too small compared to the bandwidth.

A technique that is more useful for the measurement of broad band impedances involves exciting fields in the cell by a twin lead placed along the axis. Beam tubes with a length several times their diameter are placed on either side of the accelerating gap to ensure that the localized cell fields (below cutoff) die out before reaching the end of the test system. The role of the twin lead is to induce a dipole surface current in the beam tubes of the same form as Eq. (6.26), except that Δ_x is now the spacing of the wires and $\pm I$ is the current in each wire. To accurately simulate the beam, the wave launched on the twin lead should be a pure forward (or backward)

UNCORRECTED PROOF

traveling wave, that is, reflections from the interaction with the gap should be a small perturbation. This sets an upper bound on the spacing of the wires that can be used to measure a given cell impedance and mode Q.

The impedance of the cell at any given frequency can be deduced from the perturbation in the transmitted signal due to the cell, i.e., by measuring S_{12} with a network analyzer. For accurate results, application of this technique involves a measurement of the transmission coefficient with the cell replaced by a smooth beam tube, and then subtracting this result from a measurement of the transmission with the cell in place. This technique was used to measure the transverse impedance of DARHT-I prototype cells, for example [20]. The main limitation in this approach comes from the fact that two comparable numbers must be subtracted to deduce the impedance. As a result, the accuracy of the dimensional parameters and the two S_{12} measurements must be very good to get a meaningful result.

An alternate approach was developed in the design and prototype testing of the DARHT-II induction linac cells [21, 22]. This approach also uses a twin lead to excite the RF fields in the cell, but it relies on a measurement of the radial dipole RF magnetic field in the gap $[B_r(b)]$ and the azimuthal dipole RF magnetic field in the beam tube away from the gap to determine $\eta(\omega)$ experimentally (from their ratio).

With a pure traveling wave set up by the twin lead, a measurement of the dipole B_θ at the wall some distance axially from the accelerator gap provides a direct measure of the magnitude of the "source current" in Eq. (6.26). The distance from the gap must be large enough for the cell fields (the fields created by the equivalent "negative" surface current and surface charge across the gap discussed above) to die out. The phase must be adjusted according to the distance from the loop to the gap center.

In the DARHT-II accelerator cell shown in Fig. 6.1, the loop to measure the radial RF magnetic field was inserted into the gap at a radius $r = r_p$ where the gap was a minimum (about 1.25 in. out from the beam tube radius of 5 in.). To obtain a more accurate measure of the axially-averaged radial field at $r = b$ $[\langle B_r(r = b)\rangle]$ that enters into the definition of η [see Eq. (6.28)], an interpolation scheme was used [21, 22]. This interpolation related the radial field at $r = b$ to the measured radial field at $r = r_p$, using a measurement of the azimuthal field in the gap at $r = r_p$, $\theta = 0$.

$$r_p\langle B_r(r_p)\rangle - b\langle B_r(b)\rangle = \int_b^{r_p} \mathrm{d}r\ \langle B_\theta(r)\rangle \approx (r_p - b)\langle B_\theta(r_p)\rangle. \tag{6.32}$$

The transverse impedance measurements of the DARHT-II cell obtained with this technique are presented in Fig. 6.12. As this data shows, the thin ferrite tiles inserted on the radial wall behind the insulator very effectively damped the modes. Using the DARHT-II cell dimensions in Eq. (6.30), the resistive impedance is 189 Im(η) Ω/m, giving a predicted (and observed) BBU growth rate that is minimal at beam currents of 1.5–2 kA.

We should note that we made an implicit assumption in this formulation and measurement technique that the gap width is small compared to the tube radius

UNCORRECTED PROOF

This figure will be printed in b/w

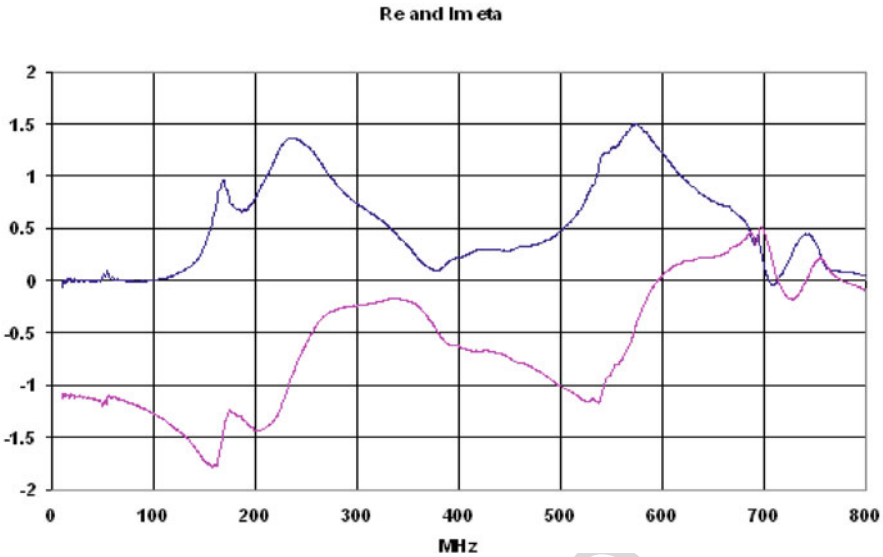

Fig. 6.12 Measurement of the real part of $\eta(\omega)$ (*lower curve*) and the imaginary part of $\eta(\omega)$ (*upper curve*) for the DARHT-II induction cell

(and wavelength). The force from the azimuthal electric field in the gap region could then be ignored compared to the radial magnetic field. Godfrey [23] has considered the contribution of the electric field to the transverse impedance for gap widths comparable or larger than the beam pipe radius. That case can lead to so-called "trapped modes" near cutoff when the gap width is larger, which can be especially dangerous because they are not damped by the cell design techniques discussed in Sect. 6.10.2.

6.11 High Average Power

Most induction accelerators constructed in the past have operated at very low average power. The heat generated by core losses was dissipated through natural conduction and convection without additional cooling. A small induction accelerator for food processing and the ETA-II were designed for high (kHz) repetition rates. Induction cell design for high repetition rates or high average power requires that an active cooling system be incorporated into the cell to insure that the average core temperature does not exceed certain limits. Short-pulse accelerators that use ferrites can be cooled by making toroids thinner, creating many cooling channels which allow circulation of the insulating fluid for heat removal. Long-pulse cells, which use tape wound cores, pose a more difficult problem. The ribbon width is limited and it must be exposed to the cooling fluid and still maintain the required voltage insulation between layers. No doubt, an induction cell for high average power poses a much greater challenge and requires careful cell design to satisfy all requirements.

UNCORRECTED

Induction cells in a synchrotron to provide acceleration and longitudinal focusing must operate at high repetition rates as discussed extensively in Chap. 11. This application has used Finemet and cooling studies indicate that in order to maintain safe temperature rise, a thinner material had to be used with a flux swing a small fraction of the total saturation flux swing, ΔB. Details of these developments are reported in Chap. 11. A proposed accelerator for free electron lasers (FEL) operating at 5 kHz CW required 1 m diameter toroids, 8 mm thick with 2 mm cooling channels to keep the PE11B or PE11BL ferrite temperature within bounds [24].

Another issue which must be taken into consideration in the cell design is the condition created when the beam load is missing. The loss of beam current can occur when there is a failure in the injector or the magnet transport system. Since the pulse generator (modulator) is designed to operate into a matched impedance including the beam, when the beam is absent, the cell voltage will step-up by an amount which is proportional to the ratio of total current to the current without the beam load. If the beam current is a very large fraction of the total current, near voltage doubling can occur at the acceleration gap if the beam is absent. The safety factors in the core volt-seconds are typically quite small and any voltage step-up will cause core saturation and voltage reversal. Depending on the severity of the saturation, nearly 100% voltage reversal can occur which can lead to breakdowns unless proper safety factors are incorporated. To prevent voltage reversal, clamping diodes are typically installed at the modulator output.

6.12 Summary of Cell Design

The requirements of the experimental program determine the basic accelerator parameters such as energy, current, pulse duration and repetition rate. Once these parameters are established, beam transport physics determine the gradient and inside radius to insure that the design is well within the stable operating range for beam breakup instabilities. The gradient and repetition rate give guidelines to establish the basic modulator technology. For example, at very low repetition rates it is acceptable to use spark gaps as switches, at medium repetition rates, thyratrons may be more appropriate and at very high repetition rates only solid state devices will be applicable. For an optimized design, it is important to determine the technology since the operating voltage level of the modulator will strongly influence the design of the cell. If spark gaps are used, a smaller number of cells at very high voltage can meet the energy requirements. If solid state devices are used, an intermediate step-up transformer or a much larger number of cells at lower voltage will be required. The cell design and choice of magnetic material to achieve the desired voltage, current and pulse duration are always done in concert with the modulator design. Once a final design is chosen a full scale prototype must be constructed to insure that all the required parameters are met and impedance measurements are made to insure that the beam breakup growth is acceptable. Extensive prototype testing at and well above the normal operating levels must also be performed to insure that the safety factors are met for long term operation.

UNCORRECTED PROOF

References

1. A. Faltens, D. Keefe, W. Salsig, and E. Hartwig. Preliminary Hardware Concepts for an Electron Ring Accelerator. *IEEE Trans. Nucl. Sci.*, NS-18:479–487, 1971. (Proceedings of the 1971 Particle Accelerator Conference, Chicago, IL, 1–3 March, IEEE).
2. L. Reginato, D. Branum, E. Cook, C. Fong, and D. Kippenhan. Advanced Test Accelerator (ATA) Pulse Power Technology Development. *IEEE Trans. Nucl. Sci.*, NS-28:2758, 1981.
3. D. Prono, D. Barret, E. Bowles, G. Caporaso, Y.-J. Chen, J. Clark, F. Coffield, M. Newton, W. Nexsen, D. Ravenscroft, W. Turner, and J. Watson. High Average Power Induction Linacs. In *Proceedings of the 1989 Particle Accelerator Conference*, page 1441, Chicago, IL, 20–23 Mar. 1989.
4. N. Christofilos, R. Hester, W. Lamb, D. Reagan, W. Sherwood, and R. Wright. High Current Linear Induction Accelerators for Electrons. *Rev. Sci. Inst.*, 35:886–890, 1964.
5. J. Beal, N. Christofilos, and R. Hester. The Astron Accelerator. *IEEE Trans. Nucl. Sci.*, NS-16:294, 1969.
6. W. Waldron and L. Reginato. Design and Performance of the DARHT Second-Axis Induction Cells and Drivers. In *Proceedings of the 24th-International Power Modulator Symposium*, pages 179–182, 26–29 June, Norfolk, VA, 2000.
7. W. Turner, G. Caporaso, G. D. Craig, J. De Ford, L. Reginato, S. Sampayan, R. Kuenning, and I. Smith. Impedance Characteristics of Induction Accelerator Cells. In *Proceedings of the 7th International Conference on High Power Particle Beams*, page 845, Karlsruhe, Germany, 4–8 July 1988.
8. J. Leiss, N. Norris, and M. Wilson. The Design and Performance of a Long Pulse High Current Linear Induction Accelerator at the National Bureau of Standards. *Part. Accel.*, 10:223–234, 1980.
9. A. Sessler and S. Yu. Relativistic Klystron Two-Beam Accelerator. *Phys. Rev. Lett.*, 54:889, 1987.
10. G. Westenskow and T. Houck. Relativistic Klystron Two-Beam Accelerator. *IEEE Trans. Plasma Sci.*, 22:750, 1994.
11. L. Reginato. Engineering Conceptual Design of the Relativistic Klystron Two-Beam Accelerator Based Power Source for 1-TeV Next Linear Collider. In *Proceedings of the 1995 Particle Accelerator Conference*, page 743, Dallas, TX, 1–5 May 1995.
12. L. Reginato. Induction Accelerator Development for Heavy Ion Fusion. *Nuovo Cimento Soc. Ital. Fis.*, 106:1445, 1993. (also Proceedings of the International Symposium on Heavy Ion Fusion, Frascati, Italy, 25–28 May, 1993.
13. T. Houck, F. Deadrick, G. Giordano, E. Henestroza, S. Lidia, L. Reginato, D. Vanecek, G. Westenskow, and S. Yu. Prototype Microwave Source for a Relativistic-Klystron Two-Beam Accelerator. *IEEE Trans. Plasma Sci.*, 24:938, 1996.
14. H. Kirk, R. Palmer, I. Gallardo, D. Kaplan, M. Green, L. Reginato, S. Yu, and Y. Fukui. Phase Rotation at the Front End of a Neutrino Factory. In *Proceedings of the 2001 Particle Accelerator Conference*, page 2026, Chicago, IL, 18–22 June 2001.
15. T. L. Houck, G. Caporaso, C. Shang, S. Sampayan, N. Molau, and M. Kro. Measured and Theoretical Characterization of the RF Properties of Stacked High-Gradient Insulator Material. In *Proceedings of the 1997 Particle Accelerator Conference*, page 2627, Vancouver, Canada, 12–16 May 1997.
16. S. E. Sampayan, G. Caporaso, D. Sanders, D. Stoddard, R. Trimble, T. Elizondo, and M. Krogh. High performance Insulator Structures for Accelerator Applications. In *Proceedings of the 1997 Particle Accelerator Conference*, page 1308, Vancouver, Canada, 12–16 May 1997.
17. R. Briggs and W. Fawley. A Simple Model for Induction Core Voltage Distributions. Technical Report LBNL-55079, Lawrence Berkeley National Laboratory, 2004. (also DARHT Tech Note No. 418).
18. C. Shang, Y.-J. Chen, T. Houck, G. Caporaso, W. Ng, N. Molau, J. Fockler, and S. Gregory. BBU Design of Linear Induction Accelerator Cells for Radiography Applications. In

UNCORRECTED PROOF

Proceedings of the 1997 Particle Accelerator Conference, pages 2632–2635, Vancouver, Canada, 12–16 May 1997.

19. R. Briggs, D. Birx., G. Caporaso, K. Neil, and T. Genoni. Theoretical and Experimental Investigation of the Interaction Impedances and Q Values of the Accelerating Cells in the Advanced Test Accelerator. *Part. Accel.*, 18:41, 1985.
20. L. Walling, P. Allison, M. Burns, D. Liska, D. McMurray, and A. Shapiro. Transverse Impedance Measurements of Prototype Cavities for a Dual-Axis Radiographic Hydrotest (DARHT) Facility. In *Proceedings of the 1991 Particle Accelerator Conference*, page 2961, San Francisco, CA, 6–9 May 1991.
21. R. Briggs, D. Birx, S. Nelson, L. Reginato, and M. Vella. Transverse Impedance Measurements of the DARHT-2 Accelerator Cell. In *Proceedings of the 2001 Particle Accelerator Conference*, pages TPH079, 1850, Chicago, IL, 18–22 June 2001.
22. R. Briggs and W. Fawley. Campaign to Minimize the Transverse Impedance of the DARHT-2 Induction Linac Cells. Technical Report LBNL-56796, Lawrence Berkeley National Laboratory, 2005. (also DARHT Tech Note No. 424).
23. B. Godfrey, Transverse Wake Potentials for Wide Radial Lines, MRC/ABQ-R-1046, March 1988 (unpublished).
24. J. Van Sant, Cooling Induction Accelerator Cores by Forced Flow Boiling PE11B Ferrite, Unpublished Beam Research Program Notes, Lawrence Livermore National Laboratory, 1986.

UNCORRECTED PROOF

Chapter 7
Electron Induction Linacs

George J. Caporaso and Yu-Jiuan Chen

UNCORRECTED PROOF

Electron induction linacs have been used for over four decades for a variety of applications. As discussed in Chap. 8, these include basic studies in magnetically confined fusion, transport of intense electron beams in various gases, the generation of electromagnetic radiation from free electron lasers, radiation processing of materials and food, and flash X-ray radiography sources.

In this chapter we will discuss the basic structure of electron induction linacs, describe the focusing system commonly used and treat the most important instabilities in these machines.

7.1 Introduction

Typical electron induction linacs incorporate focusing elements into each accelerator cell. Since the induction cells are electrically independent they may be closely placed without affecting their performance. In order to obtain the highest accelerating gradient possible, the usual configuration consists of accelerator cells grouped into blocks of 4–10 ~~that~~ are separated by short sections of transport tube called intercell regions. A typical 4-cell block is shown in Fig. 7.1. Solenoids are typically incorporated into the accelerator cells as can be seen, for example, in Fig. ~~7.2~~.

The intercell regions usually provide the pumping ports necessary to ensure adequate vacuum in the accelerator (typical pressures range from 10^{-6} to 10^{-8} Torr in long-pulse machines like DARHT-II). These pumping ports may also provide access for diagnostics such as insertable probes, cameras, etc. Diagnostics such as beam position monitors and current monitors are also generally located in these sections. Solenoids for focusing along with dipole steering coils are also typically found in intercells. The layout of an induction linac (the ETA-II at LLNL) is shown in Fig. 7.2, and the photo of the ETA-II is shown in Fig. 7.3.

G.J. Caporaso (✉)
Lawrence Livermore National Laboratory, Livermore, CA 94550, USA
e-mail: caporaso1@llnl.gov

K. Takayama, R.J. Briggs (eds.), *Induction Accelerators*, Particle Acceleration and Detection, DOI 10.1007/978-3-642-13917-8_7,
© Springer-Verlag Berlin Heidelberg 2011

This figure will be printed in b/w

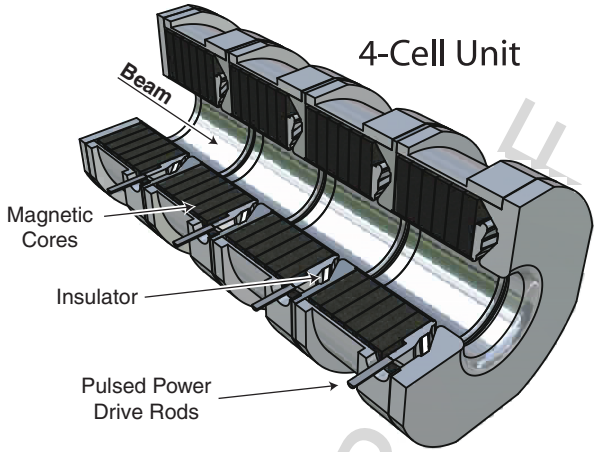

Fig. 7.1 A 4-cell block is illustrated ~~above~~. The induction cells do not interact electrically and may be placed as closely as possible to achieve maximum accelerating gradient

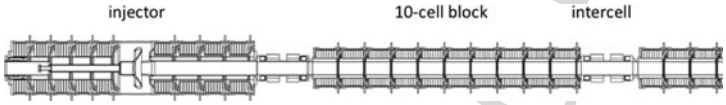

Fig. 7.2 Layouts of the ETA-II accelerator at LLNL is shown above. The machine consists of an injector with 9 induction cells and six 10-cell blocks

This figure will be printed in b/w

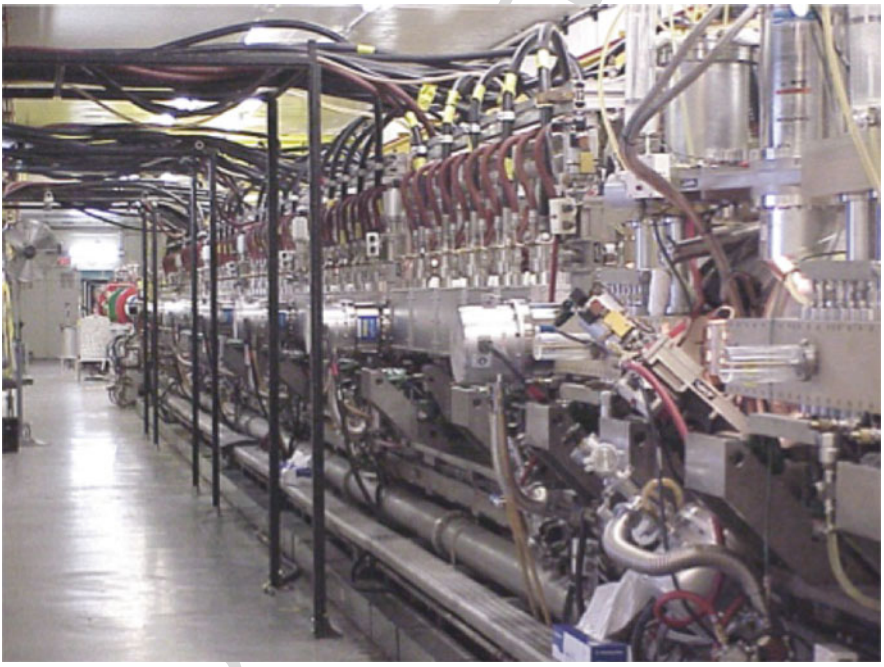

Fig. 7.3 The ETA-II accelerator at LLNL is shown above with the injector in the foreground. This accelerator consists of a 1 MeV injector with 9 induction cells followed by six 10-cell blocks. The machine produces a 5.3 MeV, 2 kA beam with a 50 ns pulsewidth and runs at 1 Hz. It has also operated at 2 kHz in burst mode as discussed in Chap. 2

The accelerator requires almost continuous focusing along its length to confine the beam against its space charge and to suppress the growth of instabilities. Electron induction linacs use solenoids to focus the beam as they are suitable for cylindrically symmetric beams and are compatible with placement into the induction cells without compromising the accelerating gradient.

The use of focusing is a double-edged sword. Since the focusing elements can never be perfectly aligned and the energy of the beam can never be perfectly constant across the pulse the beam centroid will develop progressively higher frequency distortions called *corkscrew* as the beam propagates. The beam is also subject to various instabilities as it propagates. Those of most concern are the *image displacement and beam breakup* (BBU) instabilities. Successful strategies to control all of these problems exist and will be described. We will begin by discussing beam formation.

7.2 Electron Sources

7.2.1 Cathodes

Most of the applications of the electron induction accelerators demand high current density beams, which are emitted from a conducting cathode material. There are several approaches that can be used for extracting electrons from the cathode.

Electrons in the cathode material's conduction band need to either surmount or tunnel through the potential barrier, the *work function*, between the conducting material and the vacuum interface before being extracted freely by the electric field in the electron gun. To help these electrons tunnel through the potential barrier, the electric field on the entire emitter surface needs to be in the range of 10^4 kV/cm, which is hard to do. When the electric field on the emitter surface reaches this level, it is very likely that all the conducting electrodes and beam pipe wall in the electron gun are also emitting.

We can provide electrons with additional energy by heating the cathode either with a conventional heat source or an intense laser beam, such that these electrons have large enough kinetic energy to overcome the work function of the material (typically a few tenths of an eV) and escape the surface.

The mechanism for electron emission using a conventional heating method is called *thermionic emission*. The ETA-II injector uses a thermionic dispe cathode, which is a porous tungsten disk impregnated with $6BaO-CaO-2Al_2O_3$ and coated with osmium alloy. The coatings on the thermionic cathodes usually lower the work function by roughly 50%. However, they tend to be poisoned easily. The electron gun's vacuum needs to be around 10^{-7} Torr or better. Typically, thermionic dispenser cathodes need to be heated to around 1,100°C in order to provide space charge limited emission, and hence the intrinsic electron temperature is about 0.1 eV. The thermionic emitters have been consistently delivering current density of 10–100 A/cm^2. Their high current density and low intrinsic electron temperature make them a good source for generating high brightness beams. The lifetime for operating at the space charge limited emission region is about 1,000 h at 10 A/cm^2.

UNCORRECTED PROOF

The mechanism for electron emission using a laser is called *photoemission*. So far, this kind of cathode (photocathode) has been used mainly in RF machines, in which the beam pulses are a few picoseconds to a few nanoseconds in length. A space charge limited current at about 90 A/cm^2 over 15 ns was achieved in a feasibility study at LANL [1] with a cathode made of Pb and Al. However, using photoemission to generate longer beam pulses or higher current density beams could be problematic. The high laser intensity (about 1 MW/cm^2) needed to achieve space charge limited emission will create a plasma near the cathode surface and in the anode–cathode gap. The beam quality will then be degraded by this plasma formation. Without degradation by plasma formation, the electron beam's intrinsic temperature is also about 0.1 eV.

Another approach to generate beams is to reduce the work function of the emitter in situ with electron emission. First, the electric fields are enhanced locally, which leads to field emission (breakdown). The localized breakdown produces a cold, dense plasma arising from adsorbed gasses on the emitter surface. Since plasma has a near zero work function, the anode–cathode gap electric fields can easily extract an electron current from this plasma. This emission mechanism is called *explosive emission*. This type of emitter does not require any additional heating, and is inexpensive. A typical cathode only consists of a piece of ordinary velvet [2] cloth glued with conductive epoxy to a metal plate. Simply apply an electric field greater than 16 kV/cm in the anode–cathode gap. The bound polarization charge at the tip of the dielectric fiber will enhance the electric field at the tip, which leads to plasma formation and subsequent electron emission. Depending on the distribution of the velvet's tufts, electron emission could be uniform and up to 1 kA/cm^2. The intrinsic temperature of the emitted electrons is in the range of 0.5–2 eV [2, 3]. The plasma gap closure velocity is reasonably low at about 2 mm/μs. Since cathode poisoning is not an issue, the vacuum in the gun region can be 1–2 orders higher than that for thermionic cathodes. Its only obvious disadvantage is that the velvet fibers will erode during a beam pulse. Velvet cathodes have been used in single-pulse machines, such as ATA and on the first axis of DARHT. The lifetime of velvet emitters is about 10^5 shots for regular velvet and 10^6 for velvets coated with a cesium iodide salt [3].

7.2.2 Electron Guns

Figure 7.4 shows the configuration of LLNL's 1 MeV, 2 kA ETA-II injector. This injector consists of nine induction cells and a diode. There are 5 induction cells to the left of the diode and 4 cells to the right of the diode with the electron beam going to the right. The beampipe and the inner bores of those induction cells at the anode side form a transmission line. Voltage waves created in those cells travel down the transmission line and provide the voltage on the anode electrode. Similarly, the cathode stalk and the inner bores of the induction cells at the cathode side form another transmission line. Voltages generated at those cells would be applied to the cathode. Each induction cell provides a voltage at 111.1 kV, and the total anode–cathode

UNCORRECTED PROOF

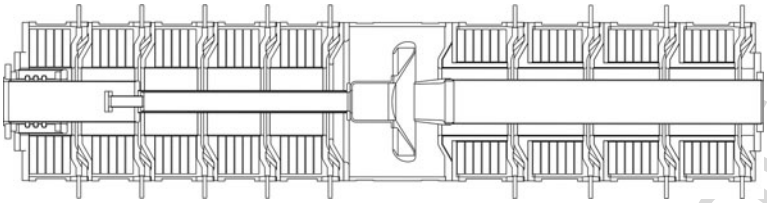

Fig. 7.4 Configuration of LLNL's 1 MeV, 2 kA ETA-II injector

gap voltage is 1 MV. Once the beam enters the anode entrance, the space charge dominated beam will not be accelerated while it propagates in the injector beampipe. One may prefer to minimize the distance that the space charge dominated beam would travel before entering the accelerator by putting all the induction cells at the cathode side. However, the cathode stalk would be long for this configuration, which may be difficult to design and maintain mechanical alignment. To minimize the cathode stalk length by putting all the cells at the anode side is also not desirable since it maximizes the distance that the space charge dominated beam has to travel before being accelerated. The optimal configuration is to minimize the distance between the anode entrance and the accelerator entrance and the cathode stalk length simultaneously. The ETA-II injector, as shown in Fig. 7.4, has 4 cells at the anode side and 5 cells at the cathode.

The ETA-II diode is very similar to the schematic of the diode region shown in Fig. 7.5. The entire system is cylindrically symmetric about the axis of the accelerator. ~~Later in Sect. 7.4, we will discuss that a~~ nonzero canonical angular momentum, an invariant, lead~~s~~ to an increase of the effective beam emittance. To minimize the canonical angular momentum, one or two bucking coils are used to cancel external focusing magnetic fields at the cathode so that the electrons would be born in a magnetically field-free region. The Pierce-angled cathode shroud is at the same voltage

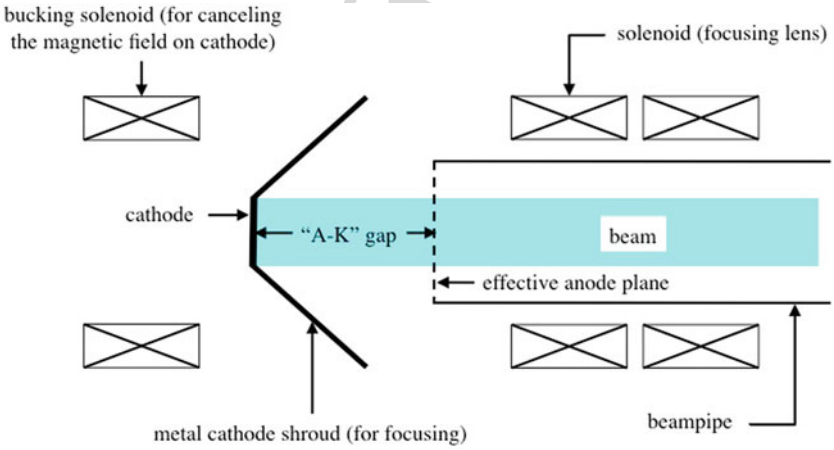

Fig. 7.5 Diagram of a diode region of a typical injector

as the cathode and is used to shape the potential contours near the cathode. This provides focusing for the electrons in that region and also guides the electrons to, ideally, produce a laminar flow. Once the extracted beam leaves the area immediate to the cathode surface, it is held together (focused) by an array of solenoids wrapped around the anode pipe. Although the detailed geometry of the diode configuration will affect the emitted current density, the Child-Langmuir law for space charge limited current density emitted from a planar diode given as

$$J_0 = \frac{4}{9}\sqrt{\frac{2e}{m}}\frac{\epsilon_0 V_0^{3/2}}{d^2} = \frac{2.33 \times 10^{-6} V_0^{3/2}}{d^2} \tag{7.1}$$

provides a reasonable estimation for the emitted current density [4, 5]. Note that the Child-Langmuir law describes the emission of a non-relativistic beam. H. Ivey provided a modified space-charge-limited emission law for a relativistic beam [6]. As shown in Fig. 7.6, the relativistic effects suppress the electron emission somewhat.

Generally, to obtain a small emittance and high current beam, the cathode area should be small while the field stress in the diode region should be high. This may lead to unwanted emission from electrodes due to excessive field stress on the electrode surfaces. While electrons emitted at the tip of the shroud, where the field stress is largest, cannot enter the anode entrance and spoil the beam emittance, electrons emitted from the shroud near the cathode can easily be captured and phase-mix with the beam. These electrons are born at a large angle, θ_{sh} with respect to the laminar flow. They can greatly increase the beam emittance. Figure 7.7 shows PIC simulations of how a small fraction of electrons, 0.8% of the total ETA-II beam current, emitted from the inner radius of the shroud are captured by the beam as it is transported between the cathode and anode [7]. These unwanted electrons cause ~~very~~ large emittance growth. Let n be the fraction of beam current field-emitted from the shroud with respect to the total extracted current. The factor of emittance growth is approximately given by $1 + n\theta_{sh}/\theta_{th}$, where θ_{th} is the intrinsic thermal angle of electrons emitted from the cathode. To avoid this source of emittance growth, injectors should use larger area cathodes with minimum field stress. Also, the shroud electrode should be made of a material that is resistant to electron emission.

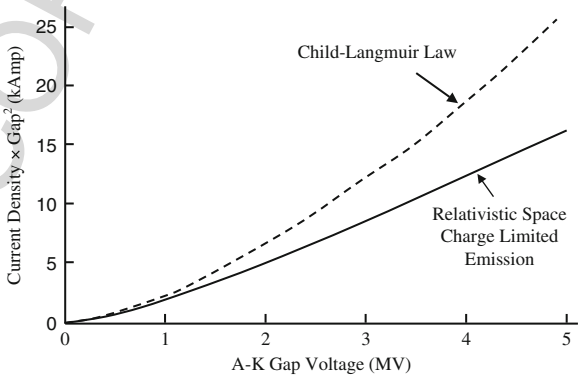

Fig. 7.6 Comparison of the relativistic space-charge-limited current and Child-Langmuir law

UNCORRECTED PROOF

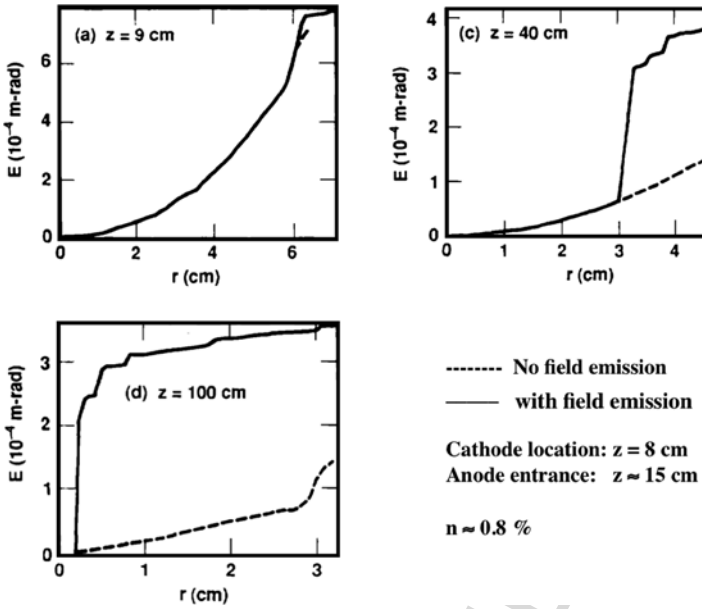

Fig. 7.7 Normalized emittance, E, of the enclosed beam within radius r vs. r is plotted with and without the presence of field emitted electrons from the shroud. The plots, given at various transport distances, show the degradation of beam emittance resulting from mixing in a small number of field-emitted electrons from the shroud (0.8% of the total beam)

7.3 Beam Dynamics in Induction Machines

7.3.1 Basic Force Equation

We wish to consider the motions of both individual charged particles and collections of charged particles (beams). The motions of all particles, charged or otherwise, are governed by

$$\frac{\mathrm{d}\mathbf{p}}{\mathrm{d}t} = \mathbf{F}, \tag{7.2}$$

where $\mathbf{F}$ is the force vector which acts on the particle whose momentum vector is given by $\mathbf{p}$. This equation holds for all forces and is valid for relativistic as well as non-relativistic motion (note that the familiar $m\mathbf{a} = \mathbf{F}$ is just a special case of Eq. (7.2) which is valid when the mass is constant). For a charged particle with charge q the force is just given by the *Lorentz Force*

$$\mathbf{F}_L = q[\mathbf{E} + \mathbf{v} \times \mathbf{B}] \tag{7.3}$$

where $\mathbf{E}$ is the electric field and $\mathbf{B}$ is the magnetic field.

UNCORRECTED PROOF

For an electron moving along the z-axis and subject to only transverse forces the equation of motion becomes

$$\gamma_b m_e \frac{\mathrm{d}\mathbf{v}}{\mathrm{d}t} = -e[\mathbf{E} + \mathbf{v} \times \mathbf{B}]_\perp \tag{7.4}$$

where the subscript on the Lorentz force indicates that we are just taking the transverse component. Here

$$\gamma_b = \frac{1}{\sqrt{1 - \frac{\mathbf{v}^2}{c^2}}} \tag{7.5}$$

and $\gamma_b m_e$ is the "transverse mass". If acceleration is present (due to a z-component of electric field from an accelerating cell for instance) then we must replace the left hand side of Eq. (7.4) by $\mathrm{d}(\gamma_b m_e \mathbf{v})/\mathrm{d}t$. From this point on we will assume that we have purely transverse forces.

A very important case ~~that occurs frequently~~ in practice is that of transverse velocities ~~which are~~ small compared to the longitudinal velocity. Equivalently, whenever $\partial x/\partial z$ and $\partial y/\partial z$ are *both* substantially less than 1 we speak of the motion as being "paraxial" (nearly parallel to the axis). This is frequently the case for a relativistic particle and allows us to simplify the dynamics by replacing t with z as the independent variable in the force equation.

If $v_\perp^2/v^2 \ll 1$ then we have that $v_z \simeq v$ (in practice this is usually a good approximation if $\partial x/\partial z \leq 1/3$). Under these conditions we can write

$$\frac{\mathrm{d}}{\mathrm{d}t} \simeq v\frac{\mathrm{d}}{\mathrm{d}z} \simeq v_z\frac{\mathrm{d}}{\mathrm{d}z} \tag{7.6}$$

for a single particle.

With this approximation we may rewrite the equation of motion (7.4) as

$$\gamma_b \beta^2 m_e c^2 \frac{\mathrm{d}^2\mathbf{r}}{\mathrm{d}z^2} = -e[\mathbf{E} + \mathbf{v} \times \mathbf{B}]_\perp, \tag{7.7}$$

where $\mathbf{r}$ is the transverse position vector.

7.3.2 Coordinate Description of a Beam

We wish to consider the analog of Eq. (7.7) that is appropriate for a collection of particles (a beam) instead of just one. If we had N particles in our beam we could just hang a subscript on $\mathbf{r}$ and write Eq. (7.7) for each of them.

We could also regard the beam as a continuous fluid. In this case the beam dynamics will be a function of time (or equivalently, z) and some other quantity

UNCORRECTED PROOF

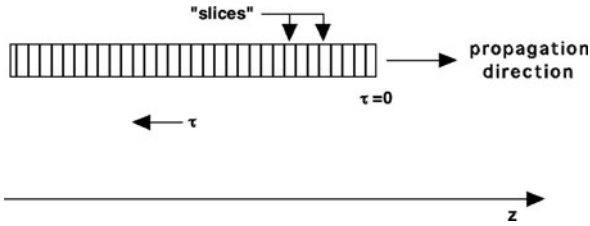

Fig. 7.8 Beam coordinate system

that labels the position of the particle along the beam. We will imagine that the beam can be divided into imaginary "slices" labeled by a coordinate τ that has the definition

$$\tau \equiv t - \frac{z}{v}. \tag{7.8}$$

τ is usually defined so that it is zero at the front or head of the beam and increases toward the tail.

The quantity τ is a local coordinate in the beam frame (i.e., if you were riding along with the beam, τ would measure the distance back from the head of the beam divided by v). Another way to think of τ is that if you had an array of beam position monitors along the accelerator that you were examining with oscilloscopes, the time axis on each scope trace would actually be τ. In general, all quantities we would want to compute are functions of z and τ. So if we have some function $f(z, \tau)$, then its total time derivative is

$$\frac{\mathrm{d}f(z, \tau = t - z/v)}{\mathrm{d}t} = \left.\frac{\partial f}{\partial z}\right|_{\tau} \frac{\mathrm{d}z}{\mathrm{d}t} + \left.\frac{\partial f}{\partial \tau}\right|_{z} \left(\frac{\mathrm{d}t}{\mathrm{d}t} - \frac{1}{v}\frac{\mathrm{d}z}{\mathrm{d}t}\right) = v \left.\frac{\partial f}{\partial z}\right|_{\tau}, \tag{7.9}$$

and our analog of Eq. (7.7) for a continuous beam becomes simply

$$\gamma_b \beta^2 m_e c^2 \frac{\partial^2 \mathbf{r}(z, \tau)}{\partial z^2} = -e[\mathbf{E} + \mathbf{v} \times \mathbf{B}]_{\perp}. \tag{7.10}$$

7.3.3 Focusing in a Solenoidal Field

Let us consider a solenoid [8] that is one of the most commonly used focusing systems for electrons (virtually all electron induction accelerators use solenoidal focusing).

Because the magnetic field lines must close on themselves (since the divergence of **B** is zero), there must be a radial as well as an axial component of field in a finite length solenoid:

$$\mathbf{B} = \hat{\mathbf{e}}_r B_r + \hat{\mathbf{e}}_z B_z. \tag{7.11}$$

UNCORRECTED PROOF

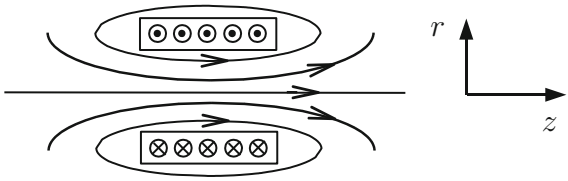

Fig. 7.9 Schematic of a solenoid with current coming out of the page in the upper plane and entering the page in the lower plane. The *curves* wrapping around the solenoid indicate the magnetic field lines

We can estimate this radial field by using the fact that the divergence of the magnetic field vanishes. We have (with no azimuthal field)

$$\nabla \cdot \mathbf{B} = 0 = \frac{1}{r}\frac{\partial}{\partial r}(rB_r) + \frac{\partial B_z}{\partial z}. \tag{7.12}$$

Now near the z-axis we have approximately that

$$B_r \simeq -\frac{r}{2}\frac{\partial B_z(z,0)}{\partial z}, \tag{7.13}$$

where we have integrated Eq. (7.12) with respect to r by taking the z-derivative of B_z to be a constant (at its on-axis value). The radial component causes a divergence of the field lines at either end of the solenoid. These are referred to as "fringe fields." The normalized B_z field and B_r/r are plotted in Fig. 7.10.

Solenoids can focus a beam and confine the transverse motion of its centroid. We will consider the idealized case of a continuous, constant solenoidal field (in actuality, the focusing is provided by many discrete solenoids usually placed so close together that the field is treated as continuous to a first approximation). The case of a magnetic field that varies in z can be treated by the same methods but is somewhat more complicated. In what follows we will consider only a constant field. In that case the magnetic field is just

$$\mathbf{B} = \hat{\mathbf{e}}_z B_0. \tag{7.14}$$

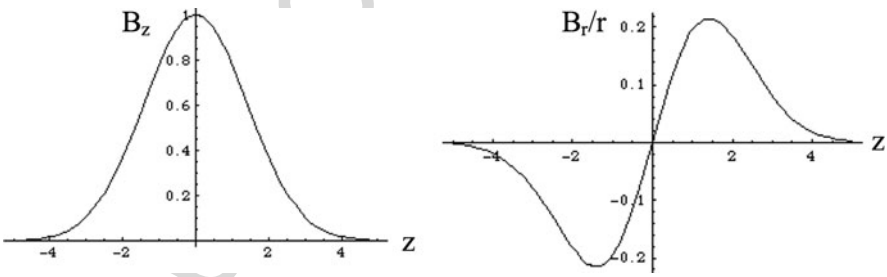

Fig. 7.10 Plots of the normalized z and r components of the field of a solenoid

UNCORRECTED PROOF

The equation of motion just becomes

$$\gamma_b \beta^2 m_e c^2 \frac{\partial^2 \mathbf{r}}{\partial z^2} = -e\mathbf{v} \times \mathbf{B}. \tag{7.15}$$

Using Eq. (7.14) this becomes

$$\frac{\partial^2 \mathbf{r}}{\partial z^2} = -\frac{e}{\gamma_b \beta^2 m_e c^2} \left[\beta c \frac{\partial x}{\partial z} \hat{\mathbf{e}}_x + \beta c \frac{\partial y}{\partial z} \hat{\mathbf{e}}_y + \beta c \hat{\mathbf{e}}_z \right] \times \hat{\mathbf{e}}_z B_0. \tag{7.16}$$

Retaining only transverse components of force this becomes

$$\frac{\partial^2 \mathbf{r}}{\partial z^2} = -\frac{e B_0}{\gamma_b \beta m_e c} \left[-\hat{\mathbf{e}}_y \frac{\partial x}{\partial z} + \hat{\mathbf{e}}_x \frac{\partial y}{\partial z} \right]. \tag{7.17}$$

Finally, these can be simplified as

$$x'' + k_c y' = 0, \tag{7.18}$$

and

$$y'' - k_c x' = 0, \tag{7.19}$$

where a prime denotes differentiation with respect to z and where we define the *cyclotron wavenumber* k_c as

$$k_c \equiv \frac{e B_0}{\gamma_b \beta m_e c} = \frac{B_0(\mathrm{kg})}{1.703 \gamma_b \beta} (\mathrm{cm}^{-1}). \tag{7.20}$$

The cyclotron wavenumber is a measure of the focusing strength of the solenoid.

The easiest way to solve the coupled set of Eqs. (7.18) and (7.19) is to use *phasors*. A phasor is a complex quantity that we can use to combine Eqs. (7.18) and (7.19) into a single equation. We define the phasor ξ as

$$\xi \equiv x + iy. \tag{7.21}$$

Multiplying Eq. (7.19) by i and adding it to Eq. (7.18) and using the definition (7.21) we have

$$\xi'' - i k_c \xi' = 0. \tag{7.22}$$

Once we solve Eq. (7.22) we can immediately find x and y as

$$x = \mathrm{Re}(\xi), \tag{7.23}$$

UNCORRECTED PROOF

and

$$y = \mathrm{Im}(\xi), \tag{7.24}$$

The solution to Eq. (7.22) is just

$$\xi = A + Be^{ik_c z}, \tag{7.25}$$

where A and B are complex constants that will be determined by the initial conditions on x, y, x' and y'. We have

$$\xi(0) = x(0) + iy(0) = A + B, \tag{7.26}$$

while

$$\xi'(0) = x'(0) + iy'(0) = ik_c B. \tag{7.27}$$

Thus

$$\xi(z) = \xi(0) + \frac{i\xi'(0)}{k_c} - \frac{i\xi'(0)}{k_c} e^{ik_c z}. \tag{7.28}$$

Taking the real and imaginary parts and using Eqs. (7.26) and (7.27) we find that

$$x(z) = x(0) - \frac{y'(0)}{k_c} + \frac{y'(0)}{k_c} \cos k_c z + \frac{x'(0)}{k_c} \sin k_c z, \tag{7.29}$$

and

$$y(z) = y(0) + \frac{x'(0)}{k_c} - \frac{x'(0)}{k_c} \cos k_c z + \frac{y'(0)}{k_c} \sin k_c z. \tag{7.30}$$

Let us consider a simple example with $x(0) = y(0) = x'(0) = 0$ and $y'(0) = y'_0$. Then we have

$$x(z) = -\frac{y'_0[1 - \cos k_c z]}{k_c}, \tag{7.31}$$

and

$$y(z) = \frac{y'_0}{k_c} \sin k_c z. \tag{7.32}$$

Projected onto the x–y plane this motion is just a circle. In the laboratory frame the orbit describes a helix since it is advancing in z.

UNCORRECTED PROOF

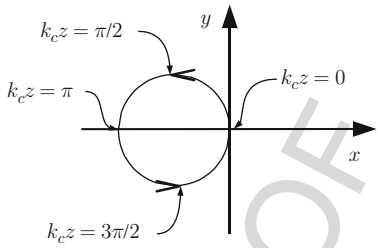

Fig. 7.11 Projection of the particle orbit onto the x–y plane for the example in the text

It is not clear how the motion depicted in Fig. 7.11 describes focusing. We will find that when viewed from a special reference frame this motion will appear intuitively to provide focusing. We will first do this mathematically and then show how it works physically.

Let us return to Eq. (7.22) and solve it in another way. We can remove the first derivative by use of a standard mathematical trick. We define a new dependent variable Ω such that

$$\xi = \Omega e^{\frac{ik_c z}{2}}, \tag{7.33}$$

and substitute it into Eq. (7.34). We have

$$\xi' = \left(\Omega' + \frac{ik_c\Omega}{2}\right) e^{\frac{ik_c z}{2}}, \tag{7.34}$$

and

$$\xi'' = \left(\Omega'' + ik_c\Omega' - \frac{k_c^2\Omega}{4}\right) e^{\frac{ik_c z}{2}}. \tag{7.35}$$

Substitution of these expressions into Eq. (7.22) yields

$$\Omega'' + \frac{k_c^2\Omega}{4} = 0. \tag{7.36}$$

We note that Eq. (7.36) is a harmonic oscillator equation with *betatron wavenumber* given by $k_c/2$. What we have done with the transformation given by Eq. (7.33) is to go into a rotating reference frame that is spinning with angular "velocity" given by $k_c/2$ which is called the *Larmor wavenumber* or "frequency" (the rotating frame is called the Larmor frame). When viewed in this frame the motion described by Eqs. (7.31) and (7.32) is an oscillatory motion in a single plane which goes through the origin. Figure 7.12 shows the Larmor frame and its relationship to the laboratory frame.

Let us reexamine the motion shown in Fig. 7.11. We will label various points corresponding to increments of $k_c z$ equal to $\pi/2$ in both the laboratory and Larmor frames as shown in Fig. 7.13.

UNCORRECTED PROOF

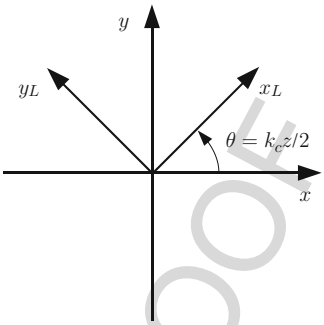

Fig. 7.12 The Larmor frame and its relationship to the laboratory reference frame

The orbit starts at position 1 which is at the origin in both coordinate systems. By the time the particle has advanced to position 2 in the lab frame, the Larmor frame has rotated by such an amount that the particle is along its positive y-axis. By position 3 the Larmor frame has rotated counter-clockwise by 90° so that position 3 appears further out along its positive y-axis. By position 4 the electron appears to be moving down along the positive y-axis of the Larmor frame and by the time the electron has moved to position 5 it has completed one cyclotron orbit in the lab frame *but only half a betatron orbit in the Larmor frame*. At this point the Larmor frame has rotated 180° counter-clockwise so that the negative-y axis is pointing "up" in the lab frame. Therefore, as the electron makes its second orbit in the lab frame it will be seen to move up and down along the negative y-axis in the Larmor frame. Upon completion of its second orbit the Larmor frame would have rotated a full 360°. This picture is essentially unchanged even if the magnetic field changes with propagation distance.

Thus far we have looked at the focusing effect of an electron in a constant, axial field and we found that transverse components of velocity were needed in order for there to be any transverse force components. If the electron is moving purely parallel to the field no forces will be generated. Of course, real focusing systems have solenoids of finite length so that there will be fringe fields. These fringe fields will give rise to transverse components of velocity which the main, axial field can

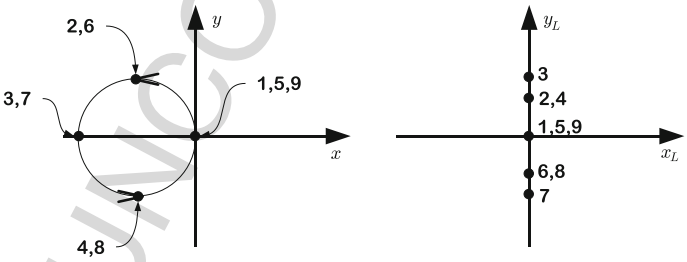

Fig. 7.13 Motion of an electron in a uniform solenoidal field as observed over two complete orbits in the laboratory frame (*left*) and in the Larmor frame (*right*)

UNCORRECTED PROOF

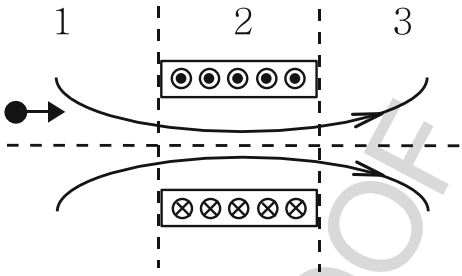

Fig. 7.14 Fields of a solenoid divided into two fringe field regions and an interior region of approximately constant axial field

then act on to give focusing. The actual mechanism can be understood in terms of a three-stage process depicted in Fig. 7.14.

We divide the fields of the solenoid arbitrarily into three regions. In region 1 a charged particle moving parallel to the axis of the solenoid is acted upon by the *radial* component of the field giving rise to an *azimuthal* velocity. In the interior region (region 2) the situation is roughly what we have just investigated, a constant axial field. The azimuthal velocity is now acted upon by the axial field to produce a radial (focusing) force. As the particle leaves the solenoid in region 3 it encounters a radial field of opposite sign to that in region 1 which spins the particle back down, removing its azimuthal velocity. The particle then leaves the solenoid with a net kick towards the axis and no rotation.

Solenoids whose polarities alternate from one to the next can also be used to stably transport a beam and have certain advantages. Magnetic and electric quadrupoles can also be used to focus and guide beams. Magnetic quadrupoles have generally been employed only for downstream beamlines in electron induction linacs as described in detail in Chap. 8.

7.4 Envelope Equations

There are several types of envelope equations that can be found in the literature. One that is widely used in electron induction linacs is that due to Lee and Cooper [9]. It is an equation for the RMS (root mean square) radius of a cylindrically symmetric beam and is correct for arbitrary radial density profiles (since almost all induction linacs use solenoidal focusing the beam is generally cylindrically symmetric inside the accelerator).

7.4.1 Lee-Cooper Envelope Equation

We will sketch the derivation of this envelope equation. We start from the single particle equation of motion for a particle subjected to a radial force $F(r)$:

$$\gamma_b \beta^2 m_e c^2 \frac{\partial^2 \mathbf{r}}{\partial z^2} = F(r)\hat{\mathbf{e}}_r. \tag{7.37}$$

UNCORRECTED PROOF

We now dot $\mathbf{r}$ into this equation to get

$$\gamma_b \beta^2 m_e c^2 \mathbf{r} \cdot \frac{\partial^2 \mathbf{r}}{\partial z^2} = F(r) r. \tag{7.38}$$

Now

$$\mathbf{r} \cdot \frac{\partial^2 \mathbf{r}}{\partial z^2} = \frac{\partial^2}{\partial z^2}\left(\frac{\mathbf{r} \cdot \mathbf{r}}{2}\right) - \left(\frac{\partial \mathbf{r}}{\partial z}\right)^2, \tag{7.39}$$

so that Eq. (7.38) can be written as

$$\gamma_b \beta^2 m_e c^2 \left[\frac{\partial^2}{\partial z^2}\left(\frac{r^2}{2}\right) - \left(\frac{\partial \mathbf{r}}{\partial z}\right)^2\right] = F(r) r. \tag{7.40}$$

We now average this equation over the beam profile. The average of r^2 is just the square of the RMS radius R. The second term in brackets in Eq. (7.40) is just the square of the total transverse velocity so that its average is the square of the RMS transverse velocity V (when using z as the independent variable we will often speak of a quantity such as $\partial x/\partial z$ as a *velocity* even though it is dimensionless and is in fact an angle). Performing the average yields

$$\gamma_b \beta^2 m_e c^2 \left[\frac{\partial^2}{\partial z^2}\left(\frac{R^2}{2}\right) - V^2\right] = \overline{F(r) r}, \tag{7.41}$$

where the bar over the right hand side indicates an average over the beam. Expanding the second derivative gives (where a prime denotes differentiation with respect to z)

$$\gamma_b \beta^2 m_e c^2 (R R'' + R'^2 - V^2) = \overline{F(r) r}. \tag{7.42}$$

We can now write this as

$$R'' = \left(\frac{V^2 - R'^2}{R}\right) + \frac{\overline{F(r) r}}{\gamma_b \beta^2 m_e c^2 R}. \tag{7.43}$$

We must now define a quantity called the *emittance* which is a measure of the area in transverse phase space occupied by the beam (actually it is the area in transverse *trace* space x–x' as opposed to phase space which is x–p_x). For a cylindrically symmetric beam the RMS emittance E is given by

$$E = R\theta_t, \tag{7.44}$$

where θ_t is the RMS random transverse velocity at a point where the beam has $R' = 0$. The quantity $\gamma\beta E$ is called the *normalized RMS emittance* and is constant

UNCORRECTED PROOF

if the forces on the beam are linear in radius. When these forces are not linear ~~then~~ the emittance may grow and the envelope equation becomes less accurate as a computational tool to evaluate beam behavior.

The condition that the emittance is conserved implies that the external forces are linear in r and that the beam undergoes *self-similar* (profile preserving) radial motion. Under these assumptions we may decompose the transverse velocity into a coherent part and a random residual part

$$\mathbf{V} = R' \frac{\mathbf{r}}{R} + \boldsymbol{\theta}_t. \tag{7.45}$$

Now if we square Eq. (7.45) and average over the beam we obtain

$$V^2 = R'^2 + \theta_t^2 + 2\frac{R'}{R}\overline{\mathbf{r} \cdot \boldsymbol{\theta}_t}. \tag{7.46}$$

The last term in Eq. (7.46) vanishes since it is the average of the radial component of the random velocity which has zero mean. Therefore we have that

$$\theta_t^2 = V^2 - R'^2, \tag{7.47}$$

so that with the help of Eq. (7.44) we may write Eq. (7.43) as

$$R'' = \frac{E^2}{R^3} + \frac{\overline{F(r)r}}{\gamma_b \beta^2 m_e c^2 R}. \tag{7.48}$$

Equation (7.48) is a simplified form of the beam envelope equation. The force $F(r)$ in general includes the beam's own space charge fields and the external focusing force.

Let us consider the beam's space charge fields first. When viewed in the lab frame the beam has a line charge density of $I(r)/\beta c$ which produces a radial electric field

$$E_r = \frac{I(r)}{2\pi\epsilon_0 \beta c r}, \tag{7.49}$$

where $I(r)$ is the current enclosed as a function of radius.

Now the beam also appears in the lab frame as a moving current so that it produces an azimuthal component of magnetic field

$$B_\theta = \frac{\mu_0 I(r)}{2\pi r}. \tag{7.50}$$

The total (radial) Lorentz force on a charged particle in the beam is given by

$$F(r)_s = e[E_r - \beta c B_\theta] = e\left[\frac{I(r)}{2\pi\epsilon_0 \beta c r} - \frac{\mu_0 I(r)\beta c}{2\pi r}\right] = \frac{e I(r)}{2\pi\epsilon_0 \gamma_b^2 \beta c r}, \tag{7.51}$$

UNCORRECTED PROOF

where we have used the fact that $\gamma_b^{-2} = 1 - \beta^2$. The subscript s on the left hand side of Eq. (7.51) refers to the fact that we are computing the radial force due only to the beam's self fields. The net self force causes the beam to expand.

Let us now consider the average of $F(r)_s r$ over the beam:

$$\overline{F(r)_s r} = \frac{e\overline{I(r)}}{2\pi\epsilon_0\gamma_b^2\beta c}. \tag{7.52}$$

To compute the average over the beam of any quantity A we use the prescription

$$\overline{A} = \frac{1}{I}\int_0^\infty 2\pi r J(r) A \mathrm{d}r, \tag{7.53}$$

where $J(r)$ is the current density. This simply weights the quantity $A(r)$ by the amount of current near that radius and is the continuum analog of summing the quantity A_i for a beam particle over all the particles in the beam and dividing by the total number. But

$$J(r) = \frac{1}{2\pi r}\frac{\mathrm{d}I(r)}{\mathrm{d}r}, \tag{7.54}$$

so that Eq. (7.52) can be written as

$$\overline{F(r)_s r} = \frac{e}{2\pi\epsilon_0\gamma_b^2\beta c I}\int_0^\infty I(r)\frac{\mathrm{d}I(r)}{\mathrm{d}r}\mathrm{d}r = \frac{eI}{4\pi\epsilon_0\gamma_b^2\beta c}. \tag{7.55}$$

Using this result in Eq. (7.48) gives the envelope equation

$$R'' = \frac{E^2}{R^3} + \frac{I}{(\gamma_b\beta)^3 I_0 R} + \frac{\overline{F(r)_f r}}{\gamma_b\beta^2 m_e c^2 R} \tag{7.56}$$

where the quantity I_0 which has dimensions of current is

$$I_0 = \frac{4\pi\epsilon_0 m_e c^3}{e} \cong 17.1 \text{ kA}. \tag{7.57}$$

I_0 is related to the Alfvén current I_A by $I_A = \gamma\beta I_0$ which represents a limiting current where the beam's magnetic field bends the electrons backwards and inhibits propagation in vacuum [10]. The subscript f on $F(r)$ on the right hand side of Eq. (7.56) refers to the fact that now $F(r)$ is due to external focusing forces.

We have derived Eq. (7.56) under the assumption that γ was held constant. That restriction may be removed to produce a more general envelope equation capable of handling acceleration. When external focusing is present it can be represented by a term proportional to R (this will be valid for solenoids or any other type of linear focusing system). The constant of proportionality is the square of the betatron

UNCORRECTED PROOF

wavenumber which is the analog of the oscillation frequency in a mass-spring system. The betatron wavenumber is in general a function of z. Thus we may write

$$R'' + \frac{(\gamma_b\beta)'}{\gamma_b\beta}R' = \frac{E^2}{R^3} + \frac{I}{(\gamma_b\beta)^3 I_0 R} - k_\beta^2 R. \tag{7.58}$$

Equation (7.58) is the most general envelope equation for a cylindrically symmetric beam (without canonical angular momentum that is).

There are many interesting and useful solutions to Eq. (7.58). We will examine just one of these: the equilibrium radius of the beam in a solenoidal focusing field. The condition for equilibrium is

$$R'' = R' = 0. \tag{7.59}$$

The solution of Eq. (7.58) then becomes

$$R = \sqrt{\frac{2E}{k_c}}\left[\theta + \sqrt{\theta^2 + 1}\right]^{1/2}, \tag{7.60}$$

where the dimensionless quantity θ is given by

$$\theta \equiv \frac{I}{2(\gamma_b\beta)^3 I_0 k_c E}. \tag{7.61}$$

When θ is very large the beam is said to be *space charge dominated* and the equilibrium radius asymptotes to

$$R = \sqrt{\frac{2I}{(\gamma_b\beta)^3 I_0 k_c^2}}. \tag{7.62}$$

When θ is very small the beam is *emittance dominated* and the equilibrium radius becomes

$$R = \sqrt{\frac{2E}{k_c}}. \tag{7.63}$$

7.4.2 KV Envelope Equations

So far we have discussed an envelope equation which corresponds to the RMS quantities of a beam. Another envelope equation in wide use is that due to Kapchinskij and Vladimirskij [11]. The KV distribution is a delta function in the four dimensional transverse trace space of the beam and has the property that any two dimensional projection of this distribution is uniform. Thus a KV beam has uniform density in configuration space and produces linear self fields. This beam has a hard edge and the KV are used in the presence of quadrupole focusing.

UNCORRECTED PROOF

If the situation is rotationally symmetric these equations collapse to

$$R'' = \frac{E^2}{R^3} + \frac{2I}{(\gamma_b\beta)^3 I_0 R} - k_\beta^2 R \tag{7.64}$$

where R and E now represent *edge* quantities [note the factor of 2 difference in the space charge term between this result and Eq. (7.58)].

7.5 Corkscrew Motion

An accelerator is never perfectly aligned. We will focus on the effects of chromatic aberration and misalignments of solenoidal focusing systems on the beam transverse motion in this section. An incoming beam misaligned with respect to the magnetic flux line will gyrate around the magnetic flux line regardless of whether the beam or the magnet is misaligned with respect to the machine axis. If the beam energy is constant within the pulse, the entire beam rotates at the same cyclotron frequency. Then, at any given z position along the machine, the beam is uniformly displaced in the transverse plane. However, if there is an energy variation within the beam pulse, the energy dependence of the cyclotron frequencies makes different slices of the beam rotate at different rates. Theses slices arrive at a downstream z position with different phase advances and different transverse displacements. The beam becomes twisted, and its centroid will progressively distort into a higher pitch helix as it travels downstream. If the difference in the phase advances among these slices are larger than 2π, the beam displacement of the entire beam pulse resembles a corkscrew. Hence, we call the transverse beam motion caused by chromatic aberrations and misalignments "corkscrew motion" [12, 13]. Corkscrew-type oscillations can also be found in any linear focusing system, such as alternating gradient (AG) quadrupole transport systems. An initially straight beam in an AG system will develop wiggles whose frequency upshifts as the beam propagates.

7.5.1 Corkscrew Amplitude

If a magnet is misaligned with respect to the beam, the beam will experience an error dipole field component. For an offset δs_x in the x direction, the error field is approximately

$$\delta \mathbf{B}_x \approx -\frac{\delta s_x}{2} \left.\frac{\partial B_z(z,r)}{\partial z}\right|_{r=0} \hat{\mathbf{e}}_x, \tag{7.65}$$

as given by Eq. (7.13). For a tilt $\delta\theta_x$ in the x direction, the error field is approximately

$$\delta \mathbf{B}_x \approx \left[B_z + \frac{z - z_0}{2} \left.\frac{\partial B_z(z,r)}{\partial z}\right|_{r=0} \right] \delta\theta_x \hat{\mathbf{e}}_x. \tag{7.66}$$

UNCORRECTED PROOF

For simplicity, we use phasors to represent the error field, the transverse displacement and the corkscrew amplitude in this section. The total error field of the focal system is $\delta B(z) = \Sigma \delta B_j(z)$, where

$$\delta B_j(z) = \delta B_{x,j}(z) + i\delta B_{y,j}(z), \tag{7.67}$$

and j is the index of the j-th misaligned solenoid. The displacement of the magnetic flux line of this solenoidal system is given by

$$\Delta(z) = \int_0^z \frac{\delta B(z')}{B_z}\, dz'. \tag{7.68}$$

Assuming no acceleration, the equation of motion for the beam is

$$\xi'' - ik_c\xi' = -ik_c\frac{\delta B}{B_z}, \tag{7.69}$$

where $\xi = x + iy$. Assume that the beam is perfectly aligned at the beginning of the accelerator, i.e., $\xi = 0$ and $\xi' = 0$. ~~The~~ A beam slice at location z rotates around the displaced flux line $\Delta(z)$ with a gyro-radius $|\rho(z,\tau)|$ as shown in Fig. 7.15 and its transverse displacement $\xi(z,\tau)$ is given by

$$\xi(z,\tau) = \Delta(z) - \rho(z,\tau)e^{ik_c(\tau)z}, \tag{7.70}$$

where

$$\begin{aligned}\rho(z,\tau) &= \int_0^z \frac{\delta B(z')}{B_z} e^{-ik_c(\tau)z'}\,\mathrm{d}z' \\ &= \sum_{j=1}^{n}\int_0^z \frac{\delta B_j(z')}{B_z} e^{-ik_c(\tau)z'}\,\mathrm{d}z',\end{aligned} \tag{7.71}$$

n is the index of the last magnet within distance z, and $k_c(\tau)$ is the cyclotron wavenumber. Since the error field usually is localized around the misaligned magnet

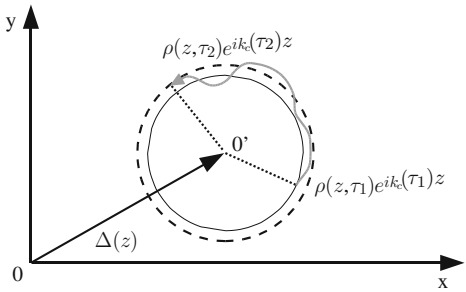

Fig. 7.15 Beam centroid gyrates around an offset magnetic flux line. Beam slices with different energies have different gyro-radii and phases

UNCORRECTED PROOF

location, we can extend the above integration range to $(-\infty, \infty)$ and rewrite the above equation as

$$\rho(z,\tau) = \sum_{j=0}^{n} \frac{\delta \tilde{B}_j(\tau)}{B_z}, \tag{7.72}$$

where

$$\delta \tilde{B}_j = \int_{-\infty}^{\infty} \delta B_j(z') e^{-ik_c(\tau)z'} \mathrm{d}z', \tag{7.73}$$

is the Fourier component of the jth error field at the cyclotron wavenumber. For a beam having an energy variation over its length, different beam slices rotate at different cyclotron wavenumbers with different gyro-radii as the beam propagates in the solenoidal system. The differential gyration within the beam pulse is called corkscrew motion, and its amplitude is given as

$$\eta(z,\tau) = \langle \rho(z,\tau) e^{ik_c(\tau)z} \rangle - \rho(z,\tau) e^{ik_c(\tau)z}, \tag{7.74}$$

where $\langle \quad \rangle$ denotes time averaging over the beam pulse. The time averaged corkscrew amplitude $A(z)$ is given as

$$A(z) = \langle \rho(z,\tau) \rho^*(z,\tau) \rangle^{1/2}. \tag{7.75}$$

The phase of the beam gyration is accumulated from the misaligned magnets' origin. When the differential phase advance $\delta k_c(\tau)z$ within the pulse is much less than 1, the corkscrew amplitude is roughly a linear function of the energy variation $\delta\gamma$, i.e.,

$$\eta(z,\tau) = \delta k_c(\tau) z \left[-i\rho(z,\tau_0) + \frac{1}{z} \left. \frac{\partial \rho(z,\tau)}{\partial k_c} \right|_{\tau_0} \right] e^{ik_c(\tau_0)z}, \tag{7.76}$$

and the time averaged corkscrew amplitude is given by

$$A(z) = \langle \delta k_c^2(\tau) \rangle^{1/2} z |\rho(z,\tau_0)| \left| 1 - \frac{1}{z} \left. \frac{\partial \rho(z,\tau)/\partial k_c}{\rho(z,\tau)} \right|_{\tau_0} \right. . \tag{7.77}$$

The second terms in Eqs. (7.76) and (7.77) are usually much smaller than the first terms since the Fourier spectrum of the error field is relatively flat around the cyclotron wavenumber. Hence, the corkscrew amplitude also increases linearly in z when the relative phase advance is small.

After the beam has traveled some distance, the relative phase advance is greater than 2π. The beam will resemble a corkscrew. The corkscrew motion is then "fully developed" with the gyro-radius as its amplitude, i.e.,

$$\eta(z,\tau_0) \cong -\rho(z,\tau) e^{i\delta k_c(\tau)z}, \tag{7.78}$$

UNCORRECTED PROOF

and the time averaged corkscrew amplitude is given by

$$A(z) \cong |\rho(z, \tau_0)| \left[1 + \frac{1}{2} \left| \frac{\partial \rho(z, \tau)}{\partial k_c} \right|_{\tau_0} \langle \delta k_c^2(\tau) \rangle^{1/2} \right]. \tag{7.79}$$

Generally, the error field δB is linearly proportional to the focusing strength B_z so that changing the focusing field will not change the Fourier spectrum of $\delta B / B_z$ while the cyclotron wavenumber changing linearly with B_z may result in different gyro-radius. If the system has random error fields like white noise, the gyro-radius would be constant regardless of the focusing field strength. Then, according to Eqs. (7.76) and (7.77), the corkscrew amplitude also ~~increase~~ linearly in B_z when the differential phase advance within the pulse is much less than 1. However, it is noteworthy that Eqs. (7.78) and (7.79) indicate that the amplitude of a fully developed corkscrew motion may not change when the focusing solenoids' strength is changed.

7.5.2 Tuning Curve Algorithm

The corkscrew motion is caused by misalignment of the system and energy variation within the beam pulse. Intuitively, one would try to reduce the magnetic flux line's transverse displacement to minimize the corkscrew motion within a beam pulse with a given energy variation. However, this method does not always reduce corkscrew amplitude. Reducing the transverse displacement of the magnetic flux line only guarantees reduction of the DC component of the error field or the z-averaged error field. Since the corkscrew amplitude depends on the Fourier component of the error field at the cyclotron wavenumber $k_c(t)$, to remove the corkscrew motion, we have to remove the Fourier component of the error field at the cyclotron wavenumber $k_c(t)$ instead.

To begin the beam steering during accelerator operation, the focusing magnet should be set to produce a chosen magnetic profile for the target beam quality. The steering procedure can be incorporated into a computerized data acquisition and control system, such as the MAESTRO [13] program used on the ETA-II. The control system acquires and processes signals from the beam position monitors. The beam displacements $x(z, t)$ and $y(z, t)$ are recorded as functions of time t at the beam position monitors. The beam centroid position over the pulse t_1 to t_2 is given by $(\langle x(z, t) \rangle, \langle y(z, t) \rangle)$. The corkscrew amplitude $\eta(z, t)$ is calculated as

$$\eta(z, t) = [x(z, t) - \langle x(z, t) \rangle] + i[y(z, t) - \langle y(z, t) \rangle], \tag{7.80}$$

and the time averaged corkscrew amplitude is calculated as

$$A(z) = \left\langle [x(z, t) - \langle x(z, t) \rangle]^2 + i[y(z, t) - \langle y(z, t) \rangle]^2 \right\rangle^{1/2}. \tag{7.81}$$

UNCORRECTED PROOF

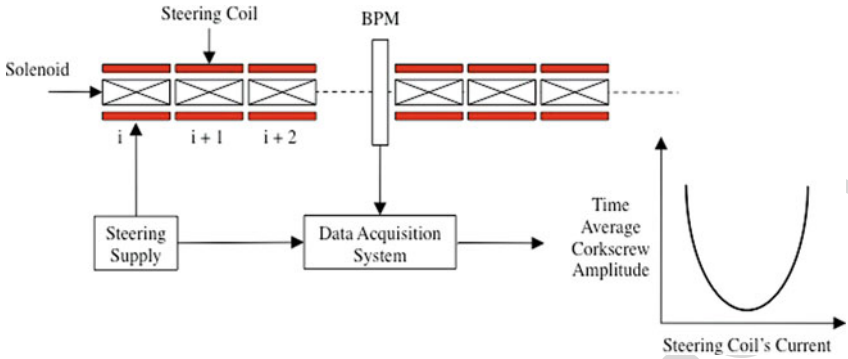

Fig. 7.16 The time-independent, dynamic beam steering algorithm reduces the corkscrew amplitude by minimizing the time averaged corkscrew amplitude

Since the corkscrew amplitude is the differential beam displacement from the averaged centroid position, the offset of the beam position monitor will not be included in the calculated corkscrew amplitude. Therefore, the time-averaged corkscrew amplitude calculated by the control system is only determined by the net error field that includes both the alignment error field and the steering field. Varying the excitation current on a steering magnet will change the magnitude of the time averaged corkscrew amplitude $A(z)$. We will obtain a well-defined minimum $A(z)$ while tuning the steering coils current to its optimal setting. Operationally the accelerator is steered iteratively, starting at the injector and sequentially adjusting a chosen steering coils current for a minimum in the time averaged corkscrew amplitude observed by a downstream beam position monitor until the end of the accelerator is reached (see Fig. 7.16). When the alignment errors are large, repeating the steering process for the whole accelerator may be needed to reach convergent settings on the steering coils.

Note that the corkscrew motion is removed when the Fourier component of the steering field at the cyclotron wavenumber cancels out the error field's Fourier component at k_c. Therefore, one can minimize the corkscrew amplitude on the BPM at the end of the accelerator while using only one pair of steering coils at the beginning of the accelerator if the steering supply can supply infinite amount of steering current, and if the displacement in the middle of the accelerator is not an issue.

Figure 7.17 shows the corkscrew motion observed on the ETA-II accelerator. For the 20-cell experiments, two beam position monitors are located at the end of the 20 cells [14]. The unsteered corkscrew amplitude was about 8 mm (see Fig. 7.17a). When the steering coils were used to straighten the magnetic flux line by using the Stretched Wire Alignment Technique (SWAT) [15–20], i.e., the DC component of the error field was minimized. The observed corkscrew amplitude was only reduced slightly from 8 to 6 mm (see Fig. 7.17b). Finally, we steered the beam by implementing the corkscrew tuning curve steering algorithm. The observed corkscrew tuning curves for all the steering coils had the shape of "V" with well-defined

UNCORRECTED PROOF

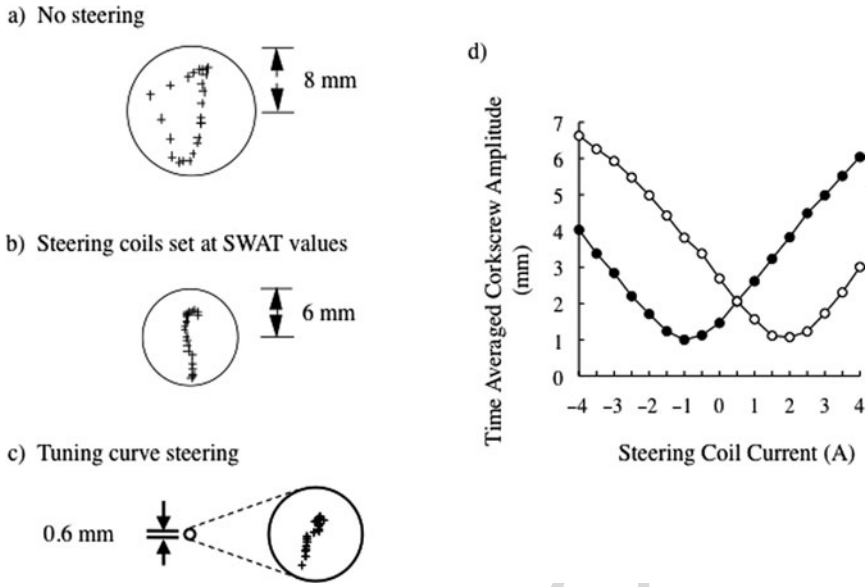

Fig. 7.17 Measured beam displacement for 40 ns on a 20-cell ETA-II experiment with (**a**) no steering, (**b**) correction of tilts by using SWAT values, (**c**) the corkscrew tuning curve steering algorithm, and (**d**) observed ETA-II corkscrew tuning curves for the horizontal and the vertical steering coils at the last injector cell [15]

minimums, and that for the steering coil pair at the last injector cell are shown in Fig. 7.17d. We had observed one order of magnitude reduction on the 20-cell ETA-IIs corkscrew amplitude, and the final corkscrew amplitude was reduced to 0.6 mm (see Fig. 7.17c). A similar corkscrew amplitude reduction was also achieved on the FXR accelerator by using this tuning algorithm [21, 22].

7.6 Instabilities

7.6.1 Image Displacement Instability

Both instabilities to be discussed in this section depend on the beam current. This is a parametric instability and arises because an offset beam is subjected to a periodic defocusing force at each accelerating gap. This force arises from the lack of cancellation of the electric and magnetic image forces at the gap [23, 24]. The presence of the gap nearly eliminates the restoring force to the beam centroid provided by the image current. The gap, however, only minimally perturbs the destabilizing force from the image charge. The model geometry is shown in Fig. 7.18. We will assume that the image current forces are absent over the gap while the image charge forces are unperturbed from their smooth pipe value. We can then Fourier analyze the spatial dependence of this force and define a gap

UNCORRECTED

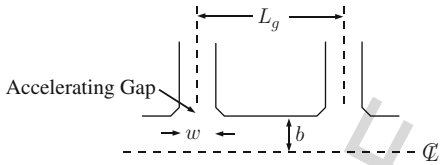

Fig. 7.18 Periodic-gap geometry for image displacement and BBU calculations is shown ~~above~~

occupation function $g(z)$. In terms of this function the equation of motion for the centroid is

$$\xi'' - ik_c\xi' - p^2 g(z)\xi = 0. \tag{7.82}$$

We remove the first derivative term as we did in Sect. 7.3.3 by defining $\xi = \Omega e^{ik_c z/2}$. Then we obtain

$$\Omega'' + \frac{k_c^2}{4}\Omega - p^2 g(z)\Omega = 0, \tag{7.83}$$

where p^2 is given by

$$p^2 = \frac{2I}{\gamma\beta^3 I_0 b^2}. \tag{7.84}$$

Here $g(z)$ is given by

$$g(z) = \frac{w}{L_g} + \frac{2}{\pi}\sum_{n=1}^{\infty}\frac{1}{n}\sin\left(\frac{n\pi w}{L_g}\right)\cos\left(\frac{2\pi n z}{L_g}\right). \tag{7.85}$$

If we retain the first two terms in the expansion for $g(z)$ we will obtain the *Mathieu equation*

$$\Omega'' + \left[\frac{k_c^2}{4} - k^2 - \frac{2p^2}{\pi}\sin\left(\frac{\pi w}{L_g}\right)\cos\left(\frac{2\pi z}{L_g}\right)\right]\Omega = 0, \tag{7.86}$$

where k^2 is given by

$$k^2 = \frac{2Iw}{\gamma\beta^3 I_0 b^2 L_g}. \tag{7.87}$$

Here L_g is the distance between gaps, w is the effective gap width, and b is the pipe radius. By defining $\zeta = 2\pi z/L_g$ we may cast this equation into a standard form

$$\frac{\partial^2\Omega}{\partial\zeta^2} + [a - 2\epsilon\cos(\zeta)]\Omega = 0, \tag{7.88}$$

UNCORRECTED PROOF

with a and ϵ given by

$$a = \frac{L_g^2}{4\pi^2}\left[\frac{k_c^2}{4} - k^2\right], \tag{7.89}$$

$$\epsilon = \frac{p^2 L_g^2}{2\pi^3}\sin\left(\frac{\pi w}{L_g}\right). \tag{7.90}$$

The solutions to Eq. (~~7.87~~) may be stable or unstable depending on the values of a and ϵ. A plot of the boundaries between stable and unstable solutions is shown ~~below~~. The shaded regions are stable. An approximation for the shape of the stability boundary between $a = 0$ and $a = 1/4$ is given by

$$a(\epsilon) = \frac{1}{4} - \epsilon - \frac{\epsilon^2}{2}. \tag{7.91}$$

Applying this condition for the first stability region $0 \le a \le 1/4$ requires

$$\epsilon < \sqrt{\frac{3}{2} - 2a} - 1. \tag{7.92}$$

Note that $k_c^2 \sim \gamma^{-2}$ while $k^2 \sim \gamma^{-1}$ so that if the solenoidal field strength is not increased with acceleration to higher energies eventually ~~a~~ will become negative and the beam motion will become unstable. At that point the average defocusing force of the gaps will be stronger than the applied focusing.

This instability can be of concern for very high current machines where some novel accelerating cell geometries have been developed to minimize both the image displacement effect and the Beam Breakup Instability [25]. The constraints imposed upon accelerator design and magnetic field tune by the image displacement force are further discussed in Sect. 7.7.1.

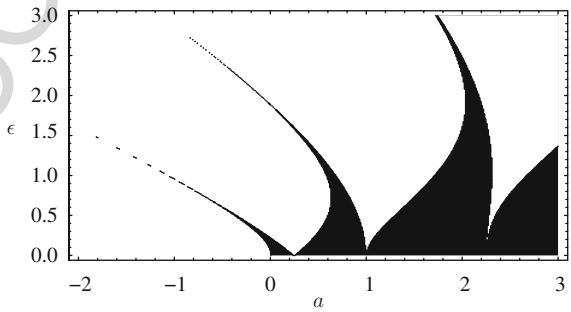

Fig. 7.19 Stability boundaries of the Mathieu equation. The dark regions are stable

UNCORRECTED PROOF

7.6.2 Beam Breakup Instability (BBU)

This is perhaps the most serious instability for a long, high current linac and sets the focusing requirements and current limit for the machine (an exception may occur for high current, heavy ion linacs where the focusing required to confine the beam against its own space charge forces may be a more demanding requirement than suppressing BBU). Historically, the instability was discovered circa 1957 but gained prominence when SLAC was turned on. As initially designed, SLAC had only ∼10 betatron wavelengths for the entire 2 mile accelerator. The appearance of BBU necessitated the installation of extra quadrupoles to limit the number of e-folds of growth [26].

The instability arises from the beam interacting with the dipole TM modes of the accelerating cavities. These modes have z-components of electric field that extract energy from the beam and have transverse magnetic fields that act to deflect the beam. In most high current linacs the accelerating cavities are far enough apart that electromagnetic fields from one cell do not appreciably excite modes in adjacent cells. This leads to what is termed *cumulative* BBU where there are only local interactions between the cavities and the beam.

7.6.2.1 Continuous System Model

We will treat a set of model equations for the instability that approximates the accelerator structure as a continuous system. This requires that there be many gaps per betatron wavelength. Any phenomena that depend upon the periodic spacing of the cavities will be lost in this model but it yields the most important features of the instability. In addition, we will assume continuous solenoidal focusing although the method and the results can be easily extended to any type of smoothed focusing system.

In general there will be many dipole RF modes. When the beam passes by the accelerator gap it will experience a transverse Lorentz force from the mode magnetic field. This force will result in a change in transverse momentum of the beam. Let us define Δ as the average change in angle of the beam per unit length

$$\Delta \equiv \frac{\Delta p_x + i\,\Delta p_y}{p_z L_g} = -\frac{e}{\gamma_b \beta m_e c}\int_{\text{gap}} \left(\hat{\mathbf{e}}_x \cdot \beta c \hat{\mathbf{e}}_z \times \hat{\mathbf{e}}_y B_y + i\hat{\mathbf{e}}_y \cdot \beta c \hat{\mathbf{e}}_z \times \hat{\mathbf{e}}_x B_x\right)\left(\frac{\mathrm{d}z}{\beta c}\right). \tag{7.93}$$

From now on we will take $\beta = 1$. The dipole modes in the cell are in turn excited by the transverse beam oscillations as described in Sect. ~~7.10.1~~. With a beam displacement ξ varying as $\exp(i\omega t)$ the frequency dependent response of the cell can be characterized by the transverse interaction impedance discussed in Sect. 6.10. Using the definition of transverse impedance in Eq. (6.29), the change

UNCORRECTED PROOF

in angle per unit length can be related to the beam centroid oscillation amplitude as [27, 28]

$$\Delta = -\frac{ieZ_t(\omega)I}{L_g\gamma_b m_e c^2}\xi. \tag{7.94}$$

We now complete the set of model equations by writing the equation of motion for the beam centroid

$$\frac{\partial}{\partial z}\left(\gamma_b\frac{\partial\xi}{\partial z}\right) - i\gamma_b k_c\frac{\partial\xi}{\partial z} = \gamma_b\Delta, \tag{7.95}$$

where we have explicitly allowed for acceleration and variable focusing strength. A detailed analysis of the general case with varying energy and focusing strength is presented in the following Section, assuming a single high Q mode. Here we derive a useful scaling law for the instability growth rate by considering the dispersion equation of a uniform system (constant focusing strength and constant beam energy). With a beam centroid displacement of the form

$$\xi \sim \exp(i\omega\tau - ikz) \tag{7.96}$$

from Eqs. (7.94) and (7.95) we have the following solution for the wavenumber $k(\omega)$

$$k(\omega) = -\frac{k_c}{2} \pm \left[\frac{k_c^2}{4} + iA(\omega)\right]^{1/2} \tag{7.97}$$

where

$$A(\omega) = \frac{eZ_t(\omega)I}{L_g\gamma_b m_e c^2}. \tag{7.98}$$

It is easy to show that the instability is convective in the lab frame [29], so the amplification over a distance z as a function of the excitation frequency can be computed from $\mathrm{Im}(k)$ at $\mathrm{Re}(\omega)$. In most cases of interest, the focusing strength is strong enough to make

$$A \ll \frac{k_c^2}{4} \tag{7.99}$$

In this case, the amplification after N accelerator cells ($N = z/L_g$), is

$$\xi \sim \exp\left[\frac{NI}{B_0 c}\mathrm{Re}\big(Z_t(\omega)\big)\right]. \tag{7.100}$$

UNCORRECTED PROOF

7.6.2.2 Instability Growth with a Single High Q Mode

If we take the single mode model we can express the transverse impedance as

$$Z_t(\omega) = \frac{i\omega_0^3 (Z_\perp/Q)/c}{\omega_0^2 - \omega^2 + i\omega\omega_0/Q}. \tag{7.101}$$

The parameter $Z_\perp/Q$ is called the transverse shunt impedance of the mode and determines the degree to which the mode is excited by the beam. The real and imaginary parts of the impedance are plotted in Fig. 7.20. The real part is responsible for BBU as we have shown. The value of the imaginary part of Z_t at zero frequency is responsible for the image displacement force. The actual impedance will be the sum of the contributions from all of the RF dipole modes in the cell. If the modes are well separated the peaks of the real part will be almost unaffected by the presence of the other modes. However, all the modes will contribute to the value of the imaginary part at zero frequency.

We consider an initial value problem to obtain the asymptotic growth rate, and use the Laplace transform notation $s = i\omega$. If the cavities are quiescent when the head of the beam passes by

$$\frac{\partial^2 \tilde{\xi}}{\partial z^2} + \left(\frac{1}{\gamma_b}\frac{\partial \gamma}{\partial z} - ik_c\right)\frac{\partial \tilde{\xi}}{\partial z} - \frac{h(s)}{\gamma_b}\tilde{\xi} = 0, \tag{7.102}$$

where a tilde denotes the Laplace transform and the function $h(s)$ is

$$h(s) = \frac{\omega_0^2 G}{s^2 + \frac{\omega_0}{Q}s + \omega_0^2}. \tag{7.103}$$

Here the quantity G is given by

$$G = \frac{4\pi\epsilon_0\omega_0}{L_g}\frac{I}{I_0}\left(\frac{Z_\perp}{Q}\right). \tag{7.104}$$

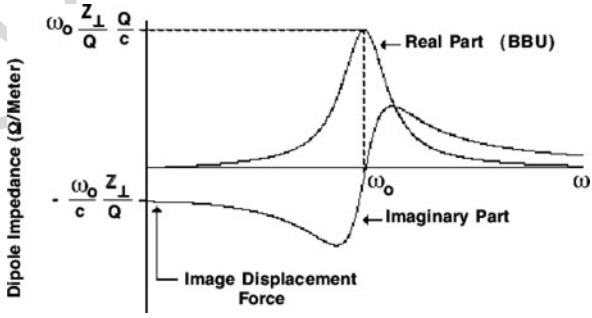

Fig. 7.20 Single mode dipole cell impedance for $Q = 4$

UNCORRECTED PROOF

We proceed to remove the first derivative terms by defining

$$\tilde{\xi} = \frac{\tilde{\Omega}}{\sqrt{\gamma_b}} \exp\left\{\frac{i}{2}\int_0^z k_c \mathrm{d}z'\right\}. \tag{7.105}$$

Substitution into Eq. (7.102) yields

$$\frac{\partial^2 \tilde{\Omega}}{\partial z^2} + \left[\frac{k_c^2}{4} - \frac{h(s)}{\gamma_b} + \frac{i}{2}\frac{\partial k_c}{\partial z} - \frac{1}{2\gamma_b}\frac{\partial^2 \gamma}{\partial z^2} + \frac{1}{4\gamma_b^2}\left(\frac{\partial \gamma}{\partial z}\right)^2 + \frac{i k_c}{\gamma_b}\frac{\partial \gamma}{\partial z}\right]\tilde{\Omega} = 0. \tag{7.106}$$

We now consider the case of uniform acceleration and put

$$\gamma_b = \gamma_0 + \lambda z. \tag{7.107}$$

We now assume that k_c changes very little in a cyclotron wavelength, i.e. that $k_c^2 \gg k_c'$ and also that $k_c \gg \lambda/\gamma_b$. Then Eq. (7.106) becomes

$$\frac{\partial^2 \tilde{\Omega}}{\partial z^2} + \left[\frac{k_c^2}{4} - \frac{h(s)}{\gamma_b}\right]\tilde{\Omega} \cong 0, \tag{7.108}$$

which has the WKB solution

$$\tilde{\Omega} \approx \frac{A(s)}{\left[\frac{k_c^2}{4} - \frac{h(s)}{\gamma_b}\right]^{1/4}} \exp\left\{i\int_0^z \left[\frac{k_c^2}{4} - \frac{h(s)}{\gamma_b}\right]^{1/2} \mathrm{d}z'\right\} + \text{c.c.} \tag{7.109}$$

Let us consider a beam that is injected into the accelerator with an aiming error but with no initial displacement. Then $\xi(0,\tau) = 0$ and $\xi'(0,\tau) = \xi_0'$ and we find that

$$\tilde{\xi}(z,s) = \frac{\xi_0'}{s}\sqrt{\frac{\gamma_0}{\gamma}}\frac{\exp\left\{\frac{i}{2}\int_0^z k_c \mathrm{d}z'\right\}}{\left[\frac{k_c^2(0)}{4} - \frac{h(s)}{\gamma_0}\right]^{1/4}\left[\frac{k_c^2}{4} - \frac{h(s)}{\gamma_b}\right]^{1/4}} \sin\left\{\int_0^z \left[\frac{k_c^2}{4} - \frac{h(s)}{\gamma_b}\right]^{1/2} \mathrm{d}z'\right\}. \tag{7.110}$$

In order to somewhat simplify Eq. (7.110) we will make the *strong focusing* approximation. Specifically, we require

$$\frac{k_c^2}{4} \gg \frac{h(s)}{\gamma_b}. \tag{7.111}$$

We will see later that this is satisfied if $\frac{k_c^2}{4} \gg \frac{GQ}{\gamma_b}$. We use this condition to neglect $h(s)$ in the denominator of Eq. (7.110) while we expand the radical in the exponent

UNCORRECTED PROOF

and keep the first term in $h(s)$. It is this term that will yield the asymptotic growth rate. We define $\phi(z)$ and $\Gamma(z)$ as

$$\phi(z) = \int_0^z k_c \mathrm{d}z', \tag{7.112}$$

$$\Gamma(z) = \int_0^z \frac{\mathrm{d}z'}{\gamma_b k_c}. \tag{7.113}$$

Then we may write Eq. (7.110) as

$$\tilde{\xi}(z,s) \approx \frac{\xi_0'}{ik_c(0)s}\sqrt{\frac{\gamma_0 k_c(0)}{\gamma k_c}}[e^{i\phi(z)-ih(s)\Gamma(z)} - e^{ih(s)\Gamma(z)}]. \tag{7.114}$$

In order to obtain the inverse Laplace transform of Eq. ~~(7.111)~~, we must compute integrals of the form

$$I_\pm \equiv \frac{1}{2\pi i}\int_{c-i\infty}^{c+i\infty} \frac{\mathrm{d}s}{s} e^{s\tau \pm ih(s)\Gamma(z)}, \tag{7.115}$$

where the contour is taken to the right of all the singularities of the integrand. Consider the exponent of Eq. (7.115):

$$\Lambda_\pm = s\tau \pm ih(s)\Gamma(z). \tag{7.116}$$

Let us define a dimensionless variable σ and θ such that

$$s = \omega_0 \sigma, \tag{7.117}$$

and

$$\theta = \frac{\omega_0 \tau}{G\Gamma(z)}. \tag{7.118}$$

With these definitions $\Lambda_\pm$ becomes

$$\Lambda_\pm = G\Gamma(z)\chi_\pm = G\Gamma(z)\left[\theta\sigma \pm \frac{i}{\sigma^2 + \frac{\sigma}{Q} + 1}\right], \tag{7.119}$$

and $I_\pm$ becomes

$$I_\pm = \frac{1}{2\pi i}\int_{c-i\infty}^{c+i\infty} \frac{\mathrm{d}\sigma}{\sigma} e^{G\Gamma(z)\chi_\pm(\sigma)}. \tag{7.120}$$

We will evaluate these integrals by the saddle point method. The asymptotic solution resulting from this procedure will become increasingly valid as $G\Gamma$ gets larger. The saddle points are found from solutions of

UNCORRECTED PROOF

$$\frac{\partial \chi_\pm}{\partial \sigma} = \theta - \frac{(\pm i)\left(2\sigma + \frac{1}{Q}\right)}{\left(\sigma^2 + \frac{\sigma}{Q} + 1\right)^2} = 0. \tag{7.121}$$

There are two limiting cases corresponding to $\theta \ll 1$ and $\theta \gg 1$.

7.6.2.3 Long-Pulse BBU

Now we consider the important and interesting case $\theta \gg 1$. In order to satisfy Eq. (7.121) we must have $\sigma^2 + \sigma/Q + 1 \to 1$, i.e. σ must be close to the resonant frequency. So σ is approximately

$$\sigma \cong -\frac{1}{2Q} \pm i, \tag{7.122}$$

where we have neglected terms of order $1/Q^2$. At this point we [redacted]t know which sign to choose in Eq. (7.122). We now substitute into Eq. (7.118) to obtain

$$\left(\sigma^2 + \frac{\sigma}{Q} + 1\right)^2 \sim \frac{(\pm i)(\pm 2i)}{\theta} = \pm\frac{2}{\theta}. \tag{7.123}$$

The solutions to this equation give the saddle points. It turns out that the dominant contributions will come from the saddle points with an overall minus sign in Eq. (7.123). One can verify this by solving for the saddle points and then inserting them into the expression for $\chi_\pm$ and looking for the largest real part. Thus the dominant saddles are found as

$$\begin{aligned} \sigma_{0+} &\approx -\frac{1}{2Q} + i + \frac{1}{\sqrt{2\theta}}, \\ \sigma_{0-} &\approx -\frac{1}{2Q} - i + \frac{1}{\sqrt{2\theta}}. \end{aligned} \tag{7.124}$$

If $\theta < 2Q^2$ the dominant saddle points will lie to the right of the imaginary axis and there will be no contribution from the pole at the origin. If $\theta > 2Q^2$ the saddle points will lie to the left of the imaginary axis and there will be a contribution from the pole to the integrals in Eq. (7.120) but the saddle point contributions will dominate. These choices give

$$\chi_\pm(\sigma_0) \approx \pm i\theta - \frac{\theta}{2Q} + \sqrt{2\theta}. \tag{7.125}$$

and

$$\frac{1}{2}\frac{\partial^2 \chi_\pm(\sigma_0)}{\partial \sigma^2} \approx 2\left(\frac{\theta}{2}\right)^{3/2}. \tag{7.126}$$

UNCORRECTED PROOF

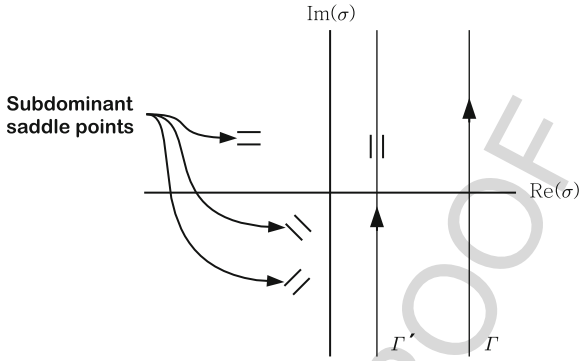

Fig. 7.21 Complex σ plane for I_+

We see from Eq. (7.126) that the steepest descent paths are vertical in the complex σ plane (i.e., if we put $\sigma - \sigma_0 = \eta e^{i\lambda}$ we will find that $\lambda = \pi/2$). We now have all the pieces needed to assemble the solution

$$\xi(z,\tau) \sim \frac{\xi_0'}{k_c(0)}\sqrt{\frac{\gamma_0 k_c(0)}{\gamma_b k_c(z)}}\frac{e^{i\phi/2}}{2\sqrt{\pi G\Gamma}}\left(\frac{2}{\theta}\right)^{3/4} e^{G\Gamma\left(-\frac{\theta}{2Q}+\sqrt{2\theta}\right)}\cos\left(\frac{\phi}{2}-\omega_0\tau\right). \tag{7.127}$$

Where the magnitude of the growth is given by

$$|\xi(z,\tau)| \sim \frac{|\xi_0'|}{2\sqrt{\pi G\Gamma k_c(0)}}\sqrt{\frac{\gamma_0 k_c(0)}{\gamma_b k_c(z)}}\left(\frac{2}{\theta}\right)^{3/4} e^{G\Gamma\left(-\frac{\theta}{2Q}+\sqrt{2\theta}\right)}. \tag{7.128}$$

Let us write out the exponential term in the growth formula:

$$G\Gamma\mathrm{Re}(\chi) = -\frac{\omega_0\tau}{2Q} + \sqrt{2\omega_0\tau G\Gamma}. \tag{7.129}$$

Examination of this equation reveals that there is unique time τ_p for which the exponent is a maximum. For late times the growth is damped by the losses in the cavities. Differentiating Eq. (7.129) and equating the result to zero yields τ_p as

$$\omega_0\tau_p = 2Q^2 G\Gamma. \tag{7.130}$$

The location of the peak growth in the pulse moves further back towards the pulse tail as the beam propagates down the accelerator (increasing Γ). This is an example of a *convective* instability. Eventually the peak of the growth will propagate out the tail of the pulse leaving behind a growth envelope that is monotonically increasing from head to tail.

The value of the exponent, which occurs at τ_p, is

$$G\Gamma\mathrm{Re}(\chi)_{\max} = GQ\Gamma, \tag{7.131}$$

UNCORRECTED PROOF

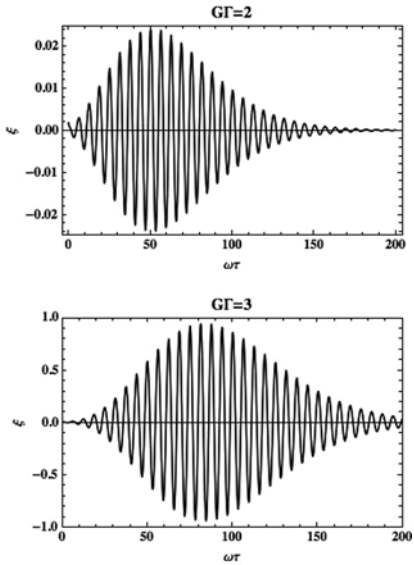

Fig. 7.22 Convective behavior of long-pulse BBU

and the maximum magnitude of the growth is

$$|\xi(z,\tau)| \sim \frac{|\xi_0'|}{2\sqrt{\pi G\Gamma k_c(0)}}\sqrt{\frac{\gamma_0 k_c(0)}{\gamma_b k_c(z)}}\,\frac{e^{GQ\Gamma}}{Q^{3/2}}. \tag{7.132}$$

Figure 7.22 ~~below~~ shows the value of $|\xi|$ versus τ at two different values of $G\Gamma$ that correspond to two different axial positions down the accelerator. The rapid oscillations are occurring at the frequency of the RF mode. Note the scale change between the two plots.

The maximum exponent, Eq. (7.131), has different functional forms depending on the focusing scheme used. The equation turns out to be correct for any type of smooth linear focusing if we just replace k_c by $2k_\beta$. For a constant field with or without acceleration we have

$$k_\beta = \frac{k_0}{\gamma_b} \to \Gamma = \frac{z}{2\gamma_b k_\beta}, \tag{7.133}$$

while if the field is ramped as $\sqrt{\gamma_b}$ we have

$$k_\beta = \frac{k_0}{\sqrt{\gamma_b}} \to \Gamma = \frac{\sqrt{\gamma_b}-\sqrt{\gamma_0}}{\lambda k_0}. \tag{7.134}$$

Finally, if the field is ramped proportionally to γ_b we have

$$k_\beta = k_0 \to \Gamma = \frac{1}{2\lambda k_0}\log\left(\frac{\gamma_b}{\gamma_0}\right). \tag{7.135}$$

UNCORRECTED

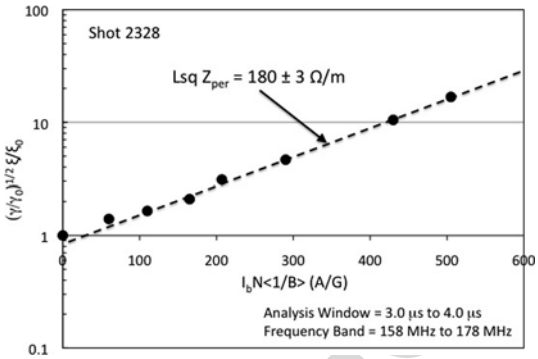

Fig. 7.23 BBU growth versus $GQ\Gamma$ in the DARHT-II accelerator is shown ~~above~~ on a semi-log scale showing the exponential growth [30]

The parameter GQ that appears in the growth exponent is proportional to the product of all three RF mode parameters $\omega_0(Z_\perp/Q)Q$, which we can recognize as the peak of the resistive part of the transverse impedance for the single pole model (Eq. 7.101). Indeed, the e-folding rate in Eq. (7.133) for the case of a uniform focusing field is the same as Eq. (7.100).

The growth of BBU versus distance is shown for the DARHT-II machine ~~below~~ [30]. ~~The growth is indeed exponential as expected.~~ Note that the measurements performed correspond to BBU growth due to the low frequency peak of the mode spectrum shown in Fig. 6.12. The growth is indeed exponential as expected and the inferred transverse impedance (from the BBU growth) is very close to the value determined by the technique described in Sect. 6.10.3.

7.7 Induction Linac Design Considerations

7.7.1 Optimal Focusing Strategy

The output beam of a high current accelerator may be required to drive a free electron laser or other device with a high energy selectivity. A typical requirement for a variety of applications of these beams is that the energy variation across the useful portion of the pulse (generally called the "flat top") be no larger than a few percent. This relatively small energy variation raises the possibility that practical machines could be constructed such that $\omega_s\tau_p \ll 1$. An obvious way to satisfy this criterion is to use a weak focusing field. However, a weak focusing field will invite BBU growth. We will shortly see that there is a unique way to grade the focusing strength so as to minimize the phase advance of a machine for a given level of BBU growth [31].

Let us recall that the number of e-folds of BBU in the long-pulse limit (the regime of operation of most high current linacs) is

$$\mathrm{Re}(\Lambda) = GQ\Gamma = GQ\int_0^z \frac{\mathrm{d}z'}{2\gamma_b k_\beta}. \tag{7.136}$$

UNCORRECTED PROOF

We also need the betatron phase advance:

$$\phi_\beta = \int_0^z k_\beta \mathrm{d}z'. \tag{7.137}$$

We take the case of constant average acceleration

$$\gamma_b(z) = \gamma_0 + \lambda z. \tag{7.138}$$

Then we may express Eqs. (7.136) and (7.137) as integrals over γ:

$$\mathrm{Re}(\Lambda) = GQ\Gamma = \frac{GQ}{2\lambda}\int_{\gamma_0}^{\gamma_\infty} \frac{\mathrm{d}\gamma'}{\gamma' k_\beta(\gamma')}, \tag{7.139}$$

$$\phi_\beta = \frac{1}{\lambda}\int_{\gamma_0}^{\gamma_\infty} k_\beta(\gamma')\mathrm{d}\gamma', \tag{7.140}$$

where γ_∞ is the value of γ at the end of the accelerator.

The problem now is to minimize (7.140) subject to the constraint Eq. (7.139). That is, we wish to specify a fixed number of e-folds of BBU growth and find the functional form of $k_\beta(\gamma)$ that minimizes the betatron phase advance. To solve this problem we minimize the auxiliary integral

$$\phi_\beta = \frac{1}{\lambda}\int_{\gamma_0}^{\gamma_\infty} \left[k_\beta(\gamma') + \frac{\mu GQ}{2\gamma' k_\beta(\gamma')}\right]\mathrm{d}\gamma', \tag{7.141}$$

where μ is a Lagrange multiplier. We use the Euler-Lagrange equation on the integrand J of Eq. (7.141):

$$\frac{\mathrm{d}}{\mathrm{d}\gamma}\left(\frac{\partial J}{\partial k'_\beta}\right) - \frac{\partial J}{\partial k_\beta} = 0, \tag{7.142}$$

where k'_β is the derivative of k_β with respect to γ. This condition reduces simply to

$$\frac{\partial J}{\partial k_\beta} = 0 = 1 - \frac{\mu GQ}{2\gamma_b k_\beta^2}, \tag{7.143}$$

with the solution

$$k_\beta = \sqrt{\frac{\mu GQ}{2\gamma_b}}. \tag{7.144}$$

By examining the expressions we have derived for the betatron wavenumber of various types of focusing systems the result in Eq. (7.144) tells us that the optimum way

UNCORRECTED PROOF

to grade the strength of the focusing system is to have the solenoidal field strength be proportional to $\sqrt{\gamma}$.

We can now determine ~~m~~ by substitution into the constraint equation (7.139) as

$$\sqrt{\mu} = \frac{\sqrt{2GQ}}{\lambda \mathrm{Re}(\Lambda)} \left(\sqrt{\gamma_\infty} - \sqrt{\gamma_0}\right). \tag{7.145}$$

So we can now find the values of k_β and ϕ_β as

$$k_\beta = \frac{\sqrt{2GQ}}{\lambda \mathrm{Re}(\Lambda)} \frac{\left(\sqrt{\gamma_\infty} - \sqrt{\gamma_0}\right)}{\sqrt{\gamma_b}}. \tag{7.146}$$

$$\phi_\beta = \frac{2GQ}{\lambda^2 \mathrm{Re}(\Lambda)} \left(\sqrt{\gamma_\infty} - \sqrt{\gamma_0}\right)^2. \tag{7.147}$$

From Eqs. ~~(7.132)~~ and ~~(7.136)~~ it is clear that increasing the pipe radius b will have high leverage in lowering the phase advance and number of BBU e-folds in an accelerator. In fact a figure of merit may be defined for an accelerator transport system that is just

$$\phi_\beta \mathrm{Re}(\Lambda) = \frac{2GQ}{\lambda^2} \left(\sqrt{\gamma_\infty} - \sqrt{\gamma_0}\right)^2. \tag{7.148}$$

For a given choice of energy and beam current this figure can be minimized by using a larger pipe and higher accelerating gradient.

The DARHT-I accelerator at LANL was the first induction machine to be designed using some of these considerations [32]. Cost and availability of ferrite led to the choice of pipe radius as 7.5 cm. A Γ of 3 was chosen as a design goal for a beam current of 3 kA. The fact that the two pulsed power drive rods were close to the accelerating gap locations led to a splitting of the BBU mode impedances in the horizontal and vertical direction. This splitting led to an effective impedance that was lower than that in either plane since the mode frequencies in the two directions were different by about 20%.

In order to achieve a high beam brightness from the velvet cathode an injector voltage of 4 MV was chosen. The machine consists of 64 cells with an accelerating voltage of 250 kV each. A minimum accelerating gap was chosen as 1.5 cm to be consistent with the breakdown strength of the vacuum electrodes while minimizing the transverse impedance. An initial magnetic field was chosen at 250 Gauss in order to avoid problems with the image displacement effect and to minimize the phase advance for corkscrew. Increasing the magnetic field with energy by a modest factor leads to a BBU exponential gain of approximately 3.

UNCORRECTED PROOF

7.8 Nonlinear Focusing to Suppress BBU

7.8.1 Motivation for Nonlinear Focusing Systems

Electron beams propagating in accelerators always deviate from the axis due to misalignments of focusing elements, injection errors or "error" fields. In addition, there are a variety of instabilities that may lead to amplification of this transverse motion. It has long been known that nonlinear focusing systems will lead to *phase mix damping* of particle motion. Phase mixing occurs when particles in a thin axial slice of the beam have a distribution of betatron wavelengths. This leads to a damping of the motion of the centroid since after several oscillations the particle orbits will loose phase coherence. If the spread in betatron wavelengths is sufficiently large, some instabilities like BBU, can actually be suppressed while the behavior of others is qualitatively changed. ~~Phase~~ mixing does not occur in linear focusing channels since the betatron frequency in a quadratic potential (which yields a linear restoring force) is independent of the amplitude of the motion. In a nonlinear channel the potential is anharmonic so that the betatron frequency is amplitude dependent and phase mixing will occur. The focusing systems to be discussed in this section was motivated by the desire to incorporate phase mix damping.

7.8.2 Laser Generated Ion Channel

If the accelerator could be filled with a suitable low-pressure gas a plasma channel could be produced by propagating a laser beam along the axis. When a relativistic electron beam encounters the plasma its radial electric field expels the plasma electrons, leaving behind a positively charged ion channel.

All that is required for phase mixing is that the ion density profile be non-uniform in radius. The potential well created by the ions will then be anharmonic. We will see in Sect. ~~7.3~~ that only a small degree of nonlinearity may be required in order to suppress instabilities. Only 0.1 mTorr pressure of a gas such as benzene or ~~n,~~ AQ2

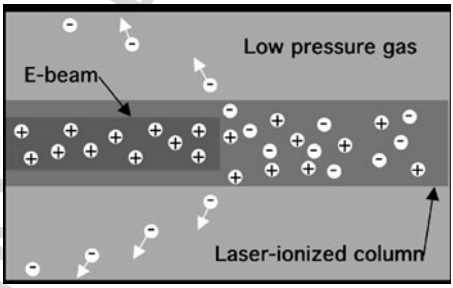

Fig. 7.24 Laser guiding scheme. The accelerator tube is filled with a dilute gas that is ionized by a laser pulse, producing a plasma column. The radial electric field of the electron beam expels the plasma electrons leaving behind a positively charged column that focuses the beam

UNCORRECTED PROOF

n-diethyl aniline is required to produce a strong channel. KrF lasers producing several hundred ~~milliJoule~~ pulses have been used to ionize channels on the order of 100 m in length [33, 34]. Today high intensity, short-pulse lasers can ionize virtually any gas in any ionization state.

Consider a uniform density ion channel of radius a with total linear charge density λ. The radial electric field of this channel is then

$$E_r = \frac{\lambda r}{2\pi\epsilon_0 a^2} \quad \text{for} \quad r \le a, \tag{7.149}$$

$$E_r = \frac{\lambda}{2\pi\epsilon_0 r} \quad \text{for} \quad r > a, \tag{7.150}$$

We can consider two extreme cases. If the beam fits within the channel it experiences a linear focusing force and we may write its envelope equation as

$$R'' = \frac{E^2}{R^3} - \frac{2c\lambda R}{\gamma_b \beta^2 I_0 a^2}, \tag{7.151}$$

with equilibrium radius

$$R = \left[\frac{\gamma\beta^2 I_0 a^2 E^2}{2c\lambda}\right]^{\frac{1}{4}}, \tag{7.152}$$

and

$$k_\beta = \frac{1}{a}\left[\frac{2c\lambda}{\gamma\beta^2 I_0}\right]^{\frac{1}{2}}. \tag{7.153}$$

If the beam is very much larger than the channel then we have ~~wire like~~ focusing and the envelope equation becomes

$$R'' = \frac{E^2}{R^3} - \frac{2c\lambda}{\gamma_b \beta^2 I_0 R}, \tag{7.154}$$

with equilibrium radius

$$R = \left[\frac{\gamma\beta^2 I_0 E^2}{2c\lambda}\right]^{\frac{1}{2}}, \tag{7.155}$$

and an approximate k_β given by

$$k_\beta \approx \frac{2c\lambda}{\gamma_b \beta^2 I_0 E} = \frac{2c\lambda}{\beta I_0 E_n}. \tag{7.156}$$

UNCORRECTED PROOF

Note the slow dependence of k_β on γ. In the case of a large or *harmonic channel* ~~(Eq. 7.153)~~ k_β varies as $\gamma^{-1/2}$ while for a wire-like channel ~~(Eq. 7.156)~~ (or a wire) it has virtually no energy dependence.

Laser guiding has been remarkably successful in suppressing the beam breakup instability and other sources of transverse beam motion but it is not without difficulties. Most of the troubles can be traced to the fact that the ions are not stationary on the time scale of the beam pulse. From the point of view of an ion in the channel, it experiences the radial electric field of the beam that will cause it to oscillate about the beam axis with "sloshing" frequency

$$\omega_s = \sqrt{\frac{eI}{2\pi\epsilon_0\beta c M a_b^2}}, \tag{7.157}$$

where a_b is the beam edge radius and M is the ion mass. For 10 kA and singly ionized benzene the sloshing time can be on the order of tens of ns. The mobility of the ions can give rise to a potent instability known as ion-hose which must be considered for long-pulse machines such as DARHT-II.

7.8.3 Phase Mix Damping of BBU

Beam breakup can grow very quickly in a high current accelerator but the characteristic e-folding length is generally long compared to a betatron wavelength. In fact, this is implied by the condition for strong focusing

$$k_\beta^2 \gg \frac{GQ}{\gamma_b} \rightarrow k_\beta z \gg \frac{GQz}{\gamma_b k_\beta} \sim GQ\Gamma. \tag{7.158}$$

This raises the possibility that a small spread in the betatron wavenumber due to some nonlinearity in the focusing system may lead to a damping rate that is at least as large as the growth rate. If that condition can be achieved we may expect the instability to be suppressed. We anticipate that a spread in betatron wavenumber will yield a damping rate of roughly Δk_β so that in order to suppress BBU we must have

$$\Delta k_\beta \geq \frac{GQ}{\gamma_b k_\beta}. \tag{7.159}$$

We will see that this argument works very well.

Consider the free oscillations of a system of undamped, non-interacting oscillators with a distribution of frequencies that are all labeled by their frequency k:

$$x_k'' + k^2 x_k = 0. \tag{7.160}$$

The distribution of frequencies $f(k)$ is normalized such that

$$\int_{-\infty}^{\infty} f(k)\mathrm{d}k = 1. \tag{7.161}$$

UNCORRECTED PROOF

The ensemble average of the displacement is given by

$$\bar{x}(z) = \int_{-\infty}^{\infty} f(k) x_k(z) \mathrm{d}k. \tag{7.162}$$

Suppose all oscillators have an initial displacement of x_0 with zero initial x'. Then the solution to Eq. (7.160) is just

$$x_k(z) = x_0 \cos(kz). \tag{7.163}$$

Let us choose $f(k)$ to be a Lorentzian,

$$f(k) = \frac{\Delta k/\pi}{(k - k_0)^2 + (\Delta k)^2}, \tag{7.164}$$

where Δk is the half width of the distribution at half height. Now we can compute $\bar{x}$ as

$$\bar{x}(z) = \frac{x_0 \Delta k}{\pi} \int_{-\infty}^{\infty} \frac{\cos(kz)}{(k - k_0)^2 + (\Delta k)^2} \mathrm{d}k = x_0 \cos(k_0 z) e^{-\Delta k z}. \tag{7.165}$$

We could have achieved the same result from an equation for $\bar{x}$ that reads

$$\bar{x}'' + 2\Delta k \bar{x}' + (k_0^2 + \Delta k^2)\bar{x} = 0. \tag{7.166}$$

That is, the ensemble average oscillates with frequency $\sqrt{k_0^2 + \Delta k^2}$ and has an effective linear damping term $2\Delta k \bar{x}'$. If we had made a different choice for $f(k)$, we would not have obtained an exponential damping term. We might have obtained z^{-1} or z^{-2} for $kz \gg 1$ or some other dependence but the result would have been a damped oscillation.

This result suggests a crude way of modeling phase mix damping of BBU. We can simply add a linear damping term to the equation of motion for the beam centroid and work through the growth theory again.

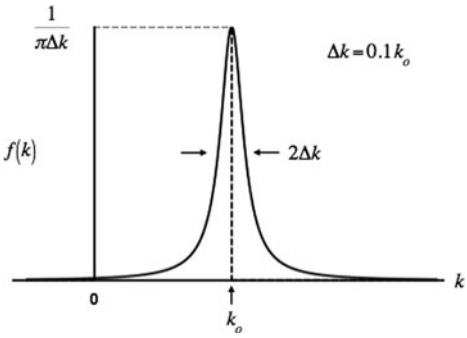

Fig. 7.25 Lorentzian distribution

UNCORRECTED PROOF

We consider the case of an ion channel guided beam with the channel radius assumed to be larger than that of the beam. This is the usual condition for a long transport region where the Rayleigh range of the laser would prevent holding a very tight focus over an extended distance. The focusing of the channel is described by Eq. (7.153) which we use to modify Eq. (7.95) to get

$$\frac{\partial^2 \xi}{\partial z^2} + \frac{1}{\gamma_b}\frac{\partial \gamma_b}{\partial z}\frac{\partial \xi}{\partial z} + \frac{2\Delta k_0}{\sqrt{\gamma_b}}\frac{\partial \xi}{\partial z} + \frac{k_0^2}{\gamma_b}\xi = \Delta, \tag{7.167}$$

where we have added a damping term characterized by the wavenumber spread $\Delta k_0/\sqrt{\gamma_b}$. Now the variable ξ stands for either x or y since there is no coupling between motion in the two planes as there was with solenoidal guiding.

If we again Laplace transform Eq. (7.167) and use (7.94) and (7.101) with $s = i\omega$ we may eliminate Δ to obtain

$$\frac{\partial^2 \tilde{\xi}}{\partial z^2} + \frac{1}{\gamma_b}\frac{\partial \gamma_b}{\partial z}\frac{\partial \tilde{\xi}}{\partial z} + \frac{2\Delta k_0}{\sqrt{\gamma_b}}\frac{\partial \tilde{\xi}}{\partial z} + \left(\frac{k_0^2}{\gamma_b} - \frac{h(s)}{\gamma_b}\right)\tilde{\xi} = 0. \tag{7.168}$$

We now make the transformation

$$\tilde{\xi} = \frac{\tilde{\Omega}}{\sqrt{\gamma_b}} e^{-\Delta k_0 \int_0^z \frac{dz'}{\sqrt{\gamma_b}}}, \tag{7.169}$$

and obtain the equation for $\tilde{\Omega}$ as

$$\frac{\partial^2 \tilde{\Omega}}{\partial z^2} + \left(\frac{k_0^2 - h(s)}{\gamma_b}\right)\tilde{\Omega} \cong 0, \tag{7.170}$$

where we have made the additional assumption that $(\Delta k_0)^2 \ll k_0^2$. Equation (7.170) is of the form (7.105) with the replacement of $k_c^2/4$ by k_0^2/γ. We could write down the solution directly but at this point we are interested in finding the condition to suppress BBU.

Let us evaluate the exponent for the long-pulse case where we are at the point in the pulse of maximum growth. The real part of the exponent in the expression for ξ contains the term $GQ\Gamma$ as well as a part from the transformation (7.169). Thus the total real exponent is

$$\mathrm{Re(exp)} = -\Delta k_0 \int_0^z \frac{dz'}{\sqrt{\gamma_b}} + GQ \int_0^z \frac{dz'}{2k_0\sqrt{\gamma_b}}. \tag{7.171}$$

Both integrals have the same z dependence so that we will have no growth if

$$\Delta k_0 \geq \frac{GQ}{2k_0}. \tag{7.172}$$

UNCORRECTED PROOF

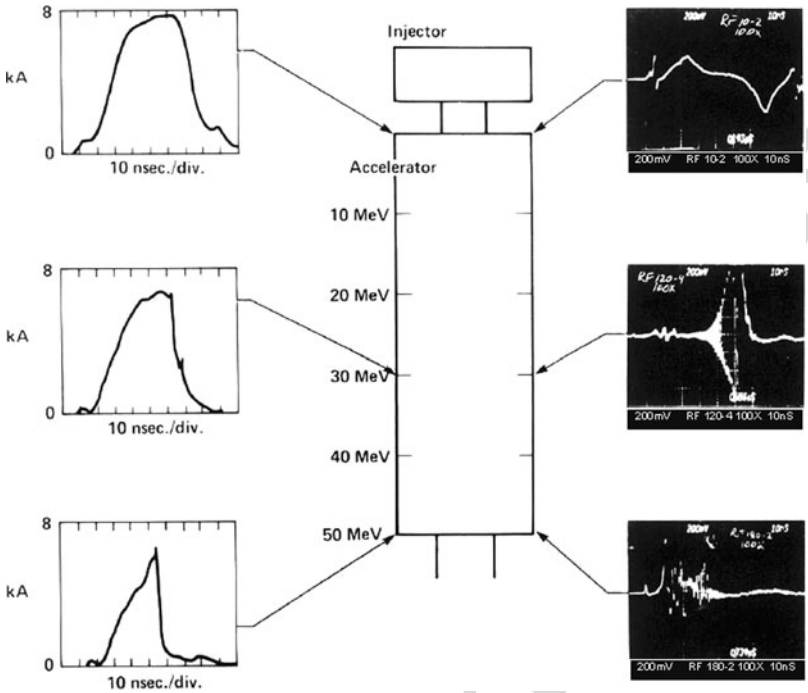

Fig. 7.26 A schematic of the ATA is shown in the *center above*. Beam current traces at different axial locations are shown on the *left*. Along the *right* side are shown outputs from loops that respond to the time changing azimuthal magnetic field caused by the rapid centroid motion of the BBU. The 830 MHz oscillations are evident in the traces

If we divide both sides of this expression by $\sqrt{\gamma}$ we will see that it is just equal to our original guess, Eq. (7.159). This result is borne out by the results of a more rigorous calculation [35].

This method was used to suppress BBU in the ATA machine [33]. With the nominal 3 kGauss guide field in the accelerator there were more than 10 *e*-folds of BBU growth for a 10 kA beam. By introducing low pressure benzene gas and a laser beam along the axis through a hole in the cathode BBU was completely suppressed. Figure 7.26 ~~below~~ shows the shortening of the beam pulse due to loss of the tail to large amplitude BBU.

The use of the laser guiding technique completely suppressed the instability and permitted transport of the full 10 kA beam without the use of any guiding magnetic field in the accelerator whatsoever. The results of this technique are shown in Fig. 7.27.

UNCORRECTED

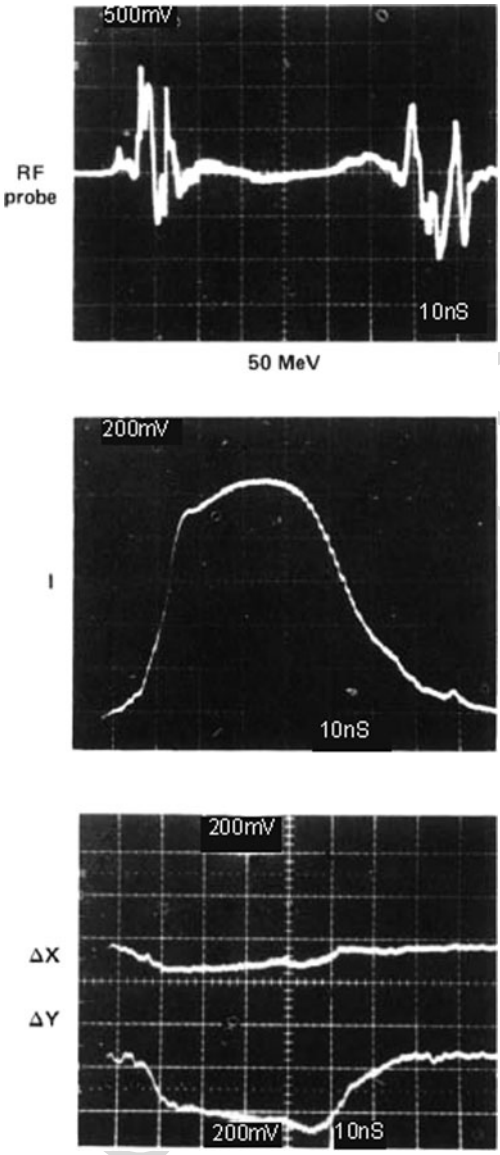

Fig. 7.27 Results of laser guiding. The *top trace* is measured at the downstream end of the accelerator (50 MeV). The body of the pulse shows an absence of 830 MHz oscillations. The *lower trace* shows the beam current at the end of the accelerator at the full 10 kA value. The beam current was fully preserved throughout the entire machine

UNCORRECTED PROOF

References

1. T. Kauppila, R. Carlson, D. Moir, and R. Ridlon. Time Resolved Emittance Measurements of an Excimer-Laser-Driven Metal Photocathode. In *Proceedings of the 1991 Particle Accelerator Conference*, page 2107, San Francisco, CA, 6–9 May 1991.
2. R. Miller. Mechanism of Explosive Electron Emission for Dielectric Fiber (Velvet) Cathodes. *J. Appl. Phys.*, 84:3880, 1998.
3. D. Shiffler, M. Ruebush, M. Haworth, R. Umstattd, M. LaCour, K. Golby, D. Zagar, and T. Knowles. Carbon Velvet Field-Emission Cathode. *Rev. Sci. Instr.*, 73:4358, 2002.
4. I. Langmuir. The Effect of Space-Charge and Initial Velocities on the Potential Distribution and Thermionic Plane Electrodes. *Phys. Rev.*, 21:419, 1923.
5. H. R. Jory and A. W. Trivelpice. Exact Relativistic Solution for the One-Dimensional Diode. *J. Appl. Phys.*, 40:2294, 1969.
6. H. Ivey. Space Charge and Transient Time Considerations in Planar Diodes for Relativistic Velocities. *J. Appl. Phys.*, 23:208, 1952.
7. Y.-J. Chen, J. Boyd, and W. Turner. Degradation of Beam Brightness by Field Emission from a Cathode Shroud. Technical Report URL-98043, Lawrence Livermore National Laboratory, 1988.
8. J. Kraus. *Electromagnetics*, 3rd edition, McGraw-Hill Book Company, New York, NY, 1983.
9. E. Lee and R. Cooper. General Envelope Equation for Cylindrically Symmetric Charged-Particle Beams. *Part. Accel.*, 7:83, 1976.
10. A. Honda. On the Maximum Current for a Self-Focusing Electron Beam. *Phys. Plasmas*, 7:1607, 2000.
11. I. Kapchinskij and V. Vladimirskij. Limitations of Proton Beam Current in a Strong Focusing Linear Accelerator Associated with the Beam Space Charge. In *Proceedings of the International Conference on High Energy Accelerators and Instrumentation*, page 274. CERN Scientific Information Service, Geneva, 1959.
12. Y.-J. Chen. Corkscrew Modes in Linear Accelerators. *Nucl. Inst. Meth. A*, 292:455, 1990.
13. W. Nexsen, S. Allen, F. Chambers, R. Jong, A. Paul, S. Sampayan, and W. Turner. Reduction of Energy Sweep of the ETA-II Beam. In *Proceedings of the 1991 Particle Accelerator Conference*, page 3103, San Francisco, CA, 6–9 May 1991.
14. W. Nexsen, D. Atkinson, D. Barrett, Y.-J. Chen, J. Clark, L. Griffith, H. Kirbie, M. Newton, A. Paul, S. Sampayan, A. Throop, and W. Turner. The ETA-II Induction Linac as a High Average Power FEL Driver. In *Proceedings of the 11th International FEL Conference*, page 54, Naples, FL, 28 Aug.–1 Sept. 1989.
15. W. Turner, S. Allen, H. Brand, G. Caporaso, F. Chambers, Y.-J. Chen, F. Coffield, F. Deadrick, T. Decker, L. Griffith, D. Lager, W. Mauer, W. Nexsen, A. Paul, V. Renbarger, and S. Sampayan. Reduction of Beam corkscrew Motion on the ETA-II Linear Induction Accelerator. In *Proceedings of the 1990 Linear Accelerator Conference*, page 435, Albuquerque, NM, 10–14 Sept. 1990.
16. S. Allen, H. Brand, F. Chambers, Y.-J. Chen, F. Coffield, F. Deadrick, L. Griffith, D. Lager, W. Mauer, W. Nexsen, A. Paul, S. Sampayan, and W. Turner. Measurements of Reduced Corkscrew Motion on the ETA-II Linear Induction Accelerator. In *Proceedings of the 1991 Particle Accelerator Conference*, page 3094, San Francisco, CA, 6–9 May 1991.
17. Y.-J. Chen. Beam Control in the ETA-II Linear Induction Accelerator. In *Proceedings of the 1992 Linear Accelerator Conference*, page 540, Ottawa, Canada, 24–28 Aug. 1992.
18. S. Allen and E. Scharlemann. The ETA-II Linear Induction Accelerator and IMP Wiggler: A High-Average-Power Millimeter-Wave Free-Electron-Laser for Plasma Heating. In *Proceedings of the 9th International Conference on High Power Particle Beams*, page 247, Washington, DC, 25–29 May 1992.
19. S. Allen, private communication.
20. D. Lager, H. Brand, W. Mauer, F. Coffield, F. Chambers, and W. Turner. Artificial Intelligence Techniques for Tuning Linear Induction Accelerators. In *Proceedings of the 1991 Particle Accelerator Conference*, page 3085, San Francisco, CA, 6–9 May 1991.

UNCORRECTED PROOF

21. B. Kulke, T. Innes, R. Kihara, and R. Scarpetti. Initial Performance Parameters on FXR. In *Proceedings of the 15th IEEE Power Modulator Symposium*, page 307, Baltimore, MD, 14 June 1982.
22. R. Scarpetti and J.-M. Zentler, private communication.
23. V. Neil. The Image Displacement Effect in Linear Induction Accelerators. Technical Report UCID-17976, University of California, 1978.
24. R. Adler, B. Godfrey, M. Campbell, D. Sullivan, and T. Genoni. The Image-Displacement Effect in Intense Electron Beams. *Part. Accel.*, 13:25, 1982.
25. R. B. Miller, B. M. Marder, P. O. Coleman, and R. E. Clark. The Effect of Accelerating Gap Geometry on the Beam Breakup Instability in Linear Induction Accelerators. *J. Appl. Phys.*, 63:997, 1988.
26. R. Helm, G. Loew, and W. Panofsky. Beam Dynamics. In R. B. Neal, editor, *The Stanford Two-Mile Accelerator*, page 168, W. A. Benjamin, Inc., New York, NY, 1968.
27. V. Neil and R. Cooper. Coherent Instabilities in High Current Linear Induction Accelerators. *Part. Accel.*, 1:111, 1970.
28. R. Briggs. Suppression of Transverse Beam Breakup Modes in an Induction Accelerator by Gas Focusing. Technical Report UCID-18633, University of California, 1980.
29. E. Lifshitz and L. Pitaevskii. *Physical Kinetics*, Pergamon Press, New York, NY, 1981.
30. C. Ekdahl, E. Abeyta, P. Aragon, R. Archuleta, R. Bartsch, H. Bender, R. Briggs, W. Broste, C. Carlson, K. Chan, D. Dalmas, S. Eversole, D. Frayer, R. Gallegos, J. Harrison, T. Hughes, E. Jacquez, D. Johnson, J. Johnson, B. McCuistian, N. Montoya, C. Mostrom, S. Nath, D. Oro, L. Rowton, M. Sanchez, R. Scarpetti, M. Schauer, M. Schulze, Y. Tang, A. Tipton, and C. Tom. Long-Pulse Beam Stability Experiments on the DARHT-II Linear Induction Accelerator. *IEEE Trans. Plasma Sci.*, 34:460, 2006.
31. G. Caporaso and A. Cole. Design of Long Induction Linacs. In *Proceedings of the 1990 Linear Accelerator Conference*, page 281, Albuquerque, NM, 10–14 Sept. 1990.
32. P. Allison, M. Burns, G. Caporaso, and A. Cole. Beam-Breakup Calculations for the DARHT Accelerator. In *Proceedings of the 1991 Particle Accelerator Conference, San Francisco*, page 520, San Francisco, CA, 6–9 May 1991.
33. W. Martin, G. Caporaso, W. Fawley, D. Prosnitz, and A. Cole. Electron-Beam Guiding and Phase-Mix Damping by a Laser-Ionized Channel. *Phys. Rev. Lett.*, 54:685, 1985.
34. G. Caporaso, F. Rainer, W. Martin, D. Prono, and A. Cole. Laser Guiding of Electron Beams in the Advanced Test Acceleration. *Phys. Rev. Lett.*, 57:1591, 1986.
35. G. Caporaso and A. Cole. High Current Electron Transport. In M. Month and M. Dine, editors, *The Physics of Particle Accelerators*, page 1615, Brookhaven National Laboratory, Upton, NY, 1992. AIP Conference Proceedings 249.

UNCORRECTED PROOF

Chapter-7

Query No.	Query
AQ1	Please provide citations for Figs. 8, 9, 19, 21, 23, 24, and 25.
AQ2	Please check the cross-reference "Sect. 7.3."

UNCORRECTED PROOF

Chapter 8
Applications of Electron Linear Induction Accelerators

Glen Westenskow and Yu-Jiuan Chen

Linear Induction Accelerators (LIAs) can readily produce intense electron beams. For example, the ATA accelerator produced a 500 GW beam and the LIU-30 a 4 TW beam (see Chap. 2). Since the induction accelerator concept was proposed in the late 1950s [1, 2], there have been many proposed schemes to convert the beam power to other forms. Categories of applications that have been demonstrated for electron LIAs include:

1. Flash Radiography
2. Free Electron Laser Drivers
3. Microwave Generators
4. Collective Accelerator Studies
5. Radiation Processing and Radiation Effects Studies
6. Production of Intense Neutron Pulses
7. Transient Chemistry Studies
8. Beam–Plasma Interactions
9. Directed Energy Weapons Research
10. Magnetic Fusion Research

Pulsed diodes have been used for all these applications as well as LIAs. In practice pulsed diodes have been limited to beam energies below 10 MeV. LIAs are considered when one desires the high beam current coupled with high beam voltage. Induction machines can simply boost the beam's energy by adding additional induction modules to the beamline.

RF accelerators, electrostatic accelerators, cyclotrons, and synchrotrons have also been used for many of these applications. However, they are limited in beam current. LIAs are typically low impedance structures that can accelerate high currents. Higher current can be achieved for RF machines by using accumulative storage rings, but add to the complexity.

G. Westenskow (✉)
Lawrence Livermore National Laboratory, Livermore, CA, USA
e-mail: GWestenskow2@gmail.com

K. Takayama, R.J. Briggs (eds.), *Induction Accelerators*, Particle Acceleration and Detection, DOI 10.1007/978-3-642-13917-8_8,
© Springer-Verlag Berlin Heidelberg 2011

UNCORRECTED PROOF

The Astron concept for magnetic fusion [1] was the application that initially motivated the invention of the LIA by Christofilios, as described in Chap. 2. Currents of several hundred amps at multi-MeV electron energies, and a burst rate around one kHz, were needed to study the injection and trapping of a circulating ring of electrons intense enough to create closed magnetic field lines for plasma confinement.

Ideas for using high intensity charged particle beams as "speed of light" directed energy weapons date back to the Second World War, although serious consideration of this possibility began in the 1950s in research on ballistic missile defense. A classified research program centered at LLNL to assess the basic feasibility of long range propagation of intense electron beams through the atmosphere was the initial motivation for the construction of the ETA and ATA. (Gsponer [3] has published a comprehensive unclassified treatment of the basic physics and technology of particle beam weapons). These accelerators were subsequently used also for Free Electron Laser research as discussed below.

The application that presently supports most of the current large operating induction accelerators is flash radiography, a diagnostic technique that helps to evaluate the performance of nuclear weapons primaries through non-nuclear hydrodynamic testing. These accelerators are used to provide radiographs of fast moving material. To acquire the image within a 100 ns time window when examining a thick object requires an intense beam. In Sect. 8.1 we will look at induction machines that were built for flash radiography, and the beam requirements for producing high resolution images.

Free Electron Lasers (FELs) have been used to convert electron beam power into coherent radiation. Typically RF accelerators are used, but reaching high peak output power requires high beam current. Research on high power, short wavelength induction based FEL's in the 1980s was motivated by its application to ballistic missile defense as part of the US Strategic Defense Initiative (see [4] for an unclassified assessment of SDI directed energy technologies). Achieving a small beam emittance as well as high current is essential to achieving good conversion efficiencies at short wavelengths. In Sect. 8.2 we discuss several high power induction machines that were used to drive free-electron lasers at millimeter wavelengths and infrared wavelengths. Currently, few of these induction accelerators are still involved in active FEL research projects.

Beam power can also be converted into microwave power by longitudinally bunching the beam, and then passing it through resonant cavities. In Sect. 8.3 we will discuss the possibility of using LIAs in the power sources of e^+e^- linear colliders. This application requires that the conversion of wall-plug power to RF power be very efficient. By reaccelerating and reusing the beam after RF power has been extracted, the efficiency of an induction machine can be enhanced. In Two-Beam Accelerators the beam is recycled many times.

In Collective Accelerators the collective fields of a large number of electrons were used to accelerator a smaller number of ions [5]. The study of collective accelerator techniques prompted the construction of several induction machines in the former USSR [6] and an early induction accelerator, the ERA injector [7] in the US. Many of the groups studying collective acceleration used pulsed diodes rather than LIAs.

UNCORRECTED PROOF

There are many other applications that require high average power. The development of low-cost high-current solid-state switches will make the use of LIAs for these applications more attractive. One method to increase the average power is to operate at higher repetition rates. In Sect. 8.4 we will briefly discuss a few applications that have been proposed for induction accelerators where high average power is important.

8.1 Linear Induction Accelerators Built for Flash X-Ray Radiography

Several large induction accelerators (> 10 MeV) have been built to produce X-ray radiographs. They are used to evaluated the performance of the primaries of nuclear weapons through non-nuclear hydrodynamic testing. A radiograph is taken of full-scale, non-nuclear mock-up of the weapon's primary during the late stages of the implosion. The images are used to obtain information on shapes, densities, and edge locations. The testing has become important for the maintenance of the nuclear weapon stockpiles without underground nuclear tests. The machines include FXR [8] and DARHT-I and DARHT-II [9] in the USA, AIRIX [10] in France, and Dragon in China [11]. X-rays with 0.5–10 MeV photon energies can deeply penetrate dense objects. The flash X-ray radiography facilities use 15–20 MeV accelerators with 1–4 kA beams. In these machines the pulse duration is kept short (< 200 ns) to avoid image blur from rapidly moving material in the objects being radiographed. To produce high resolution radiographs for a typical setup at these facilities, requires that the X-rays be created at a single small spot less than a few millimeters in width.

For an example, consider the DARHT-I Accelerator [12] at LANL. The accelerator yields a 19.8 MeV, 2 kA, 60 ns electron beam. The accelerating gradient in the accelerator is 0.47 MeV/m. The beam quality allows the beam to be focused on a thin tantalum X-ray converter to a spot less than 2 mm diameter (at 50% modulation transfer function). Bremstrahlung scattering in the converter produces a forward X-ray pulse with a dose of 500 rad measured in air a meter downstream (1rad $= 10^{-2}$J/kg). ~~An object is placed a meter downstream away from the Bremstrahlung converter, and the X-ray sensitive photographic film is placed 2 m away (along the same axis).~~ The image produced on the film is a "snap shot" of the density distribution of the object during the 60 ns X-ray pulse. The image size on the film for this case will be twice that of the object. To resolve small features of density distribution of the weapon's primary at late stages of the implosion in this setup would require that the electron spot size on the X-ray converter be comparable to the feature size being resolved. Reducing noise from scattered X-rays and neutron backgrounds is also important for obtaining good images.

8.1.1 Induction Accelerators Built for Radiography

Pulsed diodes have been used for many years to provide radiographs. In 1957 construction was started at LANL on Phermex [13], a 27 MeV RF radiography machine

UNCORRECTED PROOF

that was used to produce radiographs. By delivering about 30 A on the X-ray target, this accelerator pushed the current limit on RF accelerators. To produce a more intense high-energy X-ray burst, the first large radiography induction machine was built at LLNL. FXR was commissioned [8] in 1982, and has had several upgrades to improve its performance. The final power conditioning stage is similar to the power conditioning used in the ETA (water filled blumlein). The machine design is similar to what was later used for ATA. Initial parameter called for a 3–5 mm spot, but with a new injector and other machine upgrades [14] it has achieved a 2.5 mm X-ray spot sizes. Beam energy variation within the electron pulse duration coupled with ~~their~~ beam emittance limits their ability to further reduce the spot size (see Sect. 8.1.3).

DARHT-I, a 20 MeV linear induction accelerator [9], was built at LANL and first operated in 1999. The beam energy flatness was improved over FXR. Their injector also produced a lower emittance beam. The beam parameters were mentioned in the previous section. The design of the French AIRIX machine [10] is similar to DARHT-I machine, with several improvements in the cell design.

An interesting new development for radiography is the DARHT-II accelerator [12]. The DARHT-I and DARHT-II beamlines are perpendicular to each other, allowing two simultaneous views of the same object. The accelerator voltage pulse for DARHT-II has a 1.6 μs duration. However, only short ~~burst~~ of electrons are desired

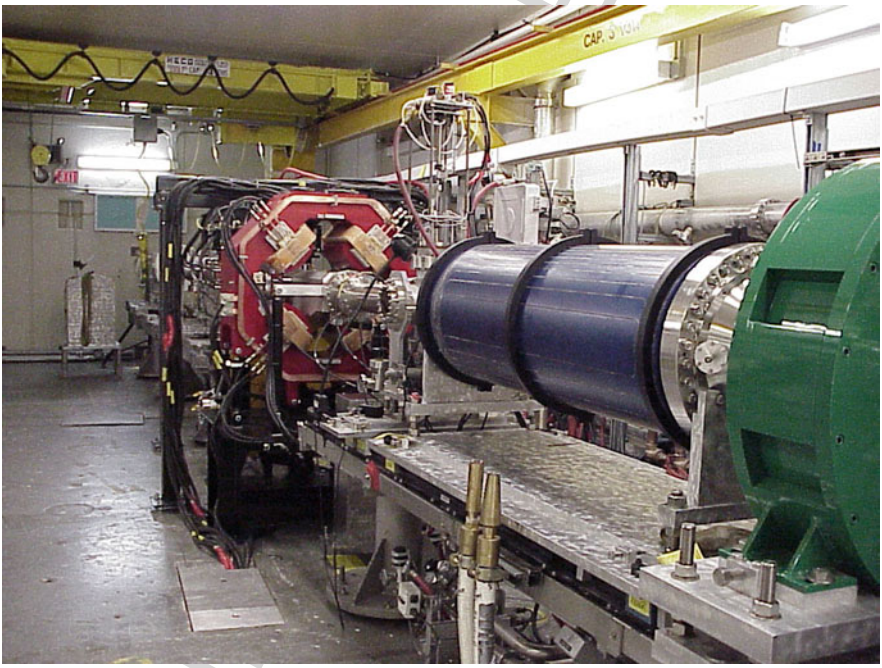

Fig. 8.1 DARHT-II Kicker and septum region installed on the ETA-II beamline for pretesting. The beam is running from the *right* to the *left* in the picture

UNCORRECTED PROOF

on target. During most of the accelerator pulse the beam is bent down into an electron collector. About 4 times during the 1.6 μs pulse, the fields of the kicker (shown in Fig. 8.1), a pulsed stripline, counters the static downward force of a dipole magnet, and allows the beam to propagate onto the target. Having additional images during the implosion aids the designer with more information on the movement of the material during the implosion. The multi-pulse capability required the development of fast gated electronic cameras for extraction of the radiographic images.

A variation of the LIA machines used to produce radiographs is the Inductive Voltage Adder [15] (IVA). This approach uses high voltage diodes employing magnetically insulated transmission lines. Various diode configurations such as the magnetically immersed diode and the rod pinch diode have been studied. The "cells" of the adder and pulse power system are similar to that used in induction accelerators. However, the current is carried almost to the target by a metal rod placed along the center axis. The cathode to target distance is only a few centimeters. Although ~~IVA~~, used for radiography can produce a high radiation dose by using very high currents, its beam spot size on the X-ray converter tends to be large when it is operating with the high beam current. By reducing the image magnification (moving the film closer to the object) they can somewhat compensate for the larger spot size. For the same object, the conventional LIAs with better beam quality can produce smaller spots and do not need the higher doses that are typical of pulsed diode. Issues with X-ray scatter in the object and in the environment need to be considered to produce a good radiograph.

8.1.2 Beam Requirements

We now will discuss the beam requirements for flash X-ray radiography. These will include the dose, pulsewidth, photon energy and X-ray spot size, as these will all impact either the sensitivity or resolution of the radiographs.

Typically radiation transport simulations are performed to determine the required beam parameters. To understand the need for an intense beam we will roughly estimate the number of photons that reach a segment of the detector after passing through a dense object.

Let us consider the case of X-rays transported through a 5 cm thick uranium slab placed 1 m from the electron X-ray converter, and that the forward X-ray dose is on the order of 500 rad in front of the slab. As shown in Fig. 8.2, photons below 0.5 MeV will be highly attenuated as they pass through Uranium. The scattering coefficient for a 1 MeV photon in uncompressed Uranium is about 1.47/cm. After passing through a 5 cm length of uncompressed Uranium, the unscattered photons contribution to the radiation pulse is about 0.3 rad if no collimators or anti-scattering grids are used between the X-ray source and the uranium slab. Then, for a section of the detector located 2 m from the X-ray source and shadowed by the slab, the dose from unscattered photons is only about 0.08 rad. Only 0.016% of initial X-ray photons reach the detector without bring scattered. If collimators and grids are used

UNCORRECTED PROOF

This figure will be printed in b/w

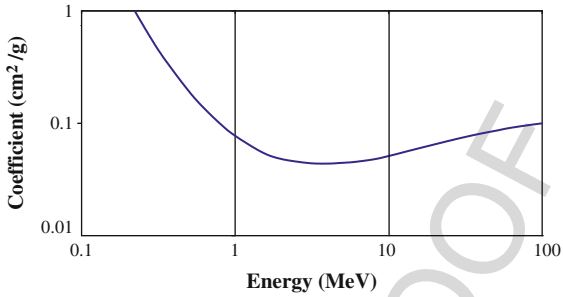

Fig. 8.2 Coefficients for photon transport in Uranium from data listed in [16]

at any location, this number would be significantly lower. The X-ray dose is almost a cubic power of the beam energy for a fixed beam current, and is linearly proportional to the current. Higher beam current can be used to increase X-ray dose at the detector.

Once you have sufficient flux through the object, the next problem is getting the transmitted X-rays to deposit sufficient energy into the film or scintillator to record the radiograph. The 0.08 rad radiation dose would deposit about 10^{-10} J in a 1 mm^2 section of a 100 μm thick film. This energy is equivalent to stopping about 1,000 0.5 MeV photons. The amount of energy deposited in the film can be increased by using thin Tantalum sheeting in front of the film to create a radiation shower. The DARHT-II electronic detectors [9] have ∼ 250,000 segmented LSO scintillators that are used to convert X-rays to light. The pixel size is 1 mm by 1 mm. The light is lens-coupled onto a mosaic of large-area charge-coupled devices (CCD). These new electronic detectors can work with lower X-ray doses than photographic film.

In the introduction we remarked that the X-ray spot size should be small. We will now look at the requirement on the beam parameters to obtain a small spot at the Bremsstrahlung converter. We will approximate the spot size as if we were using a thin lens. Take the example of DARHT-I, the normalized beam emittance, $\varepsilon \sim 1{,}500$ mm-mrad, the energy spread is $|\Delta\gamma|/\gamma < 1\%$. If the facility uses a solenoid for the final focusing with focal length $f_0 = 30$ cm and with a coefficient of spherical aberration $C_x = 5 \times 10^{-5}$ mm^{-2}, then the rms final focus spot size, R_{out}, is roughly given by [17]:

$$R_{\text{out}}^2 \sim \left(\frac{\varepsilon}{R_{\text{in}}} f_0\right)^2 + \left(2R_{\text{in}}\frac{\Delta\gamma}{\gamma}\right)^2 + (C_x R_{\text{in}}^3)^2$$

where R_{in} is the beam size at the input of the solenoid. Figure 8.3 plots the final spot size as a function of the input radius. For the conditions mentioned above, adjusting R_{in} to 24 mm will produce a minimum for R_{out} of about 1 mm on the converter. A 1 mm rms spot size is equivalent to 2.66 mm spot (50% modulation transfer function) assuming a Gaussian distribution for particles in the beam.

UNCORRECTED PROOF

This figure will be printed in b/w

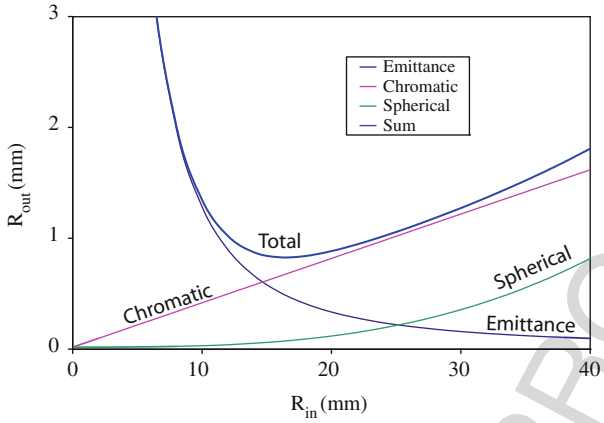

Fig. 8.3 Final spot size as a function of the initial beam radius. The contributions to the spot size from the beam emittance, chromatic aberration, and spherical aberration of the focusing system terms are shown as well

8.1.3 Target Issues

A 2 kA, 50 ns beam focused to 2 mm spot will vaporize the Tantalum material used in the Bremsstrahlung X-ray targets. The Tantalum ions at the front of the neutralized plasma plume will typically move at less than 1 cm/μs. A more serious issue are light ions that are desorbed from the front surface early within the pulse. If water has been absorbed on the front surface, hydrogen ions will be released when the target is struck by the beam. The light hydrogen ions will be accelerated by the fields of the electron beam, and move upstream rapidly along the beam path. These ions' space charge fields will partially neutralize the beam's space charge fields. A change in the focusing upstream of the target will lead to a change in spot size at the target [18]. Furthermore the change in the spot size is time dependent, and results in a larger average spot size than what would be possible for a narrower time window. For good radiographic resolution, mitigation [18] is needed to control the spot size growth.

8.2 Free Electron Lasers Driven by LIAs

The intense beams produced by induction machines enable high-power coherent radiation production. The free electron laser (FEL) is one proposed scheme to convert beam power into microwave power. LIA driven FELs have demonstrated record power levels. In this section we will discuss several experiments that used LIAs to drive FELs.

UNCORRECTED PROOF

The first experiment using an induction accelerator to drive a free-electron laser was carried out at the Naval Research Laboratory (NRL) [19]. They obtained 4 MW at 30 GHz with a corresponding efficiency of 3%. A few years later the beam from the Experimental Test Accelerator (ETA) was used to drive the ELF wiggler. This experiment demonstrated that high peak power production was possible, and that the power extraction efficiency could be high with a tapered wiggler. To test the concept with higher power beams, and at shorter wavelengths, FEL experiments at 10.6 μm were performed at the Advanced Test Accelerator (ATA). The success of the ATA experiment was limited by ATA's beam quality. We will also look at efforts to use ~~LIAs~~ driven FELs to produce ∼ 200 GHz power for electron cyclotron heating in magnetic confinement tokamak fusion devices in this section. For this application the average power is important.

8.2.1 ELF Experiments on the ETA Accelerator

In 1986 high microwave power production was achieved [20] on the ELF wiggler using the ETA induction accelerator at LLNL. A 3.5 MeV 850 A electron beam was used to produce over 1 GW of power at 35 GHz. About 34% of the beam power entering the wiggler was converted into microwave power. With 50 kW signal injected into the front of the untapered ELF wiggler, a 34 dB/m gain was measured for a 3-m wiggler. The FEL would saturate (see Fig. 8.4) in 1.3 m with a 180 MW output. If the wiggler field was tapered the output level could grow to 1.0 GW. In these experiments the wiggler field provided the vertical focusing to keep the electron beam small as it passed through the wiggler. Horizontal focusing was provided by pulsed quadrupoles located outside the wiggler.

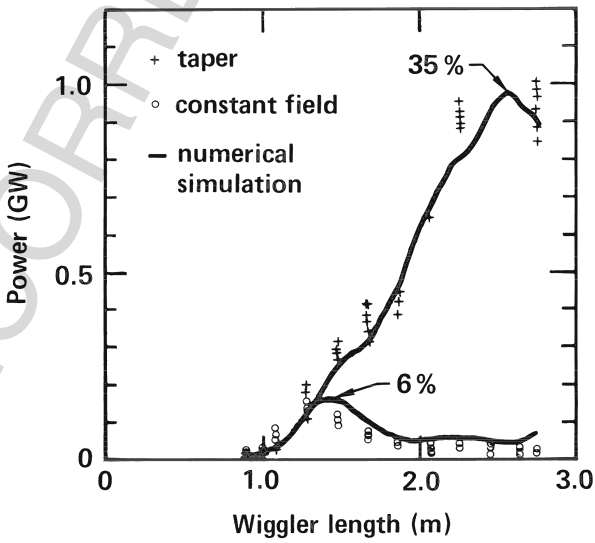

Fig. 8.4 Power levels in ELF wiggler

UNCORRECTED PROOF

Power production on ELF was limited by the electron beam's longitudinal space charge. For these experiments, the 2.5 MeV ETA field-emission injector would produce a 3 kA beam. A long narrow-bore tube immersed in 3 kG magnetic field was used to selected the "colder" portion of the beam for the FEL experiments. The beam's normalized emittance at the wiggler entrance was 300 cm-mrad. Allowing more of the ETA current to pass through the tube, by increasing the magnetic field, would not increase the FEL output power.

The large space charge in a tightly focused beam prevents the beam from being bunched effectively. At 35 GHz the electron bunches were separated by about 1 cm. For operation with an electron beam energy of 3.5 MeV and an average beam current of 850 A the longitudinal space charge forces are large. The pulse length from the injector was about 30 ns, but due to the chromatic nature of the beam transport and the time variation of the beam energy, the FEL pulses were only 10–20 ns in duration.

Other FEL experiments done for similar wavelengths using LIAs were summarized in Table 8.1. All these experiments produced lower power levels than the ELF experiment, although most of these experiments achieved saturation.

Table 8.1 LIA based FEL experiments

Country	Institution	Energy [MeV]	Current [A]	Frequency [GHz]	Power [MW]	References
USA	NRL	1.35	200	30	4	[19]
USA	LLNL – ELF	3.5	850	35	1,000	[20]
Japan	Osaka University	1.6	150	35	0.5	[21]
USA	LLNL – IMP	6	2,500	140	2,000	[22]
USA	LLNL – Palladin	45	800	30,000	25	[23]
China	IFP	3.5	950	35	140	[24]
Japan	KEK	1.5	450	9.4	100	[25, 26]
Russia	JINR	0.8	200	31	39	[27]
France	CESTA	2.2	800	35	100	[28]

8.2.2 Short Wavelength Radiation Production Using the ATA Accelerator

In the 1980s short wavelength FELs were considered one of the most promising direct energy weapon concepts in the US Strategy Defense Initiative (SDI) for defense against incoming missile attacks. Ground based LIA driven FELs were seen as one of the leading methods to generate the intense laser beams needed for

UNCORRECTED PROOF

boost phase intercept of missiles with relay mirrors. The SDI application required 10–100 MW average powers at around one micron wavelengths for several minutes. With typical wiggler periods of a few centimeters, it was necessary to use beam energies > 50 MeV to obtain near infrared radiation. At the shorter wavelengths, and with typical brightness, it was necessary to make the wiggler long to obtain high power. The generation, and the atmospheric propagation, of an intense laser beam at the required peak and average power levels were the major research and development issues.

Experiments on the production of short-wavelength radiation using an induction accelerator were done on the ATA accelerator using the Palladin wiggler(see Fig. 8.5). Radiation at 10.6 μm was amplified using a 45 MeV 800 A electron beam. Experiments were done using either a 15 or a 25 m long wiggler. The wiggler had a 8 cm magnetic period. The seed power was provided by using either a 37 kW or a 5 MW CO_2 laser. Using the 5 MW drive laser, an FEL output power of 50 MW was measured. The power conversion efficiency was 0.16%. With 14 kW drive (coupled to corrected mode at entrance of the wiggler) a gain of 27 dB in a 15 m wiggler was measured. Measurements of the optical beam spot size, and agreement with simulations, indicated gain guiding [29]. The optical beam spot only grew from 8 mm at the entrance to 10 mm after 15 m (3 Rayleigh ranges).

ATA accelerator used laser guiding to control the transverse beam motion, such as the beam breakup instability (see Sect. 7.8.2 on laser guiding). Before firing the

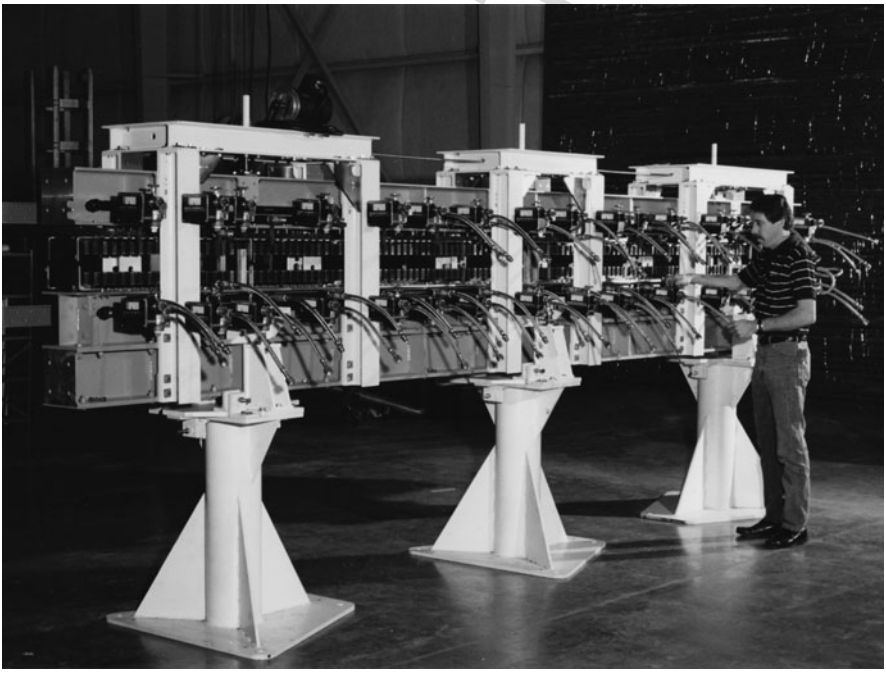

Fig. 8.5 A 5-m section of the Palladin Wiggler

UNCORRECTED PROOF

injector, an excimer laser would produce an ion channel in a low density gas that filled the accelerator transport line. The strong non-linear ion-channel focusing field degraded the beam quality within a few betatron wavelenghts. The beam quality was further spoiled in the transition from the ion-channel guiding transport to the vacuum transport used for the FEL.

At the end of the ATA accelerator the beam's core (∼300 A) had a low emittance (650 mm-mrad), while the total beam's (2,700 A) emittance was 11,000 mm-mrad. A quadrupole emittance selector, located in the transition region between the accelerator exit and the FEL entrance, was used to select the lower emittance core of a 3 kA beam. At peak power production only about 800 A was passed to the wiggler. Tuning for more current entering the wiggler would introduce electrons with higher transverse energy. These electrons would not stay in phase with the 10.6 μm radiation. Although only indicative of the required electron beam quality, for maximum geometrical overlap of the laser radiation and the electron beam, the beam's emittance should be on the order of:

$$\varepsilon_x \sim \frac{\gamma\lambda}{\pi} = 300 \text{ mm-mrad} \tag{8.1}$$

where λ is the wavelength of the radiation, and ε_x is the normalized edge emittance. This relationship does not include effects of the focusing fields. In the Palladin experiments the radiation wavelength, λ, was 10 μm. Simulations show that a tapered wiggler has reduce sensitivity to beam quality.

8.2.3 Use of Induction Accelerators to Produce Millimeter Wavelength Power for Tokamak Heating

Plasma heating is an important process in magnetic confinement fusion energy devices. There were efforts in the US [MTX at LLNL [22]] and Japan [JAERI at NAKA [30]] to use induction accelerator driven FELs to produce 140–600 GHz power for electron cyclotron heating (ECH) of plasmas in tokamak fusion devices. An FEL output at multi-megawatt average power levels lasting for several seconds were desired.

The ETA-II accelerator, capable of supporting a 50-pulse burst, was run at 2 kHz for a series of Tokamak experiments. Many bursts contained pulses with peak power on the order of 1 GW at entrance of the MTX. Feedback systems helped maintain beam parameters constant during the burst, but large deviations in output power were still present within a burst (see Fig. 8.6). Energy variation within the individual accelerator pulses led to the spikes in the output power. This operation required that the magnetic cores be rapidly reset and the electron beam source (M-type cathodes) be able to supply sufficient electrons to remain space charge limited during the burst.

There was a small effort at LLNL exploring the feasibility of a 250 GHz CARM [31] driven by a 2 MeV LIA. CARMs can produce higher frequency radiation at lower beam energy than an FELs. However, they also require a lower emittance beam for good performance.

UNCORRECTED PROOF

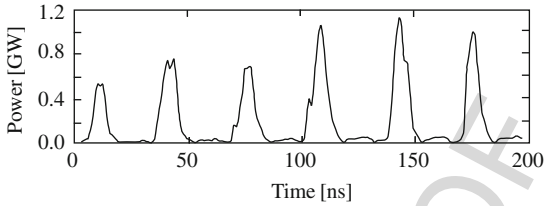

Fig. 8.6 Microwave power at the entrance of MTX. About 500 μs of base signal has been removed between each pulse to show multiple pulses on the same plot (reproduced from [22])

8.3 Two-Beam Accelerators

~~Based on the success of induction driven FELs in producing high peak power microwaves a proposal [32] was put forward to use this capability to produce microwave power to drive e^+e^- linear colliders for high-energy physics.~~ Although the ELF experiment produced high peak power, it was not efficient in terms of average *wall-plug* power to average beam power conversion. Only a small fraction of the wall-plug power was converted to microwaves. It was realized that instead of starting fresh with a new electron source for each FEL section, that the spent beam from an FEL could be reaccelerated, and used again to drive another FEL. One could make the process very efficient, if the reacceleration could be repeated many times. Energy is converted from the high-current low-voltage LIA drive beam into RF power which is fed to high gradient structures in the high-energy beamline (see Fig. 8.7). The higher current drive beam runs parallel to the main high-energy beam. This concept became known as Two-Beam Accelerator (TBA).

In the FEL–TBA approach, the output RF phase is sensitive to variations in beam parameters. In the overmoded waveguides typically used for FELs driven by LIAs, there is significant power in coupled non-fundamental modes. Small variations in drive beam current or voltage results in both phase drift within a pulse and pulse-to-pulse phase variations. Due to this problem, and the difficulties in maintaining a high quality beam in a long system usable for an FEL, it was proposed [33] to change

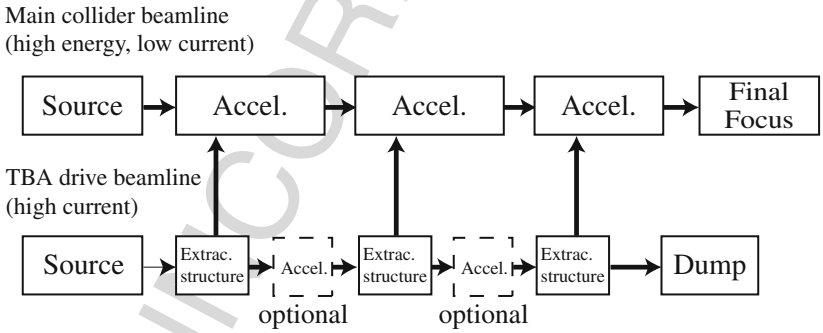

Fig. 8.7 The two beamlines of an RK–TBA with the LIA shown in the *lower* beamline. The beam passing through the induction cells is bunched at the resonate frequency of the accelerating structures in the *top* beamline

UNCORRECTED PROOF

the RF coupling mechanism from an FEL to resonant microwave structures similar to those used in klystrons. A research effort based on this concept was started [34]. We will focus on this approach in this section.

As a power source candidate for linear colliders, two-beam-accelerators have the inherent advantage of high efficiency for power conversion from drive beam to RF. In addition, induction-linac-based TBAs have favorable scaling with high frequencies (> 11.4 GHz) and high accelerating gradients (> 100 MV/m). The technical challenges for making TBAs into realizable power sources lie in the dynamics of the drive-beam which must propagate over long distances. In particular, the beam-break-up instability ~~though~~ a long multi-cavity relativistic klystron version (RK–TBA) is known to be severe. While BBU suppression techniques, such as placing the cavities at betatron nodes, have been successfully demonstrated for a few cavities, a scenario with acceptable BBU control over many traveling-wave cavities needed be constructed. Similarly, the longitudinal stability of the RF bunches over a multi-cavity TBA would need to be demonstrated. In addition to technical feasibility, a case for economic attractiveness is no less essential for the viability of the TBA as a power source.

Longitudinally, the beams will debunch because of space charge and RF-induced energy spread. To counter these debunching effects, the RF output cavities are inductively detuned. This can be accomplished in a traveling wave extraction unit by making the phase velocity of the traveling-wave structure faster than the velocity of the particles. The particle bunch lags behind the decelerating crest of the wave, and the energy loss becomes phase dependent, with the particles at the bunch tail losing the least energy (see Fig. 8.8). Kinematics lead to a "catching up" of the tail with the bunch front and subsequent synchrotron oscillations in stable RF buckets. After

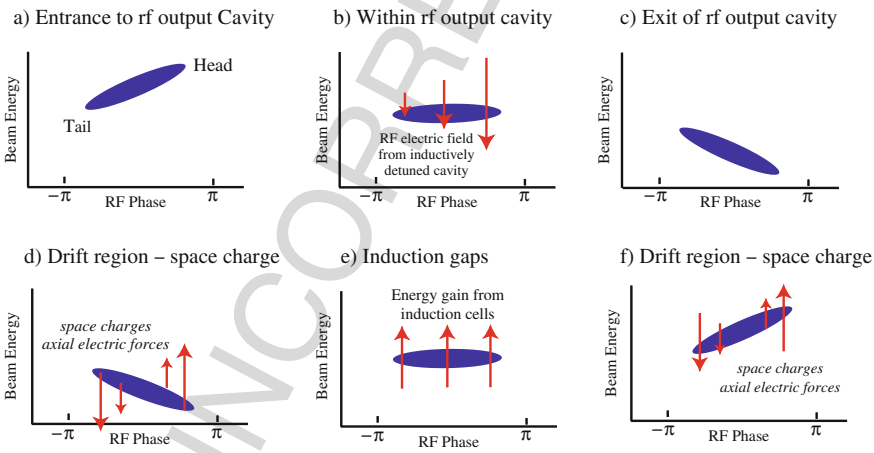

Fig. 8.8 RF bucket evolution through a section of the RK–TBA. **(a)** Entrance to rf output cavity. **(b)** Within rf output cavity. **(c)** Exit of rf output cavity. **(d)** Drift region – space charge. **(e)** Induction gaps. **(f)** Drift region – space charge

UNCORRECTED PROOF

microwave power extraction, the beam energy would be restored using induction cells. In the RK–TBA scheme, inductively detuned cavities were used, and drift distance kept short so that the beam was still bunched as it entered the next cavity.

The goal of the RK–TBA program was to reaccelerate 150 times before restarting with a fresh source. This requires design of the extraction structures with damping at the beam-breakup (BBU section) frequency and that the distance between power extraction be some multiple of a half of a betatron wavelength [35]. The surface field stress, for a given output power, could be reduced by using short traveling-wave structures instead of conventional standing-wave cavities. Damping was introduced into the structures to reduce the resonant Qs of the higher order frequencies [36]. RF power of 426 MW was achieved in a single structure for a 30 ns period using a 4 MeV, 500 A bunched beam [35].

After the 150 reaccelerations, the plan was to start with a new source. To provide the power for a 3 TeV center-of-mass energy collider, about 76 subsections would be used (see Fig. 8.9).

The initial bunches could be created at lower energy by imposing a longitudinal energy variation. However, at high beam energy a chopping techniques was utilized to produce the initial bunching. Once partial modulation is achieved, it can be enhanced by the use of gain cavities, similar to what is done in klystrons [37].

There are tight requirements on the high-energy beams in a TeV collider in order to obtain the needed luminosity to study high energy physics events. These requirements impose tight requirements on the RF power source. Meeting these requirements, while maintaining high efficiency, and low construction cost made the RK–TBA a higher risk approach than the more conventional klystron approach.

Work continued at KEK to look at FELs as a power sources for linear colliders. A new version, "Klystron-Like Free Electron Laser" TBA, was introduced and studied [38]. Figure 8.10 shows a layout for this scheme. The output phase of each FEL section was determined by the drive RF into that section, not by the phase of the bunched beam leaving the previous section. They propose using Ion-Channel Guiding [39] throughout the accelerator and the FEL to reduce the transverse beam instabilities.

This figure will be printed in b/w

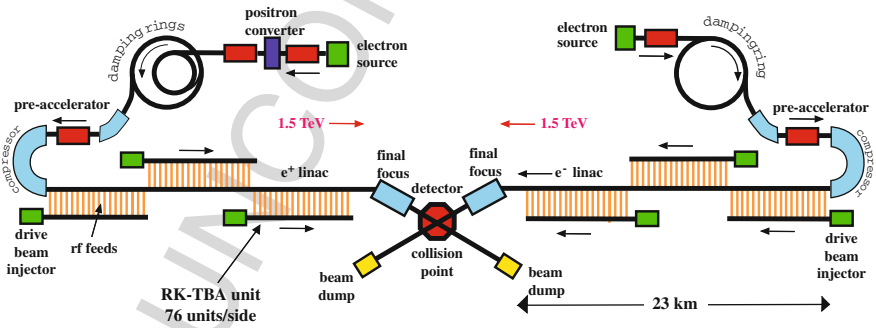

Fig. 8.9 Proposed layout for RK–TBA

UNCORRECTED PROOF

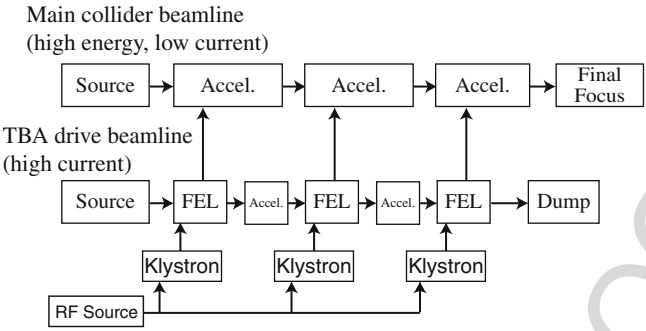

Fig. 8.10 Proposed layout for the KEK FEL–TBA

8.4 High Average Power Applications

Many RF accelerators' industrial applications could also be accomplished with induction machines. What needs to be developed for many of these applications are compact high-average-power reliable pulsed power systems. In this section we will look at a few these applications where the use of induction accelerators have been considered.

Millimeter and microwave wavelength FELs driven by LIAs could produce radiation for beaming power into space [40]. From space to ground power beaming is not now considered practical due to the high construction cost of space based systems. For ground to space power beaming, short-wavelength operation is advantageous in reducing antenna sizes. Beaming to low earth orbit could be done using S-band frequencies. However, for geosynchronous orbit, or beyond, power beaming would require very large receiver antennas in space unless higher frequencies are used. Power beaming for lunar bases, or for space propulsion have been considered. Takayama [41] has proposed a 17 GHz 100 MW version using an FEL driven by a 15 MeV 3 kA electron beam. Other possible applications for microwave FELs include planetary radar and lightning control [42].

LIAs have been used for radiation processing for extending food shelve life. Accelerators provide a more controlled (and environmentally acceptable) radiation source than radioactive material. One would like to operate them at energies below the level where neutrons are produced to avoid issues with long-term activation. The cost, size, lack of portability, and the need for radiation shielding has discouraged the use of LIAs for this application. Radiation from accelerators has also been used for sterilization of materials. Surface sterilization does not require highly penetrable radiation and may be better matched to pulsed diodes.

There have been several proposals to use electron induction machines for material processing. The energy deposited can be used to harden surface materials, or can be used to produce a surface layer with improve characteristic. For an example consider transformation hardening of steel using high energy electron beams [43]. Electrons with a 6 MeV energy will penetrate several millimeters into steel

UNCORRECTED PROOF

before stopping. This range provides the ability to modify the material properties of a deep surface layer. Lasers which are more often used for this mission, deposit their energy within ~10 μm of the surface layer. The electron beam deposits energy volumetrically within the deeper surface layer. In this example the rapid heating partially dissolves carbides present in the microstructure of the steel, and then when the material is rapidly cooled it forms martensite, which hardens the steel (see Fig. 8.11) The hardened layer was free of solidification-related defects such as cracking and porosity. Experiments [44] on Titanium alloys purified the surface from oxygen and carbon impurities. Bombardment with ion beams can also result in improved characteristics [45, 46]. At higher energy fluence electrons beam could be used for deep bonding processes. An example would be to provide improve welds in the thick plates used for hulls on large marine ships. The pulse duration is important to the modification process. Beams could be used to study first-wall materials in Magnetic Fusion Reactors [47].

Higher beam energies can be reached in a compact system using a two-beam accelerator approach. The beam from an LIA would be used to generate microwaves that would be feed to an RF accelerator. An example where this may be useful would be for X-ray lithography. Electron beams from RF accelerators have been used to investigate X-ray lithography. X-ray lithography could produce integrated circuits with smaller features (0.2 μm) than what is currently possible. The X-rays could be generated using electron storage rings, but a more compact sources would be appealing.

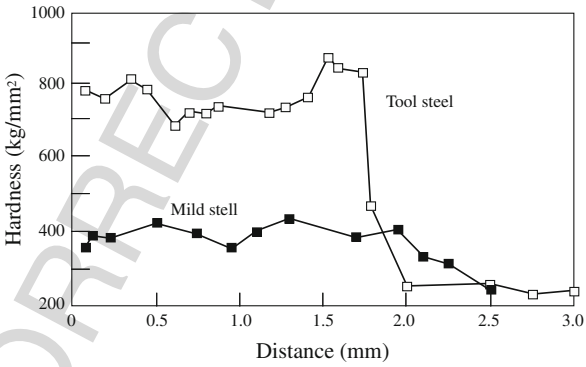

Fig. 8.11 Microhardness comparison of transformation tool steel and mild steel after the steel was bombarded by 6 MeV, 1.25 kA beam operating at 500 kHz. The surface fluence was ~20 J/mm^2 (reproduced from [43] with permission)

8.5 Conclusion

LIAs can produce high-energy high-power beams that could be used for many applications. They are employed in applications that require combinations of beam current, beam voltage, and pulse length that are not easily obtained using RF accelerators or pulsed diodes. RF linacs can produce long trains of high energy particles, but the currents are typically below one Amp. Their average power can reach several megawatts, and typically the beam quality has been better than what has

UNCORRECTED PROOF

been achieved in LIAs. Pulsed diodes do not scale easily to high beam voltage, and the beam quality typically is poor for high-current (> 10 kA) beams.

We expect that in the future there will be more applications that require a combination of beam parameters best suited to LIAs. When overall system efficiency is important the concept of recycling the spent beam can be used to improve their performance. To date there has not been a widespread use of LIA technology for commercial or military applications. However, LIAs do continue to play an important role for flash radiographic, and as research tools.

Newer power switching technologies or more compact accelerator architectures, such as the dielectric wall accelerator (DWA) [48] will alter the choice of accelerator type chosen for a given mission. High average power LIA applications await the development of low-cost, reliable pulse-power components, and a better understanding of the physics of intense beam transport.

References

1. N. Christofilos. Astron thermonuclear reactor. In *Second UN International Conference on Peaceful Uses of Atomic Energy*, Vol. 32, page 279, Geneva, Switzerland, 1958.
2. N. Christofilos, R. Hester, W. Lamb, D. Reagan, W. Sherwood, and R. Wright. High Current Linear Induction Accelerator for Electrons. *Rev. Sci. Inst.*, 35:886, 1964.
3. A. Gsponer. The Physics of High-Intensity High-Energy Particle Beam Propagation in Open Air and Outer-Space Plasmas, Report ISRI 82-04.56 (Independent Scientific Research Institute, Oxford, OX4 4YS, Jan. 11, 2009) pp. 257 E-print arXiv:physics/0409157v3, available at http://arXiv.org/abs/physics/0409157.
4. D. Pines. (editor). APS Study: Science and Technology of Directed Energy Weapons. *Rev. Mod. Phys.*, 59:S1–S202, 1987.
5. C. Olson and V. Schumacher. *Collective Ion Acceleration*. Springer, Berlin, 1979.
6. G. Dolbilov. High Current Induction Linacs at JINR and Perspective of their Applications for Acceleration of Ions. In Y. Batygin, editor, *AIP Conference Proceedings No. 480*, pages 85–98, Saitama, Japan, Dec. 1998. The American Institute of Physics, Woodbury, NY.
7. R. Avery, G. Behrsing, W. Chupp, A. Faltens, E. Hartwig, H. Hernandez, C. Macdonald, J. Meneghetti, R. Nemetz, W. Popenuck, W. Salsig, and D. Vanecek. The ERA 4 MEV Injector. *IEEE Trans. Nucl. Sci.*, NS-18:479–482, 1971.
8. B. Kulke and R. Kihara. Recent Performance Improvements on FXR. In *Proceedings of the 1983 Particle Accelerator Conference*, pages 3030–3032, Santa Fe, NM, 21–23 Mar. 1983.
9. M. Burns, B. Carlsten, T. Kwan, D. Moir, D. Prono, S. Watson, E. Burgess, H. Rutkowski, G. Caporaso, Y.-J. Chen, Y. (Judy) Chen, S. Sampayan, and G. Westenskow. DARHT Accelerators Update and Plans for Initial Operation. In *Proceedings of the 1999 Particle Accelerator Conference*, pages 617–621, New York, NY, 29 Mar.–2 Apr. 1999.
10. E. Merle, F. Bombardier, J. Delvaux, M. Mouillet, O. Pierret, J. Ribes, and C. Vermare. Progress with the 2–3 kA Airix Electron Beam. In *Proceedings of the 2002 European Particle Accelerator Conference*, pages 2649–2651, Paris, France, 3–7 June 2002.
11. J. Deng, B. Ding, L. Zhang, H. Wang, G. Dai, N. Chen, Z. Dai, Z. Zhang, J. Shi, W. Zhang, J. Li, X. Liu, Y. Zie, M. Wang, L. Wen, H. Li, J. Wang, Z. Xie, and M. Wang. Design of the Dragon-I Linear Induction Accelerator. In *Proceedings of the 2002 Linear Accelerator Conference*, pages 40–42, Gyeongju, Korea, 19–23 Aug. 2002.
12. M. Burns, B. Carlsten, H. Davis, C. Ekdahl, C. Fortgang, B. Cuistian, F. Merrit, K. Nielsen, C. Wilkinson, K. Chow, W. Fawley, H. Ruthowski, W. Waldron, S. Yu, G. Caporaso, Y.-J. Chen, E. Cook, S. Sampayan, J. Watson, G. Westenskow, and T. Hughes. Status of the

UNCORRECTED PROOF

DARHT Phase 2 Long-Pulse Accelerator. In *Proceedings of the 2001 Particle Accelerator Conference*, pages 325–329, Chicago, IL, 18–22 June 2001.

13. D. Venable, D. Dickman, J. Hardwick, E. Bush, R. Taylor, T. Boyd, J. Ruhe, E. Schneider, B. Rogers, and H. Worstell. Phermex: A Pulsed High-Energy Radiographic Machine Emitting X-Rays. Technical Report LA-3241, Los Alamos National Laboratory, 1967.
14. W. DeHope, D. Goerz, R. Kihara, M. Ong, G. Vogtlin, and J. Zentler. An Induction Linac Test Stand. In *Proceedings of the 2005 Particle Accelerator Conference*, pages 2455–2457, Knoxville, TN, 16–20 May ~~2001~~.
15. I. Smith. Induction Voltage Adders and the Induction Accelerator Family. *Phys. Rev. Spec. Topics Accel. Beams*, 7:064801, 2004.
16. D. Lide. (editor). *CRC Handbook of Chemistry and Phyics*. CRC Press, Boca Raton, FL, 89th edition, 2008. see Photon attenuation coefficients, Sec. ?10–288?
17. Y.-J. Chen. Final Focus Spot Size in a Solenoid Focusing System. Technical Report UCRL-ID-152620, Lawrence Livermore National Laboratory, 2003. https://e-reports-ext.llnl.gov/pdf/242705.pdf
18. Y. Chen, G. Caporaso, F. Chambers, S. Falabella, F. Goldin, G. Guethlein, E. Lauer, J. McCarrick, R. Neurath, R. Richardson, S. Sampayan, and J. Weir. Beam Physics in X-Ray Radiography Facilities. In *Proceedings of the International Workshop on Recent Progress in Induction Accelerators*, pages 167–173, Tsukuba, Japan, 29–31 Oct. 2002.
19. C. Roberson and P. Sprangle. A Review of Free Electron Lasers. *Phys. Fluids*, 1:3, 1989.
20. T. Orzechowski, B. Anderson, J. Clark, W. Fawley, A. Paul, D. Prosnitz, E. Scharlemann, S. Yarema, D. Hopkins, A. Sessler, and J. Wurtele. High Efficiency Extraction of Microwave Radiation from a Tapered Wiggler Free Electron Laser. *Phys. Rev. Lett.*, 57:2172, 1986.
21. T. Akiba, K. Imasaki, K. Tanaka, S. Migamoto, K. Mima, Y. Kitagawa, S. Nakea, S. Kuruma, C. Yamanaka, M. Fukuda, N. Ohigashi, and Y. Tsunawaki. Induction Linac FEL Experiment at ILE. In *Proceedings of the 7th International Conference on High Power Particle Beams*, pages 1306–1311, Karhlsruhe, Germany, 4–8 July 1988.
22. E. Hooper, S. Allen, M. Brown, J. Byers, T. Casper, B. Cohen, R. Cohen, M. Fenstermacher, J. Foote, K. Hoshino, C. Lasnier, P. Lopez, M. Makowski, M. Marinak, W. Meyer, J. Moller, W. Nevins, K. Oasa, T. Oda, K. Odajima, T. Ogawa, T. Ohgo, B. Rice, T. Rognlien, G. Smith, B. Stallard, K. Thomassen, and R. Wood. MTX Final Report. Technical Report UCRL-ID-116263, Lawrence Livermore National Laboratory, 1994.
23. J. Weir, T. Orzechowski, J. Miller, Y. Chong, F. Chambers, G. Deis, K. Halbach, and J. Edighoffer. Results of the PALADIN Experiment. In *Proceedings of the International Congress on Optical Science and Engineering*, Paris, France, 24–28 Apr. 1989.
24. D. Bainan, D. Jianjun, H. Shenzong, S. Jinsui, Z. Wenjum, L. Qing, and H. Yi. Free Electron Laser Amplifier Experiments Based on 3.5 MeV Linear Induction Accelerator. In *Proceedings of 1995 Particle Accelerator Conference*, pages 246–247, Dallas, TX, 1–5 May 1995.
25. K. Takayama, J. Kishiro, K. Ebihara, T. Ozaki, S. Hiramatsu, and H. Katoh. 1.5 MeV Ion-Channel Guided X-Band Free-Electron Laser Amplifier. *J. Appl. Phys.*, 77:5467–5469, 1995.
26. K. Saito, K. Takayama, T. Ozaki, J. Kishiro, K. Ebihara, and S. Hiramatsu. X-Band Pre-bunched FEL Amplifier. *Nucl. Inst. Meth. A*, 375:237–240, 1996.
27. N. Ginzburg, A. Kaminsky, A. Kaminsky, N. Peskov, S. Sedykh, A.S. Sergeev, and A.P. Sergeev. Experimental Observation of Mode Competition and Single Mode Operation in JINR-IAP Millimetter-wave FEM Oscillator. In *Proceedings of the 7th International Workshop on Linear Colliders*, page CD ROM, Zvenigorod, Russia, 29 Sept.–3 Oct. 1997.
28. T. Lefevre, J. Gardelle, P. Gouard, J. Rullier, J. Donohue, S. Lidia, and C. Vermare. The FEL Driven Two-Beam Accelerator Studies at CESTA. In *Proceedings of the 2000 Linear Accelerator Conference*, pages 869–871, Monterey, CA, 21–25 Aug. 2002.
29. C. A. Brau. *Free-Electron Lasers*, pages 197–201, Academic Press, Inc, Boston, MA, 1990.
30. K. Sakamoto, T. Kobayashi, S. Kwasaki, Y. Kishimoto, S. Musyoki, A. Watanabe, M. Takahashi, H. Ishizuka, M. Sato, and M. Shiho. Millimeter Wave Amplification in a Free Electron Laser with a Focusing Wiggler. *J. Appl. Phys.*, 75:36–42, 1994.

UNCORRECTED PROOF

31. B. Kulke, M. Caplan, D. Bubp, T. Houck, D. Rogers, D. Trimble, R. VanMaren, G. Westenskow, D. McDermott, N. Luhmann, and B. Danly. Test Results from the LLNL 250 GHz CARM Experiment. In *Proceedings of the 1991 Particle Accelerator Conference*, pages 766–768, San Francisco, CA, 6–9 May 1991.
32. A. Sessler. The Free-Electron Laser as a Power Source for a High Gradient Accelerating Structure. In *Workshop on Laser Acceleration of Particles*, page 154, New York, NY, 18–23 Feb. 1982. AIP Conference Proceedings No. 91.
33. A. Sessler and S. Yu. Relativistic Klystron Version of the Two-Beam Accelerator. *Phys. Rev. Lett.*, 58:2439, 1987.
34. G. Westenskow, T. Houck, and S. Yu. Transverse Instabilities in a Relativistic Klystron Two-Beam Accelerator. In *Proceedings of the 16th International Linear Accelerator Conference*, pages 263–267, Ottawa, Canada, 24–28 Aug. 1992.
35. T. Houck, G. Westenskow, J. Haimson, and B. Mecklenburg. Chopperton II. In *Proceedings of the 1995 Particle Accelerator Conference*, pages 1524–1526, Dallas, TX, 1–5 May 1995.
36. J. Haimson and B. Meckelenburg. Suppression of Beam Induced Pulse Shortening Modes in High Power RF Generator TW Output Structures. In *Intense Microwave and Particle Beams III*, pages 209–219, Los Angeles, CA, 20 Jan. 1992. SPIE Proceedings Vol. 1629-71.
37. T. Houck, F. Deadrick, G. Giodano, E. Henestroza, S. Lidia, L. Reginato, D. Vanecek, G. Westenskow, and S. Yu. Prototype Microwave Source for a Relativistic Klystron Two-Beam Accelerator. *IEEE Trans. Plasma Sci.*, 24:938–946, 1996.
38. K. Takayama. Stability of a Klystron-Type Free-Electron Laser in the Steady-State Regime: Macroparticle Approach. *Phys. Rev. Lett.*, 63:516–519, 1989.
39. K. Takayama and S. Hiramatsu. Ion-Channel Guiding in a Steady-State Free-Electron Laser. *Phys. Rev. A*, 37:173–177, 1988.
40. J. Swingle. Technical Options for High Average Power Free Electron Millimeter-Wave and Laser Devices. In *Second Beamed Space-Power Workshop*, page 191, Hampton, VA, 28 Feb.–2 Mar. 1989. NASA Conference Pub. No. 3037.
41. K. Takayama, S. Hiramatsu, and M. Shiho. CW 100 MW Microwave Power Transfer in Space. *J. British Interplanetary Soc.*, 44:573, 1991.
42. M. Shiho, A. Watanabe, S. Kawasaki, H. Ishizuka, K. Takayama, J. Kishiro, T. Shindo, and T. Fujioka. ~~Lighting~~ Control System Using High Power Microwave FEL. *Nucl. Inst. Meth. A*, 375:396–400, 1996.
43. J. Elmer, M. Newton, and A. Smith. Transformation Hardening of Steel Using High Energy Electron Beams. *Welding J.*, 73:5291–5299, 1994.
44. N. Nochovnaya, V. Shulov, D. Proskurovski, and V. Rotshtein. Modification of Titanium Alloy Parts Properties by Intensive Current Electron Beams. In *Proceedings of the 11th International Conference on High Power Beams*, pages 813–816, Prague, Czech Republic, 10–14, June 1996.
45. T. Renk, P. Provencio, S. Prasad, A. Shlapakovski, A. Petrov, K. Yatsui, W. Jiang, and H. Suematsu. Material Modification Using Intense Ion Beams. In *Proceedings of the IEEE*, Vol 92, No. 7, pages 1057–1081. IEEE, 2004. IEEE No. 0018-9219/04.
46. A. Pogrebnjak. Utilizaton of High Power Ion Beams and High Current Electron Beams for Modification of Metalline Materials. In *Proceedings of the 10th International Conference on High Power Beams*, pages 232–235, San Diego, CA, 20–24 June 1994.
47. Y. Gofman. Use of Charged Particle Beams for Research of Mechanical Behaviour on Thermonuclear Reactor First Wall Candidate Materials. In *Proceedings of the 11th International Conference on High Power Beams*, pages 805–808, Prague, Czech Republic, 10–14 June 1996.
48. G. Caporaso, S. Sampayan, Y.-J. Chen, D. Blackfield, J. Harris, S. Hawkins, C. Holmes, M. Krogh, S. Nelson, W. Nunnally, A. Paul, B. Poole, M. Rhodes, D. Sanders, K. Selenes, J.Sullivan, L. Wang, and J. Watson. High Graident Induction Accelerator. In *Proceedings of the 2007 Particle Accelerator Conference*, page TUYC02, Albuquerque, NM, 25–29 June 2007.

UNCORRECTED PROOF

Chapter 9
Ion Induction Accelerators

~~Steven M. Lund,~~ John J. Barnard~~,~~ and Kazuhiko Horioka

The description of beams in RF and induction accelerators share many common features. Likewise, there is considerable commonality between electron induction accelerators (see Chap. 7) and ion induction accelerators. However, in contrast to electron induction accelerators, there are fewer ion induction accelerators that have been operated as application-driven user facilities. Ion induction accelerators are envisioned for applications (see Chap. 10) such as Heavy Ion Fusion (HIF), High Energy Density Physics (HEDP), and spallation neutron sources. Most ion induction accelerators constructed to date have been limited scale facilities built for feasibility studies for HIF and HEDP where a large numbers of ions are required on target in short pulses. Because ions are typically non-relativistic or weakly relativistic in much of the machine, space-charge effects can be of crucial importance. This contrasts the situation with electron machines, which are usually strongly relativistic leading to weaker transverse space-charge effects and simplified longitudinal dynamics. Similarly, the bunch structure of ion induction accelerators relative to RF machines results in significant differences in the longitudinal physics.

In this chapter, ion sources and injectors are covered in Sect. 9.1. Ion sources have different practical issues than electron sources (see Sect. 7.2). Longitudinal dynamics ~~is~~ covered in Sect. 9.2 while emphasizing strong space-charge issues specific ion induction accelerator applications.

9.1 Ion Sources and Injectors

Induction ion accelerator applications with high space-charge intensity need high perveance beam sources in pulses that typically range from ∼10 ns to ∼10 μs. Compared with electron beam generation, ions are more difficult to extract from the source. The generation, extraction, and propagation of the ions are strongly influenced by both longitudinal and transverse space-charge effects and plasma phenomena. Currents of high-power ion beam sources are limited by the gap structure

~~S.M. Lund~~ (✉)
Lawrence Livermore National Laboratory, Livermore, CA 94550, USA
e-mail: ~~smlund~~@llnl.gov

K. Takayama, R.J. Briggs (eds.), *Induction Accelerators*, Particle Acceleration and Detection, DOI 10.1007/978-3-642-13917-8_9,
© Springer-Verlag Berlin Heidelberg 2011

UNCORRECTED PROOF

and the properties of the ion source. Important properties include the available ion current-density, the ion species and purity (including their charge state), and the stability of the emitting surface. We first review basic physical concepts required for understanding the gap dynamics (Sect. 9.1.1), including: space-charge limited flow (Child-Langmuir emission), plasma limited flow (Bohm criterion) and the ion emitting surface in plasmas, transverse and longitudinal beam emittance, electrode geometry, transients in the diode, and longitudinal accelerative cooling. Then we review specific ion sources presently employed or showing promise for high current induction accelerators (Sect. 9.1.2) and finally review several complete injector systems (Sect. 9.1.3).

9.1.1 Physics of High Current-Density Ion Sources

Options for ion sources depend on the available ion current-density and beam transport limitations associated with the injector geometry. To evaluate options, we need to know the relationship between plasma parameters, the space-charge field, and the attainable ion current-density.

1D Child-Langmuir extraction: In low energy transport, particularly within the beam extraction section (diode), the charged particle motion is dominated by the space-charge field. We estimate [1, 2] the steady-state (mid-pulse) current produced of a species-pure ion beam when there is a voltage of magnitude V applied across a gap of distance d, as illustrated in Fig. 9.1. The flow is assumed to be independent of transverse radius and varies only with longitudinal position z in the gap. The source can represent any pure species ion emitter which can produce adequate current-density. In steady state, the continuity equation implies that the axial current-density $J_z = \rho v_z$ is constant as a function of z, where ρ is the charge-density of the beam and v_z is the axial particle velocity in the gap. The one-dimensional Poisson equation $\partial^2\phi/\partial z^2 = -\rho/\epsilon_0$ governs the relation between the electrostatic potential ϕ and the charge-density ρ. The velocity is related to ϕ by the steady-state (non-relativistic) momentum equation $m v_z \partial v_z/\partial z = -q\,\partial\phi/\partial z$ yielding the energy

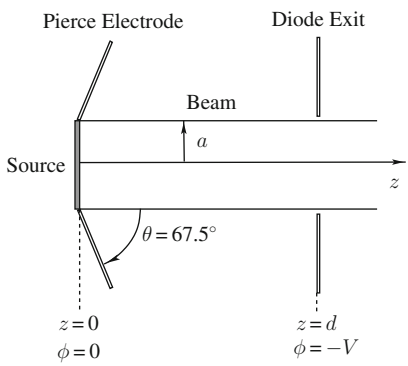

Fig. 9.1 Diode geometry

UNCORRECTED PROOF

conservation equation $(1/2)mv_z^2 = -q\phi$. Here we have assumed zero pressure (cold beam) in the momentum equation. For convenience, the potential ϕ is chosen to be zero at the emitter and $-V$ at the diode exit. The charge-density ρ in the Poisson equation can thus be expressed in terms of ϕ yielding the differential equation:

$$\frac{\mathrm{d}^2\Phi}{\mathrm{d}z^2} = \frac{J_z}{\epsilon_0 v_z} = \frac{J_z}{\epsilon_0}\left(\frac{m}{2q\Phi}\right)^{1/2}. \tag{9.1}$$

Here we have denoted $\Phi \equiv -\phi$ for the sake of clarity to minimize negative signs in the derivation. We multiply Eq. (9.1) by $\mathrm{d}\Phi/\mathrm{d}z$ and integrate to obtain:

$$\frac{1}{2}\left(\frac{\mathrm{d}\Phi}{\mathrm{d}z}\right)^2 = \frac{J_z}{\epsilon_0}\left(\frac{2m}{q}\right)^{1/2}\Phi^{1/2} + C \tag{9.2}$$

Here, C is an integration constant. We further assume that space-charge is plentiful enough that it may be extracted from the emitting surface (or from a plasma source) at $z = 0$ such that the longitudinal field $E_z = \partial\phi/\partial z$ is reduced to zero right at the surface. This is the so-called "space-charge limited emission" condition. If more space-charge were extracted, it would create an electric field that would be directed towards the emitter and thus prevent further emission. The steady-state condition occurs when $\partial\Phi/\partial z = 0$ is maintained at the emitter. This condition (together with the condition that $\Phi = 0$ at $z = 0$) requires $C = 0$ in Eq. (9.2). Taking the square root of Eq. (9.2) and solving the resulting differential equation (again subject to $\Phi = 0$ at $z = 0$), yields

$$\Phi(z) = \frac{3^{4/3}}{2^{5/3}}\left(\frac{J_z}{\epsilon_0}\right)^{2/3}\left(\frac{m}{q}\right)^{1/3} z^{4/3}. \tag{9.3}$$

Setting $\Phi = V$ at $z = d$, gives $\Phi = V(z/d)^{4/3}$ and so V satisfies,

$$V = \frac{3^{4/3}}{2^{5/3}}\left(\frac{J_z}{\epsilon_0}\right)^{2/3}\left(\frac{m}{q}\right)^{1/3} d^{4/3}. \tag{9.4}$$

Solving for the current-density J_z yields the so-called Child-Langmuir Law for the current-density of space-charge limited emission:

$$J_z = J_{\mathrm{CL}} \equiv \chi\frac{V^{\frac{3}{2}}}{d^2}, \tag{9.5}$$

where

$$\chi = \frac{4\epsilon_0}{9}\sqrt{\frac{2q}{m}}. \tag{9.6}$$

UNCORRECTED PROOF

In addition to the space-charge effect, voltage breakdown limits the value of V used for beam extraction. Empirically it has been found that [3] for small gap distances (for $d \lesssim 1$ cm) there is an electric field maximum of around 100 kV/cm that gives a reasonable design upper limit to avoid electrical breakdown across the gap. In this regime, the maximum voltage V V_{BD} corresponding to this limit therefore scales with d as $V_{\mathrm{BD}} \simeq 100$ kV $(d/1$~~1~~cm). For gap distances larger than $d = 1$ cm however, a smaller electric field is required to ent breakdown, and in this case the design limit scales as $V_{\mathrm{BD}} \simeq 100$ kV$(d/1$~~1~~ cm$)^{1/2}$. Substituting these relations into Eq. (9.5) gives

$$J_z \propto \frac{V^{3/2}}{d^2} \propto \begin{cases} d^{-1/2} & d \lesssim 1 \text{ cm}, \\ d^{-5/4} & d \gtrsim 1 \text{ cm}. \end{cases} \tag{9.7}$$

Therefore, the current-density decreases as the gap length increases in operation close to the breakdown limit.

For a circular beam with constant radius a within the gap, the extractable total ion current I is given by,

$$I = \pi a^2 J_{\mathrm{CL}} = \pi \chi \left(\frac{a}{d}\right)^2 V^{\frac{3}{2}}. \tag{9.8}$$

The radius of the diode aperture is typically slightly larger than the beam radius a. If a is too large compared with the gap width d, the equi-potential lines will be distorted and the negative lens effect [4] can become large. Pierce electrodes (see Fig. 9.1 and the subsection below) are employed to shape the field and maintain approximate 1D flow. Even with Pierce electrodes, to avoid beam aberrations, the aspect ratio of the extraction gap a/d is typically limited to $a/d < 0.25$ [5]. This scaling implies that for a fixed aspect ratio, the maximum extractable beam current depends only on the extraction voltage as $I \propto V^{\frac{3}{2}}$. Note that these scaling relations imply that when producing high current using a single beam, the current-density decreases as the beam current increases.

Transverse beam emittance: The ion temperature at the source, together with radius of the source determine the initial transverse phase-space area, or equivalently the emittance, of the beam. We assume a uniform current-density at the source so that $\langle x^2 \rangle_\perp = a^2/4$ and we also assume a nonrelativistic Maxwell Boltzm dis-tribution in the spread of particle angles, so that $\frac{1}{2} m v_z^2 \langle x'^2 \rangle_\perp = k_B T_i/2$. Here, a and T_i are the beam radius and ion temperature at the source, respectively, and k_B is Boltzmann's constant. Both of the assumptions above are good near the emitting surface. If there is no angular divergence in a, then $a' = 4\langle xx' \rangle_\perp / a = 0$, and the initial normalized emittance $\varepsilon_{nx} = 4\gamma_b \beta_b [\langle x^2 \rangle_\perp \langle x'^2 \rangle_\perp - \langle xx' \rangle_\perp^2]^{1/2}$ (see [1]) at the source is

$$\varepsilon_{nx} = 4 \left\langle x^2 \right\rangle_\perp^{1/2} \left\langle \frac{v_x^2}{c^2} \right\rangle_\perp^{1/2} = 2a \left(\frac{k_B T_i}{mc^2}\right)^{1/2}. \tag{9.9}$$

UNCORRECTED PROOF

Here, $v_x = \mathrm{d}x/\mathrm{d}t \simeq \beta_b c x' = v_z x'$ has been applied in the nonrelativistic limit with $\gamma_b = 1$. Assuming conservation of normalized emittance, then the unnormalized emittance $\varepsilon_x = c\varepsilon_{nx}/v_z$ exiting the diode can be expressed as,

$$\varepsilon_x = 2a\left(\frac{k_B T_i}{m v_z^2}\right)^{1/2} = \sqrt{2}a\left(\frac{k_B T_i}{qV}\right)^{1/2}, \tag{9.10}$$

where $qV = \frac{1}{2}mv_z^2$ is the ion kinetic energy at the diode exit. Beam optical aberrations (non-linear transverse electric fields) will increase the emittance from the initial source value given by Eq. (9.10). Electrodes near the edge of the beam are used to shape the electric field so that nearly parallel flow can be maintained (see Pierce electrodes subsection below) and aberrations minimized. However, because the electrodes cannot be made to be ideal, diode normalized emittance can be significantly higher than Eq. (9.9).

Longitudinal beam emittance and accelerative cooling: Analogously to the transverse case the longitudinal phase-space area in our ideal 1D diode is also conserved. Here the appropriate phase-space variables are those that form conjugate pairs, such as the longitudinal energy $\mathcal{E}_z \equiv p_z^2/2m$ and arrival time t, or the longitudinal momentum p_z and the longitudinal position z. At the source there is a spread in longitudinal energy corresponding to the temperature at the source, such that $\langle \delta p_z^2 \rangle/(2m) = k_B T_i/2$. Here, $\langle \cdots \rangle$ denotes an average over the 6D distribution function, and δp_z and $\delta \mathcal{E}_z$ are the difference between the longitudinal momentum and energy of a particle and their respective means. After passing through an ideal diode, all particles receive the same energy increment qV so the spread in longitudinal energy remains the same as it is at the source. For a pulse duration at the source τ_p, the duration at the exit will also be τ_p, so the longitudinal (normalized) emittance that is proportional to $\langle \delta \mathcal{E}_z^2 \rangle^{1/2}\tau_p$ will be conserved as expected. But the consequence of having a conserved normalized emittance implies that the temperature of the beam (as measured in the co-moving frame) is drastically reduced.

To calculate the energy spread in the co-moving frame, it is most convenient to first calculate δv_z for a particle in the laboratory frame. For a non-relativistic boost, velocities are additive, so the velocity difference δv_z and momentum difference δp_z in the co-moving frame are the same as those quantities in the lab frame. Since $\mathcal{E}_z = p_z^2/2m$, it follows that $\delta \mathcal{E}_z = p_z \delta p_z/m$, or $\delta \mathcal{E}_z/\mathcal{E}_z = 2\delta p_z/p_z$. If we denote subscript "source" and "exit" for quantities at the diode source and exit respectively, then the longitudinal temperature in the co-moving frame $k_B T_{z,\mathrm{exit}}$ is given by:

$$\frac{k_B T_{z,\mathrm{exit}}}{2} = \frac{\langle \delta p_{z,\mathrm{exit}}^2 \rangle}{2m} = \frac{\langle \delta \mathcal{E}_{z,\mathrm{exit}}^2 \rangle}{4\mathcal{E}_{z,\mathrm{exit}}} = \frac{\langle \delta \mathcal{E}_{z,\mathrm{source}}^2 \rangle}{4\mathcal{E}_{z,\mathrm{exit}}} = \frac{3}{16}\frac{(k_B T_{\mathrm{source}})^2}{\mathcal{E}_{z,\mathrm{exit}}} \tag{9.11}$$

Here, the final equality uses the result that, for a Maxwell-Boltzmann distribution, the average $\langle \delta \mathcal{E}_z^2 \rangle = 3(k_B T)^2/4$. As can be seen from Eq. (9.11) the longitudinal

UNCORRECTED PROOF

temperature of the beam $k_B T_{z,\text{exit}}$ has decreased by a factor of order $k_B T_{\text{source}}/\mathcal{E}_{z,\text{exit}}$. For $k_B T_{\text{source}} \sim 0.1$ eV, and $\mathcal{E}_{z,\text{exit}} \sim 10^5$ eV, the temperature has decreased by a factor of order 10^{-6}. This large reduction in temperature can be seen as a result of the effective lengthening of the beam. Since the initial longitudinal length of the beam is of order $\delta p_{z,\text{source}} \tau_p / m$, and the length of the beam at the diode exit is of order $p_{z,\text{exit}} \tau_p / m$, the beam has been stretched by a factor $p_{z,\text{exit}}/\delta p_{z,\text{source}}$ so the momentum spread $\delta p_{z,\text{exit}} = \delta p_{z,\text{source}}^2 / p_{z,\text{exit}}$ has gone down by the same factor, implying that the temperature has gone down by a factor $\sim k_B T_{\text{source}}/\mathcal{E}_{z,\text{exit}}$, consistent with Eq. (9.11).

Whereas the length of the beam has gone up by a large factor (with a concomitant decrease in the longitudinal temperature), the transverse dimension of the beam (and transverse temperature) remain nearly constant. The distribution function in the beam frame has thus become highly anisotropic. This can lead to dynamic instabilities [6–8] that saturate when the longitudinal temperature approaches the transverse temperature. Collisions also tend to reduce the magnitude of the anisotropy by transferring momentum from the transverse degrees of freedom into longitudinal momentum spread. This is known as the Boersch effect [1]. Even though collisions are generally negligible in beams, since longitudinal cooling is so extreme, the few collisions that do occur can increase the longitudinal temperature to a value far higher than given by Eq. (9.11).

Plasma sources: the Bohm criterion and ion emission surface: Many high current-density ion sources rely on extraction from a plasma surface. Important phenomena in plasma-based high current-density include: escape of electrons from the emitter, drift of ions toward the plasma surface, acceleration of ions, injector geometry and applied fields, space-charge and plasma effects and associated transport limitations.

When an electric field is applied to the source plasma, the externally applied ~~filed~~ field is shielded by the plasma sheath. The characteristic distance over which the electric field is excluded is the *Debye length* [9, 10]

$$\lambda_D = \sqrt{\frac{\epsilon_0 k_B T_e}{e^2 n_e}} = 743 \text{ cm} \sqrt{\frac{T_e/(\text{eV})}{n_e/(\text{cm}^{-3})}}. \tag{9.12}$$

Here, $-e$ is the electron charge, and T_e and n_e are the electron temperature and density. Because the ions are extracted from the plasma through the sheath region so long as the dimensions of plasma volume are much larger than λ_D, this is the basic scale length of the plasma source. In plasma ion sources, the boundary between electrically neutral source plasma and the sheath region is called the *ion emission surface*. The ion emission surface, the emitted current, and the geometry and biases of the injector structures will determine the ion optics.

The current of ions extracted is limited by the available ion current-density through the sheath and/or the space-charge field in the extraction gap. When ions are extracted from a stationary plasma, the current-density is limited by the thermal motion of the source plasma. Assuming a Maxwellian velocity distribution in the

UNCORRECTED PROOF

source plasma, we can derive the characteristic *Bohm current-density* which gives the available current-density of ions [4]. The Bohm current-density is

$$J_B = 0.6en_i \left(\frac{\kappa T_e}{m_i}\right)^{\frac{1}{2}}, \tag{9.13}$$

where n_i is the plasma ion density and m_i is the ion mass. Equation (9.13) indicates that high current-density sources require higher temperature plasmas. On the other hand, the intrinsic emittance of the beam emerging from the ion source is given by Eq. (9.10).

Because the equilibration time between electrons and ions ~~are~~ usually long enough, the Bohm limit can not be directly related with the intrinsic beam emittance. However these indicate that the relation between the available current-density and the intrinsic beam emittance is a trade-off; increasing the current level means decreasing the quality of extracted beam.

The optics of ions extracted strongly depend on the plasma source. Figure 9.2 shows a schematic of the stationary ion emitting surface in a long-pulse plasma source. Here, we define the "anode" as the ion emitting surface, and the "cathode" as the diode exit. (In general, current flows from anode to cathode.) When the ion supply is sufficient to extract, the current and the beam optics are governed by the self field in the extraction gap. If the Bohm current-density is less than the Child-Langmuir current-density ($J_B < J_{CL}$), then the source is starved and a concave emission surface results which produces an over-focused beam as illustrated in Fig. 9.2(a). Conversely, if $J_B > J_{CL}$, then there is an excess supply of ions resulting in a convex emission surface and produces a divergent beam as illustrated in Fig. 9.2(b). For good beam optics, a slightly starved source is considered preferable. This guiding principle limits the aspect ratio of the extraction gap [11].

Pierce electrodes: As discussed above, Child-Langmuir flow is based on the assumption of a one-dimensional (longitudinal) geometry. In fact, diodes have finite

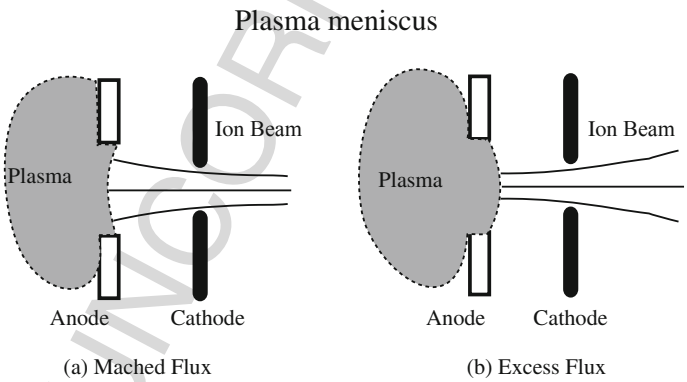

Fig. 9.2 Behavior of the ion emitting surface in extraction from a stationary source plasma for starved (**a**) and excess (**b**) source current-density

UNCORRECTED PROOF

transverse extent and so are intrinsically multi-dimensional. Nevertheless, electrodes can be introduced (see Fig. 9.1) that allow the beam to be terminated at a finite radius, yet maintain the same electrical field, velocity, and charge-density, as in the case of a one-dimensional Child-Langmuir flow over the full radial profile of the beam. This can be easily seen in the case of a ribbon beam that propagates in the z direction and is infinite in the y-direction but has some finite width in the x-direction. We take $x = 0$ to be one of the edges of the beam (with $x > 0$ vacuum). We wish to calculate surfaces of equipotentials, such that the potential satisfies the Child-Langmuir potential $[\Phi(x = 0, y, z) = V(z/d)^{4/3}]$ and also maintains the 1D condition that the transverse electric field is zero $\partial\phi(x = 0, y, z)/\partial x = 0$ along the edge of the beam. A solution that satisfies both conditions can be found using complex variables. Let $w = z + ix$. Then let $\Phi(x, z)$ be the real part of a complex function $F(w) \equiv \Phi(x, z) + i\mu(x, z)$. If $F(w)$ is an analytic function (i.e. its derivative exists and is independent of direction over some domain in the w plane), then Φ and μ satisfy the Laplace equation over that domain. This suggests that we take $F(w) = V(w/d)^{4/3}$ so that along the surface $x = 0$, $\Phi(x = 0, z) = V(z/d)^{4/3}$ implying that $\Phi(z)$ satisfies the Child-Langmuir potential. The real part of $F(w)$ can be written:

$$\mathrm{Re}[F(w)] = \Phi(x, z) = V(x^2 + z^2)^{2/3} \cos\left[\frac{4}{3}\tan^{-1}\left(\frac{x}{z}\right)\right] \tag{9.14}$$

Note that $\Phi(x, z) = \Phi(-x, z)$ so that $\partial\Phi/\partial x|_{x=0} = 0$, as required.

If the source ($z = 0$) is at the equipotential $\Phi = 0$, then the equipotential surface that originates at $x = 0$ and $z = 0$ can be shown from Eq. (9.14) to satisfy $0 = \cos[4\tan^{-1}(x/z)/3]$ implying that $\tan^{-1}(x/z) = 3\pi/8 \simeq 67.5°$. The coordinates of the equipotential passing through $x = 0$ and $z = z_0$ satisfies:

$$z_0^{4/3} = (x^2 + z^2)^{2/3} \cos\left[\frac{4}{3}\tan^{-1}\left(\frac{x}{z}\right)\right] \tag{9.15}$$

By placing conductors along these equipotentials the Child-Langmuir potential is enforced along the edge and therefore throughout the beam. In particular at $z = 0$ an electrode placed at approximately 67.5° from the z-axis is known as a Pierce electrode, and is intended to ensure an initial parallel flow from the source. Electrodes may be placed at larger z along curves given by Eq. (9.15) such as at the diode exit, so that Φ satisfies Eq. (9.14) between electrodes, and therefore ensures Child-Langmuir potential along the beam boundary.

For the case of an axisymmetric cylindrical beam (in contrast to a ribbon beam), there is no simple analytic solution such as Eq. (9.15), but numerical results indicate that at $z = 0$ the same "Pierce angle" of 67.5° is obtained. However, for finite z_0 the curves are different, but qualitatively similar, and instead of lying on surfaces that are independent of y the surfaces are independent of azimuth θ in the axisymmetric case [12].

As discussed above, despite the use of electrodes at, for example, the diode emitter and diode exit, if the diameter of the aperture a is too large compared with the

UNCORRECTED PROOF

gap width d, the equi-potential lines will be distorted [4]. This is due to the finite thickness and radius of curvature of conductors that are needed to avoid breakdown, and because fields arising because of departures from the ideal Child-Langmuir geometry can leak in from beyond the exit of the diode.

Diode transients: We saw in the previous section that adding angled electrodes at the edge of the beam compensates for the absence of space-charge beyond the radius of the beam, and thus ensures that the electric field in the location where there is charge-density obeys Child-Langmuir flow. Similarly, during the initial transit of the beam head through the diode, the lack of space-charge in front of the head requires compensation to avoid the effects of the vacuum electric field that occurs between the head of the beam and the exit of the diode. In this case, the compensation is in the form of a time dependent voltage waveform, that is adjusted so that during the initial transit of the head of the beam, the electric field at the head is the same as if there were Child-Langmuir flow. The effect of space-charge between any point in the diode and the diode exit is to reduce the field relative to what it would be if the diode were at the same voltage, but had no space-charge. Therefore, the required waveform will increase with time until the head of the beam reaches the diode exit at which time the potential drop across the diode $\Phi(d)$ will reach the full voltage V for steady Child-Langmuir flow.

We may calculate the required waveform as follows [13]. Suppose the head of the beam is at position z_0 [see Fig. 9.3(a)], with constant current-density J_z at all points between $z = 0$ and $z = z_0$ but $J_z = 0$ between z_0 and the position of the diode exit ($z = d$). If the desired steady-state voltage is V, the potential difference between 0 and z_0 is just the Child-Langmuir potential Φ to the point z_0, $\Phi = V(z_0/d)^{4/3}$. The desired electric field at z_0 is the Child-Langmuir electric field at that point, so $-\partial\phi/\partial z = \partial\Phi/\partial z = (4/3)(V/d)(z_0/d)^{1/3}$. The potential difference between the beam head and the diode exit is $d - z_0$ times this electric field. Summing the potential drops between 0 and z_0 and between z_0 and d yields the desired potential drop across the gap $\Phi(d, z_0)$. Here, we have added a second argument on Φ to indicate that the potential $\Phi(d)$ is calculated when the beam head is at axial position $z = z_0$. We obtain:

$$\begin{aligned}\Phi(d, z_0) &= V\left(\frac{z_0}{d}\right)^{4/3} + \left(\frac{4V}{3d}\right)\left(\frac{z_0}{d}\right)^{1/3}(d - z_0)\\ &= V\left[\frac{4}{3}\left(\frac{z_0}{d}\right)^{1/3} - \frac{1}{3}\left(\frac{z_0}{d}\right)^{4/3}\right]\end{aligned} \tag{9.16}$$

The location of the beam head (z_0) as a function of time can be found by solving the Child-Langmuir energy equation, which can be viewed as a differential equation relating the longitudinal velocity of a particle to the Child-Langmuir potential,

$$\frac{1}{2}m\left(\frac{\mathrm{d}z_0}{\mathrm{d}t}\right)^2 = qV\left(\frac{z_0}{d}\right)^{4/3}. \tag{9.17}$$

The solution to Eq. (9.17), subject to the initial condition $z_0 = 0$ at $t = 0$, is $z_0 = d(t/\tau)^3$, where $\tau = 3d[m/(2qV)]^{1/2}$ is the "transit time" for a particle undergoing

UNCORRECTED PROOF

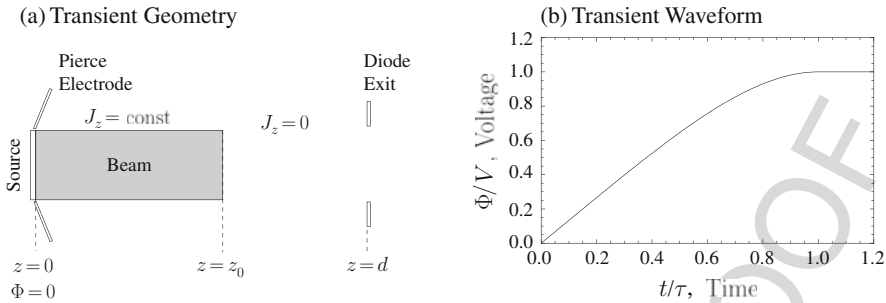

Fig. 9.3 Geometry for transient beam-head calculation (**a**) and the required voltage waveform for an ideal, sharp beam-head (**b**)

Child-Langmuir flow to traverse the diode. Expressing the potential $\Phi(d, z_0)$ in Eq. (9.16) in terms of t instead of z_0 yields

$$\Phi(d,t) = \begin{cases} V\left[\frac{4}{3}\left(\frac{t}{\tau}\right) - \frac{1}{3}\left(\frac{t}{\tau}\right)^4\right], & 0 < t < \tau, \\ V, & t \geq \tau. \end{cases} \tag{9.18}$$

Equation (9.18) specifies how the applied voltage should ramp in time and is plotted in Fig. 9.3(b). Typically this ramping is achieved approximately by raising Φ from 0 to V in a time τ in order to keep the current-density constant during the start up of the diode. If the voltage is turned on with a rise time longer or shorter than this characteristic time τ, beam current oscillations will occur. Such oscillations can have negative consequences since a mismatched beam can strike the aperture, producing secondary particle emission, etc. A similar calculation for the transit of the tail of the beam through the gap yields a rising voltage at the end of the pulse. In this case, a third electrode is needed to cut off the current flow, in the presence of the rising voltage, by allowing the local bias near the source to turn off the space-charge limited emission.

9.1.2 Ion Sources

A large number of ion emitters exist [14] with differing characteristics concerning current-density capability, species purity, transverse emittance, momentum spread, transverse phase-space distortions. In this section we briefly survey features of several technologies and provide references where more details can be found. Electron sources are discussed in Sect. 7.2 and have very different technological issues than ion sources.

Hot-plate sources: A conventional method for extracting metallic ions with low emittance but modest current-density is to use a shaped solid plate as the source. An advantage of plate ion sources is the high degree of control of the shape of the emitting surface, which is a well defined solid boundary which is stable over the

UNCORRECTED PROOF

pulse and can be shaped to minimize aberrations. The emitting surface is precisely defined over a wide area with the shaped geometry of the source material. A 17 cm diameter alumino-silicate source was developed and it produced 0.8 A of 1.8 MeV K^+ ions with emittance $\varepsilon < 1.0$ mm-mrad [15, 5, 16]. Various types of material have been employed for hot-plate sources. Alumino-silicates are commonly coated onto tungsten substrates and used for injection of alkali metal ions (Li^+, K^+, Na^+, and Cs^+). Alumino-silicates have a crystal structure with long tunnels, so that alkali ions may flow freely within (even though the material is not a conductor of electrons). The work function to remove these alkali metals (as singly charged ions) from the alumino-silicate is small, so the temperature of the hot-plate need only be raised to ~ 0.1 eV $= 1{,}000°$C (in contrast to plasma sources in which $k_B T_i \sim 1$ eV) to produce significant quantities of singly charged ions. The low ~~temperatures~~ gives rise to a lower intrinsic emittance. Alumino-silicates are thermionic emitters, with the emission satisfying the Richardson-Dushman equation [17], which states that the current-density is proportional to $T_i^2 \exp(-q\phi_w/k_B T_i)$, where ϕ_w is the effective work function of the material. Thermionic emitters are chosen to have low ϕ_w.

In addition to thermionic emitters (such as alumino-silicates), so-called "contact ionization" sources are also employed as hot-plate sources. These are typically refractory metals, such as tungsten or porous tungsten, that are doped with a surface layer of an alkali carbonate. These emitters have high work functions that exceed the ionization potential of the metallic atoms in the alkali carbonates so when the alkali metal is thermally desorbed there is a high probability it will be desorbed as an ion. If the alkalis are not continuously replenished by feeding material onto either the front or rear surface of the tungsten, the doped tungsten sources will tend to deplete and have smaller lifetimes than the alumino-silicate sources. This follows because the amount of alkali metal that can be "doped" onto a surface layer (a fraction of a mono-layer thick) is less than can be contained in the volume of the alumino silicates. Contact ionization sources also tend to have larger ratio of emitted neutrals to emitted ions than do alumino-silicate sources, which accounts for most of the depletion at typical source temperatures.

Because both alumino-silicate and contact ionization sources operate at a hot-plate temperature of about $k_B T_i \sim 0.1$ eV, they produce sources which are relatively charge state pure due to the large values of the second ionization potential of the alkali metals. Due to modest ion depletion rates, pulse durations can generally be as long as the driving circuit can maintain voltage.

Gas discharge plasma sources: Most high current-density gas-discharge ion sources rely on extraction from a stationary, high-density and high-temperature plasma, which is produced from a neutral gas by electron impact ionization. To produce the ions, energetic electrons in the discharge plasma must liberate bound electrons. The ionization processes depend on the collision rate. Consequently, the electron density and temperature should be sufficiently high for efficient ionization. Recent experiments on these sources have demonstrated current-densities more than 100 mA/cm^2 [5]. However, as later discussed in the Section on multi-beamlet sources, this extraction scheme suffers from the current-density and emittance trade

UNCORRECTED PROOF

off. Charge exchange of the ions with the background gas in the extraction gap is also an issue.

The usual process to make high charge-state ions is to liberate successive bound electrons by by the electron impact ionization. The process can be characterized by the parameter $J_e\tau_i = en_e v_e \tau_i$, where J_e is the electron current-density and τ_i is the ion confinement time. The important parameters for the discharge plasma ion source are the electron temperature $k_B T_e$, electron density n_e, electron current-density J_e, and the ion confinement time τ_i. A large flux of high-energy electrons is needed to produce a dense plasma of highly-stripped ions.

Vacuum arc sources: Metallic plasmas produced with vacuum arc discharges are also candidates for high current-density ion beams [11, 18]. Highly ionized ions formed from a vaporized metal arc plasma are utilized as an ion source. The available current-density and stability depend on the behavior of the arc and the electrode configuration. Typically, only ions of one charge state are desired for acceleration. Because the vacuum arc plasma is intrinsically transient, control of the surface fluctuations and the ionization degree are critical issues. In order to suppress the fluctuation, a number of types of grid controlled ion sources have been developed [4].

ECR sources: Electron Cyclotron Resonance (ECR) sources are plasma sources which are in widespread use for the production of high charge-state ions [19]. The source plasma is produced without cathodes using RF driven ECR heating of an initially neutral gas. They are reliable and stable because they do not have any consumable components except the beam source. High charge-state ions are produced by the impact of energetic electrons with neutrals and ions within a "minimum-B" magnetic field configuration used to both stably confine the plasma and allow for cyclotron instability. To increase the rate of ionization, the electron temperature ($k_B T_e$) is typically driven from 1 to 10 keV. On the other hand, the ion temperature ($k_B T_i$) should be held as low as possible because higher ion temperature produces an extracted beam with higher intrinsic emittance (see Sect. 9.1.1). In ECR sources, due to selective heating of electrons, ions in the source plasma can be low temperature. Because the plasma frequency is a function of the cut-off plasma density, microwave sources with higher frequencies are needed to reach higher plasma density in ECR ion sources. Recently, techniques have been developed that allow use of solid materials as the beam source, which extend the performance to a wide range of heavy ions. However, the available current-~~density~~ of massive ions from solid materials in ECR sources is order of $\sim 100\,\mu$A [20].

EBIS sources: Electron Beam Ion Sources (EBIS) can produce extremely high charge-state ions. The EBIS device uses a nearly monoenergetic electron beam to bombard a neutral gas and produce highly-charged ions by electron impact ionization [21]. The electron beam only passes through the gas usually one time in a high vacuum. An electrostatic ion trap then stores ions produced with the desired charge state which can then be injected in an accelerator.

EBISs have provided the highest charge-state ions of all types of ion sources. Even fully stripped bare uranium nuclei are expected to be possible. However, only pulses with $\sim 10^{11}$ particles are possible with present trap technology. The relatively

UNCORRECTED PROOF

low intensity of ions and difficult engineering requirements in the EBIS device are disadvantages for high current-density ion sources. However, a highly efficient EBIS using axially oscillating electrons is promising to enhance the number of extractable charges [14, 22, 23].

Laser sources: Laser irradiation of materials can produce dense plasmas from which ions can be extracted and formed into a beam. Such laser produced plasma sources provide a possible solution for high current-density and/or high charge-state ion extraction as well as high power applications. The target material is ablated as a dense drifting plasma that allows ion extraction exceeding conventional current-density limits. Properties of the ablation plasma are a strong function of the laser power density as well as the target geometry and material properties. Simplicity of operation, small size, and the capability to produce a wide variety of ion species with low emittance are advantages of laser ion sources. However, laser ion sources are in a developmental phase and further research is required for practical, economical source technology with high charge state purity and low characteristic spreads in energy and angular diversion. A laser ion source which overcomes that Bohm limit by direct ion injection has been proposed [24, 25] and research is progressing on sources employing ultra-high intensity, short-pulse lasers to irradiate thin foils [26, 27].

Negative ion sources: Negative ions are important for high flux neutral beam injectors in magnetic fusion devices [28] and have possible induction accelerator applications. Recent studies indicate that negative ions would be a possible source for high current ion accelerators, including drivers for Heavy Ion Fusion (HIF) [29]. The use of negative ions in beam transport can mitigate electron-cloud effects of concern for positive ions in high perveance sections. The vacuum requirements for accelerating and transporting high energy negative ions are estimated to be essentially the same as for positive ions. The halogens with their large electron affinities appear to be the most attractive candidates for high current negative ion sources. If desired, the beams could be photodetached to neutrals. An experiment conducted at LBNL using chlorine in an RF-driven source obtained a negative chlorine current-density of 45 mA/cm^2 under the same plasma conditions that gave a 57 mA/cm^2 positive chlorine current [29].

9.1.3 Example Injectors

Several example ion injectors are briefly reviewed to illustrate both typical working systems and design approaches made to achieve high currents.

Simple hot-plate diode: An example of a hot-plate diode is shown in Fig. 9.4. The Pierce electrode, source, exit electrode, and insulating support structure are shown in the figure. The flat, alumino-silicate source is 2.54 cm diameter and a 300 keV, 26 mA (apertured), long-pulse K^+ beam is extracted. The source is heated to ~0.1 eV and the $a = 10$ mm radius (apertured) extracted beam has measured emittance $\varepsilon_x = 14.2$ mm-mrad, which is a factor of 1.7 times higher than calculated

UNCORRECTED PROOF

This figure will be printed in b/w

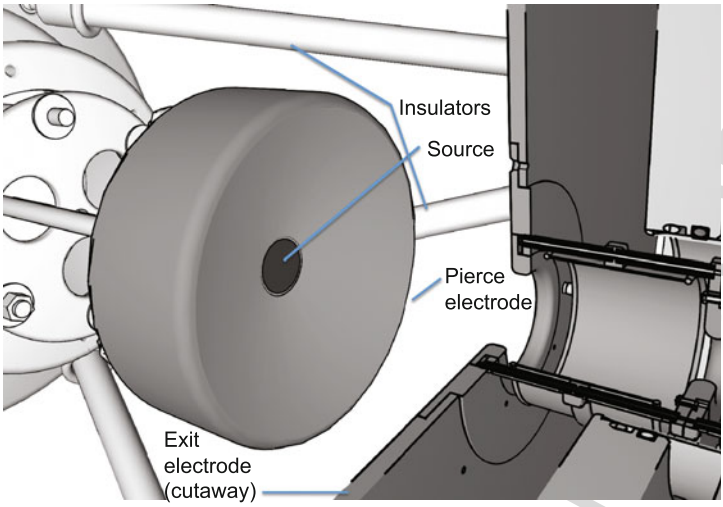

Fig. 9.4 A mechanical drawing of a hot-plate diode used on the NDCX-1 experiment at LBNL. One quarter of the exit electrode is cut away for viewing the source geometry (drawing courtesy M. Leitner, LBNL, 2010)

using Eq. (9.10) with $T_i = 0.1$ eV. Such emittance growth factors above simple ideal estimates are typical for hot-plate sources and are thought to result from nonlinear fields produced from both space-charge effects and the diode geometry.

Multi-beamlet sources: A possibility of overcoming the current-density limit with low beam emittance is to use multiple sources. Multiple-beam systems are well developed for neutral particle injectors and ion propulsion devices [30]. As can be seen from Eq. (9.9), the normalized emittance ε_{nx} is proportional to $T_i^{1/2}$. The beam brightness B is proportional to $I/\varepsilon_{nx}^2 \sim J_z/T_i$. But from the Child-Langmuir Law (Eq. 9.14) $J_z \sim V^{3/2}/d^2$; combined with the voltage breakdown law ($V \sim d^{1.0 \text{ to } 0.5}$), implies that the current-density scales as $J_z \sim V^{-1/2 \text{ to } -5/2} \sim d^{-1/2 \text{ to } -5/4}$ (cf. Eq. 9.7). Thus, small sources give high current-density, and so high beam brightness. The total beam current I, on the other hand is proportional to $\pi a^2 J_z$, and since maintaining good beam optics requires keeping $d/a >$ a constant (~ 4), $I \sim J_z d^2 \sim V^{3/2}$. So large current scales with large voltage and large sources. Applications that require both high brightness and high current are faced with a compromise. One way around the contradictory limitations, is by employing a multiple "beamlet" design where each small beamlet has high brightness, and then combining many beamlets into a single high current beam.

In low-energy, space-charge-dominated sections, high current-density miniature beamlets are contained in pre-accelerator grids. After the pre-acceleration, the beamlets are merged together to form a single beam composed of multiple beamlets. Independent control of individual beamlets allows steering for beam merging and focusing adjustments for envelope matching to be fulfilled simultaneously alleviating the need for usual matching sections between the source and transport lattice.

UNCORRECTED PROOF

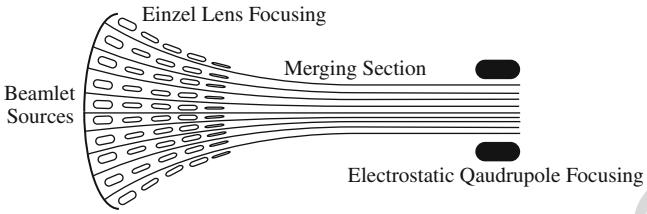

Fig. 9.5 Ion injector with multiple ion source beamlets

A multi-beamlet injector has been developed where 119, 2.2 mm diameter miniature Ar^+ beamlets with ~100 mA/cm^2 current-density are merged to single 70 mA, 400 keV beam with emittance $\varepsilon_x = 250$ mm-mrad [5, 31, 32]. A schematic of this injector is shown in Fig. 9.5. Simulations and experiment show that emittance growth is dominated by nonlinear space-charge effects in the merging process rather than the initial ion temperature, but that final emittance can be modest [33, 32].

Direct ion extraction from drifting plasma: One potential path towards increasing the ion current-density without increased emittance is to use a drifting plasma as an ion source. In case of plasma injection, the extractable current from a moving plasma is

$$J_i = q n_i v_d, \tag{9.19}$$

where v_d s the drift velocity of the source plasma [34]. The source plasma can be an electro-magnetically accelerated plasma or a laser ablation plasma. Based on this concept, ~~a~~ drifting and point-expanding plasma sources have been proposed for high current ion injectors [35].

However, in case of direct ion extraction from a drifting plasma, shape and position of the ion emitting surface is difficult to control. Behavior of the emitting surface is determined by the balance between the current produced by the plasma and the ability to extract ions in the effective acceleration gap. Figure 9.6 shows an illustration of the behavior of the space-charge potential of the direct injection gap. Although the dynamics driven by highly transient source plasma is still under investigation, it has been demonstrated that a high current-density, charge selected, and low emittance ion beam is possible to extract from a laser ablated expanding plasma [36, 37]. Experimental results show that the matching problem in which the plasma meniscus change is overcome when the operating condition is controlled to supply ions close to the space-charge limited current of the effective gap. At this matching condition, the plasma flux equals the effective space-charge limited value, and the emission surface becomes stationary. Using this configuration, a copper beam with $J_z = 100$ mA/cm^2 was produced with emittance $\varepsilon = 0.25$ mm-mrad, and flattop pulse duration 500 ns [24].

UNCORRECTED PROOF

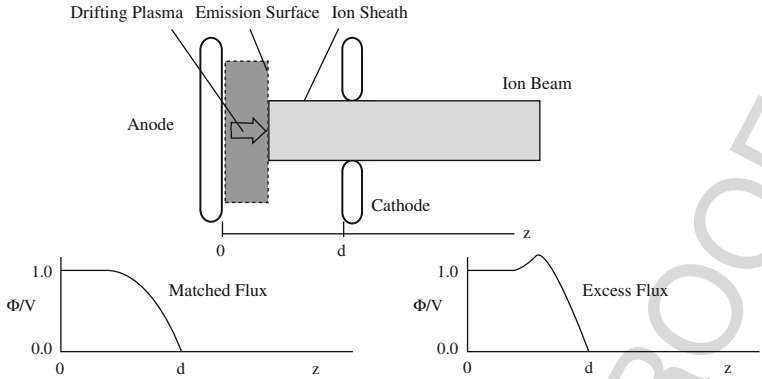

Fig. 9.6 Schematic of high current-density ion extraction from a drifting plasma

9.2 Longitudinal Beam Dynamics

One of the most significant differences between the physics of RF-accelerators and induction accelerators is the longitudinal dynamics resulting from the two different pulse formats. RF-accelerators generally form "micropulses" resulting from electric fields harmonically varying in time with frequency in the 100 MHz to several GHz range (corresponding to micropulses spanning ~0.1 wavelength, of order 0.1–1.0 ns). Macro pulses are formed by strings of micropulses. Induction accelerators have no micro-pulses; instead macro-pulses in the ~20 ns to ~10 μs range are formed, which typically do not vary in current or energy during the "flattop" part of the pulse, and have ends which are confined by the application of electrical fields (sometimes called "ear" fields) which provide extra acceleration at the trailing end ("tail") of the pulse and some deceleration (relative to the flattop) at the leading end ("head") of the pulse. Since the beam length is typically large relative to the radius, analysis is often carried out using a "g-factor" approximation to the longitudinal electric field, to be discussed below.

The most complete solution to the coupled particle and field equations for the ions in a beam is obtained through numerical simulation. It is noted that 3D particle-in-cell methods, as well as direct Vlasov equation integrators have been used to describe both the longitudinal and transverse beam behavior most accurately. However, their details are not discussed here, because they are beyond the scope of the book.

9.2.1 Fluid Equation Approach

It is useful (for both a basic understanding of the beam physics and for accelerator design) to characterize the parallel beam dynamics using a reduced set of equations from the full Vlasov-Maxwell set. When the Vlasov equation is averaged over the

UNCORRECTED PROOF

transverse coordinates and over the longitudinal velocity, a set of longitudinal fluid equations may be obtained. Since ion beam dynamics in induction accelerators is typically non-relativistic, for simplicity we use a non-relativistic formulation:

$$\frac{\partial \lambda}{\partial t} + \frac{\partial \lambda v}{\partial z} = 0 \tag{9.20}$$

$$\frac{\partial v}{\partial t} + v\frac{\partial v}{\partial z} = \frac{q}{m}E_z \tag{9.21}$$

Here, z is the longitudinal coordinate, t is time, $\lambda \equiv \int \rho \mathrm{d}x\mathrm{d}y$ is the line charge density, ρ is the charge density, v is the average longitudinal fluid velocity, and E_z is the longitudinal electric field (the sum of the space charge and externally applied field) averaged over the transverse coordinates. In Eq. (9.21), an additional term ($= -\frac{q\pi a^2}{m\lambda}\frac{\partial p}{\partial z}$ where p is the one dimensional pressure averaged over the beam radius a) has been dropped, because it is generally much smaller than the space charge term. To close the equations, a relationship between the electric field arising from space charge and the distribution of charge must be found.

9.2.2 "g-Factor" Descriptions of E_z

For an axisymmetric beam and infinite in longitudinal extent, Poisson's equation can be solved elementarily:

$$E_r = \frac{\lambda(r)}{2\pi\epsilon_0 r} \tag{9.22}$$

Here r is the radial coordinate, and $\lambda(r)$ denotes the line charge within radius r [and λ without an argument denotes $\lambda(r \to \infty)$]. When variations in r are much more rapid than variations in z then

$$\frac{\partial^2 \phi}{\partial z^2} \ll \frac{1}{r}\left(\frac{\partial}{\partial r} r \frac{\partial \phi}{\partial r}\right) \tag{9.23}$$

and we may calculate the beam potential by integrating radially from the pipe radius (where $\phi = 0$) to the radius r. If the charge density ($\rho = \rho_0$) is constant within the beam ($r < a$) and $\rho = 0$ outside of the beam ($r > a$) then the potential can be written:

$$\phi = \int \frac{\partial \phi}{\partial r}\mathrm{d}r = \begin{cases} \frac{\lambda}{2\pi\epsilon_0}\left[\frac{1}{2}\left(1 - \frac{r^2}{a^2}\right) + \ln\frac{b}{a}\right] & 0 < r < a \\ \frac{\lambda}{2\pi\epsilon_0}\ln\frac{b}{r} & a < r < b \end{cases} \tag{9.24}$$

Now, $E_z = -\partial\phi/\partial z$ may be calculated:

$$\frac{\partial \phi}{\partial z} = \frac{1}{2\pi\epsilon_0}\left[\frac{1}{2}\left(1 - \frac{r^2}{a^2}\right) + \ln\frac{b}{a}\right]\frac{\partial \lambda}{\partial z} - \frac{1}{2\pi\epsilon_0}\left[1 - \frac{r^2}{a^2}\right]\left(\frac{\lambda}{a}\right)\frac{\partial a}{\partial z}. \tag{9.25}$$

UNCORRECTED PROOF

If $\rho = \text{const}$, then $\lambda/a^2 = \text{const}$, and

$$\frac{\partial \lambda}{\partial z} = \frac{2\lambda}{a}\frac{\partial a}{\partial z}, \tag{9.26}$$

so that

$$\frac{\partial \phi}{\partial z} = \frac{1}{2\pi\epsilon_0}\left(\ln\frac{b}{a}\right)\frac{\partial \lambda}{\partial z}. \tag{9.27}$$

Thus,

$$E_z = \frac{-g}{4\pi\epsilon_0}\frac{\partial \lambda}{\partial z}, \tag{9.28}$$

where $g \equiv 2\ln(b/a)$. The assumption of $\rho = \text{const}$ is most closely satisfied for space-charge dominated beams. When the beam is emittance dominated, the beam radius is not determined by λ so $\partial a/\partial z \simeq 0$. In that case,

$$\left\langle \frac{\partial \phi}{\partial z} \right\rangle = \frac{1}{2\pi\epsilon_0}\left[\frac{1}{2}\left(1 - \left\langle \frac{r^2}{a^2}\right\rangle\right) + \ln\frac{b}{a}\right]\frac{\partial \lambda}{\partial z}. \tag{9.29}$$

Here, the $\langle \ldots \rangle$ denotes an average taken over the radial coordinate. For a circular beam that has uniform density with respect to radius, $\langle r^2/a^2 \rangle = 1/2$, so that for emittance dominated beams, $g = 2\ln(b/a) + 1/2$. For beams that are intermediate between space charge dominated or emittance dominated, or are not uniform over radius, numerical evaluation may be required to accurately calculate g.

Combining Eqs. (9.21) and (9.28) yields:

$$\frac{\partial v}{\partial t} + v\frac{\partial v}{\partial z} = \frac{-qg}{2\pi m\epsilon_0}\frac{\partial \lambda}{\partial z} \tag{9.30}$$

The fluid equations (9.20) and (9.30) may now be solved, since the electric fields are treated as a local function of the line charge density, and the equations form a closed set.

9.2.3 Rarefaction Waves

One application of the fluid equations derived in Sects. 9.2.1 and 9.2.2 is the analysis of the longitudinal beam evolution of an initially uniform beam at the head or tail of the beam, as the space charge self-field acts to cause the beam to expand. As a mathematical simplification [38, 39] we assume that the line charge density initially makes a step in z from its constant value λ_0 to zero at the position of the the beam

UNCORRECTED PROOF

end, which we place at $z = 0$. (Here we take z to be measured in the beam frame.) Expanding Eqs. (9.20) and (9.30) yields:

$$\frac{\partial \lambda}{\partial t} + v\frac{\partial \lambda}{\partial z} + \lambda\frac{\partial v}{\partial z} = 0 \tag{9.31}$$

$$\frac{\partial v}{\partial t} + v\frac{\partial v}{\partial z} + \frac{qg}{2\pi m\epsilon_0}\frac{\partial \lambda}{\partial z} = 0 \tag{9.32}$$

It is convenient to define $\Lambda \equiv \lambda/\lambda_0$, $V \equiv v/c_s$ and $\zeta \equiv v_0 z/c_s$ and $s \equiv v_0 t$ where $c_s^2 \equiv qg\lambda_0/4\pi\epsilon_0 m$, and v_0 is the beam velocity. Then Eqs. (9.31) and (9.32) become:

$$\frac{\partial \Lambda}{\partial s} + V\frac{\partial \Lambda}{\partial \zeta} + \Lambda\frac{\partial V}{\partial \zeta} = 0 \tag{9.33}$$

$$\frac{\partial V}{\partial s} + V\frac{\partial V}{\partial \zeta} + \frac{\partial \Lambda}{\partial \zeta} = 0 \tag{9.34}$$

We may try a similarity solution in the variable $x \equiv \zeta/s = v_0 z/(c_s s) = z/(c_s t)$. Since $\partial x/\partial s = -x/s$, and $\partial x/\partial \zeta = x/\zeta$, so that $\partial \Lambda/\partial s = (x/s)d\Lambda/dx$, etc., then Eqs. (9.33) and (9.34) can be expressed as a matrix equation:

$$\begin{bmatrix} V - x & \Lambda \\ 1 & V - x \end{bmatrix} \begin{bmatrix} \frac{\partial \Lambda}{\partial x} \\ \frac{\partial V}{\partial x} \end{bmatrix} = 0. \tag{9.35}$$

The substitution of the similarity variable x was successful in changing the fluid equations (which are partial differential equations in two independent variables) into a set of ordinary differential equations (with one independent variable), which is much easier to solve. For a nontrivial solution to exist, the determinant of the matrix in Eq. (9.35) must vanish. This implies that

$$\Lambda = (V - x)^2. \tag{9.36}$$

Taking the derivative of Eq. (9.36), and combining with the lower equation in Eq. (9.35) yields the simple equation: $\mathrm{d}V/\mathrm{d}x = 2/3$. The general solution to (9.35) is then:

$$V = \frac{2}{3}x + C \tag{9.37}$$

$$\Lambda = \left(-\frac{1}{3}x + C\right)^2 \tag{9.38}$$

To evaluate the integration constant C, we make use of the boundary and initial conditions. If the initial beam is such that $\Lambda = 1$ for $z < 0$ and $\Lambda = 0$ for $z > 0$, it is apparent that for $t > 0$, the solution extends from position x_- to position x_+, where $x_- < 0$ and $x_+ > 0$. Since $\Lambda = 1$ at $x = x_-$, the solution requires $x_- = 3C - 3$.

UNCORRECTED PROOF

Similarly, $\Lambda = 0$ at $x = x_+$, requires $x_+ = 3C - 3$. To establish the constant C, we note that mass at positive z, originated at $z < 0$, so that mass conservation requires $-x_- = \int_{x_-}^{x_+} \Lambda(x)\mathrm{d}x$. From this constraint, simple algebra shows that $C = 2/3$, implying $x_- = -1$ and $x_+ = 2$. So the complete solution is:

$$\Lambda = \begin{cases} 1 & x < -1 \\ (-\frac{x}{3} + \frac{2}{3})^2 & -1 < x < 2 \\ 0 & x > 2 \end{cases} \tag{9.39}$$

$$V = \begin{cases} 0 & x < -1 \\ \frac{2}{3}(x+1) & -1 < x < 2 \\ 0 & x > 2 \end{cases} \tag{9.40}$$

The solution is plotted in Fig. 9.7. One qualitative feature of the solution is the space charge driven expansion of the tip of the beam away from the beam interior at twice the space charge wave speed ($x = 2$), and a rarefaction wave propagating towards the beam interior at a speed equal to the space charge wave speed ($x = -1$).

This figure will be printed in b/w

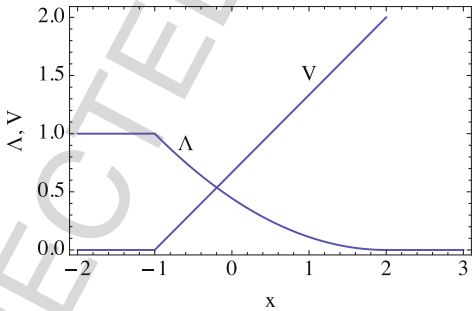

Fig. 9.7 Normalized line charge density Λ and velocity V in a self-similar space charge rarefaction wave, plotted against normalized position $x \equiv z/(c_s t)$

9.2.4 "Ear Fields"

As we have seen in Sect. 9.2.3, longitudinal space charge acts to increase the beam length. In order, to counteract the space charge, induction accelerators can employ externally imposed electric fields (so-called "ear fields," so named because the voltage profile resembles the floppy ears of a dog with one ear up and one ear down). These electric fields are also known as "barrier buckets."

For a beam with a line charge that is a constant over a length ℓ_{flat} but that falls off parabolically in the ends (each of length ℓ_{end}), the line charge can be written:

$$\lambda = \lambda_0 \begin{cases} 1 & |z| < \ell_{\text{flat}}/2 \\ 1 - (|z| - \ell_{\text{flat}}/2)^2/\ell_{\text{end}}^2 & \ell_{\text{flat}}/2 < |z| < \ell_{\text{flat}}/2 + \ell_{\text{end}} \\ 0 & \ell_{\text{flat}}/2 + \ell_{\text{end}} < |z| \end{cases} \tag{9.41}$$

UNCORRECTED PROOF

Here z is the longitudinal coordinate measured in the beam frame, with beam center at $z = 0$. Use of Eqs. (9.41) and (9.28) results in an ear field equal to:

$$E_z = \frac{\text{sign}[z] g \lambda_0}{\pi \epsilon_0} \begin{cases} 0 & |z| < \ell_{\text{flat}}/2 \\ (|z| - \ell_{\text{flat}}/2)/\ell_{\text{end}}^2 & \ell_{\text{flat}}/2 < |z| < \ell_{\text{flat}}/2 + \ell_{\text{end}} \\ 0 & \ell_{\text{flat}}/2 + \ell_{\text{end}} < |z| \end{cases} \tag{9.42}$$

The maximum ear field for the line charge density (see Eq. 9.41) occurs at $|z| = \ell_{\text{flat}}/2 + \ell_{\text{end}}$ (i.e. the very tip of the beam) where it has value E_z (max) $= g\lambda_0/(\pi\epsilon_0\ell_{\text{end}})$. Other models for the line charge density distribution, of course, will yield different results, but the value above is useful for order of magnitude estimates. As an example, for $\lambda_0 = 0.25\,\mu$C/m, $\ell_{\text{end}} = 0.3$ m, and $g = 1$, an electric field of 30 kV/m must be supplied to by the average accelerating gradient of the induction modules to keep the beam ends confined.

9.2.5 Longitudinal Waves

Just as pressure variations in a gas result in sound waves, line charge density fluctuations in a beam result in space charge waves. We may calculate some of the properties of space charge waves using the longitudinal fluid equations (9.20) and (9.21). For ease of calculation, we work in the beam frame, and we consider a long beam (ignoring the effects of the ends of the beam). We consider an equilibrium with uniform line charge density λ_0 and because we are working in the beam frame, zero equilibrium velocity ($v_0 = 0$). If we let $\lambda = \lambda_0 + \lambda_1$ and $v = v_0 + v_1$ and substitute into Eqs. (9.20) and (9.21), and linearize, we find:

$$\frac{\partial \lambda_1}{\partial t} + \lambda_0 \frac{\partial v_1}{\partial z} = 0 \tag{9.43}$$

$$\frac{\partial v_1}{\partial t} + \frac{c_s^2}{\lambda_0} \frac{\partial \lambda_1}{\partial z} = 0 \tag{9.44}$$

Here $c_s^2 \equiv q g \lambda_0/(4\pi\epsilon_0 m)$. Combining Eqs. (9.43) and (9.44) results in the familiar wave equation,

$$\frac{\partial^2 \lambda_1}{\partial t^2} - c_s^2 \frac{\partial^2 \lambda_1}{\partial z^2} = 0 \tag{9.45}$$

This has the well known general solution

$$\begin{aligned} \lambda_1 &= \lambda_0 \left(f_+[u_+] + f_-]u_-] \right), \\ v_1 &= c_s \left(-f_+[u_+] + f_-[u_-] \right). \end{aligned} \tag{9.46}$$

UNCORRECTED PROOF

Here, $u_\pm = z \pm c_s t + C_0$, where C_0 is an arbitrary constant, and f_+ and f_- are arbitrary functions. From the solution, one can show that a pure density perturbation at $t = 0$ will decompose into a forward and backward going wave at later times. A sub class of solutions to Eq. (9.45) are harmonic solutions of the form $\lambda_1 = \tilde{\lambda_1} \exp[i\omega' t \pm ik'z]$. Here primes are a reminder that quantities are being calculated in the beam frame. Substitution into Eq. (9.45) yields the dispersion relation:

$$\omega' = \pm c_s k' \tag{9.47}$$

Thus the phase and group velocity of waves of all frequencies in the beam frame is c_s, the "space-charge wave" speed, which is consistent with the more general solution (9.46).

9.2.6 Longitudinal Instability

In the previous section, the equations assumed that image charge and currents did not change the longitudinal dynamics. However, image currents are impeded by the induction gaps, giving a high effective impedance. Further resistance in the pipe wall adds to the impedance although ~~is~~ usually gives a much smaller contribution to the impedance. Further, the gaps can act like capacitors which also changes the dynamics of the image current. We may model the physics of these interactions in the simplest case by placing a resistor and capacitor in parallel with a current source (equal to the image current). (See Fig. 9.8.) We may assume that a voltage ΔV is induced by the resistive and capacitive effects per induction module, each separated by a distance L. The image current is a current source, and must satisfy

$$I = C\frac{\mathrm{d}\Delta V}{\mathrm{d}t} + \frac{\Delta V}{R} \tag{9.48}$$

The average electric field $E = -\Delta V L$. Define $C^\dagger = CL$ and $R^* \equiv R/L$. Let $I = I_0 + I_1 \exp[-i\omega t]$ and $E = E_0 + E_1 \exp[-i\omega t]$ then linearizing Eq. (9.48) yields:

$$Z^* \equiv \frac{-E_1}{I_1} = \frac{R^*}{1 - i\omega C^\dagger R^*} \tag{9.49}$$

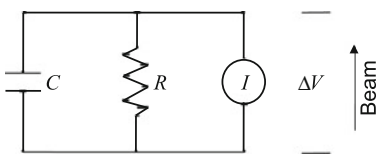

Fig. 9.8 Circuit representation of one module of many, each separated by a distance L

UNCORRECTED PROOF

Now let's return to the 1D fluid equations. Let $\lambda = \lambda_0 + \lambda_1 \exp[-i(\omega t - kz)]$ and $v = v_0 + v_1 \exp[-i(\omega t - kz)]$ then linearizing Eqs. (9.20) and (9.21) *in the lab frame (in which $v_0 \neq 0$)* and using the generalized impedance $Z^*(\omega) \equiv -\frac{E_1}{I_1}$ and $I_1 = \lambda_0 v_1 + v_0 \lambda_1$ yields,

$$\begin{bmatrix} \omega - kv_0 & -k\lambda_0 \\ \frac{-c_s^2 k}{\lambda_0} + \frac{iqZ^*(\omega)v_0}{m} & \omega - kv_0 + \frac{iqZ^*(\omega)\lambda_0}{m} \end{bmatrix} \begin{bmatrix} \lambda_1 \\ v_1 \end{bmatrix} = 0 \tag{9.50}$$

The determinant of Eq. (9.50) must vanish for non-trivial solutions, which yields the dispersion relation:

$$(\omega - kv_0)^2 - c_s^2 k^2 + \frac{iqZ^*(\omega)\lambda_0 \omega}{m} = 0 \tag{9.51}$$

We may use a Galilean transformation to calculate the wave vector and frequency in the comoving beam frame ($\omega' = \omega - kv_0$ and $k' = k$, where prime indicates comoving frame variables). In terms of beam frame variables the dispersion relation, Eq. (9.51) can be expressed as:

$$\omega'^2 - c_s^2 k'^2 + \frac{iqZ^*(\omega', k')}{m}\lambda_0(\omega' + k'v_0) = 0 \tag{9.52}$$

Here, $Z^*(\omega', k') \equiv Z^*(\omega = \omega' + k'v_0)$.

Let us now first examine the dispersion relation Eq. (9.52) when only resistance is present. Rearranging Eq. (9.52) gives,

$$\omega' = \pm c_s k' \sqrt{1 - \frac{iqR^*\lambda_0}{mc_s^2 k'^2}(\omega' + k'v_0)}. \tag{9.53}$$

Using the definition of c_s and assuming that the effects of the resistive term are small ($\omega'/k' \simeq c_s$), and that the space charge wave speed is much less than the ion beam velocity ($c_s \ll v_0$) yields

$$\begin{aligned} \omega' &= \pm c_s k' \sqrt{1 - \frac{i4\pi\epsilon_0 R^*}{g}\frac{v_0}{k'}} \\ &= \pm c_s k' \left(1 + \left(\frac{2\Gamma_R}{c_s k'}\right)^2\right)^{1/4} \times \left(\cos\left[\frac{1}{2}\tan^{-1}\left(\frac{2\Gamma_R}{c_s k'}\right)\right]\right. \\ &\quad \left. -i\sin\left[\frac{1}{2}\tan^{-1}\left(\frac{2\Gamma_R}{c_s k'}\right)\right]\right) \end{aligned} \tag{9.54}$$

$$\omega' \simeq \pm c_s k' \mp i\Gamma_R \qquad \text{for } 2\Gamma_R/(c_s k') << 1 \tag{9.55}$$

UNCORRECTED PROOF

Here, $\Gamma_R \equiv 4\pi\epsilon_0 c_s v_0 R^*/(2g)$. Since the linearized quantities (such as λ_1 and E_1) were assumed to vary as $\exp[i(k'z - \omega' t)]$ choosing the upper sign in the dispersion relation Eq. (9.55), implies that $\omega' = c_s k'$ so that a line of constant phase $z = c_s t$, is forward propagating in the beam frame, and we find that the imaginary part of ω' is less than zero, which yields a decaying perturbation: $\lambda_1 \propto \exp[-\Gamma_R t]$. Similarly, choosing the lower sign in the dispersion relation (9.54) yields a backward propagating, growing wave. We define a logarithmic gain factor G by

$$G \equiv \Gamma_R t = \frac{4\pi\epsilon_0 c_s v_0 R^* t}{2g} \tag{9.56}$$

G is essentially the number of e-folds a backward propagating perturbation will grow in time t. The gain of a perturbation will be limited by the finite time in the accelerator (t_{res}) or the finite propagation time from head to tail (ℓ_b/c_s), where ℓ_b is the bunch length. If the former condition holds, G is proportional to $c_s \propto \lambda_0^{1/2}$ and so G is intensity dependent. However, if the latter condition holds $G \simeq 4\pi\epsilon_0 v_0^2 R^* \Delta t/(2g)$ where Δt is the pulse duration. Note that in this case G is independent of the current.

9.2.7 Effects of Capacitance on Longitudinal Instability

As discussed above, a more general lumped circuit model that describes the module impedance includes a capacitor in parallel with a resistor. The capacitance includes the "parallel plate" capacitance of the induction gap, and could include externally added capacitance to mitigate longitudinal instability. When Eq. (9.49) is inserted into Eq. (9.51) the lab frame dispersion relation becomes:

$$(\omega - kv_0)^2 - c_s^2 k^2 + \frac{iqZ^*(\omega)\lambda_0\omega}{m} = 0 \tag{9.57}$$

When capacitance is included in the lumped circuit the full Eq. (9.49) is needed. Separating the real and imaginary components of Eq. (9.49) yields:

$$Z^*(\omega) = \frac{R^*}{1 - i\omega C^\dagger R^*} = \frac{R^* + i\omega C^\dagger R^{*2}}{1 + \omega^2 C^{\dagger 2} R^{*2}} \tag{9.58}$$

Inserting Eq. (9.58) into Eq. (9.51) yields:

$$(\omega - kv_0)^2 - c_s^2 k^2 - \frac{q\omega^2 C^\dagger R^{*2}\lambda_0}{m(1 + \omega^2 C^{\dagger 2} R^{*2})} + \frac{iqR^*\lambda_0\omega}{m(1 + \omega^2 C^{\dagger 2} R^{*2})} = 0 \tag{9.59}$$

UNCORRECTED PROOF

Expressed in terms of Γ_R and the space charge wave speed c_s, the dispersion relation becomes:

$$(\omega - kv_0)^2 - c_s^2 k^2 - \frac{2\Gamma_R (c_s/v_0)\omega^2 C^\dagger R^*}{(1+\omega^2 C^{\dagger 2} R^{*2})} + \frac{2\Gamma_R (c_s/v_0)\omega}{(1+\omega^2 C^{\dagger 2} R^{*2})} = 0 \tag{9.60}$$

Equation (9.60) can be expressed in the beam frame as:

$$\omega'^2 - c_s^2 k'^2 - \frac{2\Gamma_R (c_s/v_0)(\omega' + k'v_0)^2 C^\dagger R^*}{(1+(\omega'+k'v_0)^2 C^{\dagger 2} R^{*2})} + \frac{2\Gamma_R (c_s/v_0)(\omega' + k'v_0)}{(1+(\omega'+k'v_0)^2 C^{\dagger 2} R^{*2})} = 0 \tag{9.61}$$

It is clear, that if $C^\dagger$ is large, the second and third term can be reduced, thus reducing the instability growth rate. In particular, if $2(v_0/c_s)\Gamma_R R^* C^\dagger << 1$, then the third term in Eq. (9.61) will be much less than the second, so the real part of the dispersion relation will not be significantly changed, and thus $\omega' \simeq c_s k'$. In that case, the steps leading to Eq. (9.56) can be repeated leading to:

$$\begin{aligned}
\omega' &= \pm c_s k' \sqrt{1 - i\frac{2\Gamma_R}{c_s k' \left(1 + (k' v_0 R^* C^\dagger)^2\right)}} \\
&= \pm c_s k' \left(1 + \left(\frac{2\Gamma_R}{c_s k' \left(1 + (k' v_0 R^* C^\dagger)^2\right)}\right)^2\right)^{1/4} \\
&\quad \times \left(\cos\left[\frac{1}{2}\tan^{-1}\left(\frac{2\Gamma_R}{c_s k' \left(1 + (k' v_0 R^* C^\dagger)^2\right)}\right)\right]\right. \\
&\quad \left. -i \sin\left[\frac{1}{2}\tan^{-1}\left(\frac{2\Gamma_R}{c_s k' \left(1 + (k' v_0 R^* C^\dagger)^2\right)}\right)\right]\right)
\end{aligned} \tag{9.62}$$

$$\omega' \simeq \pm c_s k' \mp i \frac{\Gamma_R}{1 + (k' v_0 R^* C^\dagger)^2} \quad \text{for} \quad \frac{2\Gamma_R}{c_s k' (1 + (k' v_0 R^* C^\dagger)^2)} << 1 \tag{9.63}$$

The growth rate now depends on k' (at large k'). For a perturbation with k' less than $2\pi/l_b$ the perturbation wavelength would be longer than the beam length l_b, and so the perturbation is not likely to grow. So if $2\pi v_0 R^* C^\dagger / l_b > 1$, the second term in the denominator of the imaginary term of Eq. (9.63) will significantly reduce the growth rate.

Consider an example, from a proposed application discussed in Chap. 10, a high current heavy ion accelerator for inertial fusion. Typical designs might have beams with ion velocities $v_0 = 10^8$ m/s, current $I = 3$ kA, bunch length $l_b = 10$ m, $g = 1.8$, $R^* = 100\,\Omega$/m, yielding a resistive growth rate $\Gamma_R = 1.5 \times 10^5$ s^{-1}. The logarithmic gain G would be $\Gamma_R l_b / c_s = 3$ if the growth time were limited by head to tail growth, or $\Gamma_R l_{\text{acc}}/v_0 = 1.5$ if the growth time were limited by the

UNCORRECTED PROOF

This figure will be printed in b/w

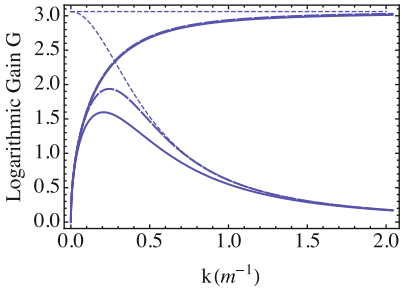

Fig. 9.9 Logarithmic Gain G of the longitudinal instability as a function of perturbation wavenumber k, for $R^* = 100\,\Omega/\text{m}$, $C^\dagger = 0$ (*upper curves*) and $C^\dagger = 2 \times 10^{-10}$ F-m (*lower curves*), after a growth time corresponding to l_b/c_s, where $l_b = 10$ m and $c_s = 4.9 \times 10^5$ m, calculated from numerical solution (*solid curves*) to Eq. (9.51), analytic solutions from Eqs. (9.54) and (9.62) (*long dashed curves*) and asymptotic expressions from Eqs. (9.55) and (9.63) (*short dashed curves*). Other parameters are given in the text

length of the accelerator l_{acc}, here assumed to be 10^3 m. If $C^\dagger = 5 \times 10^{-12}$ F-m the growth, there would be a measurable reduction in growth. Simulations [40] using above parameters with 40 times larger capacitance, show essentially no growth of a perturbation. Figure 9.9 shows the the logarithmic gain obtained from the exact numerical solution of Eq. (9.51), using the parameters above, together with the analytic solutions discussed above.

The above calculations may be repeated with finite inductance in the circuit equation. The lesson to draw is that for high current applications, beam interactions with the structure of the accelerator need to be assessed and, if necessary, addressed. This low frequency longitudinal resistive instability is only one example of beam/accelerator interactions. See Chap. 7 for an example of a high frequency transverse beam/accelerator interaction known as the beam-break-up instability (or BBU).

9.3 Transverse Dynamics Issues

As mentioned in Introduction, the physics of transverse ion dynamics in induction linacs has been not covered here. Beam dynamics in the non-relativistic and space-charge dominated regime, which characterizes ions in induction linac, has been extensively developed for RF linacs as well as induction linacs. A lot of articles are available in Journal papers [41] and related topics have been given as lectures at the established US particle accelerator schools [42]. In addition, there are crucial and practical issues to design a beam transport line and analyze the behavior of ion beam there. They are listed below.

1. Beam envelope mismatching originating from perturbations in the lattice parameters or beam loss through the beam line [42].
2. Coupling effects between transverse and longitudinal motions arising in longitudinal beam manipulations [43–45].

UNCORRECTED PROOF

3. Beam halo driven by nonlinear space-charge effects or beam core breathing [46].
4. Two stream instability caused by the coherent interaction with electron clouds emitted from the surrounding surface or created as a result of ionization of residual gas atoms [47].
5. Transverse instability (BBU) caused by wake fields in the surrounding devices [4].

~~Discussions on these subjects are rather professional and beyond the scope of this book.~~ Readers who are interested in these subjects will be advised to refer related articles shown above and should be able to get useful information from the recent proceedings of accelerator conference such as PAC, EPAC, APAC, and IPAC.

References

1. M. Reiser. *Theory and Design of Charged Particle Beams*, Wiley, New York, NY, 1994.
2. R. Miller. *An Introduction to the Physics of Intense Charged Particle Beams*, Plenum Press, New York, NY, 1982.
3. A. Chao and M. Tigner, editors. *Handbook of Accelerator Physics and Engineering*, World Scientific, New York, NY, 1999. A. Faltens, p. 475.
4. S. Humphries. *Charged Particle Beams*, Wiley, New York, NY, 1993.
5. J. Kwan. High Current Ion Sources and Injectors for Induction Linacs in Heavy Ion Fusion. *IEEE Trans. Plasma Sci.*, 33:1901, 2005.
6. E. Startsev, R. Davidson, and H. Qin. Anisotropy-Driven Collective Instability in Intense Charged Particle Beams. *Phys. Rev. Spec. Topics Accl. Beams*, 8:124201, 2005.
7. E. Startsev, R. Davidson, and H. Qin. Nonlinear δf Simulation Studies of Intense Charged Particle Beams with Large Temperature Anisotropy. *Phys. Plasmas*, 9:3138, 2002.
8. S. Lund, D. Callahan, A. Friedman, D. Grote, I. Haber, and T. Wang. Theory of an Electrostatic Instability Driven by Transverse-Longitudinal Temperature Anisotropy in Space Charge Dominated Beams. In *Proceedings of the 1998 Linear Accelerator Conference*, pages 372–376, TU2004, New York City, NY ~~?days? + ?month?~~ 1998. AQ1
9. R. Davidson. *Physics of Nonneutral Plasmas*. Addison-Wesley, Reading, MA, 1990. Re-released, World Scientific, Singapore, 2001.
10. R. Davidson. Electrostatic Shielding of a Test Charge in a Nonneutral Plasma. *J. Plasma Phys.*, 6:229, 1971.
11. I. Brown. *The Physics and Technology of Ion Sources*, Wiley, New York, NY, 1989.
12. A. Forrester. *Large Ion Beams: Fundamentals of Generation and Propagation*.—Wiley-Interscience, New York, NY, 1988.
13. ~~M. Lampel and M. Tiefenback. An Applied Voltage to Eliminate Current Transients in a One-Dimensional Diode. 1983.~~ AQ2
14. R. Becker. Electron Beam Ion Sources and Traps. *Rev. Sci. Inst.*, 71:816, 2000.
15. J. Kwan, F. Bieniosek, E. Henestroza, L. Prost, and P. Seidl. A 1.8 MeV K+ Injector for the High Current Beam Transport Experiment. *Laser Part. Beams*, 20:441, 2002.
16. F. Bieniosek, C. Celata, E. Henestroza, J. Kwan, L. Prost, P. Seidl, A. Friedman, D. Grote, S. Lund, and I. Haber. 2-MV Electrostatic Quadrupole Injector for Heavy-Ion Fusion. *Phys. Rev. Spec. Topics Accel. Beams*, 8:010101, 2005.
17. L. Smith and R. Breitwieser. ~~Riahcrdson~~ Dushman Equation Monograph. *J. Appl. Phys.*, 41: 436–437, 1970.
18. H. Rutkowski, D. Hewett, and S. Humphries, Jr. Development of Arc Ion Sources for Heavy Ion Fusion. *IEEE Trans. Plasma Sci.*, 19:782, 1991.

UNCORRECTED PROOF

19. V. Semenov, V. Skalyga, A. Smirnov, and V. Zorin. Scaling for ECR Sources of Multicharged Ions with Pumping at Frequencies from 10 to 100 GHz. *Rev. Sci. Inst.*, 73:635, 2002.
20. D. Wutte, S. Abbott, M.. Leitner, and C. Lyneis. High Intensity Metal Ion Beam Production with ECR Ion Sources at the Lawrence Berkeley Laboratory. *Rev. Sci. Inst.*, 73:521, 2002.
21. A. Kponou, E. Beebe, A. Pikin, G. Kuznetsov, M. Batazova, and M. Tinov. Simulation of 10 A Electron-Beam Formation and Collision for a High Current Electron-Beam Ion Source. *Rev. Sci. Inst.*, 69:1120, 1998.
22. R. E. Marrs. *Experimental Methods in the Physical Sciences 29A: ATOMIC, MOLECULAR, AND OPTICAL PHYSICS: CHARGED PARTICLES.* Academic Press, San Diego, CA, 1995.
23. J. Sun, N. Nakamura, M. Tona, C. Yamada, H. Watanabe, S. Ohtani, and Y. Fu. Growth of Ionization Balance from F-like to Bare Ions of Heavy Atoms in an Electron Beam Ion Trap. *Plasma Fusion Res.*, 3:052, 2008.
24. M. Nakajima, N. Kobayashi, K. Horioka, J. Hasegawa, and M. Ogawa. Direct Extraction of Ions from Expanding Laser Ablation Plasma. Technical Report Reserach Report NIFS-PROC-61, page 149, National Institute for Fusion Science, Toki, Japan, 2005.
25. M. Okamura, T. Katayama, R. Jameson, T. Takeuchi, T. Hattori, and H. Kashiwagi. Scheme for Direct Plasma Injection into an RFQ Linac. *Laser Part. Beams*, 20:451, 2002.
26. A. Henig, S. Steinke, M. Schnürer, T. Sokollik, R. Hörlein, D. Kiefer, D. Jung, J. Schreiber, B. Hegelich, X. Yan, J. Meyer ter Vehn, T. Tajima, P. Nickles, W. Sandner, and D. Habsy. Radiation-Pressure Acceleration of Ion Beams Driven by Circularly Polarized Laser Pulses. *Phys. Rev. Lett.*, 103:245003, 2009.
27. B. Hegelich, B. Albright, J. Cobble, K. Flippo, S. Letzring, M. Paffett, H. Ruhl, J. Schreiber, R. Schulze, and J. Fernández. Laser Acceleration of Quasi-Monoenergetic MeV Ion Beams. *Nature*, 439:441–444, 2006.
28. W. Cooper. Neutral Beam Injectors for the International Thermonuclear Experimental Reactor. *Phys. Fluids B*, 4:2300, 1992.
29. L. Grisham, S. Hahto, S. Hahto, J. Kwan, and K. Leung. Experimental Evaluation of a Negative-Ion Source for a Heavy-Ion Fusion Negative-Ion Driver. *Nucl. Inst. Meth. A*, 544: 216, 2005.
30. Y. Hayakawa and S. Kitamura. Ion Beamlet Divergence Characteristics of Two-Grid Multiple-Hole Ion Thruster. *J. Propulsion Power*, 15:377–382, 1999.
31. J. Kwan, F. M. Bieniose, D. P. Grote, and G.A. Westenskow. Compact Multibeamlet High-Current Injector for Heavy-Ion Fusion Drivers. *Rev. Sci. Inst.*, 77:03B503, 2006.
32. G. Westenskow, J. Kwan, D. Grote, and F. Bieniosek. High-Brightness Heavy-Ion Injector Experiments. *Nucl. Inst. Meth. A*, 577:168–172, 2007.
33. D. Grote, E. Henestroza, and J. Kwan. Design and Simulation of a Multibeamlet Injector for a High Current Accelerator. *Phys. Rev. Spec. Topics Accel. Beams*, 6:014202, 2003.
34. M. Dembinski, P. K. John, and A. G. Ponomarenko. High-Current Ion Beam from a Moving Plasma. *Appl. Phys. Lett.*, 34:553, 1979.
35. K. Horioka, J. Hasegawa, M. Nakajima, H. Iwasaki, H. Nakai, K. Hatsune, M. Ogawa, K. Takayama, J. Kishiro, M. Shiho, and S. Kawasaki. Long-Pulse Ion Induction Linac. *Nucl. Inst. Meth. A*, 415:291, 1998.
36. M. Yoshida, J. Hasegawa, J. Kwan, Y. Oguri, K. Horioka, and M. Ogawa. Grid-Controlled Extraction of Low-Charged Ions from a Laser Ion Source. *Japanese J. Appl. Phys.*, 42:5367, 2003.
37. M. Ogawa, M. Yoshida, M. Nakajima, J. Hasegawa, S. Fukuda, K. Horioka, and Y. Oguri. High-Current Laser Ion Source Based on a Low-Power Laser. *Laser Part. Beams*, 21:633, 2004.
38. L. Landau and L. Lifshitz. *Fluid Mechanics*, Pergamon Press, Elmsford, New York, NY, 1987.
39. A. Faltens, E. Lee, and S. Rosenblum. Beam End Erosion. *J. Appl. Phys.*, 61:5219, 1987.
40. D. Callahan. *Simulations of Longitudinal Beam Dynamics of Space-Charge Dominated Beams for Heavy Ion Fusion*. PhD thesis, University of California at Davis, 1994.

UNCORRECTED PROOF

41. S. Lund and B. Bukh. Stability Properties of the Transverse Envelope Equations Describing Intense Ion Beam Transport. *Phys. Rev. Spec. Topics Accel. Beams*, 7:024801, 2004.
42. J. Barnard and S. Lund. U.S. Particle Accelerator School Courses. *Beam Physics with Intense Space-Charge*, Annapolis, MD, 16–27 June 2008, Lawrence Livermore National Laboratory, LLNL-AR-407617 and Lawrence Berkeley National Laboratory, LBNL-1097E; *Beam Physics with Intense Space-Charge*, Waltham, MA, 12–23 June 2006, Lawrence Livermore National Laboratory, UCRL-TM-231628 and Lawrence Berkeley National Laboratory, LBNL-62783; *Intense Beam Physics: Space-Charge, Halo, and Related Topics*, Williamsburg, VA, 19–20 January, 2004, Lawrence Livermore National Laboratory, UCRL-TM-203655 and Lawrence Berkeley National Laboratory, LBNL-54926; *Space-Charge Effects in Beam Transport*, Boulder, CO, 4–8 June, 2001, Lawrence Berkeley National Laboratory, LBNL-49286. Course notes are also archived on the US Particle Accelerator School web site: http://uspas.fnal.gov/
43. H. Okamoto and H. Tanaka. Proposed Experiments for the Study of Beam Halo Formation. *Nucl. Inst. Meth.*, A-437:178, 1999.
44. T. Kikuchi and K. Horioka. Beam Behavior Under a Non-stationary State in High-Current Heavy Ion Beams. *Nucl. Inst. Meth.*, A-606:31, 2009.
45. L. Groening, I. Hoffmann, W. Barth, W. Bayer, G. Clemente, L. Dahl, P. Forck, P. Gerhard, M. S. Kaiser, M. Maier, S. Mickat, T. Milosic, and S. Yaramyshev. Experimental Evidence of Space Charge Driven Emittance Coupling in High Intensity Linear Accelerators. *Phys. Rev. Lett.*, 103:224801, 2009.
46. J. Wei, W. Fisher, and P. Manning, editors. *Beam Halo Dynamics, Diagnostics, and Collimation, AIP Conference Proceedings No. 693*. The American Institute of Physics, Woodbury, New York, NY, 2003.
47. A. Molvik, Experiments and Simulations of Electrons in a Linac with 4 μs Duration Ion Beam, (Electron ~~Could~~ Feedback Workshop, March 13–15, 2007), available at http://physics.indiana.edu/~shylee/ap/mwapc/epws.html

UNCORRECTED PROOF

Chapter-9

Query No.	Query
AQ1	Please provide days and month for “Lund et al. (1998),” if necessary.
AQ2	Please provide complete details for “Lampel and Tiefenback (1983)”.

UNCORRECTED PROOF

Chapter 10
Applications of Ion Induction Accelerators

John J. Barnard and Richard J. Briggs

UNCORRECTED PROOF

As discussed in Chap. 9, the physics of ion induction accelerators has many commonalities with the physics of electron induction accelerators. However, there are important differences, arising because of the different missions of ion machines relative to electron machines and also because the velocity of the ions is usually non-relativistic in these applications. The basic architectures and layout reflects these differences. In Chaps. 6, 7, and 8 a number of examples of electron accelerators and their applications were given, including machines that have already been constructed. In this chapter, we give several examples of potential uses for ion induction accelerators. Although, as of this writing, none of these applications have come to fruition, in the case of heavy ion fusion (HIF), small scale experiments have been carried out and a sizable effort has been made in laying the groundwork for such an accelerator. A second application, using ion beams for study of High Energy Density Physics (HEDP) or Warm Dense Matter (WDM) physics will soon be realized and the requirements for this machine will be discussed in detail. Also, a concept for a spallation neutron source is discussed in lesser detail.

10.1 Driver for Heavy Ion Fusion (HIF)

To understand the energy, current, and power requirements for a HIF ion induction accelerator, it is useful to start at the target. Consideration of the final focus, which ultimately determines the final spot radius and hence beam intensity, places constraints on the beam brightness, which together with the target requirements, specifies the macro requirements on the beam (such as beam energy, current, and emittance). Working upstream from the final focus, requirements on the accelerator and injector can then be set. In early studies of HIF, RF as well as induction options were considered [1] and indeed RF approaches continue to be pursued [2]. Most of the US research has been focused on induction accelerator approaches to HIF, because of the perceived ability of the induction technology to produce pulses of

J.J. Barnard (✉)
Lawrence Livermore National Laboratory, Livermore, CA, USA
e-mail: jjbarnard@llnl.gov

K. Takayama, R.J. Briggs (eds.), *Induction Accelerators*, Particle Acceleration and Detection, DOI 10.1007/978-3-642-13917-8_10,
© Springer-Verlag Berlin Heidelberg 2011

high peak power affordably. But even with a downselect to induction acceleration many beam and architecture choices remain to be made, such as the ion energy and focusing system, and the number and arrangement of beamlines and induction corelines. In this section, we give three examples of HIF driver concepts, to illustrate some of these possibilities.

10.1.1 Requirements Set by Target Physics

Beams of heavy ions are but one of several possible methods of delivering energy to an inertial confinement fusion (ICF) target (see e.g. [3]). Light ions, lasers, "z-pinches," and electrons have also been proposed. ICF targets come in two general varieties: direct drive, where the driver beam illuminates a capsule (containing the fusion fuel) directly, and from all sides, and "indirect drive" where the driver beam heats a "hohlraum," and the hohlraum produces X-rays which illuminate the capsule. In both cases, the heated outer layers of the capsule are ablated outward, driving a fuel shell inward. The inward driven shell compresses the gas fuel within the shell and the shell itself, to the point where the gas reaches the temperature required for fusion of the reactants, and at a density sufficient to stop a significant fraction of the reaction byproducts (in the case of Deuterium-Tritium fuel, alpha-particles), causing "ignition" and "burn" to occur. The implosion of the shell must be isotropic, otherwise hot material will mix with cool material preventing ignition. The use of hohlraums allows the capsule to be illuminated very uniformly, minimizing the seed for Rayleigh-Taylor instability, a possible source of anisotropic implosion. Further the ion beams need not be distributed over four π steradians. Typically, ion beams are directed at two (or a few) radiation converters, which can be located near the ends of, and at various points within, the cylindrical hohlraums. However, the use of a hohlraum is less efficient; more of the energy of a driver pulse is used in heating the hohlraum material, instead of imploding the capsule. Consequently, indirect drive requires the driver to be more efficient in converting "wall-plug" energy into beam energy. Accelerators (and particularly induction accelerators operating at high current) can be highly efficient and so that indirect direct drive is an option for HIF. Direct drive has also been suggested for HIF, and there has a recent resurgence of interest in direct drive targets for HIF because of the potential for high gain, low energy targets [4]. However, with direct drive targets in order to achieve uniform illumination the ion beams must illuminate all four π steradians. This may require a final focusing system with beams converging at large angles out of the plane of the accelerator or targets designed such that ion deposition occurs from a limited number of angles, but nevertheless produces uniform compression. If the compression is sufficiently isotropic, the efficient coupling of beam energy into fuel shell kinetic energy, can significantly reduce the total energy required by the driver [4].

As the ion mass increases at fixed ion energy, the ion range decreases, and the shorter range of heavier ions, allows one to use ions of high energy that can still be stopped within a small range R (roughly the product of mass density ρ and physical stopping distance). Short range (0.015–0.15 g/cm^2) is desired to minimize

UNCORRECTED PROOF

the amount of material that is heated by the ions. High ion energy is desirable, to minimize the amount of current transported to the target, allowing the use of conventional accelerators and assure focusability. Ultimately, though, high ion energy can translate to high cost and therefore accelerators which optimize acceleration and transport costs must be chosen. Typical parameters for recent HIF targets are: ion range 0.03 g/cm^2, main pulse energy of 0.5–7 MJ, pulse duration of about 2–8 ns, focal spot radius of $\sim$ 1.8 mm. Recent US designs include distributed radiator target [5], closely coupled targets [6], so-called "hybrid targets" [7, 8] ~~and~~ direct drive targets [4].

10.1.2 Final Focus Limits

Targets driven by heavy ion beams require the ability to focus ion beams onto small spots. Typical systems designs indicate that within the accelerator, the beam radius can be of order centimeters, whereas at the final focal spot on the target, beam radii of order millimeters are required, so radial compression factors of order ten are required. Target gain, and hence the overall cost of electricity is a sensitive function of the final spot radius on target. To get an appreciation of the factors which help determine the spot size, we present here simple models similar to what could be used in a systems code, in which algebraic relations are used to model many aspects of the driver system and to develop a self-consistent model of a heavy ion driven inertial fusion power plant. Because of the sensitivity of spot radius on target gain, careful attention needs to be paid to the part of the model that calculates the spot radius. Recent research has investigated the feasibility of using nearly complete neutralization of the beam in the target chamber in order to remove the effects of space charge (known as neutralized ballistic transport). Neutralized ballistic focusing experiments, analytic calculations, and simulations all point to the possibility of focusing highly neutralized ($>$ 99%) beams.

First we consider constraints on the beam assuming unneutralized ballistic transport to the target. When focusing the beam through a final convergent angle θ, if the beam is not neutralized, space charge is one of the elements that limits the final beam radius. Starting with the envelope equation (see e.g. [9]), we may make an estimate on how much space charge can be focused to a particular spot size.

$$a_x'' + \frac{(\gamma_b\beta_b)'}{(\gamma_b\beta_b)}a_x' + \kappa_x a_x - \frac{2Q}{a_x + a_y} - \frac{\varepsilon_x^2}{a_x^3} = 0. \tag{10.1}$$

After the beam passes through the final focusing element $\kappa_x = 0$, if the spot is circular, $a_x = a_y$, and $\beta_b' = 0$, so that Eq. (10.1) can be integrated, assuming the perveance Q and the emittance ε_x are conserved,

$$\frac{a_x'^2}{2} - Q\ln(a_x) + \frac{\varepsilon_x^2}{2a_x^2} = \frac{a_{x0}'^2}{2} - Q\ln(a_{x0}) + \frac{\varepsilon_x^2}{2a_{x0}^2} \tag{10.2}$$

UNCORRECTED PROOF

Here subscript 0 indicates evaluation just outside the final focus element. If we identify the value of a_x at the focus to be r_s, and the convergence angle θ to be $a'_{x0} \simeq a_{x0}/d$ where d is the distance between the last magnet and the final focus, we may rearrange Eq. (10.2) as:

$$\theta^2 = 2Q\ln(\theta d/r_s) + \varepsilon_x^2\left(\frac{1}{r_s^2} - \frac{1}{a_{x0}^2}\right) \tag{10.3}$$

The perveance can be expressed (non-relativistically) as $Q = \lambda/(4\pi\epsilon_0 V)$ where qV is the final ion energy, q is the ion charge, and λ is the line charge density ($\lambda = Q_c/(\beta c\Delta t_f)$), where Q_c is the charge in each beam, βc is the ion velocity and Δt_f is the pulse duration at final focus. The total charge $Q_{c\text{tot}} = N_b Q_c$, where N_b is the total number of beams. If the beams are not neutralized in final focus, Eq. (10.3) can be expressed as a lower limit on the number of beams (by neglecting the emittance term):

$$N_b > \frac{Q_{c\text{tot}}\ln(\theta d/r_s)}{2\pi\epsilon_0\theta^2 V\beta c\Delta t_f} \tag{10.4}$$

For a multi-beam linac with final energy of 4 GeV total charge $Q_{c\text{tot}}$ of 1,650 μC, and convergence angle $\theta = 0.015$ rad, $\sim$ 220 beams would be required. For the recirculator design of [10] with a total charge $Q_{c\text{tot}}$ in all beams of 400 μC, convergence angle $\theta = 0.03$ rad, and $\beta = 0.3$ (corresponding to 10 GeV), N_b could be as small as 4.

The thermal contribution to spot size places a limit on the normalized emittance ε_N. Again using (10.3) (assuming space charge has been neutralized) a requirement on the emittance may be estimated:

$$\varepsilon_N < \beta\theta r_s = 8\ \text{mm-mrad}\left(\frac{\beta}{0.2}\right)\left(\frac{\theta}{0.015}\right)\left(\frac{r_s}{2.5\ \text{mm}}\right)$$

Chromatic aberration limits for transport through quadrupole or solenoid lenses place a limit on the momentum spread,

$$\frac{\Delta p}{p} < \frac{r_s}{\alpha_c\theta d} = 3\times 10^{-3}\left(\frac{r_s}{2.5\ \text{mm}}\right)\left(\frac{0.015}{\theta}\right)\left(\frac{5\ \text{m}}{d}\right)\left(\frac{6}{\alpha_c}\right),$$

where d is the distance from target to final focusing magnet, and α_c is a constant depending on magnet layout and type. For quadrupole systems, $\alpha_c \simeq$ 4–6 and for solenoid final optics $\alpha_c = 2$.

Geometric aberrations limit the convergent angle for uncorrected optics, $\theta \lesssim 0.015$ rad (see [11]), although the general scaling for this limit has not been thoroughly explored. Using octupoles [12], it was found that this limit could be relaxed, and designs as large as $\theta = 0.030$ rad have been considered.

UNCORRECTED PROOF

The target power requirements place limits on the 3D space coordinates of the beam (pulse length and beam radius r_s) while final focus optics place constraints on the 3D momentum coordinates ($\Delta p/p$, ε_{nx}/r_s, and ε_{ny}/r_s), necessary to reach the spot radius r_s. Additionally because of Liouvilles theorem, the final 6D phase volume occupied by the beam will be at least as large as the initial volume. This constraint can be expressed [13] by a "dilution factor" D, which is a ratio of the initial to final 6D volumes and is a measure of how much room for emittance dilution exists in any particular driver concept:

$$D = \frac{\varepsilon_{Nf}^2 \Delta p_f \ell_f}{\varepsilon_{Ni}^2 \Delta p_i \ell_i} \tag{10.5}$$

Here ℓ_i and ℓ_f are the initial and final bunch lengths of the beam. If we assume the focusing limits on emittance and momentum spread discussed above, for the recirculator [10] (in which $\varepsilon_{Nf} < 8$ mm-mrad, $\varepsilon_{Ni} = 0.5$ mm-mrad, $p_i/p_f = 1.7 \times 10^{-2}$, $\ell_f = 1$ m, $\ell_i = 340$ m, $\Delta p/p_f < 1.4 \times 10^{-3}$, and $\Delta p/p_i \gtrsim 10^{-3}$ from assumed voltage errors in the injector), we find that there is phase-space dilution allowance $D \simeq 62$, which allows for only a factor of 4 growth in phase area in each of the three directions. This relatively small leeway is largely a result of the large initial pulse duration chosen in the recirculator [10], to reduce the number of beams. As one increases the number of beams as in the linac designs the constraint relaxes.

(Note that $D > 1$ is a minimum requirement. If coupling between the transverse and longitudinal directions is not sufficiently strong, the areas of individual phase space projections in each direction (i.e. ε_{Nx}, ε_{Ny}, or Δpl) will individually be non-decreasing, which in some cases can result in a stronger constraint on allowable emittance dilution.) Particle-in-cell simulations are needed to determine the emittance growth through the accelerator (see e.g. [14]).

10.1.3 Accelerator Architectures for Inertial Fusion Energy

Several induction accelerator architectures have been proposed for heavy ion driven Inertial Fusion Energy (IFE) (see e.g. [15–17]). Multiple beam linacs with quadrupolar or solenoidal focusing have been proposed to transport and accelerate the high line-charge densities required. Linacs with both high and low ion charge-to-mass ratio have been explored, with significantly different architectures, arising mainly from the different accumulated ion voltage, and current requirements. Circular layouts of induction accelerators or "recirculators" have also been investigated, for the purpose of achieving a cost savings by reusing induction cores and focusing elements. Recirculators are treated in this chapter (rather than in Chap. 11) due to the expected commonality of the beam dynamics with linear accelerators, although there is also some commonality between induction synchrotrons and recirculators, as well. In all of these concepts, final peak power is achieved by compressing the beam longitudinally in a final "drift compression" section. Both linear drift sections and compressor rings have been explored conceptually.

UNCORRECTED PROOF

An important choice of architecture is that between the linac and a circular machine. Because of the need to optimize the bore radius as the beam accelerates, the, purely circular designs have been composed of several rings. Hybrid designs are also possible, with combinations of linac and ring. Other design questions include which focusing system (electric quadrupole, magnetic quadrupole, or solenoid) to use, whether or not to merge beams, and what number of beams to use – all of which must be answered as a function of ion energy throughout the machine. Also, the optimal charge state and mass must be chosen. These different architectures and beam parameters lead to different emittances and imply different constraints on the final focus.

Another, important variable, is the impact of the architecture on the development path to a fusion driver. The development path refers to the sequence of machines that would be built, ultimately leading to a fusion power plant. Some work has been done on a "modular" approach, defined here as the development of a complete accelerator (a module), which would take a beam to the final energy required for a driver, but not necessarily the final current. The IFE driver would then consist of, for example, 10–20 identical copies of the module, that together could deliver the required current on target. An advantage of the modular approach is that all the issues involving the accelerator would be resolved in developing the prototype for the single module. The development path is thus attractive in the sense that risks in achieving the accelerator goals are removed before investing in a large driver-scale system. A disadvantage of this approach, is that the cost of a modular driver is inherently larger than an optimized multiple beam accelerator. Also, the issues involving multiple beam overlap at the target are still not resolved until the final driver, so that the risk reduction is only partial.

We will describe in detail three example accelerator concepts that illustrate some of the physics and technology considerations for an IFE driver:

1. The multiple beamline, single-coreline, quadrupole-focused linac (hereafter multi-beam linac); (A coreline is defined here as the set of beamlines which thread a common set of induction cores).
2. A "modular" design, with low-energy solenoidal focusing, comprised of 20 corelines, each consisting of a single-beamline.
3. The recirculator, composed of three rings, and four beamlines and one coreline throughout.

We take the 2002 Robust Point Design as an example of the multiple-beam linac [18]. This example has 120 beams that are magnetically focused. The main reasons for having large beam numbers are three-fold: First, the large beam number maximizes the current transport through a fixed core radius, minimizing the core volume. Second, the large beam number allows a larger ratio of the required final six-dimensional phase-space volume to the initial volume out of the injector. This allows a larger increase in the transverse and parallel normalized emittances, allowing a greater safety factor in permissible emittance dilution. Third, recent LLNL target designs require a large number of beams for symmetry considerations [6, 7, 5].

UNCORRECTED PROOF

In the modular approach [16, 19], the final beam energy is reduced by a factor of ten from the nominal quadrupole approach. This requires an increase in total charge on target by the same factor. However, the reduced final energy, requires much less core-material – one of the cost drivers in an induction accelerator. Also, at sufficiently low energies solenoids become more favorable for transporting charge as will be seen. Since the core material has been drastically reduced by going to lower energy, it becomes feasible to consider, multiple "core-lines," which are essentially identical accelerator copies. The different scaling of transportable current of solenoids can lead to optimal designs with small numbers of beams.

Cost reduction is the main motivation for the recirculator approach, achieved through the multiple use of induction cores and quadrupoles during each acceleration sequence using the circular layout. When the required ion energy is sufficiently large, the recirculator is more compact than a multi-beam linac at the same energy. In the design of [10], the circumference $\sim$2 km is dictated by the radius of curvature of a 10 GeV ion in a $\sim$2 Tesla dipole magnetic field (at an average dipole occupancy of 0.33). In the linac approach the maximum accelerating gradient (of 1–2 MV/m) determines the scale of the machine (length $\sim$ 2–4 km at 4 GeV). The size of the induction cores also tends to be reduced in a recirculator, because reuse of the cores allows a smaller accelerating gradient to be used, with an associated reduction in core size.

Now let us examine the major elements of induction accelerators, emphasizing the scaling relationships of the induction cores, focusing elements, and bending elements on the variables which distinguish the three example architectures, such as number of beams, pulse duration, and accelerating gradient. Figure 10.1 shows the unit structure of a multiple beam linac, called the "half-lattice period" (hlp). Because quadrupoles focus in pairs with alternating field gradients the complete

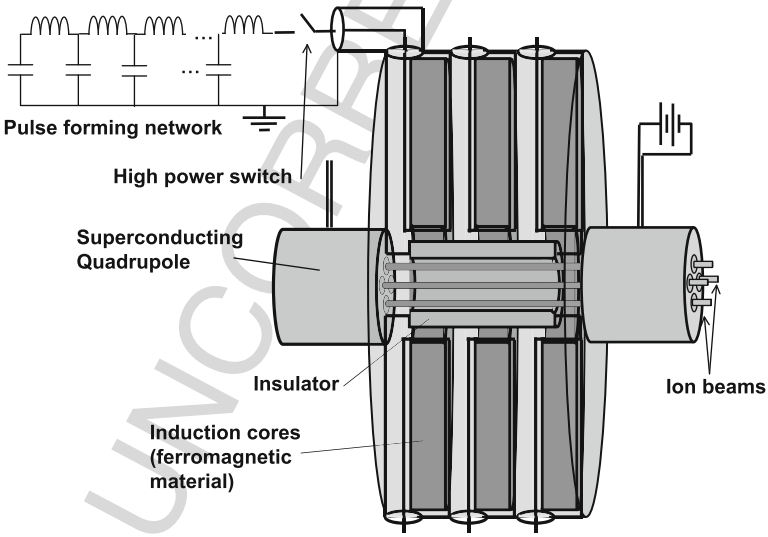

Fig. 10.1 A typical half-lattice-period of a multiple beam quadrupole linac for heavy ion fusion

UNCORRECTED PROOF

lattice period consists of a pair of hlp's. The complete accelerator consists of 100's to 1,000's of hlp's. Quadrupoles are replaced by solenoids in some high current low ion energy designs, such as in some modular designs. In the recirculator a dipole bend is added to the half-lattice period. We will return to the three concepts and explicitly discuss the advantages and key issues associated with each.

10.1.4 Induction Acceleration and Energy Loss Mechanisms

Acceleration is achieved in all three concepts by the use of a series of induction modules, each module adding an energy increment to the beam. The induction cell consists of the induction core, which is an annulus of ferromagnetic material and a modulator, which consists of a set of capacitors or a pulse forming network for energy storage and a switch. The principle is the same as that of a transformer, in which the beam (which threads the core) acts like a "one-turn" secondary of the transformer (see Chap. 3). As in the case of a transformer, Faraday's law relates the voltage increment ΔV, and pulse duration Δt to the cross-sectional area of the annulus A and the change in magnetic flux ΔB (see Sect. 3.5):

$$\Delta V \Delta t = A \Delta B. \tag{10.6}$$

Since the total volume of ferromagnetic material (such as Metglas, or Ferrite) is a major cost of the accelerator, keeping either the pulse duration short or the voltage increment small is essential to having cores of reasonable areas and volumes. In the linac approaches, a high voltage gradient is desirable to minimize costs. In the recirculator approach, the cores are reused, so the voltage gradient can be reduced and/or pulse durations can be longer. In the recirculator example examined in this paper this flexibility is used to increase the pulse duration in the early part of the machine and reduce the number of beams.

The modulators in a recirculator will be different from those chosen in any of the linac approaches. In the linac examples, a voltage pulse is a applied to the core just once per "shot" so the repetition rate is the rate at which the fusion targets are shot, a few Hz. In the recirculator example the cores are fired once each lap, so repetition rates up to of order 100 kHz are required. Further, as the beam accelerates, the pulse repetition rate increases, and because of the velocity increase and bunch compression the pulse duration decreases. The modulators on a linac are envisioned as pulse forming networks of capacitors and inductors (see Chap. 4), which form a pulse of a fixed duration and fixed waveform, after being initiated by a high-power switch such as a thyratron. The recirculator designs use capacitors for energy storage, which are discharged using arrays of solid state switches (MOSFETS), to both initiate and terminate the pulse. Arrays are required because many switches are required in series to hold the required voltage, and in parallel to carry the required current. Although, arrays of solid-state switches are individually more expensive than the pulse forming network approach, the smaller number of modulators required in a recirculator permits their use, despite their higher unit cost. As costs decrease in

UNCORRECTED PROOF

time, it will be necessary to reevaluate whether or not solid state switches will be affordable for linacs, as the main switch for the induction cores. They already may be competitive for auxiliary tasks, such as lower power correction pulses.

For a fusion power plant to be practical, the driver must be highly efficient in converting wall plug power into beam power. Efficiencies in the range of 20–30% are calculated to be possible using induction acceleration. One of the main sources of energy loss in induction linacs is dissipative losses in the induction cores (see Sect. 5.4). "Eddy current" losses arise when inductive electric fields within the cores create currents, producing resistive losses. Again using Faraday's law, the inductive field E is proportional to geometric factors times $\partial B/\partial t \simeq \Delta B/\Delta t$. The current density J is given by $J = \sigma_c E$, where σ_c is the conductivity, so that the power lost per unit volume is proportional to $J \cdot E \sim \sigma_c E^2 \sim \Delta B^2/\Delta t^2$. Over the course of a pulse of duration Δt the energy dissipated per unit volume is thus proportional to $\sigma_c \Delta B^2/\Delta t$. This argument applies to tape wound cores (ribbons), where the eddy currents are within each layer of tape (as in Metglas).

As the pulse duration gets very long, the eddy current losses go toward zero. Hysteresis losses contribute a second form of energy loss. This is the energy required to reorient the domains of magnetic flux along the imposed field direction. As the rate of change of the flux goes to zero this loss approaches a value proportional to the total change in flux ΔB. Empirically, the losses per unit volume $\mathcal{L}$ can be expressed approximately as in Chap. 5 (cf. Eq. 5.2):

$$\mathcal{L} \simeq 750 \left(\frac{\Delta B}{2.5\ \text{Tesla}}\right)^2 \left(\frac{1\ \mu s}{\Delta t}\right) + 100 \left(\frac{\Delta B}{2.5\ \text{Tesla}}\right)\ \text{J/m}^3. \tag{10.7}$$

Here the coefficients depend on the choice of magnetic material which in this case is Metglas 2605-S2.

Consider an accelerator that has a constant acceleration gradient [15] $\mathrm{d}V/\mathrm{d}s = (V_f - V_i)/N_{\text{gap}}L$. Here subscripts i and f indicate initial and final values respectively, and N_{gap} is the number of accelerating cores encountered by the beam (which for a recirculator is equal to the number of turns times the number of half-lattice periods in the ring). As an illustration, consider a pulse duration that decreases linearly with distance (or voltage), so that

$$\Delta t = \Delta t_i + (\Delta t_f - \Delta t_i)\frac{V - V_i}{V_f - V_i}. \tag{10.8}$$

In that case, the total loss in the inductive cores $\mathcal{L}_{tot}$, under these assumptions is given by:

$$\begin{aligned}\mathcal{L}_{\text{tot}} = &\left[4.7\ \text{MJ}\left(\frac{\mathrm{d}V/\mathrm{d}s}{1\ \text{MV/m}}\right)\left(\frac{0.5\ \text{m}}{R_{\text{out}} - R_{\text{in}}}\right)\left(\frac{0.8}{\eta_{\text{core}}}\right) + 0.63\ \text{MJ}\right] \\ &\times \left(\frac{R_{\text{out}} + R_{\text{in}}}{1\ \text{m}}\right)\left(\frac{V_f - V_i}{10\ \text{GV}}\right)\left(\frac{\Delta t_i + \Delta t_f}{1\ \mu\text{s}}\right)\end{aligned} \tag{10.9}$$

UNCORRECTED PROOF

Here, the core inner and outer radii are given by R_{in} and R_{out}, respectively, and η_{core} is the ratio of the core length to the distance between accelerating gaps. Note that core losses can be reduced by going to small accelerating gradients and by increasing core volume so that the cores operate away from saturation. Both effects will reduce the first term in $\mathcal{L}_{\text{tot}}$, and can be carried out until hysteresis dominates the core loss. The recirculator operates at a much lower accelerating gradient and therefore will have more efficient acceleration. High-charge state machines have much lower V_f and can also have more efficient acceleration when operating at high current through each core.

In recirculators, a second major source of energy loss is present. As the energy of the beam increases during the acceleration of a beam pulse, so too must the dipole field which bends the beam. The scale over which the acceleration occurs is a few milliseconds, which is faster than the permissible ramping time of present-day superconducting magnets. Conventional magnets must be used, with losses generally proportional to the magnetic field energy (proportional the square of the field B). In the magnets under consideration for recirculators, losses arise from four major sources [20]. These are:

1. Resistive losses in the conducting wire coils (proportional to $I^2RP \sim B^2P$, where I is the current, R is the wire resistance, and P is the residence time of the beam within the ring).
2. Eddy currents within the conductors ($\sim B^2x^3/P$ where x is the width of the wire).
3. Eddy current losses in the laminated iron yokes needed to confine and direct the magnet flux (also proportional to B^2/P).
4. Hysteresis loss in the iron.

In driver recirculator designs $\sim$40 MJ of magnetic energy is stored in the magnetic field. Efficient recovery of this energy for subsequent pulses is required to achieve overall high efficiency of the accelerator. Dipole designs (including the effects of cooling channels) in which $\sim$90% of the magnetic energy is reused each pulse appear achievable.

10.1.5 Scaling of the Focusing Systems

In the absence of acceleration, the envelope equations for the three focusing systems can be expressed as:

$$\frac{\mathrm{d}^2 a_x}{\mathrm{d}s^2} = \frac{\varepsilon^2}{a_x^3} + \begin{cases} \dfrac{2Q}{a_x+a_y} \pm \dfrac{V_q}{V}\dfrac{a_x}{r_p^2}, & \text{Electric Quadrupole} \\ \dfrac{2Q}{a_x+a_y} \pm \left(\dfrac{qB_q^2}{2mV}\right)^{1/2}\dfrac{a_x}{r_p}, & \text{Magnetic Quadrupole} \\ \dfrac{Q}{a_x} + \dfrac{\omega^2 a_x}{v_z^2} - \dfrac{\omega\omega_c a_x}{2v_z^2}, & \text{Solenoid} \end{cases} \tag{10.10}$$

UNCORRECTED PROOF

Here, a_x and a_y are the envelope radii in the x- and y-directions, $Q = \lambda/(4\pi\varepsilon_0 V)$ is the perveance, qV is the ion energy, q and m are the charge and mass of the particle, ω is the rotation frequency of the beam envelope, ω_c is the cyclotron frequency, ε is the unnormalized beam emittance, v_z is the axial beam velocity, and r_p is the clear aperture (beam-pipe) radius. For the quadrupole case, the equation for a_y is found by interchanging a_x with a_y in Eq. (10.10). For the solenoid case, the beam is axisymmetric, i.e., $a_x = a_y = a$. Also in the solenoid case, the focusing results from the difference between the outward centrifugal force due to beam rotation and the inwardly directed $v_\theta B_z$ force, where v_θ is the azimuthal beam rotation velocity and B_z is the solenoidal magnetic field. In addition, space charge and emittance tend to defocus the beam.

In the quadrupole case the beam alternately receives "kicks" which focus then defocus, but since the focusing occurs when the beam is at larger radius where the kicks are stronger, there is an average net focusing. We may average over a lattice period to obtain a smooth approximation to the focusing [21]. In the solenoid case, we may maximize the focusing by choosing $\omega = \omega_c/2$. Then, all three focusing systems may be represented approximately by an envelope equation for the average beam radius a

$$\frac{\mathrm{d}^2 a}{\mathrm{d}s^2} = \frac{\varepsilon^2}{a^3} + \frac{Q}{a} - k^2 a. \tag{10.11}$$

Here,

$$k^2 \equiv \begin{cases} \frac{1}{4r_p^2}\left(\frac{\eta L}{r_p}\right)^2 \left(\frac{V_q}{V}\right)^2, & \text{Electric Quadrupole,} \\ \frac{1}{8}\left(\frac{\eta L}{r_p}\right)^2 \left(\frac{qB_q^2}{mV}\right), & \text{Magnetic Quadrupole,} \\ \frac{\eta}{8}\left(\frac{qB_s^2}{mV}\right), & \text{Solenoid.} \end{cases} \tag{10.12}$$

Here, η is the fractional quadrupole or solenoid occupancy in the lattice. Note that for electrostatic quadrupoles k^2 is proportional to $1/V^2$ whereas for magnetic quadrupoles k^2 varies as $1/V$ suggesting that at low voltages electrostatic quadrupoles will be more effective than magnetic quadrupoles. Note also that for quadrupole focusing the focusing constant increases as the lattice period increases, whereas for solenoids the constant is independent of lattice period.

The particle undergoes quasi-harmonic betatron motion with wave number k. The phase advance (in the absence of space charge) σ_0 is approximately given by $\sigma_0 = 2kL$ designated per lattice period $2L$. Note that for aligned solenoids the period $2L$ contains a single magnet, but two magnets for alternating solenoids, whereas there are two quadrupoles in period $2L$.

For all three systems, the phase advance cannot be made arbitrarily large. Envelope/lattice instabilities set in for $\sigma_0 \gtrsim \pi/2$ [22–24].

By eliminating the lattice period $2L$ in favor of σ_0, and equating the space charge term Q/a to the focusing term $k^2 a$ in Eq. (10.7) (ignoring the normally small

UNCORRECTED PROOF

contribution from the emittance term), we may calculate the maximum transportable line charge density per beam λ_b. This is one form of the so-called "Maschke limit:"

$$\lambda_b = \begin{cases} 0.9\ \frac{\mu\text{C}}{\text{m}} \left(\frac{\sigma_0}{1.4}\right) \left(\frac{a/r_p}{0.7}\right)^2 \left(\frac{\eta}{0.7}\right) \left(\frac{V_q}{80\ \text{kV}}\right) & \text{Electric Quad} \\ 1.0\ \frac{\mu\text{C}}{\text{m}} \left(\frac{\sigma_0}{1.4}\right) \left(\frac{a/r_p}{0.7}\right)^2 \left(\frac{\eta}{0.7}\right) \left(\frac{B_q}{2\ \text{Tesla}}\right) \left(\frac{(q/e)/A}{1/200}\right)^{1/2} & \\ \qquad \times \left(\frac{V}{2\ \text{MeV}}\right)^{1/2} \left(\frac{r_p}{6\ \text{cm}}\right) & \text{Magnetic Quad} \\ 0.03\ \frac{\mu\text{C}}{\text{m}} \left(\frac{a/r_p}{0.7}\right)^2 \left(\frac{\eta}{0.7}\right) \left(\frac{B_s}{2\ \text{Tesla}}\right)^2 \left(\frac{(q/e)/A}{1/200}\right) \left(\frac{r_p}{6\ \text{cm}}\right)^2 & \text{Solenoid} \end{cases} \tag{10.13}$$

Here, A is the mass of the ion in amu. Note that the line charge density limit per beam λ_b increases with voltage V only for the magnetic quadrupoles, which leads to the choice of magnetic quadrupoles for the high energy section for two of the three example concepts described here. Note also that, although the line charge density limit for the solenoids has a smaller coefficient at the nominal values of the field and pipe radius indicated, λ_b increases with the square of $B_s r_p$, whereas for the quadrupoles it rises linearly with $B_q r_p$.

Also note that λ_b is independent of r_p for electrostatic quadrupoles, proportional to r_p for magnetic quadrupoles, and r_p^2 for solenoids. We define a second relevant quantity λ_{tot} equal to the total line charge that can be transported through an induction core of fixed inner radius R_{in}. We follow the argument of Bangerter [25], adding solenoidal focusing to the discussion.

The number of beams N_b threading each induction core is proportional to $(R_{\text{in}}/r_q)^2$ where r_q is the outer radius of the quadrupole or solenoid (for large N_b) (see Fig. 10.2). Assuming that r_q/r_p is constant as one changes the number of beams, then the total transportable line charge $\lambda_{\text{tot}} \sim V_q N_b$ for electric quadrupoles, $B_q N_b^{1/2}$ for magnetic quadrupoles, B_s^2 for solenoids. Further, $V_q \sim r_p^{1/2\ \text{to}\ 1}$ to avoid breakdown, and for small magnetic field values B_q and B_s are proportional to I_m/r_p where I_m is the total current in the magnet. But $I_m \sim J_{\text{crit}} r_p^2$ where J_{crit} is the critical current density for superconducting magnets, and is assumed here to be only weakly dependent on field strength. Thus B_q and B_s are proportional to r_p for fixed ratio r_q/r_p which suggests that $\lambda_{\text{tot}} \sim N_b^0$ (for magnetic quadrupoles) and $\lambda_{\text{tot}} \sim N_b^{-1}$ (solenoids). For large r_p and magnetic fields, for technological and economic reasons the magnets are designed at nearly constant maximum values, so that $\lambda_{\text{tot}} \sim N_b^{1/2}$ (for magnetic quadrupoles) and $\lambda_{\text{tot}} \sim N_b^0$ (solenoids). Summarizing these scalings, we find:

$$\lambda_{\text{tot}} \sim \begin{cases} N_b^{1/2\ \text{to}\ 3/4}, & \text{Electric Quadrupole} \\ N_b^{0\ \text{to}\ 1/2}, & \text{Magnetic Quadrupole} \\ N_b^{-1\ \text{to}\ 0}, & \text{Solenoids} \end{cases} \tag{10.14}$$

UNCORRECTED PROOF

This figure will be printed in b/w

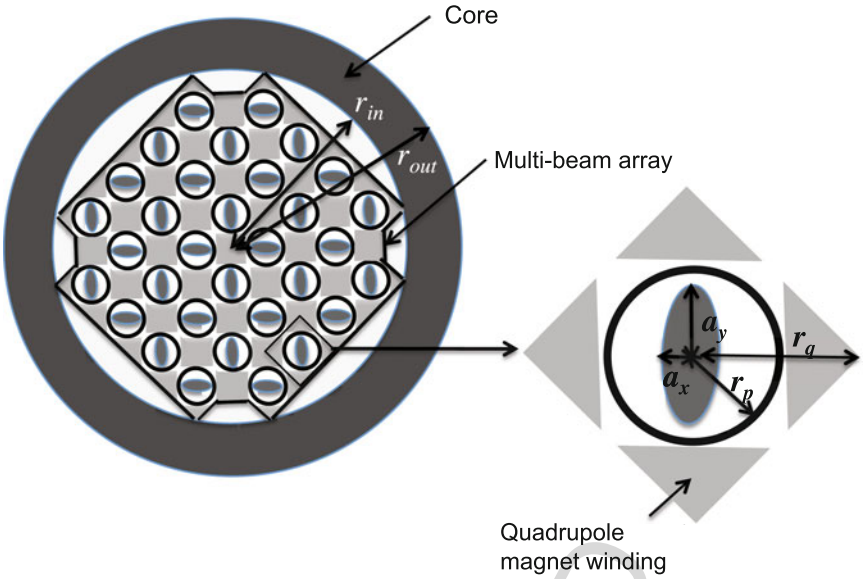

Fig. 10.2 A quadrupole array showing multiple beamlines with shared conductors threading a single induction coreline

From Eq. (10.9), it is apparent that for electrostatic quadrupoles a larger number of beams is optimal, for magnetic quadrupoles larger numbers of beamlines are somewhat favored, but for solenoids a smaller number of beamlines will be optimal. Indeed, (a/r_p) multiplies the above expression, and since finite alignment precision suggests that a/r_p tends to zero as a tends to zero (or N_b tends infinity), even for electric quadrupoles an upper limit on the number of beams for maximum transportable current is reached. It is thus apparent how the scaling of transportable current leads to a large number of beams in accelerators with electric quadrupole "front ends," and a small number of beams in an accelerator with solenoids in the low energy section.

10.1.6 Accelerator Scaling with Charge-to-Mass Ratio

In order to obtain a qualitative understanding of how accelerator costs scale with charge-to-mass ratio q/m we may consider a simplified example using quadrupole transport to illustrate the scaling. In comparing drivers which use different charge-to-mass ratios, target requirements constrain the driver to maintain the same pulse energy $Q_{\text{ctot}}V_f$, the same pulse duration at the target Δt_t, and the same ion range R. Here Q_{ctot} is the total charge in the bunch, and qV_f is the final ion energy. A crude low order approximation (but sufficient for our purposes) of the mass and energy dependence of the range R is that R depends only on β where βc is the ion velocity. (This neglects a slow decrease in range as the atomic mass increases, at fixed β).

UNCORRECTED

Under these assumptions $qV_f/m \simeq$ constant. This directly implies that $V_f \sim m/q$ and $Q_{c\text{tot}} \sim q/m$. For a linac the accelerator length L_{acc} decreases for large q/m since $L_{\text{acc}} \sim V_f/(\mathrm{d}V/\mathrm{d}s) \sim m/q$. Here $\mathrm{d}V/\mathrm{d}s$ is the maximum accelerating gradient, which is typically $\sim$ 1–2 MV/m for induction linacs. For larger q/m the space charge increases. For a concrete comparison, we make the additional assumption that the voltage, pulse duration, and geometry of the injector (such as r_p) are fixed, but that as q/m is altered the number of beams changes to account for the changes in required space charge. Under those assumptions,

$$\begin{aligned} N_{bi} &\sim \frac{Q_{c\text{tot}}}{\ell_{bi}\lambda_{bi}} \sim \left(\frac{q}{m}\right)^{1/2}, && \text{Electric Quadrupole,} \\ N_{bf} &\sim \frac{Q_{c\text{tot}}}{\ell_{bf}\lambda_{bf}} \sim \left(\frac{q}{m}\right), && \text{Magnetic Quadrupole.} \end{aligned} \tag{10.15}$$

Above $Q_{c\text{tot}} \sim q/m$ (for both electric and magnetic quadrupoles), $\ell_{bi} \sim (q/m)^{1/2}$ and $\lambda_{bi} \sim 1$ (for electric quadrupoles), while $\ell_{bf} \sim 1$ and $\lambda_{bf} \sim 1$ (for magnetic quadrupoles), and where subscripts i and f represent initial and final, respectively.

We again assume for this example that the pulse duration decreases linearly with distance [see Eq. (10.8)]. The required total volt-second capability of the accelerator is given by $\int \Delta t(\mathrm{d}V/\mathrm{d}s)\mathrm{d}s = \int \Delta t \mathrm{d}V \sim m/q$. Hence the inner radius of core $\sim N_b^{1/2} \sim (q/m)^{1/2 \text{ to } 1/4}$, and the total core volume and core costs $\sim (m/q)^{1/2 \text{ to } 3/4}$. This result suggests that there can be a cost savings associated with larger q/m. As will be discussed in the next section, the challenges for this approach arise from more stringent requirements at the final focus and at the injector.

10.1.7 Multi-Beam Linac with Quadrupole Focusing

The multi-beam linac has undergone the most research over the last 20 years. See Fig. 10.3 for a schematic of the various elements and beam manipulations in a multiple-beam linac approach to heavy ion fusion. Systems codes have been developed which [26] to put each of the various accelerator configurations onto a common cost and efficiency basis. The codes have been applied to accelerator designs that have been specifically tailored to recent LLNL target designs [8]. One design, hereafter called the Robust Point Design or RPD [18] consisted of 120 beams of singly charged Bismuth (injected with a pulse energy of 1.6 MeV and pulse duration of 30 μs.) Since the target required a prepulse at lower energy (3.3 GeV), once this prepulse energy is reached, 48 of the beamlines are transported outside the main induction cores while the remaining 72 beams continue acceleration to 4 GeV. The main pulse exits the accelerator at 200 ns and undergoes drift compression, reaching approximately 9 ns at the target. (The prepulse is similarly compressed from 200 to approximately 38 ns). The pulse shape is built up from five different "rectangular" pulses having varying pulse width and phase, but add to a desired pulse shape determined by target physics. Another design [26] consisted of 192 beams transported with electrostatic quadrupoles to 100 MeV after which the beams merged

UNCORRECTED PROOF

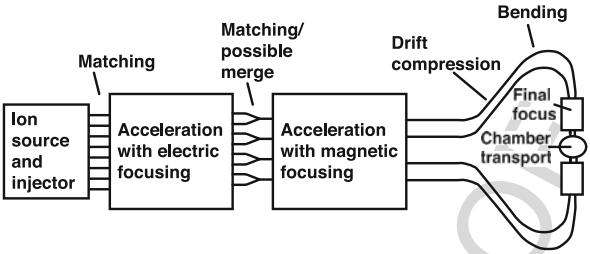

Fig. 10.3 The multiple beam linac approach to heavy ion fusion, with various beam manipulations indicated

into 48 beams transported by magnetic quadrupoles. In addition to the beneficial transport properties of electric quadrupoles at low energy, they also tend to clear electrons out of the beam, which is most critical at low energy. At low energy, the pulse duration is long so the beam is most vulnerable to electron accumulation, since the longer time allows ionized residual gas particles time to reach the walls liberating electrons and ions, and thus possibly causing emittance dilution to the latter part of the beam.

Although, heavy ion fusion relies on technology that has been validated on other accelerators, including induction accelerators, the ion beam intensity required for heavy ion fusion has not been achieved on any existing machine. For the multibeam linac concept some of the key physics and technology issues, that would require validation in a HIF research program (see e.g. [27]) include:

1. Control and alignment of multiple-beam arrays. Since there have been few experiments with such large arrays of ion beams, there have been few attempts to quantify the requirements on the alignment and control system.
2. Transport of beams with large head-to-tail velocity tilt. This is an issue which affects all of the accelerator concepts and ultimately becomes a question of what velocity tilt can be transported without inducing mismatch oscillations on the beam.
3. Inter-beam interactions in gaps. In a high gradient machine the acceleration gaps are either longer or are graded, making this issue more important for this concept. Methods for shielding the beams within the gaps need to be assessed.
4. Emittance dilution from merging. The question of whether or not to merge is ultimately an issue of system optimization (some designs have, in fact, no merging), since the emittance dilution associated with a beam merge must be accounted for in an optimized design. Simulations and recent experiments [28] will help resolve this issue.
5. Electron-cloud effect. During magnetic quadrupole or solenoid transport electrons (originating from the walls, created by ion or secondary impacts, or from collisions with the residual gas) can accumulate in long pulses and if sufficiently dense degrade beam quality [29, 30].
6. Cost. The driver cost must be evaluated carefully for this concept as well as any concept for HIF.

UNCORRECTED PROOF

Fig. 10.4 The MBE-4 induction accelerator that demonstrated acceleration and compression of four beams in an electrostatically focused accelerator

A multi-beam linac (MBE-4) with four beams was constructed at LBL in 1982. It provided a proof of principle for simultaneous acceleration and compression of four beams in an induction linac to 2 MeV [31]. See Fig. 10.4.

10.1.8 Modular Drivers

As discussed earlier, a key question is how to create a sequence of accelerators which allow key concept validations without risking large capital investments. In an effort to solve that problem, the "modular" approach whereby, a complete subset or "module" of an HIF driver can be created and tested at a fraction of the cost ($\sim$5–10%) of a complete driver. The driver then consists of tens to hundreds of identical copies of each module, all focused onto the target. Examples of modular designs are given in Yu et al. [19] and Logan [32]. One approach to accomplish this task is based on a linac that is solenoidally focused, and has a final energy of only a few 100 MeV instead of a few GeV. Figure 10.5 shows one module of a concept that accelerates stripped Rubidium, charge state +9, through 100 MV (with a resulting ion energy of 900 MeV). As in the multi-beam linac, there are several manipulations required to reach the intensities required for HIF. In Fig. 10.6 each

AQ1

UNCORRECTED

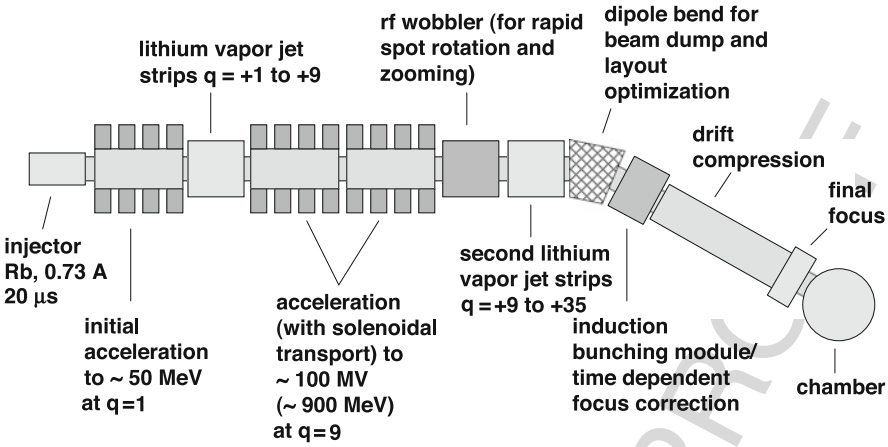

Fig. 10.5 A typical accelerator "module" in the modular, solenoid based, multiple linac approach to heavy ion fusion [32]

accelerator module lies on one of two cylindrical surfaces, and the drift sections lie on cones with polar opening angles of 10° and 55°.

There are a number of key issues associated with this concept. The accelerator requires a large current ~~and~~ ion source. No experience with such sources has as of yet been obtained. A second major concern is aberrations from the fringe fields of laterally adjacent solenoids. Multiple beam arrays are not as naturally compatible as they are with quadrupoles. With solenoids, the flux through the end of one solenoid interacts in a non-axisymmetric manner with the flux from an adjacent one, producing large non-linear field aberrations, unless the flux from the solenoids is contained or they are separated a sufficient distance. A third issue is the control of backflowing electrons flowing down magnetic field lines and achieving high energy going through multiple gaps. Alternating the field direction longitudinally in adjacent solenoids has been suggested, but flux lines which terminate on the walls may be a source for electrons and thus may do more harm than good.

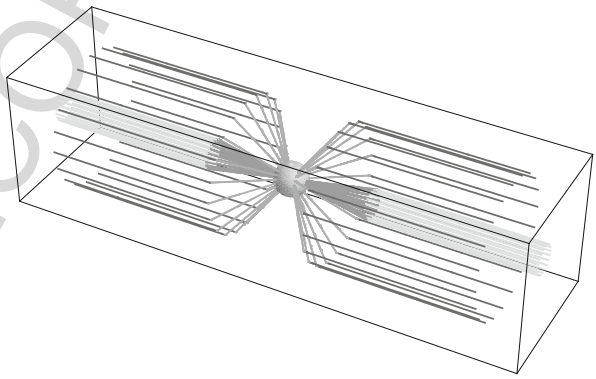

Fig. 10.6 The layout of the modular, multiple-linac approach of [32]. Each module is ∼ 100 m in length (see Fig. 1)

AQ2

UNCORRECTED PROOF

10.1.9 Recirculator

is 10.8 the right eq?

The recirculator as envisioned in [10] consisted of several rings, each increasing the [illegible]ctor of about 10 and decreasing the pulse duration by a factor of about [illegible]. 10.7. The prime motivation for the study was to see if it was possible to substantially reduce the cost of the accelerator relative to a linac design. Further, the authors tried to design a machine with a small number of beams, favoring the simplicity of four beams relative to the complexity of the large number of beams in the linac approach, and eliminating the need to merge beams with the associated emittance growth. Designing a machine with fewer beams, however, meant the design relied on large initial pulse durations in order to satisfy the constraint of Eq. ~~(10.8)~~. Since the recirculator can operate at a reduced acceleration gradient (because the accelerator components are reused over the course of ∼100 turns), long pulse durations can be entertained more easily in a recirculator than in a linac, without requiring very large induction cores [see Eq. ~~(10.1)~~].

is 10.1 the right eq?

However, because of the smaller accelerating gradient, the beam covers a much larger pa[illegible] residual gas and charge-changing collisions of beam par[illegible]ore problematic in a recirculator, and the poorly understood effects of lost beam and ionized residual gas hitting the wall, producing additional outgassing (a beam intensity dependent effect) needs experimental verification to establish that the vacuum behaves as predicted. As indicated above, the efficiency of ramped dipoles is crucial to the recirculator design, since the recycled dipole energy is larger than the beam energy itself. Insertion/extraction of multiple beams into and out of the ring also requires validation. In one recirculator design study [10] the beam lines were arrayed in a square pattern within the bend sections (to minimize core volume), but were arrayed vertically in the insertion/extraction section to facilitate use of the rectangular quadrupoles used for getting the beam into and out of the ring. This arrangement allowed path equalization by exchanging inner

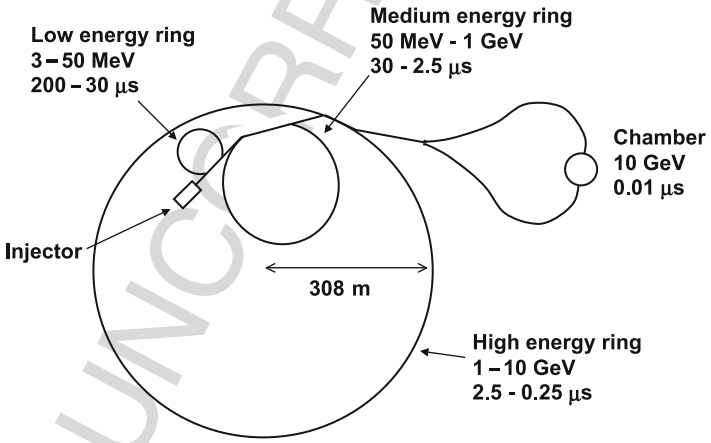

Fig. 10.7 The layout of the recirculator from [10]

UNCORRECTED PROOF

beams with outer beams in the bends. Use of superconducting quadrupoles provides an efficient focusing system and constant magnetic field. As the beam accelerates, the tune changes rapidly, effectively passing through resonances. As a result, the recirculator operates in a space-charge-dominated regime, far exceeding the Laslett tune shift limit of conventional circular accelerators. Validation of this operation point experimentally is a key goal of the bending and recirculation experiments that took place at LLNL [33, 34] and are taking place at the University of Maryland [35, 36]. Finally, the long pulse durations which enabled a small number of beams to be accelerated at the beginning of the accelerator, imply larger momentum spread at the end of the accelerator, and there is less leeway for phase space dilution. Injectors with smaller voltage errors or achromatic final focusing systems would be beneficial to recirculators with long initial pulse duration. Also, recirculators with more beams and shorter pulses (hence closer in concept to "circular" linacs) need evaluation.

10.1.10 Beam Manipulations

There are number of non-standard techniques that are envisioned for induction-accelerator-based HIF. As indicated above one of these techniques increases the current and hence peak power by increasing the velocity of the tail of the beam relative to the head, thus compressing the beam longitudinally. This is one benefit from using non-relativistic beams where velocities are significantly different than the speed of light, so that a relatively small fractional change in energy $\Delta E/E$ results in a significant fractional change in velocity ($\Delta v/v \sim \Delta E/2E$) instead of ($\Delta v/v \sim (1/\gamma_r^2)\Delta E/E$) for an ultra-relativistic beam, where γ_r is the relativistic factor [$\gamma_r = (1 - v^2/c^2)^{1/2}$]. As was shown in Chap. 9, the decreasing line charge density at the beam ends creates an electric field which tends to cause the beam to expand longitudinally. For a beam which decreases monotonically from the center (as for example a beam that has a parabolic line charge density with longitudinal coordinate z) there is an outward longitudinal force over the entire beam length (except the beam center). From the earliest concepts for HIF, it was realized that this space charge force would act to remove a velocity tilt that is imposed on the beam, and under some circumstances could remove the tilt, just as the beam was passing through the final focus magnets. By coinciding this "stagnation" point with the location of the center of the final focus magnet system, minimal chromatic aberrations would result, limited only by intrinsic thermal spread of the compressed beam and any residual velocity tilt not removed by the stagnation.

We may make estimates of the magnitude of the velocity tilt needed and the length of the drift section by appealing to the longitudinal envelope equation:

$$\frac{\mathrm{d}^2\ell_b}{\mathrm{d}s^2} = \frac{\varepsilon_z^2}{\ell_b^3} + \frac{12gqQ_c}{4\pi\epsilon_0 m v^2 \ell_b^2} - K(s)\ell_b. \tag{10.16}$$

Here, ℓ_b is the length of a beam with a parabolic density profile, g is the "g-factor" (cf. Eq. (9.28)), Q_c is the total charge in the beam, $K(s)$ is a possible linear

UNCORRECTED PROOF

longitudinal focusing field (which we assume to be zero in the drift section), and ε_z is the longitudinal emittance. For non-neutralized drift compression, the longitudinal emittance may be ignored, since the intense space charge will generally cause stagnation before the emittance term has effect. (For neutralized drift compression, the longitudinal emittance limits the ultimate minimum pulse duration). Setting $K(s) = \varepsilon_z = 0$, and integrating Eq. (10.16) once we obtain:

$$\frac{1}{2}\left(\frac{\mathrm{d}\ell_b}{\mathrm{d}s}\right)^2 + \frac{12gqQ_c}{4\pi\epsilon_0 m v^2 \ell_b} = \frac{1}{2}\left(\frac{\mathrm{d}\ell_{b0}}{\mathrm{d}s}\right)^2 + \frac{12gqQ_c}{4\pi\epsilon_0 m v^2 \ell_{b0}} \tag{10.17}$$

Noting that at the longitudinal focus $\mathrm{d}\ell_b/\mathrm{d}s = 0$, and $\mathrm{d}\ell_{b0}/\mathrm{d}s = \Delta v/v$, where Δv is the difference between the velocity of the tail of the beam and the head, we may calculate the required velocity tilt $\Delta v/v$:

$$\frac{\Delta v}{v} = \sqrt{\frac{24gqQ_c}{4\pi\epsilon_0 m v^2 \ell_{bf}}\left(1 - \frac{\ell_{bf}}{\ell_{b0}}\right)} \tag{10.18}$$

Here, ℓ_{b0} and ℓ_{bf} are the bunch length at the beginning of the drift length, and at the focus respectively. The drift length can be estimated noting that the length of the beam is reduced to its final length during the time it takes to transit the drift length:

$$l_{\text{drift}} \simeq \frac{(\ell_{b0} - \ell_{bf})}{\Delta v/v} \tag{10.19}$$

In some designs with large line charge densities, the idea of neutralized drift compression in which a plasma is injected along the propagation path has also been advanced. In this case, the neutralizing plasma eliminates the chance of vacuum breakdown, and eases the requirements on longitudinal compression. In this case, the minimum pulse duration occurs when longitudinal emittance limits further bunch compression. In contrast to unneutralized drift compression, in ~~neutralized~~ drift compression, the final velocity spread will be that spread by the tilt imposed to compress the beam (since space charge is no longer acting to remove the tilt). In that case, however, it has been suggested that time dependent chromatic corrections be used to minimize chromatic aberrations. The time dependent chromatic corrections would occur at a position upstream of the final focus at a point where the beam has sufficiently long pulse duration (~100 ns) so that time dependent quadupolar magnetic or electric field temporal ramps may be imposed, at reasonable power levels. The correctors must be sufficiently close to the final focus so that accumulated phase advance differences do not put unreasonable requirements on the precision of the correctors.

Other possible beam manipulations include beam merging [28] and beam splitting [37]. The former has been considered as a way to compensate for the different scaling of focusing of electric and magnetic quadrupoles. (Electric quadrupole transport is generally optimum at a smaller bore radius than magnetic quads.)

UNCORRECTED PROOF

As of this writing, the National Ignition Facility is poised to achieve the first ignition of inertial confinement fusion targets, using a laser as the driver. If it is successful, the uncertainty about whether targets can ignite will be eliminated, and a major step toward the realization of inertial fusion energy will have been achieved. The focus will then shift to the best driver (and best chamber options) for inertial fusion energy. As discussed in this chapter, there appear to be several attractive options for heavy ion accelerators to fill the role of the driver. At the same time, we have outlined the areas where further research is needed to push the accelerator frontier into an unprecedented regime of ion beam power and intensity. But this regime is an area where induction accelerators could play a natural role.

10.2 Other Applications of Ion Induction Accelerators

10.2.1 High Energy Density Physics and Warm Dense Matter Physics

Although accelerators driving HIF targets to temperatures of ~200 eV may be a decade or more in the future, accelerators that could drive targets to a few eV may be much closer at hand. The field of High Energy Density Physics seeks to explore the properties of matter with energy densities greater than about 10^{11} J/m^3 which corresponds to temperatures greater than 1 eV at solid density [38, 39]. Also, a regime at lower temperatures [the Warm Dense Matter (WDM) regime], with temperatures greater than about 0.1 eV, and densities at 1–100% of solid density is of interest to a variety of scientists. Induction accelerators are also well suited to investigate these regimes, because large pulse energies are required to heat matter to this temperature, and the heating must be done rapidly to avoid hydrodynamic and other means of cooling the matter.

The WDM regime is particularly interesting because it is at the cross-roads of strongly- and weakly-coupled plasmas (where ion kinetic energies can be of order the Coulomb potential energy between neighboring ions), and is at the border of degenerate and classical electron behavior (where the electron Fermi energy can be of order of the electron thermal energy). This crossroads where small parameters are no longer small, is a challenge for theorists, and confrontation of experiment with theory is essential to understand the behavior of matter at these temperatures and densities. Further, the regime can include exotic plasmas that have had little study. An example of such a plasma is pure ion plasma consisting of positively and negatively charged ions (such as bromine) with many fewer electrons than ions. Such a plasma may have similarities to electron-positron plasmas, since the species masses are essentially equal, and may also have electrical properties analogous to semi-conductors. Also of interest, is the boundary of the liquid-vapor regions in the density-temperature phase plane of many materials [40]. The precise location of the "critical point" (indicating the density and maximum temperature of the two phase region) is not known for many metals. Also, the interior of the gaseous planets and

UNCORRECTED PROOF

low mass stars falls squarely within the regime of WDM [38]. Spacecraft have given planetary scientists exquisitely precise measurements of the gravitational moments of the planets Jupiter and Saturn, and the equation of state becomes one of the central uncertainties in matching the calculated gravitational moments from planetary models to the observed moments from spacecraft trajectories [41]. Finally, the hydrodynamics of plasmas heated by ions, may be of interest in its own right. Instabilities can be significantly modified by the energy deposition process itself.

For quantitative WDM and HEDP experiments with heavy ions it is desirable to heat the sample as uniformly as possible. One would also like to utilize the ion beam pulse energy as efficiently as possible. Both of these objectives are fulfilled by operating near the Bragg peak (see Fig. 10.8). With a helium ion beam, for example, the required voltage is about 1 MeV, while with Ne^{+1} or Na^{+1} it is about 20 MeV. To heat an Al foil to 1 eV, the number of Ne ions required in a sub nanosecond pulse that is focused to ~1 mm radius is about 2×10^{11}, or a pulse energy of about 1 J. These requirements are extremely modest compared to those of a heavy ion driver for inertial fusion. (More conventional accelerators are also being used to explore the WDM regime, but at a much higher ion energy (far above the Bragg peak) at larger range, but less efficient use of ion energy (cf. e.g: [42])).

Taken as a whole, a facility for using heavy ion beams to heat matter to Warm Dense Matter conditions will have unique characteristics (relative to lasers, pulsed-power experiments, diamond anvil, or gas gun experiments) that will allow scientific exploration of this regime. Among these characteristics are: precise control of energy deposition (a result of highly diagnosable and controllable ion current and ion energy, characteristic of accelerator-based heating); uniformity of energy

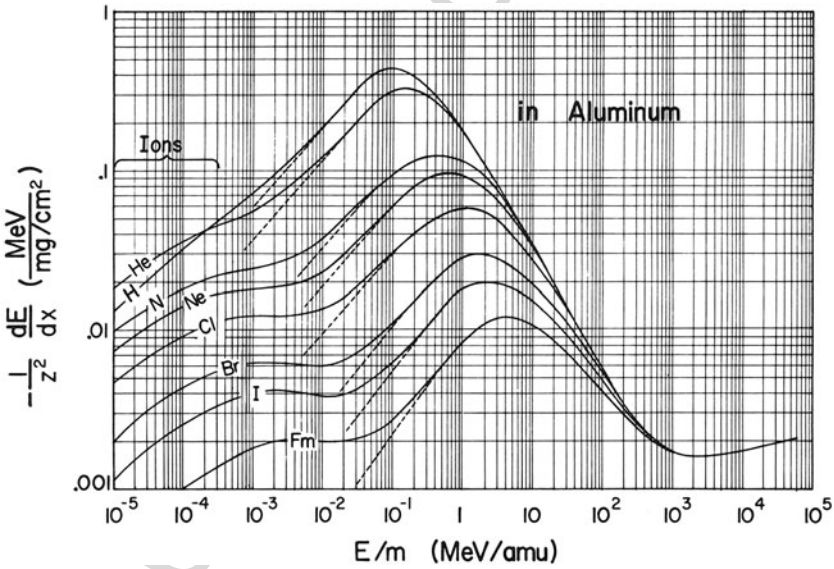

Fig. 10.8 Ion stopping rate in Aluminum as a function of energy, and ion mass (from [44])

deposition (a result of isochoric heating characteristic of ion deposition the Bragg peak); large sample sizes compared to diagnostic resolution volumes; (a result of a broad choice of ion masses and ion energies, allowing range optimization); a variety of potential targets (e.g. both conductors and insulators may be heated by ion beams); relatively long times to achieve equilibrium conditions (concomitant with the large sample sizes); a benign environment for diagnostics (low debris and radiation background, owing to the relatively low ion energy of order a few MeV/amu); high shot rates (10 per hour to 1 per second easily achievable with accelerator technology); multiple beamlines/target chambers (possible due to beam switching); sites with easy access for broad participation by university scientists and students.

By consideration of ion beam phase-space constraints, both at the injector, and at the final focus, and consideration of simple equations of state and relations for ion stopping, approximate conditions at the target foil may be calculated [43]. Thus, target temperature and pressure may be calculated as a function of ion mass, ion energy, pulse duration, velocity tilt, and other accelerator parameters. We connect some of these basic parameters to help illustrate the requirements on an ion induction accelerator for the investigation of WDM.

We first examine ion stopping, or $\mathrm{d}E/\mathrm{d}X$, where E is the ion energy and $X \equiv \int \rho \mathrm{d}z$ is the integrated range of the ion (see [44]). For heating solid aluminum (at room temperature) over a range of ion mass from 4 amu (helium) to 126 amu (iodine), the energy loss at the peak of the $\mathrm{d}E/\mathrm{d}X$ curve ($\mathrm{d}E/\mathrm{d}X|_{\max}$) may be parameterized approximately as

$$\frac{1}{Z^2}\left.\frac{\mathrm{d}E}{\mathrm{d}X}\right|_{\max} \simeq 1.09\,\frac{\mathrm{MeVcm}^2}{\mathrm{mg}}A^{-0.82}, \tag{10.20}$$

where Z and A are the ion nuclear charge and atomic mass, respectively. Expressing $\mathrm{d}E/\mathrm{d}X|_{\max}$ as a function of A yields

$$\left.\frac{\mathrm{d}E}{\mathrm{d}X}\right|_{\max} \simeq 0.35\,\frac{\mathrm{MeVcm}^2}{\mathrm{mg}}A^{1.07}. \tag{10.21}$$

Thus, the peak energy loss rate increases (nearly linearly) with ion atomic mass. Similarly, the ion energy E at the peak increases with ion mass nearly quadratically with A according to

$$E_{\max} \simeq 0.052\ \mathrm{MeV}A^{1.803}, \tag{10.22}$$

where $E_{\max}$ is E at $\mathrm{d}E/\mathrm{d}X|_{\max}$.

Target temperature uniformity is another important consideration. It has been pointed out [45] that target temperature uniformity can be maximized in simple planar targets if the particle energy reaches the maximum in the energy loss rate $\mathrm{d}E/\mathrm{d}X$ when the particle has reached the center of the foil. For any specified fractional deviation in target temperature (assuming the energy is deposited in a time short so that no hydrodynamic, radiative, or other cooling has occurred) one can

UNCORRECTED PROOF

determine the energy at which the ion must enter and exit the foil. From the curves of $\mathrm{d}E/\mathrm{d}X$ [44] we find that for the entrance energy to have less than a 5% lower energy loss rate relative to the peak in $\mathrm{d}E/\mathrm{d}X$, $\Delta E/E \lesssim 1.0$, where ΔE is the difference in ion energy between entering and exiting the foil, and E is the energy at which $\mathrm{d}E/\mathrm{d}X$ is maximum. The spatial width of the foil Δz, for a 5% temperature non-uniformity is then given by:

$$\Delta z = \frac{\Delta E}{\rho \left.\frac{\mathrm{d}E}{\mathrm{d}X}\right|_{\max}} \simeq 0.77\ \mu\ A^{0.733} \left(\frac{\rho_{\mathrm{al}}}{\rho}\right) \tag{10.23}$$

Here, we used $\rho_{\mathrm{al}} = 2.7$ g/cm^3 to convert the range into a physical distance. So by using materials of low density such as metallic foams, for example, the width of the foil can be relatively large, which allows longer heating times and accesses interesting densities.

The sound speed c_s is given by $c_s = (\gamma P/\rho)^{1/2} = (\gamma[\gamma - 1]U/\rho)^{1/2}$. Here, γ is the thermodynamic parameter equal to the ratio of specific heats. For an instantaneously heated target a rarefaction wave propagates inward at about c_s while matter flows outward at about $3c_s$ (for a monatomic gas) [46]. Thus, for measurement of material properties, heating needs to occur on a time scale such that the rarefaction wave does not progress so far as to render the full density region of the foil smaller than some minimum diagnosable spatial scale over the duration of the pulse.

In order to calculate more accurately the sound speed and the temperature achieved in the heating, one needs to understand the relation between energy density and target temperature. For a perfect ionized gas, the energy density is $(3/2)(1 + Z^*)(nkT)$ where Z^* is the ionization state, and n is the number density of atoms plus ions. However for solids, interaction energy of the atoms in the solid must be included, and typically for WDM the ionization state is low. For solids, the energy density is often well approximated by $3nkT$. As a first estimate, we assume $3nkT$ since we are normally interested in material with $Z^* \sim 1$. We may compare with models developed by Zeldovich and Raizer and summarized [47] or by using the Thomas Fermi model for calculating the distribution of electrons within an atom (see [48] and references therein for a description).

Using the scaling described above for ion beam stopping, the time scale for hydrodynamic expansion, and the equation of state, we are able to make estimates of the required beam parameters for exploring the Warm Dense Matter regime. Table 10.1 gives examples of requirements for Ne^{+1} ($A = 20.17$) at foil entrance energy (E_{incident}) of 19 MeV, The energy at the center of the foil (E_{center}) and the energy at the exit of the foil (E_{exit}) are listed in the caption to the table. Three different mass densities of Aluminum target are given: Solid density (2.7 g/cm^3) and 10 and 1% of solid, which can be produced by making an aluminum "foam." In turn for each target density, three target temperatures are shown. The table is based on a minimum diagnosable length scale $\Delta z_{\min}$ of 40 μ. It is clear from the table that solid density, although resulting in the highest energy density, requires very short pulse durations, because the foil width is smaller than $\Delta z_{\min}$ and only a

UNCORRECTED PROOF

Table 10.1 Target parameters for a Neon beam ($Z = 10$, $A = 20.18$, $E_{\text{incident}} = 20.1$ MeV, $E_{\text{center}} = 12.1$ MeV, $E_{\text{exit}} = 7.7$ MeV, and $\Delta z_{\min} = 40\ \mu$ (from [49])

ρ (g/cm^3)(% solid)	0.027 (1%)			0.27 (10%)			2.7 (100%)		
Foil thickness (μ)	480			48			4.8		
kT (eV)	3.1	4.8	15	4.2	7.3	18	5.9	12	22
Z^*	1.1	2.1	2.7	0.56	1.7	2.6	0.56	1.2	2.5
$\Gamma_{ii} = Z^2 e^2 n_i^{1/3}/kT$	0.45	1.1	0.95	0.30	0.63	1.4	0.30	0.70	1.6
$N_{\text{ions}}/(r_{\text{spot}})^2/10^{12}$	1	3	10	1	3	10	1	3	10
Δt ns	84	48	27	3.8	2.2	1.2	0.04	0.03	0.014
U(J/m^3)/10^{11}	0.15	0.045	0.15	0.15	0.45	1.5	1.5	4.5	15

small rarefaction wave propagation distance is allowed. But for the 1 and 10% cases, the foil is larger than $\Delta z_{\min}$, so that the rarefaction wave propagation distance can be 10's or 100's of microns, with concomitantly longer pulse duration. In all cases the plasma temperature is in the few to tens of eV, and the required number of particles is in the order of 10^{12}–10^{13} particles, for equivalent focal spot radii of 1 mm.

We may make simple estimates for the contribution to the spot size from chromatic effects (i.e. for the effects of a velocity spread) from particular optical systems, under the assumption that a beam plasma neutralizes both a drift compression region and the final focus. Here we choose a "thick" solenoidal lens in which a beam enters a solenoid with zero convergence angle and focuses to a spot within the solenoid. The focused beam can be shown to have a radius from emittance and chromatic effects r_{spot} given approximately by:

$$r_{\text{spot}}^2 \simeq \left(\frac{\pi r_0}{2}\right)^2 \left(\frac{\Delta v_{\text{spread}}}{v}\right)^2 + \left(\frac{2\varepsilon_x f}{\pi r_0}\right)^2 \tag{10.24}$$

Here, f is the focal length, i.e., the distance from the entrance of the solenoid to the focal spot, and ε_x is the beam emittance. Also, r_{spot} and r_0 are the beam radii ($= 2^{1/2}\langle r^2\rangle^{1/2}$) at the focal spot and entrance to the solenoid respectively, and $\varepsilon_x = 4(\langle x^2\rangle\langle x'^2\rangle - \langle xx'\rangle^2)^{1/2})$ is the unnormalized emittance. The quantity r_{spot} is minimum when $r_0^2 = (2/\pi)\varepsilon_x f/(\Delta v_{\text{spread}}/v)$ and has the value given by

$$r_{\text{spot}}^2 = 2\varepsilon_x f \frac{\Delta v_{\text{spread}}}{v}. \tag{10.25}$$

Simulations [50, 51] and analysis [43] shows that the beam intensity is not uniformly distributed over the spot radius, but is peaked resulting in somewhat higher central intensities than would be inferred from Eq. (10.25). Other effects such as the defocusing effect from the induction buncher, and the physics of beam neutralization are considered in [52].

At minimum pulse duration a velocity "tilt" becomes a velocity spread, so achieving high beam intensity will limit the velocity tilt.

It is apparent from Eq. (10.25) that a large velocity spread has deleterious effects in the focusing. Thus a larger velocity tilt will allow a shorter pulse but will yield

UNCORRECTED PROOF

a large overall spot. If the longitudinal emittance is small a larger velocity tilt is not needed to achieve the short pulse duration. Thus to obtain a small spot there are tradeoffs that can be made between longitudinal and transverse emittance; a different optimization might be made if one is easier to minimize than the other. This may be made more explicit by expressing Eq. (10.25) in terms of the transverse and longitudinal normalized emittances:

$$r_{\text{spot}}^2 = \frac{4\varepsilon_{nx}\varepsilon_{nz} f}{3^{1/2}\beta^3 c\Delta t} \tag{10.26}$$

Here, ε_{nx} is the normalized x-emittance ($= \beta\varepsilon_x$) and ε_{nz} is the normalized z (longitudinal) emittance (defined here as $= 3\beta(\langle z^2\rangle\langle z'^2\rangle - \langle zz'\rangle^2)^{1/2}$), f is the final focal length, β is the final velocity in units of c and Δt is the final pulse duration. A prime indicates derivative with respect to path length.

We may use the ion stopping equations, together with injector and final focus equations to examine the overall target performance as a function of ion energy, mass and other parameters. At the injector end, the normalized emittance may (ideally) be related to the temperature T_s and radius r_b of the source (cf. Eq. (9.9)):

$$\begin{aligned}\varepsilon_{nx} &= 2r_b\left(\frac{kT_s}{mc^2}\right)^{1/2}\\ &= 0.81\ \text{mm-mrad}\left(\frac{r_b}{4\ \text{cm}}\right)\left(\frac{20.1}{A}\right)^{1/2}\left(\frac{kT_s}{2\ \text{eV}}\right)^{1/2}\end{aligned} \tag{10.27}$$

Even if the injector emittance is dominated by optical aberrations an effective temperature may be used in Eq. (10.27). To avoid voltage breakdown, the diode gap distance d must be sufficiently large (cf. Eq. (9.7)):

$$d = 0.01\ \text{m}\left(\frac{V_d}{100\ \text{kV}}\right)^2 \quad \text{if } d > 1\ \text{cm} \tag{10.28}$$

Since we are considering large currents, $d > 1$ cm is appropriate, we may combine Eqs. (10.27) and (10.28) to obtain an equation for the final emittance

$$\varepsilon_f = 29\ \text{mm-mrad}\left(\frac{4}{\Delta}\right)\left(\frac{kT_s}{2\ \text{eV}}\right)\left(\frac{V_d}{400\ \text{kV}}\right)^2\left(\frac{20\ \text{MeV}}{qV_f}\right)^{1/2}. \tag{10.29}$$

The Child-Langmuir current is (cf. Eq. (9.15))

$$\begin{aligned}I &= \left(\frac{4\pi\epsilon_0}{9}\right)\left(\frac{2q}{m}\right)^{1/2}\left(\frac{V_d^{3/2}}{\Delta^2}\right)\\ &= 0.6\,A\left(\frac{20}{A/q}\right)^{1/2}\left(\frac{4}{\Delta}\right)^2\left(\frac{V_d}{400\ \text{kV}}\right)^{3/2}.\end{aligned} \tag{10.30}$$

UNCORRECTED PROOF

Here $\Delta = d/r_b$ which is usually in the range 2.5–8 to minimize nonlinearities. Here we choose 4 as a typical nominal value. The total charge $I\Delta t$ is

$$I\Delta t = 0.12\ \mu\text{C}\left(\frac{20}{A/q}\right)^{1/2}\left(\frac{4}{\Delta}\right)^{2}\left(\frac{V_d}{400\ \text{kV}}\right)^{3/2}\left(\frac{\Delta t_d}{200\ \text{ns}}\right), \tag{10.31}$$

and the final pulse energy E_{pulse} is

$$E_{\text{pulse}} = V_f I\Delta t = 2.4\ \text{J}\left(\frac{20}{A/q}\right)^{1/2}\left(\frac{4}{\Delta}\right)^{2}\left(\frac{V_d}{400\ \text{kV}}\right)^{3/2} \times\left(\frac{\Delta t_d}{200\ \text{ns}}\right)\left(\frac{V_f}{20\ \text{MV}}\right). \tag{10.32}$$

Equations (10.27), (10.28), (10.29), (10.30), and (10.31) describe the phase space and total charge obtainable from an injector. The final target energy density U can be calculated from the total pulse energy, spot radius, foil thickness,

$$U = \frac{2V_f I\Delta t}{3\pi r_{\text{spot}}^2\Delta z} \tag{10.33}$$

and the target temperature can be expressed as:

$$\begin{aligned} kT_{\text{targ}} &\simeq \frac{2UA_{\text{targ}}m_{\text{amu}}}{3(Z^*+1)\rho} \\ &= 3\ \text{eV}\left(\frac{A_{\text{targ}}}{27}\right)\left(\frac{3}{Z^*+1}\right)\left(\frac{2\ \text{eV}}{kT_s}\right)^{1/2}\left(\frac{0.05}{\Delta v/v_{\text{tilt}}}\right)\left(\frac{q}{1}\right)^{0.32} \\ &\left(\frac{4}{\Delta}\right)\times\left(\frac{\Delta t_d}{200\ \text{ns}}\right)\left(\frac{V_d}{400\ \text{kV}}\right)^{-1/2}\left(\frac{V_f}{20\ \text{MV}}\right)^{0.815}\left(\frac{0.7\ \text{m}}{f}\right). \end{aligned} \tag{10.34}$$

Here m_{amu} is mass of an atomic mass unit. As discussed before, the target temperature in Eq. (10.34) can be achieved if the pulse duration is sufficiently small compared to the hydro time. The pulse duration at the target Δt_t can be expressed as

$$\begin{aligned} \Delta t_t &= \frac{2\varepsilon_{nz}Am_{\text{amu}}c}{qV_f\Delta v/v_{\text{tilt}}} \\ &= 1\ \text{ns}\left(\frac{\varepsilon_{nz}}{8\ \text{mm-mrad}}\right)\left(\frac{20\ \text{MeV}}{V_f}\right)\left(\frac{A/q}{20}\right)\left(\frac{0.05}{\Delta v/v_{\text{tilt}}}\right), \end{aligned} \tag{10.35}$$

where $\Delta v/v_{\text{tilt}}$ is the head-to-tail tilt imposed on the beam during final drift compression.

UNCORRECTED PROOF

These equations give estimates of the requirements for an induction linac (or any pulsed ion beam driver) using Bragg peak heating, neutralized drift compression and final solenoidal focus for the purpose of investigating Warm Dense Matter. Other concepts which choose different technological assumptions (for example, the use of time-dependent focusing) can change the requirements on the beam.

Experiments [53] using the technique of compressing [54] and focusing an ion beam in a neutralizing plasma to heat up targets began in 2009 on the NDCX I experiment at LBNL [55]. These experiments used 300–350 keV singly charged potassium ion beam, with a 30 A, 120 ns pulse section of the several microsecond pulse, that was compressed by a factor ∼60 to a 2 ns pulse. The velocity tilt was imparted by a separate induction buncher after a four solenoid transport section. A 1–2 m drift section followed during which plasma was injected by means of a ferro-electric plasma source. Four cathodic arc plasma sources, pointing upstream from beyond the final focus solenoid, supplied plasma into the solenoid and final focus region. Much of the several microsecond pre-pulse could be used to heat the ion beam because the hydrodynamic motion was not significant, until vaporization occurred. NDCX I has reached target temperatures of about 0.5 eV. The experiment is shown in Fig. 10.9.

A follow on experiment, NDCX II was designed [56, 57] to reach WDM conditions using the Bragg peak of Li. The design called for an ion energy of 2–3 MeV, and total charge of 0.03–0.06 μC in a compressed pulse 1 ns in duration. A CAD drawing of the experiment is shown in Fig. 10.10. The plan called for reusing the induction cores and other hardware including the pulse power systems from the decommissioned LLNL ATA accelerator. The NDCX II accelerator is under construction at the time of this writing.

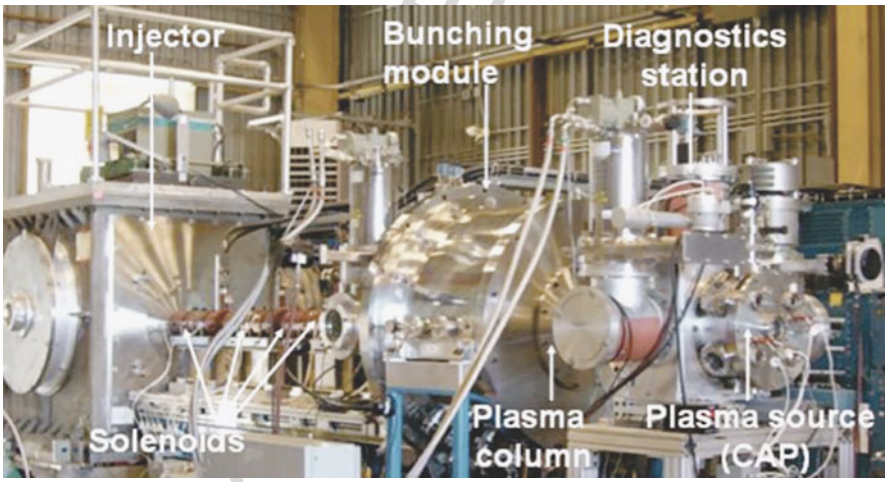

This figure will be printed in b/w

Fig. 10.9 The neutralized drift compression experiment (NDCX I) at LBNL in 2009

UNCORRECTED PROOF

This figure will be printed in b/w

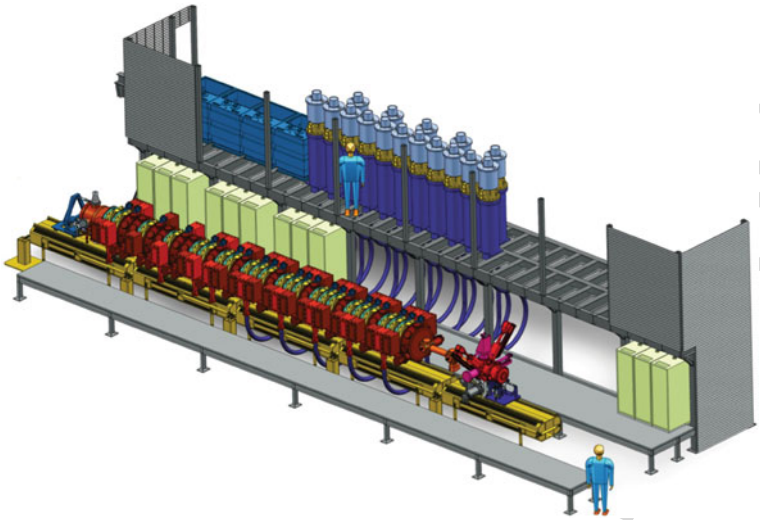

Fig. 10.10 A CAD drawing of the NDCX II experiment planned for completion at LBNL in 2012

10.2.2 Neutron Spallation Source

Neutron scattering science requires intense sources since the interaction of neutrons with matter is relatively weak. Research reactors have been used as sources for many years. The ILL reactor at Grenoble represents the most advanced capability, producing a neutron flux over 10^{15} cm^{-2}s^{-1}. With research reactors choppers are required to convert the continuous neutron flux into short pulses for time-of-flight separation into a monochromatic neutron beam. Pulsed accelerator-based spallation sources have now been shown to be viable options with significant advantages over reactors in the efficiency of neutron utilization and the avoidance of serious security and environmental protection issues. Indeed two major new facilities designed for average beam powers of order 1 MW are now beginning operation: the SNS in the USA [58] and J–PARC [59] in Japan. Both of these facilities are so-called "short pulse" (SP) spallation sources: a millisecond time scale negative ion beam from an RF linac is stacked in a storage ring and then extracted to deliver a sub-μs proton beam on a target. An alternate accelerator-based neutron source concept is the so-called "long pulse" (LP) spallation source. In this approach a few millisecond proton beam pulse is accelerated in an RF linac and sent directly to a target. The neutron pulse produced in the target can then be chopped to an even shorter duration (if desired) as in the reactor approach. This approach is currently being considered in Europe as the basis for a next generation spallation source that will deliver a time average neutron flux equivalent to the ILL reactor (the 5 MW ESS).

A short pulse spallation neutron source requires delivery of intense ~1 GeV proton pulses of < 1 μs duration on a target at a typical repetition rate of 50–60 Hz. The fact that these parameters were a "natural fit" to the capabilities of induction linac

UNCORRECTED PROOF

technology was noted in the 1980s by Denis Keefe [60]. The relative "immaturity" of induction linac technology for accelerating protons at the GeV scale prevented its serious consideration as an option at that time. If induction technology began to be applied more widely, however, with some of the new applications discussed in this book, this situation might change at some time in the future.

The great disparity between the maturity of negative ion RF accelerators and storage rings, and ~1 GeV induction accelerators operating at high CW power levels and accelerating protons, makes it difficult to do an honest comparison between the two for this application. On fundamental grounds, however, it would certainly seem probable that going through all the manipulations involved in accelerating a millisecond negative ion pulse in an RF accelerator, stripping and stacking them as protons in a storage ring, and extracting the protons in sub microsecond pulses will ultimately limit the scaling of this technical approach to higher powers cost effectively. In fact the intensity limitation on the number of protons per bunch in a storage ring is a serious constraint in the RF approach, and it appears to have been a major factor in the recent decision by the European ESS team to choose the LP approach for a 5 MW capability.

To illustrate the general parameter range involved, consider a 5 MW spallation source (a next generation facility like the ESS). Assuming 1 GeV protons (for efficient neutron production), 100 μ C pulses are required assuming a repetition rate of 50 Hz. As an example (not optimum necessarily), a single channel 3 T solenoid transport system can transport a proton line charge density of 2.6 μ C/m assuming a beam radius of 1.5 cm. The beam pulse length would then be 38 m through the accelerator. The injector would need to produce a 60 A, 1.6 μs proton beam pulse. These injector parameters are not unreasonable based on MFE neutral beam source developments in the 1980s, but this area clearly represents one of the developments that would be required. At the accelerator output, the pulse length would be about 160 ns and the current would be 600 amps. Note that the pulse length is less than a microsecond over most of the machine. The short pulse length and high beam current facilitate the design of high efficiency, high gradient induction cells, as in the HIF application.

Spallation sources do need to have very high reliability and availability to be accepted by the neutron scattering community. The beam transport also needs to be very low loss to avoid issues of remote handling and the associated costs. It therefore will likely remain the case that serious consideration of induction linacs in this application will not occur without significant demonstrations at an appropriate scale. There is obviously a high degree of synergism with the HIF system, so one avenue might be making the next major HIF experimental facility compatible with demonstrating proton beam acceleration as an SNS prototype.

References

1. Initial research on accelerators for heavy ion fusion can be found in the early workshops on the topic: ERDA summer study of heavy ions for inertial fusion, Lawrence Berkeley Laboratory, LBL-5543 (1976); Proceedings of the HIF Workshop, Brookhaven National Laboratory,

UNCORRECTED PROOF

17 Oct., 1977, BNL-50769 (1977); Proceedings of the HIF Workshop, Argonne National Laboratory, 19–26 Sep., 1978, ANL-79-41 (1978); Proceedings of the HIF Workshop, Berkeley, CA, 29 Oct.–9 Nov., 1979, Lawrence Berkeley Laboratory, LBL-10301 (1980); Proceedings of more recent heavy ion fusion symposia can be found in: Particle Accelerators 37–38 (1992); Il Nuovo Cimento A 107 (1993); Fusion Engineering and Design 32–33 (1996); Nucl. Instr. Meth. A 415 (1998), 464 (2001), 544 (2005), 577 (2007) and 606 (2009).

2. I. Hofmann and G. Plass. (editor). The HIDIF-Study. Technical Report GSI-98-06, GSI, 1998.
3. J. Lindl. *Inertial Confinement Fusion: the Quest for Ignition and Energy Gain Using Indirect Drive*. Springer, New York, NY, 1998.
4. B. Logan, L. Perkins, and J. Barnard. Direct Drive Heavy-Ion-Beam Inertial Fusion at High Coupling Efficiency. *Phys. Plasmas*, 15:072701, 2008.
5. M. Tabak and D. Callahan-Miller. Design of a Distributed Radiator Target for Inertial Fusion Driven from Two Sides with Heavy Ion Beams. *Phys. Plasmas*, 5:1895, 1998.
6. D. Callahan-Miller and M. Tabak. Progress in target physics and design for heavy ion fusion. *Phys. Plasmas*, 7:2083, 2000.
7. D. Callahan, M. Herrmann, and M. Tabak. Progress in heavy ion target capsule and hohlraum design. *Laser Part. Beams*, 20:3:405–410, 2002.
8. D. Callahan, D. Clark, A. Koniges, M. Tabak, G. Bennett, M. Cuneo, R. Vesey, and A. Nikroo. Heavy-Ion Target Physics and Design in the USA. *Nucl. Inst. Meth. A*, 544:9–15, 2005.
9. M. Reiser. *Theory and Design of Charged Particle Beams*, Wiley, New York, NY, 1994.
10. J. Barnard, A. Brooks, J. Clay, F. Coffield, F. Deadrick, L. Griffith, A. Harvey, D. Judd, H. Kirbie, V. Neil, M. Newton, A. Paul, L. Reginato, G. E. Russel, W. Sharp, H. Shay, J. Wilson, and S. Yu. Study of Recirculating Induction Accelerators as Drivers for Heavy Ion Fusion. Technical Report UCRL-LR-108095, Lawrence Livermore National Laboratory, 1991.
11. D. Neuffer. Geometric Aberrations in Final Focussing for Heavy Ion Fusion. Technical Report ANL-79-41, Argonne National Laboratory, 1978.
12. D. Ho, I. Haber, and K. Crandell. Octupole Correction of Geometric Aberrations for High-Current Heavy Ion Beams. *Part. Accel.*, 36:141–160, 1991.
13. D. Judd. Phase space constraints on some heavy-ion inertial-fusion igniters and example designs of 1 mj rf linac systems. Technical Report ANL-79-41, p. 237, Argonne National Laboratory, 1978.
14. D. Grote, A. Friedman, G. Craig, W. Sharp, and I. Haber. Progress Toward Source-to-Target Simulations. *Nucl. Instr. Meth. A*, 464:563, 2001.
15. J. Barnard, R. Bangerter, A. Faltens, T. Fessenden, A. Friedman, E. Lee, B. Logan, S. Lund, W. Meier, W. Sharp, and S. Yu. Induction Accelerator Architectures for Heavy Ion Fusion. *Nucl. Inst. Meth. A*, 415:218, 1998.
16. E. Lee. Solenoid Transport for Heavy Ion Fusion. *Nucl. Inst. Meth. A*, 544:187–193, 2005.
17. S. Yu, R. Abbott, R. Bangerter, J. Barnard, R. Briggs, D. Callahan, C. Celata, R. Davidson, C. Debonnel, S. Eylon, A. Faltens, A. Friedman, D. Grote, P. Heitzenroeder, E. Henestroza, I. Kaganovich, J. Kwan, J. Latkowski, E. Lee, B. Logan, P. Peterson, D. Rose, P. Roy, G.-L. Sabbi, P. Seidl, W. Sharp, and D. Welch. Heavy Ion Fusion (HIF) Driver Point Designs. *Nucl. Inst. Meth. A*, 544:294–299, 2005.
18. S. Yu, W. Meier, R. Abbott, J. Barnard, T. Brown, D. Callahan, C. Debonnel, P. Heitzenroeder, J. Latkowski, B. Logan, S. Pemberton, P. Peterson, D. Rose, G-L. Sabbi, W. Sharp, and D. Welch. An Updated Point Design for Heavy Ion Fusion. *Fusion Sci. Technol.*, 44:266–273, 2003.
19. S. Yu, J. Barnard, R. Briggs, D. Callahan, C. Celata, L. Chao, R. Davidson, C. Debonnel, S. Eylon, A. Friedman, E. Henestroza, I. Kaganovich, J. Kwan, E. Lee, M. Leitner, B. Logan, W. Meier, P. Peterson, L. Reginato, D. Rose, P. Roy, W. Waldron, and D. Welch. Towards a Modular Point Design for Heavy Ion Fusion. *Fusion Sci. Technol.*, 47:621–625, 2005.
20. T. Godlove. Heavy Ion Recirculating Induction Linac Studies. *Part. Accel.*, 37–38:439–451, 1992.
21. M. Reiser. Periodic Focusing of Intense Beams. *Part. Accel.*, 8:167–182, 1978.

UNCORRECTED PROOF

22. M. G. Tiefenback. *Space-Charge Limits on the Transport of Ion Beams in a Long Alternating Gradient System*. PhD thesis, University of California at Berkeley, CA, 1986.
23. I. Hofmann, L. Laslett, L. Smith, and I. Haber. Stability of the Kapchinskij-Vladimirskij (K-V) Distribution in Long Periodic Transport Systems. *Part. Accel.*, 13:145–178, 1983.
24. S. Lund and S. Chawla. Space-Charge Transport Limits of Ion Beams in Periodic Quadrupole Focusing Channels. *Nucl. Inst. Meth. A*, 561:203–208, 2006.
25. R. Bangerter. The Induction Approach to Heavy-Ion Inertial Fusion: Accelerator and Target Considerations. *Il Nuovo Cimento*, 106:1445, 1993.
26. W. Meier, R. Bangerter, and A. Faltens. An Integrated Systems Model for Heavy Ion Drivers. *Nucl. Inst. Meth. A*, 415:249–255, 1997.
27. C. Celata. Scientific Issues in Future Induction Linac Accelerators for Heavy-Ion Fusion. *Nucl. Inst. Meth. A*, 544:142–150, 2005.
28. P. Seidl, C. Celata, A. Faltens, W. Fawley, W. Ghiorso, and S. Maclaren. Progress on the Scaled Beam Combining Experiment at LBNL. *Nucl. Inst. Meth. A*, 415:243–248, 1998.
29. J.-L. Vay, M. Furman, P. Seidl, R. Cohen, A. Friedman, D. Grote, M. Kireeff Covo, A. Molvik, P. Stoltz, S. Veitzer, and J. Verboncoeur. Studies of the Physics of Space-Charge-Dominated Beams for Heavy Ion Inertial Fusion. *Nucl. Inst. Meth. A*, 577, 2007.
30. A. Molvik, M. Kireeff Covo, R. Cohen, A. Friedman, S. Lund, W. Sharp, J.-L. Vay, D. Baca, F. Bieniosek, C. Leister, and P. Seidl. Quantitative Experiments with Electrons in a Positively Charged Beam. *Phys. Plasmas*, 14:056701, 2007.
31. W. Fawley, T. Garvey, S. Eylon, E. Henestroza, A. Faltens, T. Fessenden, K. Hahn, L. Smith, and D. Grote. Beam Dynamics Studies with the Heavy-Ion Linear Induction Accelerator MBE-4. *Phys. Plasmas*, 4:880, 1997.
32. B. Logan. Exploring a Unique Vision for Heavy Ion Fusion. Technical Report HIFAN, Lawrence Berkeley Laboratory, 2008.
33. T. Sangster, J. Barnard, T. Cianciolo, G. Craig, A. Friedman, D. Grote, E. Halaxa, R. Hanks, G. Kamin, H. Kirbie, B. Logan, S. Lund, G. Mant, A. Molvik, W. M. Sharp, S. Eylon, D. Berners, T. Fessenden, D. Judd, L. Reginato, H. Hopkins, A. Debeling, W. Fritz, and J. Meredith. Status of Experiments Leading to a Small Recirculator. *Nucl. Inst. Meth. A*, 415:310–314, 1998.
34. L. Ahle, T. Sangster, D. Autrey, J. Barnard, G. Craig, A. Friedman, D. Grote, E. Halaxa, B. Logan, S. Lund, G. Mant, A. Molvik, W. Sharp, S. Eylon, A. Debeling, and W. Fritz. Current Status of the Recirculator Project. In *Proceedings of the 1999 Particle Accelerator Conference*, pages 3248–3250, New York, NY, 29 March–2 April 1999.
35. R. Kishek, S. Bernal, Y. Cui, T. Godlove, I. Haber, J. Harris, Y. Huo, H. Li, P. O'Shea, B. Quinn, M. Reiser, M. Walter, M. Wilson, and Y. Zou. HIF Research on the University of Maryland Electron Ring (UMER). *Nucl. Inst. Meth. A*, 544:179–186, 2005.
36. J. Wang, S. Bernal, P. Chin, T. Godlove, I. Haber, R. Kishek, Y. Li, M. Reiser, M. Venturini, R. York, and Y. Zou. Studies of the Physics of Space-Charge-Dominated Beams for Heavy Ion Inertial Fusion. *Nucl. Inst. Meth. A*, 415, 1998.
37. C. Celata, F. Bieniosek, and A. Faltens. Transverse Splitting of Intense Heavy-Ion Beams in the IRE and in an HIF Driver. *Nucl. Inst. Meth. A*, 464:533–538, 2001.
38. National Research Council Committee on High Energy Density Physics, Plasma Science Committee. *Frontiers in High Energy Density Physics: the X-Games of Contemporary Science*. National Academies Press, Washington, DC, 2003.
39. National Task Force on High Energy Density Physics. Frontiers for Discovery in High Energy Density Physics. ~~Technical Report ??,~~ Office of Science and Technology Policy, National Science and Technology Council Interagency Working Group on the Physics of the Universe, 2004. AQ3
40. R. More, H. Yoneda, and H. Morikami. Short Pulse Lasers and Electron Dynamics in Warm Dense Matter. *J. Quant. Spectros. Radiat. Trans.*, 99:409–424, 2006.
41. T. Guillot. The Interiors of Giant Planets: Models and Outstanding Questions. *Annu. Rev. Earth Planet. Sci.*, 33:493–530, 2005.

UNCORRECTED PROOF

42. N. Tahir, A. Shutov, I. Lomonosov, A. Piriz, G. Wouchuk, C. Deutsch, D. Hoffmann, and V. Fortov. Numerical Simulations and Theoretical Analysis of High Energy Density Experiments at the Next Generation of Ion Beam Facilities at Darmstadt: The Hedgehob Collaboration. *High Energy Density Phys.*, 2:21–34, 2006.
43. J. Barnard, P. Seidl, J. Coleman, and D. Ogata. Estimates of Energy Fluence at the Focal Plane in Beams Undergoing Neutralized Drift Compression. In *Proceedings of the 2008 Linear Accelerator Conference*, page MOP031, Victoria, Canada, 28 Sept.–3 Oct. 2008.
44. L. Northcliffe and R. Schilling. Range and Stopping-Power Tables for Heavy Ions. *Nucl. Data Tables*, A7:233, 1970.
45. L. Grisham. Moderate Energy Ions for High Energy Density Physics Experiments. *Phys. Plasmas*, 11:5727, 2004.
46. L. Landau and E. Lifshitz. *Fluid Mechanics*. Pergamon Press, New York, NY, 1959. see Chapter 10.
47. R. Harrach and F. Rogers. Comparison of Two Equation-of-State Models for Partially Ionized Aluminum: Zeldovich and Raizer's Model Versus the Activity Expansion Code. *J. Appl. Phys.*, 52:5592, 1981.
48. S. Atzeni and J. Meyer ter Vehn. *The Physics of Inertial Fusion: Beam Plasma Interaction, Hydrodynamics, Hot Dense Matter*. Oxford University Press, Inc, New York, NY, 2004.
49. J. Barnard, R. Briggs, D. Callahan, R. Davidson, A. Friedman, L. Grisham, E. Lee, R. Lee, B. Logan, C. Olson, D. Rose, P. Santhanam, A. Sessler, J. Staples, M. Tabak, D. Welch, J. Wurtele, and S. Yu. Accelerator and Ion Beam Tradeoffs for Studies of Warm Dense Matter. In *Proceedings of the 2005 Particle Accelerator Conference*, pages 2568–2570, Knoxville, TN, 16–20 May 2005.
50. D. Welch, J. Coleman, P. Seidl, P. Roy, E. Henestroza, E. Lee, A. Sefkow, E. Gilson, T. Genoni, and D. Rose. Source-to-Target Simulation of Simultaneous Longitudinal and Transverse Focusing of Heavy Ion Beams. *Phys. Rev. Special Topics – Accelerators and Beams*, 11, 2008.
51. A. Sefkow, R. Davidson, I. Kaganovich, E. Gilson, P. Roy, P. Seidl, S. Yu, D. Welch, D. Rose, and J. Barnard. Optimized Simultaneous Transverse and Longitudinal Focusing of Intense Ion Beam Pulses for Warm Dense Matter Applications. *Nucl. Inst. Meth. A*, 577:289–297, 2007.
52. I. Kaganovich, R. Davidson, M. Dorf, E. Startsev, A. Sefkow, J. Barnard, A. Friedman, E. Lee, S. Lidia, B. Logan, P. Roy, P. Seidl, and D. Welch. Designing Neutralized Drift Compression for Focusing of Intense Ion Beam Pulses in Background Plasma. In *Proceedings of the 2009 Particle Accelerator Conference*, page TH3GA103, Vancouver, Canada, 4–8 May 2009.
53. F. Bieniosek, E. Henestroza, M. Leitner, B. Logan, R. More, P. Roy, P. Ni, P. Seidl, W. Waldron, and J.Barnard. High-Energy Density Physics Experiments with Intense Heavy Ion Beams. *Nucl. Inst. Meth. A*, 606:146–151, 2009.
54. P. Roy, S. Yu, E. Henestroza, A. Anders, F. Bieniosek, J. Coleman, S. Eylon, W. Greenway, M. Leitner, B. Logan, W. Waldron, D. Welch, C. Thoma, A. Sefkow, E. Gilson, P. Efthimion, and R. Davidson. Drift Compression of an Intense Neutralized Ion Beam. *Phys. Rev. Lett.*, 95:234801, 2005.
55. P. Seidl, A. Anders, F. Bieniosek, J. Barnard, J. Calanog, A. Chen, R. Cohen, J. Coleman, M. Dorf, E. Gilson, D. Grote, J. Jung, M. Leitner, S. Lidia, B. Logan, P. Ni, P. Roy, K. Van den Bogert, W. Waldron, and D. Welch. Progress in Beam Focusing and Compression for Warm-Dense Matter Experiments. *Nucl. Inst. Meth. A*, 606:75–82, 2009.
56. A. Friedman, J. Barnard, R. Briggs, R. Davidson, M. Dorf, D. Grote, E. Henestroza, E. Lee, M. Leitner, B. Logan, A. Sefkow, W. Sharp, W. Waldron, D. Welch, and S. Yu. Toward a Physics Design for NDCX-II, an Ion Accelerator for Warm Dense Matter and HIF Target Physics Studies. *Nucl. Inst. Meth. Phys. Res. A*, 606:6–10, 2009.
57. A. Friedman, J. Barnard, R. Cohen, D. Grote, S. Lund, W. Sharp, A. Faltens, E. Henestroza, J.-Y. Jung, J. Kwan, E. Lee, M. Leitner, B. Logan, J.-L. Vay, W. Waldron, R. Davidson, M. Dorf, E. Gilson, and I. Kaganovich. Beam Dynamics of the Neutralized Drift Compression Experiment-II, a Novel Pulse-Compressing Ion Accelerator. *Phys. Plasmas*, ~~2010. in press.~~ AQ4

UNCORRECTED PROOF

58. S. Henderson. Spallation Neutron Source Progress, Challanges and Upgrade Options. In *Proceedings of the 2008 European Particle Accelerator Conference*, page 2892, Genoa, Italy, 23–27 June 2008.
59. M. Kinsho. J-PARC Progress and Challanges of Protron Synchrotrons. In *Proceedings of the 2008 European Particle Accelerator Conference*, page 2897, Genoa, Italy, 23–27 June 2008.
60. D. Keefe and E. Hoyer. Proton Induction Linacs as High-Intensity Neutron Sources. Technical Report LBL-12855; CONF-8106120-4, Lawrence Berkeley Lab, 1981.

UNCORRECTED PROOF

Chapter-10

Query No.	Query
AQ1	We have changed Fig. 10.6 as Fig. 10.5 as per caption. Please check and confirm.
AQ2	Please update the figure number in figure cross reference.
AQ3	Please provide the Technical Report No.
AQ4	Please update the reference (57) “Friedman, 2010”.

UNCORRECTED PROOF

Chapter 11
Induction Synchrotron

Ken Takayama

UNCORRECTED PROOF

The concept of a synchrotron employing induction acceleration devices is described [1]. The concept becomes more clear when one contrasts the *Induction Synchrotron* with an RF synchrotron, which has been employed in all high-energy circular accelerators since being independently invented by McMillan [2] and Veksler [3]. In the Induction Synchrotron, the accelerating devices of a conventional synchrotron, such as an RF cavity, are replaced with induction devices. Acceleration and longitudinal confinement of charged particles are realized with independently driven induction devices. This concept of separated-function longitudinal dynamics brings about a significant freedom of beam handling relative to conventional circular accelerators, typically in which radio-frequency waves in a resonant cavity simultaneously take both roles of acceleration and longitudinal confinement. Associated with this separated-function, various aspects are realized such as the formation of a *super-bunch*, which is an extremely long-bunch with a uniform line-density. Newly developed injection/extraction schemes, which make use of unique features of the Induction Synchrotron, are illustrated with the help of computer simulations. Longitudinal beam dynamics are unique as compared with RF synchrotrons. Elementary descriptions of barrier bucket acceleration are given. Transition crossing used to be one of the biggest issues in RF-synchrotrons. We contrast transition crossing in the RF and induction cases. It is found that the induction approach allows considerably more freedom to address issues. Technical details of key components of the induction accelerating cell and the switching power supply driving the cell are given.

11.1 Principle of Induction Synchrotron

The Induction Synchrotron employs induction cells for the acceleration and longitudinal confinement of charged particles. The two functions of acceleration and confinement can be independently achieved with induction step-voltages. This aspect

K. Takayama (✉)
High Energy Accelerator Research Organization (KEK), Tsukuba 305–0801, Japan
e-mail: ken.takayama@kek.jp

K. Takayama, R.J. Briggs (eds.), *Induction Accelerators*, Particle Acceleration and Detection, DOI 10.1007/978-3-642-13917-8_11,
© Springer-Verlag Berlin Heidelberg 2011

is an essential point why the Induction Synchrotron proposed by Takayama and Kishiro [1] is distinguished from the preceding concepts, such as recirculating LIAs, described in Chap. 2, or an Induction Synchrotron accelerator proposed by Putnam [4]. For the purpose of contrasting novel features of the Induction Synchrotron with the RF synchrotron, we present a brief review of the longitudinal beam dynamics in a conventional RF synchrotron. In the conventional RF synchrotron, the acceleration and longitudinal focusing are realized with radio-frequency waves (RF) in a well-known manner. Figure 11.1 shows the relation between a bunch of charged particles and the RF voltage in time. In the figure we assume that particles in the bunch have positive charge and the particle energy is below the transition energy.

A synchronous particle, which is located at the center of a bunch, is accelerated with a net magnitude of RF voltage, that is, $V_{\mathrm{RF}} \sin \phi_s$, where V_{RF} is the amplitude of the RF voltage and ϕ_s is called the synchronous phase. The energy of a synchronous particle is ramped with the magnetic guiding-fields to synchronously keep the bunch centered in the machine aperture. A particle in the bunch-head is accelerated less with respect to the synchronous particle, and conversely, a particle in the bunch-tail is accelerated more. Thus particles are focused towards the synchronous particle, while losing or gaining energy. All of the particles in the bunch are confined in the longitudinal direction. This focusing is provided by the inherent gradient in the RF voltage about the synchronous particle. All of the particles are simultaneously accelerated due to the voltage being positive for all. This is the well-known phase stability and a principle of resonant acceleration in the RF synchrotron [5]. In this sense, the RF synchrotron may be called a combined-function accelerator in the longitudinal direction. This principle was independently recognized by McMillan [2] and Veksler [3] in 1945. However, a gradient focusing force is not the only possible way to achieve the longitudinal confinement of the particles. Electric fields, which are generated at both ends of the beam bunch using opposite sign voltages, as shown in Fig. 11.2, are capable of providing longitudinal focusing forces. A particle entering into a negative-voltage region, after drifting through a zero-voltage region, is decelerated and turns back to move toward the synchronous particle. It passes by the synchronous particle, while drifting with a constant energy along the time axis or the orbit axis. Once it reaches the positive voltage region, it is gradually accelerated, and again turns back towards the synchronous particle at the center of the bunch. The above process repeats every cycle of longitudinal synchrotron oscillation as the

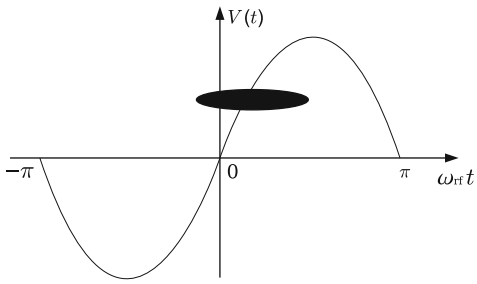

Fig. 11.1 RF voltage and a bunch of charged particles

UNCORRECTED PROOF

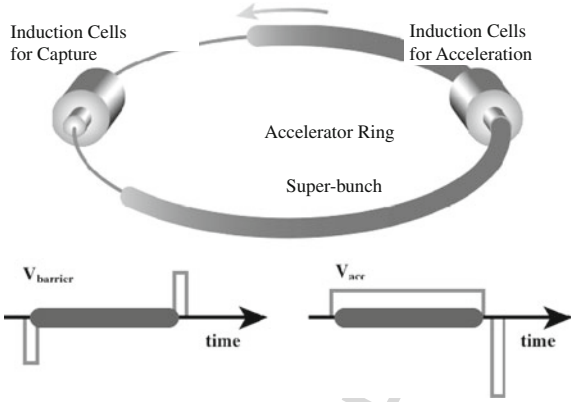

Fig. 11.2 Schematic view of the Induction Synchrotron and step-voltage profiles for confining and acceleration

bunch goes through induction cells along the accelerator circumference. The process is nothing but phase stability. If an accelerating voltage pulse covering the time-duration between the pair of voltage pulses for longitudinal confinement is provided, the coherent acceleration of all the particles in the bunch will be guaranteed.

11.1.1 Review of Phase Dynamics in an RF Synchrotron

Here, we present a mathematical formulation to quantitatively understand the essential differences of longitudinal beam dynamics in the RF synchrotron and the Induction Synchrotron. The synchrotron oscillation for both cases is derived from discrete acceleration equations presented below. We assume that the RF and induction devices are localized at specific positions of the accelerator ring. The particle energy E and phase ϕ are chosen as dynamical parameters to describe the particle motion. E is the total energy of the particle of interest right before entrance into an acceleration gap and ϕ is the RF phase that the particle sees while passing through the gap. Then we have

$$\begin{aligned}(\Delta E)_{n+1} &= (\Delta E)_n + eV_{\mathrm{RF}}(\sin\phi_n - \sin\phi_n^s),\\ \phi_{n+1} &= \phi_n + \frac{2\pi h\eta}{(\beta^s)^2 E^s}(\Delta E)_{n+1} + (\phi_{n+1}^s - \phi_n^s) + \Delta\phi_{\mathrm{RF},n+1},\end{aligned} \tag{11.1}$$

with

$$(\Delta E) = E - E^s, \qquad \phi = \omega_{\mathrm{RF}} t, \qquad \eta = \frac{1}{\gamma_{\mathrm{T}}^2} - \frac{1}{\gamma_s^2},$$

Here, the subscript n denotes the n-th turn and the superscript s refers to quantities associated with the ideal synchronous particle. h is the harmonic number, ω_{RF} and V_{RF} are the angular frequency and voltage of the RF, η is the so-called slippage factor, γ_{T} is the transition energy, and $\Delta\phi_{\mathrm{RF},n+1}$ is the shift of the RF phase which usually occurs at transition crossing. The set of the discrete equations are

UNCORRECTED PROOF

averaged over a time period for a single turn, $T_0 = 2\pi/\omega_0$, where ω_0 is the angular rotation frequency of the synchronous particle. Introducing a convenient variable, $W = \Delta E/\omega_{\mathrm{RF}}$, we obtain a continuous equation of motion:

$$\begin{aligned} \frac{\mathrm{d}W}{\mathrm{d}t} &= \frac{eV_{\mathrm{RF}}}{2\pi h}(\sin\phi - \sin\phi^s), \\ \frac{\mathrm{d}\phi}{\mathrm{d}t} &= \frac{\omega_{\mathrm{RF}}^2\eta}{(\beta^s)^2E^s}W. \end{aligned} \tag{11.2}$$

For small-amplitude oscillations, we can define the well-known synchrotron frequency as follows. The upper equation is expanded in terms of $\Delta\phi \equiv \phi - \phi^s$. Since $\sin\phi - \sin\phi^s = \sin(\Delta\phi + \phi^s) - \sin\phi^s \cong \Delta\phi\cos\phi^s + \sin\phi^s - \sin\phi^s$, Eq. (11.2) reduces to

$$\begin{aligned} \frac{\mathrm{d}W}{\mathrm{d}t} &\cong \frac{eV_{\mathrm{RF}}\cos\phi^s}{2\pi h}\Delta\phi, \\ \frac{\mathrm{d}\Delta\phi}{\mathrm{d}t} &\cong \frac{\omega_{\mathrm{RF}}^2\eta}{(\beta^s)^2E^s}W. \end{aligned} \tag{11.3}$$

Taking the time-derivative of the lower equation and instituting the upper equation, we have

$$\frac{d^2\Delta\phi}{\mathrm{d}t^2} = \frac{\omega_{\mathrm{RF}}^2\eta}{(\beta^s)^2E^s}\frac{\mathrm{d}W}{\mathrm{d}t} = \frac{eV_{\mathrm{RF}}\omega_{\mathrm{RF}}^2\eta\cos\phi^s}{2\pi h(\beta^s)^2E^s}\Delta\phi. \tag{11.4}$$

Here, temporal changes in other parameters except for W and $\Delta\phi$ are ignored. Thus, the synchrotron frequency is given as

$$\omega_s = \frac{\omega_{\mathrm{RF}}}{\beta^s}\sqrt{\frac{eV_{\mathrm{RF}}\eta\cos\phi^s}{2\pi hE^s}}. \tag{11.5}$$

The set of canonical equations in Eq. (11.2) can be obtained from the Hamiltonian,

$$H(\phi, W; t) = \frac{\omega_{\mathrm{RF}}^2\eta}{2(\beta^s)^2E^s}W^2 + \frac{eV_{\mathrm{RF}}}{2\pi h}\left[\cos\phi - \cos\phi^s + (\phi - \phi^s)\sin\phi^s\right]. \tag{11.6}$$

For a time-period sufficiently short, where temporal changes in the physics parameters for the synchronous particle are ignored, the Hamiltonian can be regarded as a constant of motion. We can obtain contour lines from $H(\phi, W; t) = H(\phi_0, W_0; t_0) = \text{const}$. A particle with a contour inside the separatrix shown in Fig. 11.3, is stably confined while accelerated. The area of the separatrix in phase space, is obtained by integrating the difference between the upper half and lower half of the phase volume in $\Delta p/p(\phi)$, bounded by the separatrix. The volume decreases with increasing magnitude of the synchronous phase ϕ^s, assuming the RF voltage V_{RF} remains constant. The phase-space area available for acceleration is much less

UNCORRECTED PROOF

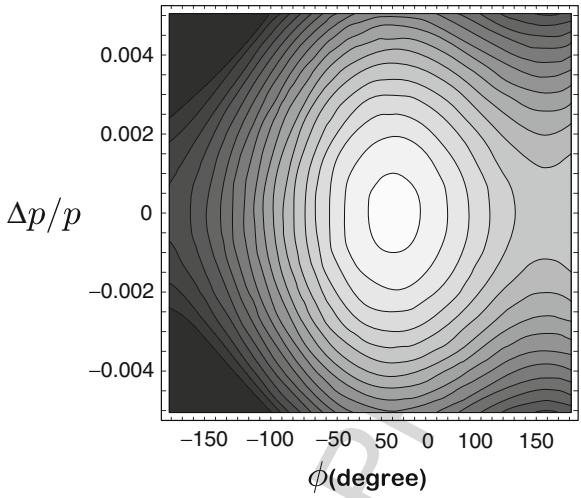

Fig. 11.3 Hamiltonian contours in phase-space and the RF bucket

than $2\pi(\Delta p/p)_{\max}$, where $(\Delta p/p)_{\max}$ is the maximum height of the separatrix, suggesting that the total number of particles subject to acceleration is notably limited due to Liouville's Theorem. This is a fundamental limit of the RF synchrotron.

As mentioned, the temporal change in the synchronous phase is determined by V_{RF} and the ramped bending fields $B(t)$. The synchronous particle is subject to the force-balance in the transverse direction, $m\gamma^s c\beta^s = e\rho B$. where ρ is the bending radius. γ^s is uniquely determined by

$$\gamma^s = \sqrt{1 + \left[\frac{e\rho}{mc}B\right]^2}. \tag{11.7}$$

Consistent with this equation, the synchronous energy $E^s (= \gamma^s mc^2)$ changes according to the discrete equation:

$$E^s_{n+1} = E^s_n + eV_{\mathrm{RF}}(t)\sin\phi^s_n.$$

Averaging over the rotation period, we obtain

$$\frac{\mathrm{d}E^s}{\mathrm{d}t} \cong \frac{E^s_{n+1} - E^s_n}{T_{n+1}} = \frac{eV_{\mathrm{RF}}(t)}{T_{n+1}}\sin\phi^s_n = \frac{eV_{\mathrm{RF}}(t)c\beta^s}{C_0}\sin\phi^s(t),$$
$$mc^2\frac{\mathrm{d}\gamma^s}{\mathrm{d}t} = \frac{eV(t)c\beta^s}{C_0}\sin\phi^s(t),$$

where C_0 is the ring circumference and $T_{n+1} = C_0/c\beta^s_{n+1}$. This equation gives

$$\phi^s(t) = \sin^{-1}\left[\frac{mcC_0\mathrm{d}\gamma^s/\mathrm{d}t}{eV_{\mathrm{RF}}(t)\beta^s}\right]. \tag{11.8}$$

UNCORRECTED PROOF

From Eq. (11.1) and Eq. (11.2), we have

$$\phi^s(t) = \sin^{-1}\left[\frac{\rho C_0}{V_{\mathrm{RF}}(t)}\frac{\mathrm{d}B}{\mathrm{d}t}\right]. \tag{11.9}$$

The change in $\phi^s(t)$ is significant in a rapid cycling synchrotron. For a slow cycling synchrotron, it is almost constant over the entire acceleration time-period, except at the beginning and last stage of the acceleration.

11.1.2 Phase Dynamics in the Induction Synchrotron

In an Induction Synchrotron, the required voltage pulses are generated by induction cells. Longitudinal bunch confinement and acceleration require different types of voltage-pulses, as shown in Fig. 11.2. The pair of the step-voltages shown in Fig. 11.2 has a focusing effect on the particles. A voltage with different polarity and the same height at the ends of the bunch is known as a barrier voltage. Barrier voltages were first proposed in the form of an isolated sinusoidal RF voltage by Griffin et al. [6], and experimentally realized by Blaskiewicz and Brennan [7]. In an Induction Synchrotron, the barrier voltage is introduced in the form of step-barrier voltages added to a circular ring. The step-voltage for acceleration has an asymmetric pulse profile, in which the pulse length has to be flexible to meet the various requirements of beam handling. The reset pulse may be short in time and high in voltage to keep the bunching factor large. It is noted that for both type of step voltages the integration of the voltage in time must always be zero in order to protect the magnetic core from saturating. The formulation for the step-barrier bucket acceleration is given below. The net voltage, which a particle entering into the devices with the phase $\phi = \omega_0 t$ experiences, is given by

$$V(\phi) = \begin{cases} V_{\mathrm{ac}} - V_{\mathrm{bb}} & (\phi^s - \Delta\phi/2) - \phi_{\mathrm{pulse}} \le \phi \le (\phi^s - \Delta\phi/2)\,, \\ V_{\mathrm{ac}} & (\phi^s - \Delta\phi/2) \le \phi \le (\phi^s + \Delta\phi/2)\,, \\ V_{\mathrm{ac}} + V_{\mathrm{bb}} & (\phi^s + \Delta\phi/2) \le \phi \le (\phi^s + \Delta\phi/2) + \phi_{\mathrm{pulse}}, \end{cases} \tag{11.10}$$

where V_{ac} is the accelerating voltage that is constant in time, V_{bb} is the barrier voltage, $\Delta\phi$ is the inner distance between the barrier voltages in phase, and ϕ_{pulse} is the barrier pulse length. Then, the changes in energy and phase are given by discrete equations analogous to Eq. (11.1),

$$\begin{aligned} (\Delta E)_{n+1} &= (\Delta E)_n + e\left[V(\phi_n) - V_{\mathrm{ac}}\right], \\ \phi_{n+1} &= \phi_n + \frac{2\pi\eta}{(\beta^s)^2 E^s}(\Delta E)_{n+1} + (\phi^s_{n+1} - \phi^s_n). \end{aligned} \tag{11.11}$$

UNCORRECTED PROOF

In the continuous limit, Eq. (11.11) becomes

$$\frac{\mathrm{d}W}{\mathrm{d}t} = \frac{e\,[V(\phi) - V_{\mathrm{ac}}]}{2\pi},$$
$$\frac{\mathrm{d}\phi}{\mathrm{d}t} = \frac{\omega_0^2 \eta}{(\beta^s)^2 E^s} W. \tag{11.12}$$

Here a convenient variable, $W = \Delta E/\omega_0$ is introduced. These canonical equations can be derived from the Hamiltonian,

$$H(\phi, W; t) = \frac{\omega_0^2 \eta}{2(\beta^s)^2 E^s} W^2 - \frac{e}{2\pi} \int^{\phi} \left[V(\phi') - V_{\mathrm{ac}}\right] \mathrm{d}\phi'. \tag{11.13}$$

The contours, which are orbits of the particles in phase space for fixed initial conditions, are shown in Fig. 11.4. The separatrix, which is called a barrier bucket, is clear. The contours inside the separatrix have a race-track, or almost rectangular, shape. Their figures in both sides are functions of the barrier parameters, such as V_{bb} and ϕ_{pulse}. Since $\Delta\phi$, by which the bunch-length is mainly determined, is a free parameter, one can control its length as desired insofar as it does not exceed the ring circumference and allows for reset time. This is a completely different feature from that of the RF-type synchrotron. This characteristic allows us, in principle, to have an almost circumference-long bunch in the accelerator ring, in principle. Such a long bunch has been called a *super-bunch*.

The synchrotron oscillation frequency for the Induction Synchrotron is defined in a similar manner to that in the RF synchrotron. However, the synchrotron frequency for a small amplitude does not make sense, because it fully depends on the longitudinal emittance as evaluated below. The synchrotron period consists of two parts.

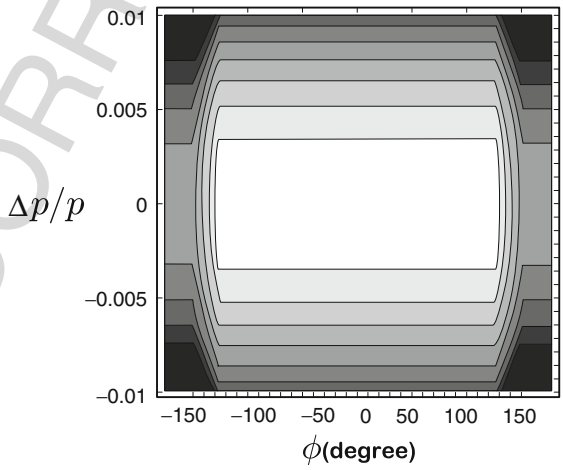

Fig. 11.4 Hamiltonian contours in phase space and the barrier bucket

UNCORRECTED PROOF

One results from the drift through the no-focusing region, and the other is from an oscillation period in a V-shape potential. Each of them is derived as follows. From Eq. (11.12), we straightforwardly have the drift time-period τ_d,

$$\tau_d = \frac{2\Delta\phi(\beta^s)^2 E^s}{\omega_0^2|\eta|W} = \frac{2\Delta t}{|\eta|(\Delta p/p)}, \tag{11.14}$$

where $\Delta t = \Delta\phi/\omega_0$ is the time between the barrier pulses. The time-period τ_b, within which a round trip in the V-shape potential takes, is obtained as follows. In this potential, the equations of motion are given by

$$\frac{\mathrm{d}W}{\mathrm{d}t} = -\frac{eV_{\mathrm{bb}}}{2\pi},$$
$$\frac{\mathrm{d}\phi}{\mathrm{d}t} = \frac{\omega_0^2\eta}{(\beta^s)^2 E^s}W.$$

The second-order differential equation for ϕ and its solution with an initial condition of $\phi(0) = 0$ are

$$\begin{aligned} \frac{\mathrm{d}^2\phi}{\mathrm{d}t^2} &= -\left(\frac{eV_{\mathrm{bb}}}{2\pi}\right)\left[\frac{\omega_0^2\eta}{(\beta^s)^2 E^s}\right] \equiv \kappa, \\ \phi(t) &= \frac{1}{2}\kappa t^2 + \dot{\phi}(0)t = t\left(\frac{1}{2}\kappa t + \dot{\phi}(0)\right). \end{aligned} \tag{11.15}$$

From Eq. (11.15), τ_b is obtained in the form of

$$\tau_b = -\frac{4\dot{\phi}(0)}{\kappa} = \left(\frac{8\pi}{eV_{\mathrm{bb}}}\right) = 4T_0\left[\frac{(\beta^s)^2 E^s}{eV_{\mathrm{bb}}}\right]\left(\frac{\Delta p}{p}\right). \tag{11.16}$$

Thus, the synchrotron period τ_{sync} in an Induction Synchrotron is given by

$$\tau_{\mathrm{sync}} = \tau_d + \tau_b = \frac{2\Delta t}{|\eta|(\Delta p/p)} + 4T_0(\beta^s)^2\left(\frac{E^s}{eV_{\mathrm{bb}}}\right)\left(\frac{\Delta p}{p}\right). \tag{11.17}$$

In the extreme relativistic limit with $\beta^s \cong 1$,

$$\tau_{\mathrm{sync}} \cong 2T_0\left[\left(\frac{\Delta t}{T_0}\right)\frac{1}{|\eta|(\Delta p/p)} + 2\left(\frac{E^s}{eV_{\mathrm{bb}}}\right)\left(\frac{\Delta p}{p}\right)\right]. \tag{11.18}$$

In most cases, the first term derived from the drift contribution dominates the synchrotron period. The synchrotron frequency is given by $f_s = 1/\tau_{\mathrm{sync}}$. The synchrotron frequency of a low-momentum particle is extremely small. It is shown later that this characteristic brings about a notable feature in phase mixing between particles, which takes a crucial role in coherent instabilities of a super-bunch.

UNCORRECTED PROOF

The barrier-bucket height is one of the useful parameters when one considers barrier-bucket acceleration. Its height is obtained from the Hamiltonian as follows. The bucket height $W_{\max}$ satisfies

$$H(\phi_{\max}, 0; 0) \equiv 0 = \frac{\omega_0^2 \eta}{2(\beta^s)^2 E^s} W_{\max}^2 + \Phi(0), \tag{11.19}$$

where

$$\Phi(0) = -\frac{e}{2\pi} V_{\mathrm{bb}} \phi_{\mathrm{pulse}} = -\frac{e V_{\mathrm{bb}} \omega_0 \tau_{\mathrm{pulse}}}{2\pi}.$$

Here, τ_{pulse} is the barrier pulse width. From Eq. (11.19), we have

$$\begin{aligned} W_{\max} &= \sqrt{\frac{(\beta^s)^2 E^s}{\omega_0 |\eta|} \frac{e V_{\mathrm{bb}} \tau_{\mathrm{pulse}}}{\pi}}, \\ \left(\frac{\Delta p}{p}\right)_{\max} &\equiv \frac{\omega_0 W_{\max}}{(\beta^s)^2 E^s} = \frac{\omega_0}{(\beta^s)^2 E^s} \sqrt{\frac{(\beta^s)^2 E^s}{\omega_0 |\eta|} \frac{e V_{\mathrm{bb}} \tau_{\mathrm{pulse}}}{\pi}} \\ &= \frac{1}{\beta^s} \sqrt{\frac{1}{|\eta|} \left(\frac{e V_{\mathrm{bb}}}{E^s}\right) \frac{2\tau_{\mathrm{pulse}}}{T_0}}. \end{aligned} \tag{11.20}$$

The expression in Eq. (11.20) suggests that the barrier bucket height is proportional to the square root of the product of the barrier voltage and its pulse length. It is useful to calculate the necessary value of $V_{\mathrm{bb}} \tau_{\mathrm{pulse}}$ for a given beam and ring parameters specified in terms of $(\Delta p/p)_{\max}$, η, E^s, and T_0.

11.2 Beam Handling

How is a super-bunch generated and accelerated in an Induction Synchrotron? What notable features of beam handling in the Induction Synchrotron are distinguished from that in the RF synchrotron? So far, a novel injection method, which makes the best use of step-barrier confining, has been proposed, and the feasibilities have been numerically investigated [1]. Here, the results of these studies are summarized. We consider a hadron accelerator complex, schematically shown in Fig. 11.5, consisting of an ion source, a pre-injector, such as RFQ, an H^- injector linac, a booster synchrotron, a second synchrotron, a third synchrotron, and a collider. Usually, the booster synchrotron is a rapid cycling synchrotron, and the following downstream synchrotrons are slow cycling synchrotrons. For simplicity, all synchrotrons belonging to the complex are assumed to be induction synchrotrons. For the convenience of readers, it is pointed out that FNAL has extensively developed beam handling techniques by the barrier voltages, which are generated in the wide-band RF cavity by a solid-state RF amplifier. Meanwhile, the idea of ion bunch confinement utilizing

UNCORRECTED PROOF

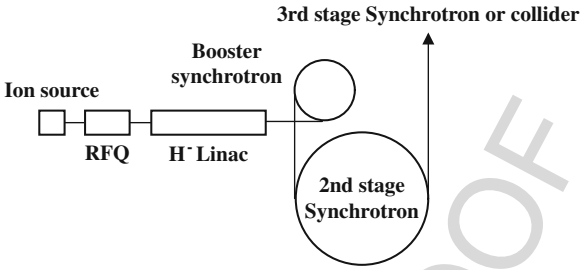

Fig. 11.5 Schematic view of a hadron induction accelerator complex

ear-like fields, which is described Sect. 9.2.2, have been proposed for the beam manipulation in a HIF beam driver. These beam handling techniques are similar to the barrier bucket beam manipulation given here, although there are big differences in their operational features or machine parameters.

11.2.1 Beam Injection

For a rapid cycling synchrotron, a symmetric painting scheme is the most promising injection method in order to increase the injected beam intensity. This method takes a maximum advantage of the capacity of the barrier bucket. At first we consider chopped-mode H^- injection. A macro-pulse is chopped from a continuous beam by a chopper located upstream of the injector H^- linac, so that its pulse-length meets the barrier-pulse duration in the first synchrotron (booster) of the accelerator complex. The bunching mechanism in the H^- linac converts the macro-pulse into a train of micro-pulses. Since a single-bunch mode of operation of the booster synchrotron is assumed, a single step-barrier bucket must be prepared for particle capture. Just after leaving the linac with the designed injection energy in the booster ring E_{inj}, the micro-pulse train enters into an RF cavity, which is called an energy splitter and operated at half of the linac RF-frequency. Consequently, the micro-pulse train is injected into the booster ring with a symmetric energy spread about E_{inj}, as shown in Fig. 11.6. Namely, the micro-bunches split into two groups in energy space. One group is the upper side in the barrier bucket, and the other is the lower side. By making the RF voltage of the energy splitter ramp in time or phase sweep, the barrier bucket is painted with micro-pulses through the injection process. Figure 11.7 shows a typical painting process in the longitudinal phase-space. In this example, the 3 GeV booster of the J-PARC facility in Japan [8] is chosen. The bunch trains injected earlier diffuse into a racetrack-shape ring, with a relative location in the phase-space determined by the injection timing. In this manner, a uniformly distributed long bunch, called a super-bunch, is created at the end of the injection process. The line density of the resulting super-bunch is shown in Fig. 11.7.

The bunching factor is one of the most important beam parameters when one considers the space-charge limit on the beam intensity. The bunching factor B_f

UNCORRECTED PROOF

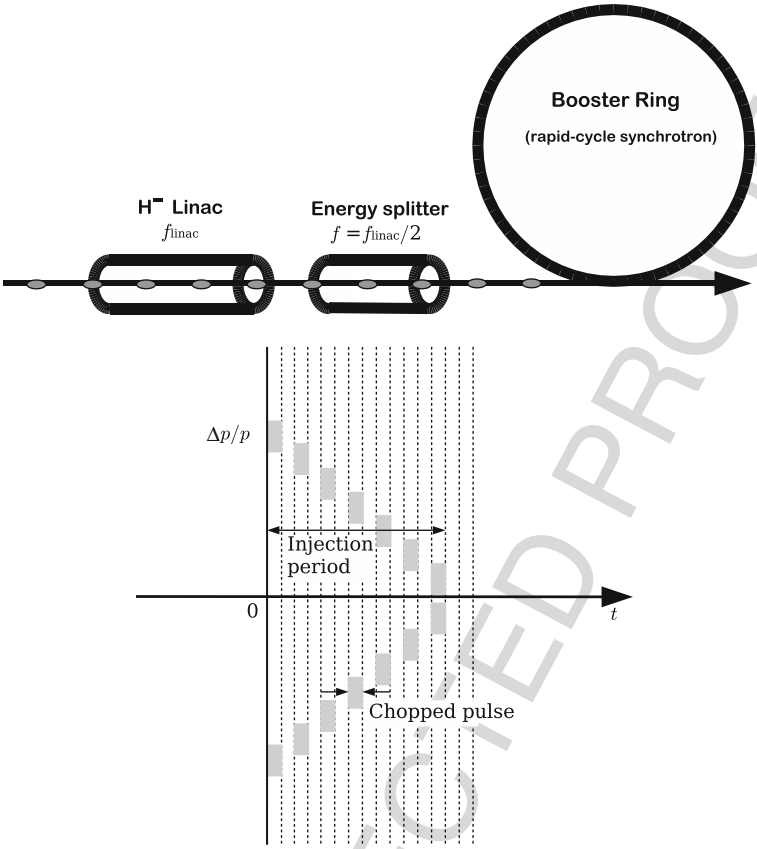

Fig. 11.6 Symmetric painting

is defined by the ratio of average to peak beam intensity. Computer simulations indicate that a bunching factor of $B_f = 0.78$ is achievable at the end of the injection process. In an RF synchrotron driven with single harmonic RF, B_f is typically between 0.25 and 0.3. For the case driven with dual harmonic RFs [9], B_f is typically estimated to be around 0.4–0.5. As is well-known, the transverse space-charge beam limit for a particular synchrotron is quantified using the Laslett tune-shift, which is expressed in the following form when effects from the metallic aperture are neglected [10]:

$$\Delta\nu \propto \frac{Nh}{\beta\gamma^2 B_f \varepsilon}, \tag{11.21}$$

Here, N is the number of particles per bunch, h is the harmonic number ($h = 1$ for the Induction Synchrotron), ε is the normalized emittance. Usually, the magnitude of the space-charge tune-shift is limited to about 0.25. Note that the Laslett tune-shift

UNCORRECTED PROOF

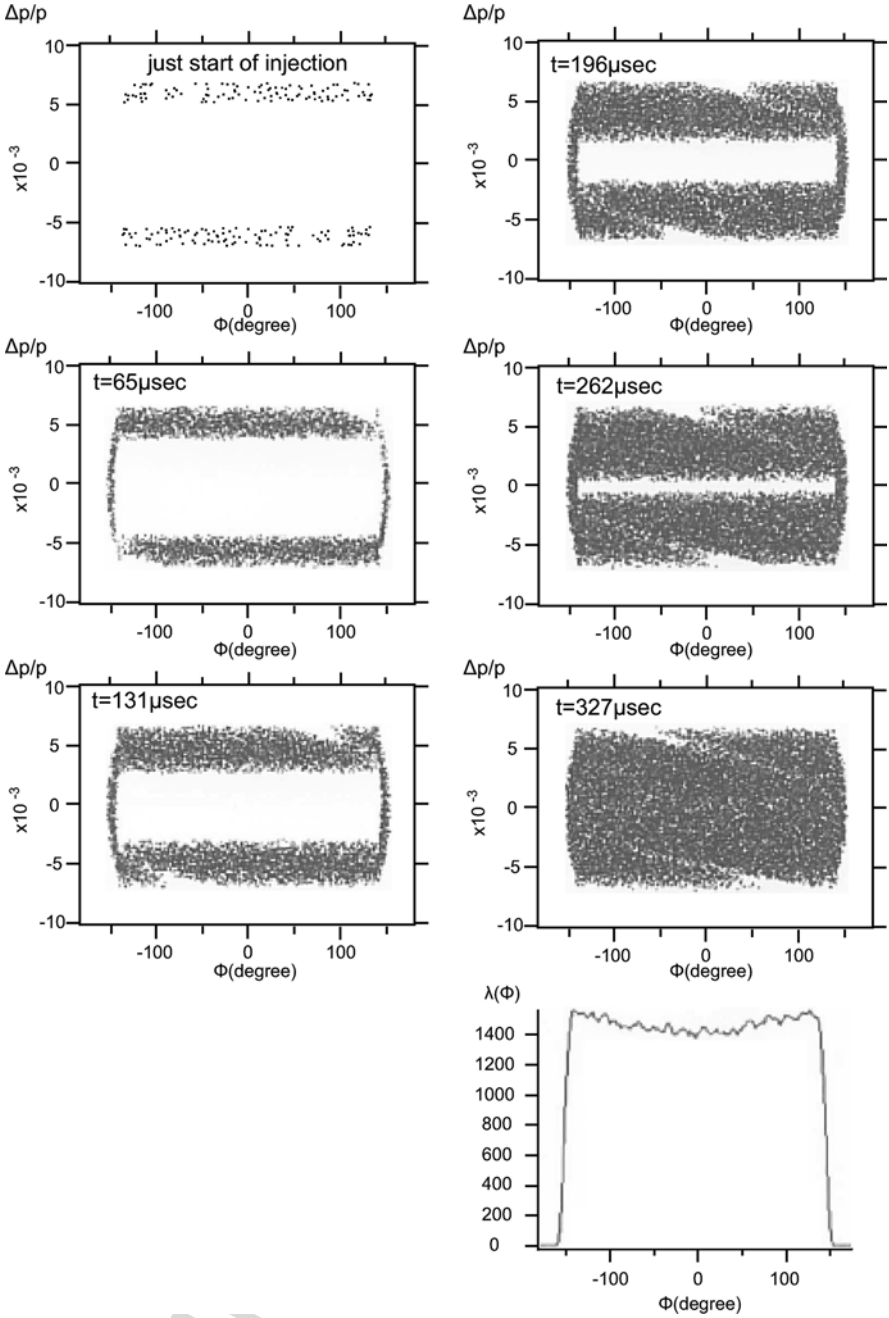

Fig. 11.7 Computer simulation of symmetric painting in phase-space (ϕ, $\Delta p/p$) for the J-PARC 3 GeV Ring. Phase space snapshots in time are shown from the first stage of injection to the last. The final line density of the super-bunch is also shown. Beam and machine parameters: $N = 8 \times 10^{13}$, $b/a = 1.8$ (averaged aspect ratio of the vacuum chamber), injection period of 330 μs, $h = 1$ (harmonic), $C_0 = 313.5$ m (circumference), $E_{\text{inj}} = 400$ MeV, $\gamma_{\text{T}} = 8.77$, $V_{bb} = 200$ kV (barrier voltage)

is inversely proportional to B_f. Large B_f allows a large value of N. In order to keep $\Delta\nu$ under the limiting value and increase N, increasing B_f is a solution allowed by the super-bunch formed with the symmetric painting technique.

11.2.2 Beam Stacking and Super-Bunch Formation

Barrier bucket stacking of super-bunches in a slow cycling synchrotron is a natural progression. An upstream booster synchrotron delivers super-bunches at its operational cycle to a second downstream synchrotron. The transferred super-bunch is captured in a barrier bucket. Figure 11.8 shows a typical example of the stacking process. The captured super-bunch is adiabatically moved toward the stacking core. Then it is released at the location adjacent to the core by pausing trigger signals of the barrier pulse for capture. At the same time, the trigger signal of the reset pulse for the stacking barrier is delayed by the length of a subsequent injected super-bunch. Then, the subsequent super-bunch begins to merge into the core. The process is repeated until a single super-bunch with the desired length and momentum spread is formed for acceleration in this ring. This technique is applied in other downstream synchrotrons.

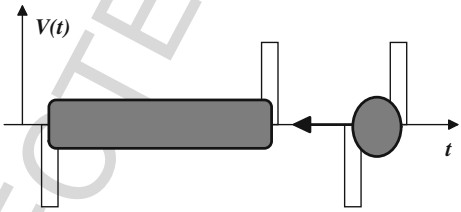

Fig. 11.8 Schematic view of barrier-bucket stacking

11.2.3 Transition Crossing

At the transition energy, the polarity of the barrier-pulse is changed to provide longitudinal focusing without being interrupted in time. This is, in principle, same as a phase-jump in an RF synchrotron. This is achieved by changing the trigger timing of the barrier-pulses. Even in an Induction Synchrotron, problems arising from transition crossing, such as non-adiabatic phase motion, are analogous to those in an RF synchrotron. Both edges of the super-bunch extend in the momentum direction due to nonadiabaticity, as shown in Fig. 11.9, where the machine parameters of the KEK 12 GeV-PS are assumed. This phenomenon is caused by the fact that particles are being placed in the barrier regions continuously without the phase motion at transition. The barrier-bucket height can be controlled independently by reducing the barrier voltage in the vicinity of the transition energy without affecting the acceleration. Accordingly, one can avoid a deformed bunch shape with a large momentum spread, which may violate dispersive limits of the ring in some ~~case,~~ as

UNCORRECTED PROOF

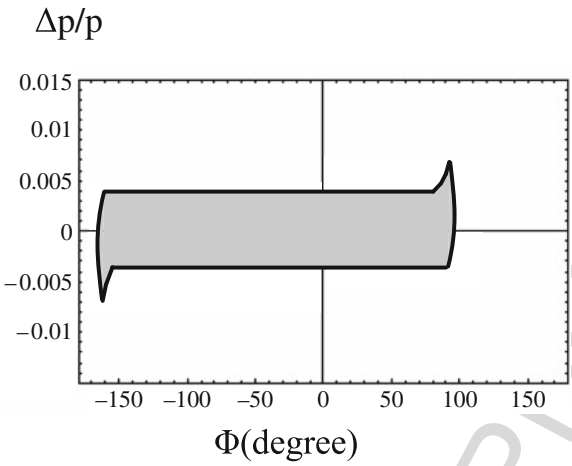

Fig. 11.9 Super-bunch in phase space just at the transition energy. Both edges of the bunch are modified due to non-adiabaticity in the transition crossing process

shown in Fig. 11.9. Transition crossing in the Induction Synchrotron can be called *focusing-free transition crossing*.

It is instructive to compare focusing-free transition crossing in an Induction Synchrotron with nominal transition crossing in the RF synchrotron [11]. Nominal transition crossing in the RF case has caused various problems, such as an asymmetric bunch shape due to nonlinear kinematic effects [12–14], and microwave instabilities (see Fig. 11.10) in addition to non-adiabatic motion. The latter is caused when rapid increases of the beam line charge density, which is inevitable in the vicinity of the transition energy, are combined with narrow-band impedances distributed along the accelerator ring [15]. Results of a numerical simulation are shown in Fig. 11.10. Inclined bunch shapes caused due to the non-adiabaticity take place for every RF bucket. Here $h \neq 1$ is assumed. The line charge density increases by about 50% from that in a region far from the transition energy. Unfortunately, it is impossible to reduce the RF voltage in order to avoid these phenomena, because a constant acceleration rate has to be maintained. This is one of the disadvantages of a combined-function synchrotron in the longitudinal direction.

The Induction Synchrotron needs a long step-voltage pulse for acceleration, and a droop in such a long step-voltage pulse is typically inevitable. The droop is approximately modeled as a gradient in the voltage in time. The gradient causes longitudinal defocusing of a super-bunch below the transition energy, and longitudinal focusing above the transition energy. Simulation results assuming a few percent droop have indicated a fatal blowup in the longitudinal emittance of a super-bunch [16]. With respect to this point, super-bunch acceleration by a long step-voltage with droop is not conceivable. It is discussed in the literature [16] how such droop limitations can be counteracted. Super-bunch acceleration in an Induction Synchrotron may force us to reconsider a transition-free synchrotron lattice [8, 17], which requires many independently excited quadrupole magnets.

UNCORRECTED PROOF

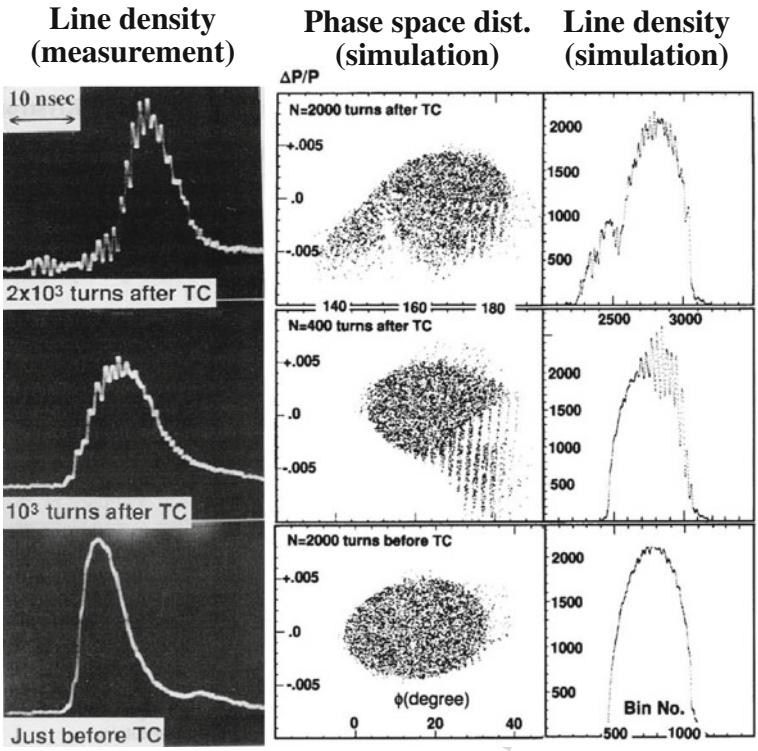

Fig. 11.10 Typical microwave instability observed just above the transition energy [15]. TC means transition crossing

11.3 Induction Devices for an Induction Synchrotron

The key components required to realize an Induction Synchrotron are an induction accelerating cell and a pulse modulator driving the cell. These devices, however, are notably different from similar devices employed in linear induction accelerators that have been described in early chapters. The unique characteristics are the repetition rate and the duty factor. Another constraint is that the pulse modulator has to be positioned well outside the induction cell placed in the accelerator tunnel if high radiation is anticipated, because the solid-state power switching elements obtainable at present cannot survive high radiation dose. Thus, the pulse modulator which is later called the switching power supply needs to be connected with the accelerating cell through a long transmission cable to allow adequate shielding. In order to reduce reflections from the load, a matching resistance is installed at the end of the transmission cable. The induction accelerating system consists of an induction cell with a matching load, a transmission cable, a pulse modulator, and a DC power supply. A system capable of generating a step-pulse with 2 kV output voltage and 18 A output peak current at 1 MHz repetition frequency with 50% duty factor has been demonstrated at KEK [18].

UNCORRECTED PROOF

11.3.1 Equivalent Circuit Model

An equivalent-circuit model for the induction accelerating system is presented in Fig. 11.11, where all of the circuit components are connected in parallel. For simplicity, the circuit parameters are assumed to be independent of the frequency, and constant. The model for an induction cell and beam loading, which is in principle same as the equivalent circuit-model given in Chap. 3, will be described in Sect. 11.4.1.

The switching power supply is represented as a full-bridge switching circuit. R is the resistance representing the core and eddy-current losses in the magnetic material. L is the inductance, which is dominated by the magnetic material. C is the cell capacitance, which is mainly determined by the mechanical cell structure including the ceramic gap, insulation materials, and coolant properties. The matching load Z satisfies the first order matching condition,

$$\frac{1}{Z_0} = \frac{1}{Z} + \frac{1}{R},$$

where Z_0 is parallel to the cell and represents the characteristic impedance of the transmission cable. The energy stored in the primary capacitor bank is continuously charged by the upstream DC power supply and is transferred downstream in a programmed switching sequence synchronized with the circulation of the beam around the ring. Assuming that an idealized rectangular-shape pulse voltage is generated just after the switching power supply, the induced accelerating voltage between both terminals of the cell inductance, is analytically obtained by solving a set of circuit equations modeling the transmission line shown below. Denote $V(t)$ and $I(t)$ as the voltage and current at the lower end of the transmission cable, and I_Z, I_R, I_C, I_L as

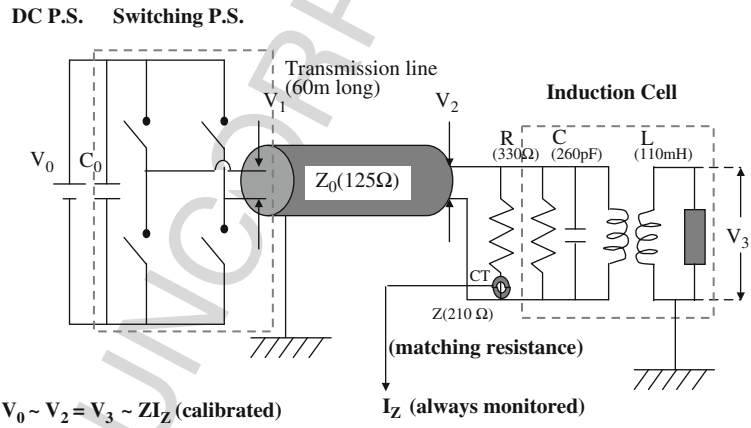

Fig. 11.11 Equivalent circuit for the induction accelerating system

UNCORRECTED PROOF

the current-flow through each labeled circuit component. Then circuit equations can be expressed as:

$$V(t) = Z \cdot I_Z = R \cdot I_R = \frac{1}{C}\int I_C \, \mathrm{d}t' = L\frac{\mathrm{d}I_L}{\mathrm{d}t}, \tag{11.22}$$

$$I(t) = I_Z + I_R + I_C + I_L. \tag{11.23}$$

Here, $V(t)$ and $I(t)$ are described by the terms of the forward/backward waves denoted with superscript +/- as follows: $V(t) = V^+(t) + V^-(t)$, $I(t) = I^+(t) + I^-(t)$, where $I^+(t) = V^+(t)/Z_0$ and $I^-(t) = -V^-(t)/Z_0$. Substituting these relations into Eqs. (11.22) and (11.23) and evaluating I_Z, I_R, I_C, and I_L from Eq. (11.22), we obtain the ~~followings~~ differential equation for $V^+(t)$ and $V^-(t)$:

$$\begin{aligned}\frac{1}{Z_0}(V^+ - V^-) = \left(\frac{1}{Z} + \frac{1}{R}\right)(V^+ + V^-) + C(\dot{V}^+ + \dot{V}^-) \\ + \frac{1}{L}\int_0^t (V^+ + V^-)\mathrm{d}t'.\end{aligned} \tag{11.24}$$

Because the forward wave $V^+(t)$ is known, the backward wave $V^-(t)$ is uniquely determined by Eq. (11.24). The Laplace transform in time of $V^+(t)$ with initial conditions $V^+(0) = A$ and $\mathrm{d}V^+/\mathrm{d}t(0) = 0$ is A/s. The initial condition $V^+(0) = A$ gives $V^-(0) = -A$, because of $V(0) = 0$. If we denote the Laplace transform in time of $V^-(t)$ by $g(s)$ and a Laplace transform in time is made on Eq. (11.24), we obtain

$$\begin{aligned}\frac{1}{Z_0}\left(\frac{A}{s} - g\right) = \left(\frac{1}{Z} + \frac{1}{R}\right)\left(\frac{A}{s} + g\right) + C(A + s \cdot g) \\ + \frac{1}{L}\left(\frac{1}{s}\frac{A}{s} + \frac{g}{s}\right).\end{aligned} \tag{11.25}$$

Here,

$$\int_0^\infty \frac{\mathrm{d}V^-(t)}{\mathrm{d}t} e^{-s \cdot t} \, \mathrm{d}t = -V^-(0) + s \cdot g(s) = A + s \cdot g(s)$$

is used. Evaluating $g(s)$ from Eq. (11.25), we have

$$g(s) = -A\frac{s^2 - (1/CZ_2)s + (1/CL)}{s \cdot \left[s^2 + (1/CZ_1)s + (1/CL)\right]}, \tag{11.26}$$

where $1/Z_1 = 1/Z_0 + 1/Z + 1/R$ and $1/Z_2 = 1/Z_0 - 1/Z - 1/R$. We calculate the inverse Laplace transform in time of $g(s)$ to obtain,

$$V^-(t) = -A\left[1 - \frac{2}{CZ_0\varphi}e^{-\gamma t}\sinh(\varphi t)\right], \tag{11.27}$$

UNCORRECTED PROOF

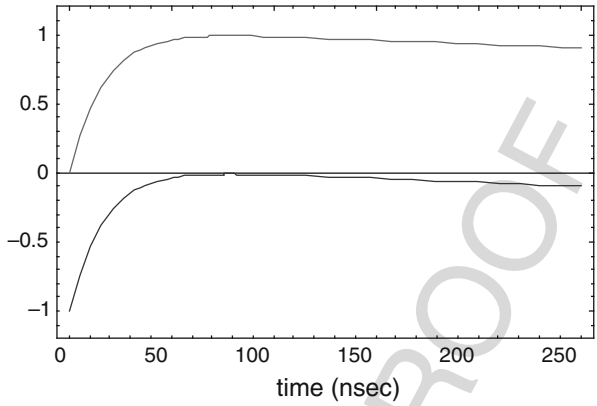

Fig. 11.12 Normalized output voltage (*upper*) and reflected voltage (*bottom*)

where

$$\gamma \equiv \frac{1}{2Z_1C}, \qquad \varphi \equiv \frac{1}{2}\sqrt{\left(\frac{1}{Z_1C}\right)^2 - \frac{4}{LC}}.$$

Using Eq. (11.27) and assuming the circuit parameters of the KEK induction accelerating system described in Sect. 11.3.2, $V^-(t)$ and $V(t)$ are illustrated in Fig. 11.12.

The voltage rise time is determined by C and the negative slope or droop in the voltage is approximated by $\exp(-Z_1t/L)$; it is a function of the magnitudes of L and Z_1, where Z_1 is the equivalent impedance in Sect. 6.2. We can realize that the divergence of $V(t)$ from the incident rectangular pulse shape is caused by the backward wave. The backward wave propagates through the transmission cable, and is reflected at its other end with a different boundary condition, and returns to the side of the load. This process is repeated, while decreasing in magnitude du to power dissipation in the resistances. Details of the reflection ringing are omitted, here. How the circuit elements are determined or chosen is now discussed.

11.3.2 Induction Cell

Practical parameters: The induction cells employed in the Induction Synchrotron are, in principle, the same as those used in a linear induction accelerator, which are described in detail in Chaps. 3 and 6. The induced voltage through the induction accelerating cell is described by Eq. (3.2) as

$$V\tau = -B_{\max}nS, \tag{11.28}$$

Here $S = wd$ is the cross-section of the single disk-shape magnetic material of thickness d and width w, V is the induced voltage across an induction accelerating

UNCORRECTED PROOF

cell consisting of n disks (or bobbins if the magnetic material is thin tapes), τ is the pulse length, and $B_{\max}$ is the maximum flux. Assuming the required energy gain ΔE per turn, the number of induction accelerating cells required is determined by $N = \Delta E/(ZeV)$, where Z is the charge state of ion. Since τ and ΔE are fixed by the machine requirement, the parameters of n, $B_{\max}$, and S are optimized by minimizing the heat deposited in the magnetic material and the total cost consistent with any constraints on the available space in the beam-line.

Magnetic material and cooling: The choice of the magnetic material, as discussed in Chap. 5, is important. In a case of high repetition rate operation such as an Induction Synchrotron, a choice of low-loss material is essential. The core-loss depends on the magnetization rate $\mathrm{d}B/\mathrm{d}t$ and the actual flux swing ΔB ($\ll B_s$) different from the flux swing, $B_r + B_s$, shown in Sect. 5.4. Based on the magnetization models [19], a formula for the core-loss in a minor-loop excitation has been empirically obtained in the following form

$$\mathcal{E}\left[\frac{J}{m^3}\right] = (c_1 + c_2\Delta B)\left(\frac{d}{\rho}\right)\left(\frac{\mathrm{d}B}{\mathrm{d}t}\right)^{1/2} + c_3(\Delta B)^2\left[\frac{d^2}{(\rho B_s)}\right]\left(\frac{\mathrm{d}B}{\mathrm{d}t}\right). \quad (11.29)$$

Here the first and second terms represent contributions from the bar-domain model and saturation wave model, respectively, B_s is the saturation inductance in Tesla, d is tape thickness in 10 μm, ρ is resistivity of material in μΩm, and $\mathrm{d}B/\mathrm{d}t$ is in Tesla/μs. Coefficients of c_1, c_2, and c_3 depend on material. The parameters for a nanocrystalline material Finemet [20], which has been employed in the first experimental demonstration of the Induction Synchrotron, are:

Tape Thickness:	$d = 1.6$	$c_1 = -0.44$
Resistivity:	$\rho = 1.1$	$c_2 = 24.7$
Saturation Inductance:	$B_s = 1.35$	$c_3 = 10.6$

Substituting the operating values of ΔB and $\mathrm{d}B/\mathrm{d}t$ into Eq. (11.29) and multiplying the result by a total volume of the magnetic core and a repetition rate, we can estimate the average power loss in Watts.

Cooling of the induction cell is a critical issue of the system design for high repetition rate. Cooling requirements depend on the type of magnetic material and which kind of coolant is acceptable. In the case of a nanocrystalline alloy such as Finemet, which is a conducting material and corrosive in water, the coolant can be air, electrically insulating inert perfluorocarbon fluid, insulating oil, or helium gas. It should be noted that the cell capacitance, which is a function of the dielectric constant of the coolant as well as the acceleration gap material, such as ceramic, determines the pulse rise and fall times, as shown in Eq. (11.27). In order to optimize the cooling efficiency, the temperature distribution in the induction cell is calculated by using a commercially available software package, such as ANSYS. Accordingly, the computer analysis aids the design of the cooling channel and coolant flow speed to maintain the magnetic core temperature below the critical point.

UNCORRECTED PROOF

Cell impedance: In order to determine the actual cell impedance, specifically the cell inductance L, resistance R representing the magnetization and eddy current losses, and capacitance C, three methods are normally used:

(1) Network-analyzer measurement assuming a LCR parallel circuit model and CW small amplitude excitation.
(2) Induced voltage measurement in a single pulse excitation.
(3) Measurements of voltage induced between the input terminals by a circulating beam.

First, we know the *inductance* and *resistance* in the AC mode excitation, $L(\omega) = [\mu' + (\mu'')^2/\mu']L_0$ and $R(\omega) = \omega[\mu'' + (\mu')^2/\mu'']L_0$, where the complex permeability, $\mu = \mu' - j\mu''$, of Finemet is known as a function of ω and provided by its manufacturer and L_0 is the core inductance in air taking account of the packing factor of the core material. The theoretical expression of the cell impedance in the parallel circuit model is given by $1/Z(\omega) = 1/R(\omega) + j[\omega C - 1/\omega L(\omega)]$ and the capacitance is independent of the drive frequency. We can determine the constant cell capacitance C so as to fit the theoretical impedance curve as a function of ω to the result obtained by the method (1).

Since the induction cell is typically driven in the pulse mode with a large amplitude excitation, the most accurate values of L and R are obtained with pulse excitation with magnetization rates similar to those of the actual experiments.

2.5 *kV engineering model*: An induction cell [18] employed in the KEK 12 GeV synchrotron is shown in Fig. 11.13. The electrical parameters of each unit of the induction cell are given in the previous Magnetic material and cooling subsection, which were determined from design considerations previously outlined [18]. Four unit-cells with a 2.5 kV output voltage per unit are mechanically combined into a single module for convenience of installation. Because the inner conductor with four ceramic gaps is common to four unit-cells, but both sides of each gap are electrically

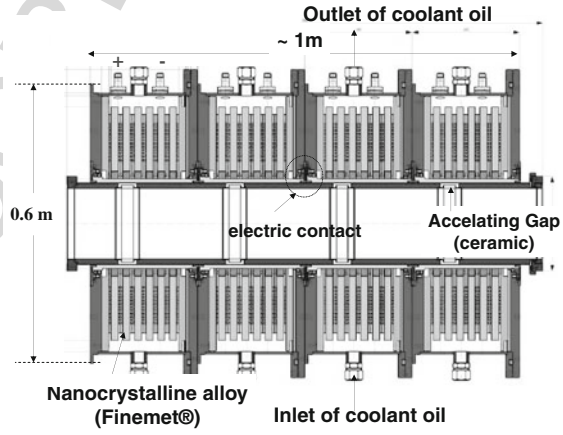

Fig. 11.13 Quartet of induction cells (4 × 2.5 kV) employed in the KEK PS

UNCORRECTED PROOF

connected to the outer edges of each cell, a particle is accelerated with the same voltage passing these gaps.

11.3.3 Switching Power Supply (Power Modulator)

Full-bridge switching circuit: For the barrier bucket, a full-bridge switching circuit, which is depicted in the equivalent circuit of Fig. 11.11, is employed because of its simplicity. The power modulator must be capable of generating bipolar rectangular shaped voltage pulses. A high repetition rate performance in the MHz range is required for typical applications. In addition, a fast rise/fall rate is required. Continuous wave (CW) high repetition rate operation is crucial for a ring. There are several solid-state switching elements capable of meeting these requirements as discussed in Chap. 4. One is a full-bridge type power modulator consisting of four identical switching arms. Each switching arm is composed of several MOSFETs, arranged in series and parallel. The matrix of switching elements called a switching matrix hereafter, is determined by the allowed magnitudes of source-drain voltage and current capacity of each semiconductor switch. Their gates are driven by their own individual driving circuits, which are electrically isolated from their power source with extremely low capacitance DC–DC converters. The gate signals are generated by converting light signals provided from the pulse controller, which is a part of the accelerator control system, to electrical signals using TOS-Links (opto-electronic interface). To obtain a bipolar voltage, two sets of switching arms (S1/S3 and S2/S4) are turned on and off reciprocally.

Keeping intrinsic resonances of the modulator circuit away from the operating frequency is essential to obtain the desired flat-top voltage. For this purpose, the physical area encircled by the current flow is reduced to as small a value as possible so as to minimize the stray loop inductance in the circuit. The capacitance existing in the main circuit, which is dominated by the capacitance of MOSFETs, is responsible for a particular resonance. It is effective to reduce the number of columns in the switching matrix and increase line numbers in order to maintain a sufficient rise time. On the other hand, in order to reduce the diode current leading to heat loss in the MOSFETs, the driving current has to be divided into the columns of the switching Matrix. Optimized parameters of the switching matrix depend on the application of interest.

Heating of the MOSFETs and the gate driving ICs caused by CW MHz switching rates is large and must be addressed. Dissipation of 150 W per device are typical. Each pair of MOSFETs and gate driving ICs are mounted on a copper heat-sink. A DC voltage of 2.5 kV, supplied from the DC power supply, is distributed. Each MOSFET along a line shares a slightly different voltage due to the capacitances distributed in the entire circuit – including gate driving circuits. These elements include the equivalent capacitances between the source and drain, the FET and heat-sink, the heat-sink and ground, the FET and return circuit, and the gate circuit and ground. In particular, the capacitance of the DC–DC converter to isolate the

UNCORRECTED PROOF

gate circuit from the ground takes an important role in determining the voltage balance among the MOSFETs before closing the gates. Voltage imbalance is an important issue, because the loss at turn-on is proportional to the initial voltage balance. The maximum power loss (heat generated) occurs at the MOSFET having the maximum shared-voltage. When the heating exceeds some limit, such as the junction temperature of 150°C, the MOSFET will break down. The breakdown of a single MOSFET can cause the breakdown of other MOSFETs and failure of the switching arm, and the entire pulse modulator. An inclusive design guide-line and its experimental justification has been reported in [21, 22].

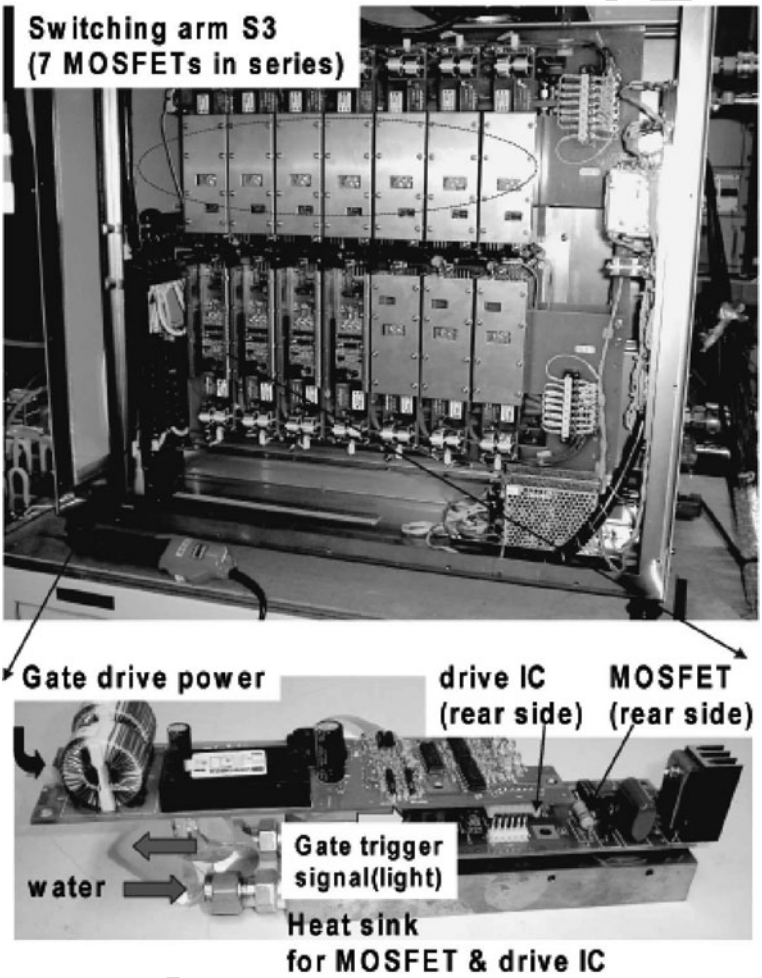

Fig. 11.14 Photo of the KEK 2.5 kV switching power supply

As an example, the switching power supply, which was developed by KEK and Nichicon Kusatsu Co. Ltd., is shown in Fig. 11.14. Specifications of the switching power supply are:

DC Power Supply:	50 kW
Output Voltage:	2.5 kV
Peak Output Current:	21 A
Duty of Pulse:	50%
Power Loss at MOSFET:	200 W

This switching power supply was successfully operated at a repetition rate of 1 MHz for 100 h, in which bipolar pulses of 2.0 kV output voltage and 250 ns pulse width were generated. The output voltage measured at the resistor load of 100 Ω is shown in Fig. 11.15. The 10–90% rise time and the 90–10% fall time were 20 and 25 ns, respectively. A flatness of 2% in the output voltage was obtained. AQ1

Half-bridge switching circuit: As mentioned earlier, a long set-pulse and short reset-pulse are required for super-bunch acceleration. A switching power supply capable of producing such a set of pulses employs a half-bridge switching circuit, in which two capacitor banks are required, as shown in Fig. 11.16. One provides a voltage for the accelerating pulse, and the other provides a higher voltage for the reset. The switching sequence is similar to that of the full-bridge switching circuit. A prototype has been demonstrated at Tokyo Institute of Technology [23, 19], in which the pulses have the same $V \times t$ product, so as to avoid core saturation. Output voltage measured is shown in Fig. 11.17. This switching architecture is conservative and the resistance of the system is determined by the higher reset voltage pulse.

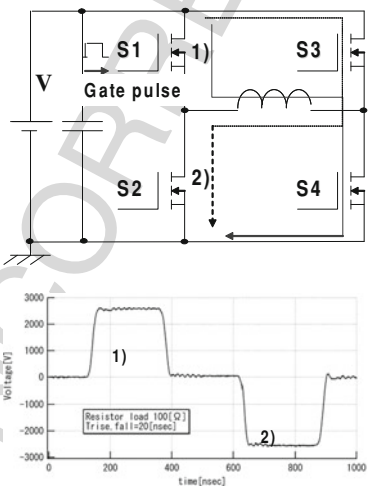

Fig. 11.15 Output voltage of the KEK 2.5 kV switching power supply (see Fig. 11.14) with a resistive load of 100 Ω

UNCORRECTED PROOF

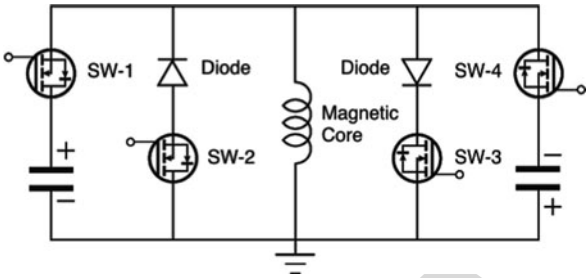

Fig. 11.16 Half bridge modulator

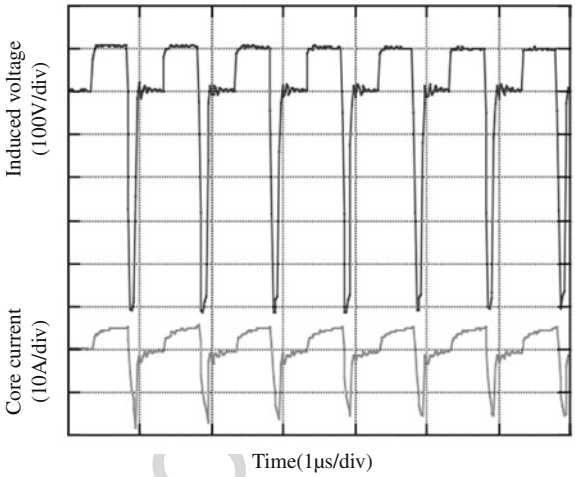

Fig. 11.17 Experimental demonstration of asymmetric voltages

A simpler and more reliable circuit architecture has been developed at KEK. In this scheme, the acceleration voltage for a long-bunch is formed by summing the relatively short pulses in time. The short pulses are generated by bipolar switching power supplies and are summed by the induction cells by appropriate timing of the pulses as illustrated in Fig. 11.18.

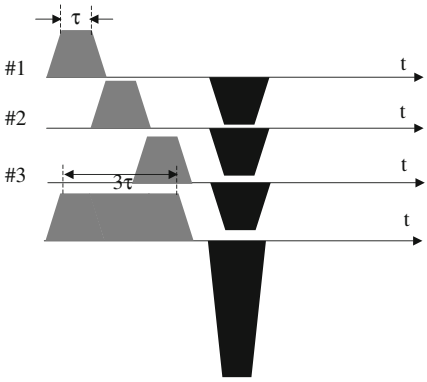

Fig. 11.18 Superposition of the short-pulse induction voltages in time

UNCORRECTED

11.4 Proof of Principle Experiment

Before the experimental demonstration of induction acceleration, the beam-cell interaction was investigated to establish the characteristics of the newly developed induction cell.

11.4.1 Beam–Cell Interaction: Beam Loading

A high energy proton beam is an ideal driving source to confirm the electric parameters of the induction cell, because any steady-state interaction of the acceleration cell with the beam itself can be ignored in a single pass excitation. A simple experiment of the induction cell excitation by a single RF bunch was conducted using the KEK 12 GeV PS [24], where the induction cell described in Sect. 11.3.2 was installed without an external driver, and its feeder line was employed to monitor the induced voltage. The proton beam was captured in the RF bucket through the entire acceleration cycle. The bunch profile slowly changed during most of the acceleration cycle because of adiabatic damping. However, the bunch length rapidly shrunk when crossing the transition energy, as discussed in Sect. 11.2.3. Since the RF voltage was switched off after achieving flat-top energy, the bunch decayed into a DC beam due to the momentum spread in the bunch. The bunch shape and the induced voltage in time were observed at various times during the acceleration cycle. The former was monitored with an inductive fast current monitor and the latter was measured by a voltage probe connected between the terminals of the attenuating resistor. In this configuration, the induction cell is treated as a current transformer. Typical profiles of bunch shapes and the induced voltages measured are shown in Fig. 11.19. Similar data taken for other circuit parameters was employed to measure the circuit parameters of the induction cell.

The induced voltage $V(t)$ satisfies the following circuit equation for the equivalent circuit driven by a beam pulse:

$$\frac{\mathrm{d}^2 V}{\mathrm{d}t^2} + \frac{1}{C}\left(\frac{1}{R} + \frac{1}{Z}\right)\frac{\mathrm{d}V}{\mathrm{d}t} + \frac{1}{LC}V = -\frac{1}{C}\frac{\mathrm{d}I_b}{\mathrm{d}t}, \tag{11.30}$$

Solved subject to the initial conditions $V(0) = 0$ and $\mathrm{d}V/\mathrm{d}t(0) = 0$. Here, I_b is the beam current, Z the external pure resistance to monitor the induced voltage, and C^* the external capacitance connected in parallel to the cell and $C = C_0 + C^*$ with C_0, R, and L are the intrinsic capacitance, resistance, and inductance of the cell, respectively. For simplicity, the frequency dependence of R and L is ignored. Making a precise estimate of C_0 and R is not easy as mentioned in Sect. 11.3.2. However, $L \cong$ const is mostly determined from the geometrical parameters of the magnetic core and the core material properties. The solution of Eq. (11.30) is

$$V(t) = -\frac{1}{\beta C}\int_0^t \mathrm{d}t' e^{-\alpha(t-t')} \sinh \beta(t-t')\dot{I}_b(t'), \tag{11.31}$$

UNCORRECTED PROOF

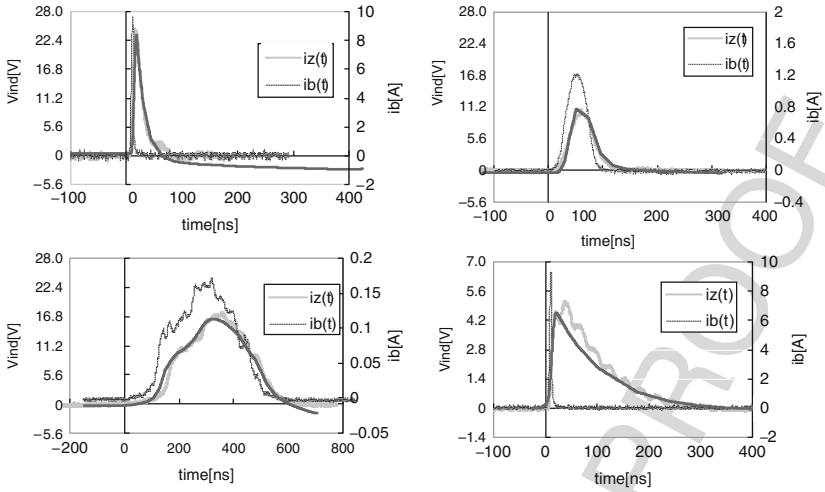

Fig. 11.19 Induced voltage and beam-current profiles with corresponding approximate analytic solutions for $Z = 60\ \Omega$. The right bottom is for $Z = 60\ \Omega$ with an additional capacitance of $C = 1{,}000$ pF

where α and β satisfy

$$\alpha = \frac{1}{2C}\left(\frac{1}{Z} + \frac{1}{R}\right), \qquad \alpha^2 - \beta^2 = \frac{1}{LC}.$$

Using the experimentally measured beam pulse profile into Eq. (11.31), we obtain an analytic expression for the induced voltage. The analytic calculations used the values

$$\begin{aligned} &\text{Capacitance:} && C = 260\ \text{pF} \\ &\text{Resistance:} && R = 330\ \Omega \\ &\text{Inductance:} && L = 110\ \mu\text{H} \end{aligned}$$

Comparisons of experimental and analytical results presented in Fig. 11.9 indicate good agreement, and consequently reasonable choices of circuit model parameters.

The induced voltage represents beam energy loss due to cell loading. The super-bunch has an intensity gradient in both of its edges, as can be seen in Fig. 11.2, which constitutes a source of beam loading. The amount of beam loading can be easily estimated using Eq. (11.31) once the beam profile is given. If the peak beam current is many Amps, cell loading can be significant. Decreasing the cell impedance is effective to mitigate beam loading effects. Powerful switching power supplies capable of carrying higher driving currents are required, assuming the same output voltage.

UNCORRECTED PROOF

11.4.2 Scenario of Proof of Principle Experiment

Proof-in-principle experiments of the Induction Synchrotron concept were carried out using the KEK 12 GeV-PS [25] in 2004–2006. The experiment was divided into three stages:

(1) Induction acceleration of a single proton bunch captured in the RF bucket.
(2) Super-bunch formation in the barrier bucket.
(3) Induction acceleration of a single super-bunch captured in the barrier bucket.

These steps are sketched schematically in Fig. 11.20. In the first stage, a single bunch trapped in an RF bucket is accelerated with a total induction voltage of 10 kV up to the flat-top energy. Here, the RF is not responsible for the resonant acceleration, and its role is simply to capture particles. A trigger signal for the induction step-voltage pulse is controlled in a manner to synchronize the revolution frequency of the beam over the entire acceleration period. In the second stage, the role of the induction voltage is transferred to that of the barrier bucket, and a single bunch injected from the 500 MeV booster is captured in the barrier bucket, creating a 600 ns long bunch regarded as a pseudo super-bunch. Finally in the third step after further installation of induction modules, a full-demonstration of the induction synchrotron concept was carried out.

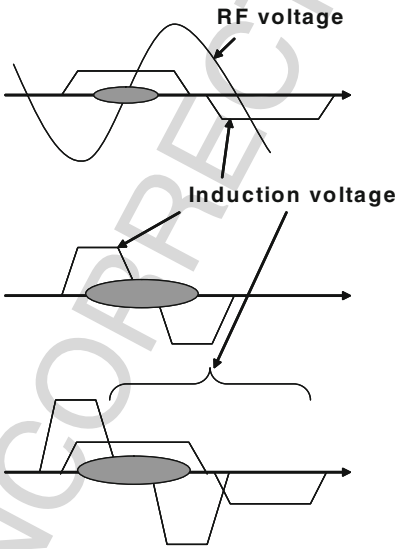

Fig. 11.20 Staging in proof of principle experiments on the KEK 12 GeV PS. 1st step (*top*): RF trapping + induction acceleration (Hybrid synchrotron), 500 MeV → 8 GeV for 6×10^{11} ppb, 2nd step (*middle*): Barrier trapping by induction step voltages at 500 MeV, 3rd step (*bottom*): Barrier trapping + induction acceleration (full induction synchrotron), 500 MeV → 6 GeV for $2 - 3 \times 10^{11}$ ppb

UNCORRECTED PROOF

11.4.3 Induction Acceleration of an RF Bunch

The system employed for the induction acceleration experiment is schematically shown in Fig. 11.21. The generation of a 2 kV voltage pulse is directly controlled by trigger pulses to the switching elements of the switching power supply. The master signal pulse is generated by the pulse sequencer of the digital signal processor (DSP) and is synchronized with the ramping of the bending magnets. Gate-driving signal patterns initiated by this master trigger signal are formulated through a pulse-pattern generator and sent to the gate controller of the switching power supply through a long coaxial cable. The pulse sequencer counts the so-called B-clock signal, which digitally counts the ramping of the guiding magnetic fields in time, and achieves the desired revolution frequency. Any delay between the accelerating pulse and a bunch monitor signal is compensated by the DSP in a programmed manner [26, 27]. The system is connected to the existing RF system through the RF signal, which shares the B-clock signal. As a consequence, a synchronized induction acceleration pulse is guaranteed. Here, the RF does not contribute to the acceleration of the beam bunch but gives the focusing force in the longitudinal direction; the beam bunch is longitudinally focused but not accelerated because the RF phase automatically adjusts to $\phi_s = 0$. The machine parameters of the KEK PS employed for the experiment are:

Circumference:	$C_0 = 339$ m
Transition energy:	$\gamma_t = 6.63$
Injection/extraction energy:	500 MeV–8 GeV
Revolution frequency:	$f_0 = 668$–877 kHz
Ramping time (transient for start/stop):	1.9 s (100 ms)
RF voltage:	$V_{\mathrm{RF}} = 48$ kV
Harmonic number:	$h = 9$
Induction voltage per turn:	$V_{\mathrm{ind}} = 5.2$ kV

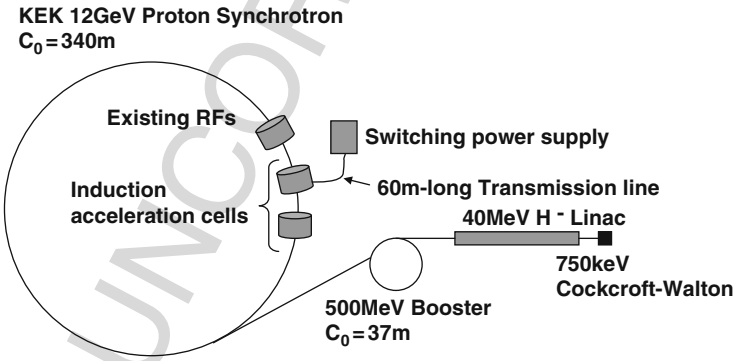

Fig. 11.21 Schematic view of the hybrid accelerating system of the KEK PS

UNCORRECTED PROOF

Experimental results: In the experiment [28], the bunch signals and signals from three current transformers (CT), which continuously monitor the current flow through the matching resistances, were displayed on the digital oscilloscope. Before the experiment, an induced voltage at a ceramic gap, an output voltage of the transmission cable, and the CT signals were simultaneously measured and the correspondence between each were well calibrated. In addition, a delayed timing of the master gate signal triggering the switching power supply was adjusted by the DSP so that the bunch signal would stay at the center of the induction voltage pulse throughout the entire acceleration cycle. Typical wave-forms of the CT signals are shown together with the bunch signal in Fig. 11.22.

Theoretical background: Under the influence of the RF voltage V_{RF} and the induction voltage V_{ind}, a charged particle receives an energy gain per turn,

$$eV_{\mathrm{acc}}(t) = e\left[V_{\mathrm{RF}}\sin\phi(t) + V_{\mathrm{ind}}\right], \tag{11.32}$$

Here, $\phi(t) = \omega_{\mathrm{RF}}t$ is the position of the particle in the RF phase. The orbit and energy of a particle are described by the two equations. From the force balance in the radial direction we obtain

$$m\gamma\frac{(c\beta)^2}{\rho} = ec\beta B(t), \tag{11.33}$$

where $B(t)$ is the bending magnetic flux density and ρ is the bending radius of the magnet. Second, from the change in energy of the reference particle

$$mc^2\frac{\mathrm{d}\gamma}{\mathrm{d}t} = \frac{ec\beta}{C_0}V_{\mathrm{acc}}(t), \tag{11.34}$$

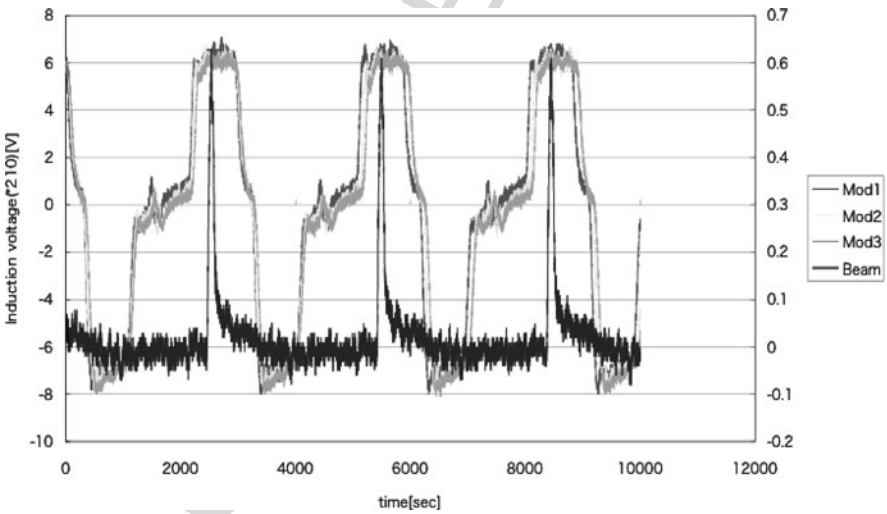

Fig. 11.22 Induction pulse wave-forms (*gray*) and a bunch signal (*solid black*) from the KEK Proton Synchrotron experiment

where C_0 is the circumference of the ring. From Eqs. (11.33) and (11.34), the accelerating voltage must satisfy the relationship, $V_{\mathrm{acc}}(t) = \rho C_0 \frac{\mathrm{d}B}{\mathrm{d}t}$, so that the particle is synchronously accelerated with ramped bending field. For the KEK proton synchrotron, the bending field is linearly ramped over 1.7 s and $V_{\mathrm{acc}} = 4.7$ kV is required. For simplicity, the induction voltage was fixed to be close to 5.1 kV.

Experimental observation: In order to confirm the induction acceleration influence, the phase signal which shows the relative position of the bunch center to the RF was measured through the acceleration cycle. Particularly, we focused on three cases:

(1) RF voltage alone.
(2) RF voltage and a positive induction voltage.
(3) RF voltage and a negative induction voltage.

From Eq. (11.32), a theoretical prediction is $\phi_s = \sin^{-1}(V_{\mathrm{acc}}/V_{\mathrm{RF}}) \sim V_{\mathrm{acc}}/V_{\mathrm{RF}} = 5.7°$ for case (1), $\phi_s = -0.66°$ for case (2), and $\phi_s = \sin^{-1}(2V_{\mathrm{acc}}/V_{\mathrm{RF}}) \sim 2V_{\mathrm{acc}}/V_{\mathrm{RF}} = 12.4°$ for case (3). In case (2), since the induction voltage is devoted to the acceleration and the RF focuses the bunch without acceleration, ϕ_s must be zero. In case (3), the RF has to provide twice the energy to the bunch relative to case (1). It follows from energy-conservation that the phase should increase by a factor of two. Observed time-evolution of the phases through acceleration are presented in Fig. 11.23. Results indicate good qualitative agreement with the theoretical predictions. For both sides of the transition, the evolution in the phase difference is clearly understandable.

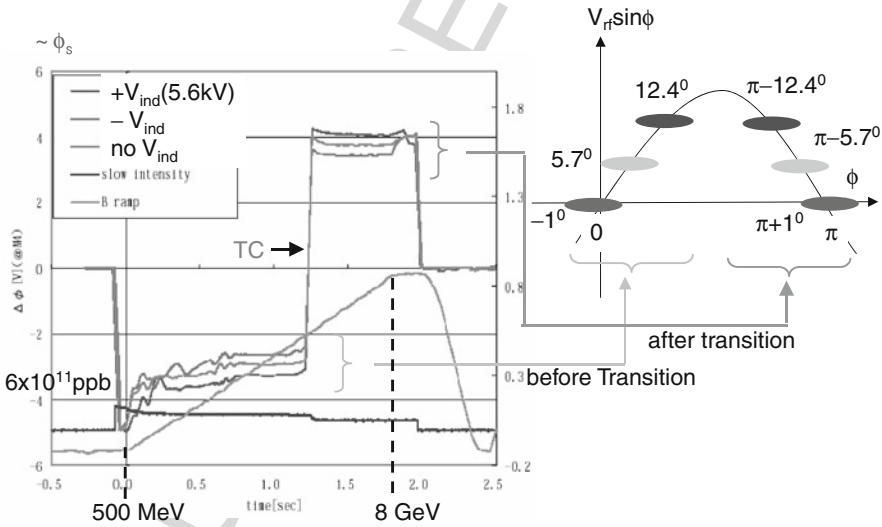

Fig. 11.23 Temporal evolution of the position of the bunch center in the RF phase

11.4.4 Confinement by Induction Barrier Voltages

Beam confinement using induction step barriers, which is crucial to achieve a super-bunch, has been demonstrated using a shallow notch potential illustrated schematically in Fig. 11.24 [27]. A single proton bunch consisting of 5.0×10^{11} protons was confined in the notch potential generated by the induction voltage $V_{\text{barrier}} = 4.7$ kV, with a pulse width $T_{\text{pulse}} = 400$ ns. Assuming a rectangular barrier voltage and $T_0 = 1.5\ \mu$s, $\beta = 0.75$, $E_0 = (500 + 938)$ MeV at injection, Eq. (11.20) gives the bucket height in momentum space of $\Delta p/p = 0.27\%$. This height is slightly lower than the momentum spread of the injected proton bunch of 0.3%. Consequently, about half of injected protons were lost over 460 ms. Experimental results are shown in Fig. 11.25 for the temporal-evolution of the bunch shape from an injection energy of 500 MeV. The bunch remains trapped in the notch potential and stretches in time over 400 ms.

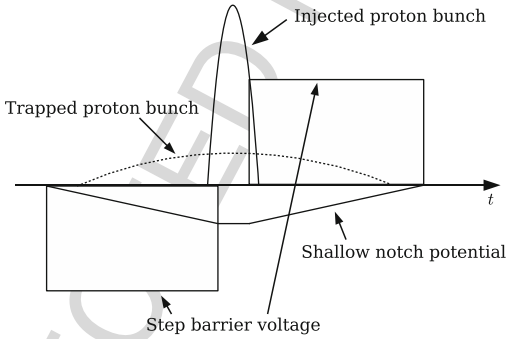

Fig. 11.24 Schematic view of the notch potential and the trapped bunch profile

11.4.5 Induction Acceleration of a Trapped Barrier Bunch – Full Demonstration of the Induction Synchrotron

The full-operation of an Induction Synchrotron requires a control system different from that of the hybrid synchrotron described in Sect. 11.4.3. Gate signals used to turn on the MOSFETs are generated by manipulating both signals monitored at the fast bunch monitor and the beam position monitors in a gate control system, which consists of a digital signal processor and active delay modules. This control system is illustrated in Fig. 11.26. Transverse beam-orbit control is the most important issue – as in any synchrotron. Without proper control, charged particles are not efficiently accelerated and can impact the vacuum chamber. The so-called ΔR-feedback system is equipped to meet this requirement in a conventional RF synchrotron, where the RF phase seen by the bunch center is automatically adjusted in real time to compensate any surplus or shortage of acceleration. A similar feedback control system is introduced for the Induction Synchrotron. In this system, the

UNCORRECTED PROOF

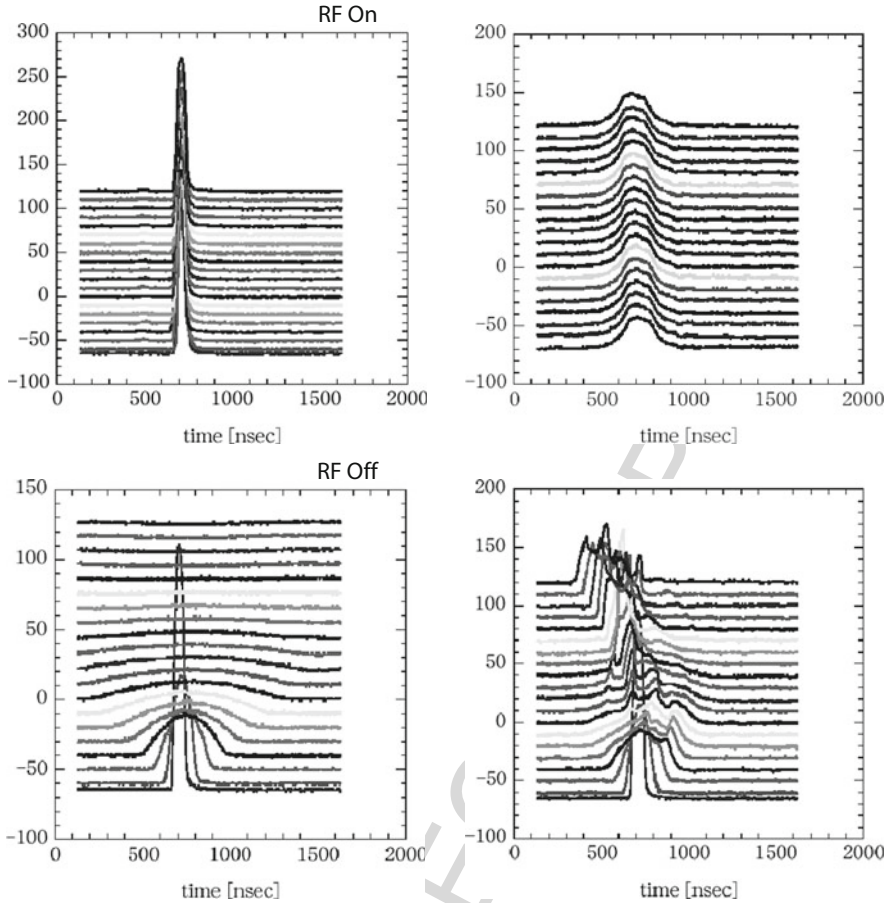

Fig. 11.25 Mountain views of the injected pulse in time. *Lower left*: RF off and just debunching of the injected pulse every 50 turns. *Upper left*: RF on and just RF trapping at 150 ms after injection every 50 turns. *Lower right*: Barrier voltage on and barrier trapping of the injected pulse just after injection every 50 turns. *Upper right*: barrier trapping at 150 ms after injection every 50 turns

gate pulse generation is determined by integrating the digital gate pulse generator with the orbit information proportional to the momentum error, $\Delta p/p$. The position monitor directly gives $\Delta R = D(s)\Delta p/p$, where $D(s)$ is the momentum dispersion function at the location of the position monitor [10]. When the signal amplitude exceeds a preset threshold value, the gate trigger signal is blocked in the DSP. Accordingly, the acceleration voltage pulse is not generated on subsequent turns until the momentum approaches the correct value, which is uniquely determined by the bending field. Note that the induction acceleration voltage per turn is always set to be a bit larger than the required voltage $\rho C_0 \mathrm{d}B/\mathrm{d}t$. The integrated gate control system is depicted in Fig. 11.26.

UNCORRECTED

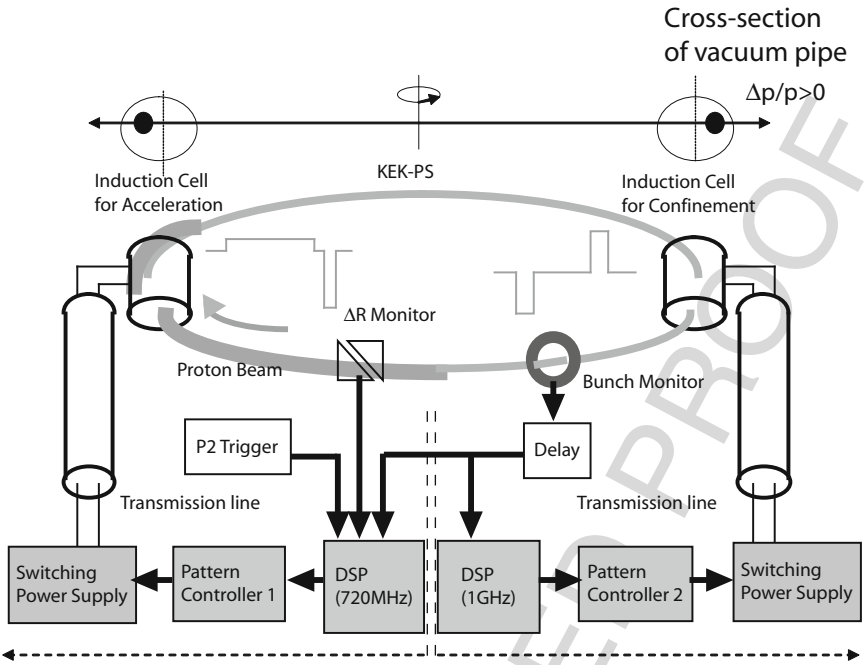

Fig. 11.26 Gate control system. P2 is timing of acceleration start

A typical example of the acceleration in the Induction Synchrotron [29] is presented, where a single 100 ns-long bunch injected from the KEK 500 MeV Booster Ring into the KEK PS was trapped in the barrier voltages shown in Fig. 11.27. The half-momentum spread of the injected beam is $(\Delta p/p)_{\max} = 0.003$ determined by measuring a debunching time of the injected beam in the KEK PS. The barrier voltages create a barrier bucket with height

$$\left(\frac{\Delta p}{p}\right)_{\text{height}} = \sqrt{\frac{2eV_{\text{bb}}\tau}{\beta^2 ET|\eta|}}. \tag{11.35}$$

Here, V_{bb} is the barrier voltage, τ the pulse width of the barrier voltage, η the slippage factor and β, E, and T are the relativistic beta, total energy, and revolution period of the synchronous particle, respectively. The net $V_{\text{bb}} = 1.8\ \text{kV} \times 6 = 10.8\ \text{kV}$ was sufficient to accommodate the injected bunch. However, the injected bunch captured by the RF bucket in the Booster ring did not match the barrier-bucket shape. Due to transient filamentation-process in the longitudinal phase-space resulting in a bunch length of 400 ns, the bunch was trapped in the barrier bucket during 450 ms just after injection. The trapped bunch was then accelerated to 6 GeV, consistent with the ramping field $B(t)$ of the guiding magnets. Because the KEK PS is operated as a slow cycling synchrotron, the ramping pattern is divided into three

UNCORRECTED PROOF

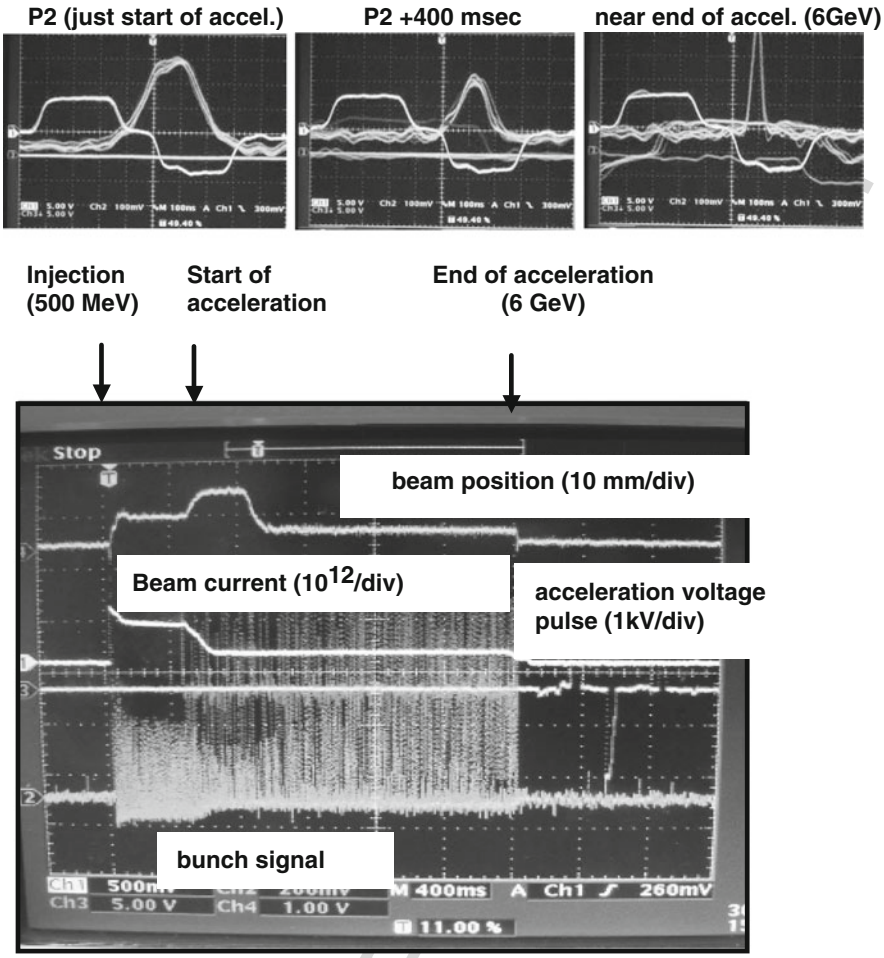

Fig. 11.27 (a) From *left* to *right*: Proton bunch trapped by step barrier voltages before acceleration, in the middle of acceleration, and at the end of acceleration. Gaussian-like, bunch signal; step barrier voltage with opposite polarity; acceleration voltage pulse with a long pulse shape. **b** Ch1, beam current (10^{12}/div); Ch2, bunch monitor signal (the amplitude is inversely proportional to the bunching factor); Ch3, gate pulse density vs. time; Ch4, central beam position (ΔR) (10 mm/div)

regions comprising two transient regions corresponding to the acceleration start and end and the long linear ramping region. The required accelerating voltage to follow this ramping pattern is described by $V_{\mathrm{acc}} = \rho C_0 \frac{\mathrm{d}B}{\mathrm{d}t}$, where ρ is the bending radius, C_0 is the circumference of the accelerator, and B is the bending magnetic flux density as a function of time. Four induction acceleration cells with an output voltage of 1.6 kV per cell were employed for acceleration. The total accelerating voltage of 6.4 kV provided by the induction acceleration cells was much larger than 3.12 kV required in the linear ramping region. A substantial beam loss at the early stage of acceleration is apparent in the second trace of Fig. 11.27b. Beyond

UNCORRECTED

that initial period, the beam intensity remained constant without any beam loss. From the previous experiment [27] described in Sect. 11.4.4, it is known that the mismatch between the bunch shape and the barrier bucket creates a fine-structure in the beam profile in time, yielding a signal from the bunch monitor with the same structure. This effect sometimes caused a timing error in the gate signal for the confinement barrier voltages, leading to a kind of bucket jitter. This occurs because the gate trigger signal is generated when the bunch signal exceeds the preset value in the gate control system and a local peak isolated from the bunch center happens to exceed this threshold. It is speculated that this mechanism is the cause of the beam loss just after injection. The other beam loss at the beginning of acceleration appears to be caused by insufficient ΔR feedback in the transient region approaching the linear ramping region. The outer edge of the beam in the horizontal direction may scrape the vacuum chamber. The bunch length gradually decreased with acceleration. Eventually it approached about 100 ns near the transition energy at 6 GeV. This is the expected adiabatic characteristics confirmed by a computer simulation assuming realistic barrier voltage parameters [30]. Throughout the entire acceleration, the central orbit of the bunch was kept at a constant value, as expected. The result is shown by the upper trace in Fig. 11.27b.

11.5 Perspective

As discussed in Chap. 12, various applications have been considered since the first proposal of the Induction Synchrotron. The super-bunch hadron collider or a proton driver for the second generation of neutrino oscillation experiments are among them. These applications rely on the realization of a super-bunch, the line density of which is just under the space-charge limit in the transverse direction. For this purpose, a long pulse-duration between the barrier voltages and a long pulse acceleration induction voltage is required. The induction acceleration module should be low impedance to minimize beam-loading effects due to a large increase in the stored beam current. The switching power supply used to drive such a low-impedance device must be capable of carrying larger arm currents. The arm currents are limited by the capability of the switching element employed. Research and development ~~works~~ on a high-current switching power supply employing newly developed solid-state switching elements, such as a mold-type SI thyristor or a SiC-JFET, are ~~is~~ being conducted in a collaboration with high-energy physics institutes, universities, solid-state material industries, and pulsed-power industries [31].

The Induction Synchrotron concept has been demonstrated in a complete manner, although there are still some unexplained phenomena. It can be concluded that the concept has been confirmed and this acceleration technology will promise a next generation of accelerator. Assuming further developments in the key devices, novel applications never realized in a conventional RF synchrotron will be expected in the future.

UNCORRECTED PROOF

References

1. K. Takayama and J. Kishiro. Induction Synchrotron. *Nucl. Inst. Meth. A*, A451:304–317, 2000.
2. E. McMillan. The Synchrotron. A Proposed High Energy Particle Accelerator. *Phys. Rev.*, 68:143, 1945.
3. V. Veksler. A New Method of Acceleration of Relativistic Particles. *J. Phys. USSR*, 9:153–158, 1945.
4. S. D. Putnam. Survey of Compact High Current Electron Accelerators. In *Proceedings of the 1987 Particle Accelerator Conference*, pages 887–891, Washington, DC, 16–19 March 1987.
5. H. Wiedemann. *Particle Accelerator Physics*. Springer, Berlin, 2007.
6. J. Griffin, C. Ankenbrandt, J. MacLachlan, and A. Moretti. Isolated Bucket RF Systems in the Fermilab Antiproton Facility. *IEEE Trans. Nucl. Sci.*, NS-30:3502, 21–23 Mar. 1983.
7. M. Blaskiewicz and J. Brennan. A Barrier Bucket Experiment for Accumulating De-bunched Beam in the AGS. In *Proceedings of the 1996 European Particle Accelerator Conference*, page 2373, Barcelona, Spain, 10–14 June 1996.
8. F. Noda. 3 GeV RCS at the JKJ. In *AIP Conference Proceedings No. 642*, pages 53–55, Batavia, IL, 8–12 Apr. 2002. FNAL, American Institute of Physics.
9. C. Prior. Studies of Dual Harmonic Acceleration in ISIS. In *Proceedings of the 12th Meeting of the International Collaboration on Advanced Neutron Sources*, pages 4–11, Abington, UK, 24–28 May 1993. RAL.
10. D. Edwards and M. Syphers. *An Introduction to the Physics of High Energy Accelerators*. Wiley, New York, NY, 1993. For instance, see page: 176.
11. E. Courant and H. Snyder. Theory of the Altaernating Gradient Synchrotron. *Ann. Phys*, 3:1, 1958.
12. K. Johnsen. Effects of non-linearities on the phase-transition. In *Proceedings of the CERN Symposium on High-Energy Accelerators 1*, pages 106–111, Geneva, Switzerland, 11–23 June 1956. CERN.
13. K. Takayama. Phase Dynamics near Transition Energy in the Fermilab Main Ring. *Part. Accel.*, 14:201, 1984.
14. J. Wei. *Longitudinal Dynamics of the Non-Adiabatic Regime on Alternative-Gradient Synchrotrons*. PhD thesis, State University of New York at Stony Brook, 1990.
15. K. Takayama, D. Arakawa, J. Kishiro, K. Koba, and M. Yoshii. Microwave Instability at Transition Crossing: Experiments and a Proton-Klystron Model. *Phys. Rev. Lett.*, 78:871, 1997.
16. Y. Shimosaki, E. Nakamura, K. Takayama, K. Torikai, K. Horioka, M. Nakajima, and M. Watanabe. Beam-Dynamic Effects of a Droop in an Induction Accelerating Voltage. *Phys. Rev. Spec. Topics Accel. Beams*, 7:014201–014208, 2004.
17. B. Erdelyi and C. Johnstone. Tracking of Three Variants of Transition-Free Lattices for a Proton Driver. *In Proceedings of the 20th ICFA Advanced Beam Dynamics Workshop on High Intensity and High Brightness Hadron Beams ICFA-HB2002, AIP Conference Proceedings No. 642*, pages 146–149, Batavia, IL, 8–12 Apr. 2002. FNAL.
18. K. Torikai, Y. Arakida, E. Nakamura, T. Kono, Y. Shimosaki, T. Toyama, M. Wake, J. Kishiro, and K. Takayama. Induction Acceleration System for a Proton Bunch Acceleration in the KEK Proton Synchrotron. In *Proceedings of the 2005 Particle Accelerator Conference*, pages TPPT014, 1679–1681, Knoxville, TN, 16–20 May 2005.
19. M. Watanabe, K. Horioka, J. Kishiro, M. Nakajima, M. Shiho, and K. Takayama. Magnetic Core Characteristics for High Rep-Rate Induction Modulator. *Rev. Sci. Inst.*, 73:1756–1760, 2002.
20. S. Nakajima, S. Arakawa, Y. Yamashita, and M. Shiho. Fe-Based Nanocrystalline FINEMET Cores for Induction Accelerators. *Nucl. Inst. Meth. A*, 331:5556, 1993.
21. K. Koseki, K. Takayama, and M. Wake. Significance of Isolation Impedance in a Solid-state Power Modulator. *Nucl. Inst. Meth. A*, 554:64, 2005.

UNCORRECTED PROOF

22. M. Wake, Y. Arakida, K. Koseki, Y. Shimosaki, K. Takayama, K. Torikai, W. Jiang, K. Nakahiro, A. Tokuchi, and A. Sugiyama. Swithing Power Supply for Induction Accelerators. In *Proceedings of the 2007 Particle Accelerator Conference*, pages MOPAN042, 251–253, Albuquerque, NM, 25–29 June 2007.
23. M. Watanabe. *Induction Voltage Modulator with Cotrollability and Repetition Capability*. PhD thesis, Tokyo Institute of Technology, 2002.
24. K. Torikai, K. Koseki, E. Nakamura, Y. Shimosaki, Y. Arakida, T. Kono, T. Toyama, M. Wake, and K. Takayama. Induction Accelerating Cavity for a Circular Ring Accelerator. In *Proceedings of the 2004 European Particle Acclerator Conference*, pages MOPLT066, 704–706, Lucerne, Switzerland, 5–9 July 2004.
25. K. Takayama, J. Kishiro, K. Koseki, K. Torikai, E. Nakamura, T. Toyama, Y. Arakida, M. Wake, H. Sato, M. Shirakata, S. Igarashi, Y. Shimosaki, M. Sakuda, D. Iwashita, K. Horioka, and M. Shiho. A POP Experiment Scenario of Induction Synchrotron at the KEK 12 GeV-PS. In *Proceedings of the 2003 Particle Accelerator Conference*, pages TPPB093, 1807, Portland, OR, 12–16 May 2003.
26. K. Torikai, K. Takayama, Y. Shimosaki, J. Kishiro, and Y. Arakida, Patent 2005198557 in Japan.
27. K. Torikai, K. Takayama, Y. Shimosaki, Y. Arakida, E. Nakamura, D. Arakawa, S. Igarashi, T. Iwashita, A. Kawasaki, J. Kishiro, K. Koseki, T. Kono, H. Sato, M. Shirakata, T. Sueno, A. Tokuchi, T. Toyama, and M. Wake. Acceleration and Confinement of a Proton Bunch with the Induction Acceleration System in the KEK Proton Synchrotron. Technical Report KEK Preprint 2005-80, KEK, 2005.
28. K. Takayama, K. Koseki, K. Torikai, A. Tokuchi, E. Nakamura, Y. Arakida, Y. Shimosaki, M. Wake, T. Kouno, K. Horioka, S. Igarashi, T. Iwashita, A. Kawasaki, J. Kishiro, M. Sakuda, H. Sato, M. Shiho, M. Shirakata, T. Sueno, T. Toyama, M. Watanabe, and I. Yamane. Observation of the Acceleration of a Single Bunch by Using the Induction Device in the KEK Proton Synchrotron. *Phys. Rev. Lett.*, 94:144801–144804, 2005.
29. K. Takayama, Y. Arakida, T. Dixit, T. Iwashita, T. Kono, E. Nakamura, K. Otsuka, Y. Shimosaki, K. Torikai, and M. Wake. Experimental Demonstration of the Induction Synchrotron. *Phys. Rev. Lett.*, 98:054801–054804, 2007.
30. T. Dixit, Y. Shimosaki, and K. Takayama. Adiabatic Damping of the Bunch Length in the Induction Synchrotron. *Nucl. Inst. Meth. A*, 582:294–302, 2007.
31. K. Nakahiro, W. Jiang, N. Shimizu, S. Yoshida, K. Nakahishi, A. Sugiyama, M. Wake, and K. Takayama. Development of High Repetition-Rate Pulse Generator Using Static Induction Thyristors. In *Proceedings of the International Workshop on Recent Progress in Induction Accelerators*, pages 88–90, Tsukuba, Japan, 7–10 Mar. 2006. KEK.

UNCORRECTED PROOF

Chapter-11

Query No.	Query
AQ1	We have changed citation Fig. 11.16 as Fig. 11.15 as per figure caption. Please check and confirm

UNCORRECTED PROOF

Chapter 12
Applications of Induction Synchrotrons

Ken Takayama

12.1 Typical Accelerator Complex Capable of Employing the Induction Synchrotron Scheme

At present there are no plans to construct a new accelerator complex fully employing the *super-bunch* induction acceleration scheme. However, it appears attractive to retrofit many existing accelerator complexes based on RF technology to the induction synchrotron accelerator technology. It is possible to do so by replacing the RF devices without any changes in major components, such as the magnets, injection/extraction devices, vacuum systems, and beam monitoring instruments. Major laboratories in the world promote unique experimental capabilities using specific hadron accelerator complexes. It is interesting to explore how a delivered beam intensity or luminosity in these accelerator complexes is increased by this replacement and consequential for applications. This replacement appears attractive for the hadron accelerator complexes of Fermi National Accelerator Laboratory (8 GeV-Booster/120 GeV-Main Injector/Tevatron) [1], Brookhaven National Laboratory (1.2 GeV-Booster/28 GeV-AGS/RHIC) [2], and CERN (28-GeVPS/450 GeV-SPS/7 TeV-LHC) [3].

12.2 Hybrid Synchrotrons

We call a *hybrid synchrotron* a synchrotron where charged particles are trapped in RF buckets and accelerated with induction voltage. This is an alternative scheme to the full *induction synchrotron* overviewed in Chap. 11; however, both machines are similar in the context of the functional separation in the longitudinal direction. Advanced features associated with the functional separation described in ~~the~~ Chap. 11 are realized in the hybrid synchrotron.

K. Takayama (✉)
High Energy Accelerator Research Organization (KEK), Tsukuba 305-0801, Japan
e-mail: ken.takayama@kek.jp

K. Takayama, R.J. Briggs (eds.), *Induction Accelerators*, Particle Acceleration and Detection, DOI 10.1007/978-3-642-13917-8_12,
© Springer-Verlag Berlin Heidelberg 2011

UNCORRECTED PROOF

12.2.1 Quasi-adiabatic Focusing-Free Transition Crossing

The method is classified as one of focusing-free transition crossing techniques, where a proton bunch passes through the transition energy with no longitudinal focusing forces, but its acceleration is assured due to flat step-voltages, which are generated with induction acceleration devices. The bunch deformation with shortening in time and stretching in momentum should disappear unless particles in the bunch are subject to confinement voltages, such as the RF voltages, for a short time period before and after the transition energy.

An adiabatic transition crossing method has been demonstrated [4]. An RF bunch can be stretched in time and compressed in energy spread as desired by adiabatically decreasing the RF voltage. If the adiabatic reduction of the RF voltage is performed for a long time period about the transition energy, then nonadiabatic features should be suppressed. This is called a quasi-adiabatic focusing-free transition crossing. In the hybrid synchrotron, in which particles are confined by an RF voltage and accelerated by an induction step-voltage (see Chap. 11), the confinement voltage can be arbitrarily manipulated as long as the particles do not diffuse beyond the accelerating voltage-pulse length. A strict acceleration voltage is necessary so that the orbit of the reference particle follows the center of vacuum chamber.

Consider a small amplitude synchrotron motion near the transition energy. The temporal evolution of the small phase difference from the synchronous particle, $\Delta\tau$, is described by the differential equation [5],

$$\frac{\mathrm{d}^2\Delta\tau}{\mathrm{d}t^2} - \frac{1}{t}\frac{\mathrm{d}\Delta\tau}{\mathrm{d}t} + \frac{4\pi e\gamma_s' t V_{\mathrm{RF}}}{mc^2\gamma_T^4 T^2}\Delta\tau = 0. \tag{12.1}$$

Here γ_T is the transition energy, T is the revolution period of the synchronous particle, V_{RF} is the RF amplitude, and the time t is measured from the transition crossing ($t = 0$). We assume that γ_s is a linear function of time, i.e,

$$\gamma_s = \gamma_T + \gamma_s' t, \tag{12.2}$$

where $\gamma_s'(\equiv \mathrm{d}\gamma_s/\mathrm{d}t)$ is the acceleration rate to satisfy the following relation

$$mc^2\gamma_s' = \frac{eV_a}{T},$$

where $V_a = \rho C_0 \mathrm{d}B/\mathrm{d}t$ is the voltage gain per turn. The slippage factor η defined in Eq. (12.1) linearly changes with time near the transition energy according to

$$\eta = \frac{1}{\gamma_T^2} - \frac{1}{\gamma_s^2} \cong \frac{2\gamma_s'}{\gamma_T^3} t. \tag{12.3}$$

UNCORRECTED PROOF

We further assume that the RF amplitude for confinement varies in time as

$$V_{\mathrm{RF}} = \pm V_0 \left| \frac{t}{t_0} \right|, \tag{12.4}$$

for a finite time period of $2t_0$, where $V_0(= \text{const})$ during the time period. The sign of the voltage is changed at transition crossing to maintain the phase stability. The synchronous particle never experiences this RF voltage because it always has zero phase. Substitution of Eq. (12.4) into Eq. (12.1) gives

$$\frac{\mathrm{d}^2 \Delta\tau}{\mathrm{d}t^2} - \frac{1}{t}\frac{\mathrm{d}\Delta\tau}{\mathrm{d}t} + 4\beta^2 t^2 \Delta\tau = 0, \tag{12.5}$$

with

$$\beta^2 = \frac{\pi e \gamma_s' V_0}{mc^2 \gamma_T^4 T^2 t_0}.$$

The independent solutions of Eq. (12.5) are $tJ_{1/2}(\beta t^2)$ and $tN_{1/2}(\beta t^2)$, where $J_{1/2}(x)$ and $N_{1/2}(x)$ are the Bessel functions of half-integer order [6]. Thus, the general solution of Eq. (12.5) is $c_1 t J_{1/2}(\beta t^2) + c_2 t N_{1/2}(\beta t^2)$ with coefficients c_1, c_2, which are determined from initial conditions. The Bessel function expressions can be expressed in terms of the elementary functions as

$$\begin{aligned} tJ_{1/2}(\beta t^2) &= t\sqrt{\frac{2}{\pi\beta t^2}}\sin(\beta t^2) = \sqrt{\frac{2}{\pi\beta}}\sin(\beta t^2), \\ tN_{1/2}(\beta t^2) &= -tJ_{-1/2}(\beta t^2) \\ &= -t\sqrt{\frac{2}{\pi\beta t^2}}\cos(\beta t^2) = -\sqrt{\frac{2}{\pi\beta}}\cos(\beta t^2), \end{aligned}$$

Using these results, we obtain

$$\Delta\tau = c_1 t J_{1/2}(\beta t^2) + c_2 t N_{1/2}(\beta t^2) = c_3\sqrt{\frac{2}{\pi\beta}}\sin(\beta t^2 + \delta). \tag{12.6}$$

In Eq. (12.6), c_3 and δ are determined by the initial condition of an individual particle at $t = -t_0$. Since the amplitude is constant in the time interval $-t_0 < t < t_0$, Eq. (12.6) shows that the maximum excursion in $\Delta\tau$ remains constant during transition crossing, suggesting that the bunch length remains constant. The synchrotron oscillation amplitude, which is subject to adiabatic damping far below the transition energy, is a function of t_0. Thus, one can create a bunch of any length desired and bunch shortening at transition crossing can be avoided.

UNCORRECTED PROOF

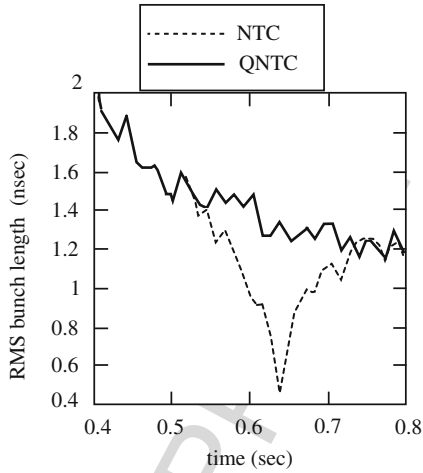

Fig. 12.1 Temporal evolution of the bunch length for two cases (simulations): normal transition crossing (NTC) and qusi-adiabatic focusing-free transition crossing

The feasibility of this method has been extensively studied with computer simulations. Figure 12.1 indicates the temporal evolution near the transition energy, assuming the machine and typical beam parameters of the KEK 12 GeV PS.

The method has been experimentally demonstrated in the hybrid synchrotron. The temporal evolution of the bunch length obtained when the RF voltage amplitude was linearly reduced to zero at the transition energy and then linearly increased according to Eq. (12.4) is shown in Fig. 12.2, together with the case without any RF amplitude reduction. The bunch length behaves as predicted by the simulation. The slight negative slope in time is attributed to adiabatic damping associated with acceleration. It is noted that the RF voltage amplitude reduction starting at time $t = t_0$, at which time the bunch length through the transient region is determined, was arbitrarily chosen. A specific bunch-length desired is obtainable by appropriately choosing t_0.

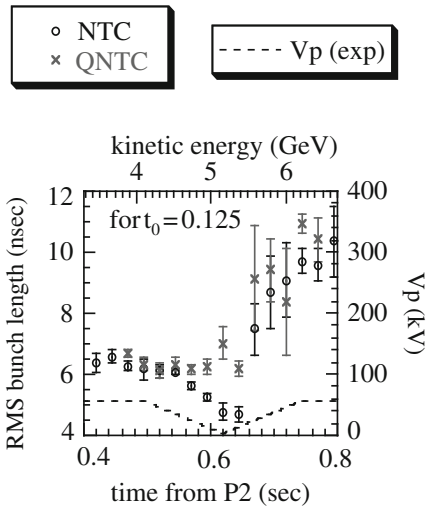

Fig. 12.2 Temporal evolution of the bunch length for two cases (experimental results): normal transition crossing (NTC) and qusi-adiabatic focusing-free transition crossing (QFTC). P2 represents the beginning of acceleration

UNCORRECTED PROOF

12.3 Super-Bunch Hadron Colliders

12.3.1 Introduction

A super-bunch hadron collider [7, 8] is a natural application of the induction synchrotron, where super-bunches trapped in the barrier buckets generated with induction step-voltages are collided at collision points. The super-bunch hadron collider promises to increase the luminosity by an order of magnitude because of its capability of accommodating a larger number of particles than a conventional hadron collider based on the RF technology such as LHC [3] and RHIC [2]. This high luminosity is achieved at the expense of risks such as parasitic beam–beam effects and coherent instabilities. On the other hand, crucial beam dynamics issues in the conventional hadron collider such as the e-p instabilities or intra-beam scattering are relaxed. These relaxations result from intrinsic characteristics of the super-bunch and from properties of the collision between super-bunches. In this section we contrast essential aspects of a *super-bunch hadron collider* with a conventional hadron collider. After the proposal of super-bunch hadron colliders, CERN had been exploring a feasibility of the super-bunch scheme in LHC as a possible upgrade path [9]. BNL also is examining the possibility for a super-bunch in the RHIC [10]. In the text, their details including the VLHC [11] with the super-bunch option are described with concrete machine and beam parameters.

12.3.2 Contrast of Coasting Beam, RF Bunch Collider, and Super-Bunch Colliders

A collision between counter-rotating continuous beams has been realized using the CERN Intersecting Storage Rings (ISR) [12] in 1971, which was also the first proton–proton collider. RF bunches were injected from the 28 GeV CERN-PS into the ISR rings and were de-bunched and accelerated up to 31 GeV with a so-called phase-displacement acceleration technique [13] then beams were collided. The ISR experimentally confirmed for the first time that the luminosity of colliders were practically limited by beam–beam interactions, the strength of which were measured by using an incoherent beam–beam tune-shift parameter. Keil et al. carefully investigated the dependence of luminosity and beam–beam tune-shifts in coasting beam colliders on machine/beam parameters and discussed possible ways to maximize the luminosity [14]. Analytical results were refined in [7, 8]. Since the phase-displacement acceleration technique is inefficient, a wide range of acceleration energy is not expected. Thus, a coasting beam collider in a high energy, TeV-class region is unlikely. Indeed, no coasting beam collider has been designed or constructed after the ISR.

The ISR itself was shutdown in a relatively short time. ISABELLE at BNL [15], which was an RF synchrotron and should have provided RF bunches for collision, was designed as a second generation of proton–proton collider and its construction was undertaken in 1978. Although it was switched to a different design

UNCORRECTED PROOF

called the Colliding Beam Accelerator (CBA) because of technical problems in the fabrication of superconducting magnets, the project was cancelled in 1983 in favor of a new machine called the Superconducting Super Collider (SSC). Fortunately, the accelerator tunnel constructed for ISABELLE was used for the Relativistic Heavy Ion Collider (RHIC) in 2001. Meanwhile, the construction of SSC began in Texas in 1991 after extensive design work [16] but the project was cancelled in 1993 because of the political decisions induced by increasing cost. The Large Hadron Collider presently being commissioned at CERN is a second proton–proton collider following two unsuccessful US projects. The future Very Large Hadron Collider, which is regarded as a last man-made circular collider, has been studied for design feasibility in US in 2001 [11], but the construction of such a collider is not envisaged within the first quarter of the century.

All hadron colliders mentioned above are RF synchrotrons. Beam bunches in these colliders except the ISR are trapped and accelerated with RF buckets. For the later convenience, we call these colliders a conventional hadron collider (CHC), because they are based on the conventional RF technology. Specific features of a CHC are summarized below: The luminosity is expressed as

$$\mathcal{L} = F\frac{k_b N_b^2 f_{\mathrm{rev}}\gamma}{4\pi\epsilon_n\beta^*}, \tag{12.7}$$

where k_b is the number of bunches per ring, N_b the number of protons per bunch, f_{rev} the revolution frequency, ϵ_n the normalized r.m.s. transverse emittance (assumed to be the same in both planes), β^* the beta-function at the collision point, and $F \leq 1$ is a reduction factor caused by the finite crossing angle Φ.

Although it is clear from the luminosity expression, in which parameters must be improved to increase the luminosity of the CHC, there are limits on the range of beam/machine parameters:

(1) The space-charge limit in the upstream accelerators imposes a limit on the ratio of the number of protons to the emittance, $\Delta\nu = N_b/\epsilon_n < 0.25$.
(2) The beam–beam limit, $\xi = \frac{N_b\gamma_0}{4\pi\epsilon_n} \leq 0.004$/Interaction Point ($\gamma_0$, classical radius of proton), which will be discussed in detail in Sect. 12.3.5.
(3) The capability of heat transfer in the cryogenetics of collider magnets gives a synchrotron radiation limit, $P_{\mathrm{rad}}(\propto k_b N_b) \leq\sim$ few watts/m.
(4) Time-resolution of present particle detectors require a minimum bunch spacing something around 5–7 m. Such bunch spacing is created by RF manipulation in the upstream accelerators. In addition, the longitudinal size of each bunch is controlled by using a higher frequency cavity in a downstream accelerator and collider and optimizing the RF voltage to match β^* so as to maximize the luminosity $\mathcal{L}$ for fixed N_b.

The beam occupancy ratio in the entire accelerator circumference, $\kappa = \sqrt{2\pi}k_b\sigma_s/C_0$, typically is limited to 1–3 %.

If the heat deposited by synchrotron radiation on the cryogenic system is removed by engineering solutions and a large number of "pile-up" events is managed by

UNCORRECTED PROOF

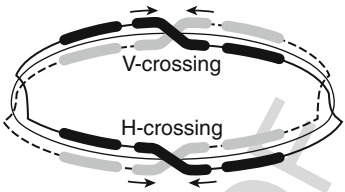

Fig. 12.3 Schematic view of a super-bunch hadron collider

future improvements in particle detectors, then the last factors to determine the ultimate achievable luminosity should be the population of bunch trains along the collider ring and the local density of each bunch. The allowable local density of each bunch depends on specific accelerators within the accelerator complex including the collider. The maximum value for the bunch density in the collider is assumed in the present discussion.

If the proton bunches occupy most of the collider circumference with an allowable momentum spread, the luminosity of hadron colliders can drastically increase. In a typical scheme, 20–30 % of the circumference can be occupied by the proton beam instead of 3–4 %. This situation is essentially like having continuous collisions between proton beams stored in two rings, as seen in Fig. 12.3.

The luminosity for such super-bunch collisions is estimated to be at least 20-times higher than for a CHC. The induction synchrotron discussed in Sect. 11.4.1 is capable of generating a super-bunch, which keeps the same momentum spread and local intensity as in the CHC scheme. After stacking super-bunches in the collider ring and accelerating them with step-voltages generated in the induction gaps to the final energy, multiple super-bunches in both rings are available for collisions. The concept and feasibility of this novel type of collider is reviewed.

12.3.3 Generation of the Super-Bunch

It is not so simple to generate super-bunches for collision in the last-stage collider ring. At the upstream stage of the accelerator complex, a seed for super-bunch must be produced. These super-bunch seeds are merged into a single super-bunch using the barrier-bucket stacking technique described in detail in Sect. 11.2 and illustrated in Fig. 12.4.

As a super-bunch is subject to adiabatic damping associated with acceleration, its bunch length can be reduced by shortening the barrier pulse distance. The momentum spread is determined from the Liouville theorem during this bunch-shortening process. Thus, further stacking of these super-bunches is possible in downstream accelerators. An example of super-bunch handling is shown in Fig. 12.4. In this example, the FNAL accelerator complex is assumed to be the injector of the VLHC. Here, note that a maximum super-bunch length is limited by a practical reason that the induction accelerating pulse-length is order of 1 μs at most, because the longer pulse demands a larger volume of magnetic core material. A barrier-bucket super-bunch seems to be ideal for colliders, because its line density and momentum

UNCORRECTED PROOF

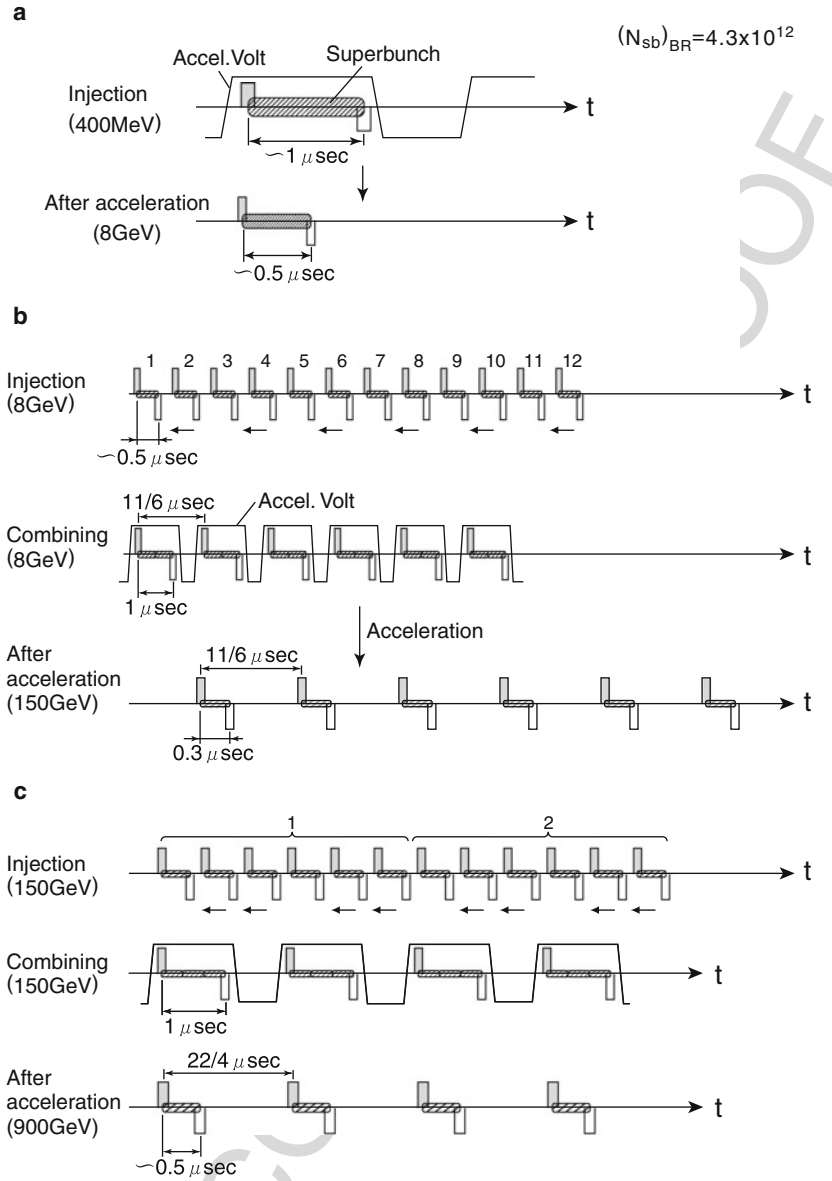

Fig. 12.4 Stacking process in the FNAL accelerator complex as an example of a hadron collider injector. (**a**) LEB (Fermilab BR, $C_o = 474.2$m), (**b**) MEB (Main injector, $C_o = 3.32$ km, $\tau_0 \simeq 11\mu$s), and (**c**) HEB (Tevatron, $C_o = 6.283$ km, $\tau_0 \simeq 22\mu$s)

UNCORRECTED PROOF

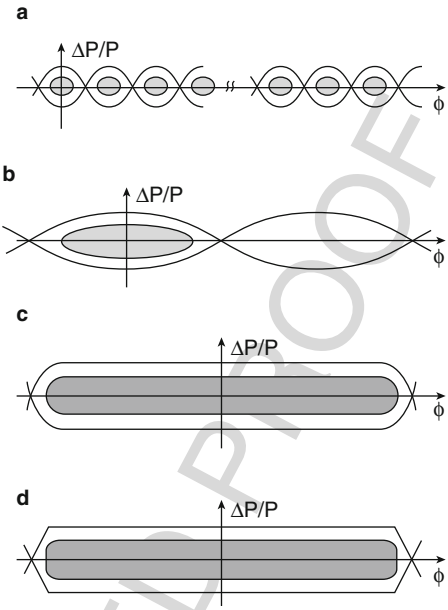

Fig. 12.5 Conventional RF bunches and various types of super-bunch. (**a**) present higher harmonic RF bunch, (**b**) Low harmonic RF super-bunch, (**c**) Super-bunch in an RF barrier bucket, and (**d**) Super-bunch in a step-barrier bucket

spread are almost uniform throughout the bunch. However, there are other types of super-bunch under consideration as shown in Fig. 12.5.

In Table 12.1, a comparison between technological approaches to form super-bunches is made.

Table 12.1 Type of super-bunch

	Low harmonic RF	RF barrier	Step barrier
Technology	Low harmonic cavity low freq. power source	Low Q RF cavity, amplified pulse voltage	Induction cell pulse modulator
Feature			
Advantage	Well-developed, small RF voltage	Already demonstrated, easy bunch formation	Easy bunch formation by controlling trigger timing, uniform line density
Disadvantage	Limited phase-space area, large momentum spread	No acceleration	Beam loading, jitter

12.3.4 Luminosity

The maximum pulse-length of the accelerating induction voltage is typically limited to order of one microsecond due to the practical size of the necessary induction-core. Thus, the collider must be occupied by multiple super-bunches, and bunch

UNCORRECTED PROOF

spacing in the ring is used to provide time to reset the magnetic materials. In the case of a VLHC-size ring, the number of super-bunches can be several hundreds (see Sect. 12.3.6). The super-bunch train can occupy a considerable fraction of the ring circumference, typically 20–30%, with a momentum spread determined by the barrier-bucket height. After the beam bunches reach the final energy, a slight accelerating voltage is applied to replenish the energy loss due to synchrotron radiation, while the super-bunches are longitudinally confined with the barrier buckets. Each of the super-bunches intersects with its own counterpart in a half time-period of the bunch length as shown in Fig. 12.3.

Consider a head-on collision between Super-Bunch A and Super-Bunch B. Assuming the super-bunch length ℓ_{sb} is much longer than the effective detector length 2ℓ, an asymmetric feature in collision in the super-bunch head/tail is ignored; a symmetric feature in the core region is taken into account in the following discussion on the luminosity. Super-Bunch A and Super-Bunch B are segmented into pieces of length ds. Particle numbers dN_{A} and dN_{B} contained in a small volume of $dxdyds$ at an arbitrary position (x, y, s) of Super-Bunch A and Super-Bunch B are

$$\mathrm{d}N_A = \rho_A(x, y, s)\mathrm{d}x\mathrm{d}y\mathrm{d}s,$$
$$\mathrm{d}N_B = \rho_B(x, y, s)\mathrm{d}x\mathrm{d}y\mathrm{d}s,$$

where $\rho_A(x, y, s)$ and $\rho_B(x, y, s)$ are the particle number density. A target-size of particles belonging to Super-Bunch B in volume dxdyds is denoted by $\sigma\mathrm{d}N_B$. The probability that a single particle belonging to Super-Bunch A collides with any particle of Super-Bunch B in the small volume dxdyds at the position (x, y, s) is then

$$\sigma\frac{\mathrm{d}N_B}{\mathrm{d}x\mathrm{d}y}.$$

The number of particles of dN_A that collide with any particles in dN_B is

$$\sigma\frac{\mathrm{d}N_B}{\mathrm{d}x\mathrm{d}y}\mathrm{d}N_A.$$

Thus the total number of particles $R(s)$ passing through the entire cross-section at s, which collide with any particles of Super-Bunch B during traversing through ds, is given by the integral

$$R(s) = \sigma\int_{-\infty}^{\infty}\int_{-\infty}^{\infty}\frac{\mathrm{d}N_B}{\mathrm{d}x\mathrm{d}y}\mathrm{d}N_A, = \sigma(\mathrm{d}s)^2\int_{-\infty}^{\infty}\int_{-\infty}^{\infty}\rho_B(x, y, s)\rho_A(x, y, s)\mathrm{d}x\mathrm{d}y.$$

The total number of particles scattering in the detector region of length 2ℓ is obtained by integrating $R(s)$ from $s = -\ell$ to $s = \ell$,

$$\int_{-\ell}^{\ell}R(s) = \sigma\mathrm{d}s\int_{-\ell}^{\ell}\mathrm{d}s\int_{-\infty}^{\infty}\int_{-\infty}^{\infty}\rho_B(x, y, s)\rho_A(x, y, s)\mathrm{d}x\mathrm{d}y.$$

UNCORRECTED PROOF

The total number of particles in Super-Bunch A, which enter into the boundary $s = -\ell$ and collide with any particles in Super-Bunch B at any location within the detector, is then

$$\frac{\ell_{\rm sb}}{{\rm d}s}\int_{-\ell}^{\ell} R(s) = \sigma\ell_{\rm sb}\int_{-\ell}^{\ell}{\rm d}s\int_{-\infty}^{\infty}\int_{-\infty}^{\infty}\rho_B(x,y,s)\rho_A(x,y,s){\rm d}x{\rm d}y,$$

where ℓ_{sb} is the a full length of the super-bunch. Multiplying this result by the bunch revolution frequency in the ring f and the number of super-bunches per ring $k_{\rm sb}$, we have a formula for a total number of proton–proton collisions per second. Dividing it by the cross-section σ, we arrive the luminosity formula,

$$\mathcal{L} = f\ell_{\rm sb}k_{sb}\int_{-\ell}^{\ell}{\rm d}s\int_{-\infty}^{\infty}\int_{-\infty}^{\infty}\rho_A(x,y,s)\rho_B(x,y,s){\rm d}x{\rm d}y. \tag{12.8}$$

Next we consider effects due to the beam crossing in the interaction region with the crossing angle Φ in the (y,s)-plane as illustrated in Fig. 12.6. We introduce primed coordinates related to the x, y, s coordinates by

$$\begin{aligned} x' &= x,\\ y' &= y\cos\Phi + s\sin\Phi \cong y + s\Phi,\\ s' &= s\cos\Phi - y\sin\Phi = s - y\Phi \cong s, \end{aligned}$$

The approximate forms are valid for the usual situation with $\Phi \ll 1$ and $s \gg x, y$.

To first order in the crossing angle Φ, the practical luminosity for one IP (interaction point) is

$$\mathcal{L} = f\ell_{\rm sb}k_{sb}\int_{-\ell}^{\ell}ds\int_{-\infty}^{\infty}\int_{-\infty}^{\infty}\rho_A(x,y,s)\rho_B(x',y',s'){\rm d}x{\rm d}y.$$

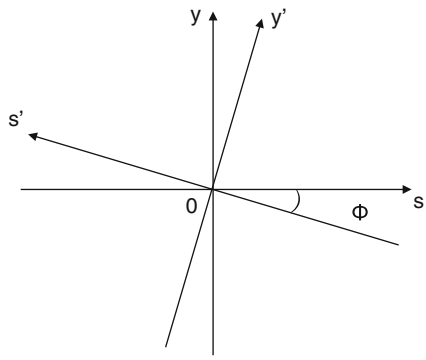

Fig. 12.6 Coordinate system

UNCORRECTED PROOF

If the transverse density profile of the super-bunches are assumed to be of Gaussian form with circular cross section, then the particle distribution may be expressed as

$$\rho_A = \frac{\lambda_A}{2\pi\sigma_A^2(s)} \exp\left[-\frac{x^2+y^2}{2\sigma_A^2(s)}\right],$$
$$\rho_B = \frac{\lambda_B}{2\pi\sigma_B^2(s')} \exp\left[-\frac{x'^2+y'^2}{2\sigma_B^2(s')}\right].$$

Here, $\sigma_A = \langle x^2\rangle^{1/2} = \langle y^2\rangle^{1/2}$ is the rms width, and λ_A and λ_B are the constant line densities. The rms beam sizes σ_A^2 and σ_B^2 are related to the beam emittance ϵ and the beta function β by

$$\sigma^2(s) \propto \epsilon\beta(s),$$

where the variation of beta function in the interaction region is described by

$$\beta(s) = \beta^* + \frac{s^2}{\beta^*},$$

with $\beta_x^* = \beta_y^* = \beta^*$. Thus, we obtain

$$\sigma_x(s) = \sigma_y(s) = \sigma^*\left[1+\left(\frac{s}{\beta^*}\right)^2\right]^{1/2},$$

where σ^* is the rms beam size at the crossing point. Evaluating $\mathcal{L}$ in the unprimed coordinate system, we have

$$\begin{aligned}\mathcal{L}_{\mathrm{SHC}}(\Phi, f) &= \frac{f\ell_{\mathrm{sb}}k_{\mathrm{sb}}\lambda_A\lambda_B}{4\pi^2(\sigma^*)^4}\int_{-\ell}^{\ell}\mathrm{d}s\int_{-\infty}^{\infty}\mathrm{d}x\int_{-\infty}^{\infty}\mathrm{d}y\,\frac{\exp\left\{-\frac{2x^2+y^2+(y+s\Phi)^2}{2(\sigma^*)^2[1+(s/\beta^*)^2]}\right\}}{\left[1+(s/\beta^*)^2\right]^2}\\ &= \frac{f\ell_{\mathrm{sb}}k_{\mathrm{sb}}\lambda^2}{4\pi^2(\sigma^*)^4}\int_{-\ell}^{\ell}\mathrm{d}s\,\frac{\exp\left\{-\frac{\Phi^2s^2}{2(\sigma^*)^2[1+(s/\beta^*)^2]}\right\}}{1+(s/\beta^*)^2}.\end{aligned} \tag{12.9}$$

Here it is assumed that all super-bunches in the collider have the same line density λ. It is interesting to compare the luminosity $\mathcal{L}_{\mathrm{SHC}}$ in the SHC with in the CHC with the local peak density of λ, using the function of c[illegible]ng angle Φ' and an effective size (2ℓ) of the particle detector. The luminosity L_{CHC}, in the CHC, where the transverse particle distribution of an RF bunch is the same Gaussian as that in

UNCORRECTED PROOF

the super-bunch and the longitudinal distribution is the Gaussian with the rms length of σ_s, is given by

$$\mathcal{L}_{\mathrm{CHC}}(\Phi') = \frac{f k_b (\sigma_s' \lambda)^2}{4(\sigma^*)^2 \sqrt{1 + \left(\frac{\sigma_s \Phi'}{2\sigma^*}\right)^2}},$$

where $\sigma_s' \equiv \sqrt{2\pi}\sigma_s$, and k_b is the number of RF bunches per ring. L_{SHC} is expressed in term of $\mathcal{L}_{\mathrm{CHC}}$ as follows,

$$\mathcal{L}_{\mathrm{SHC}}(\Phi, \ell) = 4 \frac{(k_{\mathrm{sb}} \ell_{\mathrm{sb}})}{(k_b \sigma_s')} \frac{F_{\mathrm{SHC}}(\Phi, \ell)}{\sigma_s' F_{\mathrm{CHC}}(\Phi')} \mathcal{L}_{\mathrm{CHC}}(\Phi'), \tag{12.10}$$

where F_{CHC} and F_{SHC} are the form factors described by

$$F_{\mathrm{CHC}}(\Phi') = 1/\sqrt{1 + (\Phi' \sigma_s / 2\sigma^*)^2},$$

$$F_{\mathrm{SHC}}(\Phi, \ell) = \int_0^\ell ds \frac{\exp\left(-\frac{\gamma \Phi^2 s^2}{2\beta^* \epsilon_n [1 + (s/\beta^*)^2]}\right)}{[1 + (s/\beta^*)^2]},$$

using $(\sigma^*)^2 = \epsilon_n \beta^* / \gamma$ (ϵ_n: normalized emittance). In the limit of $\Phi = 0$, $k_{\mathrm{sb}} = k_b$, $\ell_{\mathrm{sb}} = \sigma_s'$, $2\ell = \sigma_s'/2$, Eq. (12.9) becomes $L_{\mathrm{SHC}}(0, \sigma_s'/4) = L_{\mathrm{CHC}}(0)$. The factor of $(k_{\mathrm{sb}} \ell_{\mathrm{sb}})/(k_b \sigma_s')$ in Eq. (12.9) represents the relative ratio of beam occupation in the SHC/CHC ring circumference. Since ℓ_{sb} is determined by engineering limits of super-bunch acceleration as mentioned in Chap. 11, and a total number of particles contained in the super-bunch train, that is, $k_{\mathrm{sb}} \ell_{\mathrm{sb}} \lambda$ is limited by a level of allowable synchrotron radiation, the relative occupation ratio depends on an available acceleration technology and a collider of concern. For a typical example of the VHC stage-1 design, where

$$\sigma_s' = 15 \text{ cm}, \quad \beta^* = 0.5 \text{ m}, \quad \epsilon_n = 1\ \mu\text{rad},$$
$$\gamma mc^2 = 20 \text{ TeV}, \quad 2\ell = 5 \text{ m}, \quad \Phi' = 150\ \mu\text{rad},$$

and the relative occupation factor of 20 is expected, the normalized luminosity is shown as a function of Φ in Fig. 12.7. Rapid decreasing with the crossing angle is remarkable. This comes from a simple reason that collisions between continuous beams are likely to be affected by the collision angle.

The form factor $F_{\mathrm{SHC}}(400\ \mu\text{rad}, \ell)$ is depicted as a function of ℓ in Fig. 12.8. It shows that the form factor saturates beyond $\ell = 0.1$ m. This suggests that the long-range collision in space between super-bunches does not substantially contribute to the luminosity. Thus, it turns out that the value of beam occupation is crucial to obtain a high luminosity.

UNCORRECTED PROOF

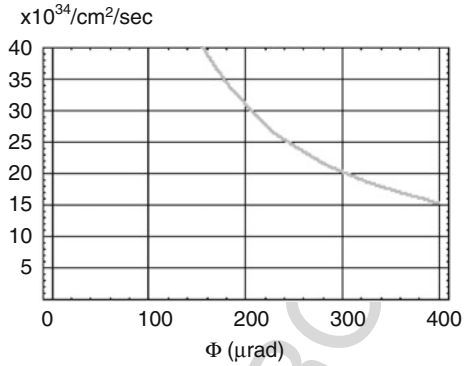

Fig. 12.7 Luminosity versus crossing angle for the VLHC stage-1 parameter

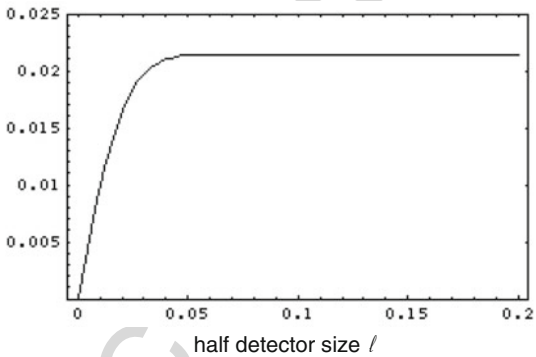

Fig. 12.8 Form factor as a function of ℓ

12.3.5 Beam–Beam Effects and Crossing Geometry

When two super-bunches collide, they exert electromagnetic forces upon each other. The forces are similar to the self space-charge forces on a particle in an intense beam. However, there are two major differences. In the self-induced space-charge force, the characteristic cancellation of electric and magnetic contributions occurs. The self space-charge forces as discussed in Sect. 7.4.1 are given by

$$e(\mathbf{E} + \mathbf{v} \times \mathbf{B}) \cong \left[\mathbf{E} + \mathbf{v} \times \left(\frac{-\mathbf{v}}{c^2} \times \mathbf{E}\right)\right] = e(1 - \beta^2)\mathbf{E} \cong \frac{e\mathbf{E}}{\gamma^2}.$$

In the limit of high energy, the force diminishes in importance. In contrast, the magnetic-field generated by the counter-part beam has the opposite sign, because the counter-part beam runs in the opposite direction. Thus, the beam–beam force is proportional to $(1$ [illegible]$)$. For the high-energy collision $\beta \to 1$, the force approaches the $2e\mathbf{E}$. Both type of space-charge forces are highly nonlinear; the extent of the

UNCORRECTED PROOF

nonlinearity depends on the transverse beam distribution. When two beams overlap, the beam–beam force takes a role of defocusing in the transverse direction, yielding a detune in the betatron oscillation frequency. A second major distinction between the two types of forces is that the single-beam space-charge force distributes around the ring circumference with modulation proportional to the envelope function $\beta(s)^{1/2}$; on the other hand, the colliding beams encounter their counter parts at only a few IPs. This suggests that the beam–beam force is quite rich in azimuthal harmonics, contrary to the single-beam space-charge force that is dominated by the 0th harmonic. This feature is important from the beam dynamics point of view, since the non-zero azimuthal harmonics are responsible for the excitation of nonlinear resonances. Even so the 0th harmonic of the beam–beam force, which represents a size of detuning in the betatron oscillation, is important to measure the strength of the beam–beam interaction.

Beyond the interaction region the colliding beams are separated from each other by the deflecting magnets and do not affect each other. Its physical distance $2\ell_{\text{int}}$ is much larger than the effective detector region 2ℓ in a modern high-energy hadron collider.

The beam–beam effects on an arbitrary particle with non-zero emittance are estimated in a term of non-resonant tune-shift (coherent tune-shift), which represents how much the betatron oscillation frequency is shifted from the machine determined bare-tune by defocusing forces exerting on a particle of concern. Its magnitude is obtained in analytical ways [17, 18] or by numerical methods, once the charge distribution of the counter rotating beam is given. The coherent tune-shift depends on the oscillation amplitude of the particle and collision geometry, as shown later. In the limit of zero-emittance, the coherent tune-shift is called an incoherent betatron tune-shift, which is related to the first term in an expansion of the beam–beam force with respect to excursion from the center of the betatron oscillation and can be expressed as

$$\Delta\nu_y = \frac{1}{4\pi}\int_0^{C_0} \mathrm{d}s\beta(s)k_y(s),$$

where

$$k_y(s) = \left(\frac{e}{mc^2}\right)\frac{1+\beta^2}{\beta^2\gamma}\left[\frac{\partial E_y}{\partial y}\right]_{y=0}.$$

For the horizontal direction, the expression is the same as the above replacing y by x. This parameter is known to be a good measure of the beam–beam effects.

Incoherent beam–beam tune shift: In the SHC scheme, the incoherent beam–beam tune shift is of big concern as well as coherent beam–beam tune shift, even with a deep crossing angle. The incoherent beam–beam tune-shift can analytically be evaluated by manipulating the non-oscillating terms in the beam–beam

UNCORRECTED PROOF

perturbing potential. The tune-shift normalized by that in the head-on collision of the CHC scheme is given in the following forms [7, 8]:

$$\frac{(\Delta\nu_x)_\Phi^{\mathrm{SHC}}}{\xi} = \frac{8\beta^*\epsilon_n}{\sigma_s'\gamma}\int_0^{\ell_{\mathrm{int}}} \frac{1+s^2/(\beta^*)^2}{\Phi^2 s^2} \times\left[1-\exp\left(-\frac{\gamma\Phi^2 s^2}{2\epsilon_n\beta^*(1+s^2/(\beta^*)^2)}\right)\right]\mathrm{d}s',$$

$$\frac{(\Delta\nu_y)_\Phi^{\mathrm{SHC}}}{\xi} = \frac{8}{\sigma_s'}\int_0^{\ell_{\mathrm{int}}} \exp\left(-\frac{\gamma\Phi^2 s^2}{2\epsilon_n\beta^*(1+s^2/(\beta^*)^2)}\right)\mathrm{d}s - \frac{(\Delta\nu_x)_\Phi^{\mathrm{SHC}}}{\xi}, \tag{12.11}$$

Here crossing in the vertical direction is assumed and $2\ell_{\mathrm{int}}$ is the size of the interaction region, $2\ell \ll 2\ell_{\mathrm{int}} \ll \sigma_{\mathrm{sb}}$. In the limit of $\Phi = 0$, $2\ell_{\mathrm{int}} = \sigma_s'/2$, Eq. (12.11) become unity. The numerical values for both directions are shown as functions of Φ in Fig. 12.9. A change in the polarity for the vertical direction beyond some critical crossing-angle is notable. This can be understood by recognizing that a particle is focused by space-charge effects as it leaves from the beam-core region, while it is defocused in the core region. Figure 12.10 graphically illustrates this point. Namely, a longer stay outside the core region gives net focusing through the interaction region beyond a certain critical crossing angle. The characteristics strongly suggests that the hybrid crossing (vertical crossing in one interaction region (IR) and horizontal crossing in the other) [7, 8] should be employed in the SHC scheme. The collider rings necessarily have twists. By the hybrid crossing, as schematically shown in Figs. 12.3 and 12.11, the beam–beam tune-shift largely diminishes for both directions. The relative tune-shifts for both directions are less than 2.0 for the crossing-angle beyond 150 μrad, where the luminosity is quite attractive, as found in Fig. 12.7. The magnitude is sufficiently acceptable, because it is equal to the integrated head-on beam–beam tune-shift in the CHC scheme with a couple of IPs.

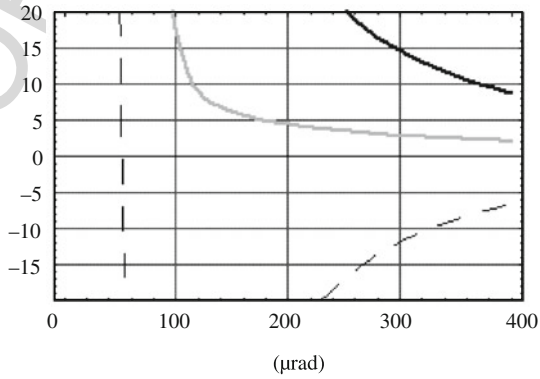

Fig. 12.9 Normalized beam–beam tune shifts for $2\ell_{\mathrm{int}} = 50$ m (*solid*, horizontal; *broken*, vertical; *gray*, sum) for the VHLC stage-1 parameter

UNCORRECTED PROOF

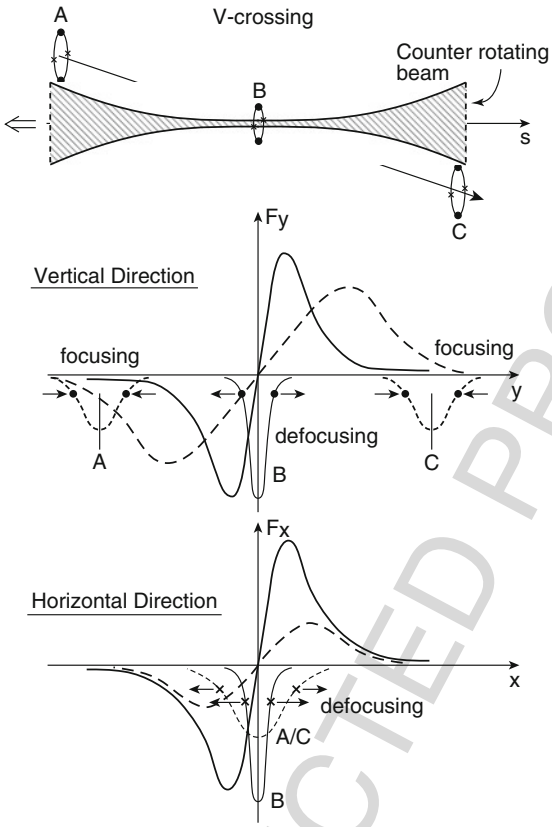

Fig. 12.10 Schematic view of space-charge focusing and defocusing in collision in the s–y plane. *Top*, geometric configuration with a track of a test particle and a change in the beam size of counter rotating super-bunch around the IP; *middle*, the space charge force exerting on the test particle in the vertical direction, where the *broken* and *solid lines* represent the forces at $s = A/C$ and B, respectively; *bottom*, the space charge force exerting on the test particle in the horizontal direction at the same azimuthal locations

Incoherent beam–beam tune-shift and crossing geometry: The beam–beam tune-shift parameters during nominal operations are rather similar to that in the CHC, assuming a same local density. Recent simulations based on the weak–strong model have indicated that an incoherent tune spread due to the continuous parasitic beam–beam interaction is bounded within a tolerable level of 0.015 without any emittance blow-up, assuming the crossing angle of 400 μrad. The full footprint on the tune space is like a bird wing, as shown in Fig. 12.12. This characteristic has been recognized in the earlier work [19]. The tune of large emittance particles locates on the tip of the wing. The footprint for a particle with the smallest emittance in the x-direction and the largest emittance in the y-direction corresponds to the upper tip of wing; meanwhile, the footprint for a particle with the other combination of emittance places on the lower tip. This feature suggests that the footprint on the

UNCORRECTED PROOF

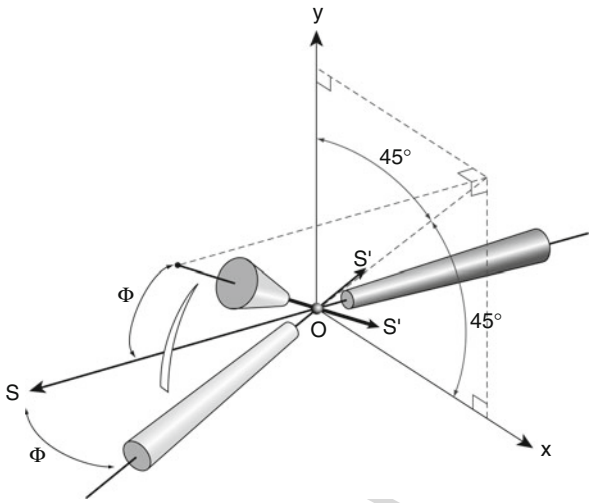

Fig. 12.11 Schematic view of the hybrid crossing and inclined crossing. The super-bunch (*gray*) subject to hybrid crossing has the crossing angle of Φ on the s–x plane; the projection of the s' axis on the x–y plane of the super-bunch subject to inclined hybrid crossing has $\pi/4$ from both axes

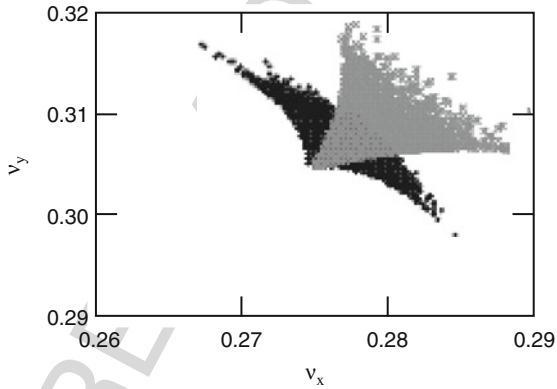

Fig. 12.12 Footprints on the tune space for the hybrid crossing (*black*) and inclined crossing (*gray*). The crossing angle of 400 μrad was assumed and other beam/machine parameters were taken from the LHC

tune space strongly depends on the collision geometry. As a matter of fact, in order to control the tune spread, the inclined crossing in addition to the hybrid crossing, as shown in Fig. 12.11, has been studied. Figure 12.12 denotes that the shape of tune spread is largely modified, substantially reducing a net spread. Details of simulation and its physics background are given in [20–22].

12.3.6 Typical Super-Bunch Collider's Parameters

The typical parameters required on the induction cells employed in the VLHC-size SHC (Superbunch VLHC) are summarized in Table 12.2. RF and beam parameters of the baseline design of VLHC are given in Table 12.3 for comparison. Their operational repetition rate is 431 kHz and the magnitudes of integrated induced voltage for confinement and acceleration are moderate.

UNCORRECTED PROOF

Table 12.2 Machine and beam parameters for the LHC

	Unit	CHC	SHC
Storage energy	TeV	7	7
Peak luminosity	$cm^{-2}s^{-1}$	10^{34}	1.5×10^{35}
Number of interaction points		2	2
Circumference	km	26.7	26.7
Revolution freq.	kHz	11.2	11.2
Injection energy	GeV	450	450
Transverse normalized emittance, rms (H & V, flat-top)	μm·rad	3.75	3.75
Initial bunch intensity		1.1×10^{11}	8.77×10^{13}
Number of bunches		2835	46
Total protons/beam		3.12×10^{14}	4×10^{15}
Av.beam current	A	0.56	7.23
Synch. radiation loss/beam	W/m	0.216	2.8
Bunch spacing	μs(m)	0.025(7.48)	1.93(580)
Bunch length rms/full	m	0.075/–	–/150
Beam occupation ratio	%	2	26
Crossing angle	μrad	200	400
β^*	m	0.5	0.5
rms beam size σ^*	m	1.58×10^{-5}	1.58×10^{-5}
Acceleration energy	TeV	6.55	6.55
Acceleration period	s	1,200	1,200
Acceleration voltage/turn	kV	480	480
Induction cell rep-rate	kHz	–	518
Unit induction cell length	m	–	0.2
Unit induction cell voltage	kV	–	2.5
Total No. of A-ICs		–	192
Total length for A-ICs	m	–	38.4
Core-loss of unit cell	kW	–	15
Total core-loss during accel.	MW	–	2.88

On the other hand, a scheme for the RHIC with three super-bunches in each ring, that fill approximately half of the circumference, has been proposed [10]. These super-bunches can be delivered to any experiment, and enough space is provided for the abort gap. Table 12.4 shows the calculated peak luminosities and luminosity lifetimes for the RHIC II and SuperRHIC conditions, where the peak current, limited at the transition energy, is the same in both cases. In addition, the parameters are arranged so that the luminosity lifetime remains constant.

12.3.7 Beam Physics Issues for the Super-Bunch Hadron Collider

12.3.7.1 Head–Tail Instability of a Super-Bunch

A dipole beam breakup mechanism of a super-bunch, called the head–tail instability, is of big concern. As mentioned in Sect. 11.1.2, the synchrotron oscillation frequency of particles trapped in the barrier bucket is small compared to the synchrotron oscillation frequency of particles in the RF bucket. This means that the

UNCORRECTED PROOF

Table 12.3 Machine and beam parameters for the VLHC (baseline design)

	Unit	CHC	SHC
Storage energy	TeV	20	20
Peak luminosity	$cm^{-2}s^{-1}$	10^{34}	1.5×10^{35}
Number of interaction points		2	2
Circumference	km	233.037	233.037
Revolution frequency	kHz	1.286	1.286
Injection energy	TeV	0.9	0.9
Transverse normalized emittance, rms (H & V, flat-top)	μm·rad	1.5	1.5
Initial bunch intensity		2.6×10^{10}	5.2×10^{13}
Number of bunches		37152	335
Total protons/beam		9.66×10^{14}	1.74×10^{16}
Av. beam current	A	0.195	3.5
Synch. radiation loss/beam	W/m	0.03	0.538
Bunch spacing	μs(m)	0.019(5.65)	2.32(695)
Bunch length rms/full	m	0.03/–	–/150
Bunch occupation ratio	%	1.2	21.6
Crossing angle	μrad	153	400
β^*	m	0.3	0.3
rms beam size σ^*	m	0.46×10^{-5}	0.46×10^{-5}
Acceleration energy	TeV	19.1	19.1
Acceleration period	s	1000	2,000
Acceleration voltage/turn	MV	14.85	7.425
Energy compensation/turn	keV	38	38
Induction cell rep-rate	kHz	–	431
Unit induction cell length	m	–	0.2
Unit induction cell voltage	kV	–	2.5
Total No. of A-ICs		–	2,970
Total length for A-ICs	m	–	594
Core-loss of unit cell	kW	–	12.5
Total core-loss during acceleration	MW	–	37

Table 12.4 Parameters for heavy ion super-bunch operation in RHIC

	Unit	RHIC II	SuperRHIC
Energy	GeV/au	100	100
Number bunches/beam		111	3
bunch intensity	10^9	1.0	800
Bunch length	m	0.3	600
Averaged beam current	A	0.11	2.4
Crossing angle	μrad	0.0	500
Peak luminisity/IP	$10^{26}cm^{-2}s^{-1}$	70	1,100
number IPs		2	2
Luminosity lifetime	h	3	3

UNCORRECTED PROOF

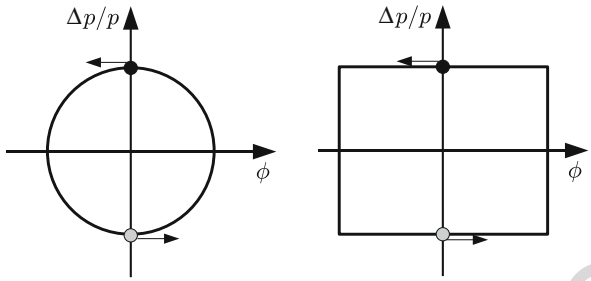

Fig. 12.13 Two macro-particle model. Two particles with the phase difference of π move along the same contour in the longitudinal phase-space for the linear RF-potential (*left*) and the barrier potential (*right*)

interchange between the head and tail particles in the super-bunch doesn't develop quickly, similar to the beam breakup instability in a linac in the limit of $\omega_s = 0$. In order to qualitatively understand the mechanism of the head–tail instability and realize differences between the RF bunch and super-bunch, an elementary model using two *macro-particles* is considered here, each with charge of $Ne/2$, where N is a total number of particles. For simplicity, it is assumed that the synchrotron motion in the RF bucket driving a change between the forward particle and retarded particle is a harmonic oscillation and a particle in the barrier bucket is just reflected at the barriers without time-delay. In addition, the betatron motion to lead to the dipole motion is also assumed to be a harmonic oscillation. In the *two macro-particle model*, an RF bunch or super-bunch consists of two particles, which are located at symmetrical positions on the same contour in the phase-space, as seen in Fig. 12.13. A simple theoretical approach to treat the two macro-particles in an RF synchrotron has been given in the text by A. Chao [23]. This approach is employed here.

Assuming that the wake fields caused by the forwarding particle are simply proportional to its position in the horizontal direction, motions of two particles in a circular accelerator, in which the retarded particle is perturbed by the wake fields, are described by the following equations, for the upper-half time-period of the synchrotron period, $0 < t < \pi/\omega_s$,

$$\begin{aligned} &\mathrm{d}^2x_1/\mathrm{d}t^2 + \omega_1^2 x_1 = 0, \\ &\mathrm{d}^2x_2/\mathrm{d}t^2 + \omega_2^2 x_2 = \left[c^2 N r_0 W_0/(2\gamma C_0)\right] x_1, \end{aligned} \tag{12.12}$$

with

$$\omega_{1,2} = (2\pi c/C_0)\left[\nu_\beta \pm \xi(\Delta p/p) f(t)\right], \tag{12.13}$$

where W_0 is the wake-function integrated over the circumference C_0, r_0 is the classical radius of proton, γ is the relativistic gamma of circulating particle, $\nu_\beta(\omega_\beta = 2\pi c\nu_\beta/C_0)$ is the betatron frequency of an on-momentum particle with $\Delta p/p = 0$ in a normal definition, ξ is the chromaticity, $\Delta p/p$ is the maximum momentum

UNCORRECTED PROOF

amplitude, and $f(t)$ is $\cos(\omega_s t)$ for the RF bucket and the step function with amplitude of unity and period of $2\pi/\omega_s$ for the barrier bucket, respectively. Here the particles are assumed to circulate with the speed of light at the first-order approximation. In the lower-half time-period of the synchrotron oscillation, $\pi/\omega_s < t < 2\pi/\omega_s$, the forwarding and retarded particles exchange their roles; the under-suffices in Eq. (12.12) must be replaced with each other. The process is repeated every synchrotron period. The betatron oscillation described by Eq. (12.12) is a harmonic oscillation with the slowly time-varying frequency ($\omega_\beta \gg \omega_s$). Its approximated solution is written in a form of WKB solution,

$$\exp\left[\pm i\int_0^t \omega_{1,2}\mathrm{d}t'\right] = \exp\left[\pm i\left(\frac{\omega_\beta}{\nu_\beta}\right)\left(\nu_\beta t \pm \xi(\Delta p/p)\int_0^t f(t')\mathrm{d}t'\right)\right]. \tag{12.14}$$

Since the Green function is easily expressed in terms of these independent solutions, the non-perturbed and perturbed solutions for Eq. (12.12) are analytically expressed as follows,

$$\begin{aligned} x_1(t) &= c_1 \mathrm{e}^{+i\phi_1(t)} + c_2 \mathrm{e}^{-i\phi_1(t)}, \\ x_2(t) &= c_1' \mathrm{e}^{+i\phi_1(t)} + c_2' \mathrm{e}^{-i\phi_1(t)} + A\int_0^t G(t,t')x_1(t')\mathrm{d}t', \end{aligned}$$

where c_1, c_2, c_1', and c_2' are determined by the initial conditions, and

$$\begin{aligned} A &\equiv \left[c^2 N r_0 W_0/(2\gamma C_0)\right], \\ \phi_{1,2}(t) &= \left(\frac{\omega_\beta}{\nu_\beta}\right)\left(\nu_\beta t \pm \xi(\Delta p/p)\int_0^t f(t')\mathrm{d}t'\right), \\ G(t,t') &= \frac{1}{-2i\omega_{1,2}}\left[-\mathrm{e}^{i(\phi_2(t)-\phi_2(t'))} + \mathrm{e}^{i(\phi_2(t')-\phi_2(t))}\right]. \end{aligned}$$

Here, we introduce a new variable

$$\tilde{x}_{1,2}(t) = x_{1,2}(t) + i\frac{x_{1,2}'(t)}{\omega_{1,2}}. \tag{12.15}$$

Their values at $t = \pi/\omega_s$ are

$$\begin{aligned} \tilde{x}_1(\pi/\omega_s) &= \tilde{x}_1(0)\mathrm{e}^{-i\phi_1(\pi/\omega_s)}, \\ \tilde{x}_2(\pi/\omega_s) &\cong \tilde{x}_2(0)\mathrm{e}^{-i\phi_2(\pi/\omega_s)} \\ &\quad + \frac{iA}{\omega_\beta}\int_0^{\pi/\omega_s} \mathrm{e}^{-i[\phi_2(\pi/\omega_s)-\phi_2(t')]}x_1(t')\mathrm{d}t'. \end{aligned} \tag{12.16}$$

UNCORRECTED PROOF

Substituting

$$x_1(t) = \frac{\tilde{x}_1^*(0)}{2}\mathrm{e}^{+i\phi_1(t)} + \frac{\tilde{x}_1(0)}{2}e^{-i\phi_1(t)},$$

into the second term of the right-hand side in Eq. (12.16), we have

$$\tilde{x}_2(\pi/\omega_s) = \mathrm{e}^{-i\phi_2(\pi/\omega_s)}\left(\tilde{x}_2(0) + \left(\frac{A}{2\omega_\beta}\right) \times \left\{\begin{array}{l} \frac{\tilde{x}_1^*(0)}{2\omega_\beta}\left(\mathrm{e}^{+i\frac{2\pi\omega_\beta}{\omega_s}} - 1\right) + \\ \tilde{x}_1(0)\left[\frac{i\pi}{\omega_s} - 2\left(\frac{\omega_\beta}{\nu_\beta}\right)\xi\left(\frac{\Delta p}{p}\right)\int_0^{\pi/\omega_s}\left[\int^{t'} f(t'')\mathrm{d}t''\right]\mathrm{d}t'\right] \end{array}\right\}\right). \tag{12.17}$$

The second term on the right-hand side of Eq. (12.17) is relatively small compared to the third term because of $\omega_\beta \gg \omega_s$. Here it is neglected. The evolution from $t = 0$ to $t = \pi/\omega_s$ is expressed in matrix form as

$$\begin{pmatrix} \tilde{x}_1 \\ \tilde{x}_2 \end{pmatrix}_{t=\pi/\omega_s} \cong \mathrm{e}^{-i\left(\frac{\pi\omega_\beta}{\omega_s}\right)}\begin{pmatrix} 1 & 0 \\ i\Gamma & 1 \end{pmatrix}\begin{pmatrix} \tilde{x}_1 \\ \tilde{x}_2 \end{pmatrix}_{t=0}. \tag{12.18}$$

Here

$$\Gamma \equiv \left(\frac{\pi c^2 N r_0 W_0}{4\gamma C_0 \omega_\beta \omega_s}\right) \times \left\{1 + i\frac{2\omega_s}{\pi}\left(\frac{\omega_\beta}{\nu_\beta}\right)\xi\left(\frac{\Delta p}{p}\right)\int_0^{\pi/\omega_s}\left[\int^{t'} f(t'')\mathrm{d}t''\right]\mathrm{d}t'\right\},$$

$$\int_0^{\pi/\omega_s}\left[\int^{t'} f(t'')\mathrm{d}t''\right]\mathrm{d}t' = \begin{cases} 2/\omega_s^2 & \text{in the RF bucket,} \\ \pi^2/2\omega_s^2 & \text{in the barrier bucket,} \end{cases}$$

Beyond $t = \pi/\omega_s$, the forward and retarded particles change their roles. Thus, the change in the parameters after a single period of the synchrotron oscillation is described by

$$\begin{aligned} \begin{pmatrix} \tilde{x}_1 \\ \tilde{x}_2 \end{pmatrix}_{t=2\pi/\omega_s} &\cong \mathrm{e}^{-i\left(\frac{2\pi\omega_\beta}{\omega_s}\right)}\begin{pmatrix} 1 & i\Gamma \\ 0 & 1 \end{pmatrix}\begin{pmatrix} 1 & 0 \\ i\Gamma & 1 \end{pmatrix}\begin{pmatrix} \tilde{x}_1 \\ \tilde{x}_2 \end{pmatrix}_{t=0} \\ &= \mathrm{e}^{-i\left(\frac{2\pi\omega_\beta}{\omega_s}\right)}\begin{pmatrix} 1-\Gamma^2 & i\Gamma \\ i\Gamma & 1 \end{pmatrix}\begin{pmatrix} \tilde{x}_1 \\ \tilde{x}_2 \end{pmatrix}_{t=0}. \end{aligned} \tag{12.19}$$

UNCORRECTED PROOF

Since the transfer matrix is known now, stability analysis of this interaction is straightforward. For a weak beam intensity, $|\Gamma| \ll 1$, its eigenvalues are

$$\lambda_{\pm} = \left(1 - \frac{\Gamma^2}{2}\right) \pm i\sqrt{1 - \left(1 - \frac{\Gamma^2}{2}\right)^2} = \mathrm{e}^{\pm i\varphi},$$

where $\sin\frac{\varphi}{2} = \frac{\Gamma}{2}$, and the eigenvectors (+ mode) and (− mode) are

$$U_+ = \begin{pmatrix} -\mathrm{e}^{i\varphi/2} \\ 1 \end{pmatrix}, \quad U_- = \begin{pmatrix} +\mathrm{e}^{-i\varphi/2} \\ 1 \end{pmatrix}.$$

An arbitrary vector at $t = 0$ is expanded in terms of a linear combination of eigenvectors as

$$\begin{aligned} \begin{pmatrix} \tilde{x}_1(0) \\ \tilde{x}_2(0) \end{pmatrix} &= -\frac{\tilde{x}_1(0) - \tilde{x}_2(0)\mathrm{e}^{-i\varphi}}{2\cos\varphi} U_+ + \frac{\tilde{x}_1(0) + \tilde{x}_2(0)\mathrm{e}^{+i\varphi}}{2\cos\varphi} U_- \\ &\approx \frac{1}{2}\left\{-[\tilde{x}_1(0) - \tilde{x}_2(0)]U_+ + [\tilde{x}_1(0) + \tilde{x}_2(0)]U_-\right\}. \end{aligned}$$

It turns out that ± modes represent the distance in the horizontal direction between two particles and the gravity of two particles. The former and latter correspond to motions of the beam size and the bunch center in a real beam, respectively. The imaginary parts of Γ give the growth rate of these modes because of $\phi = \Gamma$,

$$\begin{aligned} (\tau_{\pm})^{-1} &= \mp\frac{\mathrm{Im}(\Gamma)}{2\pi/\Omega_s} \\ &= \mp\left(\frac{c^2 N r_0 W_0}{4\gamma C_0 \nu_\beta}\right)\xi\left(\frac{\Delta p}{p}\right)\omega_s \begin{cases} 2/\pi^2 & \text{in RF bucket,} \\ 1/2 & \text{in barrier bucket.} \end{cases} \end{aligned} \tag{12.20}$$

It is noted that $\Delta p/p$ and ω_s in the barrier bucket or for the super-bunch are not independent. According to Eq. (11.17),

$$\omega_s = \frac{\pi|\eta|(\Delta p/p)}{\Delta t},$$

where $\Delta t (< C_0/c)$ is the pulse duration between the barriers and the length of super-bunch in time. In general, ω_s in the barrier bucket is extremely small compared to that in the RF bucket, provided the same magnitude of $\Delta p/p$. Even if a difference in the numerical values on the right-hand side of Eq. (12.20) is considered, therefore, the growth rate in the barrier bucket is much smaller than that in the RF bucket. A beam intensity subjected to the head–tail instability may be estimated from the following relation,

$$N_{\mathrm{super}} = \left(\frac{4}{\pi^2}\right)\frac{(\omega_s)_{\mathrm{RF}}}{(\omega_s)_{\mathrm{barrier}}} N_{\mathrm{RF}}, \tag{12.21}$$

where N_{RF} is the number of particles in a single RF bucket.

UNCORRECTED PROOF

The model and theory introduced here is quite simple. It is insufficient to understand various aspects of the head–tail instability in the super-bunch, such as oscillation modes and the instability threshold. Assuming more realistic charge distributions of water-bag and Gaussian, macro-particle simulations have been performed by two groups [24–26]. A fact that the growth rate in the computer simulation [24, 25] decreases with the super-bunch length or Δt is quite consistent to the above prediction. The threshold in the strong head–tail instability regime ($\xi = 0$) has not been observed, while some threshold has been observed for the weak head–tail instability regime [26]. Physics behind these results have not been fully understood yet.

12.3.7.2 Electron-Cloud Effects

Electron-cloud effects are important in super-bunch rings and super-bunch colliders. Electron-cloud effects were first reported in the Proton Storage Ring (PSR) at the Los Alamos National Laboratory [27]. Since then, it has been recognized that it can limit the performance of positron rings and proton–proton colliders. The electron cloud has manifested itself in a variety of ways, such as an increase in vacuum pressure, beam emittance growth and beam loss, degradation of the beam stability, and heating of the vacuum pipe. The electron cloud is known to drive both single and coupled-bunch instabilities, which is known as the e-p instability. Discussion of this instability mechanism is out of the scope of this text; readers are advised to refer to other literature such as [28] for further information. Here we focus our attention only on electron production specific to the super-bunch scheme.

Beam-induced multi-pactoring is believed to be the leading source of sustained electron production. The phenomenon of multi-bunch, beam-induced multi-pactoring was observed at the CERN PS and SPS [29]. The electron-cloud buildup is known to be sensitive to the intensity, bunch-spacing, and length of the proton bunches, and to the secondary-emission yield of electrons from the vacuum chamber surface. An electron cloud in proton colliders is produced inside the vacuum chamber by a combination of synchrotron radiation, photoemission, secondary emission, and ionization of residual gas, as illustrated in Fig. 12.14.

The major concern in the CHC, where the superconducting magnets are used, is the heat load deposited by the electrons on the beam screen inside the vacuum chamber, which prevents synchrotron radiation from intruding deeply into the superconducting magnets. In LHC, electrons emitted from the wall with an initial energy of less than 10 eV are estimated to acquire a typical energy of 200 eV in the field of a passing bunch. Eventually they transfer this energy to the beam screen. This additional heat load from the electron cloud can be much larger than that due to primary synchrotron radiation, the latter being about 0.2 W/m for the nominal LHC parameters, as mentioned in Sect. 12.3.6. This problem in LHC with a limited cooling capacity has been extensively studied by Zimmermann et al. [9]. They have shown that super-bunches are superior as a remedy against the electron cloud build up and heat load. Most of this subsection is devoted to a summary of these studies.

UNCORRECTED PROOF

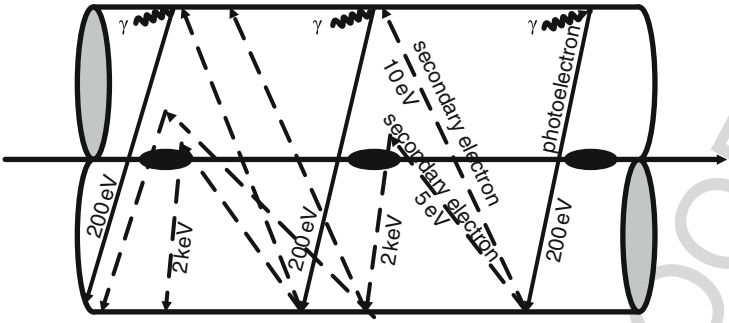

Fig. 12.14 Schematic of electron-cloud build up in the beam pipe during multiple bunch passages, via photo-emission and secondary emission (reproduced from [18] with permission)

In Fig. 12.15 the heat-load curves are given as a function of bunch population N_b for different values of the maximum secondary emission yield for perpendicular incidence, $\delta_{\max}$, which is a critical parameter for the multipacting incidence. The maximum secondary emission yield is known to depend on the surface material and its condition. A cross point of the cooling capacity and the yield in the figure will give an acceptable bunch population. The figure suggests that in order to reach the

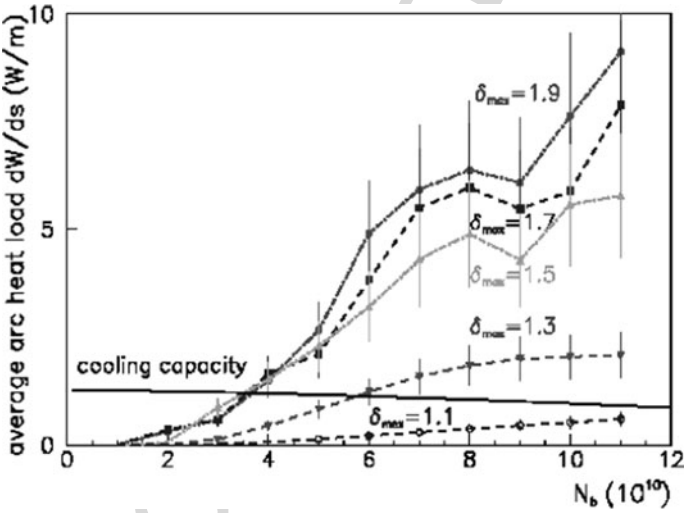

Fig. 12.15 The average LHC arc heat load and cooling capacity versus bunch population N_b, for two values of $\delta_{\max}$; the incident electron energy at the maximum is assumed to be $\epsilon_{\max} = 240$ keV, the photon reflectivity $R = 5\%$ (indicating the fraction of photoelectrons which are emitted uniformly around the chamber azimuth as compared with those on the horizontally outward side), and the photoemission yield per absorbed photon $Y = 5\%$; the elastic reflection of low-energetic electrons on the chamber wall is included. It decreases with bunch population, since at higher current more cooling must be provided for primary synchrotron radiation and image-current heating (reproduced from [9] with permission)

UNCORRECTED PROOF

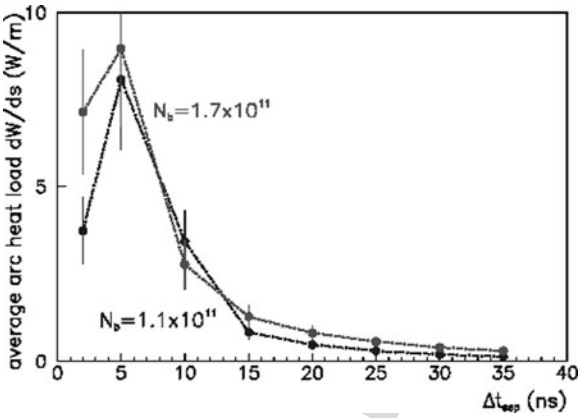

Fig. 12.16 Simulated average LHC arc heat versus bunch spacing, for the maximum secondary emission yield $\delta_{max} = 1.1$ and two bunch populations (reproduced from [18] with permission)

nominal LHC intensity of 1.1×10^{11} per bunch, a secondary emission yield close to 1.1 is required.

Figure 12.16 demonstrates that, even for a secondary emission yield as low as $\delta_{max} = 1.1$, the LHC arc heat load increases to unacceptable levels, if the bunch spacing is reduced below the nominal value of 25 ns. This precludes any luminosity upgrade based on increasing the number of bunches. It is notable, though, that for the shortest spacing 2.5 ns the heat load shows signs of a decrease. It is obvious that the limit of shorter bunch spacing is a coasting beam or a super-bunch. As a matter of fact, the heat load simulation in an LHC arc dipole indicates that its magnitude is remarkably reduced as shown in Fig. 12.17.

A uniform beam corresponds to a static electric potential. In such a potential, electrons emitted from the wall are continuously accelerated towards the centre of

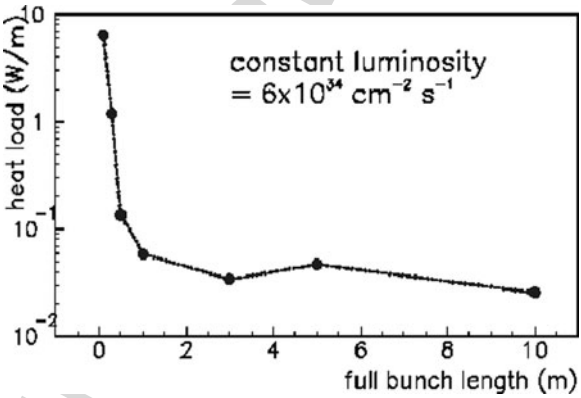

Fig. 12.17 Simulated heat load in an LHC arc dipole due to the electron cloud as a function of super-bunch length for $\delta_{max} = 1.4$, considering a constant flat-top line density of 8×10^{11} m^{-1} with 10% linearly rising and falling edges. The number of bunches is varied so as to keep the luminosity constant and equal to 6×10^{34} cm^{-2}s^{-1} (reproduced from [18] with permission)

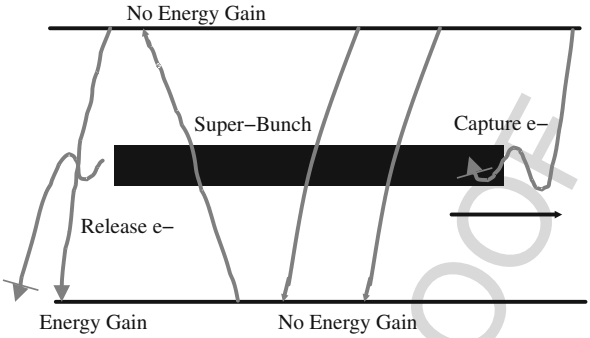

Fig. 12.18 Schematic of electron motion during the passage of a super-bunch. The average energy gain depends on the beam profile. In case of a uniform bunch, electrons do not gain any net energy from the beam, except for those emitted near the bunch tails [30]

the chamber by the electric field of the beam. On the other side of the centre, their kinetic energy decreases again, by the energy conservation law. They impact on the chamber wall with exactly the same energy at which they were emitted. Thus, in the case of a static potential or a uniform beam, no net energy is transferred from the beam to the electrons. This situation is completely different from a beam consisting of separated short bunches, where the potential is time dependent, and the passing bunches give sudden "kicks" to the electrons. The super-bunch mimics the static situation over most of its length. As illustrated in Fig. 12.18, only a small portion of electrons, emitted neat the super-bunch tail, can gain energy during their traversal through the beam. These electrons are responsible for the residual heat load. To keep the number of such electrons low and avoid the so-called "trailing-edge multipactoring", it is important that the beam profile does not decrease near the end of the bunch. If the line density decreases as $\mathrm{d}\lambda/\mathrm{d}t < 0$, the energy gain of an electron at radial position $r(t)$ is roughly described by $\mathrm{d}E/\mathrm{d}t \sim -(\mathrm{d}\lambda/\mathrm{d}t)e^2/(2\pi\epsilon_0)\ln(r(t)/b)$. A flat uniform ($\mathrm{d}\lambda/\mathrm{d}t = 0$) or slightly increasing profile ($\mathrm{d}\lambda/\mathrm{d}t > 0$) followed by a sudden edge is ideal to avoid multipactoring.

12.3.7.3 Intra-beam Scattering

The intra-beam scattering is Coulomb scattering between particles within a bunch. The spatial volume of a beam tends to increase due to the intra-beam scattering. Thus, the luminosity in hadron colliders, which sensitively depends on the spatial volume of colliding beams as understood from Eq. (12.8), is mostly determined due to the intra-beam scattering. The problem was first analyzed by Piwinski [31] and was followed by Bjorken and Mtingwa [32] . Both approaches solve the local, two-particle Coulomb scattering problem for four-dimensional Gaussian for a coasting beam and six-dimensional Gaussian for a bunched beam, assuming non-coupling between three directions. The intra-beam scattering growth-rate for a uniform super-bunch should be similar to that for a coasting beam of equal charge line-density and Gaussian-like energy-spread. Since the microscopic mechanism of intra-beam scattering is common for both cases of bunched beam and coasting beam, the difference originates from averaging over the particle distribution in the longitudinal space. Mathematical formulas useful for a super-bunch trapped in the barrier bucket,

UNCORRECTED PROOF

where a pair of steep barrier voltages with an infinitely large amplitude simply repels drifting particles to the opposite direction as depicted in Fig. 11.2, are given here.

Piwinski shows in [33] how the diffusion caused by intra-beam scattering is handled and the diffusion time is derived. Extending Piwinski's result, the rise times for the mean oscillation amplitudes and momentum spread, which determine the super-bunch dimensions, are given by

$$\begin{aligned}
\frac{1}{\tau_p} &= \frac{1}{2\sigma_p^2}\frac{\mathrm{d}\sigma_p^2}{\mathrm{d}t} = A\frac{\sigma_h^2}{\sigma_p^2} f(a,b,c),\\
\frac{1}{\tau_x} &= \frac{1}{2\sigma_x^2}\frac{\mathrm{d}\sigma_x^2}{\mathrm{d}t} = A\left[f\left(\frac{1}{a},\frac{b}{a},\frac{c}{a}\right) + \frac{D^2\sigma_p^2}{\sigma_{x_\beta}^2} f(a,b,c)\right],\\
\frac{1}{\tau_y} &= \frac{1}{2\sigma_y^2}\frac{\mathrm{d}\sigma_y^2}{\mathrm{d}t} = Af\left(\frac{1}{b},\frac{a}{b},\frac{c}{b}\right),
\end{aligned} \tag{12.22}$$

where

$$\begin{aligned}
&A \equiv= \frac{r_p^2 c}{64\pi^2}\frac{2\sqrt{\pi}N}{L}\frac{1}{\sigma_p\sigma_{x_\beta}\sigma_{y_\beta}\sigma_{x'}\sigma_{y'}\beta^3\gamma^4}, \quad \frac{1}{\sigma_h^2} \equiv \frac{1}{\sigma_p^2} + \frac{D^2}{\sigma_{x_\beta}^2},\\
&a \equiv \frac{\sigma_h}{\gamma\sigma_{x'}}, \quad b \equiv \frac{\sigma_h}{\gamma\sigma_{y'}}, \quad c \equiv \beta\sigma_h\sqrt{2\frac{d}{r_p}},\\
&f(a,b,c) = 8\pi\int_0^1 \left\{\ln\left[\frac{c^2}{2}\left(\frac{1}{\sqrt{p}} + \frac{1}{\sqrt{q}}\right)\right] - 0.5777\right\}(1-3x^2)\frac{\mathrm{d}x}{\sqrt{pq}},\\
&p \equiv a^2 + x^2(1-a^2), \quad q \equiv b^2 + x^2(1-b^2),
\end{aligned} \tag{12.23}$$

where r_p is the classical radius, N is the number of particles in the super-bunch, L is the length of the super-bunch, D is the averaged dispersion function, and d is the averaged half beam-height. Note that for a bunched beam $2\sqrt{\pi}N/L$ is replaced by N/σ_s. Equation (12.23) suggests that the rise times never depend on the length of super-bunch if the line density, N/L, is kept constant.

For a collider energy beyond LHC, the synchrotron radiation damping is known to surpass the intra-beam scattering growth rate. The equilibrium emittances will result from a balance of radiation damping, quantum fluctuations, and intra-beam scattering. Its details depend on machine and beam parameters of an individual collider.

12.3.7.4 Other Issue

The so-called Pacman effect [34] has been of concern in hadron colliders since the beginning of SSC design study. Pacman effects in the super-bunch collision have not yet been quantitatively evaluated. However, it is still possible to point out essential

UNCORRECTED PROOF

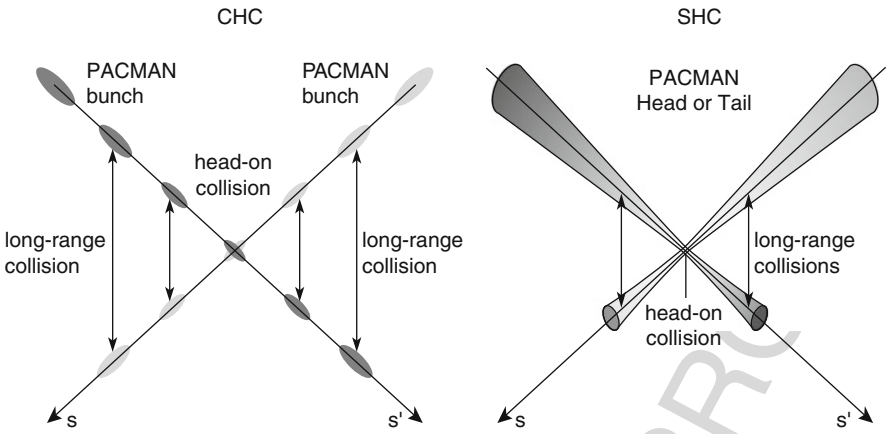

Fig. 12.19 Schematic for Pacman effects. The *left* represents asymmetric collision between the head parts of counter-rotating bunch trains. The *right* represents beginning in the super-bunch collision

differences between the RF bunch collision and super-bunch collision. In the CHC, Pacman bunches, which have no partners to guarantee symmetric collision around the collision point, are isolated in the head and tail regions in the bunch train (see Fig. 12.19). A domino-like vanishing of colliding bunches induced by this asymmetric collision has been of big concern because the blow-up of the Pacman bunches inevitably propagates into the core region of the RF bunch train. Meanwhile, the situation in the super-bunch collision is same with respect to the asymmetry. However, the head and tail of the super-bunch are always mixed in the entire region of the super-bunch due to the synchrotron oscillation. There has been no estimation how this feature can mitigate the Pacman effects.

12.4 All-Ion Accelerator – An Injector-Free Induction Synchrotron

12.4.1 Introduction

For more than 70 years since the original work by Lawrence and Livingston and other researchers in the 1930s [35], the cyclotron has evolved in its various forms. It has become a common choice for the acceleration of a wide variety of different ion species to a medium energy range of multi-hundreds of MeV/au. Any ions that have the same Z/A, where A is the mass number and Z is the charge state, can in principle be accelerated by the same cyclotron. For the acceleration of particular ions far beyond the medium energy region, RF synchrotrons have been used. In the early 1970s, heavy ions, such as N, Xe, and U, were accelerated in the Princeton Particle Accelerator [36] and the Bevatron of Lawrence Berkeley National Laboratory [37].

UNCORRECTED PROOF

Those experiments demonstrated the significance of the vacuum pressure in low and medium-energy accelerators, where beam losses due to charge-state changing of partially stripped ions are serious. These days, heavy ions, such as gold and copper, are accelerated in the Alternate Gradient Synchrotron (AGS) and the Relativistic Heavy Ion Collider (RHIC) of Brookhaven National Laboratory to serve for collider experiments [2]. Lead ions are to be accelerated in the Large Hadron Collider (LHC) of CERN for a similar purpose [3]. The heavy-ion medical accelerator of National Institute of Radiological Science in Japan (NIRS) accelerates carbon ions to 400 MeV/au, which are delivered for cancer therapy [38]; in addition, He, N, O, Ne, Si, Ar, and Fe are provided for other purposes, such as radiation-damage tests on biological cells or beam–plasma interactions. The SIS-18 synchrotron [39] of GSI is devoted to material science or warm dense matter science as described in Sect. 10.2.1, providing H, D, C, N, O, Ne, Ar, Ni, Kr, Xe, Au, Bi, and U.

Limit of resonant circular accelerators: The accelerators mentioned above are classified as resonant accelerators employing radio-frequency waves for acceleration. Electric fields varying in time give the required energy per turn and provide the focusing forces in the moving direction. This characteristic in a circular ring has been recognized to be an enormous figure of merit, and is a big reason why the RF acceleration technique has a quite long life-time since its being established. Once the synchrotron is determined to operate on protons, an RF acceleration system consisting of an RF cavity and an RF power-source is fixed. In a typical medium-energy synchrotron, the RF frequency sweeps by one order of magnitude through its entire acceleration associated with increasing the revolution frequency, where the relativistic beta changes from 0.1 to some value close to unity. The kinetic energy of an ion is described by $Amc^2(\gamma - 1)$, where γ is the relativistic gamma of the ion, and m is the proton mass; in the non-relativistic region it is approximated by $(1/2)Amc^2\beta^2$, where β is the relativistic beta. This formula suggests that the injection energy must be above $4.69A$ MeV to meet the RF frequency minimum limit. In other words, the integrated acceleration voltage in an upstream injector must be $V = 4.69(A/Z)$ MeV. So far, this required voltage has been provided by a gigantic static accelerator, such as a Van de Graaff, or by a drift-tube linac. An electro-static accelerator of larger energy than tens of MeV is not practical because of a technical limit of high-voltage breakdown and its huge cost.

Limit of drift tube linacs: A drift tube linac (DTL) is considered as the typical injector for a circular accelerator employing the RF acceleration technology. Ions in the DTL are accelerated in a gap between adjacent electrodes in the so-called π-mode, where electric fields are excited in the opposite direction during the time period when ions propagate in the electrodes. The distance L_i between the center positions of two adjacent i-th and $i+1$-th electrodes is defined by $L_i = vT/2$, where v is the velocity of ion and T is the RF period at the frequency f. It may be rewritten in the following form

$$L_i = \frac{1}{2f}\sqrt{2\frac{Z}{A}\frac{e}{m}\sum_{j=1}^{i} V_j} \tag{12.24}$$

UNCORRECTED PROOF

where V_j is the gap voltage. Once the mechanical geometry of the DTL is fixed, L_i is never changed. In addition, the RF frequency is fixed at the early stage of design. In order to accelerate an arbitrary ion of A and Z, therefore, the acceleration voltage has to be scaled proportionally to A/Z. There are two practical obstacles to the use of the DTL for acceleration of ions with a large A/Z. (1) There is no power source to meet the demand. (2) High voltage operation of the DTL will induce RF breakdown, even if a power source capable of generating the necessary voltage is available. Another possibility is to change the frequency f. Certainly, such a frequency variable DTL exists [40]. Its band is typically changed within a factor of two or three, where it is possible to cover a change in A/Z by a factor of about 5 without increasing the RF voltage. This fact seems to sound good. However, we have to also satisfy the requirement on the ion energy at the end of the DTL. The lower limit of the band-width of the RF synchrotron itself requires a minimum velocity, as mentioned earlier. The velocity of ions injected into the RF synchrotron is described by

$$v = \sqrt{2(Z/A)(e/m)V}, \tag{12.25}$$

Here $V \equiv \sum_{j=1} V_j$ is the integrated acceleration voltage in the DTL. It is apparent that the acceleration voltage has to be changed, depending on A/Z of ions of interest. Thus, it turns out that for the present purpose the RF voltage of the DTL has to be changed. Crucial issues in this case have been already mentioned.

Limit in higher harmonic operation of resonant accelerators: In principle, the acceleration of ions with a velocity far smaller than $\beta = 0.1$ in the RF synchrotron is possible by introducing the harmonic acceleration. The RF frequency, f_{RF}, is kept to be hf_0 ($h \neq 1$) through the entire acceleration, where $f_0 (= C_0/c\beta$, C_0: circumference of the ring) is the revolution frequency. In this higher harmonic acceleration, the accelerated beam is segmented into h pieces of the RF bunch. The harmonic number, h, depends on the initial velocity of the ion, that is, $\sim 1/(10\beta)$. In higher harmonic acceleration, serious beam loss at extraction is inevitable without additional beam handling. Adiabatic recapturing by lower harmonic RF after adiabatic de-bunching is required because RF bunches are uniformly distributed along the entire ring just after acceleration by the higher harmonic RF, and extraction magnets excited in a finite time will kick a substantial fraction of these higher harmonic RF bunches out of the extraction orbit. The additional RF system requires more space in the accelerator ring and the complicated beam-handling is time consuming. Higher harmonic RF acceleration of a low-energy ion beam is not impossible [41], but it is an unattractive option.

Comparison between conventional synchrotron and all-ion accelerator: In Fig. 12.20 above discussions are schematically depicted and a conclusion is arrived at that a simple structure of accelerator complex can be realized. Hereafter, a concept of injector-free synchrotron, which allows the acceleration of all species of ions in a single ring, is described in more detail. In order to overcome the above limits of the existing RF acceleration, a newly developed acceleration technology is employed for the present purpose. Such a synchrotron is called an all-ion accelerator (AIA) [42, 43]; its characteristics and key issues are discussed below.

UNCORRECTED PROOF

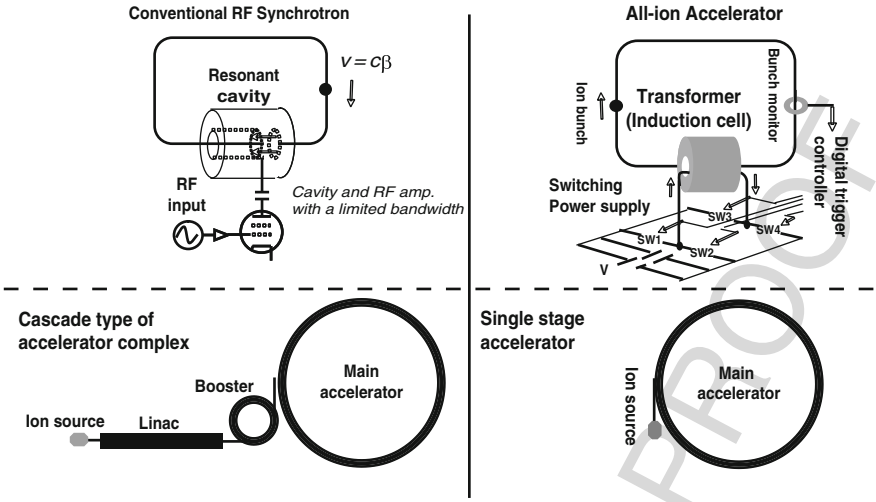

Fig. 12.20 Comparison of essential features of RF synchrotrons and all-ion accelerators based on the induction synchrotron concept

Expected roles of the AIA: So far, the irradiation of various ions on metal, magnetic material, ceramic, semi-conducting material, and polymer has been discussed to develop novel materials, such as nano-wire, nano-transistors, quantum-dots, and conducting ion tracks in diamond-like carbon [44]. Deep implantation of moderate-energy heavy ions may serve to create a new alloy in bulk size. Meanwhile, energy deposition caused by the electro-excitation associated with passing of high-energy ions through the material is known to largely modify its structure [45]. Warm dense matter science is going to drastically evolve with the aid of high-power laser and heavy-ion beams [46]. The irradiation of moderate-energy heavy-ion beams on metal in a small physical space of less than a mm in diameter and in a short time period less than 100 ns is known to create a particularly interesting state of material, where the temperature is 0.1–10 eV and the mass density is 1–10 g/cm^3. This state of matter is far from playing-grounds of solid-state physics and plasma science. Its equation of state has not yet been established, electric conductivity is not known, and the effects of the interactions between atoms are not confirmed.

12.4.2 Concept

Acceleration system of the AIA consists of induction acceleration cell, switching power-supply to drive the cell, the gate signal control system including the bunch monitors, as depicted in Fig. 12.21. A master signal for the gate signal is generated from a circulating ion-bunch signal; thus, induction pulse-voltages for acceleration and confinement are automatically synchronized with the revolution of ion bunch. This property suggests that the allowable revolution frequency is not limited if a

UNCORRECTED PROOF

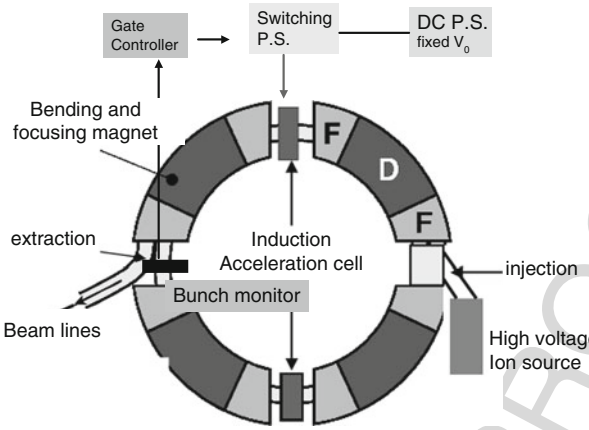

Fig. 12.21 Schematic view of the all-ion accelerator. F and D show the focusing and defocusing part in the combined function magnet, respectively. The ion-bunch signals monitored by the bunch monitor are processed with the gate controller, generating a gate signal for the switching power supply

sufficiently fast switching device is available. This is a big difference from a conventional RF synchrotron or cyclotron, where the range of the acceleration energy or ion mass is limited, since equipped RF devices usually have a finite bandwidth, as mentioned earlier. The AIA is able to accelerate all species of ions of their possible charge state from the lightest to the heaviest. In order to emphasize the unique figure of merits of the AIA, the low energy injection into the AIA is assumed, associated with a wide operational range of magnetic guiding fields. In the following subsections, the essential characteristics of the AIA are discussed, and its typical composition and numerical parameters are given. Taking as an example the KEK 500 MeV Booster Synchrotron, a rapid-cycle proton synchrotron, the beam and machine parameters when modified to an AIA would be:

Circumference	$C_0 = 37$ m
Curvature	$\rho = 3.3$ m
Minimum Field (Ar^{+18})	$B_{\min} = 0.029$ Tesla
Maximum Field (Ar^{+18})	$B_{\max} = 0.8583$ Tesla
Acceleration Voltage (Eq. 12.12)	$V_{\text{acc}} = 6.36$ kV
Machine Cycle	$f = 20$ Hz

12.4.3 Digital Acceleration and Switching Frequency

The acceleration equation for an arbitrary ion with mass $M = Am$ and charge $Q = Ze$, where m and e are the mass of a proton and unit charge, has been evaluated in Sect. 11.4.4. The following relation between the ramped bending field and the

UNCORRECTED PROOF

accelerating-voltage have to be satisfied for the orbit of an ion to stay at the center of the accelerator ring:

$$V_{\mathrm{acc}}(t) = \rho C_0 \frac{\mathrm{d}B}{\mathrm{d}t}. \tag{12.26}$$

Equation (12.26) gives the required accelerating voltage, since the ramping pattern of the magnetic field is determined first. There are two typical ramping patterns for $B(t)$:

(1) Excitation by a resonant circuit.
(2) Excitation with a pattern-controlled power supply.

Cases (1) and (2) are typically applied to rapid- and slow-cycling synchrotrons, respectively. Since the former is typical for a medium-energy synchrotron, this case is considered here. $B(t)$ is described

$$B(t) = \frac{1}{2}\left[(B_{\max} + B_{\min}) - (B_{\max} - B_{\min})\cos(\omega t)\right],$$
$$(\mathrm{d}B/\mathrm{d}t)_{\max} = \frac{\omega}{2}(B_{\max} - B_{\min}),$$

where $B_{\min}$ and $B_{\max}$ are the injection field and the extraction field, respectively, and ω is the ramping cycle. From Eq. (11.33), the relativistic $\beta\gamma$ of an ion is straightforwardly expressed in terms of $B(t)$ as

$$\beta\gamma = \left(\frac{Z}{A}\right)\left(\frac{e\rho}{mc}\right)B. \tag{12.27}$$

The revolution frequency, $f = c\beta/C_0$, is described by

$$f = \frac{c}{C_0}\sqrt{\frac{D}{1+D}}, \tag{12.28}$$

where

$$D \equiv (\beta\gamma)^2 = \left[\left(\frac{Z}{A}\right)\left(\frac{e\rho}{mc}\right)\right]^2 B^2(t).$$

Similarly, the achieved kinetic energy of the ion is represented by

$$T = Amc^2\left(\frac{1}{\sqrt{1-\beta^2}} - 1\right) = Amc^2\left(\frac{1}{\sqrt{1-\left(\frac{fC_0}{c}\right)^2}} - 1\right). \tag{12.29}$$

UNCORRECTED PROOF

Since dB/dt is not constant for the rapid-cycle synchrotron, the accelerating voltage, $V_{acc}(t)$, must change in time. Due to the nature of the induction acceleration system of a 1-to-1 transformer, the output voltage at the induction cell is the same as the output voltage of the DC power supply energizing the switching power supply. Therefore, it is difficult in a practical sense to change the acceleration voltage within one acceleration period on the order of several tens of milliseconds. Fortunately, a demanded energy gain per unit time Δt, $\Delta E = ZeV_{acc}(t)f(t)\Delta t$, is provided with a constant accelerating voltage, V_0, and a modified switching frequency, $g(t) = V_{acc}(t)f(t)/V_0$. In other words, the pulse density for acceleration is controlled. Namely, the gate trigger signal is intermittently generated. Usually, multiple induction acceleration cells are ready for acceleration. It is also possible to control in real time the number of dedicated acceleration cells. A combination of these two ways will be employed to generate the required accelerating voltage described by Eq. (12.26).

12.4.4 Longitudinal Confinement

Here, it should be noted that the switching capability of the commercially available switching element is limited to 1 MHz operation because of heat deposited on the switching element, itself. In a later region of the acceleration period in the medium energy AIA, the revolution frequency will exceed 1 MHz, as shown in Fig. 12.22. Superimposing pulse voltages intermittently triggered is a realistic technique to overcome the limited rep-rate. For instance, every induction cell devoted to confinement is simultaneously triggered every three turns in the acceleration region with a revolution frequency of 3 MHz, as can be seen in a typical example. The ion beam receives a three times larger confinement voltage than the required one in the case that the induction cells are triggered every turn.

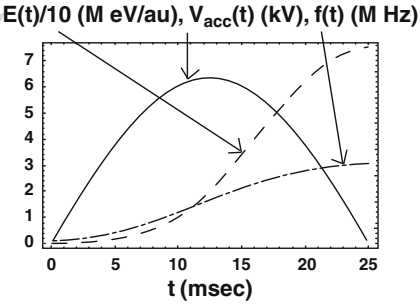

Fig. 12.22 Energy gain (*left*), required acceleration voltage (*middle*), and revolution frequency (*right*) versus time

12.4.5 Stacking and Beam Handling Through the Acceleration

A chopped ion beam is injected into the AIA in a single turn. The barrier step-voltages are excited to capture the chopped beam. From the practical limit of current

UNCORRECTED PROOF

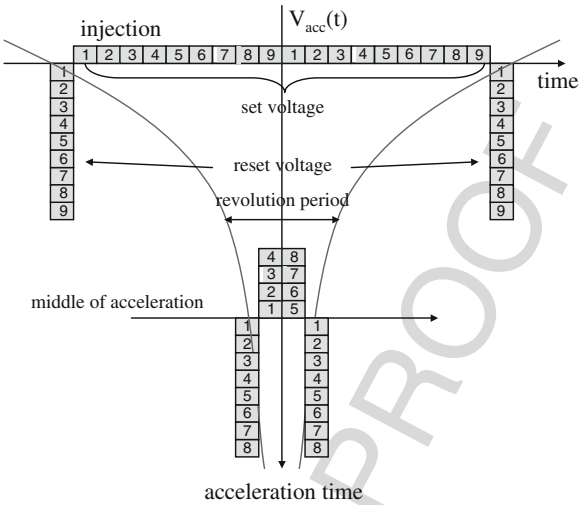

Fig. 12.23 Acceleration voltage pattern. The numbers are identification numbers of the induction acceleration cells. The set voltage is generated with an accompanying reset voltage within a single revolution period if the revolution period is larger than 1 μs. Otherwise, the acceleration cells are intermittently triggered

technology, the maximum pulse length for the induction acceleration voltage and its amplitude are of the order of 500 ns and 2 kV, respectively. The required long accelerating-voltage is generated by superimposing induction-voltage pulses with a finite pulse width, finite amplitude, and limited rep-rate, in time. Its scheme is shown in Fig. 12.23. Multiple acceleration cells driven by an individual switching power-supply entry from the beginning of acceleration and the super-imposed acceleration voltage-pulse length are shown, as well as the time-duration between the barrier voltage pulses. As the acceleration proceeds, the revolution period decreases. The entire acceleration process, which has been obtained by computer simulations [47, 48], is depicted in Fig. 12.24.

12.4.6 Transverse Focusing

Transverse focusing of an ion beam in a circular ring is also important. In a strong focusing lattice, the transverse motion of an ion is governed by the following equation:

$$Am\frac{\mathrm{d}}{\mathrm{d}t}(\gamma v_{\perp}) = -Zev_{\parallel}B'x, \tag{12.30}$$

where

$$B' \equiv \frac{\partial B_y}{\partial x}.$$

Using the orbit coordinates instead of the time-derivative, Eq. (12.30) takes the well-known form of the betatron equation. Assuming that the changes in γ and β per turn

UNCORRECTED PROOF

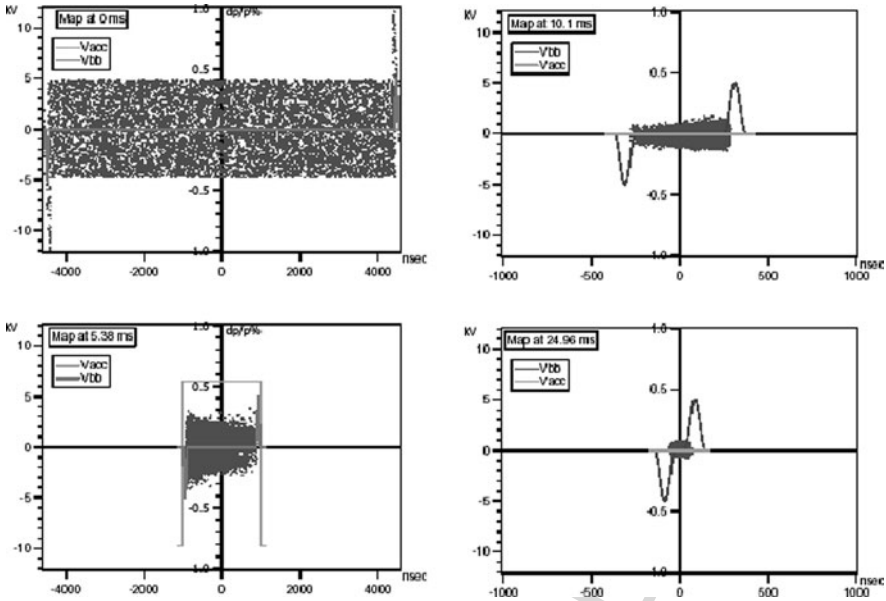

Fig. 12.24 Temporal evolution of an Ar^{18} bunch in the longitudinal phase-space. Phase plots from *left top* to *right bottom* show the ion bunch right after injection, at 5 ms, at 10 ms, and at the end of the acceleration, respectively. The output voltage (*gray*) is 1.08 kV for acceleration, and the integrated barrier voltage is 5 kV

are small, we have an approximated betatron equation,

$$\gamma_c \beta_{\parallel} \frac{\mathrm{d}}{\mathrm{d}s}\left(\frac{\mathrm{d}x}{\mathrm{d}s}\right) = -\frac{Z}{A}\left(\frac{e}{m}\right) B' x \Rightarrow \frac{\mathrm{d}^2 x}{\mathrm{d}s^2} + K(s)x = 0, \tag{12.31}$$

where

$$K(s) = \left(\frac{Z}{A}\right) \frac{e/m}{c\beta\gamma} \frac{\partial B_y}{\partial x}. \tag{12.32}$$

Substitution of Eq. (12.27) into Eq. (12.32) yields

$$K(s) = \frac{1}{B\rho} \frac{\partial B_y}{\partial x}. \tag{12.33}$$

The k-value does not depend on the ion mass or its charge state; the betatron tune for any ion or any charge state is always the same. Once any ion is injected into the AIA with an appropriate momentum, as discussed later, the transverse beam dynamics through the entire acceleration is common among all ions.

UNCORRECTED

12.4.7 Space Charge Limited Ion-Beam Intensity

A number of ions subject to acceleration in the AIA are restricted by space-charge effects at injection because of an extremely low β. Its magnitude can be estimated by the term of the Laslett tune-shift,

$$\Delta\nu \propto \frac{Z^2 N}{B_f \beta^2 \gamma^3}, \tag{12.34}$$

where N is the number of charged particles per bunch and B_f is the bunching factor. It is assumed that the beam size is uniquely determined by an acceptance of the aperture. It is believed that $\Delta\nu$ is 0.25 in the space-charge limit. Thus, the allowed magnitude of N is known from Eq. (12.34). This number has been experimentally known for the proton in the KEK 500 MeV Booster.

The space-charge limited number of ions per bunch, N_i, is straightforwardly obtained using N_p, as shown in the following equation:

$$\frac{N_i}{N_p} = \left(\frac{A}{Z^2}\right)\left(\frac{\beta_i^2\gamma_i^3}{\beta_p^2\gamma_p^3}\right)\frac{(B_f)_{\mathrm{AIA}}}{(B_f)_{\mathrm{RF}}} \cong \frac{1}{Z}\frac{V_i}{V_p}\frac{(B_f)_{\mathrm{AIA}}}{(B_f)_{\mathrm{RF}}}, \tag{12.35}$$

where the under-suffices "p" and "i" denote the parameters for a proton and an ion, respectively. Here, $(B_f)_{\mathrm{AIA}}$ is a bunching factor in the all-ion accelerator, which has been estimated to be 0.7–0.8 from extensive simulation work as described in Sect. 11.2.1. From the long experience of the KEK Booster operation for protons in the space-charge limited operation mode, where the injection voltage is $V_p = 40$ MV, we know that $N_p = 3 \times 10^{12}$ and $(B_f)_{\mathrm{RF}} = 0.3$. Substituting these numerical parameters and the injection voltage, $V_i = 200$ kV, into Eq. (12.35), we can evaluate the expected space-charge limiting current for typical ions. For three cases of $^{12}C^{+6}$, $^{40}Ar^{+18}$, and $^{197}Au^{+79}$, we obtain $N_i = 6.5 \times 10^9$, 2.2×10^9, and 0.49×10^9 per bunch, or 6.5×10^{10}, 2.2×10^{10}, and 4.9×10^9 per second, respectively. For simplicity, the same transverse emittance as that of proton is assumed here.

The beam intensity suggested here is not very high but sufficiently attractive for material science. If the extracted ion beams are focused through a kind of mini-beta focusing system familiar in colliders, the beam size can be ~~extremely minimized~~ on a metal target, creating a higher intensity beam. Bunch rotation in the longitudinal phase-space is known to compress the ion bunch in time. Accordingly, a limited region in the 3D physical space, where an ion beam manipulated in such a way looses most of its kinetic energy, will serve for warm dense matter science [49].

12.4.8 Vacuum

Vacuum is the most important parameter because the survival rate of an ion beam depends on the loss due to electron capture or stripping. This loss originates from

UNCORRECTED PROOF

electron capture or stripping as a result of the collision with residual gas molecules. Two processes will be fatal from the viewpoint of beam loss, although other ~~process~~, such as Möller scattering leading to emittance blow-up ~~is~~ likely to occur. The cross-sections of these physics process will strongly depend on the velocity of the ion beam and the achieved pressure. A simple estimation of beam intensity survival is described to help locate a requirement in the vacuum system design. Here, it should be noted that the Ar^{+Z} ions are assumed to exit the 200 kV high voltage terminal with an energy of $200(Z/A)$ keV/au, where $A = 40$. The probability of capturing one electron is given by the cross-section σ_c, and that of the loss of an electron by σ_l. These are governed by velocity dependencies of different types. A figure representing the following expression can be found from the suitable literature,

$$\sigma_c \propto Z^2\beta^{-5}, \qquad \sigma_l \propto Z^{-2}\beta^{-2} \tag{12.36}$$

Here, β indicates the relativistic beta. It is obviously practical and useful to use actual experimental results, where nitrogen is assumed as a residual gas. A major source of loss is known to be electron capture below a few MeV/au and stripping beyond that value. The survival ratio at time t from injection is given by

$$S = \frac{n(t)}{n(0)} = \exp\left[-2.12 \times 10^{27} P_{\text{torr}} \int_0^t \sigma_{\text{tot}}\beta \mathrm{d}t\right] \tag{12.37}$$

Here $\sigma_{\text{tot}} = \sigma_c + \sigma_l$ and β change with acceleration and are determined from the ramping pattern of the bending field. Substituting of $\sigma_c = \sigma_{c0}\left[\beta(0)/\beta(t)\right]^5$ and $\sigma_l = \sigma_{l0}\left[\beta(0)/\beta(t)\right]^2$, where σ_{c0} and σ_{l0} are derived from the experimental results obtained by I.S. Dmitriev [50], into Eq. (12.37) shows that a vacuum of 10^{-7} P is required to achieve a survival rate of more than 90%. It is emphasized that the injector-free all-ion accelerator must be operated under a much better vacuum condition compared with the typical vacuum of 10^{-6} P in conventional heavy ion accelerators.

12.4.9 Ion Source and Injector

The injection energy is low and its magnitude depends on an extraction voltage from an ion source. Assuming a fixed injection field, its total acceleration voltage is adjusted to

$$V \cong \frac{1}{2}\left(\frac{Z}{A}\right)\left(\frac{e\rho^2 B^2}{m}\right) = \left(\frac{Z}{A}\right) V_{\text{inj}}^p, \tag{12.38}$$

where eV_{inj}^p is the injection energy of a proton into the AIA. Ion sources such as an electron cyclotron resonance ion source (ECRIS), electron beam ion source (EBIS),

UNCORRECTED PROOF

or laser ablation ion source (LAIS) may be possible candidates. For the AIA, where ~~full stripping~~ ions are required for the high acceleration efficiency and heavy metal ions including gas ions are requested for various applications, the LAIS appears to be particularly suitable, although there is still a technical problem, such as a frequent change of the target surface. So far, a broad spectrum of charge states including a high charge state for Iron and Carbon has been demonstrated by Okamura et al. [51].

12.4.10 Summary

Various heavy ions of medium-energy delivered from the AIA should be quite attractive in a wide scope of applications from warm dense matter science to medical science. If a short acceleration gap in the induction acceleration cell and good vacuum were to be realized, even cluster ions, such as albumin of $A = 5 \times 10^4$ and $Z < 50$, could be accelerated in the AIA [52]. A large dynamic range of the guiding magnetic fields in the AIA is required to achieve an attractive high energy far beyond that of the electrostatic accelerators. In order to satisfy this demand, the choice of high field superconducting magnets may be a possible solution. However, there are two significant shortcomings that the field uniformity in the low field region is largely affected by persistent currents and the superconducting magnet cannot be rapidly ramped nor demagnetized. It is only reported that the magnetic field ramp rate up to 4 T/s with the minimum/maximum magnetic flux density of 0.5/4.0 Tesla should be achievable [53]. These features do not allow us to employ the high field superconducting magnet for the rapid cycle AIA assuming its operation at more than 10 Hz. Thus, we arrive at a concept of induction sector cyclotron [54], where the required guiding fields are constantly excited and the dynamic range of guiding fields is traded off the rotation radius within the pole gap. The induction sector cyclotron may be an interesting alternative of the AIA.

References

1. S. Mishra. High Luminosity Operation of the Fermilab Accelerator Complex. In *Proceedings of the 2003 Particle Accelerator Conference*, pages 1–5, Portland, OR, 12–16 May 2004.
2. M. Harrison, S. Peggs, and T. Roser. The RHIC Accelerator. *Ann. Rev. Nuc. Part. Sci.*, 52: 425–469, 2002.
3. The Large Hadron Collider, Conceptual Design. Technical Report CERN Report CERN/AC/95-05 (LHC), CERN, 1995. edited by P. Lefevre and T. Petterson.
4. Y. Shimosaki, K. Takayama, and K. Torikai. Quasiadiabatic, Nonfocusing Transition-Energy Crossing. *Phys. Rev. Lett.*, 96:134801–134804, 2006.
5. E. Courant and H. Snyder. Theory of the Alternating Gradient Synchrotron. *Ann. Phys*, 3:1, 1958.
6. H. Antosiewicz. *Handbook of Mathematical Functions with Formulas, Graphs, and Mathematical Tables*, Dover, New York, NY, 1970.
7. K. Takayama, J. Kishiro, M. Sakuda, Y. Shimosaki, and M. Wake. Superbunch Hadron Colliders. *Phys. Rev. Lett.*, 88:144801–144804, 2002.

UNCORRECTED PROOF

8. K. Takayama. Superbunch Hadron Colliders. In *Proceedings of the International Workshop on Recent Progress in Induction Accelerators*, pages 39–46, Tsukuba, Japan, 29–31 Oct. 2003. KEK.
9. O. Bruning, R. Cappi, R. Garoby, O. Grobner, W. Herr, T. Linnecar, R. Ostojic, K. Potter, L. Rossi, F. Ruggiero, K. Schindl, G. Stevenson, L. Tavian, T. Taylor, E. Tsesmelis, E. Weisse, and F. Zimmermann. LHC Luminosity and Energy Upgrade: A Feasibility Study. Technical Report CERN Report (LHC Project Report 626), CERN, 2002.
10. W. Fischer, M. Blaskiewicz, and J. Wei. Possible RHIC Upgrades with Superbunches. In *Proceedings of the International Workshop on Recent Progress in Induction Accelerators*, pages 5–10, Tsukuba, Japan, 7–10 Mar. 2007. KEK.
11. H. Glass, G. Foster, P. Limon, E. Malamud, P. Garbincius, S. Peggs, J. Straight, M. Syphers, J. Tompkins, and A. Zlobin. Design Study for a Staged Very Large Hadron Collider. Technical Report FNAL Report Fermilab-TM-2149, FNAL, 2001.
12. K. Johnsen. CERN Intersecting Storage Rings. *Nucl. Inst. Meth.*, 108:205–223, 1973.
13. K. Johnsen. The ISR and Accelerator Physics, Part I in A Review of Accelerator and Particle Physics at the CERN Intersecting Storage Rings. Technical Report CERN Report (CERN 84-13), CERN, 1983.
14. E. Keil. Luminosity Optimisation for Storage Rings with Low-β Sections and Small Crossing Angles. *Nucl. Inst. Meth.*, 113:333–339, 1973.
15. H. Hahn, M. Month, and R. Rau. Proton–proton Intersecting Storage Accelerator Facility ISABELLE at the Brookhaven National Laboratory. *Rev. Mod. Phys.*, 49:625–679, 1977.
16. J. Sanford and D. Matthews. Site-Specific Conceptual Design of the Superconducting Super Collider. Technical Report SSC Report (SSC-SR-2020, DE93 007234), SSC, 1990.
17. Y. Shimosaki. Crossing Geometry and Beam–Beam Tune Shift in a Superbunch Hadron Collider. Technical Report KEK-Report 2004-7, KEK, 2004.
18. F. Ruggiero, G. Rumolo, F. Zimmermann, and Y. Papaphilippou. Beam Dynamics Studies for Uniform (Hollow) Bunches or Super-bunchesin the LHC: Beam–Beam Effects, Electron Cloud, Longitudinal Dynamics, and Intra-beam Scattering. In *Proceedings of the International Workshop on Recent Progress in Induction Accelerators*, pages 131–147, Tsukuba, Japan, 29–31 Oct. 2003. KEK.
19. H. Grote. Beam–beam effects in the LHC. In *Proceedings of the Workshop on Beam–Beam Effects in Large Hadron Colliders*, pages 59–62, Geneva, Switzerland, 12–17 Apr. 1999. CERN. (CERN Report CERN-SL-99-039 AP).
20. Y. Shimosaki and K. Takayama, Beam–Beam Effects in Superbunch Collision: Weak–Strong Model, Snowmass 2001, M401 (unpublished).
21. Y. Shimosaki. Beam–Beam Effects in the Inclined Super-Bunch Crossing. In *Proceedings of the International Workshop on Recent Progress in Induction Accelerators*, pages 126–130, Tsukuba, Japan, 29–31 Oct. 2003. KEK.
22. W. Herr and J. Miles. Optimizing the LHC Interaction Region to Obtain the Highest Possible Luminosity. In *Proceedings of the 1996 European Particle Accelerator Conference*, pages 424–426, Sitges, Spain, 10–14 June 1996.
23. W. Chao. *Physics of Collective Beam Instabilities in High Energy Accelerators*, Wiley, New York, NY, 1993.
24. T. Toyama and K. Takayama. Collective Instability of a Super-Bunch. In *Proceedings of the International Workshop on Recent Progress in Induction Accelerators*, pages 148–151, Tsukuba, Japan, 29–31 Oct. 2003. KEK.
25. Y. Shimosaki, T. Toyama, and K. Takayama. Head–Tail Instability of a Super-bunch. In *Proceedings of 33rd ICFA Advanced Beam Dynamics Workshop on High Intensity and High Brightness Hadron Beams, AIP Conference Proceedings No. 773*, pages 304–306, Bensheim, Germany, 18–22 Oct. 2005. GSI.
26. G. Rumolo. Intensity Limitations by Combined and/or (Un)Conventional Impedance Sources. In *Proceedings of HHH-2004: First CARE-HHH-APD Workshop on Beam Dynamics in Future Hadron Colliders and Rapidly Cycling High-Intensity Synchrotrons, CERN-2005-006*, pages 249–259, Geneva, Switzerland, 8–10 Nov. 2005. CERN.

UNCORRECTED PROOF

27. R. Macek. Overview of New Developments on the PSR Instability. In K. Hackay and R. Macek, editors, *Proceedings of Workshop on Two-Stream Instabilities in Accelerators and Storage Rings*, Santa Fe, NM, 16–18 Feb. 2000. ANL and LANL.
28. J. Wei. Synchrotrons and Accumulators for High-Intensity Proton Beams. *Rev. Mod. Phys.*, 75:1383, 2003.
29. J. Jimenetz, G. Arduini, P. Collier, G. Ferioli, B. Henrist, N. Hilleret, L. Jensen, K. Weiss, and F. Zimmermann. Electron Cloud with LHC-Type Beams in the SPS: A Review of Three Years of Measurements. In *Proceedings of ECLOUD 02, Geneva, CERN-2002-001*, pages 17–28, Geneva, Switzerland, 15–18 Apr. 2002. CERN.
30. V. Danilov, A. Aleksandrov, J. Galambos, D. Jeon, J. Holmes, and D. Olsen. Multipacting on the Trailing Edge of Proton Beam Bunches in the PSR and SNS. In *Proceedings of Workshop on Instabilities of High-Intensity Hadron Beams in Rings, AIP Conference Proceedings No. 496*, pages 315–320, New York, NY, 28 June–1 July 1999. Brookhaven National Laboratory.
31. A. Piwinski. Intrabeam Scattering. In *Proceedings of the 9th International Conference on High Energy Accelerators*, pages 405–409, Stanford, CA, 2–7 May 1974. SLAC.
32. J. Bjorken and S. Mtingwa. Intrabeam Scattering. *Part. Accel.*, 13:115–143, 1983.
33. A. Piwinski. CAS CERN Accelerator School Advanced Accelerator Physics. Number CERN-Report 87-03, pages 402–415, 1987.
34. D. Neuffer and S. Peggs. Beam-Beam Tune Shifts and Spreads in the SSC (Superconducting Super Collider): Head On, Long Range, and Pacman Conditions. Technical Report SSC Report SSC-63, SSC, 1986.
35. E. Lawrence and M. Livingston. The Production of High Speed Protons Without the Use of High Voltages. *Phys. Rev.*, 38:834, 1931.
36. M. White, M. Isaila, K. Prelec, and H. Allen. Acceleration of Nitrogen Ions to 7.4 Gev in the Princeton Particle Accelerator. *Science*, 174:1121–1123, 1971.
37. J. Alonso, R. Avery, T. Elioff, R. Force, H. Grunder, H. Lancaster, E. Lofgren, J. Meneghetti, F. Selph, R. Stevenson, and R. Yourd. Acceleration of Uranium at the Bevalac. *Science*, 217:1135–1137, 1982.
38. Y. Hirao, H. Ogawa, S. Yamada, Y. Sato, T. Yamada, K. Sato, A. Itano, M. Kanazawa, K. Noda, K. Kawachi, M. Endo, T. Kanai, T. Kohno, M. Sudou, S. Minohara, A. Kitagawa, F. Soga, E. Takada, S. Watanabe, K. Endo, M. Kumada, and S. Matsumoto. Heavy ion synchrotron for medical use HIMAC project at NIRS-Japan. *Nucl. Phys. A*, 538:541–550, 1992.
39. P. Spiller. Challenges and Progress in the Fair Accelerator Project. In *Proceedings of the 2005 Particle Accelerator Conference*, pages 294–298, Knoxville, TN, 16–20 May 2005.
40. M. Odera, Y. Chiba, T. Tonuma, M. Hemmi, Y. Miyazawa, T. Inoue, K. Kambara, M. Kase, T. Kubo, and F. Yoshida. Variable Frequency Heavy-ion Linac, RILAC:I. Design, Construction and Operation of Its Accelerating Structure. *Nucl. Inst. Meth. A*, 227:187–195, 1984.
41. A. Ruggiero. RF Acceleration with Harmonic Number Jump. *Phys. Rev. Special Topics – Accelerators and Beams*, 9:100101–100105, 2006.
42. K. Takayama, Y. Arakida, T. Iwashita, Y. Shimosaki, T. Dixit, and K. Torikai. All-Ion Accelerators: An Injector-Free Synchrotron. *J. Appl. Phys.*, 101:063304–063307, 2007.
43. K. Takayama, K. Torikai, Y. Shimosaki, and Y. Arakida, Patent No. 3896420, PCT/JP2006/308502(2006).
44. A. Weidinger. Ion Tracks – A New Route to Nanotechnology. *Europhys. News*, 35:152–155, 2004.
45. U. Glasmacher, M. Lang, H. Keppler, F. Langenhorst, R. Neumann, D. Schardt, C. Trautmann, and G. Wagner. Phase Transitions in Solids Stimulated by Simultaneous Exposure to High Pressure and Relativistic Heavy Ions. *Phys. Rev. Lett.*, 96:195701–195704, 2006.
46. National Task Force on High Energy Density Physics. Frontiers for Discovery in High Energy Density Physics. Technical Report ??, Office of Science and Technology Policy, National Science and Technology Council Interagency Working Group on the Physics of the Universe, 2004. AQ2
47. T. Dixit, T. Iwashita, and K. Takayama. Induction Acceleration Scenario from an Extremely Low Energy in the KEK All-Ion Accelerator. *Nucl. Inst. Meth. A*, 602:326–336, 2009.

UNCORRECTED PROOF

48. T. Dixit, T. Iwashita, Y. Arakida, and K. Takayama. Digital Acceleration Scheme of the KEK All-Ion Accelerator. In *Proceedings of the 2008 European Particle Accelerator Conference*, pages 2797–2799, Genova, Italy, 23–27 June 2008.
49. T. Kikuchi, S. Kawata, and K. Takayama. Half-Mini Beta Optics with a Bunch Rotation for Warm Dense Matter Science Facility in KEK. In *Proceedings of the 2007 Particle Accelerator Conference*, pages 1541–1543, Albuquerque, 25–29 June 2007.
50. K. Takayama, T. Adachi, E. Nakamura, and H. Someya. Beam Dynamical Issues of the KEK All-Ion Accelerator. In *Proceedings of the 2008 European Particle Accelerator Conference*, pages 3227–3229, Genova, Italy, 23–27 June 2008.
51. S. Kondrashev, T. Kaneue, M. Okamura, and K. Sakakibara. Features of Ion Generation Using Nd-Glass Laser. *J. Appl. Phys.*, 100:103301–103308, 2006.
52. Y. Oguri, J. Hasegawa, M. Ogawa, K. Horioka, and K. Takayama. Beam-Plasma Interaction Experiments at PLNR and Possible Applications of Induction Synchrotrons. In *Proceedings of the International Workshop on Recent Progress in Induction Accelerators*, pages 139–145, Tsukuba, Japan, 7–10 Mar. 2006. KEK.
53. P. G. Akishin, A. V. Butenko, A. D. Kovalenko, and V. A. Mikhaylov. Field Study of the 4 T Superconducting Magnet for Rapid Cycling Heavy Ion Synchrotrons. In *Proceedings of the 2004 European Particle Accelerator Conference*, pages 1390–1392, Lucerne, Switzerland, 5–9 July 2004.
54. K. Takayama, applied for PATENT Nov. 2009.

UNCORRECTED PROOF

Chapter-12

Query No.	Query
AQ1	We have changed citation Fig. 12.14 as Fig 12.13 as per caption. Please check and confirm.
AQ2	Please provide Report number.

UNCORRECTED PROOF

Index

A

Accelerating gradient, 78
Acceleration
  barrier bucket, 257
  time varying, 89
Acceleration gradient, 75, 91
  low, 95
Accelerator classification, 2
Accelerator modules, 2
Adder, *see* Inductive adder
Adiabatic damping, 293
Advanced test accelerator, *see* ATA
AGS, 317
AIA, 316, 318, 319, 322, 324–327
AIRIX, 18, 19, 167, 168
Alfvén current, 134
All ion accelerator, *see* AIA
Alloy
  2605SC, 82
  2705M, 82
  2714, 82
  losses, 84
All-Russian Scientific and Research Institute of Experimental Physics, *see* VNIEF
Amorphous, 75, 79, 94
  alloy, 79
  annealed, 81
  permeability, 57
Anisotropy, 81
~~Applications, 165~~
~~As-cast, 79, 80, 82, 85, 94~~
Aspect ratio, 75
Astron, 8–10, 13, 15, 17, 42, 78, 87, 88, 90, 91, 97, 166
  controlled fusion concept, 8
  injector, 8–10, 15
  upgrade, 8–10, 17
ATA, 10, 12, 14, 17, 47, 61, 77, 87–90, 92, 94, 97, 98, 109, 110, 120, 160, 165, 166, 168, 172–175

B

B3–M/PEM, 19
Bar-domain model, 267
Barrier
  bucket, 255, 275
  bucket manipulation, 258
  induction step, 279
  voltage, 254
BBU, 9, 25, 32, 88, 95, 98, 107, 111, 119, 142, 144, 149, 151–155, 157–160, 174, 177
  long-pulse, 149, 151
  nonlinear focusing suppression, 155
  phase mix damping, 157
B-clock signal, 276
Beam-beam effect
  parasitic, 291
Beam-beam force, 300
Beam-beam interaction, 291, 301
Beam-beam limit, 292
Beam breakup, 305
Beam breakup instability, *see* BBU
Beam loading, 274
Beam propagation in air, 12
Beam screen, 311
Betatron, 3, 7, 14
Betatron equation, 323
Betatron wavelength, 155, 157
Betatron wavenumber, 135
Bevatron, 316
B–H relationship, 32, 90
Bias circuit, 59
Birx, 13, 88
Bjorken, 314
Blumlein, 11, 12, 15, 46, 47, 60, 93, 168
  coaxial, 47

UNCORRECTED PROOF

K. Takayama, R.J. Briggs (eds.), *Induction Accelerators*, Particle Acceleration and Detection, DOI 10.1007/978-3-642-13917-8,
© Springer-Verlag Berlin Heidelberg 2011

liquid dielectric, 47
Bohm criterion, 186, 190
Bunched beam, 314
Bunching factor, 258
Bunch spacing, 292

C
Capacitance
core-gap, 106
CARM, 175
Cathode, 169
M-type, 175
photocathode, 120
velvet, 120, 154
CBA, 292
Cell
aspect ratio, 91
configuration, 89
design, 87
impedance, 88
inductance, 88
interaction, 90
long-pulse, 91, 94
Cell configuration, 89
Cell efficiency, 93
Centre d'Etudes Scien. et Tecniques d'Aquitaine, Le Barp, France, *see* CESTA
CERN PS, 311
CESTA, 19
Chao, 307
Characteristic impedance, 40, 41, 43, 46
Child-Langmuir current, 240
Child-Langmuir flow, 186
Christofilos, 8, 9
Chromaticity, 307
Circuit parasitics, 52
Circuit schematic
induction unit, 30
CLIA, 17, 42
Closing switch, 60
Cluster ion, 327
Coasting beam, 314
Coercive field, 81
Coercive force, 75, 79
Coherent instability, 256, 291
CO_2 laser, 174
Collective accelerators, 165, 166
Collider
proton-proton, 291
Colliding beam accelerator, *see* CBA
Collision geometry, 304
Compensation, 34
load, 88
Compensation network, 87, 88, 90, 93, 97
Constant voltage, 92
Core
distribution of electrical stress, 34
impedance, 33, 88
impedance collapse, 33
laminated, 34
laminations, 78
magnetization, 89
packing factor, 57
saturation, 93
segmentation, 96
volt-second product, 33, 57, 65, 88
Coreless induction accelerator, 3, 15
Corkscrew, 119, 136, 138, 139, 141
Coupled cavity linac, 2
Crossing angle, 297
Crystallization, 79
Curie point, 77
Cyclotron, 2, 316
Cyclotron wavenumber, 127, 137, 138

D
DARHT, 120
DARHT–I, 12, 17, 18, 47, 110, 111, 154, 167, 168, 170
DARHT–II, 13, 17, 46, 80, 82, 83, 85, 87, 88, 90–92, 94, 97–99, 103–105, 107, 110–112, 117, 152, 157, 167, 168, 170
DC–DC converter, 269
Dielectric constant, 35
Dielectric wall accelerator, 181
Digital signal processor, 276
Dimensional resonance, 76
Diode transient, 193
Directed energy weapons, 12, 13, 165, 166
Dmitriev, 326
Dragon, 167
DRAGON–I, 18, 19
Drift compression, 219
Drift tube linac, 2, 317, 318
Droop, 90, 93, 262
DTL, *see* Drift tube linac
Dual axis radiographic hydrodynamic testing, *see* DARHT
Dubna, Russia, *see* JINP
DWA, *see* Dielectric wall accelerator

E
Ear fields, 204
EBIS, 326
ECRIS, 326
Eddy current, 76, 79, 223
Efficiency, 77

UNCORRECTED PROOF

Electro-excitation, 319
Electron capture, 325
Electron-cloud effect, 311
Electron-proton instability, 291, 311
Electron ring accelerator, *see* ERA
Electron ring collective ion acceleration, 11, 15
Electron stripping, 325
Electrostatic accelerator, 3, 317
ELF wiggler, 172, 173, 176
Embritttled alloys, 80
Energy conservation law, 314
Energy density loss, 77, 81
Energy deposition, 319
Energy loss, 81
Equation of state, 319
Equivalent circuit model, 88, 89, 264
ERA, 10–12, 15, 17, 47, 75, 87, 166
  injector, 10, 11, 166
Erwin Marx, 48
ESS, 243, 244
ETA, 10, 12, 17, 47, 61, 166, 168, 172, 173
ETA–II, 14, 16, 17, 36, 42, 87–89, 92, 95, 98, 110, 112, 117–122, 139–141, 168, 175
  induction cell, 36
  injector, 121
  MAG-I-D modulator, 13
ETIGO–III, 19
European spallation source, *see* ESS
Experimental test accelerator, *see* ETA

F

Fast X-ray, *see* FXR
Feedback system
  ΔR, 279
FEL, 12–14, 17, 113, 165, 166, 171–176, 178, 179
FEL–KEK, 19
Ferrimagnetic, *see* Magnetic material
Ferrite, *see* Magnetic material
  PE11B, 93
Ferrite dampers, 98
Ferromagnetic, *see* Magnetic material, 75, 94
Ferromagnetic material, 78
Field annealed, 79, 80
Filamentation
  process, 281
Final focus, 217
Finemet, *see* Magnetic material
Flash radiography, *see* Radiography
Flash x-ray radiography, 165, 167–171
Flux, 76
  remanent, 81
Flux density, 75
Flux equalizing, 96, 97
Flux swing, 33, 78, 88
FNAL, 257
Focusing system, 25
Footprint, 303
Fourier expansion, 42, 44
Free electron laser, *see* FEL
Fundamental frequency, 77
Fusion, 8
FXR, 10, 12, 17, 47, 110, 167, 168

G

Gap capacitance, 29, 30, 88
Gas reservoir, 61
Gate
  control system, 280
Gate drive circuit, 55, 56, 58, 70
g-factor, 200, 201
Godfrey, 112
Gradient, *see* Accleration gradient
Ground-Referenced switch, 46
GSI, 317
Guillemin, 42

H

Hadron collider
  conventional, 292
  super-bunch, 283, 291
Hamiltonian, 252
Hard-tube pulser, 39
Harmonic acceleration, 318
HBTS, 16, 17, 42
Head-tail instability, 305
  strong, 311
  weak, 311
Heat-load curve, 312
Heavy ion fusion, *see* HIF
HEDP, 185, 215, 235
HIF, 13–15, 185, 215, 230, 244
  modular solenoid driver, 220, 230
  multi-beam linac driver, 220, 228
  recirculator driver, 220, 232
  robust point design, 220
  target, 216
High energy density physics, *see* HEDP
High repetition-rate induction, 13
Historical perspectives, 6
Hitachi Metals Ltd., 84
Hohlraum, 216
Humphries, 2
Hybrid crossing, 302
Hybrid synchrotron, 279, 287
Hysteresis, 77

UNCORRECTED PROOF

I
I–3000, 18
IBS, *see* Intra-beam scattering
ICF, 216
IFE, 219
IGBT, 55, 64, 70–72
ILE, 19
ILL, 243
Image displacement instability, 26
Impedance
  cable, 90, 91
  narrow-band, 262
  nonlinear, 89, 92
  pulse generator, 88
  series, 93
  source, 90
  temporally decreasing, 92
Inclined crossing, 304
Inductance
  leakage, 53, 54, 57
  loop, 57
  saturated, 67
  stray, 53, 58
  unsaturated, 67
Induction accelerating cell, 263
  short pulse, 76
Induction accelerator module, 23
Induction cell, 23, 25, 54, 57, 263
  Astron, 89
  circuit, 89
  DARHT–II, 89
  impedance, 268
  inductance, 268
  inductive adder, 54
  resistance, 268
  voltage fall time, 31
  voltage rise time, 31, 32
Induction cell design, 87
  cell configurations, 87
  core segmentation, 95
  flux equalizing, 95
  high voltage, 97
  leakage, 97
  long-pulse, 91
  reset, 97
  short-pulse, 92
~~Induction cell, inductive adder, 57~~
Induction sector cyclotron, 327
Induction synchrotron, 249, 250, 279
Inductive adder, 53–59, 69
  burst mode, 53, 54
  capacitor bank, 58
  circuit topology, 53
  component layout, 55, 58
  diode clipper circuit, 57
  gate drive circuit, 55, 56
  IGBT, 55
  leakage inductance, 54, 56
  loop inductance, 58
  magnetizing current, 56, 57
  modulator design, 55
  module, 53, 54, 59
  MOSFET, 55
  output polarity, 54
  reset/bias, 53
  reset/bias circuit, 59
  snubber capacitor, 56
  solid-state switch, 55, 58
  stray loop inductance, 56
  topology, 55
  transformer, 54, 57
  transformer design, 57
  transient protection, 56
  transient suppression, 58
  trigger timing, 58
  voltage transient, 56
Inductive voltage adder, 3, 16, 169
Inertial confinement fusion, *see* ICF
Inertial fusion energy, *see* IFE
Injector, 25
  electron, *see* Electron injector
  ion, *see* Ion injector
Institute at Pontfaverger–Moronvilliers, France, *see* B3–M/PEM
Institute for laser engineering, *see* ILE
Institute for theoretical and experimental physics, *see* ITEP
Institute of fluid physics, China, 19
Insulated gate bipolar transistor, *see* IGBT
Insulation
  Inter-laminar, 80, 99
Insulator
  angled, 98
  high gradient, 98
  interface, 88, 97
Inter-laminar insulation, 80, 99
Interaction point, 297
Intercepting storage rings, *see* ISR
Interface, 97
Intra-beam scattering, *see* Scattering
Inverse laplace transform, 265
Ion implantation, 319
Ion injector, 185, 197
  ~~child-langmuir~~ flow, 186
  drifting plasma, 199, 200
  emittance, 188

UNCORRECTED PROOF

geometry, 186
hot-plate diode, 197, 198
multi-beamlet, 198, 199
pierce electrode, 188, 191
transient, 193, 194
Ion source, 185, 194
EBIS, 196
ECR, 196
gas discharge plasma, 195
hot-plate, 194, 197, 198
laser, 197
negative ion, 197
plasma, 190
vacuum arc, 196
ISABELLE, 291
Isolation inductor, 59
ISR, 291, 292
ITEP, 18
IVA, *see* Inductive voltage adder

J
JAERI, 19
Japan Atomic Energy Research Institute, *see* JAERI
JINP, 18
JLA, 19
Joint Institute for Nuclear Research, *see* JINP
J–PARC, 243
Junction temperature, 270

K
KEK, 19
PS, 261
KEK proton synchrotron, *see* KEK PS
KEK PS, 273, 275, 276, 281
KEK ps, 268
Kishiro, 250
k-value, 324

L
LAIS, 327
Laminated core, 34, 78
effective radial dielectric constant, 103
electrical stress distribution, 99
Laplace transform, 265
Large hadron collider, *see* LHC
Larmor wavenumber, 129
Laser guiding, 155, 157
Lawrence, 316
Lawrence Berkeley Laboratory, *see* LBNL
Lawrence Berkeley National Laboratory, *see* LBNL
Lawrence Livermore National Laboratory, *see* LLNL
LAX–1, 19
LBL, *see* LBNL, 9
LBNL, 9
Leakage inductance, 53, 54
pulse transformer, 53
LELIA, 19
LEUK, 18
LHC, 287, 291, 292, 305, 312, 313, 317
LIA, 18
LIA–2, 18
LIA–30, 15, 17
LIA–30/250, 16
LIA–3000, 15
LIAXF, 19
Line-type induction accelerator, 3, 15
Liouville theorem, 253
LIU–10, 18
LIU–10M, 18
LIU–30, 18
Livingston, 316
LLNL, 9
Longitudinal fluid model, 200
Longitudinal instability, 210
Longitudinal waves, 205
instability, 206
rarefaction waves, 202
Long-pulse cell, 87, 94
cross-section, 87
Long-pulse induction accelerator, 13
Long-pulse induction linac, 13
Luminosity, 291, 297
Lumped element, 40, 42
Lumped parameter network, 42
Lytkarino, Russia, *see* NIIP

M
Macro-particle model, 307
MAG-I-D modulator, 13, 14
Magnetic assist, 62, 68
Magnetic compression, 65
Magnetic compression circuit, 65–67
Magnetic core, 29
function, 88
torroidal, 67
Magnetic flux density, 66
Magnetic Fusion Energy, *see* MFE
Magnetic Material, 57, 65, 68, 75
Magnetic material
2605SC, 80, 92, 94
amorphous, 79, 93
amorphous metals, 57
As-cast, 79
dimensional resonance, 76

UNCORRECTED PROOF

energy density loss, 77
energy loss, 81
ferrimagnetic, 35, 65, 75
ferrite, 10, 11, 34, 35, 57, 75, 93, 94, 222
ferromagnetic, 34, 65, 75, 78
field annealed, 79
~~finemet~~, 84, 113, 267, 268
flux density, 66
magnetic flux swing, 66
magnetic switch, 66
manganese-zinc, 76
melt spinning, 79
metallic glass, 78
~~metglas~~, 79, 84, 92, 94, 99–102, 222, 223
nanocrystalline, 57, 78, 84, 85
nickel-zinc, 35, 76, 77
other, 83
packing factor, 57
PE11B, 77, 78, 82, 93–95, 113
permeability, 57, 65, 76
resistivity, 76
saturated, 65
spin resonance, 76
unsaturated, 65
~~vitroperm~~, 84
Magnetic modulator, 13
Magnetic switch, 42, 60, 65–69
bias, 68
core geometry, 67
design, 67
energy transfer, 66
gain, 67
hold-off time, 66
jitter, 68
magnetic flux density, 66
magnetic flux swing, 66
minimum volume, 68
reset, 68
saturated, 67
stage, 66
unsaturated, 67
winding geometry, 67
Magnetization current, 57
Magnetization loss, 81
Magnetization rate, 75, 79, 81
Magnetizing current, 29, 32, 34, 56–58, 82, 88, 90, 91, 93, 95, 99, 101
Manganese-zinc, *see* Magnetic material
Marx generator, 48–50, 60, 69
isolating elements, 49
load impedance, 49
solid-state, 50
spark gap, 49, 50
stray capacitance, 49
thyratron, 50
Maschke, 13
Massachusetts Institute of Technology, *see* MIT
Matching load, 263
Mathieu equation, 142, 143
MBE–4, 13, 17
McMillan, 249
Melt spinning, 79
Metal oxide semiconductor field effect transistor, *see* MOSFET
Metallic glass, 78, 79
Metglas, *see* Magnetic material
2605CO, 80
2605SC, 81
MFE, 244
Microtron, 14
Microwave instability, 262
Mini-beta focusing, 325
Mismatch, 283
MIT, 17
Modular solenoid driver, 220, 230
Modulator, 39–59, 65, 67, 68
~~blumlein~~, 40, 46
characteristic impedance, 40, 41, 43, 45, 46
hard-tube, 50, 51
hard-tube pulser, 39
impedance, 90
inductive adder, 51, 53–58
line-type, 39–42, 47, 48
load impedance, 41
magnetic, 65–68
~~mark generator, 49~~
~~marx~~ generator, 48–50
PFN, 39, 40, 42–48, 50
solid-state, 39, 50, 51
solid-state topology, 51
transformer coupled, 52
Modulator-solid-state, 52
Möller scattering, *see* Scattering
Momentum dispersion function, 280
Moscow Radio Technical Institute, *see* MRTI
MOSFET, 55, 56, 58, 69–72, 269, 271, 279
current sharing, 58
diode clipper circuit, 57
gate drive circuit, 58, 70
transient protection, 56
transient suppression, 58
transient voltage, 56
MRTI, 18, 84
Mtingwa, 314
MTX, 175, 176

UNCORRECTED PROOF

Multi-beam linac driver, 220, 228
Multipactoring, 311
  trailing-edge, 314
Multiple beam experiment, *see* MBE-4
Mycalex, 98
Mylar, 80, 99–101

N
Nanocrystalline, 78, 81, 85
National Bureau of Standards, *see* NBS
National bureau of standards, 13
Naval Reserach Laboratory, *see* NRL
NBS, 17
NBS prototype, 17
Negative lens effect, 188
Neutralized ballistic transport, 217
Neutrino oscillation
  experiment, 283
Nickel-zinc, *see* Magnetic material
NIIP, 18
NIRS, 317
NIST, *see* NBS
Nonlinear impedance, 89, 92
Nonlinear kinematic effect, 262
Nonlinear resonance, 301
Notch potential, 279
  shallow, 279
NPI, 18
NRL, 172
Nuclear Pysics Institute, *see* NPI

O
Okamura, 327
Osaka, Japan, *see* ILE
Oxides, 76

P
Packing factor, 57, 94, 101
Pacman effect, 315, 316
Palladin wiggler, 174, 175
Particle detector, 293
Permeability, 33, 57, 75, 76, 78, 79
  complex, 268
  relative, 76
Permittivity, 76
  effective, 76
PFL, *see* Pulse forming line
PFN, *see* Pulse forming network, 40, 42–47, 50, 60
  characteristic impedance, 43, 45, 46
  current fed, 40
  ~~fourier~~ Fourier expansion, 42
  ~~fourier~~ Fourier series expansion, 43
  load impedance, 46
  lumped element, 42, 48
  mutual inductance, 45
  network topologies, 44, 45
  series connected, 46
  stacked, 46
  tapered impedance, 46
  type E, 45
  voltage fed, 40
Phase-displacement acceleration, 291
Phase-jump, 261
Phase mix damping, 155, 157
Phase stability, 250
Phermex, 167
Physics International Company, *see* PI
PI, 17
Pierce electrode, 188, 191
PIVAR, 19
Piwinski, 314
Prepulse, 67
Princeton particle accelerator, 316
Proton driver, 283
PSI, 17
PSR, 311
Pulse
  constant voltage flat top, 87
  travel time, 90
Pulse density, 322
Pulsed power source, 30
Pulsed power system, 25
Pulse forming line, 31, 41, 42, 91, 93, 97
  Astron, 42
  characteristic impedance, 40
  load impedance, 41
Pulse forming network, 32, 90, 92
Pulse modulator, 263
Pulse rise-time, 43
Pulse Science Inc., *see* PSI
Pulse train
  bipolar, 43
Pulse transformer
  leakage inductance, 53
  step-up, 52
Pulse-shaper, 90, 91
Pulser
  characteristic impedance, 40
  line-type, 48
  transmission line, 41, 48
Putnam, 250

Q
Quantum fluctuation, 315

UNCORRECTED PROOF

R
Radio frequency quadrupole, *see* RFQ
Radio-frequency wave, 250
Radiography, 12, 13, 166
RADLAC, 17
RADLAC–I, 16, 18
RADLAC–II, 16, 18
Rarefaction wave, 204
Recirculator, 15, 17
Recirculator driver, 14, 219, 220, 232
Relativistic heavy ion collider, *see* RHIC
Relativistic two-beam accelerator, *see* RTA
~~Repetition rate, 92~~
Reset, 33, 53, 68, 97
    active, 97
    circuit, 59
    core, 97
    current, 59
Resistivity, 76, 78
Resonance, 76
Resonant acceleration, 250
Resonant accelerator, 317
Resonant transformer, 93
RF amplifier
    solid-state, 257
RF breakdown, 318
RF cavity
    wide-band, 257
RF linac, 2
RF synchrotron, 2, 249
RFQ, 2, 257
RHIC, 287, 291, 292, 305, 306, 317
Ribbon, 76
    insulated, 78
    metallic, 76
    thickness, 79
RK–TBA, *see* TBA, relativistic Klystron
Robust point design, 220
RTA, 17, 95

S
Sandia National Laboratory, *see* SNL
Sarov, Russia, *see* VNIEF
Saturate, 57
Saturation, 33, 81
Saturation wave model, 267
Saturation wave theory, 81
Scattering
    intra-beam, 291, 314, 315
    Möller, 326
SCR, *see* Thyristor
SDI, 173
Semiconductor device, 39
Separated-function, 249
Separatrix, 252
Series resonant circuit, 43
Series switch, 51
    voltage grading, 51
Series switch configuration, 51, 52
Short-pulse cell, 87
    cross-section, 87
Shunt impedance, 90
SI thyristor, 283
SiC-JFET, 283
Silicon carbide, 72
Silicon controlled rectifier, *see* SCR
SILUND, 18
SIS-18, 317
SIT, 72
SLAC, 144
SLIA, 15, 17
SNL, 18
SNOMAD–II, 14, 16, 17, 42
SNS, 243, 244
Snubber capacitor, 56
Solid-state device, 50, 53–56, 63, 64, 69–72
    IGBT, 64, 70–72
    MOSFET, 58, 69–72
    parallel operation, 55
    silicon carbide, 72
    SIT, 64, 72
    thyristors, 63, 64, 72
Solid-state switch, 50, 51, 53, 55, 57
    circuit parasitics, 52
    current sharing, 53
    gate drive circuit, 55
    inductive adder, 53–55
    load faults, 52
    MOSFET, 58
    series configuration, 51, 52
    stray inductance, 53
    transformer coupled, 52
    transient protection, 53
    trigger circuit, 51
Source
    electron, *see* Electron source
    Ion, *see* Ion source
Source impedance, 90
Space-charge force, 300
Space-charge limit, 258, 292, 325
Spallation, 185, 243
Spallation neutron source, *see* SNS
Spark gap, 12, 49, 50, 60, 61, 64
Spin resonance, 35, 76, 77
Spiral Line Induction Accelerator, *see* SLIA
SPS, 311

UNCORRECTED PROOF

SSC, 292, 315
Stacking barrier, 261
Standing waves, 76
Static induction thyristor, *see* SIT
STAUS, 18
Step-up pulse transformer, 52
STI, 64
Strategic defense initiative, *see* SDI
STRAUS–2, 18
Stray inductance, 53, 58
Stray loop inductance, 56
Strong focusing lattice, 323
Super-bunch, 255, 258, 260
    head and tail, 316
    train, 296
Superconducting magnet, 311
Superconducting super collider, *see* SSC
Surface resistance, 79
Switching circuit
    full-bridge, 264, 269
    half-bridge , 271
Switching device, 60
    closing switch, 60–65
    magnetic switch, 65
Switching transient, 56
Synchronous
    particle, 250, 251, 289
    phase, 250
Synchrotron
    oscillation, 250, 251
    rapid cycling, 257, 321
    slow cycling, 257, 321
Synchrotron frequency, 252, 256
Synchrotron radiation, 311
    damping, 315
Synchrotron radiation limit, 292

T

Takayama, 250
Target parameters, 239
TBA, 17, 176, 178
    FEL, 176
    kek fel, 178, 179
    relativistic klystron, 176–178
Tevatron, 287
Thyratron, 8, 10, 13, 42, 50, 60–65, 68, 91
    cathode depletion, 62
    fill gas, 62
    magnetic assist, 62
    recovery time, 62
Thyristor, 50, 60, 63–65, 68, 72
    gate turn-off, 64
Tokamak heating, 165, 175
Tomsk, Russia, *see* NPI
Toroid, 75, 76
Torroidal magnetic core, 67
Transformer
    1:1, 24, 53
    auto, 27, 32, 88
    leakage inductance, 57
    magnetization current, 57
    magnetizing current, 56–58
    one-to-one coupled, 88
    saturation, 57
    volt-second product, 53
Transformer coupled, 52
Transformer design, 57
Transient suppression circuit, 58
Transient voltage, 56, 90
Transition
    energy, 261
Transition crossing, 249
    focusing free, 262, 288
    quasi-adiabatic focusing-free, 288
Transmission cable, 263
Transmission line, 40
    ferrite loaded, 88
    lumped element, 88
    PFN, 40
    pulser, 40, 42
Transverse impedance, 107
    form factor, 109, 110
    interaction, 108
    measurement, 110
Trapped modes, 112
Tskuba, Japan, *see* KEK
Tune shift
    coherent, 301
    incoherent beam-beam, 291, 301
    incoherent betatron, 301
    Laslett, 259, 261, 325
Two-beam accelerator, *see* TBA

U

UHF absorber, 110
UMER, 15
University of Maryland Electron Ring, *see* UMER

V

Vacuumschmelze, 84
Van de Graaff accelerator, 3, 317
Veksler, 249
Very large hadron collider, *see* VLHC
Vitroperm, *see* Magnetic material
VLHC, 291–293, 296, 300, 304, 306
VNIEF, 18

UNCORRECTED PROOF

Volt-Seconds Product, *see* Core
Voltage transient, 53, 56

W
Wake field, 25, 307
Warm dense matter, *see* WDM, 325
WDM, 215, 235–238
Weak-strong model, 303
WKB solution, 308

Z
Zimmermann, 311

UNCORRECTED PROOF